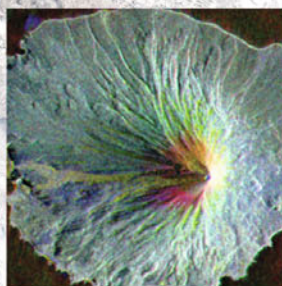


**Extra
Materials**
extras.springer.com

MONITORING VOLCANOES IN THE NORTH PACIFIC

Observations from Space



**Kenneson G. Dean
Jonathan Dehn**

 Springer

 PRAXIS

Springer Praxis Books

Geophysical Sciences

More information about this series at <http://www.springer.com/series/4110>

Kenneson Gene Dean
Jonathan Dehn
Editors

Monitoring Volcanoes in the North Pacific

Observations from Space

Editors

Kenneson Gene Dean
Geophysical Institute
University of Alaska Fairbank
Fairbanks, AK
USA

Jonathan Dehn
Geophysical Institute
University of Alaska Fairbanks
Fairbanks, AK
USA

Published in association with Praxis Publishing, Chichester, UK

Additional material to this book can be downloaded from <http://extras.springer.com>.

ISSN 1615-9748

Springer Praxis Books

ISBN 978-3-540-24125-6

ISBN 978-3-540-68750-4 (eBook)

DOI 10.1007/978-3-540-68750-4

Library of Congress Control Number: 2015958325

© Springer-Verlag Berlin Heidelberg 2015

This work is subject to copyright. All rights are reserved by the Publisher, whether the whole or part of the material is concerned, specifically the rights of translation, reprinting, reuse of illustrations, recitation, broadcasting, reproduction on microfilms or in any other physical way, and transmission or information storage and retrieval, electronic adaptation, computer software, or by similar or dissimilar methodology now known or hereafter developed.

The use of general descriptive names, registered names, trademarks, service marks, etc. in this publication does not imply, even in the absence of a specific statement, that such names are exempt from the relevant protective laws and regulations and therefore free for general use.

The publisher, the authors and the editors are safe to assume that the advice and information in this book are believed to be true and accurate at the date of publication. Neither the publisher nor the authors or the editors give a warranty, express or implied, with respect to the material contained herein or for any errors or omissions that may have been made.

Printed on acid-free paper

This Springer imprint is published by SpringerNature

The registered company is Springer-Verlag GmbH Berlin Heidelberg

Contents

Dedication to Kevin Engle	ix	2 Satellite systems and interactions	
List of contributors	xi	<i>Matthew Watson, Anupma Prakash</i>	27
Preface	xiii	2.1 Introduction and background	27
Acknowledgments	xvii	2.2 The electromagnetic spectrum	27
Extra Server Material contents	xix	2.2.1 <i>Overview, nomenclature, and mathematical framework</i>	27
List of figures	xxi	2.3 Introduction to remote sensing	32
List of tables	xxvii	2.3.1 <i>Inverse problems</i>	32
List of abbreviations and acronyms	xxix	2.3.2 <i>Modes of remote sensing</i>	32
		2.3.3 <i>Platforms and orbit types</i>	32
		2.3.4 <i>Spatial, temporal, and spectral resolution</i>	33
		2.4 Radiative transfer and atmospheric windows	35
		2.4.1 <i>Definitions</i>	35
		2.4.2 <i>Interaction of radiation with matter</i>	36
		2.4.3 <i>The radiative transfer equation</i>	39
		2.4.4 <i>The atmosphere</i>	40
		2.4.5 <i>Atmospheric windows</i>	40
		2.5 Atmospheric correction	42
		2.5.1 <i>Using empirical techniques and ground truthing</i>	43
		2.5.2 <i>Using radiative transfer models</i>	44
		2.6 The volcanological context	45
		2.6.1 <i>Overview of following chapters</i>	45
		2.6.2 <i>Past and current missions</i>	46
		2.6.3 <i>Future missions</i>	46
		2.7 Summary	46
		2.8 References	46
		3 Thermal anomalies at volcanoes	
		<i>Jonathan Dehn, Andrew J.L. Harris</i>	49
		3.1 Introduction	49
		3.2 Background	50
		3.3 The physics of thermal anomalies	52
1 Setting, history, and impact of volcanic eruptions in the North Pacific region			
<i>Kenneson Dean, Dave Rothery, John Eichelberger</i>	1		
1.1 Introduction	1		
1.2 Volcanological setting of the North Pacific	2		
1.2.1 <i>Active volcanoes of the North Pacific region</i>	3		
1.3 History of use of remote sensing for volcano studies and monitoring	9		
1.4 Impact of North Pacific eruptions on society	13		
1.5 The new perspective on monitoring volcanoes	19		
1.6 Conclusions	21		
1.7 References	21		

6.5	Conclusions	179	8.2	InSAR monitoring of deformation of Aleutian volcanoes: Case studies	244
6.6	Acknowledgments	181	8.2.1	<i>Introduction</i>	244
6.7	References	181	8.2.2	<i>Okmok Volcano</i>	244
			8.2.3	<i>Westdahl Volcano</i>	248
7	Volcanic ash transport and dispersion models		8.2.4	<i>Akutan Volcano</i>	251
	<i>Rorik Peterson, Peter Webley, Réal D'Amours, René Servranckx, Barbara Stunder, Ken Papp</i>	187	8.2.5	<i>Mt. Peulik Volcano</i>	254
			8.3	Concluding remarks	257
7.1	Introduction	187	8.4	Acknowledgments	258
7.2	Modeling techniques	189	8.5	References	258
7.3	Modeling the main physics processes in volcanic ash transport and dispersion	191	9	An overview of satellite monitoring of volcanoes	
7.3.1	<i>Advection</i>	191		<i>Kenneson G. Dean, Jeff Osinsky, Evgenii Gordeev, Sergey Senyukov, Alexander V. Rybin, Yury V. Karagusov, Nikolay S. Terentyev, Vyacheslav Guryanov</i>	261
7.3.2	<i>Diffusion</i>	192	9.1	Introduction	261
7.3.3	<i>Settling</i>	193	9.1.1	<i>Why use satellite data to monitor volcanoes</i>	261
7.3.4	<i>Aggregation</i>	193	9.1.2	<i>Types of satellite monitoring</i>	262
7.4	Initial conditions	194	9.2	Background	262
7.5	Wind fields	196	9.2.1	<i>History of satellite volcano monitoring in the North Pacific region</i>	264
7.6	Limitations and uncertainties	197	9.3	Satellite sensors and data	265
7.7	Example models	199	9.4	Acquisition of satellite data in Alaska and Russia	267
7.7.1	<i>CanERM</i>	199	9.4.1	<i>Data management and analysis: AVO Fairbanks</i>	268
7.7.2	<i>HYSPLIT</i>	200	9.4.2	<i>Data management and analysis: Petropavlovsk-Kamchatsky</i>	273
7.7.3	<i>Puff</i>	201	9.4.3	<i>Satellite data management and analysis: Yuzhno-Sakhalinsk</i>	274
7.8	Examples of VATD modeling derived ash cloud tracking	203	9.5	Data analysis for detection of volcanic activity	275
7.8.1	<i>Mount Spurr Volcano: September 1992</i>	204	9.5.1	<i>Thermal anomalies</i>	277
7.8.2	<i>Kliuchevskoi Volcano: October 1994</i>	209	9.5.2	<i>Automated detection of surface temperatures</i>	279
7.8.3	<i>Mt. Cleveland Volcano: February 2001</i>	213	9.5.3	<i>Volcanic clouds</i>	281
7.8.4	<i>Mt. Augustine Volcano: January 2006</i>	219	9.5.4	<i>Detection of opaque volcanic clouds</i>	283
7.8.5	<i>Summary of VATD modeling comparison</i>	223	9.5.5	<i>Detection of airborne ash</i>	283
7.9	Airborne ash probability distribution maps	225	9.5.6	<i>Estimating volcanic cloud height</i>	283
7.9.1	<i>Mt. Redoubt, Alaska</i>	226	9.5.7	<i>Predicting the movement of volcanic clouds</i>	287
7.9.2	<i>Bezymianny Volcano, Kamchatka</i>	226	9.5.8	<i>Use of dispersion models for hazard mitigation</i>	290
7.9.3	<i>North Pacific region</i>	227	9.6	High spatial resolution data for monitoring	291
7.10	Ramifications of airborne ash probability distribution maps	227	9.7	Reporting and communication	291
7.11	Future advances in VATD models	229	9.7.1	<i>Alaska Communication Model</i>	293
7.12	References	230	9.7.2	<i>AVO reporting and communication</i>	293
			9.7.3	<i>Communication and hazard assessments: National Weather Service/Anchorage VAAC</i>	294
8	Interferometric synthetic aperture radar (InSAR): A long-term monitoring tool				
	<i>Zhong Lu, Daniel Dzurisin, Charles Wicks Jr., John Power</i>	235			
8.1	Principles of interferometric synthetic aperture radar	235			
8.1.1	<i>Introduction</i>	235			
8.1.2	<i>Basics of interferometric SAR (InSAR)</i>	236			
8.1.3	<i>Interferogram interpretation and modeling</i>	242			
8.1.4	<i>Miscellaneous issues of InSAR processing</i>	243			

9.7.4	<i>Volcanic Ash Collaboration Tool (VACT)</i>	295		
9.8	The future of satellite monitoring of volcanic activity	296		
9.9	Conclusions	298		
9.10	Acknowledgments	298		
9.11	References	299		
10	Views of the Kamchatka–Kuriles–Aleutian volcanoes from manned spacecraft			
	<i>Peter J. Mouginis-Mark,</i>			
	<i>Thomas D. Jones</i>	303		
10.1	Introduction	303		
10.2	Mission constraints on photographic coverage	305		
10.3	Types of observations from the Shuttle and ISS	309		
10.4	Shuttle crew observations of the 1994 Kliuchevskoi eruption	314		
10.5	Shuttle radar observations of the KKA	317		
10.6	Summary	320		
10.7	Acknowledgments	321		
10.8	References	321		
11	The effects of volcanic eruptions observed in satellite images: Examples from outside the North Pacific region			
	<i>Robert Wright, Andrew J.L. Harris,</i>			
	<i>Ronnie Torres, Luke P. Flynn</i>	323		
11.1	Chapter synopsis	323		
11.2	Introduction: observing the effects of volcanic eruptions using satellite images	323		
11.3	Mt. Pinatubo, Philippines, 1991	334		
11.3.1	<i>The effects on and response of a landscape to a large ignimbrite-forming eruption</i>	334		
11.4	Mt. Etna, Italy, 1991–1993	339		
11.4.1	<i>Satellite observations of the emplacement and diversion of a large basaltic lava flow</i>	339		
11.5	Santiaguito, Guatemala, 1902–2000	342		
11.5.1	<i>Satellite observations of drainage basin impacts and hazards of prolonged effusive silicic eruption</i>	342		
11.6	Mt. Pinatubo, Philippines, 1991	345		
11.6.1	<i>Satellite observations of the atmospheric effects of a VEI-6 eruption</i>	345		
11.7	Conclusions	350		
11.8	Acknowledgments	351		
11.9	References	351		
Index				355

Dedication to Kevin Engle

Kevin Engle was a Senior Research Programmer for the University of Alaska Fairbanks (UAF) who specialized in image processing and ground receiving stations. During his studies of ocean circulation in Prince William Sound, he developed custom batch-processing tools for analysis of satellite data. Later, he became interested in the use of satellite data for environmental monitoring, including volcanoes. He became the lead engineer for installing and maintaining stations that received Advanced Very High Resolution Radiometer

(AVHRR) and Moderate Resolution Imaging Spectroradiometer (MODIS) data at UAF-GINA (Geographic Information Network of Alaska), and worked with the NOAA (National Oceanic and Atmospheric Administration) tracking station at Gilmore Creek to acquire additional satellite data from their antennas in real time. Kevin also developed radiometric and geometric correction algorithms that run as data are received at the stations. Many of the data-processing tools used at UAF-AVO (Alaska Volcano Observatory) were



Kevin Engle and the AVHRR Receiving Station, University of Alaska Fairbanks (photograph by Dayne Broderson).

initially developed by Kevin, including the automated thermal anomaly detection system (Okmok Algorithm) and the ash detection system. Kevin was an avid reader of technical articles and had the ability to comprehend and apply what he learned to the receiving stations or satellite data

analysis. The AVHRR receiving station was one of the oldest Sea Space systems that still functioned—the result of Kevin’s worldwide scrounging for parts. Kevin died suddenly at the age of 47.

Contributors

Gregg Bluth

Michigan Technological University
Houghton, Michigan, USA

Jeffrey M. Byrnes

Oklahoma State University
Stillwater, Oklahoma, USA

Simon Carn

Michigan Technological University
Houghton, Michigan, USA

Réal D'Amours

Canadian Meteorological Centre
Dorval, Québec, Canada

Kenneson G. Dean

Geophysical Institute
University of Alaska Fairbanks
Fairbanks, Alaska, USA

Jonathan Dehn

Geophysical Institute
University of Alaska Fairbanks
Fairbanks, Alaska, USA

Daniel Dzurisin

Cascades Volcano Observatory
United States Geological Survey
Vancouver, Washington, USA

John Eichelberger

University of Alaska Fairbanks
Fairbanks, Alaska, USA

Luke P. Flynn

Hawai'i Institute of Geophysics and Planetology
University of Hawai'i at Manoa
Honolulu, Hawai'i, USA

Evgenii Gordeev

Institute of Volcanology and Seismology
Far Eastern Branch of Russian Academy of Science
Petropavlovsk, Kamchatka, Russia

Vyacheslav B. Guryanov

Institute of Marine Geology and Geophysics
Yuzhno-Sakhalinsk, Russia

Andrew J.L. Harris

Université Blaise Pascal
Clermont Ferrand, France

Pavel Izbekov

Geophysical Institute
University of Alaska Fairbanks
Fairbanks, Alaska, USA

Thomas D. Jones

Florida Institute of Human and Machine Cognition
Pensacola, Florida, USA

Yury V. Karagusov

Institute of Marine Geology and Geophysics
Yuzhno-Sakhalinsk, Russia

Zhong Lu

Southern Methodist University
Dallas, Texas, USA

Peter J. Mouginis-Mark

Hawai'i Institute of Geophysics and Planetology
University of Hawai'i at Manoa
Honolulu, Hawai'i, USA

Jeffery Osiensky

National Weather Service
Anchorage, Alaska, USA

Ken Papp

Alaska Geological Materials Center
Alaska Division of Geological and
Geophysical Surveys
Eagle River, Alaska, USA

Rorik Peterson

Institute of Northern Engineering
University of Alaska Fairbanks
Fairbanks, Alaska, USA

John Power

Alaska Volcano Observatory
United States Geological Survey
Anchorage, Alaska, USA

Anupma Prakash

Geophysical Institute
University of Alaska Fairbanks
Fairbanks, Alaska, USA

Fred Prata

Norwegian Institute for Air Research
Oslo, Norway

Michael S. Ramsey

University of Pittsburgh
Pittsburgh, Pennsylvania, USA

Dave Rothery

The Open University
Milton Keynes, United Kingdom

Alexander V. Rybin

Institute of Marine Geology and Geophysics,
Yuzhno-Sakhalinsk, Russia

Sergey Senyukov

Institute of Volcanology and Seismology
Far Eastern Branch of Russian Academy of Science
Petropavlovsk, Kamchatka, Russia

René Servranckx

Canadian Meteorological Centre
Dorval, Québec, Canada

Barbara Stunder

National Oceanic and Atmospheric Administration
Camp Springs, Maryland, USA

Nikolay S. Terentyev

Institute of Marine Geology and Geophysics
Yuzhno-Sakhalinsk, Russia

Ronnie Torres

Philippine Institute of Volcanology and Seismology
Quezon City, Philippines

Matthew Watson

University of Bristol
Bristol, United Kingdom

Peter Webley

Geophysical Institute
University of Alaska Fairbanks
Fairbanks, Alaska, USA

Cynthia Werner

Cascades Volcano Observatory
United States Geological Survey
Vancouver, Washington, USA

Rick L. Wessels

Volcano Hazards Program
United States Geological Survey
Reston, Virginia, USA

Charles Wicks Jr.

Earthquake and Volcano Hazards Program
United States Geological Survey
Menlo Park, California, USA

Robert Wright

Hawai'i Institute of Geophysics and Planetology
University of Hawai'i at Manoa
Honolulu, Hawai'i, USA

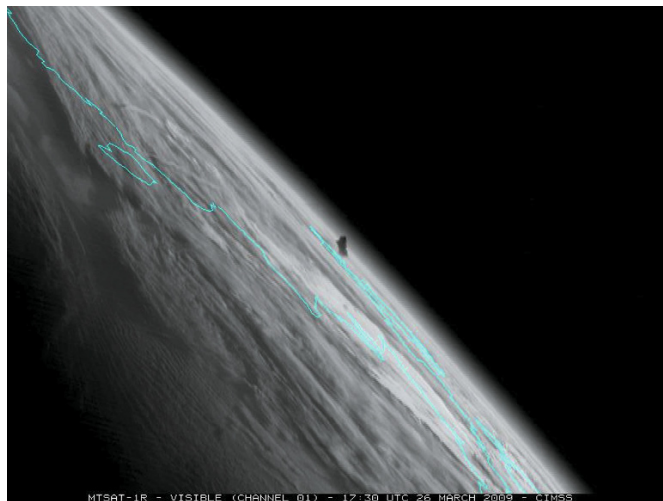
Preface

Prior to satellites and other spaceborne sensors, volcanoes in the North Pacific were not on the mental map of most volcanologists. They were far away and shrouded in clouds. We couldn't see them. There were the almost mythological eruptions of Katmai in 1912 on the American side and Bezymianny in 1956 and Tolbachik in 1975–1976 on the Russian side; few had a detailed understanding of what was happening in this part of the world.

Satellites changed this. Some of the change is specific to the region and other aspects apply to volcanism worldwide. The scale of this region was never really seen and certainly never adequately mapped before there were satellites. Also, as is the case with the volcanoes of Venus, much of the area is shrouded in clouds. Seeing through the persistent cloud cover, radar satellites permitted development of digital elevation models and the first-



Jonathan Dehn and Kenneson Dean in the Volcano Monitoring Room where satellite data are analyzed at the University of Alaska Geophysical Institute. Ken and Jon are members of the Science Team at the Alaska Volcano Observatory, University of Alaska Fairbanks (photograph by Debbie Dean).



A view of Earth from MTSAT at a height of 3,800 km (geostationary orbit). A plume (center) from the eruption of Redoubt Volcano, 2009 can be seen extending well into the atmosphere. Image is from the U.S. National Weather Service, processed by the Cooperative Institute for Meteorological Satellite Studies at the University of Wisconsin Madison.

order interpretation of major events, such as caldera formation and edifice collapse.

Likewise, and this applies globally, the true extent of great eruptions was never seen before there was satellite remote sensing. They are simply too big to see: eruption columns rising quickly to 30 km altitude and then spreading laterally hundreds of kilometers before fully coupling with wind patterns. Nor was it known that increased heat flux can also be observed from space at many volcanic vents prior to explosive eruptions, and often are precursor signals to impending activity. This new perspective has stimulated advances in understanding plume dynamics, ash and gas dispersal, and lava flow. Along with this have come several new kinds of measurements: spatial changes in surface temperature relating to eruptions in the infrared, the ash and SO₂ content of volcanic clouds in the infrared and ultraviolet, the movement and impact of these clouds, and spatially continuous surface deformation in the microwave through InSAR techniques. Remote-sensing, seismic, and deformation data together provide a more holistic picture of subsurface, surface, and airborne volcanic processes and the monitoring of activity.

Scientists at the University of Alaska's Geophysical Institute developed a reception, analysis, and information distribution system using satellite data as part of the newly formed Alaska Volcano Observatory in December 1989. At that time,

Redoubt Volcano was erupting. There were a lot of hurdles to clear to make satellite-based analyses practical. Few thought these data would be that useful, at least in an eruption response setting. Problems included: timely data access; timely coverage; timely processing of data; detection, location, and measurements; distribution of data products; and data volume (see Chapter 7 for a more detailed description of satellite data reception and analysis in a response setting).

Scientists at UAF had been experimenting with real-time access to Landsat and AVHRR data for the analysis of active surface processes for several years in the 1980s and had developed a working relationship with the NOAA Tracking Station near Fairbanks (Dean *et al.*, 1990; George *et al.*, 1992, Chapter 1). Therefore, data access did not appear to be a problem for the AVO project (early 1989–1990). However, timely access to data became a problem in that it took hours (initially) to acquire and process the data. This was critical because the speed of ash clouds can be over 45 km/h, while jet aircraft fly at 900 km/h. Therefore, by the time AVO detected and located an ash cloud it had moved hundreds of kilometers. The time required for data access is now down to minutes after the data are received by the station.

Fortunately, satellites provide timely coverage of volcanoes. Polar-orbiting satellite data were received almost hourly based on tracking several



Antennas for receiving satellite data on the roof of the Geophysical Institute, University of Alaska Fairbanks (photograph by Debbie Dean).

satellites and overlapping coverage. However, there is a period of several hours after midnight when no data were received. In the mid-1990s, data from geostationary satellites were added to the data pool thereby increasing observations to 15 minutes (at best) 24 hours per day. However, the spatial resolution of geostationary data is several kilometers per pixel compared with one kilometer at nadir for polar-orbiting data.

Another problem was detection; it was relatively simple to detect cold opaque plumes, but difficult to detect ash clouds at the time. Prata (1989, Chapter 5) had developed ash detection techniques but these were not incorporated into AVO until after 1993. Also, it was not easy to identify the location of any detected feature because the images had no geographic reference, and there were no measurable scales to determine the hazardous nature of the cloud or plume. After analysis, the high-quality images were sent as quickly as possible to the rest of AVO, by fax. Faxed images were low quality and often difficult to interpret.

A final problem was data volume. We were tracking two satellites, each with morning and evening passes, each with three orbits over Alaska daily. A swath of data was about 140 MB in volume; this required 1,680 MB of storage per day. Personal computer disk storage was typically less than 50 MB during this period.

Most of these issues were resolved over the next few years as technology advanced and UAF purchased an AVHRR receiving station in 1993. During the past 20 years our understanding of plumes, ash clouds, and thermal anomalies in terms of detection and their significance has improved significantly.

After more than 20 years of collecting data, the UAF system has developed one of the largest archives of satellite data devoted to volcanic eruptions. As part of the AVO project, students, staff, and faculty participated in the analysis and warning of hazardous conditions. To educate students on the use of these data for volcanic eruptions, a course was developed: "Remote Sensing of Volcanic Eruptions". The large satellite data archive, high frequency of volcanic activity in the North Pacific region, participation in the AVO project, and the course became the impetus for this book.

John Eichelberger
University of Alaska Fairbanks,
formerly Volcano Hazards Program Coordinator,
U. S. Geologic Survey, Reston, VA, U.S.A.

Kenneson Dean
Geophysical Institute,
University of Alaska Fairbanks,
Fairbanks, Alaska, U.S.A.

Acknowledgments

We are indebted to our many co-authors for their efforts in this time-consuming endeavor. The authors are listed at the beginning of each of their respective chapters. The intent of this book is to present the most recent satellite-based techniques to monitor and analyze an eruption, and provide warnings of potentially hazardous conditions as quickly as possible. To accomplish this, we tried to select authors who had hands-on experience with satellite data, eruptions, and associated warnings, those who were on the leading edge of technical development and those who have studied eruptions in the North Pacific region. Because many of our authors are involved in eruption response, time available for writing had to be squeezed between events over a period of time. Also, we would like to thank Pavel Izbekov for his help in describing the satellite systems and data in the Kamchatka Peninsula and Kurile Islands, Russia.

Credit for the completion of this book goes to the patience and dedication of all the authors, and that of the publisher, Springer-Praxis, including Clive Horwood of Praxis, Philippe Blondel of the University of Bath (U.K.), and Neil Shuttlewood of Originator Publishing Services (U.K.).

We are greatly indebted to the Geophysical Institute (Roger Smith, Director), to

NASA (John Labrecque), and the USGS-AVO, who provided funding and/or support for the book project. We wish to thank Dr. John Davies—a former state seismologist, one of the founding organizers of AVO, the first Coordinating Scientist of AVO—who first suggested this book in 1990, after the Redoubt eruption. It took a number of years and many eruptions since the beginning of AVO before the idea solidified. We also wish to thank Dr. John Eichelberger and Dr. Steve McNutt, second and third Coordinating Scientists for UAF-GI AVO, for their continued support and encouragement. Thanks to Shari George and Kevin Engle for helping organize and compile the earliest stages of the book.

Thanks also to our esteemed reviewers for their time and effort in detailed and frank reviews. The reviewers are Charles Connor, Jeff Freymueller, Arlin Kruegar, Christina Neal, Mike Pavolonis, Dave Pieri, Mike Ramsey, Gareth Reese, Dave Rothery, Scott Rowland, Steve Self, Andrew Tupper, Geoff Wadge, Cynthia Werner (who later became a co-author), Rick Wessels, and all of the anonymous reviewers.

Satellite data are very graphic. We encouraged the use of many figures to graphically portray the detection and analysis of volcanic plumes and clouds, and to

show spatial relationships. We are thankful to have a very talented pool of graphic artists and computer programmers at the Geophysical Institute who turned our basic figures and concepts into visual training tools. The artists include Deborah Coccia-Manning, Melissa Guy, Andy Cummins, Lynda McGilvary, and Vicki Daniels. The animations and graphics used in the *extra materials* were compiled and generated by Paul Delys.

We are very appreciative of the many students who proofed, wrote sections, made figures, and compiled and searched for data. These include Kenneth Papp, Matthew Patrick, Andrea Steffke, Courtney Kearney, Steve Smith, Joe Lovick, Peter Rinkleff, Abigail Gleason, Rachel Puchrik, Shelly Worely, Taryn Lopez, Annie Worden, Angie Ekstrand, and Lucas Moxey. We apologize if we missed anyone.

Computers are a critical element for analysis in modern science and they do not function without the help of system managers, programmers, and data entry. In that regard we wish to thank Joanne Groves and

Andrea Steffke for compiling a database of satellite observations of eruptions, Kevin Engle for his data analysis skills, Lovro Valcic who kept us organized and designed the layout of the *extra materials*, and Scott Macfarlane, Ray Skoog and Lovro Valcic, who maintained all our systems and data transfers. We thank the same people for computer system maintenance, creative programming, establishment of ftp sites and their diligence to locate, compile, and process the satellite data, generate the *extra materials*, and prevent desktop computers from catastrophic failures and data loss.

Finally, I (Ken Dean) wish to thank my wife Debbie and daughters Kristin Papp and Holly Dean for their support and toleration of my moods, worries, and concerns over the years required to complete this book. Also, a special thanks to Dr. Lara Horstmann, UAF Assistant Professor in Marine Biology, for her patience, support, and encouragement for the duration. Prof. J. Dehn would like to thank his loving wife Chris, without her this work would not have been finished.

Extra Server Material

“*extras.springer.com*” provides images, animations and the text is included. This material is also available online at <http://volcanoatlas.images.alaska.edu>. Access to the secure areas of the website requires a printed copy of this book to answer security questions. The animations take several formats, such as animated graphics interchange format (GIF) files or short videos, as currently accepted formats. Most video players will play these. All of the files can be accessed directly by opening the file “index.htm”.

This book involved a growing archive of satellite images sorted by the type of volcanic process, then the type of imagery, and finally by the volcano and event. Each of these archive entries follows a standard format showing the image, giving metadata about the image so a user can download it from the Internet, a description of the activity and how the image was useful before, during and after the eruption. An example of an atlas entry is given in the *extra materials*, the atlas itself will grow online at the website.

Figures

1.1	A map of volcanic areas of the North Pacific region	2	1.14	Eruptions in the North Pacific region	15
1.2	Generalized tectonics and faults or lineaments, and their relationship to volcanoes in the North Pacific region	3	1.15	Ash clouds and their proximity to air traffic routes in the North Pacific region	18
1.3	Map of the northern Kurile Islands, Russia, showing volcanoes that were active post 1990, others active pre 1990, and a town impacted by these eruptions	4	1.16	Examples where ash-producing eruptions in the North Pacific have impacted the United States and Canada since 1975	19
1.4	Map of Kamchatka Peninsula, Russia showing volcanoes that were active post 1990 and some that were active pre 1990	5	1.17	Time sequential composite of Puff dispersion model runs of eruptions in the North Pacific region	20
1.5	Map of Cook Inlet and Alaska Peninsula, Alaska showing volcanoes that were active post 1990 and some that were active pre 1990	6	2.1	Propagation of plane-polarized electromagnetic waves	30
1.6	Map of volcanoes in the Aleutian Islands that erupted post 1990 and the towns of Adak and Dutch Harbor	7	2.2	The relationship between frequency and wavelength	30
1.7	Map of Cascade Range, showing Mt. St. Helens that erupted post 1990 and a few volcanoes from pre 1990	8	2.3	The electromagnetic spectrum	30
1.8	Cerro Galán Caldera, Argentina	9	2.4	Planck (blackbody) curves for objects of different temperature	31
1.9	Landsat MSS image of a lava flow and plume at Sierra Negra Volcano, Galapagos Islands, 1979	10	2.5	Geostationary and low Earth orbits	33
1.10	First high spatial resolution satellite image of a hot dome	11	2.6	Instantaneous field of view and spatial resolution	34
1.11	Thermal anomalies detected on short-wave infrared satellite images on Landsat composites	12	2.7	Energy–matter interaction	35
1.12	Satellite observations of the dome at Lascar Volcano, Chile	12	2.8	Beer–Bouguer–Lambert Law	36
1.13	One of the first observations of sulfur dioxide emitted by a volcano	13	2.9	The relationship between energy and transition type	37
			2.10	Plot of Q_{EXT} vs. $X(2\pi r\lambda)$ showing Rayleigh, Mie, and non-selective scattering regimes for an andesite ash particle	38
			2.11	Three-slab radiative transfer model	39
			2.12	(a) Vertical structure of the atmosphere with respect to temperature	40
			2.12	(b) Vertical structure of the atmosphere with respect to pressure	41
			2.13	Atmospheric windows	42
			3.1	Examples of thermal anomalies shown in the MIR band 3 of AVHRR	51
			3.2	A NIMBUS II HRIR image of the North	

	Atlantic showing Iceland and activity at Surtsey Volcano	52			
3.3	Size of an AVHRR pixel with viewing angle	56	5.2	Photographs of a proximal cloud of Redoubt Volcano, April 21, 1990 and distal cloud from Spurr Volcano, September 9, 1992 from the NASA Space Shuttle	103
3.4	Pixel brightness temperature as a function of percent pixel coverage of hot and background temperatures	57	5.3	Increase in cloud aspect ratio over time as it drifts across North America	103
3.5	Energy emitted by a blackbody at different temperatures following the Planck function	59	5.4	Total, scattering, and absorption transmissions for basalt, andesite, rhyolite, and quartz as a function of wavelength	104
3.6	Examples of a thermal anomaly created by an active a'ā lava flow in several wavelengths of AVHRR and MODIS data	60	5.5	A conceptual model and corresponding example of satellite images of a plume	105
3.7	Time series of an eruption of a lava flow at Okmok Volcano	63	5.6	Spurr Volcano, September 17, 1992 AVHRR satellite data	108
3.8	A thermal anomaly of a lava dome at Bezymianny Volcano	64	5.7	The basic thermal structure of the atmosphere is defined by temperature gradients as a function of altitude which reverse at three different levels	109
3.9	Time series of lava dome growth at Bezymianny Volcano in 1998	65	5.8	Relationship between the structure of the atmosphere, plume heights, and air traffic	110
3.10	Kizimen Volcano in Kamchatka	66	5.9	The relative effect of wind and eruption vigor shown as conceptual models	111
3.11	A lahar warms pixels in the Drift River, Alaska after dome collapse at Redoubt Volcano	67	5.10	The Mt. Spurr Volcano eruption on August 19, 1992 recorded on AVHRR satellite images showing the early stages of the transition of this plume from opaque to semi-transparent	113
3.12	Time series plot of strombolian activity at Karymsky Volcano	68	5.11	Augustine volcanic eruption in January 2006	114
3.13	A strombolian eruption at Stromboli Volcano in MODIS data on April 13, 2006 and Mt. Cleveland, Alaska on May 11, 2011 in AVHRR data	68	5.12	Height estimates of the Redoubt Volcano plume on January 8, 1990 recorded on TIR AVHRR data 13 minutes after the start of the eruption	115
3.14	Katmai Lake in Alaska	69	5.13	Estimation of plume height using the trajectory method for an eruption of Kliuchevskoi Volcano, September 30, 1994	116
3.15	The basic flow chart for the Okmok II algorithm	71	5.14	A composite of AVHRR satellite images using TIR and BTD data and the conceptual model shows an early stage of a volcanic cloud at Cleveland Volcano, February 19, 2001	116
4.1	Changes detected by the Alaska Volcano Observatory using high spatial resolution data at the snow-covered summit of Mt. Spurr Volcano	82	5.15	A GOES satellite image recorded in the visible shows a plume from the eruption of Redoubt Volcano, March 24, 2009	117
4.2	ASTER VNIR/SWIR analysis of the 1986 pyroclastic flow deposits of Augustine Volcano	84	5.16	Example of plume height estimates from ground-based radar and temperatures at Augustine Volcano, January 11, 2006	118
4.3	Thermal characteristics of the 1975–1976 Tolbachik lava flows and scoria cones, Kamchatka	86	5.17	A wide range of plume heights were measured for the eruption of Augustine Volcano on January 17, 2006	119
4.4	Landsat 7 Enhanced Thematic Mapper Plus data of the eruption of Bezymianny volcano	87	5.18	An oblique photograph taken on January 14, 2006 shows a profile view of the plume recorded on a satellite image	122
4.5	TIR analysis of Black Peak Caldera, AK	88	5.19	A conceptual model of a plume showing a gas-rich region capping the ash-rich region	123
4.6	SAR data highlighting some of the volcanoes of the Kamchatka Peninsula	90	5.20	Daytime MODIS scenes showing anomalous clouds	124
4.7	Detailed radar image of Tolbachik Volcano activity from 1975 to 1976	91			
4.8	Data fusion case study for Westdahl Volcano, Unimak Island, Alaska	94			
5.1	Natural-color MODIS satellite images of plumes from Mt. Etna, Sicily, July 22, 2001 and Kilauea, Hawaii, August 7, 2008 disrupting air traffic at airports in Catania and Kona, respectively	102			

<p>5.21 Idealized radiative transfer model for calculating radiation propagation through an absorbing atmosphere and scattering layer of cloud particles. 125</p> <p>5.22 Variation of $rT = T_1 - T_2$ with T_1 for three values of the parameter β 126</p> <p>5.23 Temperature difference distributions without water vapor corrections and with corrections 128</p> <p>5.24 MODIS ash mass concentrations for an eruption of Karthala Volcano, November 2005. 129</p> <p>5.25 Sequence of GOES geosynchronous images of the eruption from Kasatochi Volcano, 2008. 135</p> <p>5.26 True-color MODIS image of the ash plume from Kasatochi Volcano on August 8, 2008 136</p> <p>5.27 MODIS ash mass retrieval for an eruption from Kasatochi. 137</p> <p>5.28 Ash mass concentrations for an eruption cloud from the eruption of Ruang, September 25, 2002. 138</p> <p>5.29 AIRS spectrum shown as a transect along a constant pixel number 139</p> <p>5.30 Spectral ratio of the top-of-atmosphere brightness temperature for a single AIRS pixel and for six different scenes 139</p> <p>6.1 Radiative forcings due to four different mechanisms 148</p> <p>6.2 Atmospheric transmission spectrum from 0.2 to 1.2 μm. 152</p> <p>6.3 TOMS SO_2 total column for the September 1992 Mt. Spurr eruption 157</p> <p>6.4 GOME SO_2 retrievals 158</p> <p>6.5 Global annual SO_2 emissions derived from SCIAMACHY monthly averages for 20 months starting in September 2004 and ending in April 2006 159</p> <p>6.6 OMI SO_2 retrievals for NOPAC volcanoes 161</p> <p>6.7 Radiative transfer calculations for the 7.3 and 8.6 μm bands of SO_2 163</p> <p>6.8 Absorbance vs. wavenumber for three SO_2 absorption bands. 165</p> <p>6.9 Results of MAP_SO2 analysis of ASTER data acquired over Augustine Volcano on January 25, 2006. 166</p> <p>6.10 TOVS/HIRS retrievals of upper troposphere/lower stratosphere SO_2 total column for the September 1992 Mt. Spurr eruption 167</p> <p>6.11 TOVS/HIRS SO_2 retrievals for Augustine, 1996. 168</p> <p>6.12 Cumulative TOVS/HIRS SO_2 for the largest eruptions sending SO_2 into the UTLS in the period 1980–2000. 169</p>	<p>6.13 MODIS 7.3 μm SO_2 retrievals for the Cleveland eruption of February 19–20, 2001. 170</p> <p>6.14 AIRS SO_2 total column retrievals for an eruption of Kliuchevskoi, March 24, 2005 172</p> <p>6.15 Concentrations for an industrial SO_2 plume derived from a ground-based thermal imaging camera system 175</p> <p>6.16 SO_2 flux derived from sequential thermal images from a ground-based thermal imaging camera. 175</p> <p>6.17 Thermal camera SO_2 retrieval for a plume from Mt. Etna, Sicily. 176</p> <p>6.18 Vertical optical depth for various atmospheric gases calculated for 55°N at 10:00 local time 177</p> <p>6.19 UV camera SO_2 retrieval and fluxes for Villarica Volcano 179</p> <p>7.1 Primary processes of advection, diffusion, and sedimentation involved in particle dispersion. 191</p> <p>7.2 Cloud and plume growth rates 192</p> <p>7.3 Schematic of an idealized initial ash cloud 195</p> <p>7.4 Major North Pacific air traffic routes, towns/airports, and volcanoes that have erupted in the past 100 years 197</p> <p>7.5 AVHRR split-window detection 205</p> <p>7.6 CanERM model airborne ash concentration predictions from Mt. Spurr's September 1992 eruption 206</p> <p>7.7 HYSPLIT model trajectories from Mt. Spurr. 207</p> <p>7.8 Puff model predictions for volcanic ash from Mt. Spurr. 208</p> <p>7.9 AVHRR split-window detection at 06:40 UTC on October 1, 1994 from the September/October 1994 eruption. 210</p> <p>7.10 CanERM model airborne ash concentration predictions from the Kliuchevskoi September/October 1994 eruption. 211</p> <p>7.11 HYSPLIT model trajectories from Kliuchevskoi beginning September 30, 1994 . . 212</p> <p>7.12 Puff model predictions for volcanic ash colored by altitude and airborne concentration from Kliuchevskoi Volcano from the September/October 1994 eruption . . . 213</p> <p>7.13 (a) Volcanic ash cloud from AVHRR at 16:55 UTC on February 19, 2001. (b) Time-sequential composite of GOES split-window data. (c) CanERM time-sequential model forecast 214</p> <p>7.14 CanERM model airborne ash concentration predictions from the Mt. Cleveland February 2001 eruption 215</p> <p>7.15 HYSPLIT model trajectories from Mt. Cleveland beginning February 19, 2001 . . 216</p>
---	--

7.16	HYSPLIT model-simulated airborne ash relative concentration from the Mt. Cleveland February 2001 eruption	216	8.9	Deformation interferograms of Okmok Volcano for the periods before and during the February–April 1997 eruption	246
7.17	Puff model predictions for volcanic ash (colored by altitude) from Mt. Cleveland.	218	8.10	Deformation interferograms of Okmok Volcano for six annual periods after the February–April 1997 eruption	247
7.18	Puff model prediction of volcanic ash cloud position at 14:00 UTC on February 22, 2001 from February 19 event at Mt. Cleveland	219	8.11	Estimated magma supply for the shallow reservoir as a function of time from 1992 to 2003.	247
7.19	AVHRR split-window detection of volcanic ash clouds during January 13, 2006 from the ongoing eruption of Mt. Augustine Volcano	220	8.12	Shaded relief image of Westdahl Volcano (a) Pre-1991 eruption interferogram of Westdahl Volcano during September 7 and November 21, 1991. (b) Interferogram showing the deflation of Westdahl Volcano during the first 20 hours of the 1991 eruption	249
7.20	CanERM model airborne ash concentration predictions from the Mt. Augustine January 2006 eruption	221	8.14	Observed interferograms showing progressive inflation for various time windows during 1991–2000	249
7.21	HYSPLIT model trajectories of 48-hour duration from Mt. Augustine beginning January 13, 2006	222	8.15	A model for the eruption cycle at Westdahl Volcano	250
7.22	HYSPLIT model-simulated airborne ash relative concentration from the Mt. Augustine January 2006 eruption	222	8.16	A Landsat-7 color-composite image draped over a DEM of Akutan Island	252
7.23	Puff model predictions of the three events at 22:20 UTC on January 13, 2006 for the Mt. Augustine Volcano	223	8.17	Deformation of Akutan Island during the 1996 seismic swarm	253
7.24	Multiple eruptions of six volcanic clouds using Puff for the Mt. Augustine events on January 13–14, 2006	224	8.18	Observed and modeled interferograms associated with the March 1996 seismic swarm of Akutan Island	253
7.25	Airborne ash probability distribution maps for Mt. Redoubt Volcano	226	8.19	(a) A shaded relief image of Mt. Peulik Volcano. (b–f) Topography-removed interferograms of Mt. Peulik Volcano that span several different time intervals	255
7.26	Airborne ash probability distribution maps for Bezymianny Volcano	227	8.20	A perspective view of topography near Mt. Peulik Volcano	256
7.27	Airborne ash probability distribution maps for 22 active volcanoes.	228	8.21	Topography-removed interferograms of Shishaldin Volcano that span several different time intervals.	257
8.1	Two SLC SAR images acquired on October 4, 1995 by the ERS-1 satellite and on October 9, 1997 by the ERS-2 satellite over the Mount Peulik Volcano	237	9.1	Location diagram of the North Pacific region.	262
8.2	An interferogram is formed by differencing the phase values of two SAR images that have been co-registered	238	9.2	The maximum areal extent of AVHRR and MODIS data received by stations used for volcano monitoring in the North Pacific region.	268
8.3	InSAR imaging geometry.	239	9.3	A swath of AVHRR data covers 2,000 × 5,000 km and has a typical file size of 100 MB	269
8.4	(a, b) An interferogram simulated to represent contributions from the topography and the orbital geometry in Figure 8.2. (c, d) Topography-removed interferogram by subtracting the interferograms	240	9.4	Nine sectors have been established containing multiple volcanoes	270
8.5	A georeferenced interferogram overlaid on a shaded relief image produced from a DEM.	241	9.5	A full swath of geometrically and radiometrically uncorrected data is received by AVO and then corrected and subsectioned to facilitate monitoring	270
8.6	Deformation interferograms for Mt. Peulik Volcano	242	9.6	Flowchart of AVO data processing and elapsed time from satellite data reception to investigation by analysts	271
8.7	Map of Alaska and the five volcanoes presented in this chapter	245			
8.8	Shaded relief image of Okmok Volcano, with outlines marking the extents of lava flows from eruptions in 1945, 1958, and 1997.	245			

<p>9.7 Example of the AVO database volcano-monitoring system 272</p> <p>9.8 A report is automatically generated by the database 273</p> <p>9.9 Examples of MODIS images distributed by the Yuzhno-Sakhalinsk Station 275</p> <p>9.10 Thermal anomalies and plumes are critical features detected on satellite data 276</p> <p>9.11 Thermal anomalies from the dome at Bezymianny Volcano on the Kamchatka Peninsula detected on MODIS data, October 25, 2000 277</p> <p>9.12 Example of validation and characterization of thermal anomalies detected on satellite data used for daily monitoring of volcanoes 278</p> <p>9.13 Time temperature or albedo graphs of activity at volcanoes are used to monitor temperature as activity changes at a volcano 280</p> <p>9.14 MODIS satellite images of the eruption showing Mt. Cleveland, Alaska, February 19, 2001 of wavelengths commonly used to detect volcanic clouds 282</p> <p>9.15 MODIS split-window satellite images of the eruption of Mt. Cleveland, Alaska, February 19, 2001 284</p> <p>9.16 Opaque and translucent volcanic clouds at Augustine Volcano, January 13, 2006, seen on AVHRR data 285</p> <p>9.17 Determination of plume height using the cloud top temperature technique 286</p> <p>9.18 Determining the height of the volcanic cloud using satellite images and dispersion models 286</p> <p>9.19 Accuracy of dispersion models for the eruption of Mt. Cleveland Volcano, February 19, 2001 289</p> <p>9.20 Dispersion models have limited use for hazard mitigation for areas within approximately 100 km of a volcano 290</p> <p>9.21 Map showing the boundaries of Volcanic Ash Advisory Centers, Volcano Observatories, and Response Teams in the North Pacific region 292</p> <p>9.22 Examples of a SIGMET and a Volcanic Ash Advisory for the eruption of Cleveland Volcano on February 19, 2001 295</p> <p>9.23 Chronology describing the communication of warnings of the eruption of Mt. Cleveland, February 19, 2001 296</p> <p>9.24 Chart showing projected timelines of satellites used for operational volcano monitoring in the North Pacific region 297</p> <p>10.1 View of the Space Shuttle <i>Atlantis</i> from the ISS, showing the location of the windows used for orbital photography 305</p>	<p>10.2 Photo of the ISS taken by an astronaut aboard the Space Shuttle on April 17, 2002 306</p> <p>10.3 Astronaut Donald Pettit on ISS Crew 6 waits for another target of opportunity to use the Kodak electronic camera and its giant 800 mm lens 307</p> <p>10.4 Space Shuttle photograph STS047-77-34 of Unimak Island and vicinity, Alaska including six volcanoes: Westdahl, Fisher, Shishaldin, Isanotski, Round Top, and Frosty 307</p> <p>10.5 Mt. Cleveland, Chuginadak Island, Aleutian Islands, Alaska erupting on May 23, 2006 308</p> <p>10.6 The ash plume and pyroclastic flows from the June 12, 2009 eruption of Sarychev Peak in the Kurile Islands, Russia 308</p> <p>10.7 A faint gas plume is seen coming from 1,730 m high Mt. Cleveland on Chuginadak Island, Aleutian Islands, Alaska 309</p> <p>10.8 Outline of the 1997 lava flow on the floor of Okmok Caldera, Unimak Island, Aleutian Islands, Alaska 310</p> <p>10.9 Akutan Volcano, Aleutian Islands, Alaska last erupted in May 1992 when localized steam and ash emissions took place 310</p> <p>10.10 Alaid Volcano, Kurile Islands, Russia 311</p> <p>10.11 At an equivalent resolution of ~8 m/pixel, the best photographs from the ISS can serve as base images for mapping volcanoes such as Prevo Peak Volcano on Simushir Island, Kurile Islands, Russia 311</p> <p>10.12 Yunaska Volcano, Aleutian Islands, Alaska last erupted in 1937 312</p> <p>10.13 Oblique view looking north across Bezymianny, Kliuchevskoi, and in the distance Shiveluch Volcanoes 312</p> <p>10.14 The two major volcanoes shown here are Kronotsky, the stratovolcano casting the shadow, and Kransheninnikov 313</p> <p>10.15 High oblique view of Opala Volcano, Kamchatka Peninsula, Russia 313</p> <p>10.16 View of the early phase of the 1994 Kliuchevskoi eruption, Kamchatka Peninsula, Russia 314</p> <p>10.17 Image number STS68-214-43 taken at 00:56:04 GMT on October 1, 1994 with a 250 mm lens on a Hasselblad camera 315</p> <p>10.18 Four views of the ash plume from Kliuchevskoi Volcano 316</p> <p>10.19 Plot of the ground tracks of STS-68, showing the data acquisitions of the SIR-C/X-SAR radar 317</p>
--	---

<p>10.20 The radar image was acquired by SIR-C/X-SAR aboard the Space Shuttle <i>Endeavour</i> on its 25th orbit on October 1, 1994 of the north flank of Kliuchevskoi Volcano and the town of Klyuchi, Kamchatka.</p> <p>10.21 Example of a single acquisition from the SIR-C radar in October 1994 of the north central Kamchatka Peninsula, Russia . . .</p> <p>10.22 Two visualization methods using digital elevation data from the SRTM were combined to produce this image: shading and color-coding of topographic height of the Kamchatka Peninsula, Russia.</p> <p>10.23 Shaded relief version of Kunashir Island, in the southern Kurile Islands, Russia just northeast of Hokkaido, Japan</p> <p>10.24 Oblique view of Urataman Volcano and Prevo Peak on Simushir Island, Kurile Islands, Russia</p> <p>11.1 (Top) Landsat MSS standard false-color composite image of Mt. St. Helens, acquired on July 29, 1972. (Bottom) Landsat TM image of Mt. St. Helens, acquired on August 26, 1986</p> <p>11.2 (Left) Landsat TM image of Montserrat, Lesser Antilles, acquired on October 9, 1989. (Right) Terra ASTER image of Montserrat acquired on September 4, 2002</p> <p>11.3 (Top left) Landsat TM image of Lascar Volcano, Chile, acquired on October 27, 1989. (Top right) Landsat ETM+ image of Lascar, acquired on May 16, 1999. (Bottom) Close-up showing the form of the pyroclastic deposit to the southeast</p> <p>11.4 ASTER-simulated true-color image of Montagu, the largest island in the remote South Sandwich Island archipelago, acquired on December 7, 2003.</p> <p>11.5 Landsat TM simulated true-color image of Socompa Volcano, Chile</p> <p>11.6 Landsat ETM+ false-color composite of Casita Volcano, Nicaragua, acquired on November 15, 1999</p> <p>11.7 (Top) Landsat TM false-color composite images of Pacaya Volcano, Guatemala, acquired on January 19, 1990 (a), February 12, 1993 (b), and February 21, 1996 (c). (Bottom) Landsat TM false-color composite images of Kilauea Volcano, Hawaii which were acquired on January 19, 1990 (a), February 12, 1993 (b), and February 21, 1996</p>	<p>318</p> <p>319</p> <p>320</p> <p>320</p> <p>321</p> <p>325</p> <p>326</p> <p>327</p> <p>328</p> <p>329</p> <p>330</p> <p>331</p>	<p>11.8 (Top) Landsat ETM+ false-color composite image of Masaya Volcano, Nicaragua, acquired on March 25, 2001. (Bottom) Landsat TM false-color composite image of Poás Volcano, Costa Rica, acquired on February 6, 1986.</p> <p>11.9 MODIS image of an eruption at Ruang Volcano, acquired at 12:50 (local time) on September 25, 2002</p> <p>11.10 NIMBUS-7 TOMS image of the ash produced by the 1982 eruption of El Chichón, Mexico.</p> <p>11.11 SPOT XS images of Mt. Pinatubo, Philippines</p> <p>11.12 (Left to right, top to bottom) SPOT XS images acquired on April 4, 1988; December 18, 1991; December 11, 1994; February 12, 1996; and December 5, 1998 of the northwestern sector of Pinatubo Volcano</p> <p>11.13 The development and containment of lahars on Pinatubo's western flank</p> <p>11.14 Sequence of SPOT images showing the denudation of vegetation caused by the June 1991 eruption and the spatial patterns of subsequent vegetation recolonization.</p> <p>11.15 Time series of Landsat TM images showing the development of the 1991–1993 Mt. Etna lava flow</p> <p>11.16 Landsat TM false-color and simulated true-color composites of Santa María Volcano and the surrounding area</p> <p>11.17 Landsat TM false-color composite of Santa María Volcano and the surrounding area</p> <p>11.18 NDVI images showing temporal variations in river aggradation downslope from Santa María Volcano</p> <p>11.19 Landsat TM false-color composite of the Pacific coast of Guatemala, showing the distribution of lahars and lahar-dammed lakes that have been produced by the ongoing activity at Santiaguito</p> <p>11.20 GMS-4 visible wavelength images of the Pinatubo eruption cloud acquired at 13:41 (a), 14:41 (b), 15:41 (c), and 16:41 (d) on June 15, 1991</p> <p>11.21 NIMBUS-7 TOMS images of the SO₂ produced by the June 15, 1991 eruption of Pinatubo, Philippines.</p> <p>11.22 SAGE-II optical depth measurements made for a period spanning the June 1991 eruption of Pinatubo</p>	<p>332</p> <p>333</p> <p>333</p> <p>335</p> <p>336</p> <p>337</p> <p>338</p> <p>341</p> <p>344</p> <p>345</p> <p>346</p> <p>347</p> <p>348</p> <p>349</p> <p>350</p>
---	---	---	--

Tables

1.1	List of eruptions in the North Pacific region from 1970 to 2013 that produced ash clouds that exceeded 6 km in height.	14	5.7	Summary of ash detection algorithms and techniques used with satellite infrared and visible channel data	134
1.2	Examples of impacts caused by airborne ash from volcanic eruptions in the North Pacific region	17	6.1	Current best estimates of the major volcanic gas emission rates to the atmosphere	147
2.1	Nomenclature of symbols used in this chapter.	28	6.2	Satellite and terrestrial (ground-based and airborne) instruments capable of detecting and determining SO ₂ and other volcanic gases	155
2.2	Regions of the electromagnetic spectrum	31	7.1	Dispersion models often used in the NOPAC region for volcanic ash forecasting	199
2.3	Past and present missions used in the observation of volcanic emissions	46	7.2	Gridded wind fields used by the Puff model in the NOPAC region	203
3.1	Landmark works on thermal volcano remote sensing with the subject, the sensor, wavelengths used, and temporal resolution	53	7.3	VATD model source parameters for the four volcanic eruption cases	204
3.2	Common features to identify the likely volcanic source of a thermal anomaly	62	8.1	Spaceborne SAR sensors capable of deformation mapping	234
4.1	List of sensors and specifications used for the Westdahl lava flow case study.	93	9.1	Characteristics of the GOES imager, AVHRR and MTSAY MVIRI sensors used for daily monitoring.	266
5.1	The stages of volcanic cloud evolution based on observations of the Mt. Spurr eruption of 1992	106	9.2	Characteristics of the MODIS sensor used for daily monitoring in the North Pacific Region	267
5.2	Generalized examples of physical values of the atmosphere at the surface, tropopause, and mesopause based on a standard atmosphere	110	9.3	Examples of image products distributed by the DMNR Receiving Station in Yuzhno-Sakhalinsk	274
5.3	Examples of the variation in height estimates for the 2006 eruptions of Augustine Volcano	121	9.4	Selected satellite bands, band combinations, and custom images used for twice-daily monitoring at AVO	277
5.4	Details of past and current satellite instruments that can be used to detect ash and generate ash mass loading maps from infrared measurements.	129	9.5	The USGS Alert Notification System for Volcanic Activity.	293
5.5	Refractive indices for water, ice, and andesite.	132	10.1	Listing of Space Shuttle flights that had the opportunity to photograph the Kuriles, Kamchatka, and the Aleutians	304
5.6	Locations of the nine Volcanic Ash Advisory Centers, satellites used to generate ash products, and the principal dispersion model(s) utilized				

Abbreviations and acronyms

AAPD	Airborne Ash Probability Distribution	a.s.l.	above sea level
AAWU	Alaska Aviation Weather Unit	ASTER	Advanced Spaceborne Thermal Emission and Reflection Radiometer
ABI	Advanced Baseline Imager		
ADGGS	Alaska Division of Geological and Geophysical Surveys	ATHAM	Active Tracer High-resolution Atmospheric Model
AFCRL	Air Force Cambridge Research Laboratories	ATSR	Along Track Scanning Radiometer
AFWA	Air Force Weather Agency (US)	AVHRR	Advanced Very High Resolution Radiometer
AIRS	Atmospheric InfraRed Sounder		
AIRSAR	AIRborne Synthetic Aperture Radar	AVIRIS	Airborne Visible InfraRed Imaging Spectrometer
AKST	Alaska Standard Time	AVO	Alaska Volcano Observatory
ALI	Advanced Land Imager	BA	British Airways
ALOS	Advanced Land Observation Satellite	BADC	British Atmospheric Data Centre
AMC	Airport Meteorological Center (Russia)	BDRF	BiDirectional Reflection Function
AMF	Air Mass Factor	BT	Brightness Temperature
AMS	American Meteorological Society (US)	BTD	Brightness Temperature Difference
ARL	Air Resources Laboratory (NOAA, US)	BUV	Backscatter UltraViolet
ARTCC	Air Route Traffic Control Center (FAA, US)	C	Celsius or Centigrade
ASA	American Standards Association	CALIOP	Cloud–Aerosol Lidar with Orthogonal Polarization (satellite)
ASCENDS	Active Sensing of CO ₂ Emissions over Nights, Days, and Seasons	CALIPSO	Cloud–Aerosol Lidar and Infrared Pathfinder Satellite Observations (satellite)
ASE	Autonomous Sciencecraft Experiment	CanERM	Canadian Emergency Response Model
ASF	Alaska Satellite Facility	CCD	Charge Coupled Device
ASI	Agenzia Spaziale Italiana (Italian Space Agency)	cm	centimeter
		CMC	Canadian Meteorological Centre

COSPEC	CORrelation SPECTrometer	ft	flow terminus
CSA	Canadian Space Agency	FT-IR	Fourier Transform InfraRed
CVO	Cascades Volcano Observatory		(radiometer, spectrometer or interferometer)
CWSU	Center Weather Service Unit (US)	ftp	file transfer protocol
D-PAF	Deutsch (German) Processing and Archiving Facility	g	gram
DEM	Digital Elevation Model	GDAS	Global Data Assimilation System
dGPS	differential Global Positioning System	GENLIN	GENeral LINE by line radiative transfer model
DLR	Deutsche Luft und Raumfahrt (German Air and Space Agency)	GEO	Geosynchronous Earth Orbit
DMNR	DalInforGeoCenter of the Ministry of Natural Resources, Yuzhno-Sakhalinsk	GFS	Global Forecast System (US, NCEP)
DMSP	Defense Meteorological Satellite Program	GIF	Graphics Interchange Format
DOAS	Differential Optical Absorption Spectrometer	GINA	Geographic Information Network of Alaska
DOASIS	DOAS Intelligent System	GIS	Geographic Information System
DOD	Department Of Defense (US)	GLI	GLobal Imager
DOMSAT	DOMestic Communications SATellite	GMS	Geostationary Meteorological Satellite
DRE	Dense Rock Equivalent	GOES	Geostationary Operational Environmental Satellite
DSP	Defense Support Program	GOES-R	Geostationary Operational Environmental Satellite—R series
DU	Dobson Unit	GOME	Global Ozone Monitoring Experiment
DVD	Digital Video Disk	GPS	Global Positioning System
ECWMF	European Centre for Medium Range Weather Forecasts	GSD	Grain Size Distribution
EDAS	Eta Data Assimilation System	GSFC	Goddard Space Flight Center
EER	Environmental Emergency Response	GUI	Graphical User Interface
EM	ElectroMagnetic	GVP	Global Volcanism Program (US)
Envisat	Environmental satellite	Gyr	Gigayear (one billion years)
EO	Earth Observation (satellite)	HIRS	High-resolution Radiation Sounder
EOS	Earth Observing System	HITRAN	High TRANsmissivity Model
EROS	Earth Resoures Observation System	HRIR	High Resolution Infrared Radiometer
ERS	European Remote Sensing (satellite)	HRPT	High Resolution Picture Transmission
ERSDAC	Earth Remote Sensing Data Analysis Center (Japan)	HYSPLIT	HYbrid Single-Particle Lagrangian Integrated Trajectory (model)
ESA	European Space Agency	IASI	Infrared Atmospheric Sounding Interferometer
ESE	East South East	IAVW	International Airways Volcano Watch
ETM	Enhanced Thematic Mapper	ICAO	International Civil Aviation Organization
ETM+	Enhanced Thematic Mapper Plus	IFOV	Instantaneous Field Of View
FAA	Federal Aviation Administration (US)	InSAR	Interferometric Synthetic Aperture Radar
FL	Flight Level	IMGG	Institute of Marine Geology and Geophysics (Sakhalin, Russia)
FLIR	Forward Looking InfraRed	IR	InfraRed
FNL	FiNaL Analyses (NCEP initialization model)		
FOV	Field Of View		

IRAS	InfraRed Astronomical Satellite	MIVIS	Multispectral Infrared and Visible Imaging Spectrometer
ISS	International Space Station	MLS	Microwave Limb Sounder
JAROS	JAPanese Resource Observation System	mm	millimeter
JAXA	Japan Aerospace eXploration Agency	MM5	Fifth Generation Mesoscale Model
JCET	Joint Center for Earth Systems Technology	MOCAGE	MOdèle de Chimie Atmosphérique à Grande Echelle (Large Stepped Atmospheric Chemistry Model)
JERS	Japanese Earth Resources Satellite	MODIS	MODerate Resolution Imaging Spectroradiometer
JMA	Japan Meteorological Agency	MODTRAN	MODerate TRANsmissivity Model
JPEG	Joint Photographic Experts Group (image format)	MOPITT	Measurement Of Pollution In The Troposphere
JPL	Jet Propulsion Laboratory	mph	miles per hour
JPSS	Joint Polar Satellite System	MSG	Meteosat Second Generation
K	Kelvin	MSH	Mount St. Helens
KAT	Kamchatka–Aleutian Tectonic	MSS	MultiSpectral Scanner
KBGS	Kamchatka Branch of the Geophysical Survey	Mt	Mount
KCCM	Kamchatka Center of Communication and Monitoring	MTSAT	Multi-functional Transport SATellite
KKA	Kamchatka–Kuriles–Aleutian (Arc)	MVIRI	Meteosat Visible and InfraRed Imager
KLM	Koninklijke Luchtvaart Maatschappij (Royal Dutch Airlines)	MW	MicroWave
km	kilometer	μm	micrometer or micron
kT a ⁻¹	kilotons per annum	NAM	North American Mesoscale (model)
KVERT	Kamchatka Volcanic Eruption Response Team	NAME	Nuclear Accident Model
LANDSAT	LAND SATellite	NASA	National Aeronautic and Space Administration (US)
LASER	Light Amplification by Stimulated Emission of Radiation	NCAR	National Center for Atmospheric Research (US)
LEO	Low Earth Orbit	NCEP	National Centers for Environmental Prediction (US)
LI-COR	Lambda Instruments CORPORATION	NDVI	Normalized Difference Vegetation Index
LOWTRAN	LOW TRANsmissivity Model	NE	North East
m	meter	NESDIS	National Environmental Satellite Data and Information Services
MASTER	MODIS/ASTER airborne simulator	NEXRAD	NEXt generation RADar
MCF	Minimum Cost Flow (algorithm)	NGM	Nested Grid Model
METI	Ministry of Economy, Trade and Industry (Japan)	NIR	Near InfraRed
MetOP	Meteorological OPERational (satellite)	nm	nanometer
Mg	Megagram (10 ⁶ grams)	NNE	North North East
MIR	Mid InfraRed	NOAA	National Oceanic and Atmospheric Administration (US)
MIRAN	Miniature InfraRed ANalyzer	NOGAPS	Navy Operational Global Atmospheric Prediction System (US)
MISR	Multi-angle Imaging SpectroRadiometer	NOPAC	North PACific
MITI	Ministry of International Trade and Industry (Japan)		

NOTAM	NOtice To AirMen	SEVIRI	Spinning Enhanced Visible and InfraRed Imager
NPOESS	National Polar-orbiting Operational Environmental Satellite System (US)	SIGMET	SIGNificant METeorological (notice)
NPP	NPOESS Preparatory Project	SIR	Shuttle Imaging Radar
NRC	National Research Council (US)	SLC	Single Look Complex
NRL	Naval Research Laboratory (US)	SMS	Synchronous Meteorological Satellite
NSF	National Science Foundation (US)	SO ₂	Sulfur dioxide
NW	North West	SPOT	Système Pour l'Observation de la Terre
NWP	Numerical Weather Prediction	SRL	Space Radar Lab (US Shuttle)
NWS	National Weather Service (US)	SRTM	Shuttle Radar Topography Mission
OCO	Orbiting Carbon Observatory (satellite)	SSA	Single Scattering Approximation
OMI	Ozone Mapping Instrument	SSW	South South West
OMPS	Ozone Mapping and Profiler Suite	STP	Standard Temperature and Pressure
PBL	Planetary Boundary Layer	STS	Space Transportation System (US Shuttle)
PC	Personal Computer	SVERT	Sakhalin Volcanic Eruption Response Team
PCI	Principal Component Image	SWIR	ShortWave InfraRed
PF	Pyroclastic Flow	t	ton (metric)
Pg	Petagram (10 ¹⁵ grams)	TES	Thermal Emission Spectrometer
PIREP	Pilot REPort	TFR	Temporary Flight Restriction
PNG	Portable Network Graphics (image format)	Tg	Teragram (10 ¹² grams)
POES	Polar Operational Environmental Satellite	TIMS	Thermal Imaging Mapping Spectrometer
ppm	parts per million	TIR	Thermal InfraRed
RA	Reverse Absorption	TIROS	Television and InfraRed Operational Satellite
RADAR	RADio Distance And Ranging	TM	Thematic Mapper
Radarsat	Radar satellite	TMS	Thematic Mapper Simulator
RAT	Robust AVHRR Technique	TOMS	Total Ozone Mapping Spectrometer
RGB	Red Green Blue	TOPSAR	TOPographic Synthetic Aperture Radar
RSMC	Regional Specialized Meteorological Center	TOVS	TIROS Operational Vertical Sounder
RST	Robust Satellite Technique	TS	Threat Score
RT	Radiative Transfer	TVAP	Three-channel Volcanic Ash Product
RTE	Radiative Transfer Equation	UAF	University of Alaska Fairbanks
RUC	Rapid Update Cycle (model, NOAA)	UAF/GI	University of Alaska Fairbanks Geophysical Institute
s	second	UARS	Upper Atmosphere Research Satellite
SAGE	Stratospheric Aerosol and Gas Experiment	UMBC	University of Maryland Baltimore County
SAR	Synthetic Aperture Radar	UNIDATA	UNiversity DATA (model)
SARTA	Stand-alone AIRS Radiative Transfer Algorithm	U.S.	United States
SBUV	Solar Backscatter UltraViolet	USGS	United States Geological Survey
sc	scoria cone		
SCIAMACHY	SCanning Imaging Absorption SpectroMeter for Atmospheric CHartography		
SEAN	Scientific Event Alert Network		

UTC	Universal Time Code	VIS	VISible (spectrum)
UTLS	Upper Troposphere Lower Stratosphere	VISSR	Visible and Infrared Spin Scan Radiometer
UV	UltraViolet	VNIR	Visible to Near InfraRed
UVB	UltraViolet B	WFO	Weather Forecast Office
VAA	Volcanic Ash Advisory (notice)	WMO	World Meteorological Organization
VAAC	Volcanic Ash Advisory Center	WRF	Weather Research and Forecasting (model)
VACT	Volcanic Ash Collaboration Tool	WSR	Weather Surveillance Radar
VAST	Volcanic Anomaly SofTware	WVC	Water Vapor Correction
VATD	Volcanic Ash Transport and Dispersion (model)	ZOLD	Zeroth Order Logarithmic Distribution
VEI	Volcanic Explosivity Index		
VHRR	Very High Resolution Radiometer		

Setting, history, and impact of volcanic eruptions in the North Pacific region

Kenneson Dean, Dave Rothery, John Eichelberger

1.1 INTRODUCTION

The focus of this book is to highlight applications and analysis of data from satellite-borne instruments for monitoring and interpreting volcanic activity. In this introductory chapter, we abbreviate “data from satellite-borne instruments” to satellite data. The techniques and procedures are described in detail to demonstrate the utility of satellite data. Our region of primary interest is the North Pacific, where many of the techniques were developed or first applied in near-real time. For this region, both monitoring and emergency response applications have been pioneered at the Alaska Volcano Observatory (AVO).

The North Pacific region is defined as the area encompassing southern Alaska and the Aleutian Islands, the Kamchatka Peninsula, the Kurile Islands, and the Cascade Volcanoes in the north-western U.S. (Figure 1.1). Volcanoes in Alaska were the initial focus for satellite monitoring by AVO but it was quickly realized that ash from explosive eruptions on the Kamchatka Peninsula drifted east, impacting Alaska. A working relationship developed with Russian scientists at the Kamchatka Volcanic Eruption Response Team (KVERT) and the Sakhalin Volcanic Eruption Response Team (SVERT) to help aid tracking of Kamchatkan and Kurile Island eruptions using satellite data. Since the coverage of satellite data received by stations at the University of Alaska Fairbanks, Geophysical Institute, referred to as the satellite station mask, extends to the Cascade Volcanoes

(Washington and Oregon), similar protocols were developed with the Cascades Volcano Observatory (CVO) for monitoring Mt. St. Helens.

Some of the busiest air traffic routes in the world cross the region. Air transport is seriously impacted by eruptions, making it critical to monitor all volcanoes in the region. Volcanic ash has damaged aircraft, or destroyed jet engines, either during landing and takeoff or at high-altitude transport and has closed airports throughout the North Pacific. Just the threat of an encounter has forced aircraft to change routes, alter flight schedules, and led to the cancellation of flights (Casadevall, 1994b). In Alaska and Kamchatka, air transportation is the primary method of travel and of transport of food, clothing, medical supplies, and other commerce for many of the villages and cities. The region also represents a critical international flight corridor, with over 20,000 passengers and more than 12 million pounds of cargo transported through it daily (Miller and Casadevall, 2000).

The successful use of satellite data for volcano monitoring in the region is due in part to the geographic and geologic setting. First, the near-polar location means that satellite orbits converge resulting in significant overlapping swaths of data which translates into many views of the same target area every day. Second, there are over 150 active volcanoes in this region that can produce potentially explosive (vulcanian to plinian) eruptions resulting in volcanic clouds that threaten local, regional, and global transportation, and population centers. The spatial perspective of satellite images is ideal for

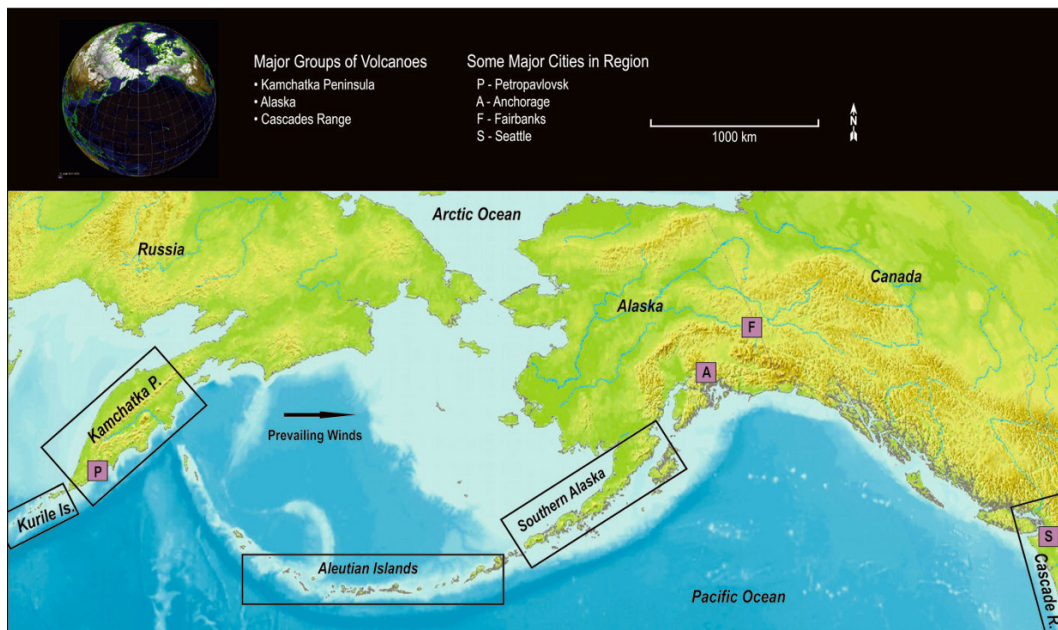


Figure 1.1. A map of volcanic areas of the North Pacific region. Some major cities near active volcanoes or that have volcano monitoring and hazard assessment facilities are shown. Regions that include the most active volcanoes are located in open rectangles. These regions are shown in more detail in Figures 1.3–1.7. The globe inset shows the northern high-latitude location of the region, which is an important factor for satellite-based studies and their potential impact on Arctic climate.

detecting and analyzing relatively short-lived volcanic clouds that drift and evolve. Third, some form of volcanic activity occurs in the region almost daily, thereby requiring constant and close scrutiny. In addition, most of these volcanoes are remote and difficult to access making them ideal targets for satellite-scale monitoring and analysis. Even though this text is focused on the North Pacific, the techniques and methods described can easily be applied worldwide and are used in locations such as Italy, Central America, and Hawaii.

1.2 VOLCANOLOGICAL SETTING OF THE NORTH PACIFIC

Most of the active and potentially active volcanoes in the North Pacific region are located near the continental coast or in island arcs. Their presence and location is related to subduction of the Pacific Ocean plate, which is generally moving northward and subducting beneath the North American plate at the rate of approximately 6 cm/yr in the

Gulf of Alaska and 8 cm/yr at the Kamchatka Trench. This subduction forms trenches along the continental–oceanic boundaries, east of the Kurile Islands and Kamchatka Peninsula (Kurile–Kamchatski Trench), central Aleutian Islands (Aleutian Trench), and the Alaska Peninsula (Alaska Trench) (Figure 1.2). Plate boundaries at the western Aleutian Islands, southeast Alaska, western Canada, and northwestern U.S. consist of transform and strike-slip faults. The most active volcanoes in recent times are located in belts parallel to the trenches. The Aleutian and Kamchatka Arc–Trench systems intersect on the Kamchatka Peninsula referred to as the Kamchatka–Aleutian Tectonic (KAT) connection (Scholl, 2007). Faulting and fracturing associated with plate collisions offer conduits for migrating magma and are associated with the significant seismic activity in the region. Globally, since 1900, three of the ten largest regional earthquakes occurred in Alaska and about one quarter of all earthquake energy released on Earth is from activity in the state (Gough and Day, 2007).

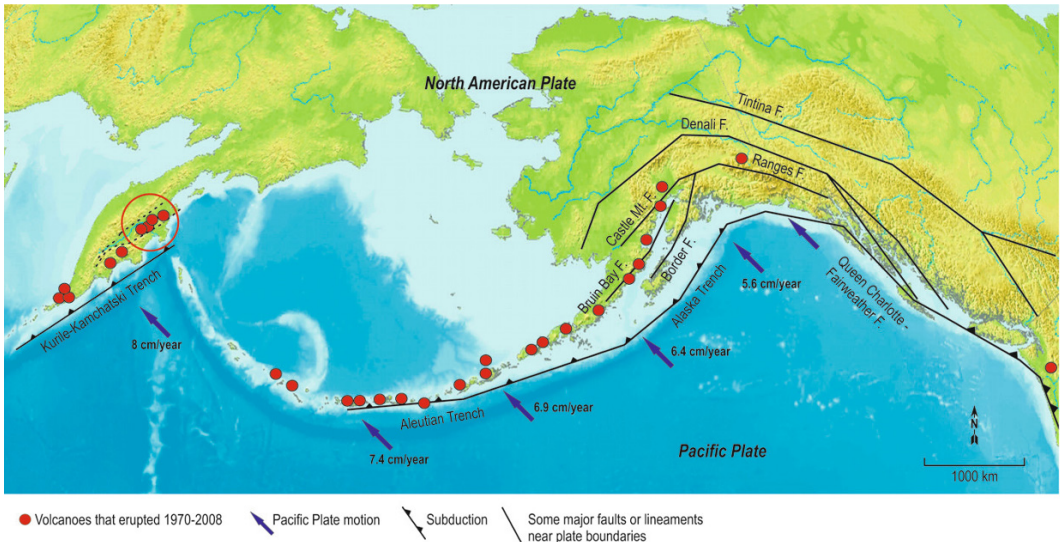


Figure 1.2. Generalized tectonics and faults or lineaments, and their relationship to volcanoes in the North Pacific region. The Kamchatka–Aleutian tectonic connection (open circle on Kamchatka Peninsula) encompasses some of the most active volcanoes in the region in recent times, including Klyuchevskoi, Bezymianny, Tolbachik, and Shiveluch. Throughout the North Pacific, there were more than 400 eruptions between 1970 and 2012 that produced ash that ascended more than 6 km (Table 1.1).

Explosive eruptions at volcanoes in the region result in volcanic clouds composed of ash and gas that drift into air traffic routes seriously impacting local and global air traffic (Miller and Casadevall, 2000) with the Anchorage, Alaska Airport, one of the busiest in the U.S. (Neal *et al.*, 1997). Facilities capable of routinely detecting and tracking these ash clouds were not available in this region prior to the establishment of AVO. Generally, eruption counts increased exponentially worldwide between 1790 and 1990 due to better communication and increased reporting (Simkin and Siebert, 1994). However, variations occur and are attributed to historical events and reporting patterns. In Alaska the average number of eruptions per year increased after 1988 when AVO was formed (Simkin and Siebert, 1994).

1.2.1 Active volcanoes of the North Pacific region

The following descriptions of North Pacific volcanic activity are in terms of eruption counts, durations, and volcanic explosivity indexes (VEIs) (Newhall and Self, 1982) and estimates are derived from Simkin and Siebert (1994), the Smithsonian

Global Volcanism website, and AVO daily observation reports from the satellite monitoring group. These statistics were compiled for two periods, post-1900 when records seem more complete and post-1990 when satellite data were first implemented for monitoring and detailed records were available.

The Kurile Islands (Figure 1.3) contain over 40 volcanoes, including stratovolcanoes, calderas, cinder cones, soma volcanoes, and submarine volcanoes. Twenty-six of them have erupted since 1900 but the most active ones are Chikurachki with 14 eruptions, Sarychev Peak with 12 eruptions, Ebeko with 10 eruptions, and Alaid with 9 eruptions. In recent times, post 1990, five of these volcanoes have erupted 12 times with Chikurachki the most active. The maximum VEI was 5 at Kharimkotan Volcano in 1933.

On the Kamchatka Peninsula there are approximately 100 volcanoes with a wide range of diverse morphologies (Figure 1.4). There are calderas within calderas, long fissures lined with cinder cones, numerous lava flows, crater lakes, stratocones, and shield volcanoes, some of which are snow-covered. Between 1900 and 2012 there were over 200 eruptions from these volcanoes. In

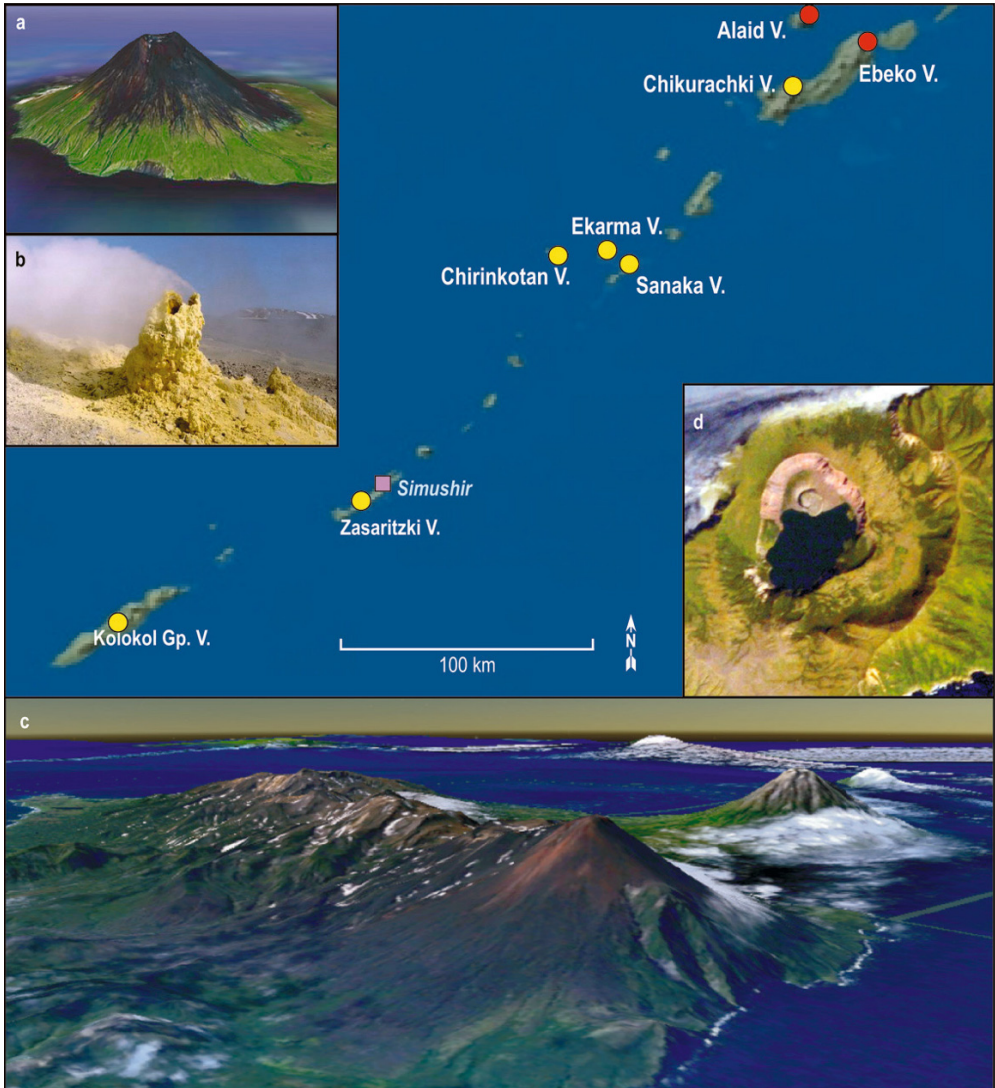


Figure 1.3. Map of the northern Kurile Islands, Russia, showing volcanoes that were active post 1990 (red), selected examples that were active pre 1990 (yellow), and a town impacted by these eruptions (purple). Some of the largest explosive eruptions in this region come from Alaid Volcano (a) shown in this north-looking, three-dimensional (3-D) perspective. Ebeko Volcano (b) is known for its sulfur deposits (source of the photograph is unknown). Chikurachki Volcano (c) is in the foreground and Fuss Peak in the background of this south-looking 3-D perspective. Zavaritzki Volcano (d) includes three nested calderas up to 10 km wide on this International Space Station NASA photograph (courtesy of NASA) (the 3-D views were generated using NASA World Wind and the shaded relief map is from Natural Earth III Texture Maps).

recent times, post 1990, there have been over 50 eruptions with durations up to 9 years. The volcanoes that erupted most frequently are Bezymianny (24 times), Kliuchevskoi (18 times), and

Shiveluch (8 times) which are located above the KAT connection (Scholl, 2007) and are some of the most active volcanoes in the region. Over a 98-year period the KAT volcanoes including Toba-



Figure 1.4. Map of Kamchatka Peninsula, Russia showing volcanoes that were active post 1990 (red) and selected examples that were active pre 1990 (yellow). The largest city, Petropavlovsk, is located less than 30 km from two active volcanoes. To the north, the town Klyuchi is also located less than 30 km from two active volcanoes. A north-looking 3-D view of volcanoes (a) of the Kamchatka–Aleutian tectonic connection is shown. A north-looking 3-D view (b) of Karymsky Lake in the foreground, Karymsky Volcano (left), and Maly Semiachik Volcano and its highly acidic crater lake in the background. Avachinsky Volcano (c) threatens Petropavlovsk (the 3-D views were generated using NASA World Wind and the shaded relief map is from Natural Earth III Texture Maps).

chik have erupted over 140 times with some of the longest durations. The largest VEI values were 5 at Bezymianny and Ksudach Volcanoes in 1955 and 1907 respectively.

In southern Alaska (excluding the Aleutian Islands) there are approximately 60 volcanoes but the most recently active ones are in the Eastern Aleutians and on the Alaska Peninsula (Figure

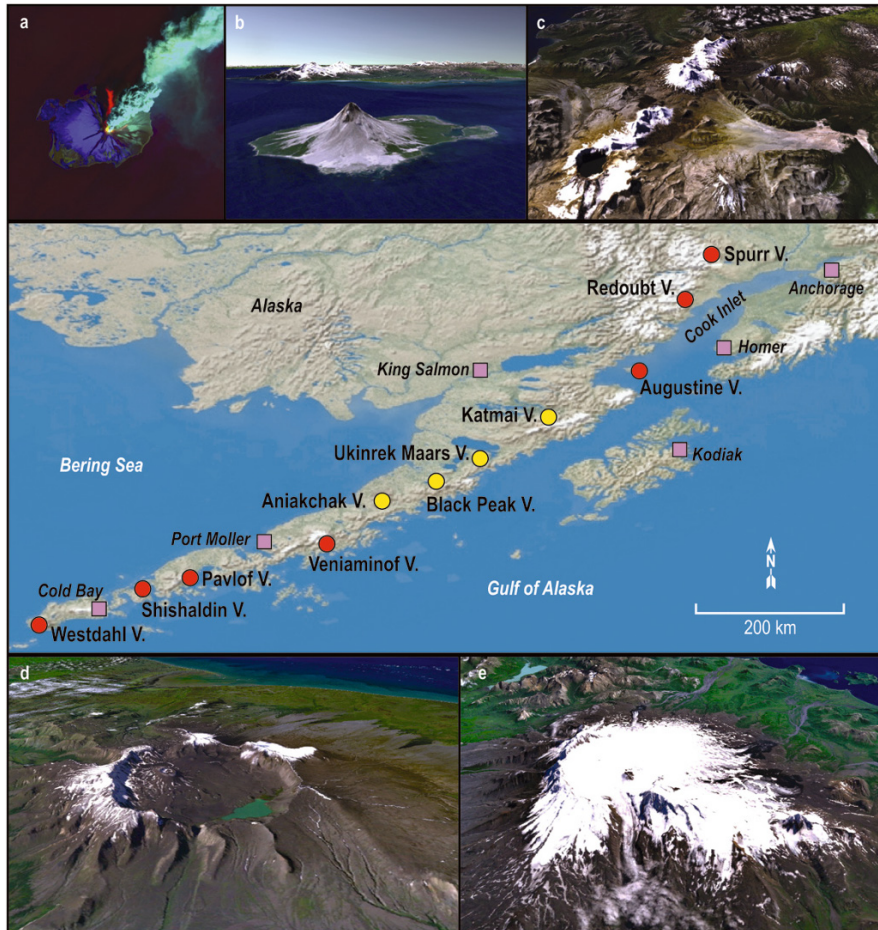


Figure 1.5. Map of Cook Inlet and Alaska Peninsula, Alaska showing volcanoes that were active post 1990 (red) as well as selected examples that were active pre 1990 (yellow). Major cities and towns (purple) and their proximity to surrounding volcanoes are shown. Eruptions of Spurr, Redoubt, and Augustine Volcanoes have seriously impacted the most heavily populated part of the state, Cook Inlet. Alaska’s largest city, Anchorage, is only 130 km east of Spurr Volcano, and Pavlof Volcano is only 56 km from Cold Bay. Augustine Volcano was recorded erupting on a Landsat image (a) in 1986 and also shown in a west-looking 3-D perspective (b). Katmai and Novarupta Volcanoes, which had the largest regional eruption in the 20th century and the Valley of Ten Thousand Smokes are shown in the east-looking 3-D perspective (c). Also, two 10 km wide calderas are shown in 3-D perspectives: Aniakhchak Volcano (d) looking east, and glacier-filled Veniaminof Volcano (e) looking south (the 3-D views were generated using NASA World Wind and the shaded relief map is from Natural Earth III Texture Maps).

1.5). Many of the Alaska Peninsula volcanoes are snow-covered stratocones. There are a few shield volcanoes, 10 km wide calderas (some filled with glaciers and lakes), maars, lava flows, domes, and cinder cones. Between 1900 and 2008 there have been 123 eruptions, 23 since 1990. The largest VEI is 6 for the full North Pacific and is attributed

to the 1912 eruption of Novarupta Volcano on the Alaska Peninsula. Significantly more detailed information became available regarding eruptions after AVO was established in 1988. Prior to this, eruptions were often reported by passing aircraft that were unknowingly in a dangerous situation. Since AVO was established aircraft have been warned of

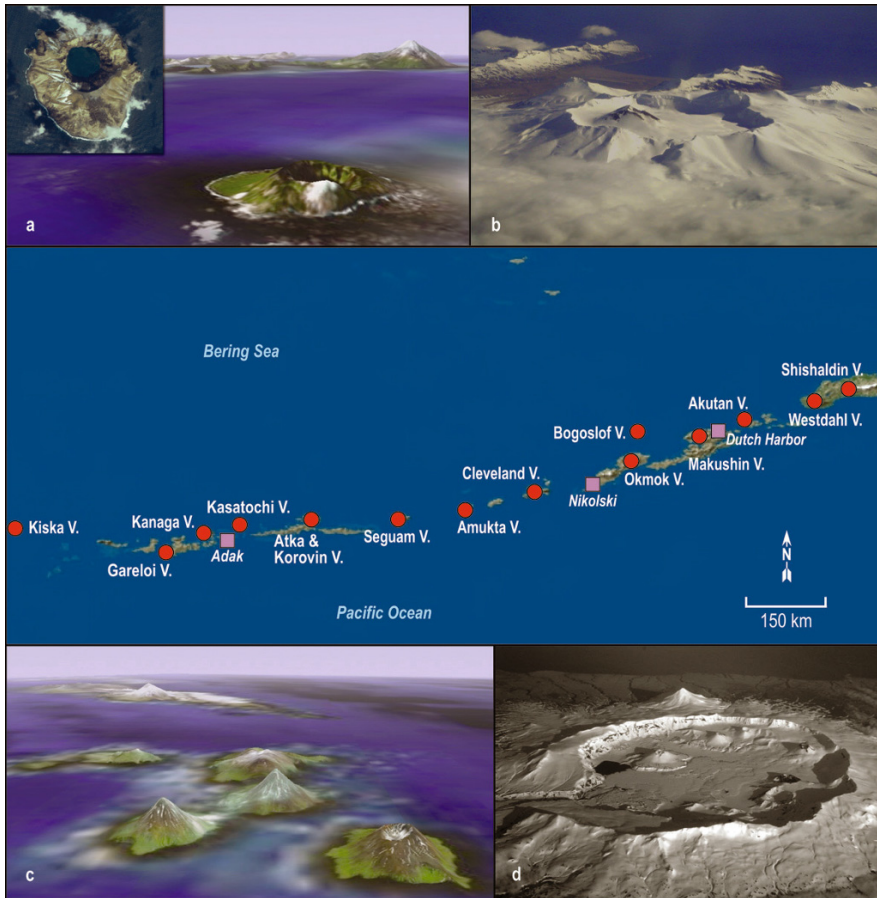


Figure 1.6. Map of volcanoes in the Aleutian Islands that erupted post 1990 (red) and towns of Adak and Dutch Harbor, the largest fisheries port in the United States. Views of selected volcanoes are shown in insets. Kasatochi Volcano (a) is in the foreground with an inset showing the crater lake, and Gareloi Volcano is in the background of this west-looking 3-D view. Kasatochi Island is less than 3 km across. Inside Akutan Volcano's 2 km wide caldera (b) is a large cinder cone. The Islands of Four Mountains (c) are shown in this east-looking 3-D view. The islands are comprised of six volcanoes. Starting from the right foreground, the volcanoes are Herbert, Carlisle, Cleveland, Tana, Kagamil, and Uliaga. Chuginadak Island (Cleveland Volcano) is less than 10 km across. Okmok Volcano (d) includes two overlapping 10 km wide calderas, numerous cinder cones, lava flows, and domes both within and on its flanks (the 3-D views were generated using NASA World Wind and the shaded relief map is from Natural Earth III Texture Maps).

volcanic clouds in advance. Three explosive eruptions that had the greatest impact in recent times were produced by Augustine Volcano (2006) in which 17 ash clouds were detected and tracked over a 5-month period; Spurr Volcano (1992) in which 3 ash clouds were detected and tracked over a 3-month period; and Redoubt Volcano (1989) in which 20 ash clouds were detected and tracked over a 7-month period.

In the Aleutian Islands (Figure 1.6) there are approximately 30 volcanoes, 20 of which have erupted since 1900. Some of these are islands that have multiple volcanoes. Most are stratovolcanoes but there are shield volcanoes, 10 km wide calderas, submarine volcanoes, cinder cones, and lava flows. Many of the volcanoes have erupted multiple times with over 135 eruptions since 1900 and over 35 eruptions since 1990. Most durations were less than

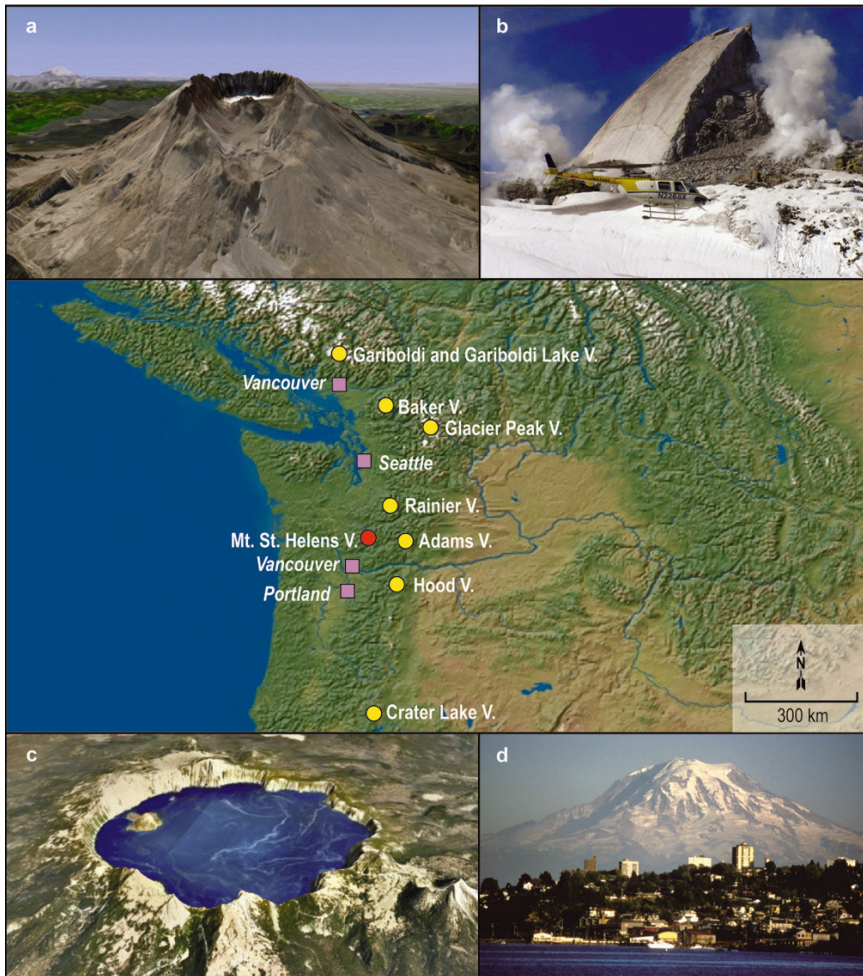


Figure 1.7. Map of Cascade Range, showing Mt. St. Helens (MSH) that erupted post 1990 (red) and a few volcanoes from pre 1990 (yellow). Views of selected volcanoes are shown in insets. MSH (a) is the most active volcano in this area in recent times (2004–2009) and is shown in this south-looking 3-D image of the 2 km wide crater and dome. A spine rock slab (b) extruded at MSH dome is shown as of April 28, 2006. Crater Lake (c) lies in a 10 km wide caldera formed about 6,850 years ago. Eruptions in this region have serious consequences due to the high population density. Mt. Rainier (d) sits just 70 km east of Tacoma, Washington. CVO is located in Vancouver, Washington (the 3-D views were generated using NASA World Wind and the shaded relief map is from Natural Earth III Texture Maps; photographs courtesy of USGS/CVO).

a few months except for Bogoslof Volcano which had an eruption that lasted approximately 2 years. Six of the volcanoes have had eruptions with VEI values of 3 which is the maximum recorded for the region in recent times. In the post-1990 period (to 2008) the most active volcanoes with known eruptions have been Cleveland with 7, Akutan and Korovin with 5, and Kanaga with 3. Eruptions of

Kasatochi and Okmok Volcanoes in 2008 produced volcanic clouds that ascended over 15 km (50,000 ft) and drifted east, impacting air traffic in North America and Europe.

In the Cascade Range region (Figure 1.7) there are approximately 60 volcanoes, 7 of which have erupted since 1900. Mt. St. Helens erupted explosively three times since 1990 but the largest event

occurred in 1980. There were six events that resulted in ash drifting over 1,000 km to the east. Even though the number of eruptions since 1900 is much smaller compared with the rest of the North Pacific, the impact of the 1980 eruption on North America was much greater. Morphologically, these volcanoes include stratovolcanoes, maars, cinder cones, shield volcanoes, complex volcanoes, large volcano fields, and a caldera.

1.3 HISTORY OF USE OF REMOTE SENSING FOR VOLCANO STUDIES AND MONITORING

This section reviews the use of satellite remote sensing to study dynamic volcanic processes, but it is worth pointing out that synoptic views from space have been responsible for the primary, basic identification of volcanoes. The discovery, using hand-held color photographs taken by Skylab astronauts (Friedman and Heiken, 1977), and independently on black-and-white Landsat Multispectral Scanner (MSS) photographic products (Francis and Baker, 1978), of the previously unrecognized 40 km long resurgent caldera Cerro Galán in northwest Argentina is a prime example (Figure 1.8). Appropriately processed multispectral satellite

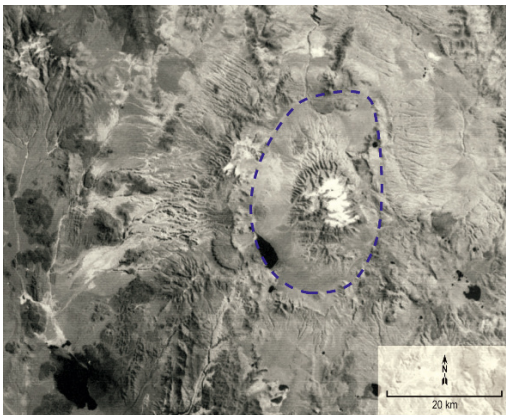


Figure 1.8. Cerro Galán Caldera, Argentina. The caldera was detected on a photographic product of Landsat MSS band 7 (800–1,100 nm) data, March 1976. Cerro Galán caldera is located to the right of center (dashed ellipse). Its resurgent dome is partly snow-covered. A dark lake abuts the southwest wall of the caldera floor. The caldera measures 40 km from north to south and 25 km from east to west.

images (De Silva and Francis, 1991) demonstrated how these data could provide an inventory of volcanoes throughout an entire province, and provide previously unreported edifice-by-edifice evidence on eruptive style, collapse history, and even basic age information at the level of pre- or post-glacial.

Now that most of the developed world has become accustomed to high-speed internet connections and low-cost (or even zero-cost) access to satellite image data, it is worth recalling how limited were the opportunities to use satellite remote sensing of volcanoes in “the old days”. In the 1960s and 1970s, the main format for satellite images was black-and-white photographs, or even computer printouts, constructed using pixel-by-pixel reconstruction at a very few capable centers. Late in the 1970s Landsat MSS images were used for geological mapping, and most people were still using black and white prints made from 1:1,000,000 scale negatives. There were also standard photographic products called “false color composites”, which were expensive and usually not well suited for geological interpretation. However, new software was available that was capable of processing digital versions of the MSS images, supplied on magnetic tape. A mainframe computer the size of a large refrigerator, requiring extensive training to learn its use, was employed to enhance surface geologic, botanical, and oceanographic features. Curiously, the main take-home product at the end of one of these sessions was typically 35 mm color slides of the processed images made by photographing the color monitor.

During the 1980s, the software grew friendlier, and specialized image-processing computers became more widespread, but they were still major items of equipment costing nearly U.S.\$100,000. During the 1990s the personal computer (PC) replaced specialist image-processing systems, and today the cost of a single academic license for one of the standard image-processing software packages (including tools for spectral analysis, geometric correction, terrain analysis, imaging radar handling, and with raster and vector GIS capabilities) is about \$4,000. Adding the price of a PC gives a total of about \$5,000, or a twentieth of the 1980 price, even without taking inflation into account. Digital data are cheaper too; the now-obsolete Landsat MSS images used to cost \$200 for a 180 × 180 km scene on magnetic tape, and when the Landsat Thematic Mapper (much more useful for thermal studies because of its short-wavelength infrared channels) began operations in the

1980s, the price was \$1,650 for a 90×90 km quarter-scene.

Although Landsat image/data prices have now fallen considerably, the emphasis among volcano remote-sensing scientists has shifted away from such systems with high spatial resolution but low temporal resolution and towards systems that offer higher temporal resolution at the expense of lower spatial resolution. This is because high temporal resolution offers greater capacity for monitoring, as well as a greater chance of avoiding cloud cover. For many purposes the concomitant loss of spatial resolution is of small importance because eruption clouds are large features, whereas the thermal radiance from small magmatic hot sources is sufficient to dominate the mid-infrared ($3\text{--}5\ \mu\text{m}$) flux from kilometer-sized pixels (Chapter 3).

Examples of volcanic eruption detection by means of satellite remote sensing can be traced back to the first decade of the space age. For example, in 1964, $3.8\ \mu\text{m}$ radiance pixels 6×6 km in size from the Nimbus I radiometer revealed a stronger thermal radiance from Kīlauea than from Mauna Loa (Gawarecki *et al.*, 1965), and the 1963–1967 eruption of Surtsey, offshore of Iceland, was apparent in similar Nimbus II data (Friedman and Williams, 1968; Williams and Friedman, 1970). Visual detection of eruption clouds can be traced back to such events as the 1973 eruption of Fernandina (Galapagos), from which a 200 km plume was noted on TIROS VHRR (the predecessor to AVHRR) images, acquired one day before the event had been noted by ground-based observers, and was also photographed by Skylab astronauts (Simkin and Krueger, 1977). An eruption of the nearby Sierra Negra Volcano (Galapagos) in 1979 produced a plume visible on Very High Resolution Radiometer imagery (VHRR) and geostationary NOAA SMS-1 imagery (SEAN, 1979), and led to the special acquisition of a Landsat MSS image of the event (Figure 1.9). In addition to the plume, this revealed incandescence from a lava channel in MSS bands 7, 6, and 5 ($800\text{--}1,100\ \text{nm}$, $700\text{--}800\ \text{nm}$, and $600\text{--}700\ \text{nm}$) at the source and traceable for about 10 km in band 7.

It is now well established that it takes an exceptionally wide or dynamic lava flow to dominate the signal in the visible or near infrared, but the deployment (from 1982) of the Landsat Thematic Mapper, with its smaller pixels, and channels in the short-wavelength infrared, opened up the possibility of detecting smaller and less radiant thermal sources on volcanoes. The first example (Figure 1.10) of

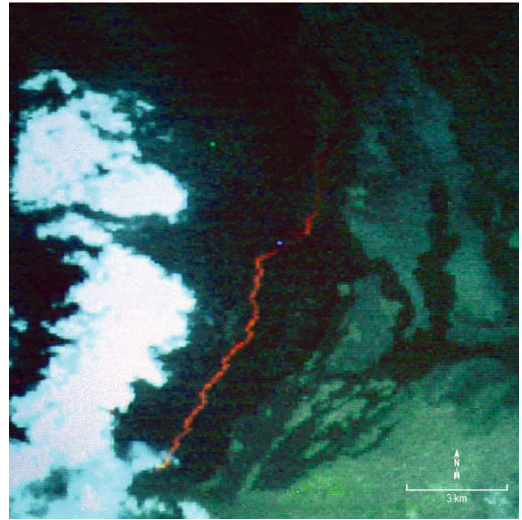


Figure 1.9. Landsat MSS image of a lava flow and plume at Sierra Negra Volcano, Galapagos Islands, 1979. The 15 km wide image is a color composite with bands 7, 6, and 5 in red, green, and blue. The image shows visible and near-infrared incandescence from a narrow lava channel. Pixels are 80 m across. The lava channel emerges from beneath the plume in the southwest and flows towards the northeast becoming less incandescent downstream as it cools, especially at shorter wavelengths.

this was the discovery of radiance in TM bands 7 and 5 ($2.08\text{--}2.35\ \mu\text{m}$ and $1.55\text{--}1.75\ \mu\text{m}$) from the shadowed floor of one of the summit craters of Lascar, Chile (Francis and McAllister, 1986). Their initial empirical report of what turned out to be a lava dome was quantified erroneously by Francis and Rothery (1987), because the mismatch between apparent, pixel-integrated temperatures in the two wavebands was not understood. Subsequently it was realized that the mismatch between pixel-integrated temperatures in adjacent channels was a result of the subpixel size of the radiating areas, and that the data carried within them information about proportional sizes and true temperatures of the radiating areas. This established the “dual band” technique as a method for extracting quantitative information on thermally radiant sources at magmatic and near-magmatic temperatures (Rothery *et al.*, 1988). It subsequently emerged that the basis of this technique had already been proposed (Dozier, 1981), principally as a way to study the temperatures of subpixel clouds on weather

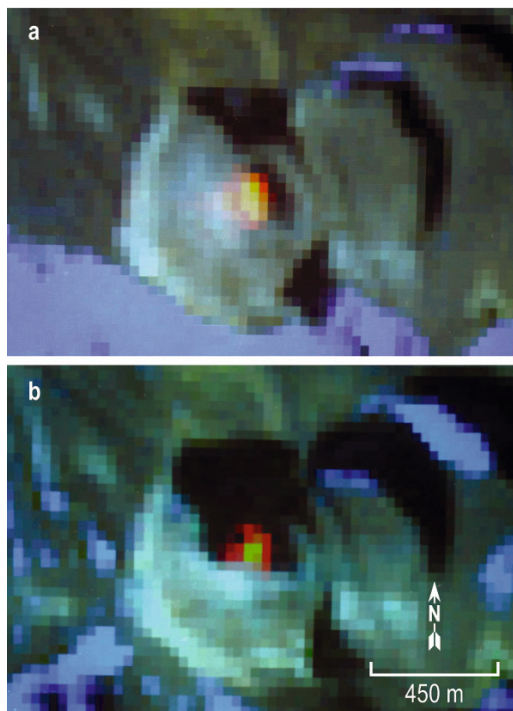


Figure 1.10. First high spatial resolution satellite image of a hot dome. The hot dome at the summit of Lascar Volcano was recorded prior to the September 16, 1986 explosive eruption. The eruption produced a 10 km high column. Image (a) was recorded on March 16, 1985 and (b) on July 21, 1985. Both are color composites with bands 7, 5, and 4 in red, green, and blue, respectively. Unambiguous thermal radiance comes from the shadowed part of the dome. Pixels are 30 m across, and these images show a 1.8 km area, from east to west.

satellite images. Examples of short-wavelength infrared radiance at several volcanoes in addition to Lascar (Rothery *et al.*, 1988) are shown for Mt. Augustine in Alaska, Erta Ale in Ethiopia, and Erebus in Antarctica (Figure 1.11). They were able to derive hot-component temperatures from the TM data, and discussed the crucial importance of basing quantitative estimates only on data that have not been resampled, and the errors that can creep into the dual-band assumptions if pixels in adjacent channels are not exactly co-registered.

Subsequent work (Oppenheimer *et al.*, 1993) improved the dual-band method by demonstrating that it made better sense to assume a value for the hot-component temperature in order to derive the

temperature of the warm background, than to assume that the background was non-radiant as a basis for estimating the temperature of the hot component. They also reported on the use of specially commissioned night-time TM images (Figure 1.12), and then showed that the radiance trends at Lascar could be tracked more cheaply and more frequently using night-time 1.6 μm data at 1 km pixel size (Wooster and Rothery, 1997).

The renaissance in the use of longer wavelength infrared weather satellite data for monitoring surface magmatic activity, which has led to the modern era of effectively real-time monitoring (Dean *et al.*, 1998, 2002, 2004; Dehn *et al.*, 2000, 2002; Wright *et al.*, 2002, 2004; Harris, 2013) can in part be traced back to studies by Andy Harris and colleagues (Harris *et al.*, 1995, 1997a, b) that put AVHRR and GOES data back into the mainstream and even established such data as capable of providing a credible proxy measurement for effusion rate (Harris *et al.*, 2000; Wright *et al.*, 2001; Lodato *et al.*, 2007).

Meanwhile, the use of remote sensing for quantitative studies of eruption clouds was beginning to take off as well, with studies of the global transport of the El Chichón 1982 cloud (Robock and Matson, 1983), of the Mt. St. Helens 1980 eruption (Sparks *et al.*, 1986), and of the Colo 1983 eruption (Malingreau and Kaswanda, 1983). Soon, efforts to use remotely sensed data to distinguish between ash-laden plumes from meteorological clouds began to bear fruit (Prata, 1989; Holasek and Rose, 1991), laying the foundations for the mature algorithms in use today. AVO began using satellite data to monitor volcanoes in 1989, starting with the eruption of Redoubt Volcano (Dean *et al.*, 1994, 1998).

Volcanic gas detection by orbital remote sensing came about with the serendipitous discovery that the Nimbus 7 TOMS (Total Ozone Mapping Spectrometer) was also capable of detecting and tracking sulfur dioxide (Figure 1.13) emplaced into the stratosphere by the 1982 El Chichón eruption (Krueger, 1983). Algorithms to measure the sulfur dioxide were soon developed, and ultraviolet spectroscopy is now a well-established method of gas plume tracking (Bluth *et al.*, 1992; Krueger *et al.*, 1995).

Radar is a particularly attractive tool for use on volcanoes because it can see through clouds and at night. Early examples of the use of radar interferometry to produce digital elevation models of volcanoes include Evans *et al.* (1992), Mougini-Mark and Garbeil (1993), and the utility of basic

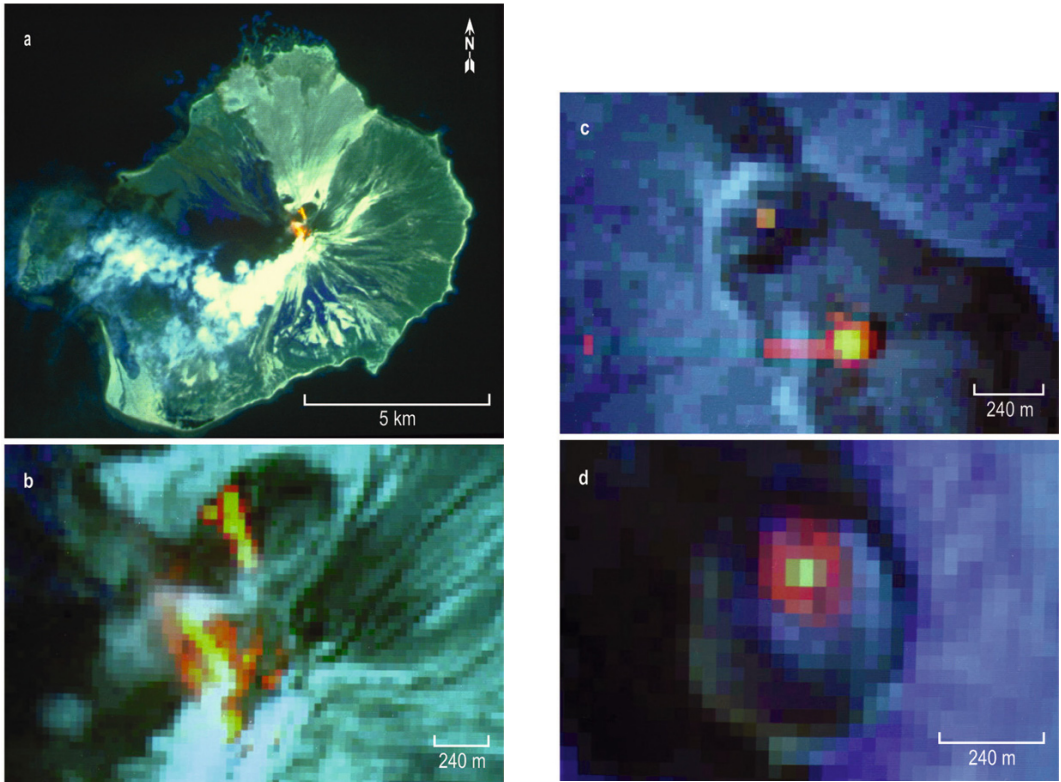


Figure 1.11. Thermal anomalies detected on shortwave infrared satellite images on Landsat TM band 7, 5, 4 composites. (a) 15 km wide view of Mt. Augustine, Alaska on April 28, 1986. (b) Enlargement of the summit area, revealing two en echelon eruptive fissures. Only one had been apparent to local observers. To the north is a radiant blocky lava flow. (c) Erta Ale, Ethiopia on January 5, 1985, providing the first confirmation of two lava lakes that have been active since 1976. (d) Mt. Erebus, Antarctica on January 26, 1986, demonstrating an active lava lake a month after the most recent ground-based observation.

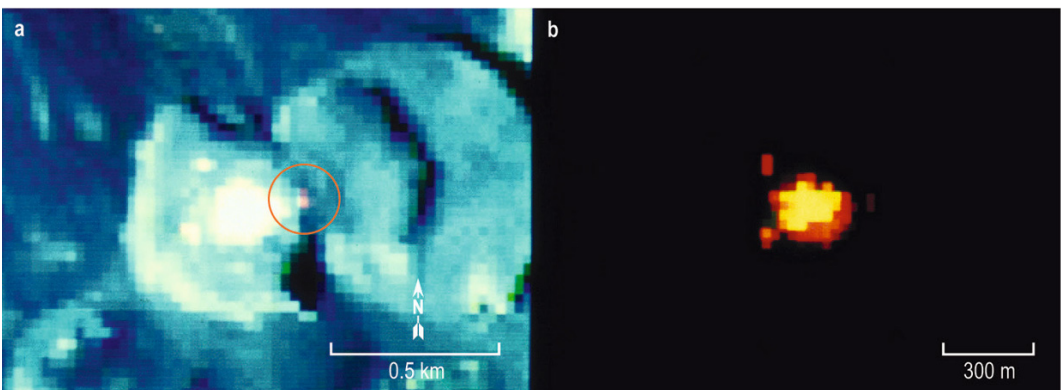


Figure 1.12. Satellite observations of the dome at Lascar Volcano, Chile. Landsat TM data recorded the dome in these color composite images using infrared bands 7, 5, and 4 as red, green, and blue. (a) A dome within the summit crater re-established itself after the 1986 eruption in this daylight image, October 27, 1989. (b) A hot dome and surrounding fumaroles are evident on November 17, 1989.

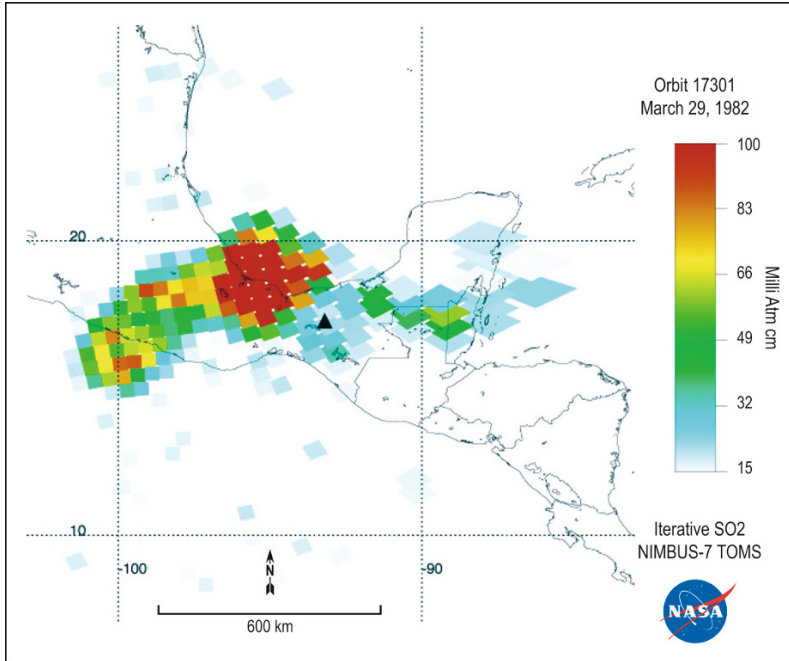


Figure 1.13. One of the first observations of sulfur dioxide emitted by a volcano. TOMS data recorded the gas emitted by the Mexican volcano El Chichón, March 29, 1982 (Krueger, 1983) (the image is a modern recalibration of data used by Krueger, courtesy of the TOMS Volcanic Emissions Group at the Joint Center for Earth Systems Technology, JCET, University of Maryland Baltimore County, UMBC).

use of radar images for mapping in cloud-ridden volcanic terrains was demonstrated by Rowland *et al.* (1993). Differential radar interferometry to detect inflation or deflation of a few centimeters requires well-constrained and appropriately chosen orbits. Success appeared to have been achieved when Massonnet *et al.* (1995) reported deflation on Etna between May 1992 and October 1993. It was subsequently shown that neglect to correct for the effect of tropospheric water vapor called these results into question (Delacourt *et al.*, 1998), but with the proper corrections made differential radar interferometry offers a powerful tool (Sigmundsson *et al.*, 1997; Lu *et al.*, 2003, 2004).

1.4 IMPACT OF NORTH PACIFIC ERUPTIONS ON SOCIETY

The NOPAC region is one of the most volcanically active areas in the world with more than 150 volcanoes, including over 70 that have been active in the past 3,500 years. Alaska alone has well over 100 volcanoes with 52 historically active since 1700

(Wood and Kienle, 1990; Miller *et al.*, 1998; AVO, 2008; Cameron, 2008). The Kamchatka Peninsula has over 100 large active or potentially active volcanoes (Fedotov *et al.*, 1991), with approximately 30 that have been active in the past 3,500 years (Ponomareva *et al.*, 2007). The northwestern U.S.A. includes 10 active and potentially active volcanoes with the most recent activity from Mt. St. Helens (1980 and 2005). Across the North Pacific region some form of eruptive activity occurs almost daily. For example, from July 2004 to April 2005 there was activity that included lava flows, dome growth, lahars, debris flows, and airborne ash (see volcano observatory websites for more details—AVO, 2008; CVO, 2008; KVERT, 2008).

Since 1970 there have been over 100 eruptions in the North Pacific region that produced ash clouds that were greater than 6 km in height (Table 1.1). However, each eruption usually consisted of multiple events over a period lasting from days to months. Taking this into account, there were approximately 300 explosive events that resulted in plumes at altitudes greater than 6 km over those 38 years (Figure 1.14). In most cases each of the

Table 1.1. List of eruptions in the North Pacific region from 1970 to 2013 that produced ash clouds that exceeded 6 km in height. There were 115 eruptions over that period when categorized by year and volcano. However, the actual activity was much greater since many of the volcanoes were active multiple times within a year (modified from compilation by P. Webley and A. Steffke, 2005–2006).

<i>Year</i>	<i>Volcano</i>	<i>Year</i>	<i>Volcano</i>	<i>Year</i>	<i>Volcano</i>	<i>Year</i>	<i>Volcano</i>
1970	Karymsky	1986	Chikurachki	1998	Kliuchevskoi	2007	Shiveluch
1972	Alaid	1986	Bezymianny	1998	Karymsky	2007	Kliuchevskoi
1973	Pavlof	1987	Kliuchevskoi	1999	Karymsky	2007	Pavlof
1974	Kliuchevskoi	1987	Cleveland	1999	Bezymianny	2007	Bezymianny
1974	Pavlof	1989	Redoubt*	1999	Shishaldin*	2007	Shiveluch
1975	Tolbachik	1990	Bezymianny	1999	Bezymianny	2008	Okmok
1975	Cleveland	1990	Redoubt*	1999	Kliuchevskoi	2008	Cleveland*
1976	Augustine*	1990	Kliuchevskoi*	2000	Kliuchevskoi*	2008	Kasatochi
1977	Bezymianny	1990	St. Helens*	2000	Shiveluch*	2008	Karymsky
1977	Ukinrek Maars	1991	Avachinsky	2000	Bezymianny*	2008	Bezymianny
1978	Westdahl	1991	Shiveluch	2000	Kliuchevskoi	2008	Shiveluch*
1979	Westdahl	1991	Westdahl	2001	Cleveland	2008	Kliuchevskoi
1979	Bezymianny*	1992	Spurr*	2001	Shiveluch*	2009	Redoubt*
1980	Bezymianny	1992	Bogoslof	2001	Bezymianny*	2009	Sarychev Peak*
1980	St. Helens*	1993	Shiveluch	2002	Shiveluch*	2009	Shiveluch
1980	Gareloi	1993	Kliuchevskoi*	2002	Kliuchevskoi	2010	Kizimen*
1980	Pavlof	1993	Bezymianny	2003	Bezymianny	2010	Shiveluch*
1981	Alaid	1994	Kanaga*	2004	Bezymianny*	2010	Kliuchevskoi*
1981	Bezymianny	1994	Cleveland	2004	Karymsky*	2011	Kizimen*
1981	Pavlof	1994	Kliuchevskoi*	2004	Shiveluch	2011	Shiveluch*
1981	Shishaldin	1995	Kliuchevskoi	2005	Kliuchevskoi	2011	Karymsky
1982	Gareloi	1995	Bezymianny	2005	St. Helens	2011	Cleveland
1982	St. Helens*	1995	Shishaldin	2005	Bezymianny	2012	Shiveluch*
1982	Bezymianny	1996	Karymsky	2005	Shiveluch	2012	Karymsky*
1983	Bezymianny	1996	Alaid	2006	Augustine	2012	Cleveland
1983	Veniaminof	1996	Pavlof	2006	Cleveland*	2013	Pavlof*
1984	Kliuchevskoi	1997	Kliuchevskoi*	2006	Bezymianny	2013	Shiveluch*
1985	Bezymianny	1997	Okmok	2006	Karymsky*	2013	Kliuchevskoi
1985	Kliuchevskoi	1997	Karymsky*	2006	Shiveluch	2013	Zhupanovsky
1986	Augustine	1997	Bezymianny	2006	Bezymianny		
1986	Pavlof	1998	Korovin	2006	Kliuchevskoi		

* Indicates multiple events or eruptions at that volcano for that year.

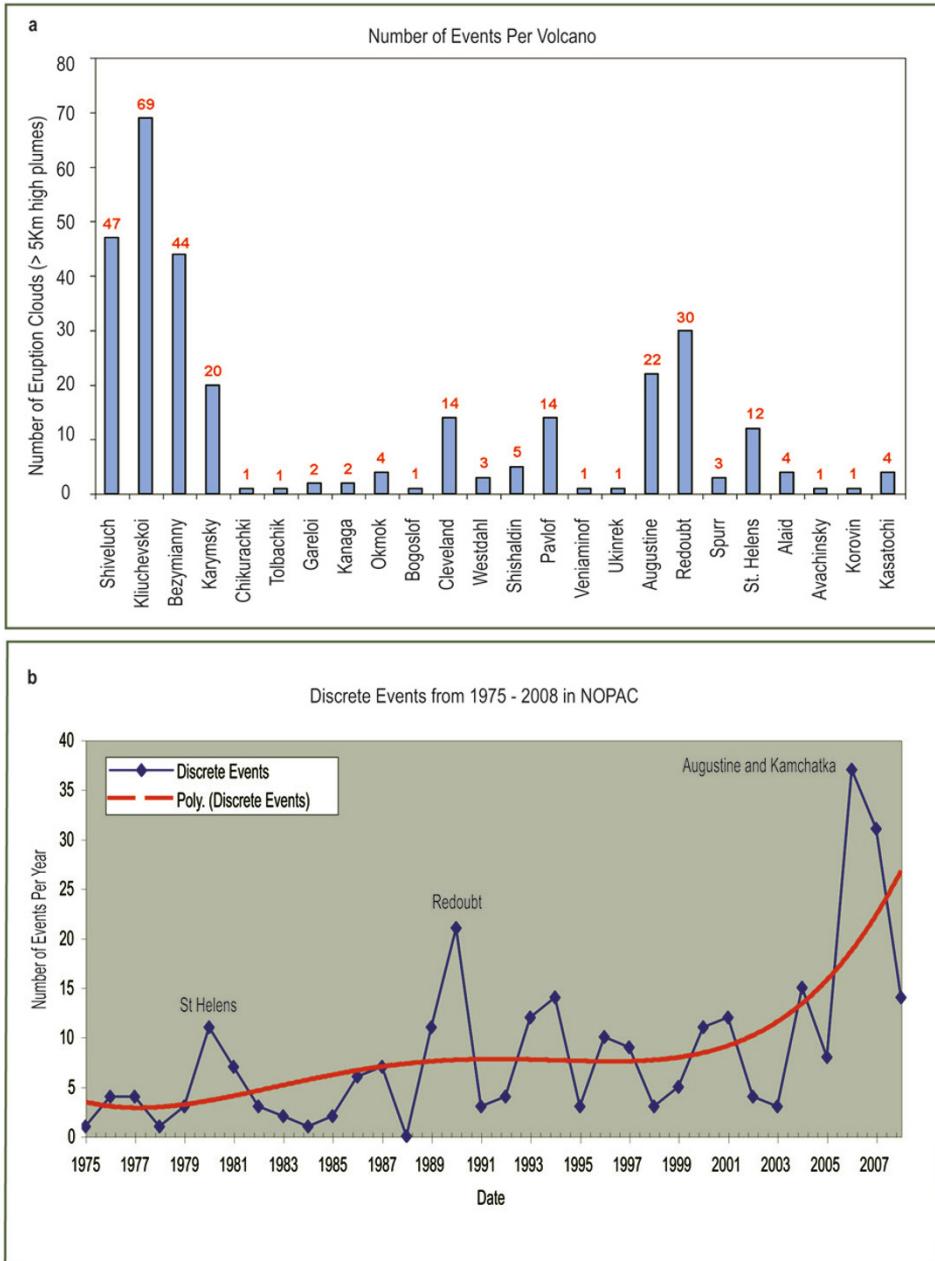


Figure 1.14. Eruptions in the North Pacific region. The graphs show the number of eruptions that produced ash clouds attaining heights greater than 6 km from 1970 to 2008, inclusive. (a) The total number of events per volcano. (b) The total number of eruptions per year shown as the best polynomial fit suggesting a gradual increase due to increased monitoring by observatories. This assessment is based on cross-referenced data from the Smithsonian Global Volcanism Program Activity Reports (Smithsonian, 2008), AVO current volcanic activity reports (AVO, 2008), KVERT Operational Reports (KVERT, 2008), and published literature (Miller and Chouet, 1994; Eichelberger *et al.*, 1995). More details are given in Table 1.1 (statistics compiled by Peter Webley and Andrea Steffke, 2005–2008).

events resulted in a separate hazard response. These events impact human health, transportation, communication, and the commerce infrastructure of the region. The best polynomial fit of the number of detected eruptions per year (Figure 1.14) shows a gradual increase between 1975 and 2008. This is attributed to the increased instrumentation and methodical monitoring of volcanoes by CVO at Mt. St. Helens and AVO, KVERT, and SVERT in Alaska, the Kamchatka Peninsula, and the Kurile Islands. AVO installed a satellite receiving station dedicated to volcano monitoring in 1993, and seismic instruments in the Aleutian Islands post 1996 after which the counts increase significantly. These instruments detect multiple events of what previously would be referred to as a single eruption, if detected at all, thereby improving our understanding of eruption processes, and hazard assessment and response.

Explosive eruptions of North Pacific volcanoes pose a serious threat to local communities and global air traffic. Recent eruptions have impacted population centers and transportation in the region in terms of ash fall, airport closure, and encounters between aircraft and volcanic clouds (Table 1.2). In Alaska and Kamchatka the two largest and most vulnerable cities are Anchorage and Petropavlovsk-Kamchatsky, respectively. Anchorage was seriously impacted by recent eruptions of Mt. Spurr (1992), 130 km to the east, Mt. Redoubt (2009), 175 km to the southwest, Mt. Augustine (2006), 285 km to the southwest, and other more distant Aleutian volcanoes, such as Okmok and Kasatochi (2008). Petropavlovsk-Kamchatsky was seriously impacted by recent eruptions of Avachinsky Volcano 25 km to the north (2001), and Koryaksky (2008) 27 km to the north. The impact that airborne volcanic ash has on the western part of the North Pacific region can be seen in a multitemporal composite compiled using satellite data from 1970 to 2005 and processed using the brightness temperature difference technique (Figure 1.15). Over the last few decades Anchorage and/or surrounding towns have repeatedly experienced ash fall, airport closures, or rerouted air traffic from the eruptions of Mt. Spurr (1953, 1992), Augustine (1976, 1986, and 2006), Redoubt (1989/1990 and 2009), Cleveland (2001), Okmok (2008), and Kasatochi (2008) (Miller and Chouet, 1994; Simkin and Siebert, 1994; Casadevall, 1994b; Keith, 1995; AVO, 2008; Guffanti *et al.*, 2008a).

Ash from some of these events has been detected, tracked, and/or impacted air traffic in

areas as far east as the Great Lakes region (Fisher *et al.*, 1997), Greenland (Schneider *et al.*, 1995), and Texas (Casadevall, 1994b) (Figure 1.16). In 2001 an aircraft taking off from San Francisco, California reported particles and a sulfur smell in the cockpit. Dispersion modeling matched the position and timing of the report, and suggested that the ash came from the recent eruption of Mt. Cleveland Volcano, Alaska, 3,500 km to the west (Simpson *et al.*, 2002; Dean *et al.*, 2004). Recently, sulfur dioxide clouds from eruptions at Okmok (2008) were detected over Europe and from Kasatochi (2008) at multiple locations in the Northern Hemisphere (even Europe) as the cloud circled the globe at least three times.

Even though activity in recent times is less frequent in the northwestern U.S.A. compared with Alaska and Kamchatka, the region is most susceptible to catastrophic impacts from eruptions due to the large population and number of cultural centers near active volcanoes. The most recent activity from volcanoes in this area includes Mt. St. Helens (1980 and 2005), Hood (1907), Mt. Rainier (1894), and Baker (1884). The impact of volcanic activity on this area was most serious during the 1980 eruption of Mt. St. Helens where cities up to 1,500 km from the volcano experienced ash fall and/or airport closures including Portland, Vancouver, Spokane, and Yakima (Table 1.2 and Figure 1.16). The area within a few tens of kilometers of the volcano was impacted by rockslides, avalanches, directed blast, ash flows, mudflows, and floods that devastated surrounding forests (Lipman and Mullineaux, 1981).

Ash dispersion modeling provides an additional perspective of the impact that ash-producing eruptions have on the western and eastern North Pacific region (Figure 1.17). In this figure the Puff dispersion model was run for all eruptions that emitted ash that ascended to heights over 6 km with a model run time of 12 h and the results compiled into a single image. The dispersion patterns seem to group in four areas: (A) Kamchatka Peninsula, (B) the Aleutian Islands, (C) Cook Inlet, and (D) the Cascade Range. This pattern is attributed to the location of the volcanoes and the wind field patterns in each area. The modeled clouds blanket the Kamchatka Peninsula, Aleutian Islands, most of continental Alaska and the northwestern U.S.A., and parts of western Canada. All the air traffic routes (white lines in Figure 1.17) in the North Pacific region cross the areas impacted by these eruption clouds.

Table 1.2. Examples of impacts caused by airborne ash from volcanic eruptions in the North Pacific region. The eruptions are reported by year but the actual activity for most volcanoes is intermittent over a period lasting from days to months (Blong, 1984; Brantley, 1990; Casadevall, 1994a; Casadevall and Krohn, 1995; Eichelberger *et al.*, 1995; Guffanti *et al.*, 2008a, b; Kienle, 1994; Miller and Casadevall, 2000; Sarna-Wojcicki *et al.*, 1981; Scott, 1994; Simpson *et al.*, 2002; Swanson and Kienle, 1988). Messages that contain significant meteorological information (SIGMETs) are broadcast to aircraft warning of hazardous weather conditions that are considered of extreme importance, including volcanic ash.

Year	Volcano	General area of impact and detection	Impact	
			Ash fall (thickness if available—mm)	Aircraft flights
2013	Kliuchevskoi	North Pacific	Light, Kamchatka	Rerouted, North Pacific
2013	Shiveluch	North Pacific	Light, Kamchatka	Rerouted, North Pacific
2009	Sarychev Peak	Global	Light, Kurile Is.	Rerouted, North Pacific
2009	Redoubt	North America Europe	Heavy, Alaska	Airport closure, Alaska; cancelled, Alaska; rerouted, North Pacific; evacuated aircraft, Alaska
2008	Kasatochi	Global	Light, Aleutian Is.	Cancelled, Alaska; rerouted, North America
2008	Okmok	North America, Europe	Light, Aleutian Is.	Rerouted, Alaska and North America
2008	Cleveland	North America	Light, Aleutian Is.	SIGMETs issued
2006	Augustine	Alaska, North America	Moderate (>5 mm), Alaska	Cancelled, Alaska; rerouted, Alaska
2004	Shiveluch	Kamchatka, North Pacific	Light (<2 mm), Kamchatka	Airport closure, Kamchatka; rerouted, North Pacific
2001	Cleveland	Alaska, North America	Light, Aleutian Is.	Rerouted, Alaska; ash and sulfur in cabin, San Francisco
1994	Kliuchevskoi	Kamchatka, North Pacific	Light, Kamchatka	Rerouted, North Pacific
1992	Spurr	Alaska, North America	Moderate (>3 mm), Alaska	Airport closure (20 h), ANC; cancelled, Alaska; rerouted, North Pacific; evacuated aircraft, Alaska
1989–90	Redoubt	Alaska, North America	Heavy, Alaska	Airport closure (days), ANC; damaged aircraft, Alaska; cancelled, Alaska; rerouted, North Pacific
1986	Augustine	Alaska, North America	Heavy, Alaska	Airport closure (days), ANC; damaged aircraft, Alaska; cancelled, Alaska; rerouted, North Pacific
1980	Mt. St. Helens	North America	Heavy (up to 90 mm), northwest U.S.A.	Multiple airport closure (up to 21 days); flight cancellations
1976	Augustine	Alaska	Light, Alaska	Damaged aircraft, Alaska; cancelled, Alaska; rerouted, North Pacific
1953	Spurr	Alaska	Heavy (up to 6 mm), Alaska	Airport closure 7 days, ANC

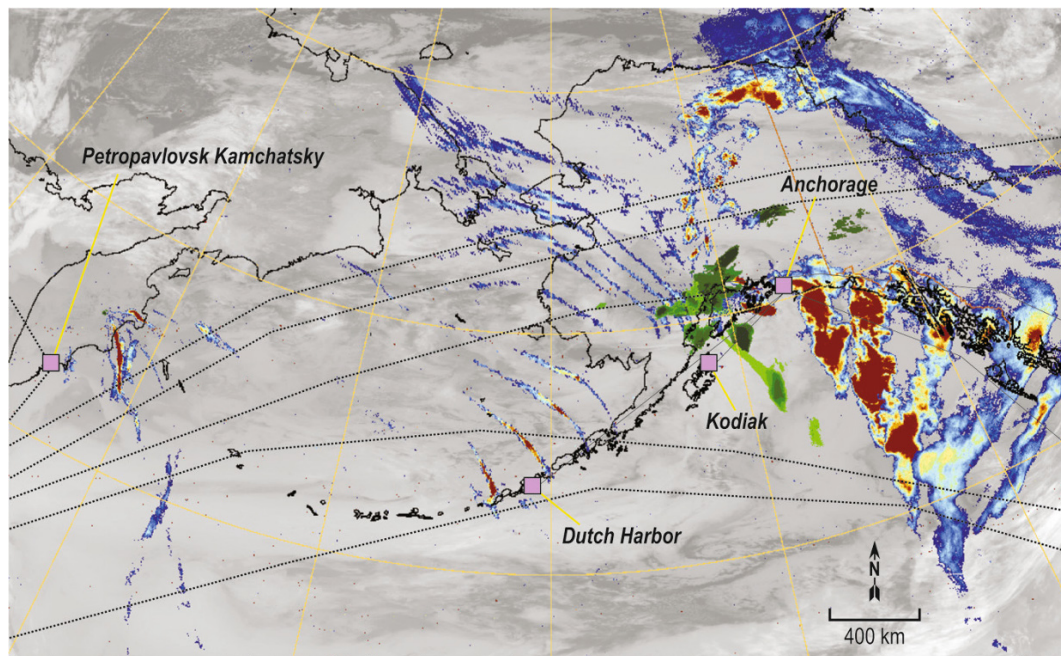


Figure 1.15. Ash clouds and their proximity to air traffic routes in the North Pacific region. More than 200 eruptions produced airborne ash that impacted the region between 1975 and 2001, many of which traverse air traffic routes at jet altitudes. Local cities and towns depend upon air traffic for transportation and delivery of commodities for survival. The figure is a multitemporal composite of opaque plumes and ash clouds derived from AVHRR satellite data. Opaque plumes (green) are derived from TIR temperature data (B4) with dark green as coldest clouds. Ash clouds are shown as blue (low-BTD signals) and red (high-BTD signals).

1.5 THE NEW PERSPECTIVE ON MONITORING VOLCANOES

One of the biggest societal gains brought by satellite observations of volcanoes has been the ability to monitor remote volcanoes that pose an ash hazard to aircraft. There have been many incidents of damage to aircraft caused by airborne volcanic ash scouring windscreens and wings, clogging instruments and air filters, and, in some cases, causing engine failure. In 1982 a Boeing 747 jet aircraft encountered an ash cloud from the eruption of Galunggung Volcano, lost power to all four engines, and dropped to within a few thousand meters of the ground before they were restarted, narrowly averting a catastrophic accident (Fisher *et al.*, 1997; Miller and Casadevall, 2000). This was the first known incident where a commercial passenger jet aircraft faced a situation where all engines failed due to environmental conditions in

the atmosphere. Satellite data (Chapter 2) and dispersion models (Chapter 7) are the only quantitative sources of information that can systematically detect (satellite data) and predict (dispersion models) the location and movement of volcanic ash clouds in the atmosphere. However, adequate monitoring of volcanoes requires multiple, independent sensors looking at different stages of volcanic activity. These include ground-based sensors (seismic and deformation) which are historically the primary instruments but in this context provide critical information in support of satellite-based deformation analysis (Chapter 8).

A network of seismic stations surrounding a volcano can detect tremors related to magma rising beneath the volcano and often permit fairly reliable forecasting of eruptions on a useful timescale (hours to a few days) including the start time (within minutes). For these purposes, data must be telemetered to an observatory in real time to be of value. Such

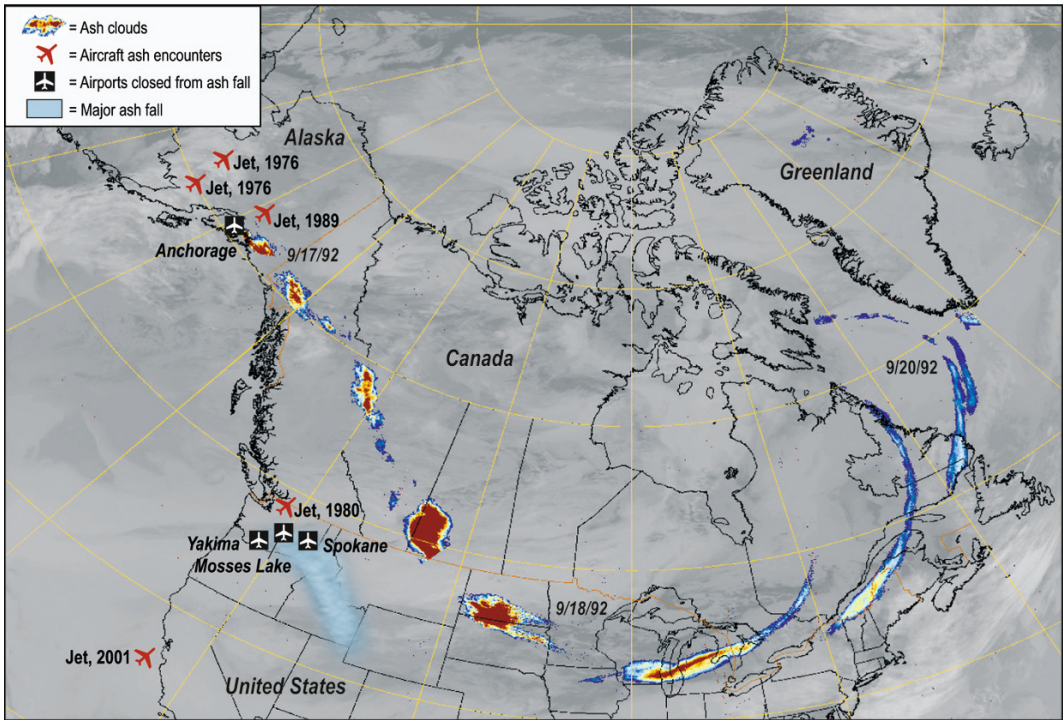


Figure 1.16. Examples where ash-producing eruptions in the North Pacific have impacted the United States and Canada since 1975. Ash clouds from four eruptions—Redoubt, 1989/1990; Spurr, 1992 (shown in above figure); Okmok, 2008; and Kasatochi, 2008—have blown across North America, seriously disrupting air traffic from coast to coast as well as throughout the North Pacific region. Aircraft have encountered airborne ash and, in one incident north of Anchorage, it was nearly fatal. Airport closures from ash fall have also seriously disrupted the transportation infrastructure in the entire region.

monitoring is relatively easy to implement near cities such as at volcanoes in the Pacific Northwest but becomes progressively more difficult as distance from existing infrastructure increases. Within the Aleutian Volcanic Arc, data from the Alaska Peninsula and the eastern Aleutian Islands is transmitted by radio, telephone line, or satellite to AVO (McNutt, 2002; Nye *et al.*, 2002; Power *et al.*, 2006). The seismic data provide critical insight on subsurface eruption processes. Conversely, satellite observations require the launching of imaging sensors that provide a synoptic view to the Earth's surface to detect and monitor changes in the landscape, surface temperatures, and volcanic clouds (Chapter 9). Equipment is needed to access, receive, and process these data in real time. Satellite data can also be used to estimate the start time of eruptions but not at the temporal resolutions of seismic data.

Volcano deformation, a powerful predictor of impending eruptions and constraint on magma dynamics, has in the past two decades undergone the revolutions of global positioning systems (GPS) and interferometric synthetic aperture radar (InSAR) satellite data (Chapter 8). The two techniques are complementary, because GPS offers time-continuous measurement of surface deformation at discrete points in space whereas InSAR offers space-continuous measurement of deformation at discrete points in time. Because it involves no field installations, InSAR has permitted a broad survey of deformation. This has revealed that many seemingly dormant volcanoes are deforming, often aseismically, a result that is as yet not fully understood. The application of GPS is fieldwork intensive and therefore has only been applied where eruptions are anticipated and/or where deformation is known to be occurring. GPS has established clear

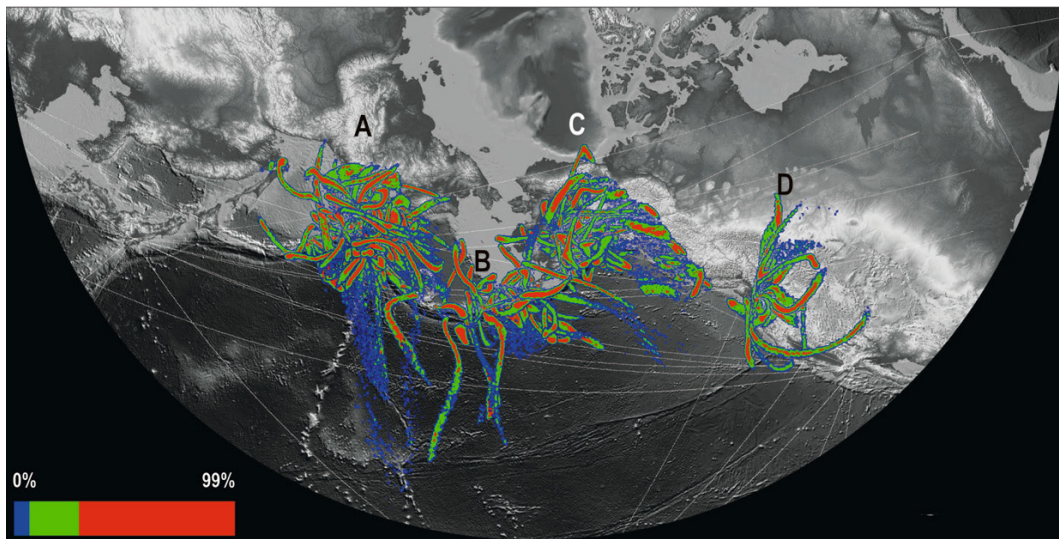


Figure 1.17. Time sequential composite of Puff dispersion model runs of eruptions in the North Pacific region. The model shows the movement and area impacted by volcanic clouds at heights over 6 km (20,000 feet) from eruptions that occurred between 1975 and 2006. Also, it shows the concentration of airborne ash relative to the total number of particles released in the model. The lines are global flight routes across the region. The model runtime is 12 hours, originating in four regions (A–D). (A) Eruptions of volcanoes in Kamchatka and the Kurile Islands. (B) Eruptions of volcanoes in the Aleutian Islands. (C) Eruptions of volcanoes in continental Alaska. (D) Eruptions of volcanoes in the Cascade Range. A longer model run would extend ash clouds well across North America.

patterns of inflation prior to eruption, and deflation during and after eruption. It has also provided new constraints on source depth of magma that complements seismic and petrologic techniques in determining the last point of magma storage before eruption. Deformation studies have also shown that seismic monitoring alone is not adequate for monitoring because magma can move without generating seismicity (Dzurisin, 2007).

Unlike seismic and deformation techniques, satellite data record surface and airborne components resulting from effusive processes (Chapter 3) and explosive processes (Chapters 5 and 6). Detection, tracking the movement, and assessing the impact of lava flows, airborne ash, and volcanic gas were problematic until satellite remote-sensing systems became available. The spatial, spectral, and temporal components of remote sensing offer a solution to this problem. As magma nears the surface adjacent rocks are heated and gases are released migrating to the surface and raising the temperature of surface rocks. The resulting thermal anomalies are often precursor signals to effusive or explosive eruptions. Thermal flux and effusive rates are estimated using time-sequential,

mid-infrared (MIR), and thermal-infrared (TIR) satellite data.

Moderate spatial resolution satellite data (Chapter 4) provide a quantitative scientific basis from which to model transient geological and meteorological hazards as well as map small-scale phenomena. Despite limited temporal coverage, moderate resolution data use has increased greatly as its capabilities have become critical for monitoring low-temperature anomalies and mapping both chemical and textural variations on volcanic surfaces. The data can also be integrated into near-real time monitoring efforts that are based primarily on high temporal/moderate spatial resolution orbital data. This synergy allows small-scale activity to be targeted for science and hazard response, and the establishment of a calibration baseline between each sensor.

Thermal-infrared (TIR) and ultraviolet (UV) satellite images can be used to quickly detect ash and gas in volcanic clouds emitted by explosive eruptions, and, by applying mathematical functions to various wavelength bands, the movement of ash can be tracked for days, or even years for some aerosols (Chapters 5 and 6). However, there are

some serious limitations in detection which is a concern considering the danger that these clouds represent. Detection of volcanic clouds is problematic since required wavelengths vary as the clouds evolve physically and chemically. The spectral signals from the clouds also vary as atmospheric conditions change and surface environmental factors beneath the cloud fluctuate. Another complication is validation and verification of satellite observations due to the changing structure and composition of the clouds, the logistics required for making measurements under dangerous conditions, and the lack of appropriate instruments. In the next decade the number of satellites with more sophisticated sensors will increase, and will continue to gain in importance and reliability for mitigation of volcanic hazards (Chapter 9).

Measurement of SO_2 in eruption plumes (Chapter 6) was a serendipitous spin-off of programs to measure O_3 in the atmosphere, since SO_2 , like O_3 , absorbs in the ultraviolet (Krueger *et al.*, 2000). Measurement of SO_2 is a favored technique for accessing the level of volcano unrest, because SO_2 is degassed with water from magma at relatively low pressure, hence at shallow depth, indicating that magma is near the surface and that an eruption is possibly imminent. In contrast, CO_2 begins exsolving at high pressure, so high CO_2 emission rates are not so diagnostic (Wallace and Anderson, 2000). One surprise from satellite measurement of SO_2 is that the gas cloud sometimes decouples from the ash cloud in an eruption (Schneider *et al.*, 1999). Also, the amount of SO_2 release is sometimes an order of magnitude more than estimated through petrological analysis (Gerlach and McGee, 1994; Gerlach *et al.*, 1996; Keppler, 1999). The petrologic technique relies on comparing the sulfur content of degassed matrix glass with that of melt inclusions in crystals, protected by their host from decompression and vapor loss and therefore representative of pre-eruption melt composition (Sparks, 2003). The difference should be sulfur lost from melt during eruption. The obvious way to explain the huge excess of SO_2 found by satellite measurements is that not all the SO_2 in the cloud came out of the melt during eruption, the so-called excess sulfur problem. It must have already been present in a vapor phase, with bubbles suspended in magma prior to eruption. Thus, remote sensing has documented unexpected and important conditions of magma storage and prerequisites for eruption.

As discussed above, satellite data do a reason-

ably good job of detecting volcanic clouds but cannot predict their movement, which is critical for hazard mitigation and assessment. Dispersion models developed for weather forecasting, climate and pollution studies, and to model the effects of nuclear wars have been found to be ideally suited for modeling the movement of volcanic clouds (Chapter 7). The models are compared with time-concurrent satellite data for validation and to define limitations in satellite detection (Dean *et al.*, 2004), and to estimate aircraft exposure to volcanic ash (Peterson and Dean, 2008).

Manned space missions provide a special perspective that complements satellite coverage (Chapter 10). Astronauts and cosmonauts on the Space Shuttle and International Space Station (ISS) can opportunistically select the optimum viewing geometry for photographs, from nadir to highly oblique angles. Being in non-Sun-synchronous orbit, they also can collect data from different times of day using shadows to accentuate the terrain, improving recognition of geomorphic features, and can notice low-level activity that may not be detected by satellites. In one example, ISS astronauts called AVO when they detected an eruption at Cleveland Volcano in May 2006. In addition, the Shuttle radar instrument has provided one of the best baseline digital elevation models of terrain and radar images for geomorphic analysis of volcanoes.

Satellite data are not only used to monitor eruptions and to analyze volcanic processes but to evaluate the impact of an eruption upon the terrain and our atmosphere (Chapter 11). Sometimes these modifications are regional or global and may be hazardous or beneficial. Case studies from worldwide examples are used to illustrate eruptions and their effect on the surrounding environment, and the attributes that make satellite remote sensing a suitable method for studying these effects.

1.6 CONCLUSIONS

AVO, KVERT, SVERT, and CVO have been monitoring volcanoes in the North Pacific for decades. During that time the rate of eruption detection has increased as the technology matures and the number of instrumented volcanoes increases. Volcanic activity has been detected in seismic, geophysical, and remote-sensing datasets used for monitoring. Each technique offers a unique but interrelated

glimpse of volcanic processes. The synergy between each provides an important synoptic approach for detection and understanding these processes.

Remote sensing is the newest family of tools and has evolved from a photographic paper product to complex digital data that measure quantifiable physical parameters. By the early 1990s data access and almost instantaneous transfer rates supported real-time monitoring of hazards associated with volcanic eruptions. The information derived from these data became invaluable for detecting surface deposits and airborne ash and gas. Satellite data coupled with dispersion modeling have become important tools to detect and track volcanic clouds that significantly impact commerce and human health. Hopefully, this book will contribute to the understanding of eruption processes, provide information for hazard assessment and mitigation, and stimulate the use of satellite data by other observatories worldwide.

1.7 REFERENCES

- AVO (2008). <http://www.avo.alaska.edu>
- Blong, R.J. (1984). *Airports and Aeroplanes, Volcanic Hazards: A Sourcebook on the Effects of Eruptions*, San Francisco, Academic Press, pp. 261–269.
- Bluth, G.J.S.; Doiron, S.D.; Schnetzler, C.C.; Krueger, A.J.; Walter, L.S. (1992). Global tracking of the SO₂ clouds from the June, 1991 Mount Pinatubo eruptions, *Geophys. Res. Lett.*, **19**, 151–154.
- Brantley, S. (Ed.) (1990). *The Eruption of Redoubt Volcano, Alaska, December 14, 1989–August 31, 1990*, USGS Circular 1061, U.S. Geological Survey, Reston, VA, p. 33.
- Cameron, C. (2008). Counting Alaska volcanoes, *EOS, Trans. Am. Geophys. Union*, **89**, V43H-07.
- Casadevall, T.J. (1994a). The 1989–1990 eruption of Redoubt Volcano, Alaska: Impacts on aircraft operations, *J. Volcanol. Geothermal Res.*, **62**, 301–316.
- Casadevall, T.J. (1994b). *Volcanic Ash and Aviation Safety: Proceedings of the First International Symposium on Volcanic Ash and Aviation Safety*, USGS Circular 2047, U.S. Geological Survey, Reston, VA, pp. 1–98.
- Casadevall, T.J.; Krohn, D. (1995). Effects of the 1992 Crater Peak eruptions on airports and aviation operations in the United States and Canada, *U.S. Geological Survey Bulletin*, **2139**, 205–220.
- CVO (2008). <http://vulcan.wr.usgs.gov/>
- De Silva, S.L.; Francis, P.W. (1991). *Volcanoes of the Central Andes*, Springer-Verlag, Berlin, 216 pp.
- Dean, K.; Bowling, S.A.; Shaw, G.; Tanaka, H. (1994). Satellite analyses of movement and characteristics of the Redoubt Volcano plume, January 8, 1990, *J. Volcanol. Geothermal Res.*, **62**, 339–352.
- Dean, K.G.; Servilla, M.; Roach, A. (1998). Satellite monitoring of remote volcanoes improves study efforts in Alaska, *EOS, Trans. Am. Geophys. Union*, **79**(35), 422–423.
- Dean, K.G.; Dehn, J.; McNutt, S.; Neal, C.; Moore, R.; Schneider, D. (2002). Satellite imagery proves essential for monitoring erupting Aleutian Volcano, *EOS, Trans. Am. Geophys. Union*, **83**(22), 241, 246–247.
- Dean, K.G.; Dehn, J.; Papp, K.R.; Smith, S.; Izbekov, P.; Peterson, R.; Kearney, C.; Steffke, A. (2004). Integrated satellite observations of the 2001 eruption of Mt. Cleveland, Alaska, *J. Volcanol. Geothermal Res.*, **135**, 51–73.
- Dehn, J.; Dean, K.; Engle, K. (2000). Thermal monitoring of North Pacific volcanoes from space, *Geology*, **28**, 755–758.
- Dehn, J.; Dean, K.G.; Engle, K.; Izbekov, P. (2002). Thermal precursors in satellite images of the 1999 eruption of Shishaldin Volcano, *Bull. Volcanol.*, **64**, 525–534.
- Delacourt, C.; Briole, C.; Achace, J. (1998). Tropospheric corrections of SAR interferograms with strong topography: Application to Etna, *Geophys. Res. Lett.*, **25**, 2849–2852.
- Dozier, J. (1981). A method for satellite identification of surface temperature fields of subpixel resolution, *Remote Sensing of Environment*, **11**, 221–229.
- Dzurisin, D. (2007). *Volcano Deformation: Geodetic Monitoring Techniques*, Springer/Praxis, Heidelberg, Germany/Chichester, U.K., 441 pp.
- Eichelberger, J.C.; Keith, T.E.C.; Miller, T.P.; Nye, C.J. (1995). The 1992 eruptions of Crater Peak Vent, Mount Spurr, Alaska: Chronology and summary, *U.S. Geological Survey Bulletin*, **2139**, 1–18.
- Evans, D.L.; Farr, T.; Zebker, H.; van Zyl, J.J.; Mouginiis-Mark, P.E. (1992). Radar interferometry studies of the Earth's topography, *EOS, Trans. Am. Geophys. Union*, **73**, 553–558.
- Fedotov, S.A.; Masurenkov, Y.P.; Svyatlovsky, A.E. (1991). *Forward, Active Volcanoes of Kamchatka*, Nauka, Moscow, Vol. 1, pp. 302.
- Fisher, R.V.; Heiken, H.; Hulén, J.B. (1997). *Volcanoes: Crucibles of Change*, Princeton University Press, Princeton, NJ, 317 pp.
- Francis, P.W.; Baker, M.C.W. (1978). Sources of two large-volume ignimbrites in the Central Andes: Some Landsat evidence, *J. Volcanol. Geothermal Res.*, **4**, 81–87.
- Francis, P.W.; McAllister, R. (1986). Volcanology from space: Using the Landsat Thematic Mapper in the central Andes, *EOS, Trans. Am. Geophys. Union*, **67**, 170–171.
- Francis, P.W.; Rothery, S.A. (1987). Using the Landsat Thematic Mapper to detect and monitor active vol-

- canoes: An example from Lascar Volcano, northern Chile, *Geology*, **15**, 614–617.
- Friedman, J.D.; Heiken, G. (1977). *Skylab 4 Observations of Volcanoes, Part A: Volcanoes and Volcanic Landforms*, NASA Special Publication—Skylab Explores the Earth No. 380, NASA, Washington, D.C., pp. 171–172.
- Friedman, J.D.; Williams, R.S. (1968). Infrared sensing of active geologic processes, paper presented at *Proceedings of the Fifth Symposium on Remote Sensing*, University of Michigan, pp. 787–815.
- Gawarecki, S.J.; Lyon, R.J.P.; Nordberg, W. (1965). Infrared spectral returns and imagery of the Earth from space and their application to geological problems, *Scientific Experiments for Manned Orbital Flight*, AAS Science and Technology Series 4, American Astronautical Society, pp. 13–133.
- Gerlach, T.M.; McGee, K.A. (1994). Total sulfur dioxide emissions and pre-eruption vapor-saturated magma at Mount St. Helens, 1980–88, *Geophys. Res. Lett.*, **21**, 2833–2836.
- Gerlach, T.M.; Westrich, H.R.; Symonds, R.B. (1996). Preeruption vapor in magma of the climatic Mount Pinatubo eruption: Source of the giant stratospheric sulfur dioxide cloud, in C.G. Newhall and R.S. Punongbayan (Ed.), *Fire and Mud: Eruptions and Lahars of Mount Pinatubo*, Washington Press, Seattle, WA, pp. 415–433.
- Gough, L.P.; Day, W.C. (2007). *Tintina Gold Province Study: Alaska and Yukon Territory, 2002–2007*, USGS Circular 38, USGS Fact Sheet 2007-3061, U.S. Geological Survey, Reston, VA.
- Guffanti, M.; Mayberry, G.C.; Casadeval, T.J.; Wunderman, R. (2008a). Compilation of disruptions to airports from volcanic activity, USGS Open-File Report 2007-1256, available only online at <http://pubs.usgs.gov/of/2007/1256/>, p. 26.
- Guffanti, M.; Mayberry, G.C.; Casadevall, T.J.; Wunderman, R. (2008b). Volcanic hazards to airports, *Natural Hazards: SI Aviation Hazards from Volcanoes*, doi: 10.1007/s11069-008-9254-2.
- Harris, A.J.L. (2013). *Thermal Remote Sensing of Active Volcanoes: A User's Manual*, Cambridge University Press, 728 pp.
- Harris, A.J.L.; Vaughan, R.A.; Rothery, D.A. (1995). Volcano detection and monitoring using AVHRR data: The Krafla eruption, 1984, *Int. J. Remote Sensing*, **16**, 1001–1020.
- Harris, A.J.L.; Blake, S.; Rothery, D.A.; Stevens, N.F. (1997a). A chronology of the 1991 to 1993 Mount Etna eruption using advanced very high resolution radiometer data: Implications for real-time thermal volcano monitoring, *J. Geophys. Res.—Solid Earth*, **102**, 7985–8003.
- Harris, A.J.L.; Keszthelyi, L.; Flynn, L.P.; Mougini-Mark, P.J.; Thornber, C.; Kauhikaua, J.; Sherrod, D.; Trusdell, F.; Sawyer, M.W.; Flament, P. (1997b). Chronology of the episode 54 eruption at Kīlauea Volcano, Hawaii, from GEOS-9 satellite data, *Geophys. Res. Lett.*, **24**, 3281–3284.
- Harris, A.J.L.; Flynn, L.P.; Dean, K.G.; Pilger, E.; Wooster, M.; Okubo, C.; Mougini-Mark, P.J.; Garbeil, H.; Thornber, C.; De la Cruz-Reyna, S. *et al.* (2000). Real-time satellite monitoring of volcanic hot spots, in P. Mougini-Mark, J.J. Crisp, and J.H. Fink (Eds), *Remote Sensing of Active Volcanism*, AGU Monograph 116, American Geophysical Union, Washington, D.C., pp. 139–159.
- Holasek, R.E.; Rose, W.I. (1991). Anatomy of 1986 Augustine volcano eruptions as recorded by multi-spectral image processing of digital AVHRR weather satellite data, *Bull. Volcanol.*, **53**, 420–435.
- Keith, T.E.C. (Ed.) (1995). The 1992 eruptions of Crater Peak Vent, Mount Spurr volcano, Alaska, *U.S. Geological Survey Bulletin*, **2139**, 220.
- Keppeler, H. (1999). Experimental evidence for the source of excess sulfur in explosive volcanic eruptions, *Science*, **284**, 1652.
- Kienle, J. (1994). Volcanic ash–aircraft incidents in Alaska prior to the Redoubt eruption on 15 December 1989, paper presented at *Volcanic Ash and Aviation Safety: Proceedings of the First International Symposium on Volcanic Ash and Aviation Safety*, USGS Bulletin 2047, pp. 119–123.
- Krueger, A.J. (1983). Sighting of El Chichón sulfur dioxide clouds with the Nimbus 7 Total Ozone Mapping Spectrometer, *Science*, **220**, 1377–1379.
- Krueger, A.J.; Walter, L.S.; Bhartia, P.K.; Schnetzler, C.C.; Krotkov, N.A.; Sprod, I.; Bluth, G.J.S. (1995). Volcanic sulfur dioxide measurements from the total ozone mapping spectrometer instruments, *J. Geophys. Res.*, **100**, 14057–14076.
- Krueger, A.J.; Schaefer, S.J.; Krotkov, N.; Bluth, G.; Barker, S. (2000). *Ultraviolet Remote Sensing Volcanic Eruptions*, AGS Monograph 116, American Geophysical Union, Washington, D.C., pp. 25–43.
- KVERT (2008). http://www.kscnet.ru/ivs/kvert/index_eng.php, English.
- Lipman, P.W.; Mullineaux, D.R. (1981). *The 1980 Eruptions of Mount St. Helens, Washington*, USGS Professional Paper, U.S. Geological Survey, Reston, VA, p. 844.
- Lodato, L.; Spampinato, L.; Harris, A.; Calvari, S.; Dehn, J.; Patrick, M. (2007). The morphology and evolution of the Stromboli 2002–2003 lava flow field: An example of a basaltic flow field emplaced on a steep slope, *Bull. Volcanol.*, **69**, 661–679.
- Lu, Z.; Fielding, E.; Patrick, M.; Trautwein, C. (2003). Estimating lava volume by precision combination of multiple baseline spaceborne and airborne interferometric synthetic aperture radar: The 1997 eruption of Okmok Volcano, Alaska, *IEEE Trans. on Geosci. Remote Sensing*, **41**, 1428–1436.
- Lu, Z.; Rykhus, R.; Masterlark, T.; Dean, K.G. (2004). Mapping recent lava flows at Westdahl Volcano,

- Alaska, using radar and optical satellite imagery, *Remote Sensing of Environment*, **91**, 345–353.
- Malingreau, J.P.; Kaswanda (1983). Monitoring volcanic eruptions in Indonesia using weather satellite data: The Colo eruption of July 28, 1983, *J. Volcanol. Geothermal Res.*, **27**, 179–194.
- Massonnet, D.; Briole, P.; Arnaud, A. (1995). Deflation of Mount Etna monitored by spaceborne radar interferometry, *Nature*, **375**, 567–570.
- McNutt, S.R. (2002). Volcano seismology and monitoring for eruptions, *International Handbook of Earthquake and Engineering Seismology*, Vol. 81A, pp. 383–406.
- Miller, T.M.; McGimsey, R.G.; Richter, D.H.; Riehle, J.R.; Nye, C.J.; Yount, M.E.; Dumoulin, J.A. (1998). *Catalog of the Historically Active Volcanoes of Alaska*, USGS Open-File Report 98-582, U.S. Geological Survey, Reston, VA.
- Miller, T.P.; Casadevall, T.J. (2000). *Volcanic Ash Hazards to Aviation*, Academic Press, San Diego, CA, pp. 915–930.
- Miller, T.P.; Chouet, B.A. (Eds.) (1994a). The 1989–1990 eruptions of Redoubt Volcano, Alaska, *J. Volcanol. Geothermal Res.*, **62**, 530.
- Miller, T.P.; Chouet, B.A. (1994b). The 1989–1990 eruptions of Redoubt Volcano: An introduction, *J. Volcanol. Geothermal Res.*, **62**, 1–10.
- Mouginis-Mark, P.J.; Garbeil, H. (1993). Digital topography of volcanoes from radar interferometry: An example from Mt. Vesuvius, Italy, *Bull. Volcanol.*, **55**, 566–570.
- Neal, C.A.; Casadevall, T.J.; Miller, T.P.; Hendley, J.W.I.; and Stauffer, P.H. (1997). *Volcanic Ash: Danger to Aircraft in the North Pacific*, USGS Fact Sheet FS 30-0097, U.S. Geological Survey, Reston, VA, p. 2.
- Newhall, C.; Self, S. (1982). The volcanic explosivity index (VEI): An estimate of explosive magnitude for historical volcanism, *J. Geophys. Res.*, **87**, 1231–1238.
- Nye, C.J.; Keith, T.E.C.; Eichelberger, J.C.; Miller, T.P.; McNutt, S.R.; Moran, S.; Schneider, D.J.; Dehn, J.; Schaefer, J.R. (2002). The 1999 eruption of Shishaldin Volcano, Alaska: Monitoring a distant eruption, *Bull. Volcanol.*, **64**, 507–519.
- Oppenheimer, C.; Francis, P.W.; Rothery, D.A.; Carlton, R.W.; Glaze, L.S. (1993). Infrared image analysis of volcanic thermal features: Lascar Volcano, Chile, 1984–1992, *J. Geophys. Res.*, **98**, 4269–4286.
- Peterson, R.; Dean, K.G. (2008). Forecasting exposure to volcanic ash based on ash dispersion modeling, *J. Volcanol. Geothermal Res.*, **170**, 230–246.
- Ponomareva, V.; Churikova, T.; Melekestsev, I.; Braitseva, O.; Pevzner, M.; Sulerzhitsky, L. (2007). *Late Pleistocene–Holocene Volcanism on the Kamchatka Peninsula, Northwest Pacific Region*, Geophysical Monograph, American Geophysical Union, Washington, D.C., p. 45.
- Power, J.A.; Nye, C.J.; Coombs, M.L.; Wessels, R.L.; Cervelli, P.F.; Dehn, J.; Wallace, K.L.; Freymueller, J.T.; Doukas, M.P. (2006). The reawakening of Alaska's Augustine Volcano, *EOS, Trans. Am. Geophys. Union*, **87**, 373–377.
- Prata, A.J. (1989). Observations of volcanic ash clouds in the 10–12 μm window using AVHRR/2 data, *Int. J. Remote Sensing*, **10**, 751–761.
- Robock, A.; Matson, M. (1983). Circumglobal transport of the El Chichón volcanic dust cloud, *Science*, **221**, 195–197.
- Rothery, D.A.; Francis, P.W.; Wood, C.A. (1988). Volcano monitoring using short wavelength infrared data from satellites, *J. Geophys. Res.*, **93**, 7993–8008.
- Rowland, S.K.; Smith, G.A.; Mouginis-Mark, P.J. (1993). Preliminary ERS-1 observations of Alaskan and Aleutian volcanoes, *Remote Sensing of Environment*, **48**, 1–25.
- Sarna-Wojcicki, A.M.; Shipley, S.; Waitt, Jr., R.B.; Dzurisin, D.; Wood, S.H. (1981). Areal distribution, thickness, mass, volume, and grain size of air-fall ash from the six major eruptions of 1980, in P.W. Lipman and D.R. Mullineaux (Ed.), *The 1980 Eruptions of Mount St. Helens*, Washington, USGS Professional Paper 1250, U.S. Government Printing Office, Washington, D.C.
- Schneider, D.J.; Rose, W.I.; Kelley, L. (1995). Tracking of 1992 eruption clouds from Crater Peak vent of Mount Spurr Volcano, Alaska, using AVHRR: The 1992 eruptions of Crater Peak vent, Mount Spurr Volcano, Alaska, *U.S. Geological Survey Bulletin*, **B2139**, 27–36.
- Schneider, D.J.; Rose, W.I.; Coke, L.R.; Bluth, G.J.S.; Sprod, I.E.; Krueger, A.J. (1999). Early evolution of a stratospheric volcanic eruption cloud as observed with TOMS and AVHRR, *J. Geophys. Res.*, **104**, 4037–4050.
- Scholl, D.W. (2007). *Viewing the Tectonic Evolution of the Kamchatka–Aleutian (KAT) Connection with an Alaska Crustal Extrusion Perspective*, American Geophysical Union, Washington D.C., pp. 3–35.
- Scott, W.E.; McGimsey, R.G. (1994). Character, mass, distribution, and origin of tephra-fall deposits of the 1989–1990 eruption of Redoubt Volcano, south-central Alaska, *J. Volcanol. Geothermal Res.*, **62**, 251–272.
- SEAN (1979). Sierra Negra, *Scientific Event Alert Network Bulletin*, **4**, 3–6.
- Sigmundsson, F.; Vaon, H.; Massonnet, D. (1997). Readjustment of the Krafla spreading segment to crustal rifting measured by satellite radar interferometry, *Geophys. Res. Lett.*, **24**, 1843–1846.
- Simkin, T.; Krueger, A.F. (1977). *Skylab 4 Observations of Volcanoes, Part B: Summit Eruption of Fernandina Caldera, Galapagos Islands, Ecuador*, NASA Special Publication No. 380—Skylab Explores the Earth, NASA, Washington, D.C., pp. 171–172.

- Simkin, T.; Siebert, L. (1994). *Volcanoes of the World*, Geoscience Press, Tucson, AZ, 349 pp.
- Simpson, J.J.; Hufford, G.L.; Pieri, D.; Servranckx, R.; Berg, J.S.; Bauer, C. (2002). The February 2001 eruption of Mount Cleveland, Alaska: Case study of an aviation hazard, *Weather and Forecasting*, **17**, 691–704.
- Smithsonian (2008). <http://www.volcano.si.edu/world/>, National Museum of Natural History.
- Sparks, R.S.J. (2003). *Models and Experiments—Dynamics of Magma Degassing, Part I: Magma Degassing*, Special Publication 213, Geological Society, London, pp. 5–22.
- Sparks, R.S.J.; Moore, J.G.; Rice, C.J. (1986). The initial giant umbrella cloud of the May 18th, 1980, explosive eruption of Mount St Helens, *J. Volcanol. Geothermal Res.*, **28**, 257–274.
- Swanson, S.E.; Kienle, J. (1988). The 1986 eruption of Mount St. Augustine: Field test of a hazard evaluation, *J. Geophys. Res.*, **93**, 4500–4520.
- Wallace, P.; Anderson, A.T. (2000). Volatiles in magma, in H. Sigurdsson, B.F. Houghton, S.R. McNutt, H. Rymer, and J. Stix (Eds.), *Encyclopedia of Volcanoes*, Academic Press, New York, pp. 149–170.
- Williams, R.S.; Friedman, J.D. (1970). Satellite observations of effusive volcanism, *Journal of the British Interplanetary Society*, **23**, 441–450.
- Wood, C.A.; Kienle, J. (1990). *Volcanoes of North America*, Cambridge University Press, 354 pp.
- Wooster, M.J.; Rothery, D.A. (1997) Thermal monitoring of Lascar Volcano, Chile, using infrared data from the along-track scanning radiometer: A 1992–1995 time series, *Bull. Volcanol.*, **58**, 566–579.
- Wright, R.; Blake, S.; Harris, A.J.L.; Rothery, D.A. (2001) A simple explanation for the space-based calculation of lava eruption rates, *Earth and Planetary Science Letters*, **192**, 223–233.
- Wright, R.; Flynn, L.P.; Garbeil, H.; Harris, A.J.L.; Pilger, E. (2002) Automated volcanic eruption detection using MODIS, *Remote Sensing of Environment*, **82**, 135–155.
- Wright, R.; Flynn, L.P.; Garbeil, H.; Harris, A.J.L.; Pilger, E. (2004) MODVOLC: Near-real-time thermal monitoring of global volcanism, *J. Volcanol. Geothermal Res.*, **135**, 29–49.

Satellite systems and interactions

I. Matthew Watson, Anupma Prakash

2.1 INTRODUCTION AND BACKGROUND

Remote sensing can be defined as “study of a target (object or phenomenon) where no physical contact with that target is made.” Instead of deriving information from direct contact, the effects of the target on the sensor, typically through some change in the information perceived, are used to derive information about the object or phenomenon. Touching the electric ring of an oven and discovering it is hot is an example of direct sampling. Observing that the ring is glowing red and deducing it is hot is the remote-sensing analog. Thus satellite-based investigation, by definition, relies on remote-sensing techniques.

Remote-sensing techniques are of considerable utility to volcanologists (e.g., Mouginiis-Mark *et al.*, 2000). By their very nature they provide observers with the opportunity to study from a distance what can be an extremely hazardous natural phenomenon. Also, the potential scale of volcanic activity lends itself to the synoptic perspective afforded by satellite-based instruments. Volcanoes may also be geographically remote, such as the Aleutians and Kuriles, or in areas of political unrest, such as in Central and Eastern Africa. Satellite remote sensing negates these problems and provides consistency and continuity of data over large areas of the Earth on a regular basis.

Volcano remote sensing is typically, though not exclusively, the study of the effects of volcanic processes on electromagnetic (EM) radiation (defined and detailed in Section 2.2) which is either gener-

ated naturally (e.g., the Sun, thermal radiation from lava flows) or artificially (e.g., laser, radar). This chapter focuses on the theory of generation, propagation, and interaction of EM radiation with volcanoes and their associated products within a wavelength range from 0.3 μm (3×10^{-7} m, ultraviolet light) through 1 m (microwaves). The aim of this chapter is to ground the reader in the necessary background of the transfer of radiation and its applied uses in remote sensing of volcanoes.

2.2 THE ELECTROMAGNETIC SPECTRUM

2.2.1 Overview, nomenclature, and mathematical framework (see Table 2.1)

Electromagnetic (EM) radiation is produced by all objects with a temperature above absolute zero, associated with the movement of charged particles within the object. EM radiation propagates as two orthogonal waves, with an electric and magnetic component, moving at right angles to the direction of wave propagation (Figure 2.1). These waves travel at a constant speed in a vacuum ($2.9979 \times 10^8 \text{ m s}^{-1}$) given by Maxwell’s equation:

$$c = \frac{1}{\sqrt{\epsilon_0 \mu_0}} \quad (2.1)$$

where c is the speed of light in a vacuum; ϵ_0 is the permittivity (the ability to polarize in response to an

Table 2.1. Nomenclature of symbols used in this chapter.

<i>Symbol</i>	<i>Meaning</i>	<i>Value and units (variable units in parentheses)</i>	<i>Defined in equation</i>
c	Speed of light in a vacuum	$3.00 \times 10^8 \text{ m} \cdot \text{s}^{-1}$	2.1
ε_0	Permittivity of free space	$8.85 \times 10^{-12} \text{ F} \cdot \text{m}^{-1}$	2.1
μ_0	Permeability of free space	$1.26 \times 10^{-6} \text{ H} \cdot \text{m}^{-1}$	2.1
ν	Frequency	(Hz)	2.2
λ	Wavelength	(μm)	2.2
E	Energy	(J)	2.3
h	Planck's constant	$6.63 \times 10^{-34} \text{ J} \cdot \text{s}$	2.3
$B_\lambda(T)$	Blackbody radiance	($\text{W} \cdot \text{m}^{-2} \cdot \mu\text{m}^{-1} \cdot \text{sr}^{-1}$)	2.4
K_B	Boltzmann constant	$1.38 \times 10^{-23} \text{ J} \cdot \text{K}^{-1}$	2.4
T	Temperature	(K)	2.4
λ_{max}	Maximum wavelength	(μm)	2.6
W	Wien's constant	$2,898 \mu\text{m} \cdot \text{K}$	2.6
π	Pi	3.14	2.7
σ	Stefan–Boltzmann constant	$5.67 \times 10^{-8} \text{ W m}^{-2} \text{ K}^{-4}$	2.7
α	Absorption coefficient	(m^{-1})	2.9
C	Concentration	($\text{mol} \cdot \text{m}^{-3}$)	2.9
l	Path length	(m)	2.9
I_{out}	Outgoing intensity	(W m^{-2})	2.9
I_{in}	Incoming intensity	(W m^{-2})	2.9
m	Refractive index	(unitless)	2.11
n	Real part of m	(unitless)	2.11
k	Imaginary part of m	(unitless)	2.11
ε	Emissivity	(unitless)	2.12
R	Reflectivity	(unitless)	2.12
F_{in}	Incident flux density	$\text{J} \cdot \text{Hz}^{-1} \text{ m}^{-2} \cdot \text{s}^1$	2.13
θ_0	Incidence angle	(radians)	2.13
γ	Bistatic scattering coefficient	(unitless)	2.14
θ_1	Exitance angle	(radians)	2.14
Q_{EXT}	Extinction efficiency factor	(unitless)	2.16
C_{EXT}	Extinction cross-section	(unitless)	2.16

<i>Symbol</i>	<i>Meaning</i>	<i>Value and units (variable units in parentheses)</i>	<i>Defined in equation</i>
r	Particle radius	(μm)	2.16
F_{out}	Measured flux density	$\text{J} \cdot \text{Hz}^{-1} \cdot \text{m}^{-2} \cdot \text{s}^1$	2.17
l_a	Absorption length	(cm)	2.17
z	Height	(km)	2.17
γ_a	Absorption coefficient	(cm^{-1})	2.19
γ_s	Scattering coefficient	(cm^{-1})	2.20
F_+	Upward flux density	($\text{J} \cdot \text{Hz}^{-1} \cdot \text{m}^{-2} \cdot \text{s}^1$)	2.20
F_-	Downward flux density	($\text{J} \cdot \text{Hz}^{-1} \cdot \text{m}^{-2} \cdot \text{s}^1$)	2.20
L_f	Upwelling (forward) radiance	($\text{W} \cdot \text{m}^{-2} \cdot \mu\text{m}^{-1} \cdot \text{sr}^{-1}$)	2.22
J_f	Path-added (forward) radiance	($\text{W} \cdot \text{m}^{-2} \cdot \mu\text{m}^{-1} \cdot \text{sr}^{-1}$)	2.22
B_f	Blackbody (forward) radiance	($\text{W} \cdot \text{m}^{-2} \cdot \mu\text{m}^{-1} \cdot \text{sr}^{-1}$)	2.23
p	Pressure	(Pa)	2.24
H	Scale height	(km)	2.24
L_W	Non-specular radiance	($\text{W} \cdot \text{m}^{-2} \cdot \mu\text{m}^{-1} \cdot \text{sr}^{-1}$)	2.25
L_A	Radiance due to aerosol	($\text{W} \cdot \text{m}^{-2} \cdot \mu\text{m}^{-1} \cdot \text{sr}^{-1}$)	2.25
L_G	Specular radiance	($\text{W} \cdot \text{m}^{-2} \cdot \mu\text{m}^{-1} \cdot \text{sr}^{-1}$)	2.25
L_S	At-satellite radiance	($\text{W} \cdot \text{m}^{-2} \cdot \mu\text{m}^{-1} \cdot \text{sr}^{-1}$)	2.25
L_R	Rayleigh radiance	($\text{W} \cdot \text{m}^{-2} \cdot \mu\text{m}^{-1} \cdot \text{sr}^{-1}$)	2.25
t	Atmospheric transmission	(unitless)	2.25
μ	Cosine of satellite zenith angle	(unitless)	2.26
μ_0	Cosine of solar zenith angle	(unitless)	2.26
ω_0	Single scattering albedo	(unitless)	2.26
$p(\theta)$	Phase function	(unitless)	2.26
τ_A	Aerosol optical depth	(unitless)	2.26
β_{EXT}	Extinction coefficient	(m^{-1})	2.27

applied electric field) of free space; and μ_0 is the permeability (the ability to magnetize in response to an applied magnetic field) of free space.

These waves have many properties of interest for remote sensors. The most pertinent are the wave's *wavelength, frequency, amplitude, and energy*.

These descriptors provide fundamental information about how EM waves interact with matter (Section 2.4) and hence can be utilized (inversely) to yield information about the object of study.

Wavelength (λ) and frequency (ν) are most easily explained. If the wave is propagating at the

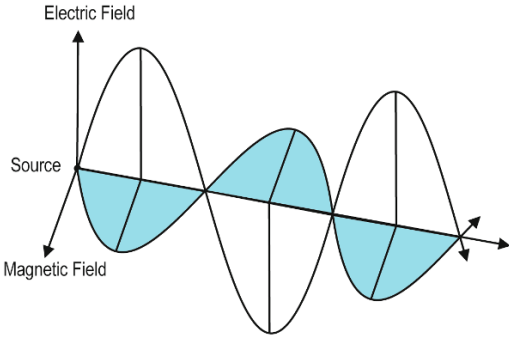


Figure 2.1. Propagation of plane-polarized electromagnetic waves.

speed of light in a given direction a certain number of peaks will pass past a stationary point over a given time interval. This is defined as the wave's frequency normally expressed in hertz (Hz) with units of oscillations per second. The wavelength of the radiation is defined as the inter-trough distance (Figure 2.2). These two properties are inversely related thus:

$$\nu = \frac{c}{\lambda} \tag{2.2}$$

The energy (E) of the wave is also related to the frequency (and thus wavelength) using the following formula:

$$E = h\nu \tag{2.3}$$

where h is Planck's constant ($6.626 \times 10^{-34} \text{ J}\cdot\text{s}$).

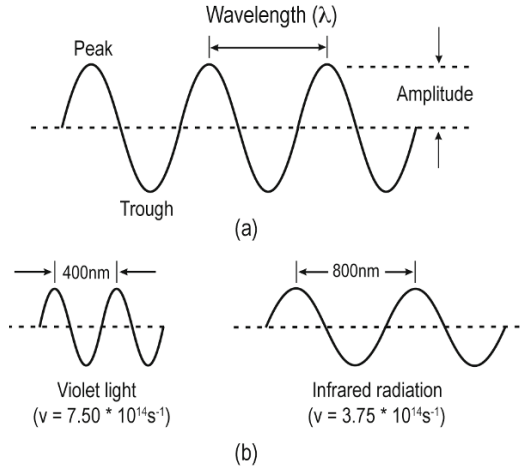


Figure 2.2. The relationship between frequency and wavelength.

Hence the amount of energy is directly proportional to the frequency and inversely proportional to the wavelength of the radiation. The entire range of possible electromagnetic energy constitutes the electromagnetic spectrum (also known as the EM spectrum or simply spectrum) (Figure 2.3). The spectrum is divided into wavelength regions with specific nomenclature. Though for most parts of the spectrum there is a general agreement on the boundaries and nomenclature of the regions and subregions, the infrared portion of the spectrum is one where there is considerable debate and little

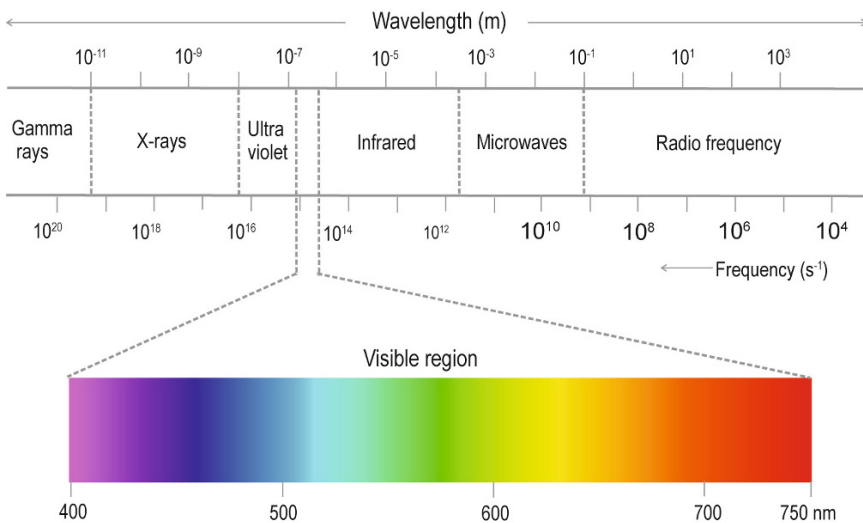


Figure 2.3. The electromagnetic spectrum.

Table 2.2. Regions of the electromagnetic spectrum.

Region	Sub-region	Popular acronym	Wavelength ranges
Gamma ray		Gamma	<0.03 nm
X-ray			0.03–30 nm
Ultraviolet		UV	0.3–0.4 mm
Visible		VIS	0.4–0.7 mm
Infrared	Near-infrared	NIR	0.7–1.3 μm
	Shortwave infrared	SWIR	1.3–3.0 μm
	Mid-infrared	MIR	3.0–8.0 μm
	Thermal infrared	TIR	8.0–14 μm
Microwave	K band		0.8–2.4 cm
	X band		2.4–3.8 cm
	C band		3.8–7.5 cm
	S band		7.5–15 cm
	L band		15.0–30.0 cm
	P band		30.0–100 cm
Radiowave			>100 cm

consensus. Throughout this book, we conform to the nomenclature given in Table 2.2.

It should be noted that, due to stratospheric ozone layer absorption, solar radiation near the Earth's surface has a short-wavelength limit at 0.29 μm (290 nm). Therefore, the region of the UV spectrum with an upper wavelength of about 290 nm is called solar-blind UV or blind UV. UV detectors with a long-wavelength cutoff below 290 nm are usually called solar-blind detectors.

In terms of remote sensing of volcanoes a range of wavelengths between 0.3 μm (3×10^{-7} m, the edge of the blind UV) and 1×10^6 μm (1 m, the far edge of the microwave region) is of special significance (see Chapter 5)

The generation of EM waves is a direct result of the oscillation of electric charge within matter. The oscillation occurs over a continuous range of frequencies and thus emits radiation at all wavelengths. However, radiation is not emitted equally at all wavelengths, rather it is distributed according to the object's emission spectrum. This spectrum

depends strongly on the temperature of the object and this interrelationship was determined by Max Planck in 1894. The discovery was aided by the concept of a *blackbody*, an object in thermal equilibrium with its surroundings that perfectly absorbs (see Section 2.4) and emits radiation. Planck was able to show that the intensity of radiation emitted by a blackbody varied with wavelength as a function of temperature as follows:

$$B_{\lambda}(T) = \frac{2hc^2}{\lambda^5 (e^{hc/\lambda K_B T} - 1)} \quad (2.4)$$

where $B_{\lambda}(T)$ is the blackbody radiance for a temperature (T); and K_B is the Boltzmann constant. Inverting the Planck function to solve for T shows that the higher the temperature the more energy is emitted at shorter wavelength (higher energy). This is also easily observed by plotting the emission spectra, derived from the Planck function, for objects of different temperature (Figure 2.4).

The position of the maximum in the emission spectrum is especially indicative of the relationship between wavelength and temperature and can be derived by setting the first derivative to zero (shown below):

$$\frac{\partial B_{\lambda}}{\partial \lambda} = 0 \quad (2.5)$$

which yields Wien's displacement law:

$$\lambda_{\max} = \frac{W}{T} \quad (2.6)$$

where W is Wien's constant (2,898 $\mu\text{m K}$).

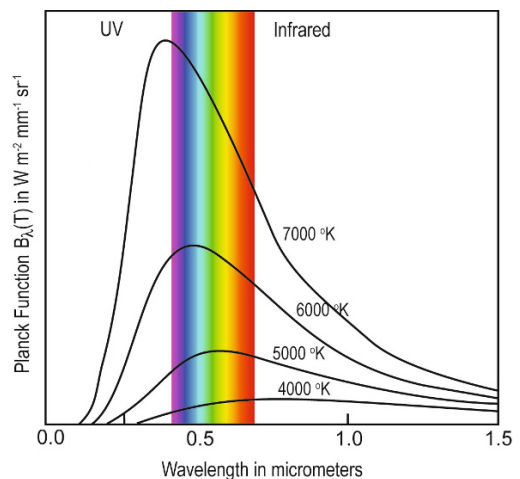


Figure 2.4. Planck (blackbody) curves for objects of different temperature.

Using Wien's displacement law yields a peak in the Planck function of $0.5\ \mu\text{m}$ for an object at $5,870\ \text{K}$ (the temperature of the surface of the Sun) and $10.0\ \mu\text{m}$ for an object at $290\ \text{K}$ (a temperature representative of the Earth's surface). This shows that the peak of the Sun's emitted radiation falls in the visible region of the EM spectrum, and the peak of Earth's emitted radiation falls in the thermal infrared region of the EM spectrum. It also shows that the Sun is emitting greater amounts of high-energy radiation relative to the Earth, because it is hotter.

It can also be observed in Figure 2.4 that the hotter an object is the more radiation it emits in total. The amount of energy emitted by an object of a given temperature over all wavelengths is described by the Stefan–Boltzmann equation, the integration of the Planck function with respect to wavelength:

$$B(T) = \int_0^{\infty} B_{\lambda}(T) d\lambda = \frac{\sigma}{\pi} T^4 \quad (2.7)$$

where σ is the Stefan–Boltzmann constant ($5.67 \times 10^{-8}\ \text{W m}^{-2}\ \text{K}^{-4}$).

This relationship indicates that the amount of energy emitted is extremely sensitive to the temperature of the object. In the case of the Sun and the Earth, an equivalent area of the Sun is emitting nearly 160,000 times as much radiation as the Earth.

2.3 INTRODUCTION TO REMOTE SENSING

2.3.1 Inverse problems

Mathematical solutions can be divided into two distinct types: forward and inverse. A simple thought experiment, involving a new species of animal, helps elucidate the differing rationales, issues, and limitations of each type. Given a complete knowledge of the animal (its height, weight distribution, skeletal structure, speed of motion, etc.) and of the ground upon which it walks (moisture content, compressibility, softness, etc.) a perfectly accurate prediction of the tracks of the animal can be made. This is a classic forward solution. The problem is well constrained and perfect knowledge of the system yields an exactly accurate result.

The inverse analog to this problem is, upon finding the tracks, deriving what the animal looked

like. Here the issues associated with inverse solution become obvious. The distance between the footprints is a function of the size of the animal and the speed at which it was traveling. Given no a priori information about the animal it is impossible to derive a unique solution to the question “how fast was the animal traveling?” The problem is ill-constrained. In this case there is one piece of information and two variables, producing not one but a suite of possible combinations of answers.

Remote sensing, by its very nature, is a study of inverse problems. As opposed to conventional field-based temperature measurement (e.g., using mercury thermometers or probes), in remote sensing the sensor does not make physical contact with the ground. Instead the temperature is derived from the amount of radiation leaving the ground, which is a function of temperature and wavelength (see Section 2.3.2 for a more complete overview). However, there are many caveats to this calculation. The amount of radiation emitted by the ground is also modulated by its emissivity (a description of the efficiency of the ground to emit). This radiation also has to travel through the atmosphere to the sensor and is therefore a complex descriptor of the ground's behavior and the composition of the atmosphere. Only by decoupling these effects can the true ground temperature be accurately determined.

2.3.2 Modes of remote sensing

Active and passive techniques are used to acquire information about the Earth's surface and/or the atmosphere by the interaction of radiation with matter. An active technique involves the generation of energy and capture of its returning signal, after having undergone some transformation. Passive remote sensing is the acquisition of radiation being produced without instrumental stimulation and records natural emission or reflection from the target. A radar system, whose sensor both transmits and receives radiation, is an example of an active sensor. An infrared instrument, simply collecting radiation being produced by a target due to its own temperature, without additional experimental stimulation, is an example of a passive sensor.

2.3.3 Platforms and orbit types

Several types of orbits exist that can be used to address different scientific issues. The two most commonly used orbits are geostationary or geosyn-

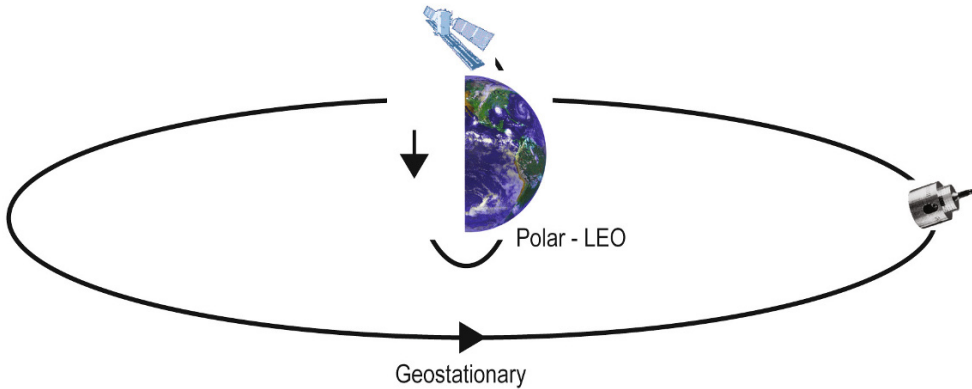


Figure 2.5. Geostationary and low Earth orbits.

chronous (GEO) and low Earth orbit (LEO) (Figure 2.5). Both have advantages and disadvantages in terms of the resolutions of the images acquired (see Section 2.3.4 for a more complete description of types of resolution and their interrelationships).

A geostationary orbit can be defined as an orbit at the distance required to keep the satellite stationary (in the Earth's frame of reference) above a single point above the equator. This is achieved by having an orbital period (the amount of time it takes to make a single orbit of the Earth) of exactly the same time as the period of a single rotation of the Earth. The distance required to achieve this orbit (from the Earth's surface) is approximately 35,800 km above mean sea level. Applications of these types of orbits include satellites designed to study large-scale systems at short intervals, such as weather satellites. Examples used by volcanologists are the GOES (Geostationary Operational Environmental Satellites) suite to observe drifting volcanic ash clouds (e.g., Ellrod and Schreiner, 2004) and thermal anomalies (Harris *et al.*, 2001).

LEO can be further subdivided into two orbit types based on their inclination relative to the poles. A polar orbit is one with an inclination of 90° . This orbit has the advantage of being able to acquire an image of almost every point on the Earth's surface. If the inclination of the orbit changes then the northernmost and southernmost parts of the globe become inaccessible. This is called the terminator effect. This is sometimes preferential, as in a near-polar, Sun-synchronous type orbit where the orbital plane of the satellite precesses (rotates) slightly to keep pace with the Earth's revolution around the Sun. This has the effect of making the satellite cross any given point on the orbit at roughly the same

time each day. This becomes important when the object of study has diurnal temporal dependence (e.g., relative humidity) or if, as in the case of Radarsat, the instrument is partially powered by solar panels that need to be constantly pointed at the Sun. Most Earth-observing satellites are therefore designed to have near-polar, Sun-synchronous LEOs, and strictly polar orbits are practically never used. LEO sensors are heavily used by volcanologists; for example, to map lava flows using Landsat (Oppenheimer, 1991) or to quantify volcanic emissions using MODIS (Watson *et al.*, 2004).

2.3.4 Spatial, temporal, and spectral resolution

Resolution refers to the resolvable limit of a system and can be broadly described as a measure of the system's accuracy. In the context of spatial, temporal, and spectral resolution, satellite data resolution can be defined using the minimum distance, time, and wavelength range covered by the satellite sensor.

The spatial resolution of a sensor is a measure of the smallest angular or linear separation between two objects that can be resolved by sensor. In a digital image, the resolution is limited by the pixel size (i.e., the smallest resolvable object cannot be smaller than the pixel size). The pixel size is determined by the sampling distance. Image resolution and pixel size are often used interchangeably. In reality, they are not equivalent. An image sampled at a small pixel size does not necessarily have a high resolution. If an instrument has a spatial resolution of 10 m, then no objects smaller than 10×10 m can

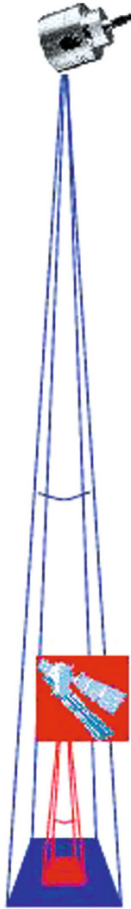


Figure 2.6. Instantaneous field of view and spatial resolution.

be distinguished from their background. This does not necessarily mean they cannot be *detected*. If the spatial resolution doubles (i.e., becomes 5 m), the image data volume increases by a factor of 4. Spatial resolution is a function of the distance from the Earth's surface and the instantaneous field of view (IFOV) of the instrument (Figure 2.6).

The temporal resolution of the instrument is a function of the repeat time; that is, the time it takes to re-acquire an image of the same point on the Earth's surface. For a geostationary orbit this is simply determined by the speed at which the data can be transferred to a receiving station and the memory of the recorder cleared. This is typically on the order of a few tens of minutes. At the other extreme a LEO satellite with a narrow swath width

might have a repeat time on the order of 15 days (typical) to several months (to give an extremely dense network of nadir tracks).

The spectral resolution of the instrument is characterized by the range of wavelengths over which a single measurement is acquired. It is a function of the width of the channel (in units of wavelength) encompassed by a measurement and the distance between the center points of separate channels. A broad single channel constitutes a panchromatic band (i.e., encompasses a significant range of wavelengths). An instrument with several discrete channels (typically on the order of 0.5–1.0 μm wide for an IR instrument) can be described as multispectral. As the number of channels increase and the spectral bandwidth of individual channels reduce (finer/higher spectral resolution), we transition from multispectral sensors to hyperspectral sensors.

The three different resolutions are not completely independent. Spatial resolution is strongly inversely related to temporal resolution, wavelength, and spectral resolution. The first relationship is somewhat obvious, the second and third less so. It can be shown that the spatial resolution of the instrument is a function of the distance to the target. The farther away the sensor is from the target the less detail can be resolved (Figure 2.6). For example, a car's license plate can be easily read by most people using the naked eye at a distance of 1 m and by no one at a distance of 1 km.

The relationship between wavelength and spatial resolution is defined by the diffraction limit of a finite aperture. Because any system's optical dimensions are in some way constrained it can be shown that angular resolution can be approximated by λ/D , where λ is the wavelength and D is the diameter of the aperture or lens. This phenomenon is best detailed in two examples (after Rees, 2001). First, consider a visible sensor 1,000 km above the surface of the Earth detecting radiation at 0.5 μm through a lens 5 cm in diameter. Using diffraction approximation it can be derived that the angular resolution is limited to about 10^{-5} radians or a spatial resolution of about 10 m. In contrast a passive microwave radiometer might have an antenna 1 m in diameter detecting radiation of 3 cm wavelength. At the same altitude (1,000 km) this would yield an angular resolution of 3×10^{-2} radians and a spatial resolution of 30 km. There are ways to circumvent the aperture limit (such as synthetic aperture radar) which are discussed in Chapter 8, but beyond the scope of this chapter.

2.4 RADIATIVE TRANSFER AND ATMOSPHERIC WINDOWS

2.4.1 Definitions

In order to ground the reader in an understanding of the behavior of radiation it is helpful to start with a series of definitions and interrelationships between the different ways EM radiation can interact with matter (Figure 2.7). The following is a series of simple definitions of the potential outcomes of radiation/matter interaction.

Absorption can be defined as the interaction of matter with radiation where a change in quantized energy level is observed. Absorption is the inter-

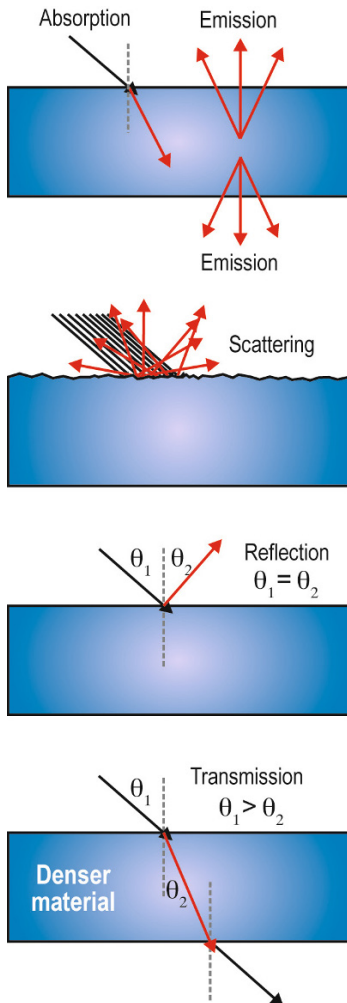


Figure 2.7. Energy-matter interaction.

action of radiation with the dipolar structure of the target in a number of different regimes of varying energy based upon the bonding of the target's molecular structure. The energy absorbed by the target is typically emitted at longer wavelengths.

Emission describes the EM radiation given out (emitted) by a target material due to its thermal state. This is a function of the temperature of the object (Planck's Law, see Section 2.2.1) and the ability of the material to absorb, emit, and reflect radiation. In general the hotter the object the more radiation (in total) it will emit, and that emitted energy will be at lower wavelength. Emission occurs in all directions.

Scattering is a description of the interaction of EM radiation with atoms, molecules, and particles where the wavelength of the radiation is unaffected (given we make the assumption that the scattering is *elastic* and ignore fluorescence) but the exitance angle is a function of the target's size, composition, and roughness. The term scattering is typically, though not exclusively, applied to atmospheric constituents; if the radiation is redirected by a surface then it is termed reflection.

Reflection describes the redirection of radiation by a surface. Again the wavelength of the radiation is unaffected. The roughness of the surface dictates the angles at which the radiation leaves the target. Note that a surface may not be uniformly rough at all wavelength scales. For a perfectly smooth target the incident angle (θ_1) is equal to the exitance angle (θ_2).

Refraction is the interaction of radiation at a surface or boundary. One conceptual idea (offered by Huygens) is that EM radiation travels at different speeds through different materials, and it is this action across the boundary that ultimately alters the direction of propagation. The ratio of the sine of the incident angle (θ_1) to propagation angle (refraction angle, θ_2) is equal to the ratio of speed in which the wave propagates through the two media.

Transmission is the lack of attenuation of EM radiation. Transmitted radiation appears to pass unscathed (in terms of intensity and wavelength) through the target. As per the concept of total energy (i.e., the total amount of radiation must sum to 1), the following relationships can be used to describe the transfer of radiation. Note that two general descriptors of the prevention of EM radiation reaching a sensor are *extinction* and *attenuation*, the sum of the processes of absorption

and scattering:

$$\left. \begin{aligned} (a) \quad & 1 = \text{absorption} + \text{scattering} + \text{transmission} \\ (b) \quad & \text{transmission} = 1 - \text{emission} + \text{scattering} \\ (c) \quad & \text{absorption} + \text{scattering} = \text{extinction} \\ (d) \quad & \text{transmission} = 1 - \text{extinction} \end{aligned} \right\} (2.8)$$

2.4.2 Interaction of radiation with matter

Energy from EM radiation cannot be destroyed (rule of the conservation of energy), only converted into a number of different states of increased energy within the target, or the wave can be deflected (in the case of scattering and reflection) and no energy transferred to the target.

The radiation attenuated (prevented from passing through the target and leaving at the same angle) can be detected as a reduction in path radiation according to the Beer–Bouguer–Lambert Law:

$$I_{\text{out}} = I_{\text{in}} e^{-\alpha c l} \quad (2.9)$$

The attenuation signal is then a function of the medium’s ability to attenuate radiation of a given wavelength (α), the concentration of the medium (c), and its path length (l) (see also Figure 2.8). In the context of remote sensing of the Earth’s surface I_{in} is the variable of interest and the exponents need to be taken into account to get an accurate description of the surface-leaving radiance (called atmospheric correction: Section 2.5). If the atmosphere itself is the target of interest then I_{in} is either known or estimated and the exponents (either singularly or collectively) are the variables of interest.

The three main processes by which radiation can be modified by the target will now be discussed in more detail. These are absorption, emission, and reflection/scattering. At thermal equilibrium absorption (coefficient α) and emission (E) are inextricably linked through Kirchhoff’s Law:

$$E_{\lambda} = \alpha_{\lambda} B_{\lambda}(T) \quad (2.10)$$

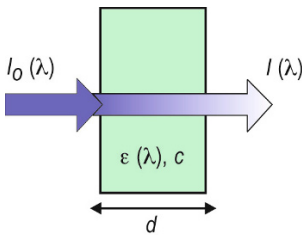


Figure 2.8. Beer–Bouguer–Lambert Law.

The fact that the absorption coefficient α is a function of wavelength is of great importance when discussing absorption and emission. The frequency (proportional to $1/\lambda$) of incident EM radiation controls what type of absorptive interaction with the target occurs. The higher the frequency the greater the energy associated with that wave and the more energetic the excitation caused by the wave–matter interaction. For example, visible radiation at a frequency of 4.3×10^{14} – 7.5×10^{14} Hz (0.4–0.7 μm wavelength) causes changes in the configuration of electrons, specifically the orbital configuration of outer (valent) shell electrons. In comparison microwave energy with a frequency of 1×10^{11} Hz (1,000 μm) alters the way in which the target’s molecules rotate. Rotational energy levels are closer together than electronic transitional energy levels and hence require EM radiation of less energy to change their state. A complete picture of which molecular mechanisms are associated with which frequencies (and wavelengths) can be seen in Figure 2.9. Note that as we are currently considering molecular interactions, the situation becomes much more complex for rigid media (e.g., solids).

The emission spectrum of a target is governed to a first order by the temperature of the target (Equation 2.4) if the target approximates a blackbody emitter. Most objects in nature do not, and their emission spectra are a complex function of the blackbody curve and the emissivity of the target. A simple thermodynamic argument can be invoked to suggest that if the target is in thermal equilibrium then it must be absorbing and emitting at the same rate (called Kirchhoff’s Law). The emissivity of the material is governed by its refractive index, a wavelength-dependent complex number (m) of the form:

$$m = n + ki \quad (2.11)$$

The real part of the refractive index (n) describes the reflective properties of the material, and the imaginary part (k) relates to the absorptive properties.

According to Kirchhoff’s law, absorption equals emission; it can therefore be deduced that the emissivity (ϵ) of an opaque surface can also be defined, as a consequence of the equation scheme (2.8) as:

$$\epsilon = 1 - R \quad (2.12)$$

Reflection and reflectivity (R) illustrate the scattering of radiation by a surface (as opposed to scattering which is a term normally reserved for the interaction of radiation with atmospheric gases

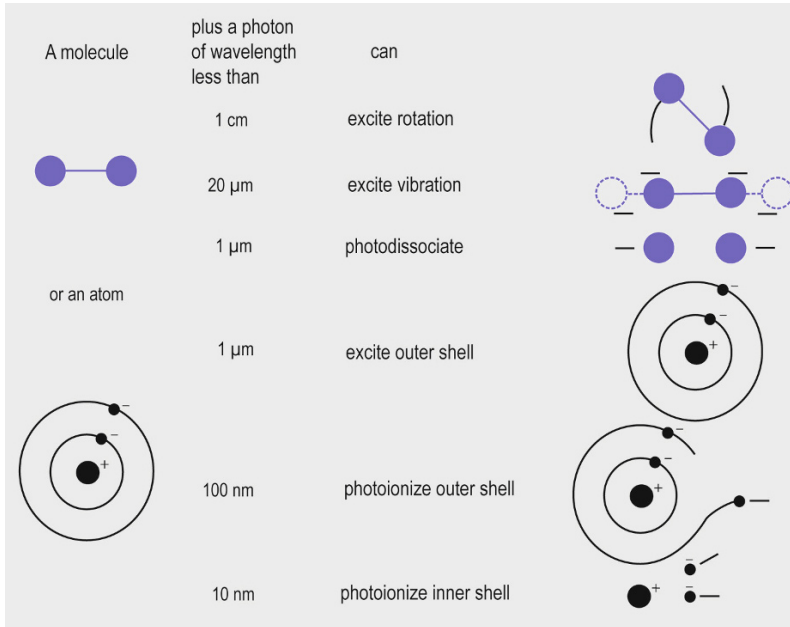


Figure 2.9. The relationship between energy and transition type.

and particles). These terms are, in reality, interchangeable and bridged by a third term, albedo. Both surfaces, such as snowpack, and aerosols, such as clouds, can be defined in terms of their albedo.

Again, the reflectivity is somewhat controlled by the refractive index, specifically (n) the real (non-imaginary) part in Equation (2.11). If a surface is opaque it can be assumed that all the radiation that is not absorbed is reflected. For a perfectly flat surface a simple description, called specular reflectance, can be assumed, where the exitance angle of the radiation is simply equal to the angle of incidence. The other end member of scattering is called Lambertian scattering, where the surface is *ideally* rough so that the incoming radiation is scattered equally in all directions.

Clearly, most surfaces are neither specular nor Lambertian but somewhere in between. This type of scattering is called non-specular, of which Lambertian is a specific and unrealistic end member. In fact, as seen in Section 2.5.2, scattering can be modeled simply as the sum of specular and non-specular reflection. Another useful descriptor is the bidirectional reflection function or BDRF defined as:

$$\text{BDRF} = \pi I_{\text{out}} / F_{\text{in}} \cos \theta_0 \quad (2.13)$$

where I_{out} is the intensity of reflected radiation; F_{in}

is the incident flux density; and θ_0 is the angle of incidence.

In radar systems BDRF is normally replaced by the *bistatic scattering coefficient* (γ):

$$\gamma = (\text{BDRF})4\pi \cos \theta_1 \quad (2.14)$$

where θ_1 is the angle between the outgoing radiation and a plane line normal to the surface.

The basic principles of scattering apply equally to reflectance. As an example, the green color of the leaves of a tree is a function of the reflectivity of the leaf. This in turn is explained by the absorption of visible light by chlorophyll pigments in the leaf. Chlorophyll absorbs strongly in all regions of the visible spectrum. However, chlorophyll absorbs slightly less strongly at the wavelength of green light, relative to other wavelengths. As a ramification of Equation (2.12) this means that green light is most reflected hence the leaf appears green.

Scattering of radiation by atmospheric constituents have an additional level of complexity when compared with a solely absorptive regime. It is a function of wavelength, scatterer size, and the angle of the incoming radiation. The mechanisms for scattering are complex and can be subdivided into three categories as a function of the ratio between the size of the scatterer and the wavelength of inci-

dent light. If the scatterer's diameter is much, much less than the wavelength of incident light then the scattering that occurs can be described using the Rayleigh scattering formula:

$$I_{\text{out}} = I_{\text{in}} [1 + \cos^2 \theta_0] \left(\frac{1}{\lambda}\right)^4 |\psi|^2 / r_p^2 \quad (2.15)$$

where ψ is the polarizability; and r_p is the distance to the particle.

This is most robustly applied to scatterers with a single oscillating dipole and indicates that scattering increases strongly as wavelength decreases. This has commonly observable ramifications including the color of the sky. The sky appears blue because N_2 and O_2 molecules in the atmosphere scatter shorter wavelengths (i.e., blue light) more than longer wavelengths from the plane of incidence. In the Rayleigh regime, light is strongly scattered at all angles relative to the angle of incidence.

The next regime (Mie scattering) occurs as the scatterer's diameter approaches the wavelength of incident light, the region where scattering is strongest. The mathematic theory is more complex than in the Rayleigh regime and the derivation of Mie scattering theory is well beyond the scope of this chapter. As a general rule, however, the larger the particle the more complicated the pattern of scattered light and the more the scattering occurs in the forward direction, until non-selective scattering (see below) predominates.

A convenient way to consider the theory is in the context of the scattering cross-section, a critical

component of the Mie derivation. The scattering cross-section represents the size of the particle required to cause the attenuation calculated if simply the geometric area is considered. Hence the extinction efficiency factor is related to the scattering cross-section thus:

$$Q_{\text{EXT}} = \frac{C_{\text{EXT}}}{\pi r^2} \quad (2.16)$$

where Q_{EXT} is the extinction efficiency factor, defined as the ratio between the extinction cross-section (C_{EXT}) and the geometric area of a particle with radius r .

Plotting the extinction efficiency factor against the size parameter $X(2\pi r/\lambda)$ is instructive in understanding the relationship within the different regimes (Figure 2.10). Here the different scattering regions are clearly delimited. As X tends towards 1 the extinction efficiency factor increases approximately as to $1/\lambda^4$ (from Rayleigh scattering theory). At the edge of the Mie region the situation becomes more complex with the addition of large-scale and small-scale oscillations. It is the presence of the edges of particles and their complex interaction that becomes increasingly important. It is the behavior of complex interference patterns that underpins Mie theory.

Rather counterintuitively the extinction efficiency factor tends towards 2 as the ratio r/λ increases into the third scattering regime, the non-selective regime past the large particle limit. Here the extinction efficiency factor is clearly independent of the r/λ ratio and remains at 2 because no

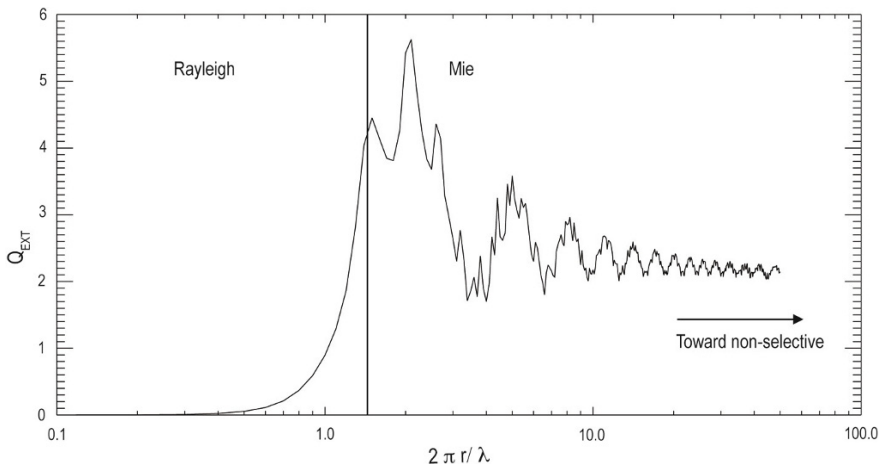


Figure 2.10. Plot of Q_{EXT} vs. $X(2\pi r/\lambda)$ showing Rayleigh, Mie, and non-selective scattering regimes for an andesite ash particle of $4\ \mu\text{m}$ radius.

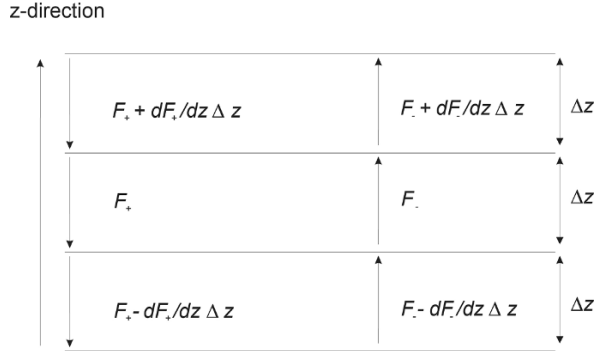


Figure 2.11. Three-slab radiative transfer model (after Rees, 2001).

matter how large particles become they still exhibit edge effects. The physical ramifications of a change of regime (from Mie to non-selective scattering) are observable in the natural world. Clouds appear white due to non-selective scattering of visible light by large ($>50 \mu\text{m}$) particles whereas sunsets are oranges and reds as the shorter wavelengths of visible light are removed by smaller atmospheric particles ($<10 \mu\text{m}$) through Mie scattering.

2.4.3 The radiative transfer equation

The previously described conceptual framework can be represented in a single mathematical form by the radiative transfer equation. The term transfer implies the propagation of radiation from one place to another. In order to discuss the radiative transfer equation in detail a physical framework of an atmosphere of several parallel slabs needs to be invoked (Figure 2.11). Here radiation can be seen to propagate to and from any of the three layers into adjacent layers.

Using the theoretic framework suggested by Rees (2001), it can be shown, from the starting point, that the density of flux (F) varies according to

$$F_{\text{out}} = F_{\text{in}} \exp\left(-\frac{z}{l_a}\right) \quad (2.17)$$

where F_{out} is the exitant flux; z is the distance (in the case of the atmosphere, height); and l_a is the absorption length coefficient and hence

$$\frac{dF}{dz} = -\frac{F}{l_a} \quad (2.18)$$

where

$$\gamma_a = \frac{1}{l_a} \quad (2.19)$$

where γ_a is the absorption coefficient.

It can be shown, given that we assume that absorption occurs in the $+z$ direction and scattering occurs only in the $-z$ direction, that the flux of radiation propagating in the forward direction through the middle slab can be described in terms of the transmission of radiation from the level below and backscattering from the level above. This can be mathematically defined as:

$$\frac{dF_+}{dz} = -(\gamma_a + \gamma_s)F_+ + \gamma_s F_- \quad (2.20)$$

where F_+ is the flux density in the $+z$ direction; F_- is the flux density in the $-z$ direction; and γ_s is the scattering coefficient.

Correspondingly the backward traveling radiation in the slab can be defined as

$$\frac{dF_-}{dz} = (\gamma_a + \gamma_s)F_+ - \gamma_s F_- \quad (2.21)$$

In order to determine the radiative transfer over three dimensions (i.e., something approximating reality) we have to move from the change in flux from one slab to another to a change in radiance. This nomenclature takes into account the fact that only considering backward scattering is a gross oversimplification. Conventionally this is done with consideration of frequency rather than wavelength. Equation (2.20) can be converted to consideration of radiance thus:

$$\frac{dL_f}{dz} = -(\gamma_a + \gamma_s)L_f + \gamma_s J_f \quad (2.22)$$

where L_f and J_f are the forward-propagating and path-added (by scattering) radiances.

Addition of an emission term yields a complete full description of radiative transfer in the $+z$

direction:

$$\frac{dL_f}{dz} = -(\gamma_a + \gamma_s)L_f + \gamma_s J_f + \gamma_a B_f \quad (2.23)$$

where B_f is the blackbody (Planck) spectral radiance of an object with temperature T .

It is important to note that the sum of the absorption and scattering coefficients is important in the radiative transfer equation. The ratio of the coefficients is critical in understanding the way a material will appear. Typically, highly particulate materials, such as clouds, appear white as the scattering coefficient overwhelms the absorption coefficient, due to the fact that the scattering coefficient is dependent on the number of particle surfaces,

whereas the absorption coefficient is not, allowing scattering to dominate.

2.4.4 The atmosphere

Knowledge of the atmosphere is important in all satellite remote sensing. Either the atmosphere is the subject of study or the effects of the atmosphere require careful removal before information about the surface can be accurately determined. The pressure profile and the vertical chemical and temperature structure of the atmosphere control its radiative effects and will be briefly described here for completeness.

The vertical temperature profile of the atmosphere has been used in the past to delimit regions

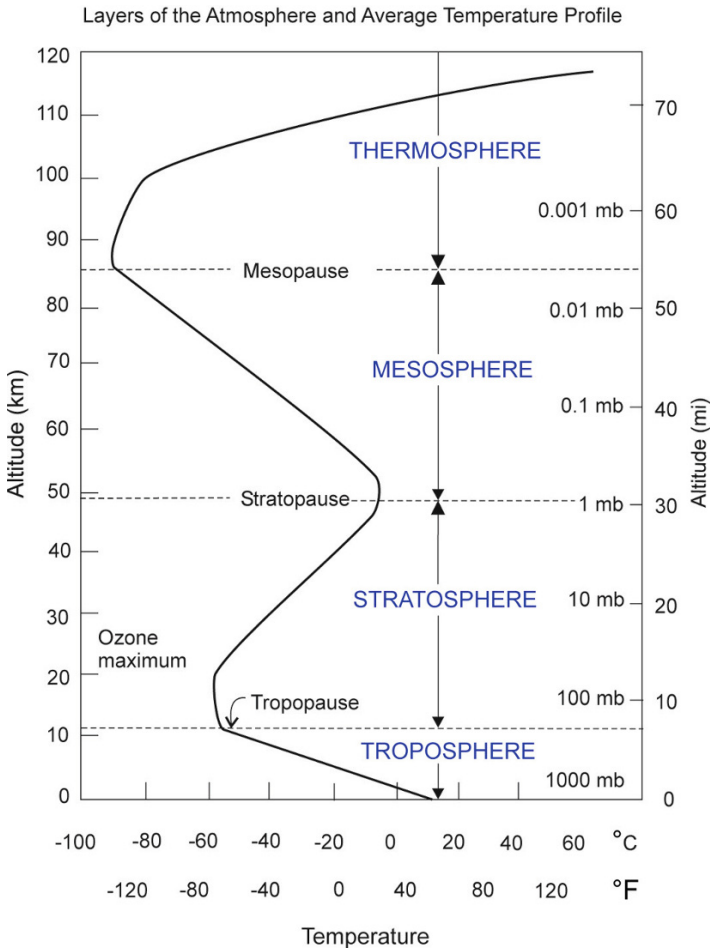


Figure 2.12a. Vertical structure of the atmosphere with respect to temperature.

of the atmosphere (Figure 2.12a). The lowest part of the atmosphere, the troposphere, is a well-mixed and turbulent regime with a negative temperature gradient (lapse rate) with increasing height. Above the troposphere is the stratosphere, a much drier layer with little vertical mixing with increasing temperature with altitude. The tropopause is the first point of inflection in the temperature profile and provides an effective boundary to all but the most buoyant air parcels. Above the stratosphere (and separated by the stratopause) is the mesosphere, another region of negative lapse rate. Above that is a second inflection (the mesopause) and another region with a positive temperature gradient, the thermosphere. In terms of volcano remote sensing, including both removal of atmospheric effects to

accurately quantify surficial products and detection of subaerial emissions, the troposphere and stratosphere are the most significant regions.

The pressure structure of the atmosphere (Figure 2.12b) is much more straightforward. Pressure decreases exponentially as a function of height and can be approximated thus

$$p(z) = p(0)e^{-z/H} \quad (2.24)$$

where p is the pressure; and H is the scale height (approximately 8 km of the troposphere).

Two ramifications of this equation are that half the mass of the atmosphere lies beneath a height of 5.5 km and 99% of the atmosphere is contained within the bottom 30 km.

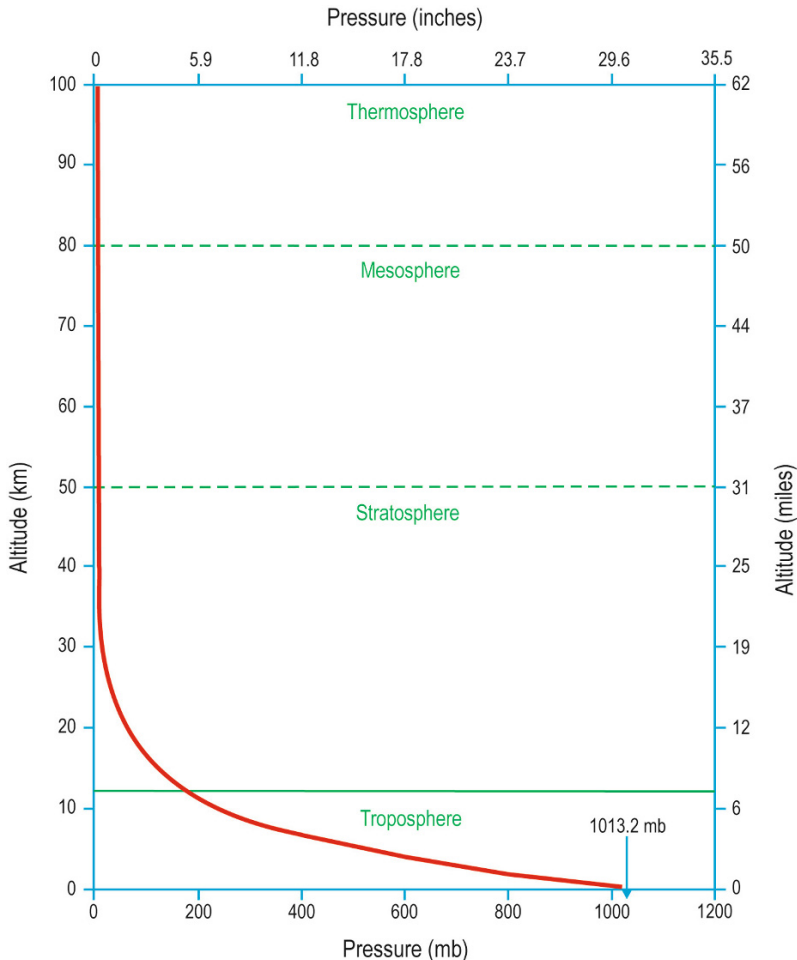


Figure 2.12b. Vertical structure of the atmosphere with respect to pressure.

The atmosphere is made up mostly of N_2 and O_2 making up 99% of the atmosphere (78% and 21%, respectively). Nitrogen is chemically and radiatively unreactive and the concentration of O_2 varies as a function of pressure. Ignoring water vapor for the moment the next two most abundant gases (Ar and CO_2) also vary as a simple function of altitude. A radiative model of the atmosphere based on these four species (>99% of the atmosphere) would actually be relatively straightforward.

It is the highly variable species, particularly H_2O and O_3 , that add the complexity in the way the atmosphere behaves radiatively. O_3 , for example, varies with altitude as a function of the UV radiation and O_2 required to make it. O_3 exists in a layer with a peak concentration at about 35 km because above this boundary there is not enough O_2 and below there is not enough UV radiation (it is strongly attenuated by the atmosphere). H_2O is even more complicated. Not only does the concentration of water vapor vary on almost every scale upon which it can be measured, it is also spectrally spectacularly complex. In terms of correcting the surface-leaving radiance for the effects of the atmosphere, understanding the vertical distribution of water vapor (also the most variable of all atmospheric species) is most critical.

2.4.5 Atmospheric windows

The atmosphere plays a vital role in the global Earth system and is studied extensively using remote-sensing techniques. Volcanic contributions, such as ash (Chapter 5) and gases (Chapter 6), perturb the atmosphere and affect the radiative transfer (and hence, potentially, climate) of the

atmosphere. Study of surficial volcanic products also requires an understanding of the atmosphere and its radiative effects. In either case the transparency of the atmosphere is critical in facilitating effective remote sensing. The atmosphere is made up of a series of wavelength regions of higher atmospheric transmission (Figure 2.13) which are targeted when the position of a satellite sensor's channels are being decided. In general, radiation of wavelengths above 10 mm are transmitted through the atmosphere and radiation below $0.3 \mu m$ is not. A second region of high opacity exists between $20 \mu m$ and 2 mm. The remaining regions, particularly those between 0.3 and $20 \mu m$ are complex and highly variable over short-wavelength ranges (Figure 2.13). The regions of high transmission are called "atmospheric windows" as they permit study of the Earth's surface (or the lower atmosphere) from space.

2.5 ATMOSPHERIC CORRECTION

Even though the atmosphere is relatively transparent at the wavelengths at which most satellite sensors operate, the atmosphere still contributes significantly to the at-satellite radiance. Whether the object of study is subaerial emissions of ash or pyroclastic deposits, correction of the detected radiance for the presence of the atmosphere is vital. This can be undertaken in a number of ways that can be binned into three categories. Empirical, or image-based techniques, determine the contribution of the atmosphere to the signal using information contained within the image only. Second, ground truthing can be used to determine the effects of the

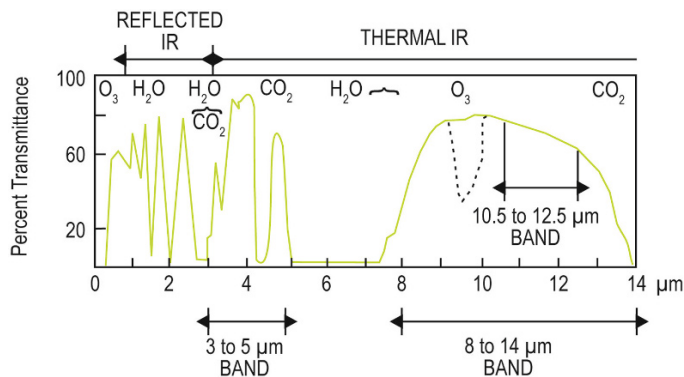


Figure 2.13. Atmospheric windows.

atmosphere by indicating what a known target would look like without the presence of an atmosphere. Third, radiative transfer models use external information about the atmosphere, specifically its vertical temperature and pressure and water vapor profile, to calculate (and hence remove) the contribution of the atmosphere.

There are advantages to all types of atmospheric corrections. Empirical techniques do not require external information, are computationally cheap, and can be undertaken simply with the image under study. Ground truthing offers an inexpensive solution that provides a quantitative and accurate solution. Modeling techniques are most robust and provide information about radiative transfer in the vertical profile, rather than a single column-averaged value.

2.5.1 Using empirical techniques and ground truthing

Intra-image atmospheric correction techniques vary depending on the wavelength range of the spectral bands of the image. As previously discussed, radiation at shorter wavelengths in the 0.3–20 μm range are much more highly scattered relative to longer wavelengths. The near UV, visible, and near IR can be considered scattering only regimes. For longer wavelengths the opposite holds true. For radiation $>8\mu\text{m}$ the atmosphere can be considered almost exclusively absorptive. Intermediate wavelengths, particularly the SWIR, must have a complete model of both scattering and absorption by the atmosphere. In short, reflected solar radiation is more likely to be mostly scattered in the atmosphere and emitted terrestrial radiation is more likely to be absorbed.

In the VNIR reflective regime the contribution of the atmosphere is likely to be a brightening of the image as incoming solar radiation is backscattered by the atmosphere before reaching the Earth. This path-added scattering explains why the horizon at distance has a paler appearance than similar features in the mid-ground and foreground. The reflectance contribution of the atmosphere can be derived using ground truthing and image-based techniques. Ground truthing involves selecting a target, typically dark in the NIR (such as a water body) and taking ground-based measurements of the reflectance of the target at some small distance above the target (on the order of centimeters to meters). This reflectance can then be assumed to truly represent the reflectance of the target, and the difference

between that measurement and the at-satellite reflectance is the contribution of the atmosphere. Ground truthing should be undertaken at several targets within the image to correct for variations in the reflectance associated with the angular dependence of scattering in the atmosphere and must also consider, in the case of water, the angular dependence of reflection (including Sun glint) as well.

The dark-pixel correction attempts to address the same problem on a much simpler level. It assumes that the reflectance of this target is zero and that any radiative contribution is from the atmosphere. The atmospheric contribution can then be removed for every pixel in the image. This must be done for all bands and makes two fundamentally flawed assumptions: (i) the reflectance from the atmosphere is constant across the image; (ii) the atmospheric correction can be adequately considered as an additive effect. Problems also occur if calibration/validation is attempted using highly absorptive targets due to low signal-to-noise ratio.

In the absorptive regime the same options are provided. Ground truthing can be undertaken to correct for the absorption of ground-leaving radiance by the atmosphere, typically seen as a darkening of the image. Typically a bright, well-known, and homogeneous target is chosen and its emissivity characterized. Given knowledge of the target's temperature, the ground-leaving radiance can be derived. Again, the difference between ground-based and satellite measurements is a function of the atmospheric contribution. An additional option is multi-angle comparison. Because the emissive regime does not have a strong angular dependence the difference in at-satellite radiance from the same target at different angles can be assumed to be representative of the additional path length through which the target is being observed. Knowledge of the path length difference, derived from known quantities such as the angle of observation and the sensor altitude, can be used in conjunction with the two measurements to quantify the contribution of the atmosphere.

Image-based calculations typically involve a channel-differencing technique. As emissive measurements are mostly confounded by the presence of water vapor the channel-differencing technique normally focuses on this issue. One such example is the "split-window" technique (e.g., Wen and Rose, 1994). As well as being used to detect volcanic ash (Chapter 6) the split-window algorithm can be used to quantify the contribution of water vapor to

the brightness temperature—the temperature given by the blackbody (Planck) calculation ignoring emissivity and/or atmospheric effects—in the 11–12 μm region. The technique works well on homogeneous, isothermal surfaces of constant emissivity, such as the sea, and less well for complex land-based background.

2.5.2 Using radiative transfer models

Several radiative transfer models currently exist to facilitate accounting for the atmospheric effects on remote-sensing observations. Of these the LOWTRAN 7 and MODTRAN models are most commonly used. The models require a priori information about the constituents in the atmosphere and then propagate ground-leaving radiation to the sensor via a series of interconnected arbitrary atmospheric levels. Meteorological data from radiosondes are normally used to constrain the atmosphere in terms of the pressure, temperature, and relative humidity. Given accurate knowledge of the atmosphere, the radiative effects of the atmosphere can be derived from a forward solution of the mathematical framework of the radiative transfer equation (Section 2.4.3).

The presence of large amounts of atmospheric aerosol is likely to confound radiative transfer models. This can be addressed with an example where an atmospheric correction is required to remove the effects of an aerosol layer above a surface of interest (e.g., water). In the VNIR it can be shown that the at-satellite radiance is a function of both the surface and atmospheric contribution. This begins with an equation where the at-satellite radiance above a surface (L_S) is given by:

$$L_S = (L_W + L_G)t + L_R + L_A \quad (2.25)$$

where L_W and L_G are the non-specular and specular reflectance from the water, respectively; t is the transmittance of the atmosphere; L_R is path-added Rayleigh (molecular) scattering; and L_A is the path-added radiance due to aerosol scattering (the quantity of interest). L_W is normally small, at least for the VNIR. L_G can be estimated using the Sun–Earth–satellite geometry and surface roughness. It is almost negligible for all but a few viewing geometries. The single scattering approximation (SSA), rather than the multiple scattering scheme, should be used in the investigation of upwelling radiation from aerosols. The use of the SSA is justified by the fact that single scattering processes dominate the transfer of radiation in most atmospheric environ-

ments. The presence of high levels of multiple scatterers (typically clouds) normally negates the need for atmospheric correction at all. The SSA can be mathematically described thus.

$$L_A = \frac{\omega_0 \mu_0 F_0}{4(\mu + \mu_0)} p(\theta) \left\{ 1 - \exp \left[-\tau_A \left(\frac{1}{\mu} + \frac{1}{\mu_0} \right) \right] \right\} \quad (2.26)$$

τ_A is the optical depth due to aerosol scattering; ω_0 is the single scattering albedo; $\mu = \cos \theta^1$, where θ^1 is the satellite zenith angle; $\mu_0 = \cos \theta_{sza}$, where θ_{sza} is the solar zenith angle and $p(\theta)$ is the scattering phase function. Aerosol optical depth is calculated by integrating the extinction coefficient (β_{EXT}) with respect to height (z):

$$\tau_A = \int \beta_{\text{EXT}} dz \quad (2.27)$$

where the extinction coefficient is given by

$$\beta_{\text{EXT}} = \int \pi r^2 Q_{\text{EXT}}(m, r) n(r) dr \quad (2.28)$$

The calculation of Q_{EXT} is complicated and the theory behind the calculation is both lengthy and well documented elsewhere (Bohren and Huffman, 1983). Several scattering codes exist for the calculation of Q_{EXT} , and its analogues Q_{ABS} and Q_{SCA} .

Some of the parameters in Equations (2.26)–(2.28) can be determined by experiment or can be modeled mathematically to produce the most likely fit, as in the case of $p(\theta)$, the scattering phase function. Equation (2.26) is reduced by the small optical depth assumption:

$$(\tau_A [(1/\mu) + (1/\mu_0)] \ll 1) \quad (2.29)$$

to:

$$L_A \approx \frac{\omega_0 F_0}{4\mu} p(\theta) \tau_A \quad (2.30)$$

L_A can be plotted against τ_A and the slope calculated. Assuming ω_0 to be 1.0 then $p(\theta)$ is given by:

$$p(\theta) = \text{slope} \frac{4(\mu)}{F_0} \quad (2.31)$$

and $p(\theta)$ can be compared with known values as a validation.

Hence, from the at-satellite radiances of two images or one image with two view angles, an understanding of the radiative effects of the aerosol layer can be retrieved and the image can be corrected for the presence of the aerosol layer.

Table 2.3. Past and present missions used in the observation of volcanic emissions.

<i>Sensor name</i>	<i>Sensor acronym</i>	<i>Spectral region</i>	<i>Target</i>	<i>Reference</i>	<i>Year</i>
Atmospheric Infrared Sounder	AIRS	TIR	SO ₂ Ash Ice Lava flow	Carn <i>et al.</i> Wright <i>et al.</i> — Patrick <i>et al.</i>	2005 2005 — 2005
Advanced Spaceborne Thermal Emission and Reflection Radiometer	ASTER	TIR	SO ₂ Ice Ash	Henney <i>et al.</i> — —	In review — —
Advanced Very High Resolution Radiometer	AVHRR	TIR	Ash Ice	Dean <i>et al.</i> Guo <i>et al.</i>	2004 2004
Geostationary Operational Environmental Satellite	GOES	TIR	Ash Ice	Gu <i>et al.</i> Rose <i>et al.</i>	2005 2000
Global Ozone Monitoring Experiment	GOME	UV	SO ₂	Khokhar <i>et al.</i>	2005
Land Satellite	LANDSAT	VIS–TIR	Lava flow	Patrick <i>et al.</i>	2005
Microwave Limb Sounder	MLS	MW	SO ₂	Read <i>et al.</i>	1993
Moderate Resolution Imaging Spectroradiometer	MODIS	TIR	SO ₂ Ash Ice ThA	Watson <i>et al.</i> Watson <i>et al.</i> Watson <i>et al.</i> Patrick <i>et al.</i>	2004 2004 2004 2005
Ozone Monitoring Instrument	OMI	UV	SO ₂	Krotkov <i>et al.</i>	2006
Scanning Imaging Absorption Spectrometer for Atmospheric Chartography	SCIAMACHY	UV	SO ₂ BRO	Afe <i>et al.</i> Afe <i>et al.</i>	2004 2004
Spinning Enhanced Visible and Infrared Imager	SEVIRI	TIR	SO ₂ Ash	— —	— —
Total Ozone Mapping Spectrometer	TOMS	UV	SO ₂	Carn <i>et al.</i>	2003
TIROS Operational Vertical Sounder	TOVS	TIR	SO ₂	Prata <i>et al.</i>	2003

2.6 THE VOLCANOLOGICAL CONTEXT

2.6.1 Overview of following chapters

In the following chapters of this book, the fundamental, underpinning physics from this chapter is applied in more detail to several specific volcanological needs, including observations of (i) volcanic

emissions to the atmosphere, (ii) temperature changes in lava domes, (iii) hazardous flows, (iv) edifice deformation, (v) spectral characteristics of surface material, and (vi) morphology and form. It should be noted that not one of the sensors used in these studies was specifically designed to observe volcanic processes.

2.6.2 Past and current missions

Data from several geostationary and low Earth orbit satellites are currently being used to study volcanic processes. Table 2.3 provides a limited summary of the popular past and current satellites and sensors used in volcano remote sensing, with examples for each sourced mainly from the study of volcanic emissions.

2.6.3 Future missions

As stated in Section 2.6.1 there has never been a dedicated satellite mission to observe volcanoes. Volcanoes are part of the lithosphere–atmosphere exchange system and are clearly important targets in terms of satellite missions primarily designed to observe something else. The fact that they make such good targets, somewhat paradoxically, means that it is unlikely to have a dedicated satellite mission to observe volcanoes. They can be (and are) observed, quantified, and monitored by numerous sensors at a range of spatial, temporal, and spectral resolutions, and it is possible to see volcanic signatures in almost all types of remote-sensing data. So, instead of discussions about future missions targeting volcanoes, we instead must talk about sensors which have the ability to observe volcanoes and their products. Rather than detail them in a table, which immediately dates a manuscript (launch dates, mission lifetimes, and mission objectives are incredibly changeable) we respectfully point the reader towards the most complete description of the forthcoming EOS missions: <http://science.hq.nasa.gov/missions/phase.html>

2.7 SUMMARY

Satellite remote sensing is now recognized and used as a valuable tool for observing and monitoring volcanoes. This is especially true when the volcano of interest is politically inaccessible, or geographically remote, or likely to erupt in the near future and viewed as a potential hazard.

Remotely sensed data, by definition, are potential solutions to inverse problems. They are inherently abstract and require careful consideration and manipulation to determine the specifics about the object or phenomenon of interest. When applied to volcanism, remotely sensed data can yield primary information about the temperature, emissivity, deformation, emitted products (both ground-based

and atmospheric), characteristics, and the lateral extent of deposits. These data can be used to determine risk, activity level, extent of impact, and potential changes in eruptive style. Ground-based monitoring is typically of higher resolutions, but has several drawbacks including a necessity for proximity to the system and an inability to qualify the system as a whole. Only from the synoptic perspective of satellite-based instrumentation can large-scale volcanic systems be studied as a whole. The volcanoes of the North Pacific are a perfect example of this. Some are so remote and inaccessible that they are currently only monitored from space.

2.8 REFERENCES

- Afe, O.T.; Richter, A.; Sierk, S.; Wittrock, F.; Burrows, J.P. (2004). BrO Emission from volcanoes: A survey using GOME and SCIAMACHY measurements, *Geophys. Res. Lett.*, **31**, L24113, doi: 10.1029/2004GL020994.
- Bohren, C.F.; Huffman, D. (1983). *Light Scattering and Absorption by Small Particles*, Wiley, New York.
- Carn, S.A.; Krueger, A.J.; Bluth, G.J.S.; Schaefer, S.J.; Krotkov, N.A.; Watson, I.M.; Datta, S. (2003). Volcanic eruption detection by the Total Ozone Mapping Spectrometer (TOMS) instruments: A 22-year record of sulfur dioxide and ash emissions., in C. Oppenheimer, D.M. Pyle, and J. Barclay (Eds.), *Volcanic Degassing*, Special Publication 213, Geological Society, London, pp. 177–202.
- Carn, S.A.; Strow, L.L.; de Souza-Machado, S.; Edmonds, Y.; Hannon, S. (2005). Quantifying tropospheric volcanic emissions with AIRS: The 2002 eruption of Mt. Etna (Italy), *Geophys. Res. Lett.*, **32**(2), L02301, doi: 10.1029/2004GL021034.
- Dean, K.G.; Dehn, J.; Papp, K.R.; Smith, S.; Izbekov, P.; Peterson, R.; Kearney, C.; Steffke, A. (2004). Integrated satellite observations of the 2001 eruption of Mt. Cleveland, *Alaska Journal of Volcanology and Geothermal Research*, **135**(1–2), July 15, 51–73.
- Ellrod, G.; Schreiner, A. (2004). Volcanic ash detection and cloud top height estimates from the GOES-12 Imager: Coping without a 12 μ m infrared band. *Geophys. Res. Lett.*, **31**, L15110.
- Gu, Y.; Rose, W.I.; Schneider, D.J.; Bluth G.J.S.; Watson, I.M. (2005). Advantageous GOES IR results for ash mapping at high latitudes: Cleveland eruptions 2001, *Geophys. Res. Lett.*, **32**, L02305.
- Guo, S.; Rose, W.I.; Bluth G.J.S.; Watson, I.M. (2004). Particles in the great Pinatubo volcanic cloud of June 1991: The role of ice, *Geochemistry, Geophysics*,

- Geosystems*, 5(5), Q05003, doi: 10.1029/2003GC000655.
- Harris, A.J.L.; Pilger, E.; Flynn, L.P.; Garbeil, H.; Mouginiis-Mark, P.J.; Kauahikaua, J.; Thornber, C. (2001). Automated, high temporal resolution, thermal analysis of Kīlauea volcano, Hawaii, using GOES-9 satellite data, *Int. J. Remote Sensing*, 22(6), 945–967.
- Henney, L.A. (2012). Remote sensing of volcanic plumes using the advanced spaceborne thermal emission and reflection radiometer. PhD dissertation, Michigan Technical University, Houghton, MI, 297 pp.
- Khokhar, M.F.; Frankenberg, C.; Beirle, S.; Kühl, S.; Van Roozendaal, M.; Richter, A.; Platt U.; Wagner, T. (2005). Satellite observations of atmospheric SO₂ from volcanic eruptions during the time period of 1996 to 2002, *Journal of Advances in Space Research*, 36(5), 879–887, doi: 10.1016/j.asr.2005.04.114, 2005
- Krotkov, N.A.; Carn, S.A.; Krueger, A.J.; Bhartia, P.K.; Yang, K. (2005). Band residual difference algorithm for retrieval of SO₂ from the Aura Ozone Monitoring Instrument (OMI), *IEEE Trans. Geosci. Remote Sensing* (in press).
- Mouginiis-Mark, P.J.; Crisp, J.A.; Fink, J.H. (2000). *Remote Sensing of Active Volcanism*, Geophysical Monograph 116, American Geophysical Union, Washington, D.C.
- Oppenheimer C. (1991). Lava flow cooling estimated from Landsat Thematic Mapper infrared data: The Lonquimay eruption (Chile, 1989), *J. Geophys. Res.—Solid Earth*, 96, 21865–21878.
- Patrick M.R.; Smellie, J.L.; Harris, A.J.L.; Wright, R.; Dean, K.; Izbekov, P.; Garbeil, H.; Pilger, E. (2005). First recorded eruption of Mount Belinda volcano (Montagu Island), South Sandwich Islands, *Bull. Volcanol.*, 67(5), June, 415–422, available at <http://dx.doi.org/10.1007/s00445-004-0382-6>
- Prata, A.J.; Rose, W.I.; Self, S.; O'Brien, D. (2003). Global, long-term sulphur dioxide measurements from TOVS data: A new tool for studying explosive volcanism and climate, in A. Robock and C. Oppenheimer (Eds.), *Volcanism and the Earth's Atmosphere*, pp. 75–92, Geophysical Monograph 139, American Geophysical Union, Washington, D.C.
- Read, W.G.; Froidevaux, L.; Waters, J.W. (1993). Microwave Limb Sounder measurement of stratospheric SO₂ from the Mt. Pinatubo volcano, *Geophys. Res. Lett.*, 20, 1299–1302.
- Rees, W.G. (2001). *Physical Principles of Remote Sensing*, Cambridge University Press, Cambridge, U.K.
- Rose, W.I.; Bluth G.J.S.; Ernst, G.G.J. (2000). Integrating retrievals of volcanic cloud characteristics from satellite remote sensors: A summary, *Philosophical Transactions of Royal Society, Series A*, 358(1770), 1585–1606.
- Watson, I.M.; Realmuto, V.J.; Rose, W.I.; Prata, A.J.; Bluth, G.J.S.; Gu, Y.; Bader, T.Yu (2004). Thermal infrared remote sensing of volcanic emissions using the moderate resolution imaging spectroradiometer, *J. Volcanol. Geothermal Res.*, 135, 75–89.
- Wen, S.; Rose, W.I. (1994). Retrieval of sizes and total masses of particles in volcanic clouds using AVHRR bands 4 and 5, *J. Geophys. Res.*, 99(D3), 5421–5431.
- Wright, R.; Carn, S.A.; Flynn, L.P. (2005). A satellite chronology of the May–June 2003 eruption of Anatahan volcano, *J. Volcanol. Geothermal Res.*, 146, 102–116.

Thermal anomalies at volcanoes

Jonathan Dehn, Andrew J.L. Harris

Abstract. Thermal anomalies occur when a pixel in a satellite image shows a higher brightness temperature than is expected relative to its neighbors. Thermal anomalies have been observed over decades at volcanoes in satellite data. Such anomalies occur for many reasons, but at volcanoes this can be an indicator of volcanic activity or even a precursor to more explosive activity. This chapter focuses on what causes thermal anomalies at volcanoes, how they are detected, and how they are used to monitor volcanoes in the North Pacific.

3.1 INTRODUCTION

It is intuitive to think that volcanoes become hot when they become active. In reality, this is often the case. It is also reasonable to think that, if the volcanic surface becomes sufficiently hot, then the emitted heat should be observable from space. Again, this is often the case. Based on these foundations, satellite-based thermal remote sensing has become a key exploration direction in, and component of, volcano monitoring. In fact, in the Alaskan experience, current satellite-based thermal remote-sensing technologies allow an eruption to almost always be detected, sooner or later, in thermal imagery, so that appropriate steps can be taken to mitigate and track the hazards represented by the eruption. Thermal data derived from the satellite-based sensor can then be related to processes on the ground through derivation of actual ground surface temperature, the amount of heat emitted, and the

mass erupted, as well as through the rate of change in shapes and sizes of thermal anomalies associated with the activity in time series data. In the case of ongoing volcanic activity, thermal imaging can provide information on the eruption type and changes in the eruption style, intensity, and magnitude in near-real time. Thermal flux can change throughout the course of an eruption, with an increase in the heat released (and thus sensed) likely being indicative of an increase in the rate that hot material is erupted from the volcano, and so can also be used to track the progress of an ongoing eruption.

Effusive volcanic eruptions will create thermal anomalies in satellite thermal data. Spatially, a thermal anomaly can be defined as an unexpected increase in the radiant temperature of a pixel relative to its neighbors. Its neighbors may be considered as pixels next to it in the same image and waveband. However, the pixel may also show differences by wavelength and time. In other words, an anomaly can be defined in terms of its spatial, spectral, or temporal divergence from the “norm”. The term “thermal anomaly” does not, however, carry any indication as to the cause of the anomaly. Thus a secondary goal, after anomaly detection, is to discover the type of activity to which a thermal anomaly relates. A key question may be, for example, is the anomaly a result of geothermal warming of the ground, heating of an aqueous crater lake, eruption of a lava flow, lake, or dome, emplacement of pyroclastics, or the emission of gas and ash.

The goal of volcano monitoring is to reliably eliminate the non-volcanic causes of thermal anomalies and to focus on volcanogenic anomalies. From a monitoring and predictive point of view, it is important to reliably distinguish between thermal anomalies associated with precursory and those associated with ongoing eruptive activity. Because low-level eruptive activity is often a precursor to more energetic effusive and explosive events, these two anomaly types may overlap and show a continuum in time. To decide whether an anomaly is building towards more energetic explosive or effusive activity often requires operator recognition of the type of activity represented by the thermal signal from spectral, temporal, or spatial clues, as well as ancillary ground-based information. From the satellite perspective, these clues can only be obtained from libraries and baseline data sets created from years of thermal data recorded for appropriate eruptive types or cycles. There are though several problems when detecting and tracking thermal anomalies in satellite data. Specifically, volcanic thermal anomalies can be obscured by, or confused with, other energy sources. These include:

- (1) Strong reflective components over snow-covered volcanic peaks or meteorological clouds near a volcano, as well as solar heating of barren rock surfaces on the volcano, can create “apparent” thermal anomalies.
- (2) Strong thermal contrasts between different ambient features, such as between lakes and their background, when the background drops below lake temperature due to a sudden snowfall.
- (3) Cloud or vapor from fumaroles and vents that may obscure volcanic anomalies or reflect sunlight to create “apparent” anomalies.
- (4) Changes in atmospheric conditions that may favor or hinder detection of warm areas. Simply, if the area is cloud free, then the anomaly can be detected; if cloud covered, it cannot be seen from the satellite perspective.
- (5) Geometric constraints, which result from geometrical considerations due to changes in the satellite’s orbital position in relation to the ground topography, so that an anomaly may be hidden from view by a ridge or crater wall.
- (6) Noise affecting the sensor or reception antenna can cause stray (apparently anomalous) pixels to appear in images which can mask subtle

anomalies or cause “apparent” electronic anomalies or “single-event upsets”.

- (7) Natural or anthropogenic signals such as fires, smoke stacks, even parking lots, sand deserts, and barren tephra fields, can create real (but non-volcanic) thermal anomalies.

Examples of several of these problems, as recorded in satellite imagery for Alaska, are given in Figure 3.1.

Volcanic rocks are also poor conductors of heat, as such they are excellent insulators. The rocks can thus dampen heat fluxes due to the presence of near-magmatic temperatures just meters below the surface. Lava flows, for example, can maintain core temperatures in excess of 500°C for years with only marginal heat loss to the surface to cause surface thermal anomalies that are undetectable. Such faint signals (of the order of a few degrees) are difficult to detect in coarse spatial resolution satellite data; higher resolution thermal imagery (Chapter 4) or hand-held/airborne thermal imaging is needed to detect these signals in advance of, or during, an eruption (as is the case, for example, over active lava tubes).

This chapter focuses on the ability to detect, measure, and track precursory and syn-eruptive thermal phenomena using satellite-based data, illustrated using examples from Alaska, the Aleutians, and Kamchatka (i.e., the region encompassed by this atlas).

3.2 BACKGROUND

Acquisition of images in the thermal infrared has been commonplace in environmental monitoring for decades. The first publicly available infrared data obtained from orbit were provided by the Television and Infrared Operational Satellite, TIROS-2, launched in 1960. Since that time there has been great interest in environmental studies focusing on thermal infrared (IR) channels, with most coming from meteorology and oceanography. However, volcanologists can use the same wavebands used by meteorologists and oceanographers to their advantage, as the same data show strong thermal anomalies over hot volcanic surfaces. Williams *et al.* (1968) and Williams and Friedman (1970), for example, were among the first to describe clear volcanic signals in “weather satellite” images provided for Iceland during Surtsey’s 1966 eruption by the Nimbus High Resolution Infrared

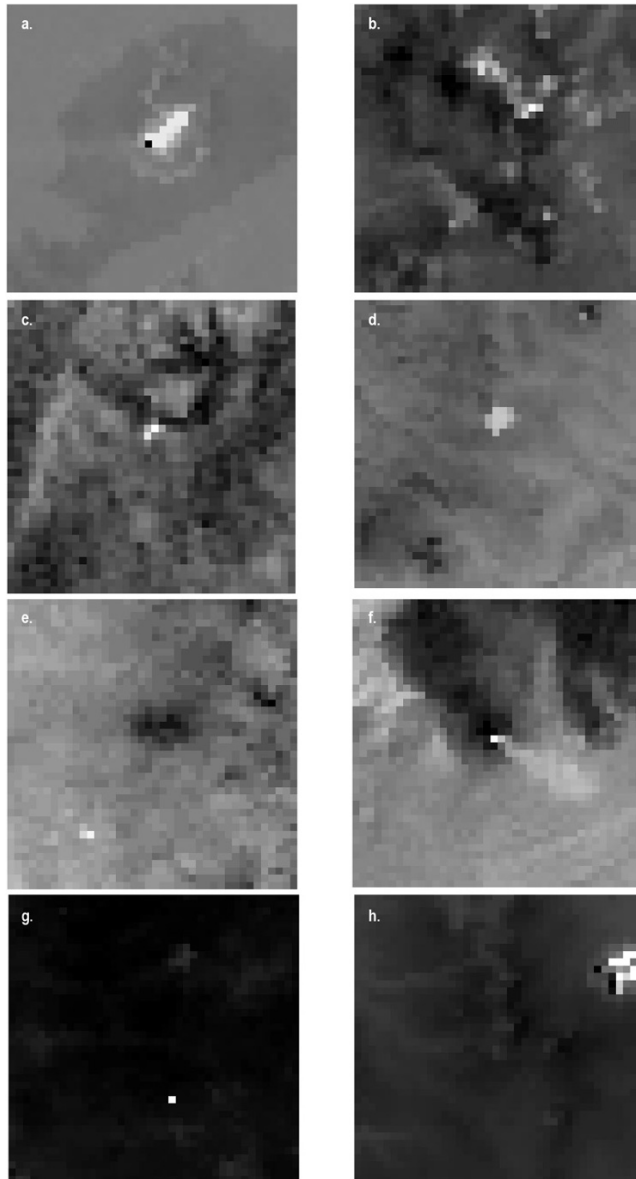


Figure 3.1. Examples of thermal anomalies shown in the MIR band 3 of AVHRR. All images are 40×40 km; north is up. (A) A lava flow at Okmok Volcano (March 14, 1998); (B) solar reflection on the snow-covered summit of Kliuchevskoi and nearby volcanoes at a time when no eruptive activity is taking place (March 22, 2009); (C) a cloud from degassing at Fourpeaked Volcano (September 18, 2006) in which the thermal signal gives no indication of ground temperatures despite the activity being volcanic; (D) Akademia Nauk Caldera Lake, its constant temperature only shows an anomaly when the background temperature decreases in the winter (October 19, 2008); (E) a clear, dry day at Tolbachik Volcano exposes the warm summit of a cinder cone, otherwise obscured by fumaroles and atmospheric interference (January 30, 2006); (F) at Shishaldin this thermal anomaly was only visible when the satellite was nearly directly overhead, allowing a view into the deep summit crater (February 9, 1999); (G) a noise pixel at Mt. St. Helens not associated with any activity (December 13, 2009); (H) a forest fire near South Sister Volcano (August 4, 2010).

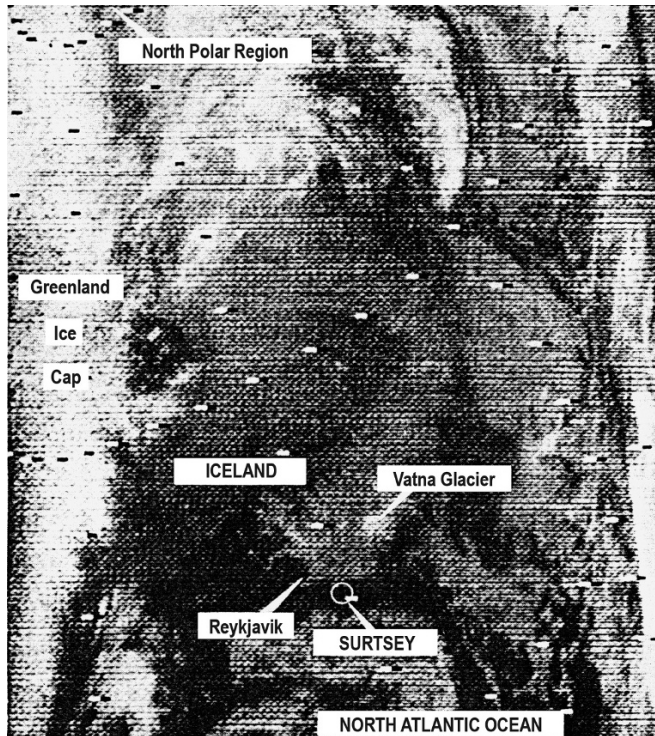


Figure 3.2. A NIMBUS II HRIR image of the North Atlantic, taken on August 22, 1967 showing Iceland and activity at Surtsey Volcano (from Williams and Friedman, 1970).

Radiometer (HRIR)—opening the door for further studies into thermal volcano remote sensing (Figure 3.2).

The launch of NOAA-2 in 1972 carried the Very High Resolution Radiometer (VHRR) and signaled the beginning of operational infrared monitoring of the Earth's surface at higher (km-scale) spatial resolutions. Higher spatial resolution still was offered by the launch of the Thematic Mapper (TM) aboard Landsat 4 in 1982. The landmark works of Wiesnet and D'Aguanno (1982), for low spatial resolution (AVHRR) data, and Rothery *et al.* (1988) for high spatial resolution (TM) data, then laid the foundation for most modern satellite-based thermal remote-sensing studies of active volcanic targets.

Table 3.1 summarizes many landmark works in thermal volcano remote sensing until ~2000. The collation reveals a two-pronged focus to thermal volcano remote sensing, with both branches, research (measurements) and operational (detection), being tightly linked. The first (research)

branch was centered on volcanological problem solving and tended to focus on the development of techniques, image interpretation, and use of thermal remote sensing to solve thematic questions regarding volcanic processes. From this focus the second (operational) branch grew. This group of studies focused on refining techniques to detect and measure volcanic thermal anomalies, as well as construction of operational tools to perform regular volcano surveillance tasks. This chapter will focus mostly on the latter.

3.3 THE PHYSICS OF THERMAL ANOMALIES

Each pixel in a satellite image has a digital number. This number is a function of the thermal radiation arriving at the sensor (see Chapter 2), and can be converted to radiance using a sensor-dependent function. Radiance (L_λ , in units of $\text{W m}^{-2} \text{sr}^{-1}$)

Table 3.1 (cont.)

<p>Heat loss and mass flux (cont.) Wright and Pilger (2008) Harris <i>et al.</i> (2009)</p>	<p>Heat loss at lava lakes Fumarole field characterization</p>	<p>MODIS FLIR</p>	<p>SWIR and TIR TIR</p>
<p>Vesicles/Spectral Kahle <i>et al.</i> (1988) Crisp <i>et al.</i> (1990) Realmuto <i>et al.</i> (1992) Crowley and Zimbelman (1997) Oppenheimer (1998) Ramsey and Christensen (1998) Ramsey and Fink (1999) Donegan and Flynn (2004)</p>	<p>Spectral dating Spectra of basalt Spectral dating Alteration mapping Spectra of natrocarbonatite Mineral spectra Vesicularity mapping Radiant response</p>	<p>TIMS TIMS TIMS AVIRIS TM and AVHRR ASTER TIMS and ASTER ETM+ and ALI</p>	<p>TIR TIR TIR SWIR SWIR and MIR SWIR, MIR, and TIR TIR SWIR</p>
<p>Detection algorithms: hot spots Wiesnet and D'Aguanno (1982) Scorer (1986) Lee and Tag (1990) Harris <i>et al.</i> (1995) Higgins and Harris (1997) Dehn <i>et al.</i> (2000) Harris <i>et al.</i> (2001) Wright <i>et al.</i> (2002a) Flynn <i>et al.</i> (2002) Di Bello <i>et al.</i> (2004) Pergola <i>et al.</i> (2004) Kervyn <i>et al.</i> (2006) Yuhaniz and Vladimirova (2009) Steffke and Harris (2011)</p>	<p>AVHRR AVHRR AVHRR AVHRR AVHRR AVHRR GOES MODIS MODIS AVHRR AVHRR MODIS Proposed Review paper</p>	<p>MIR and TIR MIR and TIR MIR MIR and TIR MIR and TIR</p>	<p>6 hours 6 hours 6 hours 6 hours 6 hours 6 hours 15 minutes 12 hours 12 hours 6 hours 6 hours 12 hours 14 minutes</p>
<p>Time series analyses Glaze <i>et al.</i> (1989) Harris <i>et al.</i> (1995) Harris <i>et al.</i> (1997b) Harris <i>et al.</i> (1997c) Wooster and Rothery (1997)</p>	<p>GOES AVHRR AVHRR GOES ATSR</p>	<p>VIS MIR and TIR MIR and TIR MIR and TIR SWIR, MIR, and TIR</p>	<p>15 minutes 6 hours 6 hours 15 minutes 3 days</p>

<p>Wooster <i>et al.</i> (1997) Wooster <i>et al.</i> (1998) Carn and Oppenheimer (2000) Harris <i>et al.</i> (2000) Harris and Thornber (1999) Mougins-Mark <i>et al.</i> (2000) Aries <i>et al.</i> (2001) Harris <i>et al.</i> (2001) Lachlan-Cope <i>et al.</i> (2001) Roach <i>et al.</i> (2001) Wooster (2001) Wooster and Rothery (2002) Dehn <i>et al.</i> (2002) Galindo and Dominguez (2002) Wright <i>et al.</i> (2002b) Calder <i>et al.</i> (2004) Rothery <i>et al.</i> (2005) Coppola <i>et al.</i> (2009) Pergola <i>et al.</i> (2009) van Manen and Dehn (2009) Koeppen <i>et al.</i> (2011) van Manen <i>et al.</i> (2011)</p>	<p>ATSR ATSR AVHRR GOES/AVHRR/ATSR GOES GOES AVHRR GOES AVHRR AVHRR ATSR ATSR AVHRR AVHRR GOES GOES MODIS MODIS AVHRR/MODIS AVHRR/MODIS MODIS AVHRR</p>	<p>SWIR, MIR, and TIR SWIR, MIR, and TIR MIR and TIR SWIR, MIR, and TIR MIR MIR MIR and TIR SWIR, MIR, and TIR SWIR, MIR, and TIR MIR and TIR MIR and TIR MIR MIR and TIR MIR and TIR</p>	<p>3 days 3 days 6 hours 15 minutes to 3 days 15 minutes 15 minutes 6 hours 15 minutes 6 hours 6 hours 3 days 3 days 6 hours 6 hours 15 minutes 15 minutes 12 hours 12 hours 6 hours 6 hours 12 hours 6 hours</p>
<p>Real-time volcano monitoring systems Dean <i>et al.</i> (1998) Schneider <i>et al.</i> (2000) Harris <i>et al.</i> (2001) Dean <i>et al.</i> (2002) Flynn <i>et al.</i> (2002) Kaneko <i>et al.</i> (2002) Dean <i>et al.</i> (2004) Pergola <i>et al.</i> (2008) Webley <i>et al.</i> (2008)</p>	<p>AVHRR GOES/GMS/AVHRR GOES GOES/GMS/AVHRR MODIS AVHRR AVHRR/MODIS/GOES AVHRR/MODIS AVHRR</p>	<p>MIR and TIR MIR & TIR</p>	<p>6 hours 15 minutes to 6 hours 15 minutes 15 minutes to 6 hours 12 hours 6 hours 15 minutes to 12 hours 6 hours 6 hours</p>
<p>Multiple resolutions Harris <i>et al.</i> (1998) Harris <i>et al.</i> (1999) Hirn <i>et al.</i> (2008)</p>	<p>AVHRR and TM AVHRR and TM ASTER and MODIS</p>	<p>SWIR, MIR, and TIR SWIR, MIR and TIR SWIR, MIR, and TIR</p>	<p>6 hours to 16 days 6 hours to 16 days 12 hours to 16 days</p>

can then be converted to a brightness temperature (T_b , in K) using the inverse Planck function:

$$T_b = \frac{\alpha_2 \cdot \nu}{\log_e \left[1 + \left(\frac{\alpha_1 \nu^3}{L_\lambda} \right) \right]} \quad (3.1)$$

where ν is the wave number (in cm^{-1}) at which the sensor operates. Wave number can be derived from the wavelength expressed in terms of microns (λ) from the relation $\nu = 10^4/\lambda$. The two constants in this equation, α_1 and α_2 , have values of $1.191066 \times 10^{-5} \text{ m W m}^{-2} \text{ sr}^{-1}/\text{cm}^{-1}$ and 1.438833 K cm . These are derived from

- Planck’s constant (h , $6.62620 \times 10^{-34} \text{ J s}$);
- the speed of light (c , $2.99793 \times 10^8 \text{ m s}^{-1}$); and

- Boltzmann constant (k , $1.38062 \times 10^{-23} \text{ J K}^{-1}$)

such that

$$\alpha_1 = 2hc^2 = 1.191066 \times 10^{-5} \text{ m W m}^{-2} \text{ sr}^{-1}/\text{cm}^{-1}$$

$$\alpha_2 = hck^{-1} = 1.438833 \text{ K cm}$$

This conversion gives the user a pixel-integrated brightness temperature (i.e., a weighted average for the temperature of all thermal surfaces falling within a pixel). As noted in Chapter 2, a pixel is not a square, but is defined by an ellipse whose aerial ground coverage depends on the pixel instantaneous field of view, viewing angle, satellite height, and topography (Figure 3.3). The integrated temperature for this ellipsoidal area is mapped into the

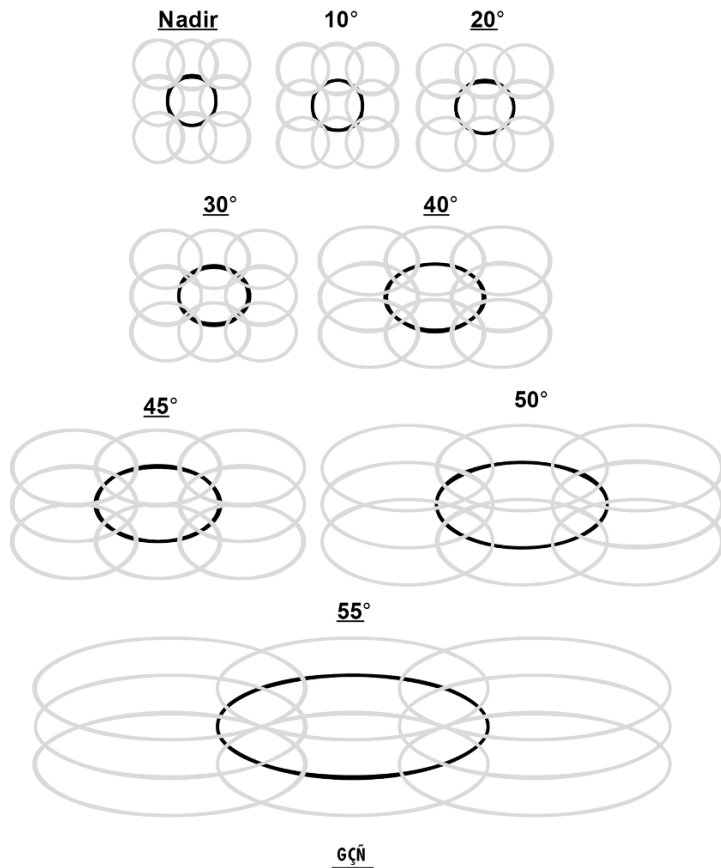


Figure 3.3. Size of an AVHRR pixel with viewing angle (from Patrick, 2002). Pixels overlap even at nadir and, as the viewing angle becomes more oblique either through satellite viewing angle or topography, the overlap grows and pixel size increases.

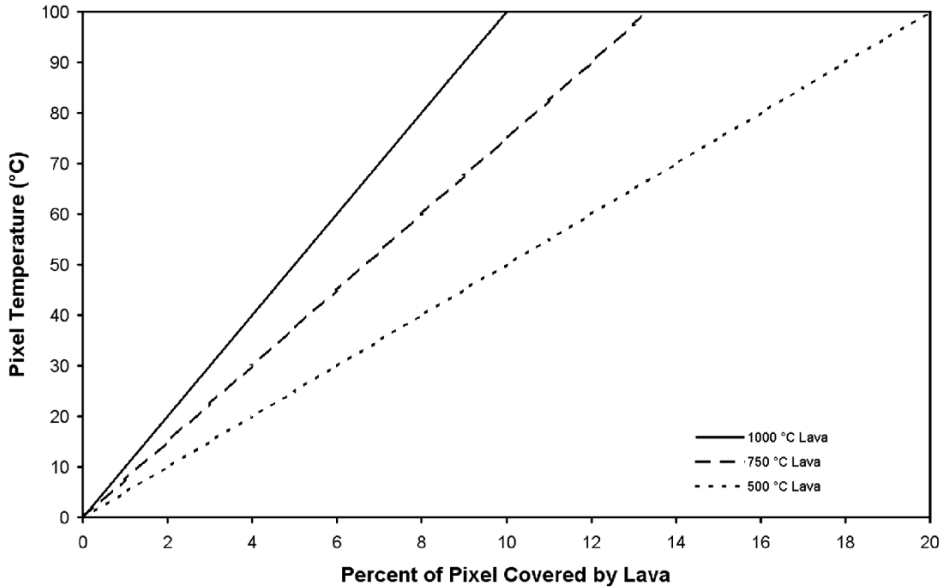


Figure 3.4. Pixel brightness temperature as a function of percent pixel coverage of hot and background temperatures. Background was chosen as 0°C, and lava temperatures of 1,000, 750, and 500°C were used. Note that lava temperatures, regardless of their area, can significantly elevate the brightness temperature of a pixel (after Harris *et al.*, 1997a). More than 5% pixel coverage almost always leads to sensor saturation.

square picture element or pixel in the image. The integrated temperature for this area may be the result of the radiant contribution of many surfaces of quite different temperatures and areas. The pixel-integrated temperature will thus not be representative of the actual temperature for any of the subpixel components; this is particularly true for temperatures over active volcanic targets which extend over a great range of temperature spanning ambient (0°C) to magmatic (1,200°C) over quite small spatial scales (i.e., a few centimeters), as shown in Figure 3.4. The maximum pixel-integrated temperature recorded by most sensors is as low as 50–60°C, so that active volcanic targets filling a significant fraction of a pixel often saturate the sensor. After all, most of the thermal sensors in orbit are on weather satellites and, thus, were never designed for use in detection of volcanic activity, but instead for cold cloud tops and cool ocean surfaces. This is a major limiting factor for volcanic thermal studies that utilize such weather satellite data, making it only possible to understand that the temperature is equal to or greater than the saturation point. Recently, some sensors (e.g., the Advanced Spaceborne Thermal Emission and Reflection radiometer ASTER, the Enhanced Thematic Mapper plus ETM+, and the

Moderate Resolution Imaging Spectroradiometer MODIS) have been designed such that some wavebands have higher saturation levels to allow acquisition of greater quantities of unsaturated data over volcanic targets.

Since the early days of thermal remote sensing, attempts have been made to extract meaningful surface temperatures from integrated brightness temperatures. For a pixel filled by a uniform thermal surface, this can be achieved through application of appropriate atmospheric and emissivity corrections. However, for a thermally mixed pixel, thermal mixture models must be applied to extract the actual surface temperatures of the various thermal components that comprise the pixel-integrated temperature. One approach commonly used with weather satellite data, where just one waveband of usable unsaturated data is typically available, is to apply a simple two-component mixture model. In this method a pixel's integrated radiance (L_v) is modeled as resulting from just two components, one hot and one cold:

$$L_v \propto L_{\text{lava}} \left(\frac{A_{\text{lava}}}{A_{\text{pixel}}} \right) + L_{\text{background}} \left(\frac{A_{\text{background}}}{A_{\text{pixel}}} \right) \quad (3.2)$$

where L_{lava} and $L_{\text{background}}$ is the radiance emitted by the lava and background (hot and cold) components of the pixel, respectively; A is the respective area of each component; and A_{pixel} is the pixel area. Because the two surfaces cannot occupy an area that is greater than, or less than, the pixel area, A_{pixel} must equal $A_{\text{lava}} + A_{\text{background}}$ and $A_{\text{lava}} + A_{\text{background}}$ must both be greater than or equal to zero. Because this mixture model involves a single equation with four unknowns, the areas and radiances of the two thermal components must be assumed to solve for the other. Because $A_{\text{lava}} + A_{\text{background}}$ must sum to one, $(A_{\text{background}}/A_{\text{pixel}})$ can be written $1 - (A_{\text{lava}}/A_{\text{pixel}})$ which reduces the number of unknowns to three. Of these, $L_{\text{background}}$ is usually estimated from surrounding cold (non-anomalous) pixels. Normally, upper and lower bounds are then assumed for the hot source radiance, which can be set from field measurements made using thermocouples, hand-held radiometers, or optical pyrometry, allowing us to solve for hot areas. However, if the hot-component area can be set using higher resolution imagery, photographs, or visits to the volcano, the equation can also be used to solve for the hot-component radiance.

This two-component model has proven useful at volcanic targets where a simple two-component surface fills the pixel, or where the majority of the integrated spectral radiance comes from just two thermal components. However, thermal surfaces at active volcanic targets can be considerably more complex than this two-component model. Wright and Flynn (2003), for example, used ground-based thermal camera data to show that more than seven thermal components may be present within a single satellite sensor pixel containing active lava. In most cases such a multi-component thermal surface is too complex to be modeled using standard multi-spectral satellite data, but clearly points to the limitations of the simple two-component system. The two-component model may, though, hold in cases in the thermal infrared where the pixel is large (100–1,000 m). In such cases, although many components are present, the hottest components are of such small area and their radiant contribution to the integrated pixel so small that a simple two-component model that assumes the majority of the radiance is from the crusted lava component and ambient background may be applied to obtain a reasonable approximation for the actual active lava area (Harris *et al.*, 1997a).

A second, slightly more complex approach is the “dual-band” method of Dozier (1981), as

initially applied to high spatial resolution (TM) satellite data for hot volcanic targets by Rothery *et al.* (1988). This model again applies a simple two-component mixture model, but uses two unsaturated bands of data. The method takes advantage of the different sensor response to a hot target at two or more wavelengths distributed across the infrared. Following Wien’s Displacement Law, peak emittance from a target moves to shorter wavelengths with increasing temperature (see Chapter 2). To show this, the Planck curve for spectral emittance from a blackbody at a given temperature can be plotted using the equation originally given by Planck:

$$L(\lambda, T) = \frac{8\pi hc}{\lambda^5} \frac{1}{e^{\frac{hc}{\lambda kT}} - 1} \quad (3.3)$$

This is done in Figure 3.5. Taking measurements at two discrete spectral points on a curve plotted for a body emitting at a certain temperature, the difference in radiant emittance between the two points can be expressed as a ratio of emitted radiance at the two points. This, in effect, represents the slope of the Planck curve for the emitter, where steeper slopes represent higher temperatures. The steepness of the slope (i.e., the difference in emitted radiance between the short or $\sim 2\mu\text{m}$ IR, mid or $3\text{--}4\mu\text{m}$ IR, and thermal or $10\text{--}12\mu\text{m}$ IR) decreases as the temperature of the emitter increases. By comparing the blackbody emission for a surface in the mid and thermal infrared (MIR and TIR), the ratio of the Planck function derived emission for the two points can be empirically solved following the approach of Ferriso and Ludwig (1965), allowing a plausible ground temperature (T , in K) to be determined:

$$T = 273.15 + 166 \exp \left[\left(\frac{\lambda_{\text{MIR}}}{\lambda_{\text{TIR}}} + 1 \right) \log \frac{L_{\text{MIR}}}{L_{\text{TIR}}} \right] \quad (3.4)$$

In this solution λ_{MIR} and λ_{TIR} are the wavelengths of the mid-infrared and thermal infrared bands used (in microns, μm), with L_{MIR} and L_{TIR} being the emitted radiances of the surface in the mid-infrared and thermal infrared, respectively.

Like the two-component, single-band model, this is an oversimplification. Inherent disadvantages lie in the real variability of the surface, emissivity, atmospheric, and surface reflection contributions to the emitted radiance in the two wavebands (Figure 3.6). Multiple bands (i.e., hyperspectral approaches, e.g., Wright *et al.*, 2010, 2011) are more useful for accurate temperature determination than use of one or two wavebands of 10–1,000 m pixel data.

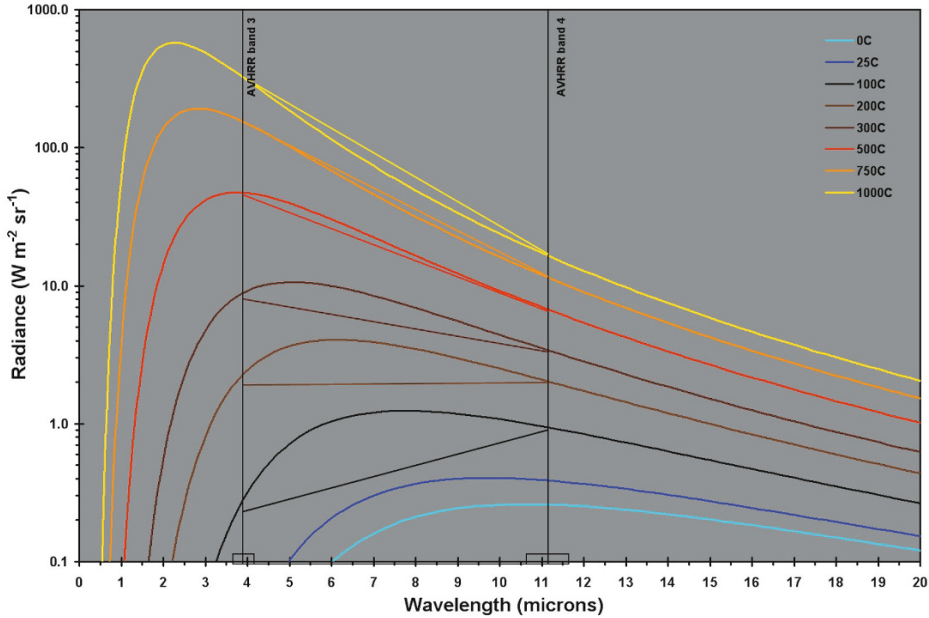


Figure 3.5. Energy emitted by a blackbody at different temperatures following the Planck function. Higher temperatures have peak energy release at shorter wavelengths following Wien's Displacement Law. By comparing the energy at a pixel in different bands (in the figure AVHRR bands 3 and 4), temperature can be estimated from these curves.

However, despite their limitations, these two methods often provide results that are in reasonable agreement with ground-truth, and are suited to the limits of data currently available for monitoring purposes (i.e., one or two bands of regularly acquired weather satellite data). These include MIR and TIR data acquired every 15 min by GOES, MTSAT, and/or SEVIRI or (nominally) every 6 h by AVHRR, and every 12 h by MODIS. For the purposes of monitoring, changes in radiance, temperature, or thermal flux occurring over time scales of tens of minutes are more important than precise derivations of accurate ground surface temperatures. Thus, although for precise science better derivations of surface thermal structures is the goal, for monitoring and time series analyses the above approximations and approaches are perfectly adequate.

3.4 VOLCANIC PROCESSES THAT PRODUCE THERMAL ANOMALIES

The thermal intensity, or magnitude, of hot spots associated with active volcanic processes is gov-

erned by the way that heat is transferred from the hot body to the surfaces defining the boundaries of the body, which the satellite-based sensor can then "see". There are three primary modes of heat transfer:

- (i) conduction (Q_k), whereby an object transmits heat through itself by molecular contact or to another object touching it;
- (ii) convection (Q_c), which involves advective heat transfer through motion in a fluid medium (liquid or gas); and
- (iii) radiation (Q_r), where heat is transmitted electromagnetically through a vacuum or gas, if the vacuum or gas is transmissive at the wavelength in question.

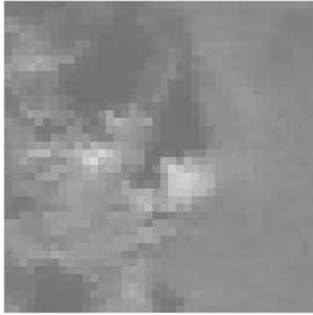
It is radiation that is measured via satellite-based sensors operating in the infrared, although the satellite sensor derived surface temperature can also be used to estimate convection.

Each mode of heat transfer follows the second law of thermodynamics (i.e., energy is transferred from a hot body to a cold body). Thus, the temperature difference between the two bodies deter-

AVHRR n19.10004.0143 01:43 UTC
zenith angle 26° sun angle 79°

MODIS a1.10004.0139 01:39 UTC
zenith angle 32° sun angle 79°

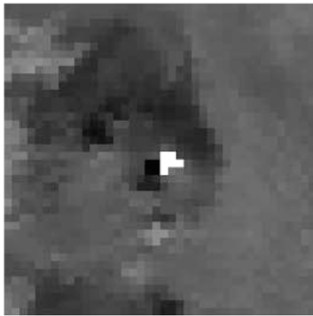
band 2 (0.72-1.10 μm)
maximum albedo 20.63



band 17 (0.89-0.92 μm)
maximum albedo 67.10



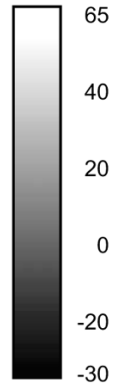
band 3 (3.55-3.93 μm)
maximum temperature 64.73°
(saturated)



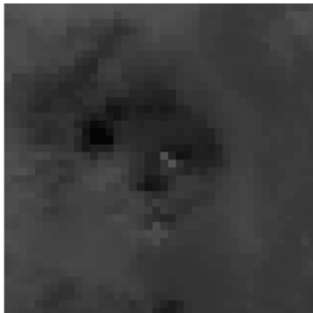
band 20 (3.66-3.84 μm) and
band 21 (3.929-3.989 μm)
maximum temperature 104.18°



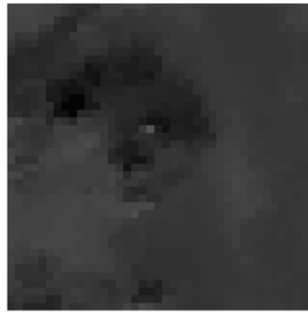
Brightness
Temperature
(°C)



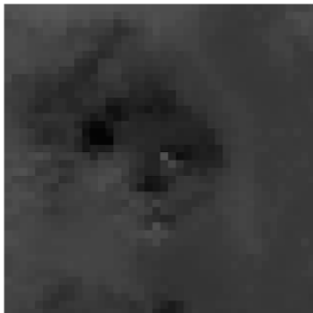
band 4 (10.5-11.5 μm)
maximum temperature -8.66°



band 31 (10.78-11.28 μm)
maximum temperature -8.48°



band 5 (11.5-12.5 μm)
maximum temperature -9.86°



band 32 (11.77-12.27 μm)
maximum temperature -9.30°

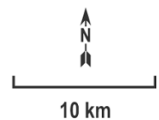


Figure 3.6. Examples of a thermal anomaly created by an active a'a lava flow in several wavelengths of AVHRR and MODIS data 5 min apart with similar viewing geometries on the NE flank of Kliuchevskoi Volcano, Kamchatka on January 4, 2010. Note higher recorded temperatures in shorter wavelengths (Wien's Law).

mines how rapidly a hot object cools and how quickly a cold body heats up. This observation can be seen in the equations that define each of the three main heat losses which show that generally hotter targets with large surface areas cool faster than cooler targets with smaller surface areas:

$$Q_k = \frac{kA\Delta T}{L} \quad (3.5)$$

$$Q_c = h_c A \Delta T \quad (3.6)$$

$$Q_r = \sigma \cdot \varepsilon \cdot \tau \cdot \psi \cdot A (T_{\text{hot}}^4 - T_{\text{amb}}^4) \quad (3.7)$$

In this equation sequence the following constants and variables are defined:

k = thermal conductivity of rock;

A = area over which heat is transferred;

ΔT = the difference in temperature between the hot and cold body;

L = the distance over which conduction is occurring;

h_c = the convective heat transfer coefficient;

σ = Stefan–Boltzmann constant;

ε = emissivity of the hot surface;

τ = atmospheric transmissivity;

ψ = the shape factor which is a function of the roughness of the surface and angle between the emitter and the receiver;

T_{hot} = the temperature of the hot body from which heat is flowing;

T_{amb} = the temperature of the cold body into which heat is flowing.

Many of these variables and constants represent complex relationships, notably the convective heat transfer coefficient and atmospheric transmissivity that are treated in Chapter 2. The shape factor helps take into account non-Lambertian radiators, those that do not radiate energy equally in all directions, but for volcanic cases it is often treated as equal to 1. For active lavas with surface temperatures above 700–900°C, the majority of heat is transferred by radiation. With cooling to ~500°C, convective heat transfer begins to account for the same amount of heat loss as radiation (e.g., Keszthelyi *et al.*, 2003).

Considering these heat transfer relationships, the most common forms of effusive volcanic activity (emplacement of lava flows, lakes, and domes)—as well as activity at hot open vents and fumarole fields—should have a predictable appearance in satellite imagery. That is, they are hot and, thus, should radiate substantial amounts of heat over a sufficiently large area in relation to that of the pixel

so as to be detectable. The resulting hot-spot properties are summarized in Table 3.2, where the criteria listed may not be definitive, but are consistent with experience from over 15 years of daily monitoring for all of the tabulated types of activity across the northern Pacific.

3.4.1 Lava flows

Lavas are often the first thing that comes to mind when considering the products of an active volcano. Lavas are typically fed from vents or fissures in the earth which more often than not were created shortly before the eruption started. It is the exception rather than the rule that a lava flow originates from the same vent over and over. Given the insulating properties of volcanic rock, the rate of rise of near-surface magma ($>0.1 \text{ m s}^{-1}$) and the speed with which a fracture can form, there is little time for an increase in temperature caused by the rise of magma to be detected by a satellite sensor (e.g., Bonneville *et al.*, 1985; Bonneville and Kerr, 1987). Following this logic it is unlikely to detect a precursory signal to a lava flow unless one has high temporal resolution on the order of minutes. The size of a lava flow vent or fissure is typically small, meters to tens of meters in size. Coarse spatial resolution sensors will have difficulty seeing a small warm target surrounded by many square kilometers of cool background material.

The high surface temperatures at active lava flows (typically 100–750°C, and up to 1,000–1,200°C over active fresh lava or hot cracks in the chilled crust) mean that radiance from even a small area of active lava can dominate and, commonly, even saturate a pixel. Hence, a time series signal for an active lava flow often jumps from background (ambient) radiances to very high, even saturating levels at the onset of effusion. Effusive eruptions can then last hours to months, even years to decades, during which time volumetric output can change including steady, waning, and/or pulsed effusion. Each of these shows characteristic trends on satellite data derived radiance times series that, thus, can likewise show the same three trends:

- waning phase during tapping of a pressurized source, as recorded during Fernandina's 1995 eruption using ATSR (Along Track Scanning Radiometer) data by Wooster and Rothery (1997);
- steady phase during overflow of an open conduit, as recorded using AVHRR data during a

Table 3.2. Common features to identify the likely volcanic source of a thermal anomaly.

<i>Type of volcanic activity</i>	<i>Expected characteristics</i>	<i>Features not expected</i>
Lava flows	<ul style="list-style-type: none"> – Basaltic or intermediate volcano – Saturated signal in successive images – MIR values much greater than TIR – Both MIR and TIR elevated – Multiple pixel anomaly 	<ul style="list-style-type: none"> – High-silica volcano – Low temperature in one image – MIR equal or less than TIR – TIR not elevated – Single pixel anomaly
Lava domes	<ul style="list-style-type: none"> – Dome-building volcano – Warm in successive imagery – Varying warm temperatures – MIR greater than TIR – MIR and TIR elevated 	<ul style="list-style-type: none"> – Basaltic shield volcano – Warm in only one image – Consistent high temperatures – MIR and TIR equal – TIR not elevated
Pyroclastic flows	<ul style="list-style-type: none"> – Explosive volcano – Previous ash eruption – Large areas covered by anomaly – Persistent warm temperatures – MIR greater than TIR 	<ul style="list-style-type: none"> – Basaltic shield volcano – No known ash eruption – Small hot area – Transient signal – MIR and TIR equal
Debris flows/lahars	<ul style="list-style-type: none"> – A source of water (lake, glacier) – A topographic gradient – MIR and TIR roughly equal – Moves from image to image 	<ul style="list-style-type: none"> – Dry or barren volcano – Little or no topography – High MIR – Stationary
Strombolian activity	<ul style="list-style-type: none"> – Basaltic or intermediate volcano – Intermittent in sequential imagery – MIR greater than TIR 	<ul style="list-style-type: none"> – High-silica volcano – Persistent over many images – MIR equal to TIR
Vulcanian/Plinian activity	<ul style="list-style-type: none"> – Explosive volcano – Thermal signal obscured by ash cloud – Ash cloud is cold 	<ul style="list-style-type: none"> – Basaltic shield volcano – Persistent thermal signal – Clouds are warm
Geothermal lakes	<ul style="list-style-type: none"> – Known presence of a lake – MIR and TIR roughly equal – Persists as ambient temperature drops 	<ul style="list-style-type: none"> – No known lake or crater – MIR greater than TIR – Temperature drops as ambient
<i>Problematic activity to reliably detect</i>		
Intrusive activity	<ul style="list-style-type: none"> – An active hydrothermal system – Subtle persistent warming 	<ul style="list-style-type: none"> – No known hydrothermal areas – Rapid warming
Volcanic gases	<ul style="list-style-type: none"> – Low but warm temperatures – Transient signal – Signal changes with time of day 	<ul style="list-style-type: none"> – High temperatures – Persistent over days – Signal persists day and night

number of summit eruptions recorded at Mt. Etna during the 1980s (Harris *et al.*, 2000);

- pulsed phase when fresh batches arrive at the erupting vent (e.g., Steffke *et al.*, 2011) or during a series of fountain-fed events (e.g., Harris and Neri, 2002); or
- any mixture of the above, as during Stromboli's 2002–2003 eruption, which showed waning and steady phases, with pulses overprinted (Calvari *et al.*, 2005; Lodato *et al.*, 2007).

When lava effusion stops, the surface begins to cool rapidly (Aries *et al.*, 2001) and the temperature decays exponentially (Hon *et al.*, 1994), as has been observed in ground-based thermal data for cooling lavas (Harris *et al.*, 2007) as well as satellite-based data (Wooster *et al.*, 1997; Patrick *et al.*, 2005a). Even so, the center of a thick lava flow may stay warm for years, where the lava can appear as a faint thermal anomaly just above the background temperature for an extended period after effusion has

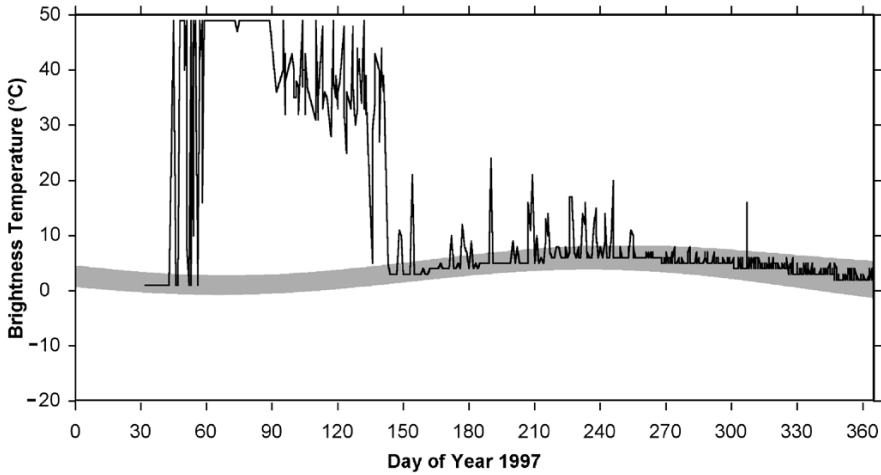


Figure 3.7. Time series of an eruption of a lava flow at Okmok Volcano (from Dehn *et al.*, 2000). No clear precursor is observed, the signal saturates, and, when effusion ends (around day 90), cooling takes place rapidly.

ceased. Etna's ~120 m thick 1991–1993 flow field, for example, was still apparent as a faint hot spot in AVHRR data up to a year after the eruption ended. At many volcanoes where active lavas have been recorded in satellite imagery, hot spots can linger for days, weeks, and months after effusion has ceased, as shown in Figure 3.7 at Okmok Volcano (Dehn *et al.*, 2000).

Spatially, lavas will often go beyond a single pixel in the satellite data, even in coarse spatial resolution sensors. In this case some structure can be seen in the data and give insight into the processes active in the lava flow. For example, a sensor will reach saturation at some level, but not trigger a “recovery” pixel until the temperature super-saturates the previous pixel. A recovery pixel occurs when the sensor resets itself, and the value at that pixel is void. They usually appear as extremely cold pixels in brightness temperature data. If these pixels only occur in one part of a large flow, this suggests hotter temperatures in that area.

Most of the models given in the introduction, as well as the derived products later in the chapter, are simplifications, requiring the lava to have fixed properties across its thermal, temporal, and spatial regimes. This is not necessarily the case; therefore, it is often best to ground-truth these data when possible, or constrain assumptions and variables in the model through higher spatial resolution data. When time-coincident supporting data sets are unavailable, it is often best to have an analyst familiar with a volcano and its products interpreting the imagery.

3.4.2 Lava domes

Lava domes occur where lava with a high yield strength and viscosity piles up over the vent (Macdonald, 1972). This lava is often of a higher silica content and lower eruption temperature than lavas involved in typically more fluid, basaltic, and andesitic lava flow forming eruptions. Lava domes also typically have lower rates of extrusion than lava flow systems and can be active for decades. However, extrusion can show a characteristic cyclic trend extending over time scales of hours to years, which often leaves a characteristic waxing–waning trend on satellite data derived thermal time series as has been observed, for example, in Landsat TM data for Santiaguito's lava dome (Harris *et al.*, 2003) and AVHRR data at Bezymianny's lava dome (Ramsey and Dehn, 2004; van Manen *et al.*, 2010b). Like lava flows, a lava dome can rapidly outgrow the size of a pixel in satellite data. Because of the ever-present crust, and steep sides, lava domes often show great variability in brightness temperature over their surface.

Because they are not topographically flat, the morphology of such domes can present a challenge to remote sensors. Domes are usually very steep, so that (for an off-nadir view) the view from the satellite may see the slope facing the sensor and not that facing away from the sensor, so that some of the energy may be hidden, and thus missed, from the satellite view. Domes are also great insulators and may even cool to near-ambient temperatures at the

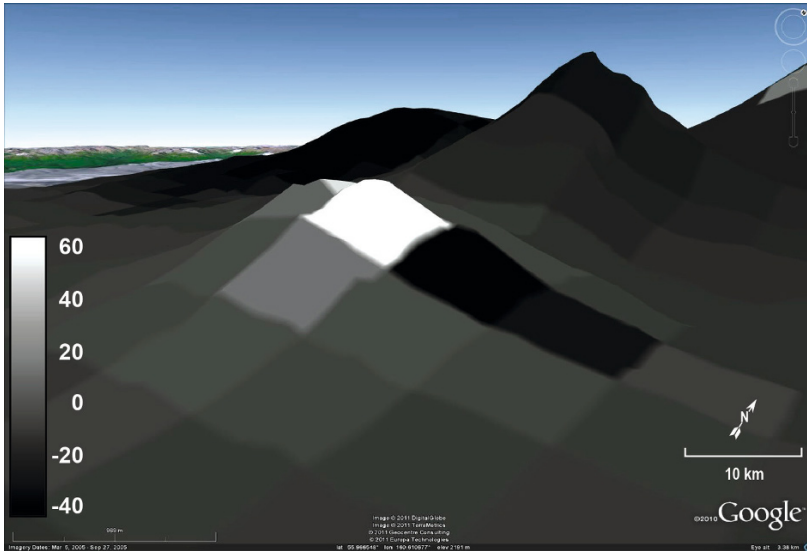


Figure 3.8. A thermal anomaly of a lava dome at Bezymianny Volcano on December 15, 2009. The view is to the northwest; each pixel is 1.1 km across. The anomaly is on the lava dome. Saturated pixels are present and have triggered a recovery pixel that appears black down the eastern flank of the dome and towards the breach in the cone created in the 1956 eruption.

surface to hide near-magmatic temperatures at their core, as has been witnessed at Santiaguito's lava dome in Guatemala (Harris *et al.*, 2002). Lava domes grow either in an endogenous fashion, inflating from within like a balloon as new lava arrives from below or, exogenously, where new lava breaks out onto the surface forming lobes or spines. Both styles of activity can give characteristic thermal signals, as recorded for Unzen's lava dome (Japan) in TM data by Wooster *et al.* (2000) and at Bezymianny's lava dome (Kamchatka) in AVHRR data by van Manen *et al.* (2010b). Depending on the size of the dome, the size of the pixel, and the nature of the extrusive activity, a thermal anomaly may or may not be apparent in the satellite sensor data and is less likely to saturate the satellite sensor than a lava flow, although during active extrusion and when using small pixels saturation can occur (Figure 3.8).

A classic thermal record for a young lava dome was recorded for Lascar Volcano in Chile using Landsat TM data by Oppenheimer *et al.* (1993a). This time series showed a waxing trend as the dome was emplaced followed by a waning trend as the dome subsided and choked the conduit, to finish with pressurization and explosion, after which the cycle began again. Established lava domes that have

been active for decades may undergo periods of growth that can be seen as thermal anomalies. Large domes like those of Bezymianny and Shiveluch Volcanoes carry significant risk of instability as they grow; a flank collapse of the dome can trigger sudden depressurization and explosions. Such failures are often preceded by cracks in the dome or new exogenously placed material at the surface, which triggers strong thermal signals (van Manen *et al.*, 2010b). During explosions, large areas of hot material may be emplaced around the dome as pyroclastic flow deposits (see Section 3.4.4) which, if the data are of sufficiently high temporal resolution, will persist in the thermal time series (Dehn *et al.*, 2000). Such a time series is given here for Bezymianny Volcano in Figure 3.9.

3.4.3 Lava lakes

These features are relatively rare at volcanoes, but can be extremely persistent and are capable of being active for decades, even centuries. Persistent lava lakes include those at Mt. Erebus, Erta Ale, and Mt. Belinda (e.g., Francis *et al.*, 1993; Oppenheimer and Francis, 1998; Patrick *et al.*, 2007). An active lava lake can be characterized by rapid overturn of the crust exposing fresh lava at the surface, so that

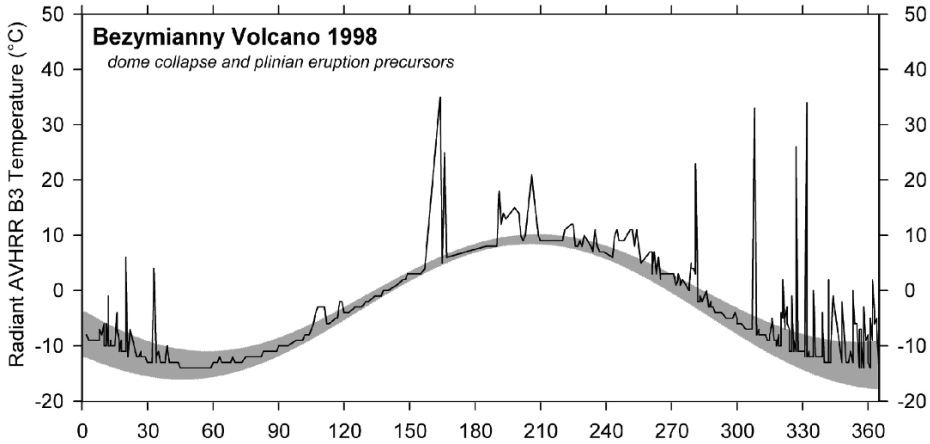


Figure 3.9. Time series of lava dome growth at Bezymianny Volcano in 1998. Often, warm pixels are seen in successive imagery, but rarely reach saturation and do not recur for days. The sudden drop in temperature to background or below after day 150 was due to a large eruption plume obscuring the anomaly from the sensor.

an intense, persistent hot spot should be apparent with relatively high or low levels of intensity depending on whether the image is captured during or between overturn. Time series for a number of lava lakes are given by Wright and Pilger (2008) and show just such a persistent (in the long term) but variable (in the short term) character.

Persistent lava lakes can be associated with lava flows and, like lava flows, typically give a very strong thermal signal to a satellite sensor. Although this leads to saturation of most thermal sensors, for very small lava lakes (on the order of a hundred square meters) in larger ($>1 \text{ km}^2$) pixels, unsaturated data could be available. As a lava lake waxes and wanes, it can overflow and marginal pixels may show variances in brightness temperature that represent this activity.

Transient lava lakes, like those at Mauna Ulu or Kupaianaha at Kīlauea Volcano in Hawaii, will crust and cool with time, showing a rapid decay of thermal signal. Like a thick lava flow, these can show weak thermal anomalies months to years after active overturn or extrusion has stopped.

3.4.4 Pyroclastic flows and block-and-ash flows

Pyroclastic flows are hot particulate flows created when an eruption column (or part of it) collapses under its own weight. Sometimes these flows can be fed by low-level ash fountaining during a sustained ash eruption when the eruption plume cannot loft

and drift, so that the ash “boils over” from the vent. Block and ash flows are typically created when a lava dome collapses, causing sudden decompression of pressurized magma within the dome. The resulting explosion creates hot pyroclastics that run down the flank of the volcano below active lava domes or large silicic lava flows. All of these pyroclastic flow types can be very hot, attaining many hundreds of degrees Celsius.

Because pyroclastic flows are often short lived, typically lasting minutes to tens of minutes, active flows are difficult to capture in satellite imagery unless the overpass is fortuitous or the acquisition is of very high temporal resolution. In addition, during an eruption, the thermal signal may also be obscured by the colder eruption cloud rising over the associated pyroclastic flow, as was observed in AVHRR and MODIS data during the 2006 eruption of Augustine Volcano by van Manen *et al.* (2010a). However, as the cloud drifts away, the hot spot associated with the warm deposit will persist for days in thermal imagery, so that cooling pyroclastic flows can be recorded in satellite thermal data, as was observed by Wooster (2001) using ASTR data following emplacement of pyroclastic flows at Lascar.

An example of thermal detection of a pyroclastic deposit in Kamchatka, using AVHRR data for an eruption at Kizimen Volcano during December 2010, is shown in Figure 3.10. During this event an explosive eruption fed a cold ash plume that initially obscured thermal signals. However, the

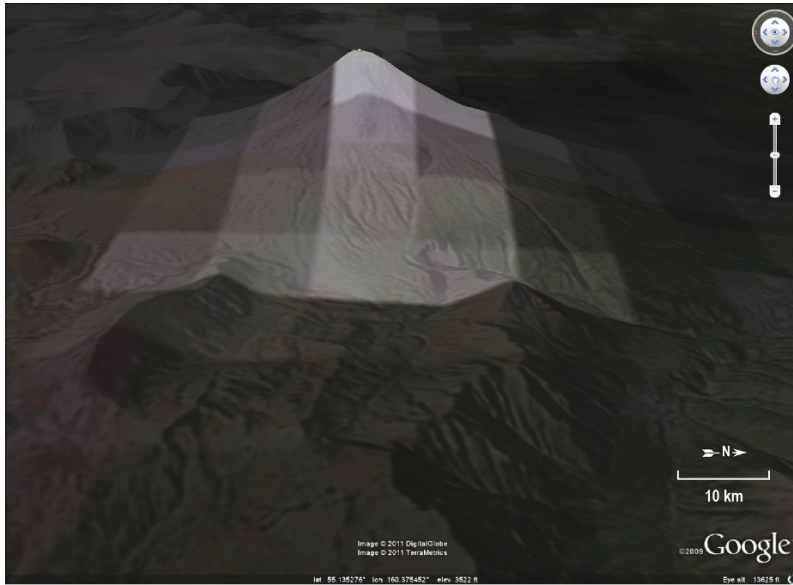


Figure 3.10. Kizimen Volcano in Kamchatka. A pyroclastic flow deposit on January 7, 2011, obscured during the eruption, warms the flanks of the volcano. The temperatures are below saturation, but cover a large area. The image n19.11007.1544 is night-time with a zenith angle of 16° . The warm temperatures cover a large area, typical of pyroclastic flow deposits.

day after the eruption a spatially large thermal anomaly (at temperatures less than saturation temperatures) was observed extending down the north-eastern flanks of the volcano. For a single deposit, these would cool quickly over the course of days, but repeated explosive eruptions at Kizimen added to the deposit to cause the thermal signal to persist for months.

3.4.5 Debris flows

Debris flows are a type of mass flow comprising a cohesive mixture of sediment, water, and often organic debris. A lahar is a specific term for a volcanogenic debris flow that involves the emplacement of mud derived from unconsolidated volcaniclastic material remobilized by water. Such debris flows can be warm: for instance, when they are triggered by hot volcanic deposits emplaced on snow or when water from a hot crater lake is released onto the flanks of a volcano. They are also short lived, usually lasting minutes to tens of minutes. As a result, their thermal signal will be transient and of low intensity. It is thus extremely rare to catch a lahar in progress in polar-orbiting satel-

lite data and, more often, satellite sensors capture a large faintly warm deposit after the event.

During the eruption of Redoubt Volcano in Alaska in 2009, however, an active debris flow was observed in thermal imagery by Peter Webley at AVO, and its progress is plotted here in Figure 3.11 using AVHRR images. The summit lava dome collapsed upon the nearby glacier, melting enough ice to create a lahar. The mixture of water and fresh pyroclastics moved along Redoubt's Drift River valley, down which its velocity was estimated using the time of the dome collapse that generated the flow and the warm flow-front at the time of the images. The velocity matched well with other independent measurements and observations made on the ground, these giving a flow velocity of about 40 km/h. In this case the debris flow was significantly warmer than the background and covered a large area, so that it showed up well in the AVHRR thermal data. However, debris flows can also have characteristic reflective properties that set them aside from their surroundings, so that the environmental change induced by the sudden emplacement of a muddy deposit can be detected from image to image if vegetation or snow is buried by the deposit (see Chapter 11).

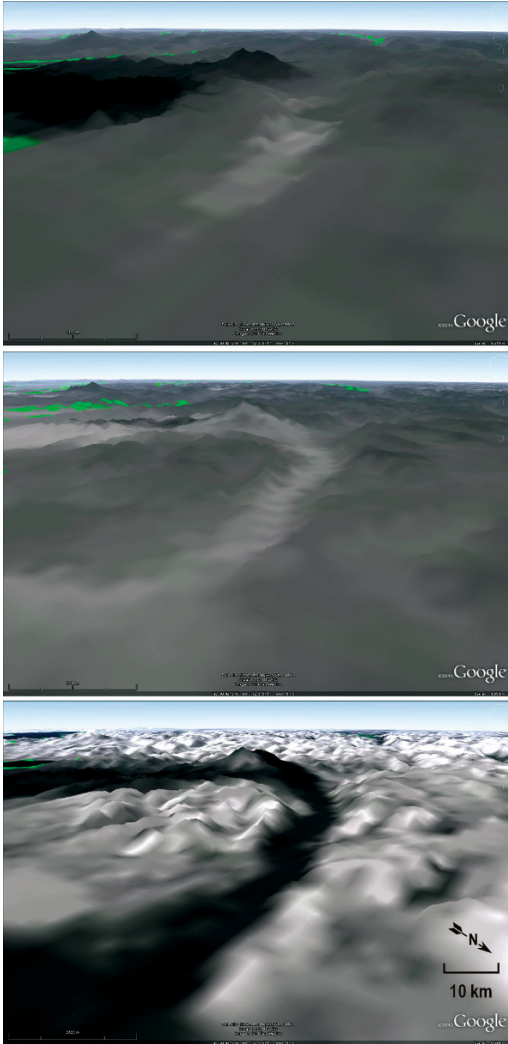


Figure 3.11. A lahar warms pixels in the Drift River, Alaska after dome collapse at Redoubt Volcano on April 4. The first MIR AVHRR image is from 14:45 UTC (n15.09094.1455), then 16:23 UTC (n15.09094.1623), the final image is a visible MODIS image from 20:35 UTC showing the black deposit (t1.09094.2035). The estimated speed of advance was about 40 km/h.

3.4.6 Explosive activity

Explosions are inherently transient at volcanoes. While strombolian and vulcanian explosions can last seconds to minutes, rarer plinian eruptions can last hours, and catastrophic events like a caldera collapse can last for days. A typical strombo-

lian event lasts seconds to tens of seconds and will emplace a small amount of hot material (bombs) near the vent (see Patrick *et al.*, 2007 for a review of strombolian eruption processes). This material may cover only a tiny fraction of even a 30 m pixel and will be incandescent for minutes at most. For an orbital sensor to catch such a brief signal, there must either be many such satellites or many such events.

Even with five AVHRR sensors and two MODIS sensors currently in orbit, the chances of catching an individual strombolian eruption are not that high. As a result, a time series plot of warm temperatures for strombolian activity shows only intermittent spikes in warm temperatures (Figure 3.12). What these satellites can record, though, are the general level of activity as expressed by the vent temperature, or area, that feeds the explosions (e.g., Harris and Stevenson, 1997).

Emplacement of material erupted during an individual strombolian eruption is unlikely to saturate a sensor, the quantity of hot material emplaced being too small (Figure 3.13). Likewise, the vents are so small that they can be quite difficult to spot in 1 km data, although they may be mapped using 120 m and 30 m data (Harris and Stevenson, 1997). However, because fire fountains will continually emit a spray of hot material for minutes to hours to feed clastogenic lava flows, such events can yield an intense thermal signal, even saturating 4 km pixels (e.g., Gouhier *et al.*, 2012).

3.4.7 Intrusive activity

Volcanoes undergo a great deal of subsurface activity, and may even undergo a large part of their growth from endogenous activity (Francis *et al.*, 1993). However, because the satellite-based sensor can only view the surface (and the edifice is a poor thermal conductor) such intrusions are often invisible from the satellite perspective. However, early work using AVHRR and TM data for Mt. Etna showed that, if data were appropriately corrected for adiabatic, emissivity, and atmospheric effects, then the surface expression of heat released by shallow intrusions may be detectable. The studies by Bonneville *et al.* (1985) and Bonneville and Kerr (1987) are classics in this regard, laying out the methodologies that need to be applied to detect the surface expressions of shallow intrusions from space-based sensors.

Intrusive activity may also have secondary, though significant, effects on existing hydrothermal

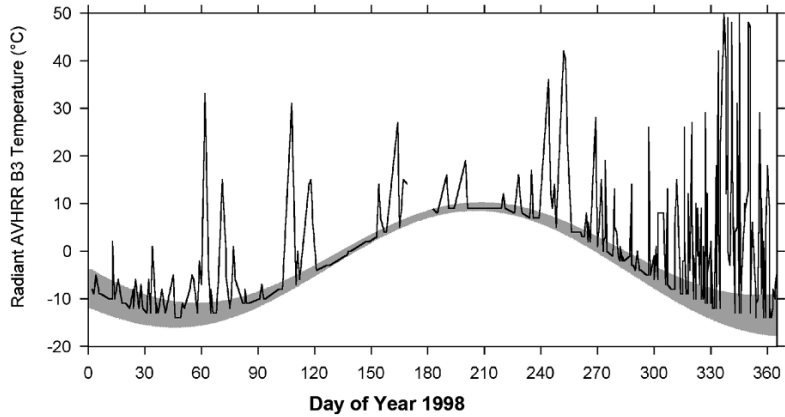


Figure 3.12. Time series plot of strombolian activity at Karymsky Volcano in 1998 (after Dehn *et al.*, 2000).

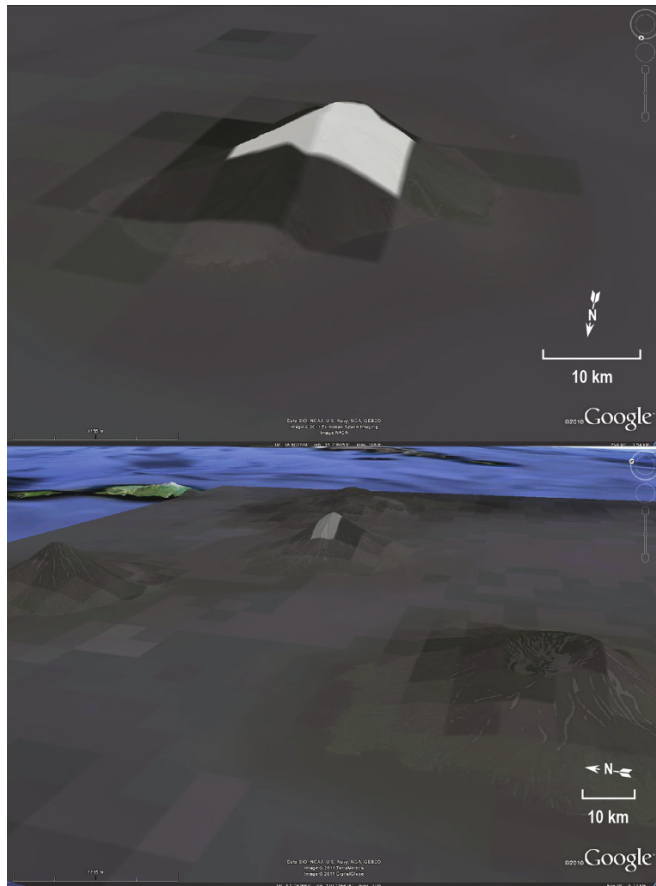


Figure 3.13. A strombolian eruption at Stromboli Volcano in MODIS data on April 13, 2006 (t1.06103.2100) and Mt. Cleveland, Alaska on May 11, 2011 in AVHRR data (n16.11131.0606). In both cases, in spite of favorable viewing conditions, no thermal anomaly was observed in the next few images.

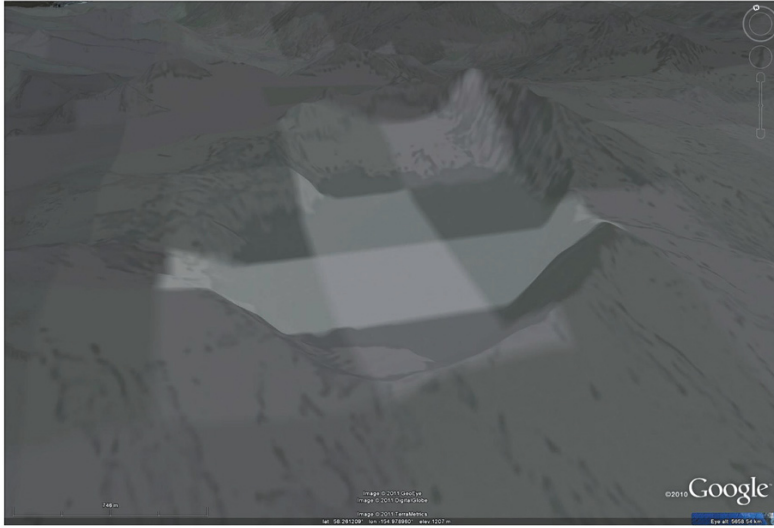


Figure 3.14. Katmai Lake in Alaska. The lake freezes only very late in the season due to heating from the volcano. In fall, when the ambient temperature drops, the lake remains nearly constant, showing this warm feature in satellite imagery.

systems, which in turn can have surface expressions. This may change the temperatures of geothermal lakes, melt snow, or cause degassing that damages plant life.

3.4.8 Geothermal lakes

Hot (and acidic) lakes of water gathering in the summit crater of a degassing volcano potentially generate a hot spot. If the lake waters are sufficiently warm and the background sufficiently cool, then the lake can be detected and its heat flux measured (Figure 3.14). However, because such lakes are typically small and relatively cool, this is the remit of high (30–120 m) spatial resolution data, where Oppenheimer (1993, 1996, 1997a, b) provides the recipes for geothermal lake detection and measurements in satellite thermal data.

Geothermal lakes are also affected by external factors, such as local weather, which may cause a change in the thermal signal that is not necessarily related to volcanic activity. However, some cases have been shown where rapid heating of a lake precedes an eruption, such as at Karymsky Volcano in Kamchatka in January 1996 (Belousov and Belousova, 2001).

3.4.9 Volcanic degassing

Thermally, volcanic degassing is expressed by the presence of hot ground broken by small (mm-to-cm wide) fumaroles. Because these are of such low thermal intensity and such small area, they are difficult to detect in 30–1,000 m pixels. Again, the methodologies proposed by Bonneville *et al.* (1985) and Bonneville and Kerr (1987) show promise, but even one of the most famous fumarole fields in the world (Vulcano, Italy) is difficult to resolve even in 120 m (TM) thermal data (Harris and Stevenson, 1997) and (currently) impossible to detect in AVHRR data. Oppenheimer and Rothery (1991) provide some guidelines for the detectability of fumarole fields but, until we have pixels of the order of one meter, consistent detection and measurement of such features may remain within the helm of airborne and ground-based thermal campaigns (e.g., Harris and Maciejewski, 2000; Matsushima *et al.*, 2003), which are of suitable spatial resolution to allow the tracking of the spatial and temporal evolution of such small (in terms of area and thermal emission) heat sources.

Broad zones of geothermal heating, such as that apparent at Yellowstone, have proved capable of detection in high spatial resolution thermal infrared data provided by ASTER (Hellman and Ramsey, 2004). However, again they are (currently)

better suited to ground-based thermal observations (e.g., Sekioka and Yuhara, 1974).

3.5 ARE THERE (SATELLITE-BASED) THERMAL PRECURSORS TO ERUPTIONS?

This is a difficult question to answer, because the exact definition of an eruption precursor is under debate. It can be argued that, because thermal activity can be observed in satellite data, then the volcano is in fact active and in eruption. In many cases this is true. However, changes in thermal activity associated with fumarole fields, lava domes, and/or strombolian systems may be precursors to larger explosive or effusive events. In such cases, trends apparent in the thermal character of these smaller events may be precursors to larger eruptions. Oppenheimer *et al.* (1993a) noted this cycle at Lascar Volcano up until 1993, where each thermal oscillation ended in an explosion. This is witnessed repeatedly over longer time scales at Bezymianny Volcano in Kamchatka from 1993 in operational monitoring at AVO (Dehn *et al.*, 2000; Ramsey and Dehn, 2004; van Manen and Dehn, 2009; van Manen *et al.*, 2010b). After the 1956 eruption of Bezymianny (Gorshkov, 1959) the lava dome has grown to reach higher than the crater rim. This dome is over 1 km in diameter and has a few episodes of dome growth each year. As described above, this growth often takes the form of a new lobe that exposes warm material to the satellite sensor. As the lobe grows it becomes unstable, oversteepening the lava dome, collapsing, and causing a sudden depressurization of the lava and associated explosion. In these cases, the thermal signal is a precursor to larger explosions. It is not, however, the case for all volcanoes with a lava dome. Just 90 km to the northeast, Shiveluch Volcano has a similar history to Bezymianny (Gorshkov and Dubik, 1970) and an active lava dome. This lava dome also has frequent periods of growth and shows thermal anomalies, yet these do not show a pattern as precursors to explosive eruptions.

Each volcano is unique. Though volcanoes and eruptions follow the same general pattern, they are complex systems that are affected by their own placement, environment, the rate of magma supply and its composition, etc. As a result, monitoring should be tailored to each volcano. This has important implications for automated detection of volcanic activity.

3.6 AUTOMATED DETECTION OF THERMAL ANOMALIES

Automated detection of thermal anomalies has long been a goal of satellite monitoring, and many methods exist that allow execution of operational hot-spot detection. Following Steffke and Harris (2011) we can define three types of hot-spot detection algorithm: contextual, temporal, and fixed threshold. While contextual approaches determine whether a pixel is thermally anomalous relative to its locally defined background, temporal approaches define normality in terms of the thermal history of a pixel and fixed approaches in divergence from a set value or threshold.

The first method proposed for automatic detection of volcanic hot spots in satellite thermal data was the contextual method of Harris *et al.* (1995). This was later packaged as VAST (Higgins and Harris, 1997) and involved comparing a (target) pixel's thermal level with that of its spatial background, as defined by the surrounding pixels. If the difference between the target and its immediate background exceeded that obtained for the maximum difference obtained from all pixels across nearby non-volcanic sectors of the image, then the pixel was flagged as "hot".

Later, a fixed threshold algorithm, Okmok (Dean *et al.*, 1998), was also implemented. Okmok, named after the volcano where it was first applied, flagged a pixel when the MIR temperature exceeded an arbitrary threshold of 35°C. The original Okmok method generated too many false alarms to be useful as a monitoring tool, but was successful in gathering time series data for baseline comparison. Later still, a multiple fixed threshold approach was applied to GOES data to allow detection of active lava at Hawaii's Kilauea Volcano (Harris *et al.*, 2001) and all volcanoes within the GOES footprint (Harris *et al.*, 2000, 2002). Probably the most well known fixed threshold algorithm is MODVOLC (Flynn *et al.*, 2002; Wright *et al.*, 2002a). The MODVOLC approach uses a normalized difference of the MIR and TIR bands, and compares this with a conservative threshold set to minimize false detections in a global data set and is thus primarily designed to detect thermal activity globally and to provide data in cases where little regular monitoring exists. This algorithm runs without user intervention and has met with great success.

The primary temporal algorithm used in volcanology is RAT (Robust AVHRR Technique),

initially proposed by Tramutoli (1998), and first applied to a volcanic target by Di Bello *et al.* (2004). Now called the Robust Satellite Technique (RST), as renamed by Pergola *et al.* (2008, 2009), the algorithm uses the temporal behavior of a pixel to assess whether it is anomalous or not. The mean and standard deviation for a pixel using images obtained from the same time of year and day are used to assess whether the current recording diverges from the “norm” or the expected value of a pixel temporally, spatially, and spectrally.

In all of these models, the anomaly in an image must pass a series of tests more complex than a simple threshold or algebraic equation in order to be considered a hot spot. By way of example, the Okmok II algorithm developed at AVO involves a Bayesian approach with a series of tests (Figure 3.15), many of which are unique to each volcano.

These are broken up into a system of credits and demerits that are assigned to each potential hot spot. Many of these are based on characteristics in Table 3.2. The list of credits and demerits is flexible, but a base set of credits includes: the bright pixel is saturated in the MIR; the MIR pixel is much brighter than the TIR pixel at the same location; the MIR pixel is over 2 standard deviations warmer

than the surrounding pixels in the same image; the MIR pixel is 2 standard deviations brighter than the same pixel in previous images; the estimated thermal flux exceeds 1 MW; the volcano is at an elevated color code. Each of these in turn can be weighted (given more than a single credit) and other credits added. As with the color code, credits and demerits are based on more than satellite data. Other geophysical data sets where available can constrain the nature of the activity when paired with satellite data (e.g., van Manen *et al.*, 2011).

There are environmental and data concerns that drive the demerits that include: the bright pixel is more than 10 km away from the volcano; the view (zenith) angle is over 40°; the image contains bad scan lines or known noise pixels; the anomaly is a complex shape with many embayments or islands; the image is cloudy; solar reflection is detected at the hot pixel. Some of these are changed or weighted depending on the volcano: for example, a shield or caldera would use the 40° zenith angle limit, but a stratocone requires a 30 or even 20° zenith angle limit to avoid not being able to see the lee side of the edifice from the satellite.

When the credits outweigh the demerits, a notice may be sent based on a second set of criteria

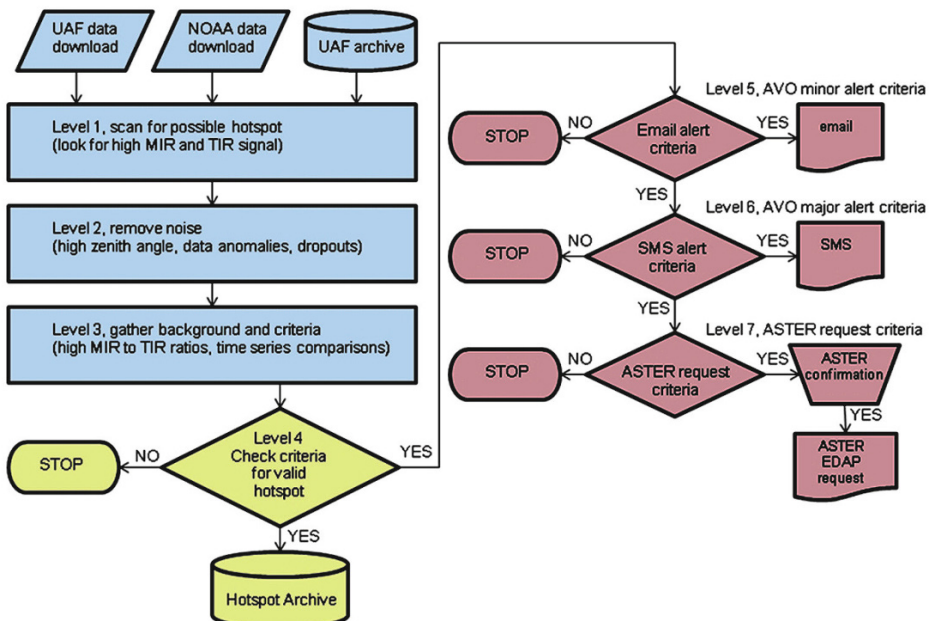


Figure 3.15. The basic flow chart for the Okmok II algorithm. The blue portion is applied to all incoming imagery. The green portions are the first discriminating criteria to detect a possible hot spot and fill the database. The red portions are the alert protocols to send messages to AVO and a request for ASTER imagery.

that assesses the severity of the anomaly. These criteria are based on operations of the observatory. An email is always sent to analysts if an anomaly is detected. If the anomaly represents a significant change at the volcano, is the first detected, or has an increase in the number of pixels or a jump in brightness, a text message is sent to analyst cell phones. If it is a first anomaly, or if no request has been sent in the last 10 days, the system automatically generates a request for higher spatial and spectral resolution data from the ASTER sensor.

3.7 HIGHER LEVEL THERMAL PRODUCTS

The most basic parameter that can be extracted from pixels selected as thermally anomalous is spectral radiance. As argued above, this can be converted to thermal energy and, as long as all anomalous pixels have been detected, selected, and used, should provide a proxy for the thermal energy involved in the volcanic process. Two higher level products that this parameter can be used to constrain are eruption type and lava discharge rate.

3.7.1 Eruption type

Some types of eruptions will have different thermal signals than others. For example, a strombolian or vulcanian emission of hot material will be a short-lived burst of small (cm-to-m scale) hot fragments that will be scattered across a pixel, generating a satellite-received thermal signal that will be weak and decay rapidly (in minutes). In contrast, an effusive emission that lasts more than a few hours should emplace a much larger area of hot material and create a stronger (and potentially more persistent—depending on the duration of the event) thermal signal that will decay less rapidly. Because of this, time series of thermal imagery may be suggestive of the eruption type (e.g., Oppenheimer *et al.*, 1993b; Dehn *et al.*, 2000; Mouginiis-Mark *et al.*, 2000; van Manen *et al.*, 2011). Examples of the temporal signature for the three primary types of hot-spot activity recorded in the North Pacific (lava flows, lava domes, and strombolian activity) are given in Figures 3.7, 3.9, and 3.12.

The size and shape of a thermal anomaly in a satellite image also gives important information about the type of activity a volcano is undergoing. In 1 km data, a lava lake or dome may be a point source of fairly fixed position and size, whereas a

lava flow may produce a more elongate anomaly of changing size. In addition to the size and shape of the anomaly, the position of the anomaly is also an important clue as to the source of the associated activity. If the anomaly is limited to the summit, it is likely a hot spot developing within central crater due to development of a hot vent, lava lake, or dome. If it is a linear feature extending down the flank of a volcano it more likely represents a fissure-fed flank eruption.

3.7.2 Discharge rate

The lava discharge rate is probably one of the most important parameters to derive. It allows both forward modeling of the areal extent potentially achieved by a volcanic flow and the source process that drives the emission at a given volumetric (or mass) flow rate. One conversion routine that exists is based on the empirical relation of Pieri and Baloga (1986) and uses lava thermal properties to convert the satellite sensor received thermal radiance to a mass or volume of erupted lava responsible for generating that response (Harris *et al.*, 1997a, 2007). The routine, however, boils down to a straightforward empirical linear relation between the erupted mass or volume flux and the satellite-received spectral radiance relation whereby (Wright *et al.*, 2001a):

$$M = xR_{\lambda} \quad (3.8)$$

where M is the mass (or volume) of lava required to give the measured signal recorded by the sensor; R_{λ} is the thermal signal recorded by the satellite-based sensor; and x is an empirically based best fitting function that links M and R_{λ} . The relation seems to give reliable results, as long as the function (x) is set appropriately. That is, the conversion needs to be set according to the environmental, rheological, and thermal insulation properties appropriate to the case in hand (Harris and Baloga, 2009), where the appropriate conversion function can be set using best fitting with field data (Harris *et al.*, 2010).

3.8 FUTURE WORK

The future of operational thermal remote sensing at active terrestrial volcanoes is uncertain. There are few plans to launch high spatial and spectral resolution sensors in the near future that use the mid or thermal infrared. MODIS currently flies aboard the Terra and Aqua platforms and, although it has

provided many new breakthroughs through its expanded spectral and spatial resolutions, newer systems using this technology are not yet finalized and another MODIS sensor will not be launched. The last AVHRR sensor was launched on NOAA-19 in 2008, and the next generation of an operational polar-orbiting infrared sensor is many years away. Fortunately, the AVHRR sensors are designed to last—the imager on NOAA-12 endured over 16 years—so there is time for development and deployment. The use of multiple platforms such as with the A-Train, a constellation of five Earth-observing sensors in the same orbital track, augments the infrared capabilities of the MODIS sensor on Aqua. This mission is primarily targeted at clouds though, as with many of the meteorological satellites (e.g. Stephens *et al.*, 2002), can be used in new ways to thermally monitor volcanoes. In addition, some military assets such as the Defense Meteorological Satellite Program (DMSP) and Defense Support Program (DSP) systems may become more available for use in volcano monitoring and research.

Geostationary capabilities are improving all the time, with new (GOES-style) sensors on GOES-R, MSG, and MTSAT allowing MIR and TIR capabilities to evolve. Better still, such data are collected at temporal resolutions of 15 min allowing fast volcanic processes to be detected, measured, and tracked at more appropriate time scales.

This direction of terrestrial sensor development seems to reflect a perception that a global constellation of coarse spatial resolution, but high temporal resolution, sensors will be sufficient for effective environmental monitoring. Although this may be true for monitoring the weather and sea surface temperatures, volcanology needs high spatial resolution to resolve subtle and (spatially) complicated thermal anomalies. However, improvements in temporal resolution (in the fast-changing world of volcano monitoring) are more important than spatial and spectral resolution. Thus, as long as meteorological satellites continue to include an all-important MIR (hot-spot detection) capability, then volcano monitoring will be viable. In fact, for fast detection, higher temporal resolution should be the goal. Detection in such low temporal resolution (4 km) data is, though, only achievable if we retain the MIR (3.9 μm) hot-volcano channel (also known as the “fire channel” for its ability to detect wild fires).

As indicated in Chapter 4, higher spatial and spectral resolution data can significantly increase

warning times for dangerous activity. It is certain that newer high-resolution sensors will be launched, but until that time future work must be constrained to improving the understanding of volcanic processes and the utilization of current data sets. An outstanding example of this is the AVHRR system, though over 25 years old at this time it is still the workhorse of volcano monitoring.

3.9 REFERENCES

- Abrams, M.; Glaze, L.; Sheridan, M. (1991). Monitoring Colima Volcano, Mexico, using satellite data, *Bull. Volcanol.*, **53**(7), 571–574, doi: 10.1007/BF00298157.
- Abrams, M.; Realmuto, V.; Pieri, D.; Buongiorno, F. (1994). Mt. Etna lava flows analyzed with remote sensing, *EOS, Trans. Am. Geophys. Union*, **75**(47), 545, doi: 10.1029/94EO02026.
- Andres, R.J.; Rose, W.I. (1995). Description of thermal anomalies on two active Guatemalan volcanoes using Landsat Thematic Mapper imagery, *Photogramm. Eng. Rem. Sens.*, **61**, 775–782.
- Aries, S.E.; Harris, A.J.L.; Rothery, D.A. (2001). Remote infrared detection of the cessation of volcanic eruptions, *Geophys. Res. Lett.*, **28**(9), 1803–1806.
- Belousov, A.; Belousova, M. (2001). Eruptive process, impact and deposits of the 1996 and ancient basaltic phreatomagmatic eruptions in Karymskoye Lake, Kamchatka, Russia, in: J. White and N. Riggs (Eds.), *Volcaniclastic Sedimentation in Lacustrine Settings*, International Association of Sedimentologists Special Publication 30, pp. 235–260.
- Bhattacharya, A.; Reddy, C.S.S.; Srivastav, S.K. (1993). Remote sensing for active volcano monitoring in Barren Island, India, *Photogramm. Eng. Rem. Sens.*, **59**, 1293–1297.
- Bonneville, A.; Kerr, Y. (1987). A thermal forerunner of the 28th March 1983 Mt. Etna eruption from satellite thermal infrared data, *J. Geodynamics*, **7**, 1–31.
- Bonneville, A.; Vasseur, G.; Kerr, Y. (1985). Satellite thermal infrared observations of Mt. Etna after the 17th March 1981 eruption, *J. Volcanol. Geotherm. Res.*, **24**, 293–313.
- Calder, E.S.; Harris, A.J.L.; Pea, P.; Pilger, E.; Flynn, L.P.; Fuentealba, G.; Moreno, H. (2004). Combined thermal and seismic analysis of the Villarrica volcano lava lake, Chile, *Revista Geológica de Chile*, **31**(2), 259–272, doi: 10.4067/S0716-0208200400020005.
- Calvari, S.; Spampinato, L.; Lodato, L.; Harris, A.J.L.; Patrick, M.R.; Dehn, J.; Burton, M.R.; Andronico, D. (2005). Chronology and complex volcanic processes during the 2002–2003 flank eruption at Stromboli volcano (Italy) reconstructed from direct observations and survey with a handheld infrared

- camera, *J. Geophys. Res.*, **110**, B02201, doi: 10.1029/2004JB003129.
- Carn, S.A.; Oppenheimer, C. (2000). Remote monitoring of Indonesian volcanoes using satellite data from the Internet, *Int. J. Rem. Sens.*, **21**, 873–910.
- Coppola, D.; Piscopo, D.; Staudacher, T.; Cigolini, C. (2009). Lava discharge rate and effusive pattern at Piton de la Fournaise for MODIS data, *J. Volcanol. Geotherm. Res.*, **184**(12), 174–192.
- Crisp, J.; Kahle, A.B.; Abbott, E.A. (1990). Thermal infrared spectral character of Hawaiian basaltic glasses, *J. Geophys. Res.*, **95**(13), 21657–21669, doi: 10.1029/JB095iB13p21657.
- Crowley, J.K.; Zimbelman, D.R. (1997). Mapping hydrothermally altered rocks on Mount Rainier, Washington, with airborne visible/infrared imaging spectrometer (AVIRIS) data, *Geology*, **25**(6), 559–562, doi: 10.1130/0091-7613(1997)025<0559:MHAROM>2.3.CO;2.
- Dean, K.; Servilla, M.; Roach, A.; Foster, B.; Engle, K. (1998). Satellite monitoring of remote volcanoes improves study efforts in Alaska, *EOS, Trans. Am. Geophys. Union*, **79**(35), 413, 422–423.
- Dean, K.G.; Dehn, J.; Engle, K.; Izbekov, P.; Papp, K.; Patrick, M. (2002). Operational satellite monitoring of volcanoes at the Alaska Volcano Observatory, *Adv. Env. Mon. Mod.*, **1**(3), 70–97.
- Dean, K.G.; Dehn, J.; Papp, K.R.; Smith, S.; Izbekov, P.; Peterson, R.; Kearney, C.; Steffke, A. (2004). Integrated satellite observations of the 2001 eruption of Mt. Cleveland, Alaska, *J. Volcanol. Geotherm. Res.*, **135**, 51–73, doi: 10.1016/j.jvolgeores.2003.12.013.
- Dehn, J.; Dean, K.G.; Engle, K. (2000). Thermal monitoring of North Pacific volcanoes from space, *Geology*, **28**(8), 755–758.
- Dehn, J.; Dean, K.G.; Engle, K.; Izbekov, P. (2002). Thermal precursors in satellite images of the 1999 eruption of Shishaldin Volcano, *Bull. Volcanol.*, **64**, 507–519, doi: 10.1007/s00445-002-0227-0.
- Denniss, A.M.; Harris, A.J.L.; Rothery, D.A.; Francis, P.W.; Carlton, R.W. (1998). Satellite observations of the April 1993 eruption of Lascar volcano, *Int. J. Rem. Sens.*, **19**(5), 801–821 doi: 10.1080/014311698215739.
- Di Bello, G.; Filizzola, C.; Lacava, T.; Marchese, F.; Pergola, N.; Pietrapertosa, C.; Piscitelli, S.; Scaffidi, I.; Tramutoli, V. (2004). Robust satellite techniques for volcanic and seismic hazards monitoring, *Ann. Geophys.*, **47**(1), 49–64.
- Donegan, S.J.; Flynn, L.P. (2004). Comparison of the response of the Landsat 7 Enhanced Thematic Mapper Plus and the Earth Observing-1 Advanced Land Imager over active lava flows, *J. Volcanol. Geotherm. Res.*, **135**(1/2), 105–126, doi: 10.1016/j.jvolgeores.2003.12.010.
- Dozier, J. (1981). A method for satellite identification of surface temperature fields of subpixel resolution, *Remote Sens. Environ.*, **11**(3), 221–229, doi: 10.1016/0034-4257(81)90021-3
- Ferriso, C.C.; Ludwig, C.B. (1965). An infrared band ratio technique for temperature determinations of hot gases, *Applied Optics*, **4**(1), 47–52.
- Flynn, L.P.; Mouginiis-Mark, P.J.; Horton, K.A. (1994). Distribution of thermal areas on an active lava flow field: Landsat observations of Kilauea, Hawaii, July 1991, *Bull. Volcanol.*, **56**, 284–296.
- Flynn, L.P.; Wright, R.; Garbeil, H.; Harris, A.J.L.; Pilger, E. (2002). A global thermal alert using MODIS: Initial results from 2000–2001, *Adv. Env. Mon. Mod.*, **1**, 37–69.
- Francis, P.W.; Rothery, D.A. (1987). Using the Landsat Thematic Mapper to detect and monitor active volcanoes: An example from Lascar volcano, northern Chile, *Geology*, **15**, 614–617
- Francis, P.; Oppenheimer, C.; Stevenson, D. (1993). Endogenous growth of persistently active volcanoes, *Nature*, **366**, 554–557
- Galindo, I.; Dominguez, T. (2002). Near real-time satellite monitoring during the 1997–2000 activity of Volcan de Colima (Mexico) and its relationship with seismic monitoring, *J. Volcanol. Geotherm. Res.*, **117**, 91–104.
- Glaze, L.; Francis, P.W.; Rothery, D.A. (1989). Measuring thermal budgets of active volcanoes by satellite remote sensing, *Nature*, **338**, 144–146.
- Gorshkov, G.S. (1959). Gigantic eruption of the Bezymianny Volcano, *Bull. Volcanol.*, **20**, 77–109.
- Gorshkov, G.S.; Dubik, Y.M. (1970). Gigantic directed blast at Shiveluch Volcano (Kamchatka), *Bull. Volcanol.*, **34**, 261–288
- Gouhier, M.; Harris, A.J.L.; Calvari, S.; Labazuy, P.; Guéhenneux, Y.; Donnadieu, F.; Valade, S. (2012). Lava discharge during Etna's 11–13 January 2011 fire fountain event tracked using MSG-SEVIRI, *Bull. Volcanol.*, **4**, 787–793, doi: 10.1007/s00445-011-0572-y.
- Gupta, R.K.; Badarinath, K.V.S. (1993). Volcano monitoring using remote sensing data, *Int. J. Rem. Sens.*, **14**, 2907–2918.
- Harris, A.J.L. (2013). *Thermal Remote Sensing of Active Volcanoes: A User's Manual*, Cambridge University Press, 728 pp.
- Harris, A.J.L.; Baloga, S.M. (2009). Lava discharge rates from satellite-measured heat flux, *Geophys. Res. Lett.*, **36**, doi: 10.1029/2009GL039717.
- Harris, A.J.L.; Maciejewski, A.J.H. (2000). Thermal surveys of the Vulcano Fossa fumarole field 1994–1999: Evidence for fumarole migration and sealing, *J. Volcanol. Geotherm. Res.*, **102**, 119–147.
- Harris, A.J.L.; Neri, M. (2002). Volumetric observations during paroxysmal eruptions at Mount Etna: Pressurized drainage of a shallow chamber or pulsed supply?, *J. Volcanol. Geotherm. Res.*, **116**, 79–95.

- Harris, A.J.L.; Stevenson, D.S. (1997). Thermal observations of degassing open conduits and fumaroles at Stromboli and Vulcano using remotely sensed data, *J. Volcanol. Geotherm. Res.*, **76**, 175–198.
- Harris, A.J.L.; Thornber, C.R. (1999). Complex effusive events at Kilauea as documented by the GOES satellite and remote video cameras, *Bull. Volcanol.*, **61**(6), 382–395, doi: 10.1007/s004450050280.
- Harris, A.J.L.; Swabey, S.E.J.; Higgins, J. (1995). Automated thresholding of active lavas using AVHRR data. *Int. J. Rem. Sens.*, **16**(18), 3681–3686.
- Harris, A.J.L.; Butterworth, A.L.; Carlton, R.W.; Downey, T.; Miller, P.; Navarro, P.; Rothery, D.A. (1997a). Low cost volcano surveillance from space: Case studies from Etna, Krafla, Cerro Negro, Fogo, Lascar and Erebus, *Bull. Volcanol.*, **59**, 49–64, doi: 10.1007/s004450050174.
- Harris, A.J.L.; Blake, S.; Rothery, D.A.; Stevens, N.F. (1997b). A chronology of the 1991 to 1993 Mount Etna eruption using advanced very high resolution radiometer data: Implications for real-time thermal volcano monitoring, *Geophys. Res. Lett.*, **102**, 7985–8003.
- Harris, A.J.L.; Keszthelyi, L.; Flynn, L.P.; Mouginitis-Mark, P.J. (1997c). Chronology of the episode 54 eruption at Kilauea Volcano, Hawaii, from GOES-9 satellite data, *Geophys. Res. Lett.*, **24**(24), 3281–3284.
- Harris, A.J.L.; Flynn, L.P.; Keszthelyi, L.; Mouginitis-Mark, P.J.; Rowland, S.K.; Resing, J.A. (1998). Calculation of lava effusion rates from Landsat TM data, *Bull. Volcanol.*, **60**, 52–71.
- Harris, A.J.L.; Flynn, L.P.; Rothery, D.A.; Oppenheimer, C.; Sherman, S.B. (1999). Mass flux measurements at active lava lakes: Implications for magma recycling, *J. Geophys. Res.*, **104**, 7117–7136.
- Harris, A.J.L.; Murray, J.B.; Aries, S.E.; Davies, M.A.; Flynn, L.P.; Wooster, M.J.; Wright, R.; Rothery, D.A. (2000). Effusion rate trends at Etna and Krafla and their implications for eruptive mechanisms, *J. Volcanol. Geotherm. Res.*, **102**, 237–270.
- Harris, A.J.L.; Pilger, E.; Flynn, L.P.; Garbeil, H.; Mouginitis-Mark, P.J.; Kauahikaua, J.; Thornber, C. (2001). Automated, high temporal resolution, thermal analysis of Kilauea volcano, Hawai'i, using GOES satellite data, *Int. J. Rem. Sens.*, **22**(6), 945–967, doi: 10.1080/014311601300074487.
- Harris, A.J.L.; Flynn, L.P.; Matias, O.; Rose, W.I. (2002). The thermal stealth flows of Santiaguito: Implications for the cooling and emplacement of dacitic block lava flows, *Geol. Soc. Am. Bull.*, **114**, 533–546.
- Harris, A.J.L.; Rose, W.I.; Flynn, L.P. (2003). Temporal trends in lava dome extrusion at Santiaguito 1922–2000, *Bull. Volcanol.*, **65**, 77–89.
- Harris, A.J.L.; Flynn, L.P.; Matias, O.; Rose, W.I.; Cornejo, J. (2004). The evolution of an active silicic lava flow field: An ETM+ perspective, *J. Volcanol. Geotherm. Res.*, **135**(1/2), 147–168.
- Harris, A.J.L.; Dehn, J.; Calvari, S. (2007). Lava effusion rate definition and measurement: A review, *Bull. Volcanol.*, **70**(1), 1–22, doi: 10.1007/s00445-007-0120-y.
- Harris, A.J.L.; Lodato, L.; Dehn, J.; Spampinato, L. (2009). Thermal characterization of the Vulcano fumarole field, *Bull. Volcanol.*, **71**(4), 441–458.
- Harris, A.J.L.; Favalli, M.; Steffke, A.; Fornaciai, A.; Boschi, E. (2010). A relation between lava discharge rate, thermal insulation, and flow area set using lidar data, *Geophys. Res. Lett.*, **37**, doi: 10.1029/2010GL044683.
- Hellman, M.J.; Ramsey, M.S. (2004). Analysis of hot springs and associated deposits in Yellowstone National Park using ASTER and AVIRIS remote sensing, *J. Volcanol. Geotherm. Res.*, **135**, 195–219, ISSN 0377-0273, 10.1016/j.jvolgeores.2003.12.012.
- Higgins, J.; Harris, A.J.L. (1997). VAST: A program to locate and analyse volcanic thermal anomalies automatically from remotely sensed data, *Comput. Geosci.*, **23**(6), 627–645.
- Hirn, B.; DiBartola, C.; Ferucci, F. (2008). Spaceborne monitoring 2000–2005 of the Pu'u O'o-Kupaianaha (Hawaii) eruption by synergetic merge of multispectral payloads ASTER and MODIS, *Geosci. Rem. Sens.*, **46**(10), 2848–2856, doi: 10.1109/TGRS.2008.2001033.
- Hon, K.; Kauahikaua, J.; Denlinger, R.; Mackay, K. (1994). Emplacement and inflation of pahoehoe sheet flows: Observations and measurements of active lava flows on Kilauea volcano, Hawaii, *Geol. Soc. Am. Bull.*, **106**, 351–370.
- Kahle, A.B.; Gillespie, A.R.; Abbott, E.A.; Abrams, M.J.; Walker, R.E.; Hoover, G.; Lockwood, J.P. (1988). Relative dating of Hawaiian lava flows using multispectral thermal infrared images: A new tool for geological mapping of young volcanic terranes, *J. Geophys. Res.*, **93**(12), 15239–15251, doi: 10.1029/JB093iB12p15239.
- Kaneko, T.; Wooster, M.J. (1999). Landsat infrared analysis of fumarole activity at Unzen Volcano: Time-series comparison with gas and magma fluxes, *J. Volcanol. Geotherm. Res.*, **89**, 57–64.
- Kaneko, T.; Yasuda, A.; Ishimaru, T.; Takagi, M.; Wooster, M.J.; Kagiyama, T. (2002). Satellite hot spot monitoring of Japanese volcanoes: A prototype AVHRR-based system, *Adv. Environ. Monit. Mod.*, **1**(1), 125–133.
- Kervyn, M.; Harris, A.J.L.; Mbede, E.; Belton, F.; Jacobs, P.; Ernst, G.G.J. (2006). MODLEN: A semi-automated algorithm for monitoring small-scale thermal activity at Oldoinyo Lengai Volcano Tanzania. In: *Quantitative Geology from Multiple Sources: IAMG Annual Conference, Liège, Belgium*.

- Keszthelyi, L.; Harris, A.J.L.; Dehn, J. (2003). Observations of the effect of wind on the cooling of active lava flows, *Geophys. Res. Lett.*, **30**(19), 1989, doi: 10.1029/2003GL017994.
- Koepfen, W.; Pilger, E.; Wright, R. (2011). Time series analysis of infrared satellite data for detecting thermal anomalies: A hybrid approach, *Bull. Volcanol.*, **73**(5), 577–593, doi: 10.1007/s00445-010-0427-y.
- Lachlan-Cope, T.A.; Connolley, W.M.; Turner, J. (2001). The role of the non-axisymmetric Antarctic orography in forcing the observed pattern of variability of the Antarctic climate, *Geophys. Res. Lett.*, **28**, 4111–4114.
- Lee, T.F.; Tag, P.M. (1990). Improved detection of hot-spots using the AVHRR 3.7 mm channel, *Bull. Am. Met. Soc.*, **71**(12), 1722–1730.
- Lodato, L.; Spampinato, L.; Harris, A.; Calvari, S.; Dehn, J.; Patrick, M. (2007). The morphology and evolution of the Stromboli 2002–2003 lava flow field: An example of a basaltic flow field emplaced on a steep slope, *Bull. Volcanol.*, **69**(6), 661–679, doi: 10.1007/s00445-006-0101-6.
- Lombardo, V.; Buongiorno, F. (2006). Lava flow thermal analysis using three infrared bands of remote-sensing imagery: A study case from Mount Etna 2001 eruption, *Rem. Sens. Env.*, **101**, 141–149.
- Macdonald, G.A. (1972). *Volcanoes*, Prentice-Hall, Englewood Cliffs, NJ, 510 pp.
- Matsushima, N.; Kazahaya, K.; Saito, G.; Shinohara, H. (2003). Mass and heat flux of volcanic gas discharging from the summit crater of Iwodake volcano, Satsuma-Iwojima, Japan, during 1996–1999, *J. Volcanol. Geotherm. Res.*, **126**, 285–301.
- Mouginis-Mark, P.J.; Snell, H.; Ellisor, R. (2000). GOES satellite and field observations of the 1998 eruption of Volcan Cerro Azul, Galapagos Islands, *Bull. Volcanol.*, **62**, 188–198.
- Oppenheimer, C. (1991). Lava flow cooling estimated from Landsat Thematic Mapper infrared data: The Lonquimay eruption (Chile, 1989), *J. Geophys. Res.*, **96**, 21865–21878.
- Oppenheimer, C. (1993). Infrared surveillance of crater lakes using satellite data, *J. Volcanol. Geotherm. Res.*, **55**, 117–128.
- Oppenheimer, C. (1996). Crater lake heat losses estimated by remote sensing, *Geophys. Res. Lett.*, **23**, 1793–1796.
- Oppenheimer, C. (1997a). Remote sensing of the colour and temperature of volcanic lakes, *Int. J. Rem. Sens.*, **18**, 5–37.
- Oppenheimer, C. (1997b). Ramifications of the skin effect for crater lake heat budget analysis, *J. Volcanol. Geotherm. Res.*, **75**, 159–165.
- Oppenheimer, C. (1998). Satellite observation of active carbonatite volcanism at Ol Doinyo Lengai, Tanzania, *Int. J. Rem. Sens.*, **19**, 55–64.
- Oppenheimer, C.; Francis, P. (1998). Implications of longeval lava lakes for geomorphological and plutonic processes at Erta Ale volcano, north Afar, *J. Volcanol. Geotherm. Res.*, **80**, 101–111.
- Oppenheimer, C.; Rothery, D.A. (1991). Infrared monitoring of volcanoes by satellite, *J. Geol. Soc. London*, **148**, 563–569.
- Oppenheimer, C.; Francis, P.W.; Rothery, D.A.; Carlton, R.W.T.; Glaze, L.S. (1993a). Infrared image analysis of volcanic thermal features: Láscar Volcano, Chile, 1984–1992, *J. Geophys. Res.*, **98**(B3), 4269–4286, doi: 10.1029/92JB02134.
- Oppenheimer, C.; Rothery, D.A.; Pieri, D.C.; Abrams, M.; Carrere, V. (1993b). Analysis of Airborne Visible/Infrared Imaging Spectrometer data of volcanic hot spots, *Int. J. Rem. Sens.*, **14**, 2919–2934.
- Patrick, M.R. (2002). Numerical modeling of lava flow cooling applied to the 1997 Okmok eruption: Comparison with AVHRR thermal imagery, M.S. thesis, University of Alaska Fairbanks, Fairbanks, 141 pp.
- Patrick, M.R.; Dehn, J.; Dean, K. (2005a). Numerical modeling of lava flow cooling applied to the 1997 Okmok eruption: Comparison with advanced very high resolution radiometer thermal imagery, *J. Geophys. Res.*, **110**(B02210), doi: 10.1029/2003/JB002538.
- Patrick, M.R.; Smellie, J.L.; Harris, A.J.L.; Wright, R.; Dean, K.G.; Izbekov, P.; Garbeil, H.; Pilger, E. (2005b). First recorded eruption of Mount Belinda volcano (Montagu Island), South Sandwich Islands, *Bull. Volcanol.*, **67**, 412–422.
- Patrick, M.R.; Harris, A.J.L.; Ripepe, M.; Dehn, J.; Rothery, D.A.; Calvari, S. (2007). Strombolian explosive styles and source conditions: Insights from thermal (FLIR) video, *Bull. Volcanol.*, **69**(7), 769–784, doi: 10.1007/s00445-006-0107-0.
- Pergola, N.; Marchese, F.; Tramutoli, V. (2004). Automated detection of thermal features of active volcanoes by means of infrared AVHRR records, *Rem. Sens. Environ.*, **93**, 311–327.
- Pergola, N.; Marchese, F.; Tramutoli, V.; Filizzola, C.; Ciampa, M. (2008). Advanced satellite technique for volcanic activity monitoring and early warning, *Ann. Geophys.*, **51**(1), 287–301.
- Pergola, N.; D'Angelo, G.; Lisi, M.; Marchese, F.; Mazzeo, G.; Tramutoli, V. (2009). Time domain analysis of robust satellite techniques (RST) for near real-time monitoring of active volcanoes and thermal precursor identification, *Phys. Chem. Earth*, **34**(6/7), 380–385, ISSN 1474-7065, 10.1016/j.pce.2008.07.015.
- Pieri, D.C.; Baloga, S.M. (1986). Eruption rate, area, and length relationships for some Hawaiian lava flows, *J. Volcanol. Geotherm. Res.*, **30**, 29–45.
- Pieri, D.C.; Glaze, L.S.; Abrams, M.J. (1990). Thermal radiance observations of an active lava flow during

- the June 1984 eruption of Mount Etna, *Geology*, **18**, 1018–1022.
- Ramsey, M.S.; Christensen, P.R. (1998). Mineral abundance determination: Quantitative deconvolution of thermal emission spectra, *J. Geophys. Res.*, **103**, 577–596.
- Ramsey, M.; Dehn, J. (2004). Spaceborne observations of the 2000 Bezymianny, Kamchatka eruption: The integration of high-resolution ASTER data into near real-time monitoring using AVHRR, *J. Volcanol. Geotherm. Res.*, **135**, 127–146, doi: 10.1016/j.jvolgeores.2003.12.014
- Realmutu, V.J.; Hon, K.; Kahle, A.B.; Abbott, E.A.; Pieri, D.C. (1992). Multispectral thermal infrared mapping of the 1 October 1988 Kupaianaha flow field, Kilauea volcano, Hawaii, *Bull. Volcanol.*, **55**(1/2), 33–44, doi: 10.1029/JB095iB13p21657.
- Reddy, C.S.S.; Bhattacharya, A.; Srivastava, S.K. (1993). Night-time TM short wavelength infrared data analysis of Barren Island Volcano, South Andaman, India, *Int. J. Rem. Sens.*, **14**, 783–787.
- Roach, A.L.; Benoit, J.P.; Dean, K.G.; McNutt, S.R. (2001). The combined use of satellite and seismic monitoring during the 1996 eruption of Pavlof Volcano, Alaska, *Bull. Volcanol.*, **62**(6/7), 385–399, doi: 10.1007/s004450000114.
- Rothery, D.A.; Francis, P.W.; Wood, C.A. (1988). Volcano monitoring using short wavelength infrared data from satellites, *J. Geophys. Res.*, **93**, 7993–8008, doi: 10.1029/JB093iB07p07993.
- Rothery, D.A.; Coppola, D.; Saunders, C. (2005). Analysis of volcanic activity patterns using MODIS thermal alerts, *Bull. Volcanol.*, **67**(6), 539–556.
- Schneider, D.J.; Dean, K.G.; Dehn, J.; Miller, T.P.; Kirianov, V.Yu. (2000). Monitoring and analyses of volcanic activity using remote sensing data at the Alaska Volcano Observatory: Case study for Kamchatka, Russia, December 1997, in: P.J. Mouginis-Mark, J.A. Crisp, and J.H. Fink (Eds.), *Remote Sensing of Active Volcanism*, American Geophysical Union Geophysical Monograph 116, Washington D.C., pp. 65–86.
- Scorer, R.S. (1986). *Cloud Investigation by Satellite*, Ellis Horwood, Chichester, U.K., 314 pp.
- Sekioka, M.; Yuhara, K. (1974). Heat flux estimation in geothermal areas based on the heat balance of the ground surface, *J. Geophys. Res.*, **79**(14), 2053–2058, doi: 10.1029/JB079i014p02053.
- Steffke, A.M.; Harris, A.J.L. (2011). A review of algorithms for detecting volcanic hot spots in satellite infrared data. *Bull. Volcanol.*, **73**, 1109–1137, doi: 10.1007/s00445-011-0487-7.
- Steffke, A.M.; Harris, A.J.L.; Burton, M.; Caltabiano, T.; Salerno, G.G. (2011). Coupled use of COSPEC and satellite measurements to define the volumetric balance during effusive eruptions at Mt. Etna, Italy, *J. Volcanol. Geotherm. Res.*, **205**, 47–53, doi: 10.1016/j.jvolgeores.2010.06.004.
- Stephens, G.L.; Vane, D.G.; Boain, R.J.; Mace, G.G.; Sassen, K.; Wang, Z.; Illingworth, A.J.; O'Connor, E.J.; Rossow, W.B.; Durden, S.L. *et al.* (2002). The CloudSat mission and the A-Train, *Bull. Am. Met. Soc.*, **93**(12), 1771–1790, doi: 10.1175/BANMS-83-12-1771.
- Tramutoli, V. (1998). Robust AVHRR Techniques (RAT) for environmental monitoring: Theory and applications, in: G. Cecchi and E. Zilioli (Eds.), *Earth Surface Remote Sensing, II: Proceedings of SPIE*, 3496, pp. 101–113.
- Urai, M. (2000). Volcano monitoring with Landsat TM short-wave infrared bands: The 1990–1994 eruption of Unzen Volcano, Japan, *Int. J. Rem. Sens.*, **21**(5), 861–872, doi: 10.1080/014311600210335.
- van Manen, S.M.; Dehn, J. (2009). Satellite remote sensing of thermal activity at Bezymianny and Kliuchevskoi from 1993 to 1998, *Geology*, **37**, 983–986, doi: 10.1130/G30179A.1.
- van Manen, S.M.; Dehn, J.; West, M.E.; Blake, S.; Rothery, D.A. (2010a). The 2006 eruption of Augustine Volcano: Combined analyses of thermal satellite data and reduced displacement, in: J.A. Power, M.L. Coombs, and J.T. Freymueller (Eds.), *The 2006 Eruption of Augustine Volcano, Alaska*, U.S. Geological Survey Professional Paper 1769, pp. 553–567.
- van Manen, S.M.; Dehn, J.; Blake, S. (2010b). Satellite thermal observation of the Bezymianny lava dome 1993–2008: Precursory activity, large explosions and dome growth, *J. Geophys. Res.*, **115**(B08205), doi: 10.1029/2009JB006966.
- van Manen, S.M.; Blake, S.; Dehn, J. (2011). A near real-time dual-band-spatial approach to determine the source of increased radiance from closely spaced active volcanoes in coarse resolution satellite data, *Int. J. Rem. Sens.*, **32**(21), 6055–6069, doi: 10.1080/01431161.2010.498452.
- Webley, P.W.; Wooster, M.J.; Strauch, W.; Saballos, J.A.; Dill, K.; Stephenson, P.; Stephenson, J.; Escobar, W.R.; Matías, O. (2008). Experiences from real-time satellite-based volcano monitoring in Central America: Case studies at Fuego, Guatemala, *Int. J. Rem. Sens.*, **29**(22), 6618–6644.
- Wiesnet, D.R.; D'Aguanno, J. (1982). Thermal imagery of Mount Erebus from the NOAA-6 satellite, *Antarctic J. U.S.*, **17**, 32–34.
- Williams, R.S.; Friedman, J.D. (1970). Satellite observation of effusive volcanism, *British Interplanetary Soc. J.*, **23**, 441–450.
- Williams, R.S.; Friedman, J.D.; Thorarinnsson, S.; Sigurgjersson, T.; Palmason, G. (1968). *Analysis of the 1966 Imagery of Surtsey Iceland*, Surtsey Research Progress Report iv, Surtsey Research Society, Reykjavik, pp. 177–192.

- Wooster, M.J. (2001). Long-term infrared surveillance of Lascar Volcano: Contrasting activity cycles and cooling pyroclastics, *Geophys. Res. Lett.*, **28**, 847–850.
- Wooster, M.J.; Kaneko, T. (2001). Testing the accuracy of solar reflected radiation corrections applied during satellite thermal analysis of active volcanoes, *J. Geophys. Res.*, **106**, 13381–13394.
- Wooster, M.J.; Rothery, D.A. (1997). Thermal monitoring of Lascar Volcano, northern Chile, using infrared data at high temporal resolution: A 1992 to 1995 time-series using the along track scanning radiometer, *Bull. Volcanol.*, **58**, 566–579.
- Wooster, M.J.; Rothery, D.A. (2002). A review of volcano surveillance applications using the ATSR instrument series, *Adv. Environ. Mon. Mod.*, **13**, 97–123.
- Wooster, M.J.; Wright, R.; Blake, S.; Rothery, D.A. (1997). Cooling mechanisms and an approximate thermal budget for the 1991–1993 Mount Etna lava, *Geophys. Res. Lett.*, **24**, 3277–3280.
- Wooster, M.J.; Rothery, D.A.; Sear, C.B.; Carlton, R.W. (1998). Monitoring the development of active lava domes using data from the ERS-1 Along Track Scanning Radiometer, *Adv. Space Res.*, **21**, 501–505.
- Wooster, M.J.; Kaneko, T.; Nakada, S.; Shimizu, H. (2000). Discrimination of lava dome activity styles using satellite-derived thermal structures, *J. Volcanol. Geotherm. Res.*, **102**, 97–118.
- Wright, R.; Flynn, L.P. (2003). On the retrieval of lava-flow surface temperatures from infrared satellite data, *Geology*, **31**(10), 893–896.
- Wright, R.; Pilger, E. (2008). Satellite observations reveal little inter-annual variability in the radiant flux from the Mount Erebus lava lake, *J. Volcanol. Geotherm. Res.*, **177**(3), 687–694.
- Wright, R.; Rothery, D.A.; Blake, S.; Harris, A.J.L.; Pieri, D.C. (1999). Simulating the response of the EOS Terra ASTER sensor to high-temperature volcanic targets, *Geophys. Res. Lett.*, **26**(12), 1773–1776.
- Wright, R.; Blake, S.; Harris, A.J.L.; Rothery, D.A. (2001a). A simple explanation for the space-based calculation of lava eruption rates, *Earth Planet. Sci. Lett.*, **192**, 223–233.
- Wright, R.; Flynn, L.P.; Harris, A.J.L. (2001b). The evolution of lava flowfields at Mount Etna, 27–28 October 1999, observed by Landsat 7 ETM+, *Bull. Volcanol.*, **63**, 1–7.
- Wright, R.; Flynn, L.P.; Garbeil, H.; Harris, A.J.L.; Pilger, E. (2002a). Automated volcanic eruption detection using MODIS, *Rem. Sens. Environ.*, **82**, 135–155.
- Wright, R.; De La Cruz-Reyna, S.; Harris, A.J.L.; Flynn, L.P.; Gomez-Palacios, J.J. (2002b). Infrared satellite monitoring at Popocatepetl: Explosions, exhalations, and cycles of dome growth, *J. Geophys. Res.*, **107**, 2153–2169, doi: 10.1029/2000JB000125.
- Wright, R.; Garbeil, H.; Davies, A.G. (2010). Cooling rate of some active lavas determined using an orbital imaging spectrometer, *J. Geophys. Res.*, **115**(B06205), doi: 10.1029/2009JB006536.
- Wright, R.; Glaze, L.; Baloga, S.M. (2011). Constraints on determining the eruption style and composition of terrestrial lavas from space, *Geology*, **39**, 1127–1130.
- Yuhaniz, S.S.; Vladimirova, T. (2009). An onboard automatic change detection system for disaster monitoring, *Int. J. Rem. Sens.*, **30**(23), 6129–6139.

Applications of high-resolution satellite remote sensing for northern Pacific volcanic arcs

Michael S. Ramsey, Jeffrey M. Byrnes, Rick L. Wessels, Pavel Izbekov

Abstract. There has been a dramatic increase in the remote-sensing data volume being acquired from Earth orbit over the past two decades. Although none of these satellite instruments were designed specifically to monitor volcanic eruptions, many government agencies and university partnerships are currently utilizing them for this task. Most rely on high temporal/moderate spatial resolution instruments (e.g., MODIS, AVHRR, GOES) to monitor transient and temporally variable anomalies such as eruption clouds and hot spots. The uses of these instruments for such purposes are detailed in Chapters 3, 4 and 6. However, in order to better develop a quantitative scientific basis from which to model transient geological and meteorological hazards as well as map small-scale phenomena, higher spatial/spectral resolution datasets are commonly needed. Whereas moderate-resolution data may be frequently received directly from the satellite at many institutes globally, access to, and temporal frequency of, coverage from high-resolution instruments has been limited because much of the data must be specially acquired and purchased using a few government (e.g., ASTER, ETM+) and commercial (e.g., IKONOS, QuickBird) providers. Despite this, high-resolution data use has increased greatly as their capabilities have become recognized. The data from these sensors are particularly useful for numerous aspects of volcanic remote sensing. For example, high spatial resolution/multi-spectral thermal infrared data are critical for monitoring low-temperature anomalies and mapping

both chemical and textural variations on volcanic surfaces. The data can also be integrated into a near-real time monitoring effort that is based primarily on high temporal/moderate spatial resolution orbital data. This synergy allows small-scale activity to be targeted for science and response, and the establishment of a calibration baseline between each sensor. The focus of this chapter is to highlight how these high spatial resolution (≤ 100 m/pixel) data, commonly with more spectral capabilities, are being used for volcanic mapping and monitoring in the North Pacific region. A review of volcanic remote-sensing research using these data is presented with attention paid to case studies of new research. These studies showcase the capabilities of higher resolution sensors to map pyroclastic flows and detect changes over time in those flows (Mt. Augustine Volcano), and to document detection of volcanic terrains using a fusion approach of data from the visible to the radar wavelengths (Westdahl Volcano).

4.1 INTRODUCTION

The use of satellite data to observe and monitor increasing volcanic activity and map the subsequent eruptive products has been documented from the early years of commercial remote sensing (Francis, 1979). This detection and monitoring of activity is an extremely valuable tool in the remote

northern Pacific region for mitigating future encounters of volcanic plumes with aircraft (Miller and Casadevall, 2000; Chapters 1 and 5). As technology has advanced and knowledge of volcanological processes and hazards has increased, progressively more complex image-processing techniques have been applied to newly acquired data in order to derive, for example, the inflation of a volcanic region using interferometric radar (Zebker *et al.*, 2000; Lu *et al.*, 2003b; Chapter 8); the existence of hot spots with both shortwave infrared (SWIR) and thermal infrared (TIR) data (Francis and Rothery, 1987; Pieri *et al.*, 1990; Abrams *et al.*, 1991; Flynn *et al.*, 1994, 2000; Chapters 1 and 3); the volume of sulfur dioxide in plumes using ultraviolet (UV) and TIR data (Krueger *et al.*, 1995; Realmuto *et al.*, 1994; Watson *et al.*, 2004; Chapter 6); and the distribution of lava textures and compositions using TIR data (Ramsey and Fink, 1999; Ramsey and Dehn, 2004; Byrnes *et al.*, 2004). Analyses such as these will continue to expand and be refined only if there is continued availability of future spaceborne high spatial resolution instruments as well as a need driven by population centers in, and travel routes through, hazardous regions.

Many remote-sensing platforms are limited in the context of systematic volcano monitoring by either poor spectral, spatial, and/or temporal resolution, so new image-processing techniques have been developed during the past two decades to maximize the utility of acquired data (Harris *et al.*, 1999; Dehn *et al.*, 2000; Ramsey and Dehn, 2004). Commonly, moderate spatial resolution (1–4 km/pixel) data from the Advanced Very High Resolution Radiometer (AVHRR), the Geostationary Operational Environmental Satellite (GOES), and the Moderate Resolution Imaging Spectroradiometer (MODIS) are used for volcanic monitoring because of their higher temporal resolution (minutes to hours) (Dehn *et al.*, 2000; Harris *et al.*, 2001; Wright *et al.*, 2004). These data are excellent for monitoring highly dynamic volcanic processes. However, with increased spatial resolution (≤ 100 m/pixel) of satellite data typically comes poorer temporal resolution (7–30 days), therefore making instruments such as the Landsat Enhanced Thematic Mapper Plus (ETM+), the Advanced Spaceborne Thermal Emission and Reflection Radiometer (ASTER), and the numerous spaceborne Synthetic Aperture Radar (SAR) instruments much less ideal for systematic monitoring. These instruments have been used for mapping small-scale features indicative of local processes (e.g., Carn,

1999; Donegan and Flynn, 2004; Patrick *et al.*, 2004) and, to a lesser degree, eruption monitoring (Ramsey and Dehn, 2004).

4.2 BACKGROUND

In remote or inaccessible locations such as the Aleutian Islands, the Kamchatka Peninsula, and the Kurile Islands, remote sensing from space commonly provides the only confirmation that an eruption had actually occurred (e.g., Dean *et al.*, 2004; Patrick *et al.*, 2005). The harsh environment and remoteness of most of the active volcanoes in the Aleutian–Kamchatka–Kurile Arc make placing field-based monitoring equipment extremely challenging and costly. The number of potentially active volcanoes that have to be continually monitored coupled with the harsh conditions has thus far precluded deployment of this field equipment in many locations. The Alaska Volcano Observatory (AVO) has pioneered the use of data from operational weather satellites for change detection on active volcanoes (i.e., increased thermal output or volcanic plume detection/tracking) over these remote volcanoes (Kienle *et al.*, 1990; Dehn *et al.*, 2000; Chapter 1).

However, in addition to volcanic monitoring using high temporal resolution data, AVO also relies on higher spatial resolution data to provide other important details. This information includes: (1) base maps for field campaigns, (2) identification and characterization of small-scale changes in volcanic behavior once activity is identified, and (3) mapping the distribution and composition of eruptive products. For example, one of the most comprehensive analyses using multiple, high spatial resolution sensors ever compiled for a single volcano (Mt. Cleveland, Aleutian Islands) was that of Smith (2005). That study utilized visible, infrared, and radar remote-sensing data from ETM+, ASTER, the European Remote-sensing Satellite (ERS)-2, and topographic data derived from the Shuttle Radar Topography Mission (SRTM) to validate moderate spatial resolution monitoring data, calculate erupted volumes, and constrain the subsequent erosion rate of new pyroclastic deposits. Analysis of the high-resolution TIR data showed volcanic activity varied with time producing an erupted volume (excluding ash) of slightly greater than 1×10^6 m³ in the first 3 months of 2001

(Smith, 2005). Continued monitoring with SAR backscatter remote-sensing data for the next 2.5 years showed that the 2001 debris flow deposit eroded at approximately 20 m² per day. Synoptic studies such as that performed at Mt. Cleveland attest to the effectiveness and utility of spaceborne instruments with resolutions better than 100 m/pixel for extracting information on eruptions in remote locations.

High spatial/moderate spectral (<20 channels in a given wavelength range) resolution airborne and spaceborne remote-sensing data are being acquired continuously by the Earth science community both to understand volcanologic processes and to validate the monitoring efforts that employ lower spatial resolution instruments (e.g., Abrams *et al.*, 1991; Harris *et al.*, 1998; Pieri and Abrams, 2004). Although airborne remote sensing provides the highest spatial resolution and spectral resolution data, its use is commonly infrequent or not feasible during eruptions due to cost, safety, the remoteness of many volcanoes, and the time needed to deploy the aircraft. However, Vaughan *et al.* (2005) document excellent results using the MODIS/ASTER airborne simulator (MASTER) during the renewed activity of Mt. St. Helens volcano in September–October 2004. More commonly, spaceborne instruments are used to monitor and map active volcanoes, particularly in the remote regions of the North Pacific. These are typically polar-orbiting multispectral imaging devices that provide spatial resolution on the scale of 10–30 m/pixel. With an average repeat time of 5–16 days, the data from these instruments provide volcanologists with the ability to detect precursory activities such as increased thermal output, ongoing activities such as dome emplacement and plume formation, and assessment of post-eruption products and damage (Abrams *et al.*, 1991; Flynn *et al.*, 1994; Harris *et al.*, 2003; Ramsey and Dehn, 2004).

The primary focus of this chapter is to describe several specific applications of high spatial resolution data to volcanologic studies of the North Pacific region, including a new data fusion case study of Westdahl Volcano designed to maximize the return from data across several regions of the electromagnetic spectrum. However, the intention of this chapter is not to summarize all high-resolution volcanologic remote-sensing studies. Readers interested in comprehensive reviews should consult Francis and Rothery (2000), Mouginiis-Mark *et al.* (2000), Ramsey and Flynn (2004), and references therein.

4.3 APPLICATIONS

4.3.1 Feature identification using VNIR data

Recent and ongoing volcano studies at AVO have begun to rely on very high spatial resolution visible to near-infrared (VNIR) commercial data from both the QuickBird and IKONOS instruments, which have spatial resolutions of 0.67 m and 1.0 m/pixel, respectively. These sensors can provide on-demand high-resolution views of new volcanic activity in a timely manner, as well as accurately geolocated base images for hazard and geologic mapping. For example, IKONOS data have been used as the primary base image for recent geologic mapping at Okmok Volcano (Begét *et al.*, 2005), whereas data from both sensors have been used as an important part of AVO's response to the 2004–2005 unrest at Mt. Spurr Volcano (Coombs *et al.*, 2006).

Elevated seismic activity and a gradual collapse of the snow and ice cap into a previously buried summit crater lake signaled renewed activity at Mt. Spurr in early July 2004. A review of historic records and photos suggested that the summit crater may have been exposed several other times over the last 60 years (Coombs *et al.*, 2006), though the most recent eruption of the summit Mt. Spurr is believed to have occurred ~5.2 kyr (Riehle, 1985). Part of the initial AVO response was to acquire both recent and new high spatial resolution images of the summit area. A series of pilot and mountaineer photographs as well as a clear IKONOS image from June 16, 2002 (Figure 4.1a) established that the summit likely showed no recent signs of ice cap deformation until June 2004 (Coombs *et al.*, 2006). During the initial response, the IKONOS image also provided a georeferenced high spatial resolution image base on which to overlay new data. A July 8, 2004 ASTER image documented the earliest stages of a new crater melt pit at the summit, and one month later (August 10, 2004) an orthorectified QuickBird image provided the first high-resolution planimetric view of summit changes (Figure 4.1b). A series of high-resolution satellite images and oblique aerial photographs spanning mid-2004 to 2005 documented the gradual expansion of the summit melt pit and changes in the crater lake (Coombs *et al.*, 2006). The summit crater, lake, and active fumaroles often persist year-round though the rate of seismic events and summit change have decreased markedly.

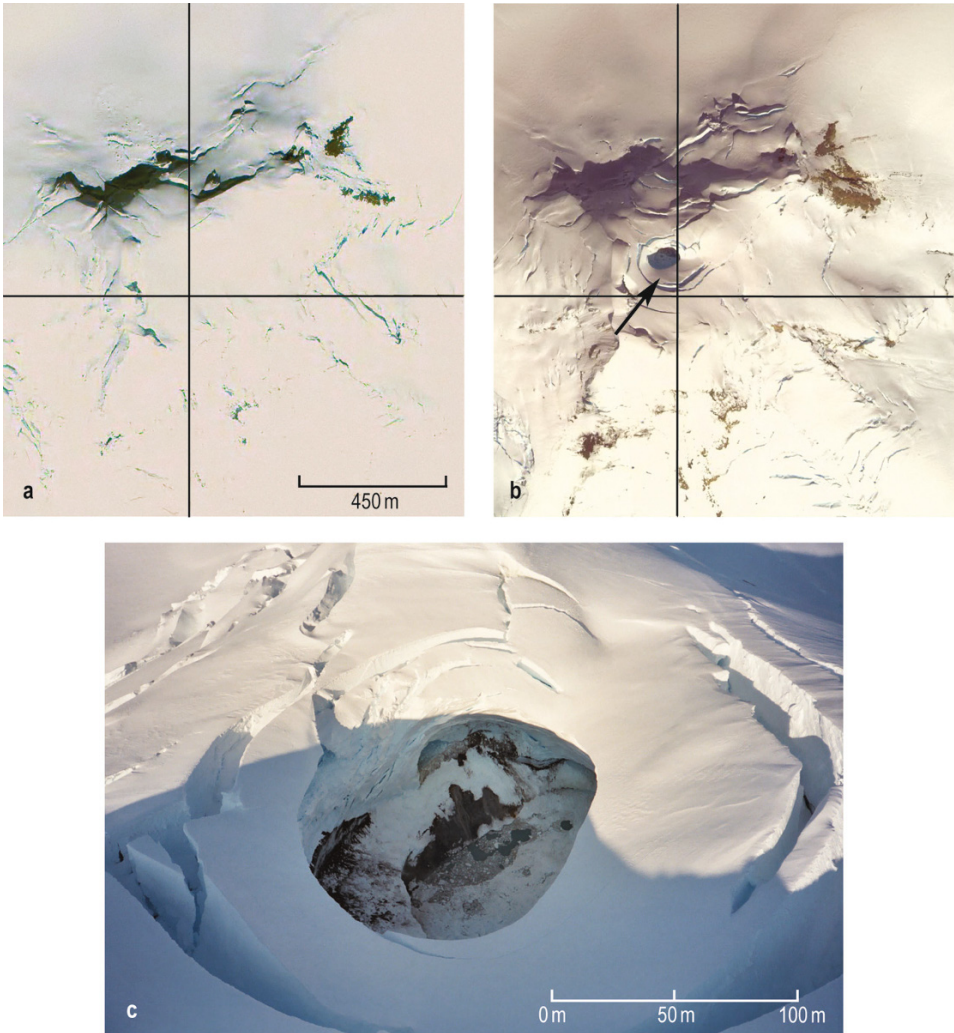


Figure 4.1. Changes detected by the AVO using high spatial resolution data at the snow-covered summit of Mt. Spurr Volcano, Alaska. (a) True-color image acquired by the IKONOS instrument (~ 1.0 m/pixel) on June 16, 2002 (© Space Imaging Corporation). (b) True-color image acquired by the QuickBird instrument (~ 0.67 m/pixel) on August 10, 2004 (© Digital Globe Corporation). Note the development of the summit melt pit and extensive local crevasse formation that began to form in June 2004 (see Coombs *et al.*, 2006 for detailed analysis). Black arrow indicates the location of the melt hole and the specific look direction of the photograph shown in (c). (c) Oblique aerial photograph of the summit crater taken by Donna Eberhart-Phillips on August 4, 2004 showing details of summit ice collapse and melting, forming the observed crater lake (image courtesy of AVO/U.S. Geological Survey).

Short reconnaissance flights from Anchorage to the summit of Mt. Spurr provided a cost-effective means to make frequent observations (Figure 4.1c), whereas the high spatial resolution data provided accurately georeferenced base images for response planning and mapping efforts at the volcano.

Unfortunately, when responding to restless volcanoes located farther out in the Aleutian Arc, reconnaissance flights present numerous weather, scheduling, and safety challenges. Regular high spatial resolution satellite observations, typically combined with in situ seismic, gas, and deforma-

tional measurements provide AVO scientists with an effective way to better document the overall state of remote restless volcanoes.

4.3.2 Compositional analysis using VNIR/SWIR data

The VNIR region of the EM spectrum is commonly used to detect weathered or altered iron oxides and trace minerals, which is important for understanding surface processes. For example, hematite is more abundant in stable landscapes, whereas goethite is more common in active erosional or depositional environments (Huntington, 1996). Vegetation detection and health is arguably the most common use of Earth-based remote sensing in this wavelength region. The strong near-infrared (NIR) reflectance associated with active photosynthesis has been used to map vegetation from the earliest days of the Landsat missions. Furthermore, minerals with significant amounts of hydroxyl (OH^-) ions in their chemical structure (e.g., hydroxyl-bearing clays, sulfates, and carbonate minerals) are most easily detected in the shortwave infrared (SWIR) region (Hook and Rast, 1990; Clark, 1993).

Combining the VNIR and SWIR subsystems of the ASTER instrument results in a spectral resolution of nine bands with 15 m/pixel (VNIR) to 30 m/pixel (SWIR) spatial resolution. This data set can be used for mapping small-scale surface changes (i.e., the presence of clay minerals associated with hydrothermal centers and the redistribution of volcanic deposits over time). Such a study was performed using data collected over Augustine Volcano in Cook Inlet (Figure 4.2). Augustine is an island volcano, which has erupted frequently in the past century and commonly produces small to moderate pyroclastic flows, lava domes, and rare large-debris avalanches (Begét and Kienle, 1992). Whereas the most recent eruption occurred in 2006, deposits of the 1986 eruption, which include numerous dome extrusions, collapse events, and pyroclastic flows, are the focus here. These deposits are preserved as unvegetated pumice and debris plains extending to the northern coastline of the island (Figure 4.2).

A new analysis of ASTER, VNIR, and SWIR data acquired over Augustine in June 2000 and April 2003 were used to map variations on the 1986 debris plain. The distribution of pyroclastic deposits from the 1986 eruption and their subsequent erosional reworking is not easily detectable with a single band of aerial photography and/or

field mapping due to the similarity of pumice clast color and morphology. However, with multiple wavelength spectroscopy and image-processing techniques, such as unsupervised classification, surface change is detectable. The unsupervised classification technique groups pixels with similar spectral response into statistical classes and assigns each a color. Figure 4.2c shows an example of unsupervised classification for ASTER-calibrated, atmospherically corrected surface reflectance data collected in 2003. This particular classification was performed using ASTER bands 1–9 (0.56–2.4 μm) and a *K*-means algorithm constrained to seven spectral classes, of which only five are visible in the image. The *K*-means unsupervised classification technique calculates initial class means evenly distributed in the data space and iteratively clusters the pixels into the nearest class using a minimum distance technique (Tou and Gonzalez, 1974). The red color class roughly correlates with lithic pyroclastic flow deposits, whereas the orange color class is more closely associated with pumiceous pyroclastic flow deposits (Waite and Begét, 1996). The other classes visible in the figure correspond to wet/submerged soil (green), coastal environments/slightly moist soils (yellow), and deep water (blue).

Another use of a well-calibrated, precisely registered, high spatial resolution data set is to measure surface changes over time. ASTER data are geolocated to within one VNIR pixel accuracy (15 m) and are ideally suited for such a study (Abrams, 2000). With the exception of the amount of snow at the summit and vigor of the vegetation, the two ASTER scenes appear to be nearly identical over the 3-year period. However, a change detection algorithm can be used to search for spectral variations of the same ground area. A difference image is computed by subtracting the initial state image from the final state image and change thresholds defined by separate color classes. Figure 4.2d is a change detection result showing the variability over time of ASTER band 3 (0.807 μm) from large (red) to small (blue). This region of the debris plain has a 3° slope and is gently incised by small seasonal runoff channels. Examination of the full-resolution data of this region shows a significant difference in the pattern and density of these channels over time (Figures 4.2e, f). It appears that surface flow due to precipitation and/or melting of snow and ice has incised new channels from 2000 to 2003 in this region, perhaps exposing material under the darker surface of the deposit. This interpretation is supported by plotting the reflectance spectra of the

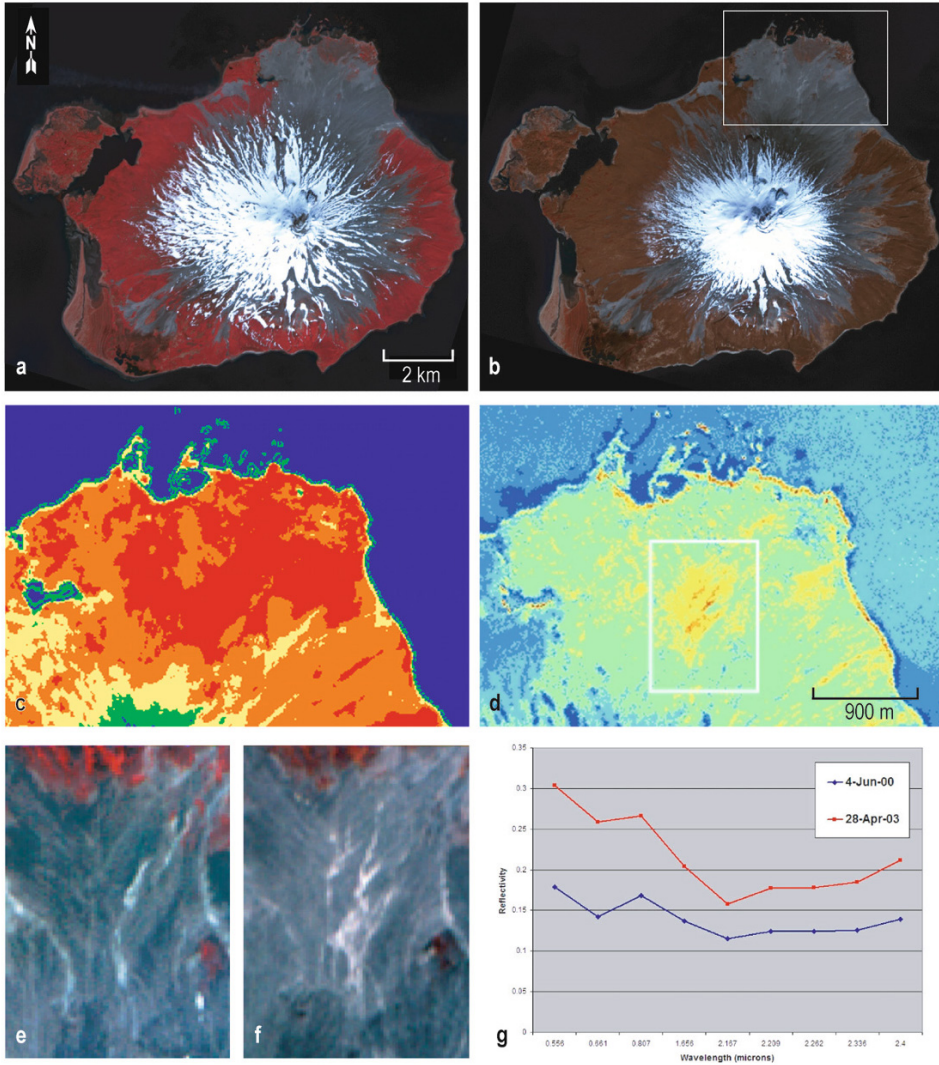


Figure 4.2. ASTER VNIR/SWIR analysis of the 1986 pyroclastic flow (PF) deposits of Augustine Volcano, Alaska. (a) VNIR color composite of the island volcano acquired on June 4, 2000 with bands 3, 2, 1 in R, G, B, respectively. Red indicates vegetation, white shows the location of snow/ice, and shades of gray mostly indicate the 1986 PF deposits on the northern shore of the island. (b) April 28, 2003 VNIR color composite—as in (a)—with the white box indicating the region shown in (c) and (d). (c) Example of an unsupervised classification highlighting the spectral differences of the PF deposits (see text for a description of the unsupervised classification technique). (d) Temporal difference image (2000–2003) of ASTER band 3 over a portion of the 1986 PF deposits. Regions of blue and green colors show less than a 10% change in reflectivity, whereas regions of red show a reflectance change of 40% or greater. Boxed area highlights the region shown in (e) and (f), and the black arrow indicates the location described in (g). (e) VNIR color composite—as in (a)—of the 1986 pyroclastic deposit. (f) Same region and color composite—as in (b)—but from 2003 image showing a detectable change on the surface, which is likely caused by formation of new fluvial channels in the deposit. (g) Average ASTER VNIR/SWIR reflectance spectra taken of the four pixels with the strongest change in spectral reflectance over the 3-year time period. The brightening of the surface (higher overall reflectance) together with little change in spectral shape indicates a surface exposed by fluvial erosion and channel incision of an unweathered pumice similar in composition to weathered pumice on the surface.

pixel with the largest detected change (Figure 4.2g). The reflectance spectra have similar morphologies indicating that the composition of the two materials is also similar. However, the increase in reflectance over all wavelength bands is obvious in 2003 data. Commonly, fresh volcanic deposits will darken (e.g., lower overall reflectance) with time in colder environments due to weathering, oxidation, and the development of surface coatings such as lichen, which are commonly black to dark brown in color.

4.3.3 Temperature analysis using TIR data

Single-channel, high spatial resolution TIR data, which first became available on the TM instruments in the 1980s, improved from 120 to 60 m/pixel spatial resolution on the later ETM+ instrument. With the launch of ASTER in late 1999, multispectral TIR data (five bands) with a similarly high spatial resolution (90 m/pixel) became a reality for the first time in Earth orbit. Both of these instruments with their increased TIR spatial and spectral sensitivity have been found to be useful for studying both large-scale thermal anomalies as well as small and relatively low-temperature features. For example, Patrick *et al.* (2004) used Landsat and ASTER data to characterize low-temperature volcanism associated with mud volcanoes in the Copper River Basin of southeastern Alaska. These features only pose a potential hazard locally and are therefore not regularly monitored, however this application of TIR analysis demonstrated the utility of such data. The relatively cool thermal anomalies could not be detected using moderate spatial resolution AVHRR data (e.g., Chapter 3).

Another example of low-temperature features that have been monitored with high spatial resolution TIR data are the vents and large lava flow at the Tolbachik volcanoes in Kamchatka (Figure 4.3). The large basaltic flows were emplaced during a fissure eruption in 1975–1976, which also produced numerous cinder cones and scoria deposits. Despite cooling for three decades, consistent temperature anomalies have been observed even at the 1 km/pixel spatial resolution of MODIS thermal data from 2000 onward. ASTER 90 m/pixel TIR data also show these persistent TIR anomalies, but in much greater detail (Figure 4.3a). The largest of these corresponds to the thickest part of the lava flow (at the terminus) and are associated with heat-emitting fractures over a large area of the flow terminus (Wessels *et al.*, 2004, 2005). The presence

of these hot cracks were confirmed with airborne and ground-based high spatial resolution thermal camera data collected in 2004 (Figure 4.3c). The availability of high spatial resolution spaceborne TIR data provides a unique opportunity for understanding the amount and long-term behavior of thermal features such as the Tolbachik lava flow. For example, it serves as a calibration target over time for ASTER TIR data. In addition, the ability to monitor changes in crater lake temperatures, fumarole fields, and quickly cooling pyroclastic deposits can signal a change in the activity state of other persistently active volcanoes.

High spatial resolution TIR data can also be used to detect and improve monitoring of high-temperature thermal anomalies commonly associated with an active eruption. Such an opportunity arose in March of 2000 with the eruption of Bezymianny Volcano on the Kamchatkan Peninsula, Russia. This event was large enough to be easily detected by the routine satellite monitoring of AVO using AVHRR data. The increased level of volcanic activity throughout the year also prompted data acquisition from higher resolution TIR instruments, such as the then recently launched ASTER and ETM+ instruments. Each acquired numerous scenes of the Bezymianny eruptive cycles throughout the remainder of 2000 (Ramsey and Dehn, 2004). During a second larger eruptive phase in the months of September–October, ASTER TIR data were used to map the thermal features on the summit dome and small pyroclastic flows. These commonly had pixel-integrated TIR brightness temperatures of greater than 90°C, which is close to the saturation threshold for ASTER. In fact, the detection of multiple 90 m pixels that are elevated to greater than 90°C generally implies the surface is covered by a significant fraction of material at >300°C (derived from 30 m/pixel SWIR data).

The ETM+ instrument also collected frequent acquisitions during the September eruption of Bezymianny. These data show the utility of high spatial resolution remote-sensing data both for discerning small-scale eruptive products as well as for documenting the changes in the volcano's state on a weekly time scale (Figure 4.4). The elevated temperatures present on the dome and pyroclastic flows were high enough to produce clearly visible elongate thermal anomalies in the 1 km/pixel resolution AVHRR data. The spatial resolution of AVHRR however was far too poor to determine the type of eruption product that produced these anomalies. Nevertheless, the ETM+ data could be used to

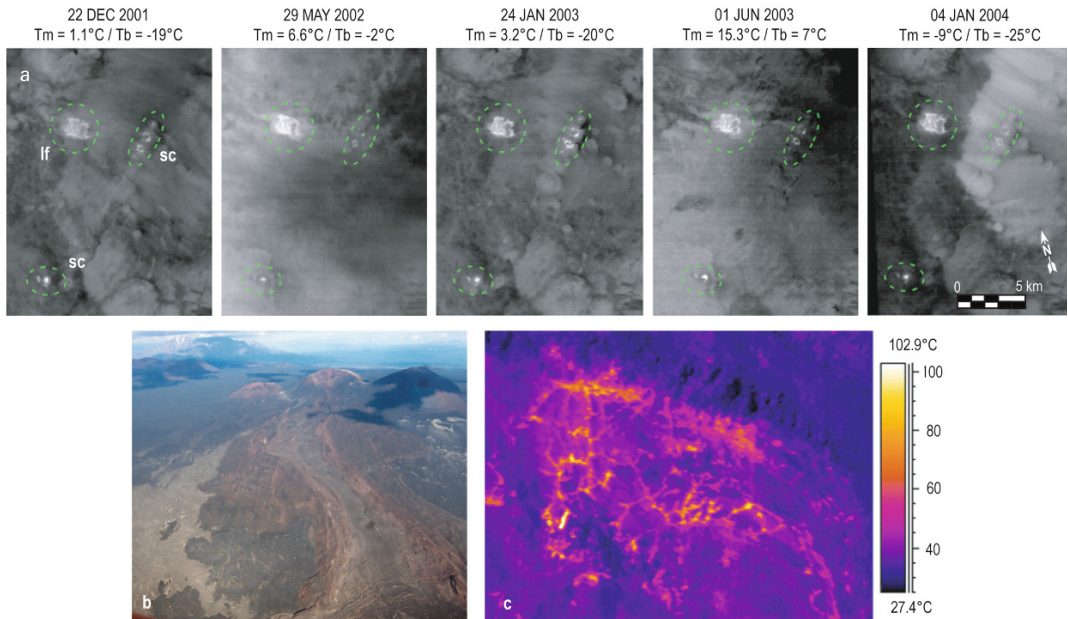


Figure 4.3. Thermal characteristics of the 1975–1976 Tolbachik lava flows and scoria cones, Kamchatka, Russia. (a) Brightness temperature images derived from ASTER TIR band 10 ($8.28\ \mu\text{m}$). The thermal anomalies are highlighted by dashed ellipses, which are centered on the summit craters of the scoria cones (sc) as well as the flow terminus (ft) of the large lava flow. Tm and Tb indicate the maximum and background temperatures, respectively, for each data set. (b) An oblique helicopter-based digital photograph of the scoria cone breached crater (center) and channeled lava flow, looking east. The white box indicates the area imaged in (c). (c) A nadir view broadband ($7.5\text{--}13.0\ \mu\text{m}$) thermal camera image of the lava flow ($\sim 0.5\ \text{m}/\text{pixel}$) acquired on the same overflight as (b). Certain FLIR images reveal temperatures as high as 150°C in several of the small fractures 30 years after the flow was emplaced demonstrating the utility of acquiring the highest spatial resolution data possible.

discriminate small-scale ($<3\ \text{km}$) pyroclastic flows confined to the southeast-trending valley as well as elevated temperatures on the dome itself. Three images collected over 5 weeks showed these thermally elevated dome pixels to have much higher temperatures than that of the surrounding area. Along the southern flank of the dome, temperatures were also elevated sufficiently to emit measurable energy in the SWIR region (Figure 4.4c). The band 7 ($2.09\text{--}2.35\ \mu\text{m}$) radiance of October 31 ETM+ data had a maximum pixel-integrated temperature of 308°C .

4.3.4 Compositional analysis using TIR data

Although volumetrically small in comparison with other lava compositions and extrusive morphologies, intermediate to silicic (e.g., andesitic to rhyolitic) domes preserve information on the

internal gas pressure, emplacement temperature, extrusion rate, and degassing state of the lava (Melnik and Sparks, 1999; Cashman and Blundy, 2000). Numerous techniques for mapping, monitoring, and modeling lava domes have been developed, with much of that work focused on older, inactive domes (Fink and Manley, 1987; Nakada *et al.*, 1995; Ramsey and Fink, 1999). Analysis of small lava domes using remote sensing is only possible with moderate to high spatial resolution data with sufficient spectral resolution (Ramsey and Dehn, 2004). Specifically, a multispectral TIR capability, such as is available with ASTER, is critical in this regard because it provides the only means to extract information on the silicate structure/composition of the minerals and the micrometer-scale to millimeter-scale surface texture of the lava dome. However, quantitative information derived from this approach relies on accurate field-based data, laboratory spectroscopy and modeling, and the

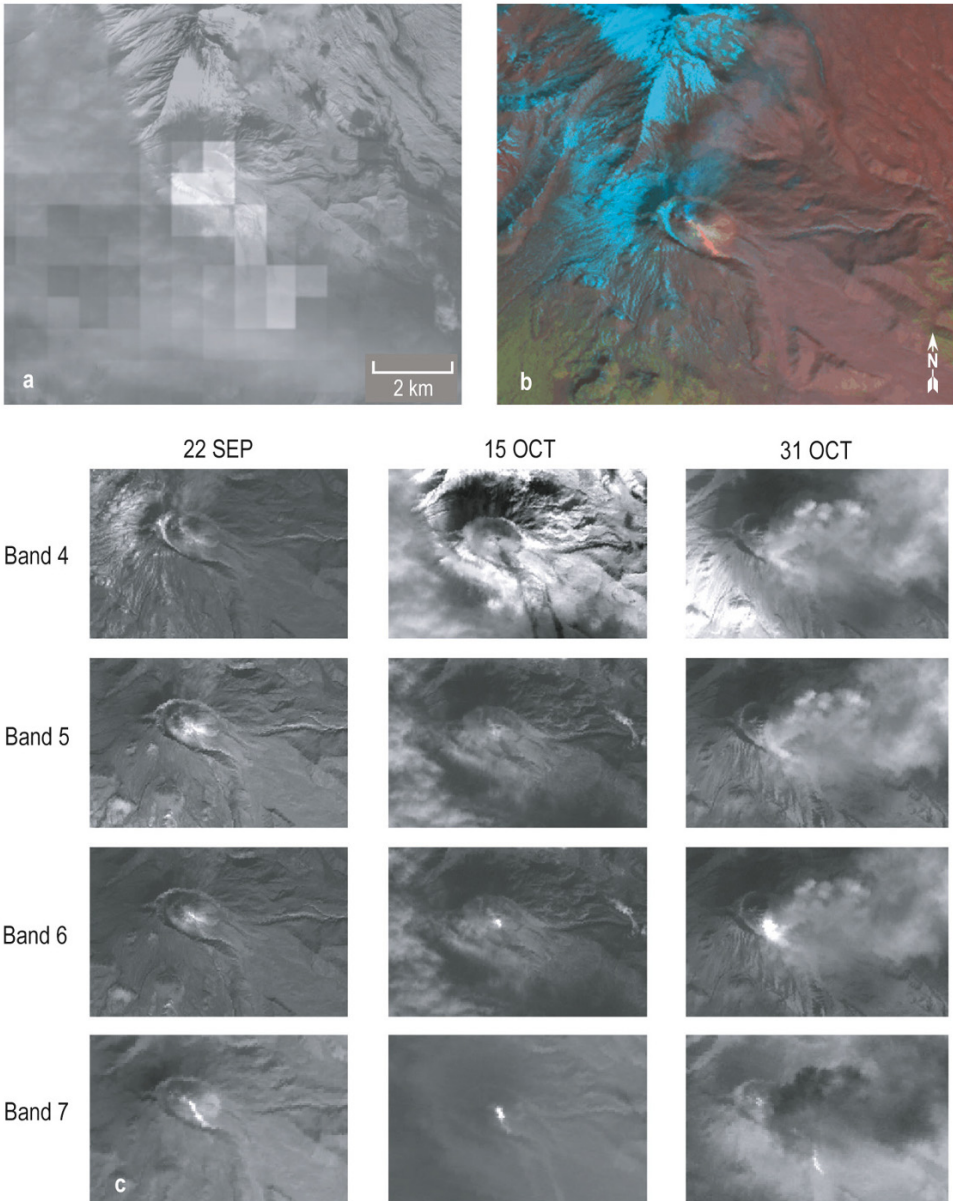


Figure 4.4. Landsat 7 Enhanced Thematic Mapper Plus (ETM+) data of the eruption of Bezymianny Volcano, Russia acquired in 2000. (a) Overlay of a typical AVHRR band 3 (3.55–3.93 μm) thermal anomaly at ~ 1 km/pixel resolution (acquired on October 31, 2000) onto the ETM+ band 4 (0.78–0.90 μm) image at 30 m/pixel (acquired on October 15, 2000). Note the elongate thermal anomaly suggesting some type of hot flow downslope from the dome. (b) False-color composite (ETM+ bands 6, 4, 2 in R, G, B, respectively) acquired on September 22, 2000 showing the thermally elevated material ($>50^\circ\text{C}$) in bright red deposited downslope (indicated by the white arrow) from the dome. (c) Time series showing three different dates and four bands of the ETM+ data. Although the eruption began in September, it was not until the October 15, 2000 data were analyzed that the emplacement of large pyroclastic flows to the south were confirmed to have occurred (indicated by the black arrow in the band 4 image from that date). Dome temperatures exceeded 100°C over this time period (Ramsey and Dehn, 2004).

continued development of new and more complex computer-based tools.

An example of ASTER TIR data used for reconnaissance mapping, later verified by detailed field and laboratory analysis, are the lava domes of Black Peak Caldera (Figure 4.5a) located between the Aniakchak and Veniaminof Calderas on the Alaska Peninsula (Adleman *et al.*, 2003; Adleman, 2005). The caldera floor of Black Peak Volcano is occupied by a complex of approximately one dozen overlapping lava domes previously identified as dacite in composition (Detterman *et al.*, 1981; Miller *et al.*, 1998). However, a decorrelation stretch of ASTER TIR night-time data collected on October 9, 2002 revealed significant differences between at least two of the intercaldera domes (Figure 4.5b). The decorrelation technique, explained in

detail by Gillespie *et al.* (1986), is a transformational stretch of the original data that highlights compositional information as color variations and surface temperature changes (which correlate to topography) as intensity (brightness) variations. The false-color red-colored and blue-colored pixels covering two adjacent domes prompted field mapping as well as laboratory (petrologic and spectroscopic) analysis of samples collected from each dome. Samples from the dome corresponding to the red pixel were found to be dacite, whereas samples from the dome corresponding to the blue pixel were found to be andesite. This verified the ASTER decorrelation stretch and laboratory spectroscopic analysis, which indicated that the domes within the caldera varied from 57 wt% SiO₂ (andesite) to 63 wt% SiO₂ (dacite) (Adleman, 2005). This study

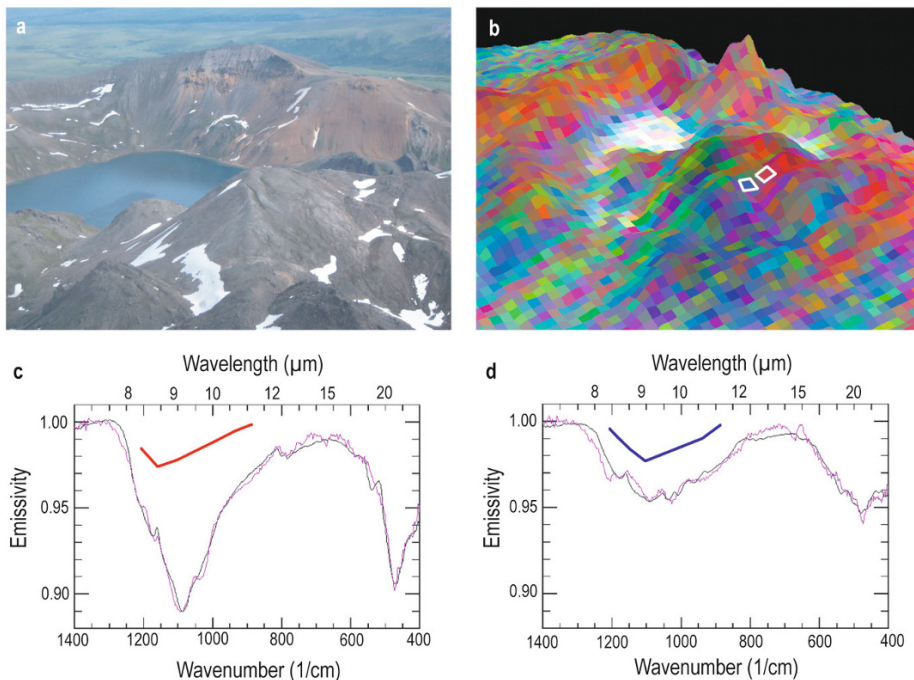


Figure 4.5. Thermal infrared (TIR) analysis of Black Peak Caldera, Alaska. (a) Aerial photograph looking NW with dome complex in the foreground and Purple Lake and the caldera wall in the background. (b) ASTER TIR decorrelation stretch image draped over a digital elevation model and oriented looking in the same relative direction as (a). The lake shows as white pixels in this false-color composite, whereas the dome mineralogy and surface coatings cause them to be displayed in shades of red (less mafic) to blue (more mafic). Two pixels investigated in the field are highlighted by the white boxes. (c) Laboratory emissivity spectrum (purple) and best case mineralogic fit (black) of a rock sample taken from the region covered by the red pixel dome. The derived five-point ASTER spectrum of that pixel is shown by the bold red line. (d) Laboratory emissivity spectrum (purple) and best case mineralogic fit (black) of a rock sample taken from the region covered by the blue pixel dome. The derived ASTER five-point spectrum of that pixel is shown by the bold blue line.

has led to a more complete understanding of the volcanic processes and timing of dome emplacement following caldera formation. Furthermore, it highlights the potential of high spatial resolution remote sensing as a cost-effective and efficient way to locate and map eruption deposits in many of the unstudied volcanic regions in the northern Pacific.

4.3.5 Morphologic analysis using SAR data

Synthetic Aperture Radar (SAR) remote sensing is a powerful tool for studying volcanic morphologies, from large-scale structures to radar wavelength scale surface roughness to detection of subradar wavelength scale morphologic changes. Radar wavelength electromagnetic radiation (~0.1–100 cm) responds to differences in the surface roughness and dielectric constant of the ground material as a function of radar wavelength, polarization, imaging geometry, and resolution. Unlike VNIR, SWIR, and TIR instruments, radar instruments typically utilize active sensors, meaning that they provide their own source of energy. Because of this and the range of wavelengths used, radar data acquisition is generally not limited by lighting conditions or clouds, which is especially useful for areas such as the North Pacific that have long periods of darkness and persistent cloud cover.

Radar analyses of volcanic surfaces include distinguishing volcanic from non-volcanic surfaces (e.g., Campbell *et al.*, 1993), delineation of lava flow textures and surface roughness (e.g., Greeley and Martel, 1988; Gaddis *et al.*, 1989, 1990; Campbell and Shepard, 1996; Byrnes, 2002; Plaut *et al.*, 2004), and distinguishing lava flows from pyroclastic deposits (e.g., Gaddis *et al.*, 1989). Additionally, topography may be measured using radar, and topographic changes may be detected using radar interferometry (e.g., Zebker *et al.*, 1992, 1996; Rowland *et al.*, 1999; Lu *et al.*, 2003a; Chapter 8).

An example of large-scale volcano morphologies evident in satellite SAR data is provided in Figure 4.6, which is a radar data mosaic for a portion of the Kamchatka Peninsula. The mosaic is composed of 17 Radarsat-1 scenes collected on January 16 and January 27, 2005. To produce the mosaic, each scene was radiometrically calibrated, georeferenced, and terrain-corrected to the 90 m spatial resolution of the SRTM digital elevation model (Gens and Logan, 2003). In order to produce the final composite, the images were mosaicked and

then filtered to reduce radar speckle (Lopes *et al.*, 1990). Radar is particularly good for illuminating structures, such as the summit crater of Kliuchevskoi, the large slope-failure scarp on the eastern portion of Kamen, the horseshoe-shaped crater and lava dome of Bezymianny, the calderas of Ushkovsky and Plosky Tolbachik, and the sector collapse of Ostry Tolbachik (Figure 4.6c). Details of surface morphologies evident in the radar data are illustrated in Figure 4.7. Specifically, discrete zones are present that display differences in surface roughness (at the 5.6 cm wavelength) along the extensive basalt flow that emanated from the Tolbachik Volcano (see also Figure 4.3), as well as a constructional channel with levees (Pieri *et al.*, 1997). Using empirical relationships between wavelength-dependent surface roughness and radar backscatter as a function of incidence angle, the radar data may be used to identify flow regimes associated with effusive volcanic deposits. For example, in the radar image there are two distinct morphologies evident on this lava flow: (1) the aforementioned channeled zone and (2) the thicker lobate terminus. The channeled portion of the flow traveled faster down a slight incline resulting in a thinner and narrower flow. This transitions into the thicker lobate portion of the flow, which had slowed during flow emplacement due to lessening of the slope.

One of the earliest high-resolution surveys of North Pacific volcanoes was conducted using radar. Rowland *et al.* (1994) examined numerous Alaskan–Aleutian volcanoes using ERS-1 data collected from 1991 to 1993, including multiple images for 10 volcanoes. They mapped three large calderas (Aniakchak, Black Peak, and Veniaminof) including the volcanic structures and constructs associated with them. The satellite SAR data were also useful for identifying surface changes associated with the eruptions of Westdahl (1991–1992) and Mt. Spurr (1992) based on pre- and post-eruption data.

Radar data from a host of instruments were later used in a study focusing on Westdahl Volcano. Dean *et al.* (2002) analyzed Seasat, ERS-1, JERS-1, and airborne SAR data collected from August 1978 to May 1996 to characterize geomorphic changes that accompanied the 1978 and 1991/1992 eruptions. Creation of a multitemporal, false-color SAR composite image aided in the interpretation of the SAR data. They found that radar backscatter alone was not always sufficient to distinguish all the lava flows of different ages, but that several large flow units and volcanic structures could be deli-

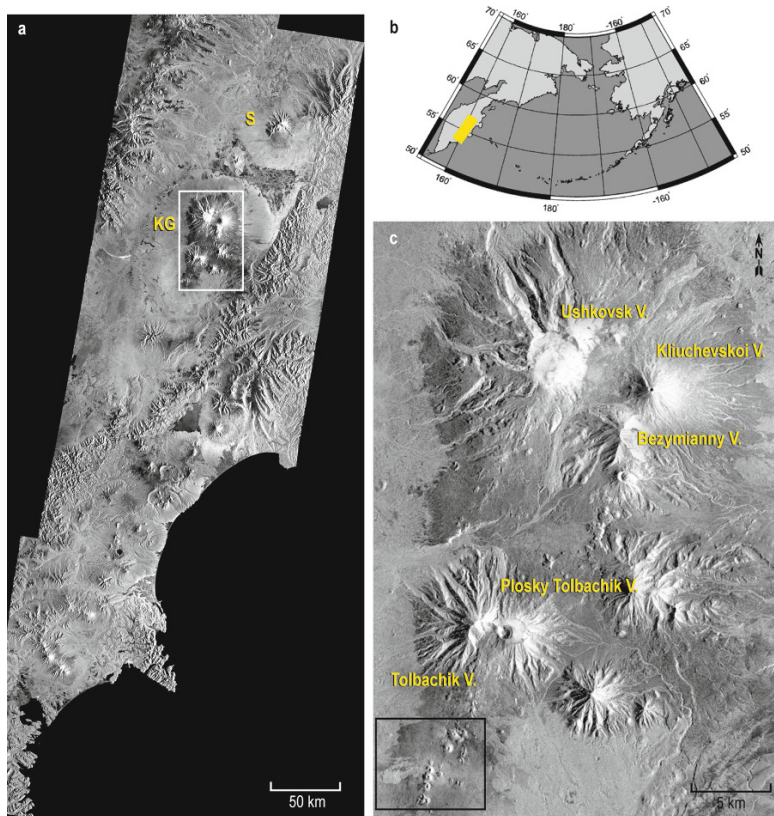


Figure 4.6. SAR data highlighting some of the volcanoes of the Kamchatka Peninsula (radar illumination is from the ESE). (a) Mosaic of Radarsat-1 SAR data collected January 2005. Sheveluch Volcano (S) and the Kliuchevskoi Volcanic Group (KG) are indicated—white box indicates the region enlarged in (c). (b) Map of the North Pacific region showing the location of the SAR mosaic (white box). (c) Portion of (a) showing the Kliuchevskoi Volcanic Group, with the black rectangle, centered on New Tolbachik flows and cones (c), indicating the region shown in Figure 4.7.

neated. They also found that the radar backscatter from the lava flow surfaces tended to decrease with age, although the trend was not ubiquitous. Brown *et al.* (under review) applied the results of Dean *et al.* (2002) to 10 ERS-2 SAR datasets in conjunction with field observations and geochemical analyses (Nicolaysen *et al.*, 1992) to determine relative ages of Holocene blocky andesite flows from Coats Caldera, Yunaska Volcano (located in the central portion of the Aleutian Arc). Their analyses indicate that the ERS-2 SAR composite may be used successfully to determine the eruption sequence for an older, caldera-breaching flow and two younger, roughly contemporaneous fissure-fed flows despite the lack of direct stratigraphic relationships between the three flows.

4.3.6 Use of satellite-derived digital elevation models (DEMs)

Digital elevation models (DEMs) have become an increasingly important tool for both visualization and analysis of data of volcanic surfaces in the northern Pacific (Dehn *et al.*, 2000; Ramsey and Dehn, 2004; Smith, 2005). DEMs are generally calculated through comparison of two images acquired under slightly different viewing conditions of the same surface. This provides the vertical information, which can be used as a base for the draping of images (e.g., Figure 4.5b), the calculation of the slope and its effect on flow emplacement, and as an input for the calculation of ground deformation using interferometric SAR (InSAR).

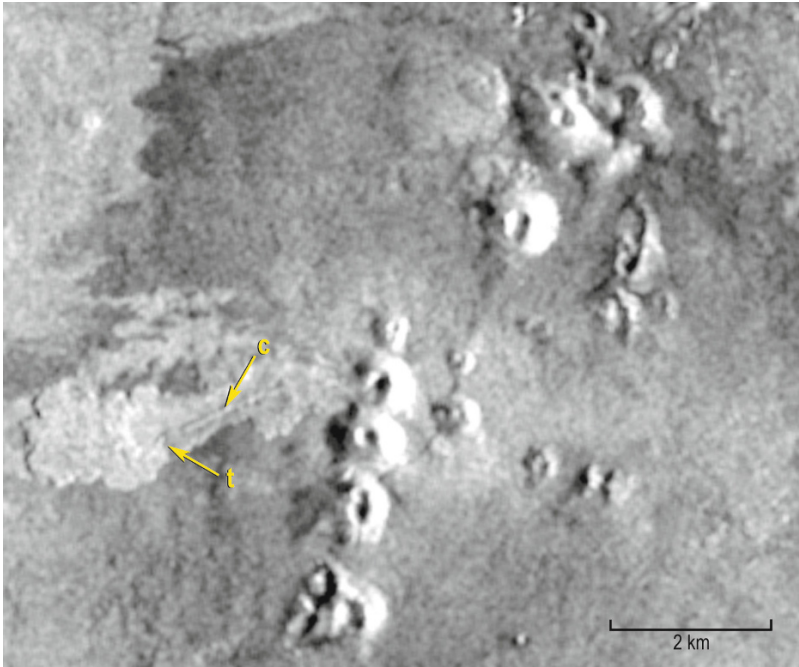


Figure 4.7. Detailed radar image of Tolbachik Volcano activity from 1975 to 1976. The data illustrate radar wavelength (5.6 cm) surface roughness differences (bright vs. dark) on the long basalt flow emanating from one scoria cone in the chain of cones associated with the NNE/SSW-trending rift zone. This is the same flow as that in Figure 4.3c shown to be warm 30 years after emplacement. It has a prominent central channel (c) with levees that end where the flow transitions (t) distally to a thicker, lobate zone with a more (radar) rough surface, although some of the increased radar backscatter may be attributable to changes in the imaging geometry across the scene. Such an increase in surface roughness with downflow distance from the vent is most likely due to thickening and deformation of the cooling crust during emplacement, which produced a much rougher slabby surface.

In addition to identifying radar wavelength scale roughness, SAR data can be used to extract deformation and surface topography using InSAR (e.g., Zebker *et al.*, 2000; Chapter 8). Two sets of SAR measurements are required in order to create an InSAR image. These may be taken synchronously and separated spatially along some baseline (e.g., SRTM, TOPSAR), taken by the same (or a similar) antenna and separated temporally by some repeat interval (e.g., ERS-1 and ERS-2), or separated spatially and temporally. Spatially separated InSAR data are used to calculate topography based on timing of the radar pulses. The relative precision of the height measurements using InSAR is orders of magnitude better than optical photogrammetry because signal phase is measured in addition to signal strength. Temporally separated InSAR measurements may be used to precisely determine deformation of the imaged surface, as described in

Chapter 8. InSAR-derived topography is limited by the baseline used, surface decorrelation, and radar shadowing in steep terrain, but can ideally measure height differences on the millimeter scale for each DEM element (Zebker *et al.*, 2000; Lu *et al.*, 2003a). For example, Lu *et al.* (2003a) used InSAR data to generate DEMs of Okmok Volcano representing the pre-1997 and post-1997 eruption topography, incorporating both satellite (ERS-1 and ERS-2) and airborne (TOPSAR) data. High-precision SAR-derived DEMs were used to calculate that 9.8 km² were resurfaced by lava flows (agreeing well with 9.47 km² calculated from Landsat data), totaling 0.129 km³–0.179 km³ of material extruded.

DEM s can also be created with data collected by optical satellite sensors (e.g., ASTER, SPOT, QuickBird, and IKONOS) using digital photogrammetry. This technique uses the image parallax from different viewing locations to calculate topog-

raphy. ASTER data are widely available and affordable as a standard data product since 2000. Daytime data collected by the sensor contain a band 3B (backward), which has the same NIR spectral response as band 3N (nadir). Band 3B serves as the stereo back-looking view and is acquired about two minutes after the 3N image. Provided there has been little to no change between the two images (e.g., clouds, etc.) the change in viewing position produces the parallax needed to create a 30 m ASTER DEM. Several different methods have been tested using ASTER band 3B/3N data over several types of terrain that produce vertical accuracies from about ± 10 m (Fujisada *et al.*, 2005) to ± 40 m (Kääb, 2005).

Ramsey and Dehn (2004) made effective use of the ASTER-derived DEM of Bezymianny Volcano on the Kamchatka Peninsula, Russia. Bezymianny's higher latitude location (56° N) and large eruption on March 14, 2000 made it an attractive target for early ASTER observations soon after the instrument was launched in December 1999. ASTER provided the first high spatial resolution, multi-spectral TIR data for a series of subplinian eruptions and subsequent pyroclastic deposits. It also provided an excellent DEM image from the VNIR data collected on May 1, 2000. In figures 6 and 7 of Ramsey and Dehn (2004) an ASTER DEM was used as a base on which to drape the TIR-derived temperature and micron-scale roughness estimates. The temperature images were chosen specifically to highlight both the non-eruptive (restive) behavior of the volcano during times where no AVHRR anomalies were seen (summer) as well as immediately following the large eruptions (April and October). Significant changes in intensity and location of the anomalous pixels were seen both on the dome as well as the cooling pyroclastic deposits. Following the large eruption in March 2000 numerous smaller hot-debris flows were emplaced in the valley southeast of the dome. The DEM provided an independent validation of the pre- and post-emplacment slope of the valleys as well as confirmation of the distance traveled by the flows and can be used as a proxy for the eruption's energy. Similarly, the micron-scale roughness images (derived from TIR emissivity data) were draped onto the lava dome itself and certain spatial and temporal patterns were seen. Large, low micron-scale roughness (<20%) regions were present and corresponded to the regions of highest thermal output. With time following the eruption in March 2000, the roughness of the dome trended higher as new

surface flows become less rough at the micron scale through surface weathering and vesicle infilling by airborne ash and/or particulates. This progression was reset in September and October when the dome was subject to a new cycle of heating, eruption, and potentially new surface flows, which again lowered the surface roughness. The monitoring of Bezymianny over 9 months in 2000 with ASTER using all the wavelength ranges and the derived DEM showed a pattern that likely represented endogenic lava dome growth and collapse following the larger eruptions.

4.3.7 Data fusion

The previous sections show that each part of the EM spectrum provides unique information to map volcanic surfaces and products. By combining the data from multiple sensors spanning the EM spectrum, the fused dataset should provide a better inference about the surface characteristics than a single sensor could achieve. The process of fusing different datasets collected on different dates with differing spatial resolutions, which are sensitive to very different surface processes/scales, can be problematic (Solberg *et al.*, 1994; Pohl and Van Genderen, 1998). One of the greatest obstacles in the successful use of stacked data from multiple instruments is registration error. To have accurate image registration, each pixel in every data layer must precisely correspond to the same places on the ground.

Several examples of volcanological studies using data fusion of radar and shorter wavelength remote-sensing datasets have been documented. Moxey *et al.* (2002) and Patrick *et al.* (2003) synthesized remote-sensing data from several sensors in order to better understand the 1997 eruption of Okmok Volcano (Alaska). Specifically, they used Landsat, ERS, and AIRSAR/TOPSAR data to characterize lava flow resurfacing that occurred within Okmok Caldera. Additionally, Patrick *et al.* (2003) incorporated high spatial resolution data (JERS, Radarsat) collected prior and subsequent to the eruption to better constrain the low spatial resolution data (AVHRR) collected during the eruption. This provided an eruption chronology and independent approaches for constraining effusion rates for an eruption that had few direct observations.

Another study was that of Lu *et al.* (2004), which combined Landsat ETM+ data, SRTM digital elevation data, and a novel application of

ERS radar data to discriminate among lava flows on the southeastern flank of Westdahl Volcano. By stacking multiple ERS radar images from one year (1992), they were able to reduce speckle noise and better differentiate between several lava flows. They showed that through careful analyses of this fused data product, they could improve upon earlier remote-sensing estimates of flow geometry and volume.

4.4 CASE STUDY

4.4.1 Analysis of Westdahl Volcano with multifrequency data

Detailed field work was carried out in the summer of 1999 (6 months prior to the launch of ASTER) at Unimak Island by authors Ramsey and Wessels. The purpose was to collect precise land cover data over various surface types at the 2–3 m spatial scale. The field surveys included sample collection, location derived from differential Global Positioning System (dGPS) measurements, and documentation of block size distribution and vegetation morphology/areal percentage of various surfaces. These surfaces included several Westdahl lava flows, vegetated soils, beach sands, and the fresh ash flows from the March 1999 eruption of Shishaldin Vol-

cano (Nye *et al.*, 2002). The survey was intended to provide ground-truth for ASTER as well as other high-resolution instruments in order to better characterize and discriminate between both volcanic and non-volcanic materials using future satellite data. These local observations can be extended to similar settings across the North Pacific in order to compile a more detailed land cover survey of the volcanic environments.

The resulting image analysis case study presented here relies on detailed field knowledge as well as ETM+ and ASTER data subsequently collected over the island. In order to constrain the extent of the study, the focus here is only on the lava flows on the eastern flank of Westdahl. This region provides many unique spectral and volcanological land cover types and can also be directly compared with the results presented by Lu *et al.* (2004). This case study briefly presents a test using co-registered ASTER, Landsat ETM+, ERS SAR, and SRTM DEM data (see Table 4.1) to map the lava flows using only standardized computer classification algorithms. The purpose of this work is to test the limits of data fusion in conjunction with land cover feature classification techniques and to illustrate where such approaches work or do not work in this situation.

The datasets were first precisely co-registered to ensure that each pixel represents the same area on the ground. ASTER 15 m VNIR data orthorectified

Table 4.1. List of sensors and specifications used for the Westdahl lava flow case study. These data were registered and resampled to the ASTER VNIR dataset (15 m/pixel) and used for image classification (see Figure 4.8).

<i>Sensor</i>	<i>Band #</i>	<i>Wavelength</i> (μm)	<i>Initial resolution</i> (m)	<i>Acquisition date</i>
ASTER	1–3	0.556–0.807	15	June 26, 2001
ASTER	4–9	1.656–2.400	30	June 26, 2001
ASTER	10–14	10.291–11.318	90	June 26, 2001
ETM+	Panchromatic	0.500–0.900	15	June 26, 2001
ETM+	1–5, 7	0.450–1.750, 2.210	30	June 26, 2001
ETM+	6	11.450	60	June 26, 2001
ERS-1	<i>C (total power)^a</i>	56,600 (5.66 cm)	12.5	1992
ERS-2	<i>C</i>	56,600 (5.66 cm)	12.5	April 18, 1999
SRTM	<i>C (DEM)</i>	56,600 (5.66 cm)	30	February 2000

^a See Lu *et al.* (2004) for a more detailed description.

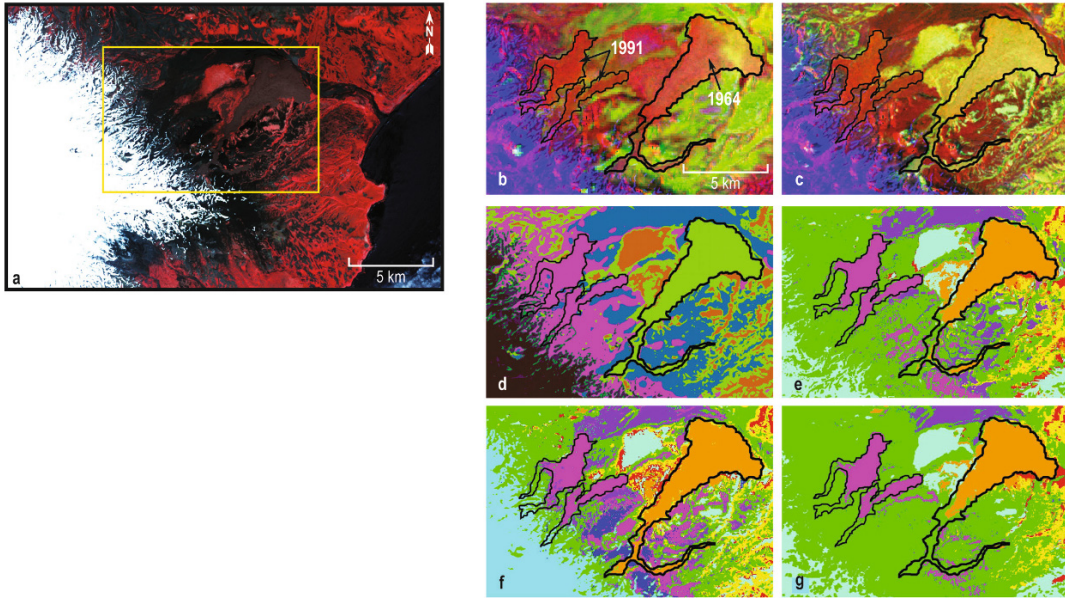


Figure 4.8. Data fusion case study for Westdahl Volcano, Unimak Island, Alaska. (a) ASTER VNIR composite (bands 3, 2, 1 in R, G, B, respectively) acquired on June 26, 2001 showing the eastern flank of Westdahl Volcano. Vegetation is displayed in red, snow/ice in white, water in black (beyond eastern coastline), and lava flows and ash flow sheets in shades of gray to black. The black rectangle indicates the extents of lava flows and ash flow sheets in (b) through (g). (b)–(g) False-color composites and automated classifications using data from ASTER, ETM+, ERS-1, ERS-2, and SRTM (see Table 4.1). The extents of the 1964 and 1991 lava flows are outlined in black in each image, and were determined by examining various band color combinations and validated by GPS data collected in the field. (b) Composite showing total ERS-1 radar power, ASTER band 12 (TIR), and ASTER band 3 (NIR) in R, G, B, respectively. (c) Composite showing total ERS-1 SAR backscatter, ETM+ band 5 (SWIR), and ASTER band 3 (VNIR) in R, G, B, respectively. (d) Decorrelation stretch of ASTER TIR radiance bands 14, 12, and 10. (e) Unsupervised classification result based on all ASTER and ETM+ data. (f) Supervised classification result of all ASTER data. (g) Supervised classification result of all ASTER, ETM+, ERS-1, and ERS-2 data.

to SRTM DEM (30 m) and checked against GPS control points provided the reference image to which all other data sets were registered. Once converted into the same projection and datum, the Landsat ETM+ bands registered very well to those of ASTER. Although terrain correction was applied to the ERS backscatter image using the SRTM DEM, the image still did not precisely register to the optical data in areas of high relief. Additional manual fitting was necessary in order to more precisely register the ERS data to the ASTER over the lava flows. A best fit polynomial achieved from affine transformation of matching control points was used to warp the ERS data. The individual bands from each sensor were then combined into one 23-band data set with all pixels resampled to 15 m (Table 4.1). This fused product was then

treated as a single data set and subjected to multi-parameter analyses and image classification.

Image products derived from the data fusion are presented in Figure 4.8. Comparison of the various products illustrates information about the volcanic surfaces and demonstrates some of the strengths and limitations of the data and the data fusion techniques. Figure 4.8b is a false-color combination of SAR total power (Lu *et al.*, 2004), ASTER TIR, and ASTER VNIR data and delineates the lower portions of the 1991 flow units from the surrounding surfaces. Much of the main 1964 flow lobe is similar in coloration to the 1991 lobe but becomes slightly more green at its distal end due to the increased signal from ASTER TIR band 12 relative to the rest of the flow; note that this distal difference does not correlate with any identifiable

features in the VNIR image (Figure 4.8a). The increase in TIR radiant emission is due to a warmer surface ($\sim 4.5^{\circ}\text{C}$) rather than higher emissivity, which would indicate a change in composition/surface texture on the lower lobe of the flow. Analysis in the field (and confirmed using standard vegetation detection ratios and the ASTER VNIR data) showed that the 1964 flow surface was highly vegetated by a dense moss cover. The SAR backscatter image also shows a slightly higher return from this portion of the flow, indicating a larger amount of centimeter-scale roughness. A blockier portion of the flow could have more non-vegetated surfaces exposed, which would explain the warmer temperature detected in the TIR and the rougher surface detected with SAR. In the false-color composite illustrated in Figure 4.8c (ERS-1 backscatter, ETM+ SWIR, ASTER VNIR in RGB, respectively), the 1991 and 1964 flow lobes are delineated from their surroundings, though the 1991 flows (especially the southernmost lobe) are not as distinct as they were when using SAR total power and TIR. Additionally, there is more contrast between the 1964 flow and pre-1964 lavas in this image relative to Figure 4.8b, indicating that at least in this case the ETM+ SWIR may be more effective for discriminating older lobe ages than the ASTER TIR. Note that the greener distal end of the 1964 flow lobe observed in Figure 4.8b is absent in Figure 4.8c indicating that the ETM+ band 5 has a fairly consistent reflectance over the entire flow lobe. It is clear that simple color composites of data from very different parts of the EM spectrum are powerful tools for discriminating surface units. A decorrelation stretch (similar to that described in the TIR data analysis of Black Peak Caldera) was constructed for ASTER TIR bands 14, 12, and 10 (Figure 4.8d). Although much of the image is fairly bland, indicating a lack of spectral diversity, the non-vegetated 1991 flow lobes are clearly delineated by the red/magenta colors. This demonstrates the utility of high spatial resolution, multi-spectral TIR for detection and mapping of relatively recent flows.

Unsupervised classification (described previously), where the discrimination of units is performed automatically based on pixel statistics, can also be an effective tool. Unsupervised classification using all bands of the ASTER and ETM+ data (Figure 4.8e) delineates much of the 1964 flow well (shown in bright green), but greatly overestimates the areal extent of the class that described the 1991 flow (shown in magenta) by incorrectly

including parts of older flows exposed at the edge of the snow pack (shown in black). A supervised classification, where the automated classifier starts with a set of user-defined spectral classes (Figure 4.8f–g) improves the classifier's ability to distinguish the 1991 flow lobes from adjacent surface units. Although all of the image composites and classifiers discussed above underestimate the 1991 flow extents on the proximal end of the lobes, this is to be expected as these regions grade into heavy snow cover at progressively higher elevations of the volcano. Additionally, supervised classifications based on either the ASTER data alone (Figure 4.8f) or the entire dataset (Figure 4.8g) underestimate the SW extents of both the 1964 and 1991 flow lobes. This is due to the small spatial scale of these flows, which allows for pixel averaging with nearby rock and snow on the volcano's flank.

Several issues related to the data fusion are evident. Although additional remote-sensing data should ideally improve the classifications, any improvements in the discrimination capability of the algorithm will strongly depend on the character and quality of the additional data. For example, inherent speckle noise in the SAR data can degrade discrimination between units with similar surface textures. Furthermore, small errors in coregistration of the various remote-sensing data sets, which may be due to differences in viewing geometry, limitations of ground control points, and other additional factors may also introduce errors in resulting classifications. Finally, it should be noted that the use of different wavelength regions will affect the resulting classification due to differences in spatial and spectral resolutions. For example, in the classification based on ASTER data alone, small-scale thermal features are represented to a lesser extent than equivalently sized visible features due to the six-fold difference in spatial resolution. Similarly, surface characteristics that are represented in the SWIR will affect the classification to a greater extent than those represented in the VNIR because there are six SWIR bands, two visible bands, and only one NIR band. Given the complexity of a target such as Westdahl and the added difficulties introduced by merging multiple bands of data that have different wavelength regions, spatial resolutions, and imaging geometries, it is evident that successfully producing and interpreting automated classifications commonly requires detailed knowledge of the target and precise controls on the remote-sensing data.

4.5 SUMMARY

In order to maximize the utility of current satellite remote-sensing instruments, moderate spatial (>100 m/pixel), high temporal (minutes–hours) resolution remote-sensing data for routine monitoring should continue, but be supplemented with high spatial (<100 m/pixel) and moderate temporal (days) resolution data as had been suggested by Wadge (2003) and Carter and Ramsey (2009). Such an approach to mapping and monitoring will maximize the utility of each class of remote-sensing instrument. High spatial resolution data are required for certain applications, such as mapping small features and low-temperature thermal anomalies, whereas multispectral capabilities, especially in the TIR region, will provide the capability to determine compositional variations. Furthermore, these high spatial resolution data will continue to serve the additional use of providing base images for field work. This chapter has demonstrated that different regions of the EM spectrum have different uses and limitations for volcanological applications in the northern Pacific region. Data fusion techniques are but one way to maximize the return from multiple data sets, although the ability to implement such methods is dependent on the type and quality of available data as well as the geometric controls on those data sets.

Overall, high-resolution satellite remote-sensing data provide a vital source of information to support monitoring, field, and other detailed studies of volcanoes. Whereas this chapter has focused on the utility of such data sets to examine active volcanoes in the North Pacific region, the techniques are applicable to the study of any volcanoes worldwide. Additional development and refinement of high-resolution remote-sensing applications to volcanology will require the continued commitment of NASA and other space agencies to the support of current data streams and the development of future remote-sensing satellite instruments, as well as innovative approaches to data analysis.

4.6 ACKNOWLEDGMENTS

The authors would like to thank the Alaska Volcano Observatory (AVO) for field support on the Unimak Island/Westdahl project, and for their continued support using high-resolution data for volcanic research. The authors would also like to

acknowledge past University of Alaska Fairbanks (UAF) graduate student research mentioned herein, in particular that by J. Adleman (Black Peak Caldera), S. Smith (Cleveland Volcano), and M. Patrick (Bezymianny Volcano). In addition, Zhong Lu (USGS) provided data and access to his analysis of Westdahl Volcano. Commercial data sets used for aspects of this research have been provided by Space Imaging Corporation (IKONOS), Digital Globe Corporation (QuickBird), the European Space Agency (ERS), and the Canadian Space Agency (Radarsat). ASTER data were provided by NASA (U.S.) and METI (Japan) and the ASTER Science Team. Research funding for Ramsey and Wessels was provided by NASA through the ASTER science project (NNG04GO69G), and for Ramsey and Byrnes by the National Science Foundation (NSF) through the Petrology and Geochemistry Program (EAR-0309631). Additional research funding for Wessels was provided by the USGS/AVO. This manuscript has benefited greatly from detailed reviews by Jeff Johnson and Laszlo Keszthelyi (USGS), David Pieri (JPL), and Scott Rowland (University of Hawaii).

4.7 REFERENCES

- Abrams, M. (2000). The Advanced Spaceborne Thermal Emission And Reflectance Radiometer (ASTER): Data products for the high spatial resolution imager on NASA's Terra platform. *Int. J. Remote Sensing*, **21**, 847–859.
- Abrams, M.; Glaze, L.; Sheridan, M. (1991). Monitoring Colima Volcano, Mexico, using satellite data, *Bull. Volcanol.*, **53**, 571–574.
- Adleman, J.N. (2005). Analysis of composition and chronology of dome emplacement at Black Peak, Alaska utilizing ASTER remote sensing data and field-based studies, M.S. thesis, University of Alaska Fairbanks, 136 pp.
- Adleman, J.N.; Larsen, J.F.; Ramsey, M.S.; McGimsey, R.G.; Neal, C.A. (2003). Analysis of composition and chronology of dome emplacement at Black Peak, Alaska utilizing ASTER remote sensing data and field-based studies, *EOS, Trans. Am. Geophys. Union*, **84**(46), Fall Meet. Suppl., Abs. V31G-07.
- Begét, J.E.; Kienle, J. (1992). Cyclic formation of debris avalanches at Mount St. Augustine Volcano, *Nature*, **356**, 701–704.
- Begét, J.E.; Larsen, J.F.; Neal, C.A.; Nye, C.J.; Schaefer, J.R. (2005). *Preliminary Volcano-hazard Assessment for Okmok Volcano, Unimak Island, Alaska*, Alaska Division of Geological & Geophysical Surveys

- Report of Investigation 2004-3, 32 pp., 1 sheet, scale 1:150,000.
- Brown, M.E.; Nicolaysen, K.; Dehn, J.; Myers, J.D. (under review). SAR and petrologic data illuminate the eruption sequence of post-caldera andesites, Yunaska Volcano, Aleutian Arc, *J. Volcanol. Geothermal Res.*
- Byrnes, J.M. (2002). Lava flow field emplacement studies of Mauna Ulu (Kīlauea Volcano, Hawaii, USA) and Venus, using field and remote sensing analyses. Ph.D. dissertation, University of Pittsburgh, Pittsburgh, 191 pp.
- Byrnes, J.M.; Ramsey, M.S.; Crown, D.A. (2004). Emplacement of the Mauna Ulu flow field, Kīlauea Volcano, Hawaii: New insights from ASTER and the MASTER airborne simulator, *J. Volcanol. Geothermal Res.*, **135**, 169–193.
- Campbell B.A.; Shepard, M.K. (1996). Lava flow surface roughness and depolarized radar scattering, *J. Geophys. Res.*, **101**, 18941–18951.
- Campbell, B.A.; Arvidson, R.E.; Shepard, M.K. (1993). Radar polarization of volcanic and playa surfaces: Applications to terrestrial remote sensing and Venus data interpretation, *J. Geophys. Res.*, **98**, 17099–17113.
- Carn, S.A. (1999). Application of synthetic aperture radar (SAR) imagery to volcano mapping in the humid tropics: A case study in East Java, Indonesia, *Bull. Volcanol.*, **61**, 92–105.
- Carter, A.J.; Ramsey, M.S. (2009). ASTER- and field-based observations at Bezmyianny Volcano: Focus on the May 2007 pyroclastic flow deposit, *Remote Sensing of Environment*, **10**, 2142–2151, doi: 10.1016/j.rse.2009.05.020.
- Cashman, K.; Blundy, J. (2000). Degassing and crystallization of ascending andesite and dacite, *Philosophical Transactions of the Royal Society*, **358**, 1487–1513.
- Clark, R.N. (1993). *Mapping Minerals with Imaging Spectroscopy*, USGS Bulletin 2039, U.S. Geological Survey, Office of Mineral Services, Reston, VA, pp. 141–150.
- Coombs, M.L.; Neal, C.A.; Wessels, R.L.; McGimsey, R.G. (2006). *Geothermal Disruption of Summit Glaciers at Mount Spurr Volcano, 2004–6: An Unusual Manifestation of Volcanic Unrest*, USGS Prof. Paper 1732-B, U.S. Geological Survey, Reston, VA, 33 pp.
- Dean, K.G.; Dehn, J.; Papp, K.R.; Smith, S.; Izbekov, P.; Peterson, R.; Kearney, C.; Steffke, A. (2004). Integrated satellite observations of the 2001 eruption of Mt. Cleveland, Alaska, *J. Volcanol. Geothermal Res.*, **135**, 51–73.
- Dean, K.G.; Engle, K.; Partington, K.; Groves, J.; Dehn, J. (2002). Analysis of surface processes using SAR data: Westdahl Volcano, Alaska, *Int. J. Remote Sensing*, **23**, 4529–4550.
- Dehn, J.; Dean, K.G.; Engle, K. (2000). Thermal monitoring of North Pacific volcanoes from space, *Geology*, **28**, 755–758.
- Detterman, R.L.; Miller, T.P.; Yount, M.E.; Wilson, F.H. (1981). *Geologic Map of the Chignik and Sutwik Island Quadrangles, Alaska 1:250,000*, Map I-1229, U.S. Geological Survey, Reston, VA.
- Donegan, S.J.; Flynn, L.P. (2004). Comparison of the response of the Landsat 7 Enhanced Thematic Mapper Plus and the Earth Observing-1 Advanced Land Imager over active lava flows, *J. Volcanol. Geothermal Res.*, **135**, 105–126.
- Fink, J.H.; Manley, C.R. (1987). Origin of pumiceous and glassy textures in rhyolite flows and domes, in: J.H. Fink (Ed.), *The Emplacement of Silicic Domes and Lava Flows*, GSA Spec. Pap. 212, Geological Society of America, Boulder, CO, pp. 77–88.
- Flynn, L.P.; Mouginiis-Mark, P.J.; Horton, K.A. (1994). Distribution of thermal areas on an active lava flow field: Landsat observations of Kīlauea, Hawaii, July, 1991, *Bull. Volcanol.*, **56**, 284–296.
- Flynn, L.P.; Harris, A.J.L.; Rothery, D.A.; Oppenheimer, C. (2000). High-spatial resolution thermal remote sensing of active volcanic features using Landsat and hyperspectral data, in P.J. Mouginiis-Mark, J.A. Crisp, J.H. Fink (Eds.), *Remote Sensing of Active Volcanism*, AGU Monograph 116, American Geophysical Union, Washington, D.C., pp. 161–177.
- Francis P.W. (1979). Infra-red techniques for volcano monitoring and prediction: A review, *J. Geological Society London.*, **136**, 355–359.
- Francis, P.W.; Rothery, D.A. (1987). Using the Landsat Thematic Mapper to detect and monitor active volcanoes: An example from Lascar Volcano, northern Chile, *Geology*, **15**, 614–617.
- Francis, P.W.; Rothery, D.A. (2000). Remote sensing of active volcanoes, *Annu. Rev. Earth Planet. Sci.*, **28**, 81–106.
- Fujisada, H.; Bailey, G.B.; Kelly, G.G.; Hara, S.; Abrams, M.J. (2005). ASTER DEM performance, *IEEE Trans. Geosci. Remote Sensing*, **43**, 2707–2714.
- Gaddis, L.; Mouginiis-Mark, P.; Singer, R.; Kaupp, V. (1989). Geologic analyses of Shuttle Imaging Radar (SIR-B) data of Kīlauea Volcano, Hawai'i, *Geol. Soc. Am. Bull.*, **101**, 317–332.
- Gaddis, L.R.; Mouginiis-Mark, P.J.; Hayashi, J.N. (1990). Lava flow textures: SIR-B radar image texture, field observations, and terrain measurements, *Photogram. Eng. Remote Sensing*, **56**, 211–224.
- Gens, R.; Logan, T. (2003). *Alaska Satellite Facility Software Tools*, Geophysical Institute, University of Alaska Fairbanks (www.asf.alaska.edu), 186 pp.
- Gillespie, A.R.; Kahle, A.B.; Walker, R.E. (1986). Color enhancement of highly correlated images: I. Decorrelation and HSI contrast stretches, *Remote Sensing of Environment*, **20**, 209–235.

- Greeley, R.; Martel, L. (1988). Radar observations of basaltic lava flows, Craters of the Moon, Idaho, *Int. J. Remote Sensing*, **9**, 1071–1085.
- Harris, A.J.L.; Flynn, L.P.; Keszthelyi, L.; Mougini-Mark, P.J.; Rowland, S.K.; Resing, J.A. (1998). Calculation of lava effusion rates from Landsat TM data, *Bull. Volcanol.*, **60**, 52–71.
- Harris, A.J.L.; Flynn, L.P.; Rothery, D.A.; Oppenheimer, C.; Sherman, S.B. (1999). Mass flux measurements at active lava lakes: Implications for magma recycling, *J. Geophys. Res.*, **104**, 7117–7136.
- Harris, A.J.L.; Pilger, E.; Flynn, L.P.; Garbeil, H.; Mougini-Mark, P.J.; Kauahikaua, J.; Thornber, C. (2001). Automated, high temporal resolution, thermal analysis of Kīlauea Volcano, Hawaii, using GOES satellite data, *Int. J. Remote Sensing*, **22**, 945–967.
- Harris, A.J.L.; Rose, W.I.; Flynn, L.P. (2003). Temporal trends in lava dome extrusion at Santiaguito 1922–2000, *Bull. Volcanol.*, **65**, 77–89.
- Hook, S.J.; Rast, M. (1990). Mineralogic mapping using Airborne Visible Infrared Imaging Spectrometer (AVIRIS) Shortwave Infrared (SWIR) data acquired over Cuprite, Nevada, *AVIRIS Airborne Geosci. Workshop Proc. 1990*, pp. 199–207.
- Huntington, J.F. (1996). The role of remote sensing in finding hydrothermal mineral deposits on Earth, in G. Bock, J. Goode (Eds.), *Evolution of Hydrothermal Ecosystems on Earth (and Mars?)*, John Wiley & Sons, Chichester, U.K., pp. 214–230.
- Kääb, A. (2005). *Remote Sensing of Mountain Glaciers and Permafrost Creep*, Geographisches Institut der Universität Zürich, 264 pp.
- Kienle, J.; Dean, K.G.; Garbeil, H. (1990). Satellite surveillance of volcanic ash plumes of the ongoing eruptions of Redoubt Volcano, Alaska, *EOS, Trans. Am. Geophys. Union*, **71**(17), Fall Meet. Suppl., 649.
- Krueger, A.J.; Walter, L.S.; Bhartia, P.K.; Schnetzler, C.C.; Krotkov, N.A.; Sprod, I.; Bluth, G.J.S. (1995). Volcanic sulfur dioxide measurements from the total ozone mapping spectrometer instruments, *J. Geophys. Res.*, **100**, 14057–14076.
- Lopes, A.; Touzi, R.; Nezry, E. (1990). Adaptive speckle filters and scene heterogeneity, *IEEE Trans. Geosci. Rem. Sens.*, **28**, 992–1000.
- Lu, Z.; Fielding, E.; Patrick, M.R.; Trautwein, C.M. (2003a). Estimating lava volume by precision combination of multiple baseline spaceborne and airborne interferometric synthetic aperture radar: The 1997 eruption of Okmok Volcano, Alaska, *IEEE Trans. Geosci. Rem. Sens.*, **41**, 1428–1436.
- Lu, Z.; Masterlark, T.; Dzurisin, D.; Rykhus, R.; Wicks, Jr., C. (2003b). Magma supply dynamics at Westdahl Volcano, Alaska, modeled from satellite radar interferometry, *J. Geophys. Res.*, **108**, 2354, doi: 10.1029/2002JB002311.
- Lu, Z.; Rykhus, R.; Masterlark, T.; Dean, K.G. (2004). Mapping recent lava flows at Westdahl Volcano, Alaska, using radar and optical satellite imagery, *Remote Sensing of Environment*, **91**, 345–353.
- Melnik, O.; Sparks, R.S.J. (1999). Nonlinear dynamics of lava dome extrusion, *Nature*, **402**, 37–41.
- Miller, T.P.; Casadevall, T.J. (2000). Volcanic ash hazards to aviation, in H. Sigurdsson, B. Houghton, S.R. McNutt, H. Rymer, J. Stix (Eds.), *Encyclopedia of Volcanoes*, pp. 915–930, Academic Press, San Francisco.
- Miller, T.P.; McGimsey, R.G.; Richter, D.H.; Riehle, J.R.; Nye, C.J.; Yount, M.E.; Dumoulin, J.A. (1998). *Catalog of the Historically Active Volcanoes of Alaska*, USGS Open-File Report 98-582, U.S. Geological Survey, Reston, VA.
- Mougini-Mark, P.J.; Crisp, J.A.; Fink, J.H. (2000). *Remote Sensing of Active Volcanism*, AGU Monograph 116, American Geophysical Union, Washington, D.C., 272 pp.
- Moxey, L.; Guritz, R.; Dehn, J.; Price, E. (2002). Surface change detection, topographic and geologic mapping of Okmok Volcano, Alaska, using high-resolution AIRSAR sensor data, paper (S1) presented at *AIRSAR Earth Science and Application Workshop*, NASA-JPL, Pasadena, CA, 10 pp.
- Nakada, S.; Miyake, Y.; Sato, H.; Oshima, O.; Fujinawa, A. (1995). Endogenous growth of dacite dome at Unzen volcano (Japan), 1993–1995, *Geology*, **13**, 157–160.
- Nicolaysen, K.E.; Myers, J.D.; Linneman, S.R.; Lamb, D. (1992). Geologic relations of the Yunaska Volcanic Complex, Central Aleutian Arc, *EOS, Trans. Am. Geophys. Union*, Fall Meeting.
- Nye, C.J.; Keith, T.E.C.; Eichelberger, J.C.; Miller, T.P.; McNutt, S.R.; Moran, S.; Schneider, D.J.; Dehn, J.; Schaefer, J.R. (2002). The 1999 eruption of Shishaldin Volcano, Alaska: Monitoring a distant eruption, *Bull. Volcanol.*, **64**, 507–519.
- Patrick, M.R.; Dehn, J.; Papp, K.R.; Lu, Z.; Dean, K.; Moxey, L.; Izbekov, P.; Guritz, R. (2003). The 1997 eruption of Okmok Volcano, Alaska: A synthesis of remotely sensed imagery, *J. Volcanol. Geothermal Res.*, **127**, 87–105.
- Patrick, M.; Dean, K.; Dehn, J. (2004). Active mud volcanism observed with Landsat 7 ETM+, *J. Vol. Geophys. Res.*, **131**, 307–320.
- Patrick, M.R.; Smellie, J.L.; Harris, A.J.L.; Wright, R.; Dean, K.; Izbekov, P.; Garbeil, H.; Pilger, E. (2005). First recorded eruption of Mount Belinda Volcano (Montagu Island), South Sandwich Islands, *Bull. Volcanol.*, **67**, 415–422.
- Pieri, D.; Abrams, M. (2004). ASTER watches the world's volcanoes: A new paradigm for volcanological observations from orbit, *J. Volcanol. Geothermal Res.*, **135**, 13–28.
- Pieri, D.C.; Glaze, L.S.; Abrams, M.J. (1990). Thermal radiance observations of an active lava flow during the June 1984 eruption of Mount Etna, *Geology*, **18**, 1018–1022.

- Pieri, D.C.; Khrenov, A.P.; Miller, T.P.; Zharinov, S.E.; Realmuto, V.; Abrams, M.; Glaze, L.S.; Kahle, A.B.; Drozhnin, V.; Divgalo, V.; Kirianov, V.; Abbott, E.; Chernobief, S. (1997). Joint effort results in first TIMS survey of Kamchatka volcanoes, *EOS, Trans. Am. Geophys. Union*, **78**(12), 125–128.
- Plaut, J.J.; Anderson, S.W.; Crown, D.A.; Stofan, E.R.; van Zyl, J.J. (2004). The unique radar properties of silicic lava domes, *J. Geophys. Res.*, **109**, E03001, doi: 10.1029/2002JE002017.
- Pohl, C.; Van Genderen, J.L. (1998). Review article. Multisensor image fusion in remote sensing: Concepts, methods and applications, *Int. J. Remote Sensing*, **19**, 823–854, doi: 199810.1080/014311698215748.
- Ramsey, M.S.; Dehn, J. (2004). Spaceborne observations of the 2000 Bezymianny, Kamchatka eruption: The integration of high-resolution ASTER data into near real-time monitoring using AVHRR, *J. Volcanol. Geothermal Res.*, **135**, 127–146.
- Ramsey, M.S.; Fink, J.H. (1999). Estimating silicic lava vesicularity with thermal remote sensing: A new technique for volcanic mapping and monitoring, *Bull. Volcanol.*, **61**, 32–39.
- Ramsey, M.S.; Flynn, L.P. (2004). Strategies, insights, and the recent advances in volcanic monitoring and mapping with data from NASA's Earth Observing System, *J. Volcanol. Geothermal Res.*, **135**, 1–11.
- Realmuto, V.J.; Abrams, M.J.; Buongiorno, M.F.; Pieri, D.C. (1994). The use of multispectral thermal infrared image data to estimate the sulfur dioxide flux from volcanoes: A case study from Mount Etna, Sicily, July 29, 1986, *J. Geophys. Res.*, **99**, 481–488.
- Riehle, J. R. (1985). A reconnaissance of the major Holocene tephra deposits in the upper Cook Inlet region, Alaska, *J. Volc. Geotherm. Res.*, **26**, 37–74.
- Rowland, S.K.; Smith, G.A.; Mougins-Mark, P.J. (1994). Preliminary ERS-1 observations of Alaskan and Aleutian Volcanoes, *Remote Sensing of Environment*, **48**, 358–369.
- Rowland, S.K.; MacKay, M.E.; Garbeil, H.; Mougins-Mark, P.J. (1999). Topographic analyses of Kīlauea Volcano, Hawai'i, from interferometric airborne radar, *Bull. Volcanol.*, **61**, 1–14.
- Smith, S.J. (2005). Chronologic multisensor assessment for Mount Cleveland, Alaska from 2000 to 2004 focusing on the 2001 eruption, M.S. thesis, University of Alaska Fairbanks, 141 pp.
- Solberg, A.H.S.; Jain, A.K.; Taxt, T. (1994). Multisource classification of remotely sensed data: Fusion of Landsat TM and SAR images, *IEEE Trans. Geosci. Remote Sensing*, **32**, 768–778.
- Tou, J.T.; Gonzalez, R.C. (1974). *Pattern Recognition Principles*, Addison-Wesley, Reading, MA.
- Vaughan, R.G.; Hook, S.J.; Ramsey, M.S.; Realmuto, V.J.; Schneider, D.J. (2005). Monitoring eruptive activity at Mount St. Helens with TIR image data, *Geophys. Res. Lett.*, **32**, L19305, doi: 10.1029/2005GL024112.
- Wadge, G. (2003). A strategy for the observation of volcanism on Earth from space, *Philosophical Trans. Royal Society London*, **361**, 145–156.
- Waite, R.B.; Begét, J.E. (1996). *Provisional Geologic Map of Augustine Volcano, Alaska*, USGS Open-File Report 96-516, U.S. Geological Survey, Reston, VA.
- Watson, I.M.; Realmuto, V.J.; Rose, W.I.; Prata, A.J.; Bluth, G.J.S.; Gu, Y.; Bader, C.E.; Yu, T. (2004). Thermal infrared remote sensing of volcanic emissions using the moderate resolution imaging spectroradiometer, *J. Volcanol. Geothermal Res.*, **135**, 75–89.
- Wessels, R.; Senyukov, S.; Tranbenkova, A.; Ramsey, M.; Schneider, D. (2004). Detecting small geothermal features at Northern Pacific volcanoes with ASTER thermal infrared data, *EOS, Trans. Am. Geophys. Union*, **85**(47), Fall Meet. Suppl., Abstract V33C-1479.
- Wessels, R.; Ramsey, M.; Dean, J.; Senyukov, S. (2005). Mapping elevated temperatures on a thirty-year-old basalt flow of New Tolbachik Volcano using satellite and ground-based thermal infrared, *EOS, Trans. Am. Geophys. Union*, **86**(52), Fall Meeting Suppl., Abstract V31A-0605.
- Wright, R.; Flynn, L.P.; Garbeil, H.; Harris, A.J.L.; Pilger, E. (2004). MODVOLC: Near-real-time thermal monitoring of global volcanism, *J. Volcanol. Geothermal Res.*, **135**, 29–49.
- Zebker, H.A.; Madsen, S.N.; Martin, J.; Wheeler, K.B.; Miller, T.; Lou, Y.; Alberti, G.; Vetrella, S.; Cucci, A. (1992). The TOPSAR interferometric radar topographic mapping instrument, *IEEE Trans. Geosci. Remote Sensing*, **30**, 933–940.
- Zebker, H.A.; Rosen, P.; Hensley, S.; Mougins-Mark, P.J. (1996). Analysis of active lava flows on Kīlauea Volcano, Hawaii, using SIR-C radar correlation measurements, *Geology*, **24**, 495–498.
- Zebker, H.A.; Amelung, F.; Jonsson, S. (2000). Remote sensing of volcano surface and internal processes using radar interferometry, in P.J. Mougins-Mark, J.A. Crisp, J.H. Fink (eds.), *Remote Sensing of Active Volcanism*, AGU Monograph 116, American Geophysical Union, Washington, D.C., pp. 179–205.

Volcanic clouds

Fred Prata, Kenneson Dean, Matthew Watson

5.1 OVERVIEW

Volcanism has been an unrivaled contributor of material to the atmosphere over the course of Earth history. Emissions from volcanoes can include gases, liquid droplets, and solid particles across a wide range of chemical variation. The primary products from active volcanism are water (in three phases), carbon dioxide, and lithic fragments derived from upwelling magma and country rock. Other gases include SO₂ (see Chapter 6), HF, HCl, HBr, H₂S, H₂O, and a host of trace gases. The mineral-based part of the plume is typically known by the catch-all term “volcanic ash”. These constituents are injected, often at very high velocity, into the atmosphere and regularly reach several kilometers in altitude. Emissions from volcanism can have dimensions of hundreds of kilometers and have been observed to circumnavigate the globe (e.g., Bluth *et al.*, 1992). Volcanic emissions typically begin as a complex, multiphase, coherent outburst from a point source (or occasionally a linear feature such as a fissure). Ash in volcanic emissions is sourced from magmatic fragmentation and subsumation of country rock. This transmits information on eruptive conditions and processes from the subsurface to the atmosphere and, eventually, forms a deposit as the ash settles out of the atmosphere. Observations of both volcanic ash in situ in the atmosphere and the subsequent deposits have been used for over three decades to infer erupted mass, eruption rate, column height, and duration of the eruption (e.g., Walker, 1971; Pyle, 1989; Wen

and Rose, 1994). Fragmentation front propagation in the conduit is at the forefront of current research into explosive volcanism (e.g., Kennedy *et al.*, 2005; Zobin and Jiménez, 2008). This imparts control over the particle size distribution of ash which can be inverted from observation, again to constrain subsurface processes.

Volcanic emissions from explosive activity are on a scale, and present hazards, that are best observed from the synoptic perspective afforded by satellite sensors. The literature is replete with examples of observation of volcanic ash in the atmosphere from satellite-borne sensors dating back 25 years (e.g., Prata, 1989a, b; Wen and Rose, 1994; Schneider *et al.*, 1999; Prata and Grant, 2001; Watson *et al.*, 2004). There are several ways to describe the style of volcanic emission; these are used interchangeably in the literature and, hence, it is worth carefully reiterating the conventional definitions.

5.2 DEFINITIONS

Volcanic cloud: airborne component of an explosive eruption and a term used to mean volcanic emissions during any type of eruption. Usually, though not always, associated with an emission that has detached from the vent.

Eruption cloud: volcanic cloud not attached to the volcano typically associated with explosive activity.

Ash or SO₂ cloud: component-specific description of volcanic emission. Something of a misnomer that encourages the community to consider emissions to be heavily dominated by a single species.

Drifting ash cloud: more complete description of emission, indicating explicitly that the cloud no longer feels any contribution from the vent.

Volcanic plume: Volcanic emission still attached to the volcano.

Whilst these descriptions appear somewhat pedantic, the issue of whether or not the emission is still being contributed to is of vital importance. For example, arguably the most important parameter retrieved by satellite is total ash mass, as it scales to eruption rate and, hence, the size of the eruption. The calculation of any mass-based parameter is significantly different in the two scenarios. A drifting cloud's mass is, by definition, independent of ongoing activity and can be observed to decrease over time as the ash falls out. Ash cloud masses (typically reported in kilotonnes) are thus derived by summing the mass of individual pixels (techniques to retrieve ash mass are discussed in Section 5.10). Conversely, a plume's mass is not a very helpful number, as the plume is continually being contributed to by the volcanic vent. Instead, an emission rate, with units of mass per unit time (typically reported in tonnes per day), is derived by slicing through the plume, integrating the transect's mass and multiplying by the plume speed.

Drifting ash clouds represent a significant hazard to aviation and can have detectable concentrations thousands of kilometers from the source. There are several well-known examples of aircraft–ash interaction, notably Galunggung (Indonesia) in 1982 (BA Flight 9) and Redoubt (Alaska) in 1989

(KLM Flight 867) (see DVD for a description of these events). In both examples a large jet airliner suffered a four-engine failure before managing to restart the engines and prevent catastrophe. Plumes, whilst still dangerous, represent a more limited threat to aircraft as they are constrained spatially to be close to the vent. However, they can still represent a significant issue for airports such as Catania (Sicily) and Kona/Hilo (Hawaii) (Figure 5.1). The airport at Anchorage is regularly affected by emissions from volcanoes in the region, depending on wind conditions. However, the most significant risk in the NOPAC region remains between aircraft at cruising altitude with drifting ash clouds from remote vents.

5.3 STRUCTURE OF VOLCANIC PLUMES AND CLOUDS

5.3.1 Plume fluid dynamics

Many excellent images of volcanic plumes have been captured over the last decades. Volcanic centers are the target of routine observations from Earth observation (EO) sensors (including ASTER and MODIS—see the prelims for a list of acronyms) causing plumes to be more regularly captured than drifting clouds. This is compounded, of course, by the fact that plumes are also much more common. This chapter is not the place to undertake a rigorous description of the fluid dynamical phenomena observed in volcanic plumes simply to pique the reader's interest. For example, the image in Figure 5.1a shows ladder-like structures that may be related to the Brunt–Väisälä frequency and image 5.1b shows the interaction of the plume with an atmospheric eddy caused by the

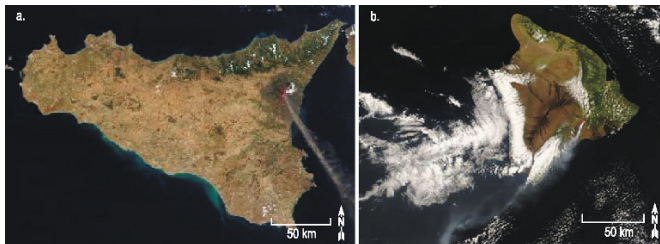


Figure 5.1. Natural-color MODIS satellite images of plumes from Mt. Etna, Sicily, July 22, 2001 (a) and Kilauea, Hawaii, August 7, 2008 (b) disrupting air traffic at airports in Catania and Kona, respectively (images are courtesy of NASA Earth Observatory website).

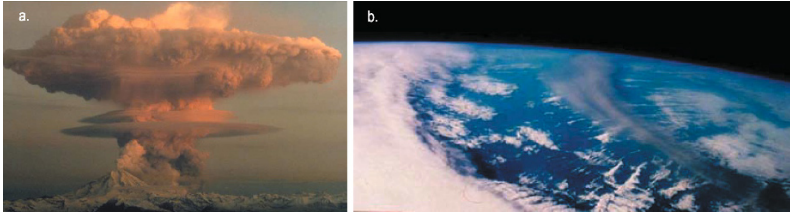


Figure 5.2. Photographs of a proximal cloud (a) of Redoubt Volcano, April 21, 1990 (courtesy of R. Clucas) and distal cloud (b) from Spurr Volcano, September 9, 1992, from the NASA Space Shuttle.

complex topography of the Big Island of Hawaii. Here the particles released from the vent are able to act as cloud condensation nuclei in the warm, tropical atmosphere.

elongate as it drifted over the conterminous United States. As a general rule, the aspect ratio (and complexity) of the cloud shape increases over time (see Mt. Spurr example, Figure 5.3).

5.3.2 Drifting ash clouds

Drifting ash clouds present a range of morphologies depending on atmospheric conditions (including wind strength and temperature structure), eruption source strength, and, critically, elapsed time since eruption. Figure 5.2 shows two classic examples, Mt. Redoubt shortly after eruption (a) showing a broadly circular shape (when viewed from above) and Mt. Spurr (b), where the cloud became very

5.4 COMPOSITION, SIZE, AND SHAPE

Volcanic ash is an unconsolidated mixture of sand to dust-sized (1 to 0.001 mm) rock and mineral fragments produced during explosive eruptions. Rock fragments are typically glassy and form as liquid magma quenches following its eruption at the Earth's surface. Mineral fragments found within the glass include plagioclase feldspar, horn-

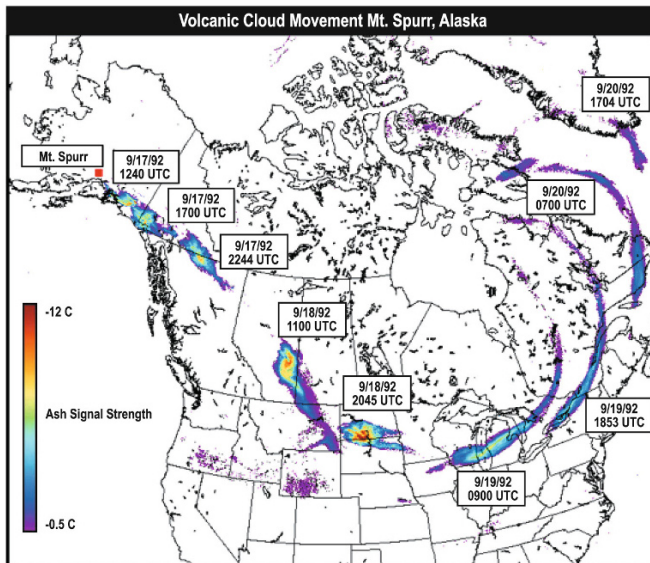


Figure 5.3. Increase in cloud aspect ratio over time as it drifts across North America. This example is from the September 1992 eruption of Mt. Spurr and is based on AVHRR brightness temperature differences—dates and times of the AVHRR images are shown in the boxes (courtesy of Dave Schneider, USGS).

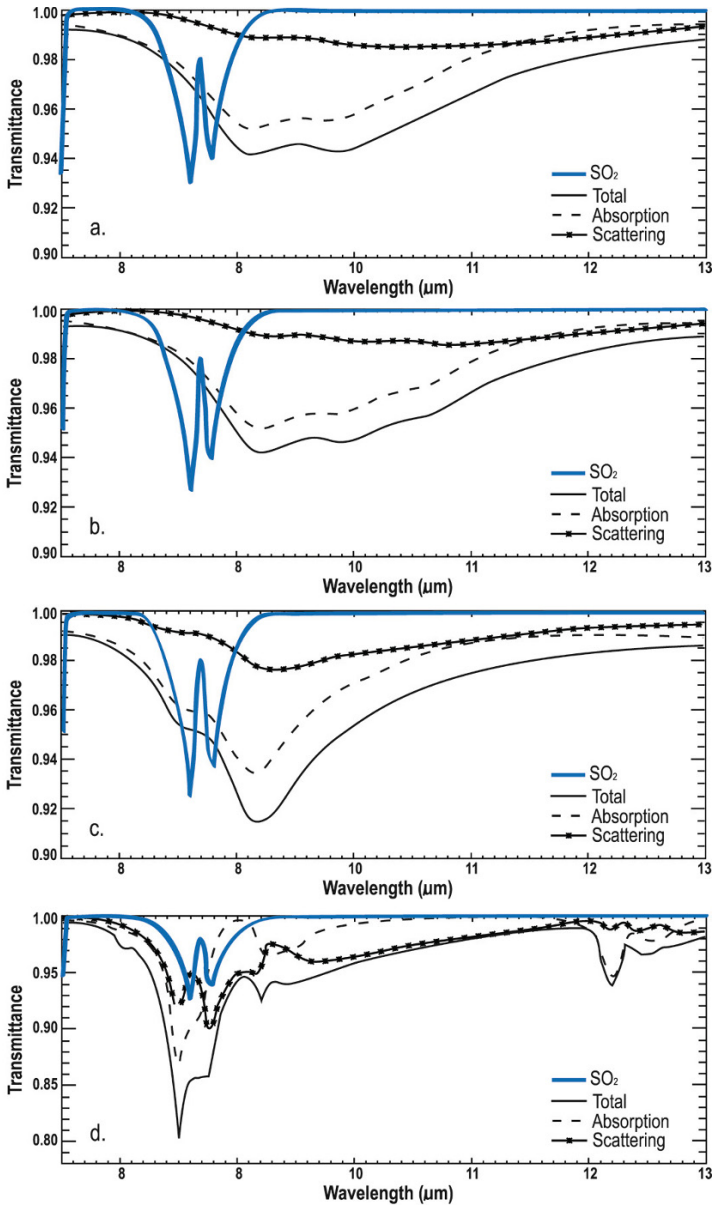


Figure 5.4. Total, scattering, and absorption transmissions for (a) basalt, (b) andesite, (c) rhyolite, and (d) quartz as a function of wavelength. The measurements are based on 10^5 particles per m^2 , a log-normal distribution with a variance of 0.74, and an effective radius of 0.5 for 7.5–13 μm . The transmittance of SO_2 is overlaid in blue. The transmittance scale in (d) is slightly longer than in (a), (b), and (c).

blende, and pyroxene. The minerals are based upon combinations of Fe, Al, K, Na, and other metals in combination with silicate groups. Mineralization, where preserved, is the pressure/temperature history of the melt on its ascent to the surface. The

amount of silica in the ash is a ramification of the magma's parent composition. This has a significant effect on the ash's radiative properties (see Figure 5.4) and our ability to distinguish it from other species (see Kearney, 2010).

The size of volcanic ash particles is an important parameter, controlling physical behavior, direct impact on humans, and the effects the ash exerts on the Earth's radiation budget (ERB). Volcanic ash is typically described in terms of the particle size distribution rather than by a single size (e.g., radius). The distributions typically have a mathematical form and are constrained by two to three additional parameters. In most cases the form is of a well-known mathematical type, log-normal (ZOLD) is often used, and the parameters completely describe the distribution (in the case of the log-normal distribution the variance and mean are sufficient).

5.5 EVOLUTION OF A VOLCANIC CLOUD

The evolution of a volcanic cloud is critical in determining its potential hazard and, given that the early stages of evolution are harder to detect (see discussion below), is also important in accurately deriving critical source parameters. An overview is provided in Figure 5.5 (after Turco, 1992).

5.5.1 Opaque clouds

Ash clouds are typically opaque when first erupted, due to the spatially constraining nature of the vent,

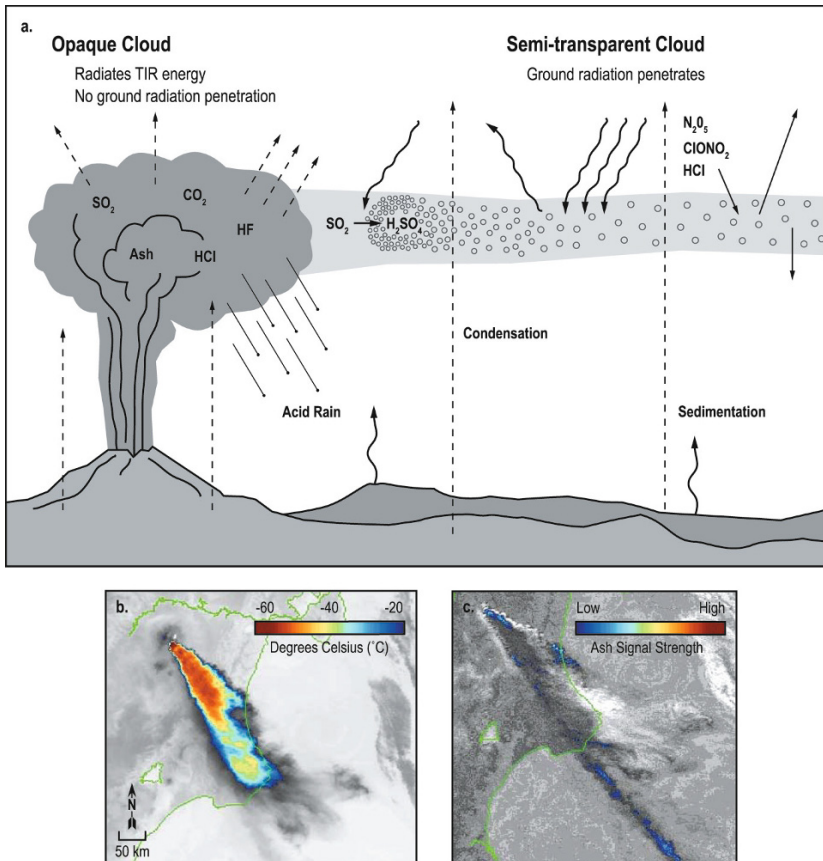


Figure 5.5. A conceptual model and corresponding example of satellite images of a plume. The model (a) shows the structure, composition, and interactions of electromagnetic energy of a typical plume (modified from Turco, 1992). AVHRR images (b) and (c) show the opaque and semi-transparent portions of the plume at Kliuchevskoi Volcano, September 30, 1994. The opaque portions are shown in the TIR (10.5–11.5 μm) image (a) as color-coded for temperature. The BTDR image (c) shows the translucent portion of the cloud as a weak ash signal along the edges of the plume (blue) with values ranging from -1 to -2 K.

Table 5.1. The stages of volcanic cloud evolution (after Rose *et al.*, 2000) based on observations of the Mt. Spurr eruption of 1992.

<i>Observable</i>	<i>Stage 1</i>	<i>Stage 2</i>	<i>Stage 3</i>
Duration after eruption stops (h)	1–4	4–24	>24
Fallout (km from volcano)	<25	25–100	>400
Area of fallout (km ²)	<300	≈5 × 10 ⁴	Discontinuous
Fallout diameter range (mm)	>0.5	0.5 to <0.01	<0.01
Fallout rate (kg/s)	>10 ⁴	<10 ⁴ –10 ²	≪10 ²
Fraction of 1–25 μm (fine) diameter ash (%)	<1	10–50	>50
Cloud area (km ²)	<10 ⁴	10 ⁴ –10 ⁶	10 ⁶ , decreasing
Mean optical depth	>2	0.5–2	<0.3
Cloud ash mass loading (kg/m ²)	>25	2–10	<3
Fraction of suspended material (%)	100–30	30–3	<3

the volume and flow rate of the eruption column, and the fluid dynamical behavior of the ash (i.e., the lack of fallout-associated eruptive thrust). For some time the plume contains a wide range (microns to centimeter-sized fragments) in a limited volume. Satellite measurements of the cloud top temperature at two infrared wavelengths (so-called split-window) are often used to distinguish ash clouds from other types of cloud by making use of brightness temperature differences (BTDs). Although split-window brightness temperature difference retrieval does not distinguish ash without some transmission of terrestrial radiation through the cloud, some information can still be obtained. Given that the cloud is opaque, the satellite will only detect radiation pertaining to the cloud top itself, specifically its temperature using thermal infrared radiance. The cloud must be completely opaque in order to retrieve its approximate radiating cloud top temperature as, otherwise, any derivation will be a function of the cloud's temperature, the ground temperature, and some modulation by the atmosphere between. The cloud's temperature is important as it can be used to determine cloud height. Height is a critical parameter in terms of hazard mitigation and is vital in determining the mass eruption rate. Calculation of the mass eruption rate can be made using the following empirical equation (Sparks *et al.*, 1997):

$$H = 1.67Q^{0.259} \quad (5.1)$$

where H is the column height; and Q is the mass

eruption rate in m³/s. The transition from opaque to transparent cloud has been observed multiple times. The classic example is the Mt. Spurr eruption cloud.

5.5.2 Semi-transparent clouds

Table 5.1 shows the stages of development of a volcanic cloud. Once the cloud becomes semi-transparent it is easier to detect with the split-window algorithm. The transition (from stage 1 to stage 2), a few hours after the eruption finishes, represents the beginnings of detectability of ash clouds using the BTD method, and the first opportunity to retrieve mass, particle radius, and optical depth. Stage 2 is characterized by a coherent drifting cloud, with fallout continuing from smaller particles (and through aggregation). After approximately 24 hours the cloud enters stage 3, where the larger particles have all fallen out and the cloud can be hundreds of kilometers from the source. This often represents the most dangerous phase of the cloud as detection is harder as the cloud thins and the cloud becomes harder to track.

5.6 EFFECTS OF EMISSION PARAMETERS ON SATELLITE DETECTION

Several parameters have a strong control on the ability to detect volcanic ash clouds using satellite

instruments with the infrared split-window (also known as brightness temperature difference or reverse absorption) technique. The first is the effective size of the particles in the cloud; there is only a fairly narrow range (1–20 μm , radii) over which the retrieval has sensitivity. This represents the region where Mie scattering and absorption dominate and is related to the ratio of the radius of the particles to the wavelength of the observed radiation, with approximate limits of $(1/2\pi) < x < 2$, where x is known as the size parameter and $x = 2\pi r/\lambda$.

This range represents only a very small fraction of the tephra (and only a small fraction of the total mass, typically <2%) produced during an eruption, although this size range can be suspended in the atmosphere for days and be transported long distances, and therefore can be a serious problem for air traffic. Within the detection limits there is a general trend that smaller particles produce a stronger BTM signal, although the relationship is not simple and is confounded by multimodal size distributions. The effective scattering radius of a particle size distribution is not a particularly reliable metric under these circumstances.

Water vapor in the atmosphere strongly affects the split-window BTM methodology. Much has been published on this effect (Rose *et al.*, 2000; Simpson *et al.*, 2000; Prata *et al.*, 2001; Yu *et al.*, 2002; Pavolonis, 2010), and it is only briefly explained here. The BTM technique relies on the fact that the shorter wavelength of the two bands used (11 μm) is more strongly affected by the presence of volcanic ash than the longer wavelength band (12 μm). This effect is countered by increasing water vapor in the atmosphere where the opposite is true. The NOPAC region represents amongst the best conditions for the algorithm due to the lack of significant amounts of water vapor at higher latitudes.

The silica content of the melt will also have a small, though significant, effect on the signal. Higher silica ash particles absorb more strongly at the shorter end (8–10 μm) of the split-window. All other parameters being equal, increasing the silica content sharpens, strengthens, and narrows the absorption feature (Figure 5.4 after Kearney, 2010) to make it have a more dramatic effect on the split-window channels. Many explosive volcanic eruptions have a higher silica content due to increasing silica which also increases viscosity and, hence, the ability of the magma to pressurize gas.

The height of the cloud also has a significant,

though again secondary, effect on the cloud's BTM signal, essentially because height controls temperature and a temperature contrast is required for the retrieval to work. The greater the contrast, the stronger the signal. This is why the retrieval is less sensitive over cold background, as it is possible under some conditions that the cloud and underlying surface temperature are similar or the cloud is warmer than the surface.

5.7 INFLUENCE OF THE ATMOSPHERE ON VOLCANIC CLOUDS

The structure of the atmosphere plays a critical role in the evolution of a plume from its injection to its dispersion. A plume is composed of a turbulent mixture of buoyant hot volcanic particles, gases from the magma, and water or atmospheric gases entrained into the eruption column (Sparks *et al.*, 1997). Condensation, sedimentation, and chemical reactions also occur (Turco *et al.*, 1983) (Figure 5.5). Satellite data are able to detect or measure plume temperature, height, movement, structure, composition, and the transition from opaque to semi-transparent cloud as it drifts away from the source volcano and disperses.

When the volcano first erupts explosively the eruption column is mostly opaque and hot but cools rapidly, usually within a few minutes, as it expands and rises in the atmosphere. The plume rise is due to the initial gas thrust, buoyancy, and vertical convection. As the plume rises it entrains air from the surrounding atmosphere, sheds heat, and becomes less buoyant. When the density equilibrates with the surrounding atmosphere it stops rising (Sparks *et al.*, 1997). Satellite data rarely record the hot phase of the erupting column. As the buoyant plume rises it cools, often to less than -50°C if in the upper troposphere, and is usually opaque (see Figure 5.6). Thermal infrared satellite data are used to detect this stage of the plume and measure its temperature. If the plume is opaque its temperature corresponds solely to material within tens of microns of the cloud top. If it has started to disperse, temperature measurements will include background energy that is transmitted through the cloud resulting in warmer temperature measurements.

The atmosphere consists of four vertical zones with varying thermal structure starting at the Earth's surface: the troposphere, stratosphere, mesosphere, and thermosphere (Figure 5.7). These zones are separated by thermal transitions called

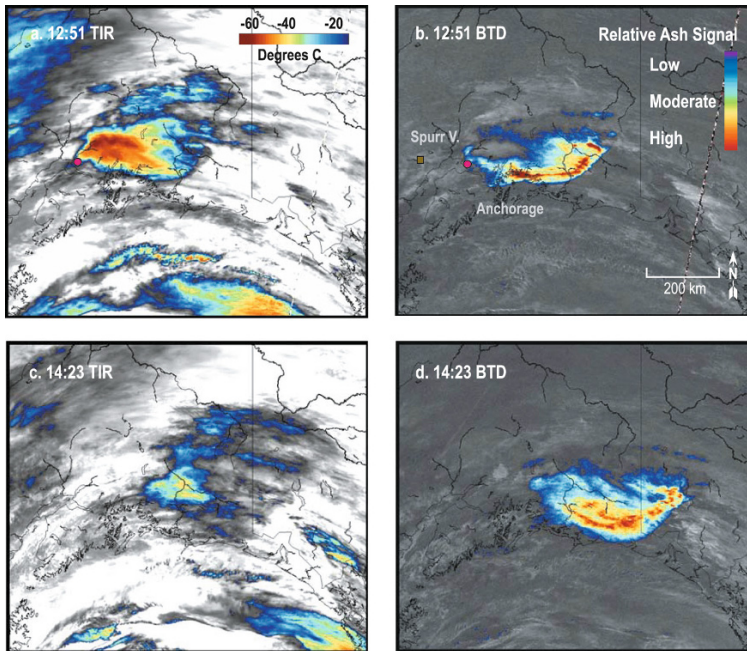


Figure 5.6. Spurr Volcano, September 17, 1992, AVHRR satellite data. These images show the transition from opaque to semi-transparent clouds in TIR (B4, 10–11 μm) and BTD data. The eruption started at 08:03 UTC and the ash cloud was recorded at 12:51 in B4 (a) and in BTD data (b). By 14:23 UTC the signal has changed as seen in B4 (c) and the BTD data (d). At 12:51 the B4 image (a) shows an opaque cloud northeast of Anchorage which is color-coded by temperature in orange and red. The temperature signal along the eastern edge of this cloud is warmer suggesting an increase in contribution from the ground beneath the cloud. In the same area the BTD data (b) show an increase in the ash signal. No ash signal is detected on the BTD image at the opaque portion of the cloud due to its opacity. At 14:23 the opacity of the plume decreased as dispersion increased (c) and the BTD signal of the ash cloud is stronger (more negative) (d).

the tropopause at 11 km, stratopause at 47 km, and mesopause at 81 km based on a standard atmosphere (Lutgens and Tarbuck, 1995). (Note that these boundaries vary in space and time and are not fixed; the values given are illustrative only.)

In recent times the highest plumes were from eruptions of Mt. Katmai which ascended to 30 km (Fierstein, 2007), Mt. St. Helens to 30 km (Holasek and Self, 1995), and Mt. Pinatubo to 40 km (Lynch and Stephens, 1996). Comparing the maximum height of these plumes with the structure of the atmosphere shows that they are below the stratopause boundary (Figure 5.8). The thermal structure of the atmosphere defines the atmospheric zone boundaries (Figure 5.7). The tropopause has a negative temperature gradient, warmest at the Earth's surface and coolest at approximately -60°C at the tropopause boundary, near 11 km, in this example. The tropopause is the boundary

where the atmospheric temperature gradient becomes positive or remains close to zero; above lies a region called the lower stratosphere with temperatures at approximately -60°C and warming to approximately 0°C at the stratopause, near 47 km, in this example. Usually, the tropopause and stratopause boundaries are not abrupt thermal reversals—but have fluctuating temperatures of a few degrees about or near the thermal gradient inflection point. These regions of fluctuating temperatures at the tropopause, stratopause, and mesopause can be 10 km thick. In addition, the tropopause is weakly stratified while the stratosphere is intensely stratified, especially at heights above 20 km. Thermal reversals and stratification in the atmosphere hinders the ascent of plumes. When a plume encounters the tropopause, temperature reversal changes the buoyancy conditions and slows or stops its ascent. Only more energetic erup-

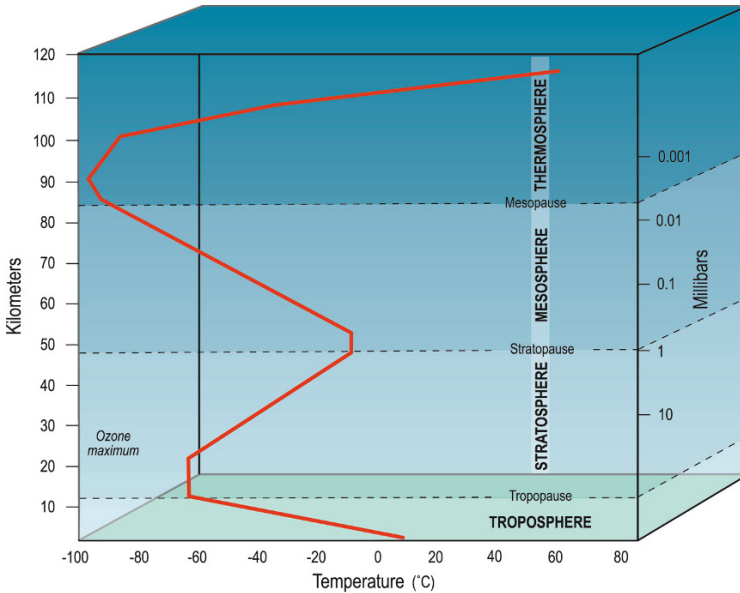


Figure 5.7. The basic thermal structure of the atmosphere is defined by temperature gradients as a function of altitude which reverse at three different levels. The pressure decreases with increasing altitude. The temperature gradients and pressure impact how a plume rises and its maximum height as it equilibrates to surrounding conditions. There are no records of a volcanic plume penetrating the stratopause. The tropopause stops or slows the rise rate of less energetic plumes where they tend to spread laterally.

tions produce plumes that are able to penetrate the tropopause and enter the stratified layers of the stratosphere (Sparks *et al.*, 1997), such as Redoubt (2009), Kasatochi and Okmok (2008), Augustine (2006), Mt. St. Helens (1980), and Katmai (1912). Most of the eruptions in the North Pacific region are unable to penetrate the tropopause, and if they do get to that height they tend to spread laterally. Modern-day jet aircraft fly at heights of 10 to 12 km which is above the tropopause but still at levels of drifting ash clouds. Ash clouds below the tropopause are a threat to local air traffic and surface infrastructure (Figure 5.8).

The height of the tropopause is not fixed but varies as a function of latitude and time. In tropical regions the boundary is 16 to 18 km, and temperatures increase sharply above this resulting in a very stable stratified atmosphere. In mid-latitudes the tropopause is about 11 km, the temperature remains fairly constant to about 20 km, and the atmosphere becomes even more stratified. In polar regions the tropopause is located at about 8 km and the atmosphere is less strongly stratified than in the tropical and middle latitudes. The tropopause tends to be a little higher, such as 10 km during the sum-

mer in polar regions (Sparks *et al.*, 1997). Due to variations in the height of the tropopause, plumes from tropical eruptions that do not have enough energy to penetrate the boundary attain greater altitudes than those in polar regions, assuming that they have similar buoyancy.

Other factors that impact plumes include atmospheric pressure, density, and water vapor density (Table 5.2). A plume will continue to rise until it comes into static equilibrium with its surrounding environment (although oscillations about and overshooting of this level also occur). A plume will be in equilibrium with its surrounding environment when the density of the plume equals the density of the surrounding environment. The density of both the plume and surrounding environment depends on the temperature, pressure, and water vapor loading. Initially, the eruption column is unsaturated but, as the column ascends, it entrains surrounding air, including moisture, and becomes saturated at approximately 8 km. Above 8 km the air pressure and moisture content is low. The heights attained by small plumes are greater in the tropics due to the moist atmosphere compared with those in the dry atmosphere in polar regions. Generally, plumes

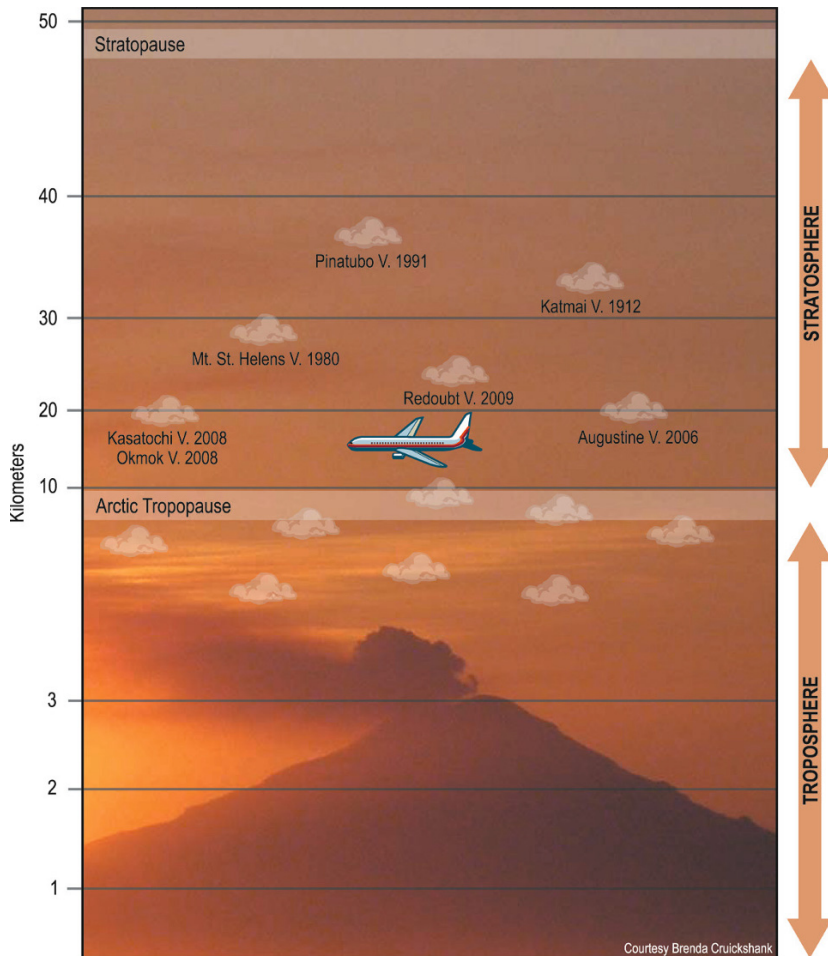


Figure 5.8. Relationship between the structure of the atmosphere, plume heights, and air traffic. Only very energetic plumes can ascend into the stratosphere, where the atmosphere is extremely stable and does not easily support vertical convection. Often an eruption will be composed of numerous plume-producing events but only the more energetic and hence dangerous plumes have sufficient energy to penetrate the tropopause. A few examples of stratospheric eruptions are shown. The weaker plumes from volcanic activity do not make it to the tropopause or are prevented from ascending beyond that boundary. Jet aircraft often fly at altitudes between 9 and 12 km, heights that energetic plumes ascend to or pass through.

Table 5.2. Generalized examples of physical values of the atmosphere at the surface, tropopause, and mesopause based on a standard atmosphere (Lutgens and Tarbuck, 1986).

Height (km)	Temperature (°C)	Pressure (kg m ⁻³)	Air density (g m ⁻³)	Water vapor density
Surface	15	1,000	1.22	8
11	-60	265	0.414	0
47	-5	2	0.004	0

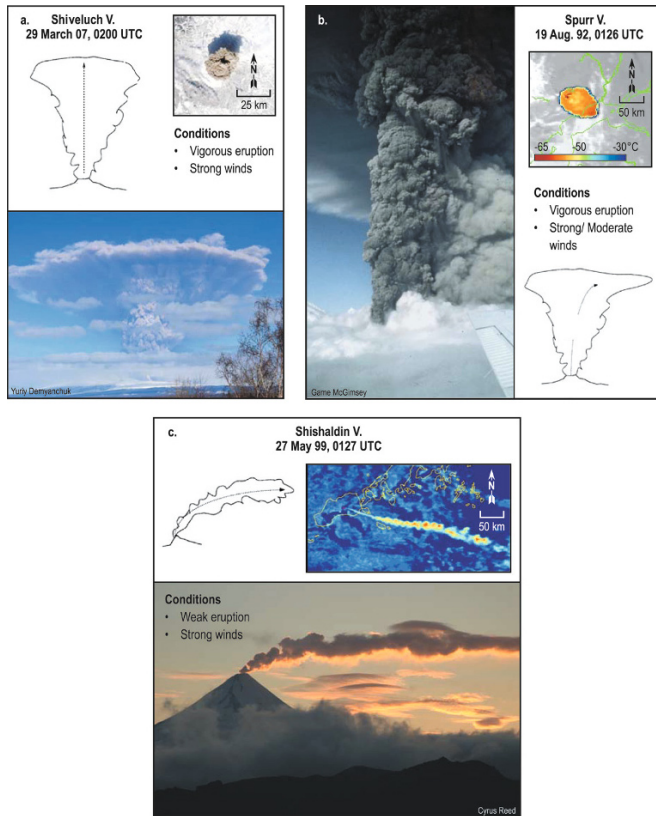


Figure 5.9. The relative effect of wind and eruption vigor shown as conceptual models (modified from Sparks *et al.*, 1997). The eruption of Shiveluch Volcano (a) shows a circular umbrella cloud above a vigorous eruption column. The MODIS color composite satellite image shows a plume and its shadow on snow-covered ground. The plume top height is 14 to 15 km with a wind speed of 13 to 15 m s^{-1} blowing to the NNE at that height. Even though the plume encountered strong winds, the highly energetic eruption resulted in a high-altitude circular plume. The eruption of Spurr Volcano (b) shows an elliptical-shaped high-altitude umbrella cloud above a vigorous eruption column. The plume top height is 14 km with a wind speed of 13 m s^{-1} blowing to the ESE at that height, elongating the plume. The AVHRR satellite image is TIR B4 which has been color-coded by temperature and recorded 31 min after the start of the eruption. The eruption of Shishaldin Volcano (c) shows a weak eruption column in high-velocity winds (13–15.5 m s^{-1}), resulting in a low-altitude bent-over plume, extending approximately 400 km to the ESE at a height of 4 km. The AVHRR satellite image is processed to detect ash clouds using the BTD technique.

whose height exceeds 12 km are not significantly impacted by atmospheric moisture (Sparks *et al.*, 1997).

Wind direction and strength impact the shape of a plume and the dispersal of ash and gas for both large and small plumes (Figure 5.9). If wind was not present then both small and large plumes would rise vertically above the source vent and spread radially forming an umbrella cloud once the neutral buoyancy height is reached or they would dissipate. A profile view of large vigorous plumes would show

that the vertical axis of the eruption column will be bent in the downwind direction and the umbrella cloud will be distorted in that direction (Sparks *et al.*, 1997). From a satellite perspective only the umbrella cloud can be observed but its shape would be elliptical instead of circular with its center displaced downwind from the position of the source vent. A profile view of small weak plumes would show a long and narrow column bent downwind. From a satellite perspective a long and narrow plume extending downwind would be observed.

Dispersion of the plumes can be mapped using high temporal resolution time-sequential satellite data such as from the GOES imaging sensor where TIR data is recorded every half hour. These images provide a snapshot in time—but not predictions of its movement. The use of gridded wind fields that include predictions of wind direction and speed in dispersion models are used to predict the movement of ash and gas clouds, which is especially useful for hazard mitigation (Searcy *et al.*, 1998). (See Chapters 7 and 9 for a more detailed discussion of dispersion modeling and its use. Animations of ash movement using dispersion models can be seen on the DVD).

5.8 CLOUD HEIGHT ESTIMATIONS

Estimating the height of plumes and ash clouds is one of the most critical components for hazard response in the North Pacific region. The height of the cloud dictates how the wind fields control movement, and this impacts how agencies and industry (especially airlines) respond to an eruption. Erroneous height estimates can result in an incorrect hazard response, such as invalid forecasts of ash cloud movement that could potentially be catastrophic. There are several quantitative methods for estimating plume and ash cloud heights: temperature, trajectory, shadow, stereoscopic, and radar. Ground observers and pilot reports (PIREPS) provide qualitative estimates. Measurements from each method do not always agree, so heights are only estimates; each method has its strengths and weaknesses. At this time, ground-based radar appears to be the most accurate and dependable method for estimating height near the vent where the particles are large enough to be detected by radar.

5.8.1 Temperature method

The temperature method involves comparing the cloud top temperature with the temperature profile of the atmosphere and requires that the cloud be opaque and the temperature equilibrated to the surrounding atmosphere. If the cloud is semi-transparent the measured temperature will include radiant energy from the underlying background, and this usually increases the measured cloud temperature resulting in an erroneously low height estimate. The most accurate cloud temperature is measured using satellite data in the 11 μm TIR band

(Sparks *et al.*, 1997; Dean *et al.*, 2004). The plume temperature is then correlated to the temperature–height profile of the atmosphere measured by radiosonde launches from airports. Ideally, there is only one temperature that correlates to one altitude unless the plume penetrates the tropopause; in those situations usually several heights will be associated with the same temperature. For example, the eruption of Spurr Volcano on August 19, 1992 was recorded on over 11 satellite images for 83.4 hours (Figure 5.5) showing the evolution of the cloud from opaque to semi-transparent (Schneider *et al.*, 1995). The cloud remained mostly opaque (Figure 5.10) for ~ 5 hours with a fairly consistent temperature ranging from -65°C (01:26 UTC), -61°C (03:31 UTC), and -63°C (05:12 UTC). These temperatures correlate to heights ranging from 11.5 to 12 km. Ground-based radar showed a height of 13.7 km (Rose *et al.*, 1995). Augustine Volcano at 01:40 UTC on January 14, 2006 is an example of multiple height estimates, as well as of the evolution of an opaque to semi-transparent cloud and its effect on temperature measurements (Figure 5.11). The first TIR B4 satellite image recorded at 01:45 UTC showed an opaque cloud with temperature of -53.5°C which correlates to height estimates of approximately 8.0 and 9.5 km which straddle the tropopause at 8.5 km. Ground-based radar indicates a height of 10.5 km and pilot reports indicate 9 to 9.5 km (Bailey *et al.*, 2010). All of these estimates are in the vicinity of the tropopause. A few hours later TIR B4 images recorded at 02:43 and at 03:27 UTC (Figure 5.11c, e) showed minimum cloud temperatures of -49.5 and -40°C , respectively, which are warmer than the cloud at 01:45 UTC and correlate to a much lower height. The plume temperature increase is almost always due to thermal contamination from the warm background indicating that the cloud has begun to disperse and is now semi-transparent. Brightness temperature difference (BTD) images (Prata, 1989a) of the cloud at 02:43 and 03:27 (Figure 5.11b, f) show an ash signal that is also indicative of a semi-transparent cloud. As shown above and discussed by others (Tupper *et al.*, 2004), height estimates are subject to error from limitations of the technique.

The location of temperature profiles from radiosonde measurements used to identify heights can also be problematic. The profiles are generated at selected airports—not at volcanoes themselves. The profiles can be located hundreds of kilometers from a volcano and may not provide a temperature profile that is representative of that above the

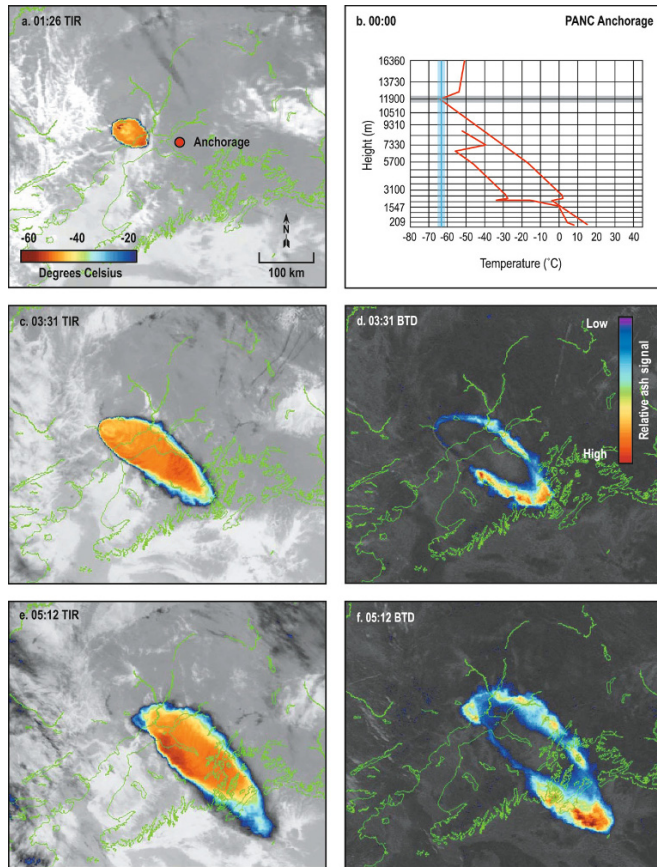


Figure 5.10. Mt. Spurr Volcano erupted on August 19, 1992 at 00:55 UTC recorded on AVHRR satellite images at 01:25, 03:31, and 05:12 UTC and show the early stages of the transition of this plume from opaque to semi-transparent. Images (a), (c), and (e) are TIR B4 (10–11 μm) data. Images (d) and (e) are BTDR data. The single TIR band data show an opaque cloud at 01:26 UTC (a) with a temperature of -65°C . The dry atmospheric profile (b) shows the thermodynamic tropopause to be at 12 km (gray line) and the atmosphere and plume temperature that corresponds to that height (blue line). Images (c) and (e) recorded at 03:31 and 05:12 UTC show the opaque cloud starting to become semi-transparent along the edges of the BTDR data (d) and (f). There is no negative BTDR signal in the core area of the cloud, because that area is still opaque. The lack of a BTDR signal suggests that the cloud temperature is not contaminated with background temperatures. The UTC time is shown on the images.

volcano. A solution to the problem is the use of gridded atmospheric models (e.g., UNIDATA) to generate profiles above a volcano. Presumably, these would be more accurate than distant sounder measurements. A comparison of rawinsonde and modeled profiles has not been systematically evaluated but qualitative comparisons suggest that these are reasonable estimates.

Another problem complicating plume temperature measurements are supercooled portions of plumes that are highly buoyant, also referred to

as the dynamic overshoot (Woods and Self, 1992; Holasek and Self, 1995). The material in the convective column ascends until it reaches its neutral buoyancy but, due to inertia, it is carried farther upward. After the inertia has dissipated, this overshoot descends to its neutral buoyancy position in the umbrella cloud probably within minutes (Sparks *et al.*, 1997). In this situation the overshoot is the coldest part of the cloud—even colder than the surrounding atmosphere—and would therefore not be used to estimate its height. Usually, the over-

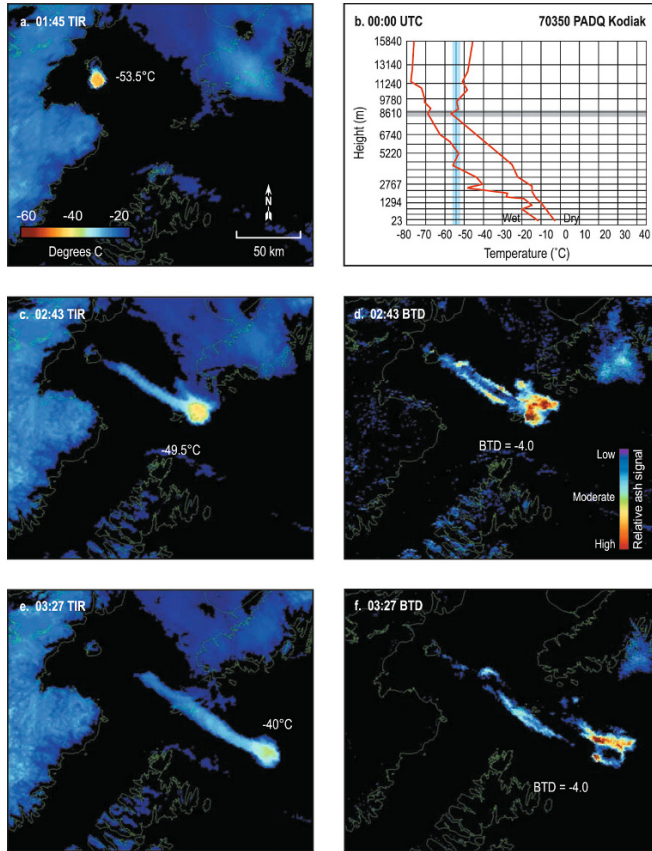


Figure 5.11. Augustine volcanic eruption in January 2006. AVHRR images recorded on January 14, 2006 show how the morphology of a volcanic cloud changes over time and impacts height estimates. Images (a), (c), and (d) are B4, (d) and (e) are BTDR, and (b) is the atmospheric temperature profile. At 01:45 UTC (a) an opaque cloud is observed with the coldest temperature of -53.5°C , the blue line in (b). This cloud correlates to a height of 8.0 and 9.5 km which straddles the tropopause at 8.6 km, the gray line in (b). At 02:43 (c) and 03:27 (e) the TIR data show that the coldest temperature of the cloud has increased to -49.5 and -40.0°C , respectively. These same images processed for BTDR (d) and (f) show a relatively strong BTDR signal of -4.0 . The increasing cloud temperature and strengthening BTDR signal is indicative of a dispersing cloud and conducive to the detection of ash. Ground-based radar measured a height over 10.5 km at 01:40 UTC and PIREPs reported 9.0 to 10.5 km. The cloud is moving to the southeast which correlates to wind fields in the atmospheric profile data at heights less than ~ 9.5 km (see Section 5.9.2). The variations in height estimates show the difficulty in precise height measurements of dynamic volcanic clouds.

shoot is above the convective column and still connected to the vent. To estimate the height of these clouds the coldest temperature in the umbrella cloud, excluding the overshoot, should be measured and compared with the atmospheric profile (Dean *et al.*, 1994). An example of a supercooled plume observed on satellite data is the eruption of Redoubt Volcano, January 8, 1990 (Figure 5.12). The satellite image was recorded at 19:11 UTC, 13

minutes after the start of the eruption. In this example the plume is circular with a diameter of approximately 40 km. The bright-red portion is the overshoot at -63°C while the coldest atmospheric temperature (Anchorage radiosonde) is approximately -55°C (Figure 5.12b). A temperature profile (Figure 5.12c) across the plume shows a low temperature of -63°C approximately at the center (topographically high), a warmer tempera-

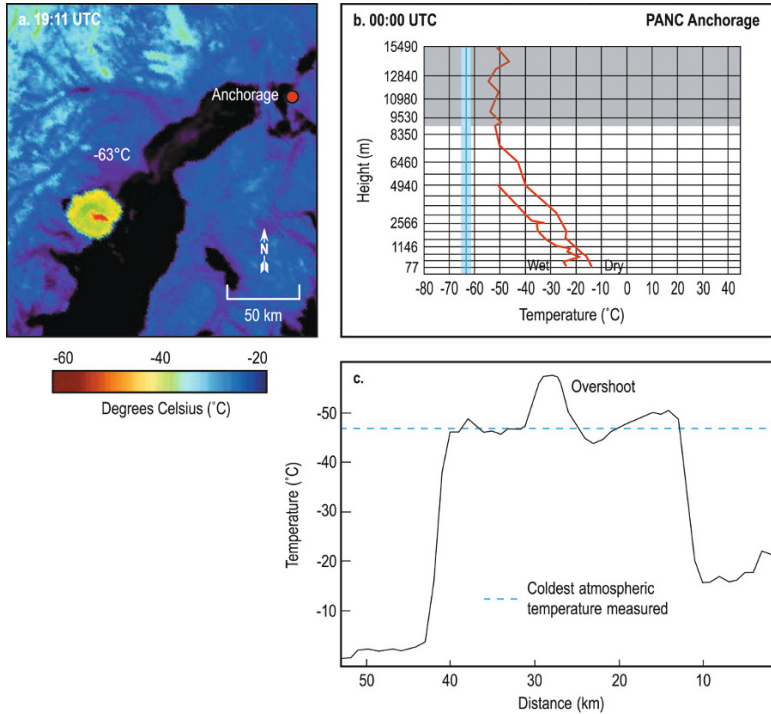


Figure 5.12. Height estimates of the Redoubt Volcano plume on January 8, 1990 recorded on TIR ($11\ \mu\text{m}$) AVHRR data (a) at 19:11 UTC, 13 min after the start of the eruption. The plume is color-coded by temperature with the coldest temperature, -63°C , shown as the blue line in (b). The coldest atmospheric temperature recorded on the radiosonde profile (b) is -55°C at 12.5 km. Therefore, the red portion of the plume has overshoot its neutral buoyancy level as shown in the temperature profile of the plume (c). The portion of the plume that appears to be neutrally buoyant has a temperature of -51°C , the dashed line in (c), and correlates to an estimated minimum height of 8.5 km based on the atmosphere temperature profile. Within a few minutes the overshoot will settle to its neutral buoyancy level probably with a temperature of approximately -55°C at 12.5 km. Previous height estimates (Dean *et al.*, 1994) range between 9–11 km and differ due to the radiosonde profiles that were used. Heights greater than 12 km have also been estimated for this eruption (Miller and Chouet, 1994).

ture trough (-44°C) surrounding the overshoot, and a cold (-51°C) topographically elevated rim. The estimated height of this plume using the temperature method is 9, 11, or 15–17 km.

The temperature method has several limitations as shown above but is a technique that often provides a first-order estimate until additional information becomes available. The limitations include multiple heights for the same temperatures, supercooled portions of plumes, masking by weather clouds, and invalid cloud temperatures due to contamination from background signals.

5.8.2 Trajectory method

Trajectories can be used to estimate cloud heights whenever there is vertical wind shear in the

atmosphere. The basic idea is to use a trajectory/dispersion model initialized using atmospheric wind data and guessing the starting height of the volcanic cloud. The resulting trajectory can be compared with a satellite observation and iterated by changing the starting height until a best fit is obtained. This process can be mathematically formalized to obtain an initial height distribution of the erupted mass (see Stohl *et al.*, 2011).

The eruption of Kliuchevskoi Volcano on September 30, 1994 is an excellent example (Figure 5.13). A satellite image recorded at 20:54 UTC shows a bifurcated plume blowing to the southeast with a segment appearing to loop beneath another segment. The Puff dispersion model shows that the lower portion of the plume is at an altitude of 4 to 8 km and the upper portion is at 8 to 12 km. The

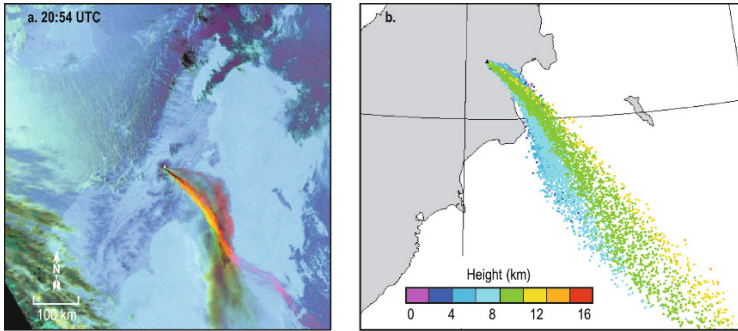


Figure 5.13. Estimation of plume height using the trajectory method for an eruption of Kliuchevskoi Volcano, September 30, 1994 at 20:54 UTC. The AVHRR color composite image (a) shows a bifurcated plume with a segment blowing southeast over the top of another segment blowing south-southeast. The Puff dispersion model (b) shows that the southeast segment (green and yellow) is at 8 to 12 km altitude and the south-southeast segment (blue) is at 4 to 8 km.

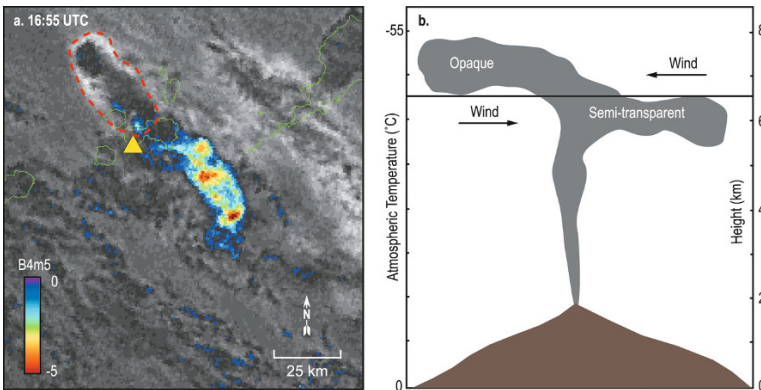


Figure 5.14. A composite of AVHRR satellite images (a) using TIR and BTM data and the conceptual model (b) shows an early stage of a volcanic cloud at Cleveland Volcano, February 19, 2001 at 16:55 UTC. The NW portion of the plume is opaque (dashed polygon) and detected on single-channel thermal infrared (TIR) B4 data with the coldest radiant temperature of -53°C , which correlates to an altitude of 8 km. The SE segment of the cloud is semi-transparent and detected on BTM data with a signal strength less than -5 . The wind shear indicated in the Puff dispersion model suggests that the SE volcanic cloud is at an altitude of approximately 6.5 km (after Dean *et al.*, 2004). Wind directions are relative to Cleveland Volcano (yellow triangle).

eruption of Cleveland Volcano on February 19, 2001 (Dean *et al.*, 2004) is an example of the separation of the opaque and semi-transparent ash cloud due to wind shear. The temperature and trajectory technique had to be used to estimate heights and analyze the structure of the cloud (Figure 5.14). The TIR ($10.5\ \mu\text{m}$) channel of an AVHRR satellite image recorded at 16:55 UTC showed an opaque cloud northwest of the volcano at a temperature of -53°C , which indicates a height of 8 km. However, further analysis of the satellite

data using the BTM technique revealed that there was also an ash-rich, semi-transparent cloud (not detected in the single-band TIR image) southeast of the volcano. Ash trajectory predictions using the Puff dispersion model indicated that there was directional wind shear at a height of approximately 7 km blowing to the southeast indicating that the ash cloud was at a height below 7 km. A conceptual model of the structure of the cloud shows how the cloud is sheared at 7 km (Figure 5.14b).

Trajectory-based height estimates have a few

limitations. Directional or velocity wind shear must be present for this technique to work, and the accuracy of the dispersion model depends upon the accuracy of the atmospheric data and gridded wind models. One of the most troublesome regions on a planetary scale is the lower 3 km of the atmosphere, in the region known as the planetary boundary layer (PBL) where turbulence dominates. Above this region, in the free atmosphere, turbulent effects can be mainly ignored in an approximate treatment of synoptic-scale motions (Holton, 2004). However, due to the height of volcanoes and the effects of an explosive eruption, the turbulence can extend a few kilometers higher in the vicinity of a volcano. The capability of gridded wind fields to accurately portray the PBL layer is variable between models. Thus, ash dispersion models at these low altitudes can be problematic. (See Chapter 7 for a more detailed discussion of dispersion models.)

5.8.3 Cloud shadow method

The cloud shadow method involves geometric principals based on the relationship between plume height and the solar elevation angle (Holasek and Self, 1995); $h = d \tan \theta$. Here h is the height of the plume, d is the shadow length, and θ is the solar elevation angle measured from the horizontal (Fig-

ure 5.15). The length of the shadow is measured on satellite data using a visible light band from the highest part of the plume which in most cases is above the volcano to the outer edge of the shadow. The tangent of the solar elevation angle (θ) is measured at the ground intersection. Simple multiplication of the tangent of θ and the distance gives an estimate. In this example a flat Earth is assumed. Greater accuracy can be attained if the curvature of the Earth is taken into account but this complicates the calculations significantly. This method has several limitations and potential sources of error that hamper its use. It requires daylight for the shadow to be formed (a problem during the long winter nights at high latitudes), the Sun must illuminate the plume obliquely, and the satellite must be in a location that permits viewing the shadow. Definitive identification of the end of the shadow can also be a problem when other shadows are present or the night terminator is in the general area. Large satellite pixels such as those in the GOES data at high latitudes can vary by a few kilometers and, thus, are not conducive to precise measurements.

5.8.4 Ground-based radar method

Ground-based radar is a relatively new technique for estimating the height of volcanic ash and is quite

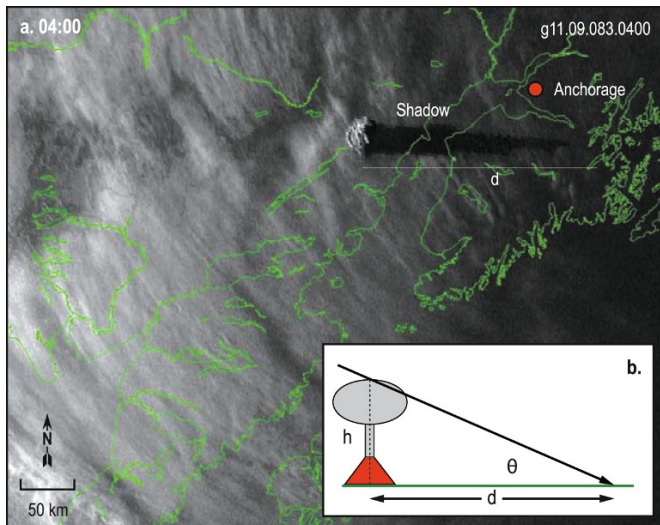


Figure 5.15. A GOES satellite image (a) recorded in the visible shows a plume from the eruption of Redoubt Volcano, March 24, 2009, 04:00 UTC. The height (h) of the plume is estimated based on the shadow length (b) and solar zenith angle (θ) where $h = d \tan \theta$. The length of the shadow (250 km) is measured on the satellite image, the solar zenith angle is 3° , and the resulting height is 12 km (40,000 ft.).

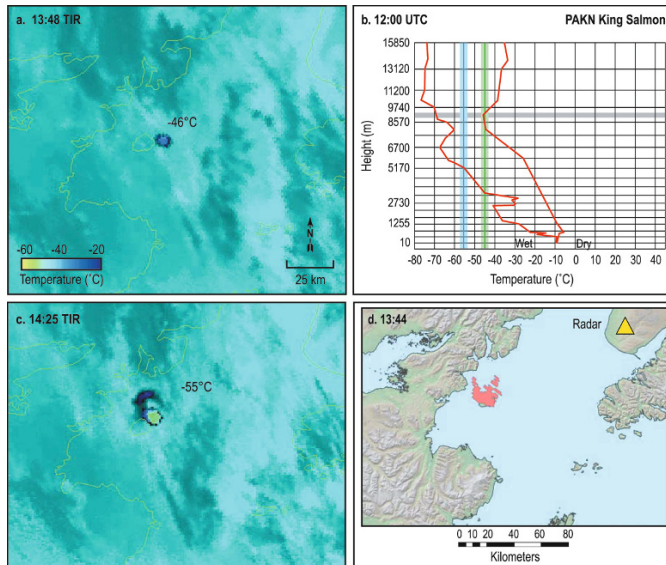


Figure 5.16. Example of plume height estimates from ground-based radar and temperatures at Augustine Volcano, January 11, 2006. Two eruptions occurred at 13:44 and 14:12 UTC. The satellite image (a) recorded at 13:48 UTC, 4 min after the first eruption, shows an opaque plume with a temperature of -46°C , the green line in (b), which corresponds to two altitudes of 7.5 and 12 km based on radiosonde data (b). A second satellite image at 14:25 UTC (c), 13 min after the second eruption started, shows a temperature of -55°C , the blue line in (b), which suggests the plume is supercooled since it is colder than the dry radiosonde profile. Ground-based radar (not shown) measured 9 km at 13:44 UTC. The tropopause, the gray line in (b), is at a height of approximately 9.1 km. A composite of radar data (d) recorded at 13:49 and 15:31 UTC shows the plan view of the particles which generally matches the location and shape of the plume observed on satellite data.

reliable when the size of the particles is large enough to be detected. The active system transmits microwave energy towards the eruption cloud which is then reflected back to the instrument by particles that are encountered. The instrument receives and processes the data which are then displayed as echo intensity (reflectivity) measured in dB (decibels). Radar energy is reflected by particles such as ash, precipitation, and ice crystals—but not gases. Radars can be operated in several ways, such as clear air or precipitation mode (affects sensitivity), and can generate a variety of products applicable to volcanic ash detection: plume top height, plan view of maximum reflectivity, and vertical or horizontal cross-sections of reflectivity (Figures 5.16 and 5.17). The temporal resolution of the scans is measured in minutes which provides unprecedented looks at the formation and collapse of eruption columns. Typical radar wavelengths used by these systems are the S, C, and X-bands. The size of ash particles detected by radar are fine (large volume $<10\ \mu\text{m}$), coarse ($10\text{--}64\ \mu\text{m}$), and lapilli ($>1\ \text{mm}$) (Rose *et al.*,

1995; Marzano *et al.*, 2006; Wood *et al.*, 2007). In the North Pacific region there are several ground-based radar instruments available (in Alaska and the Cascades). Most are the S-band Weather Surveillance Radar (WSR-88D, the “D” standing for Doppler) for monitoring weather but have been successfully used to detect volcanic ash (Wood *et al.*, 2007). The WSR radar is part of the U.S. next-generation radar (NEXRAD). The maximum range of this radar is approximately 220 km. There is also a transportable C-band instrument operated by the USGS that is dedicated to volcano monitoring (pers. comm., D. Schneider, USGS AVO) and built by Enterprise Electronics Corporation (MiniMax 100C). The maximum range of the USGS radar is 100 km. In the Cook Inlet region the WRS-88D and USGS instruments are located near Kenai (Alaska) providing coverage of the most active volcanoes in that area. There is no radar coverage for Aleutian volcanoes, but since the USGS radar is transportable it could be moved to provide coverage for other areas. In the Cascades WSR-88D instruments are

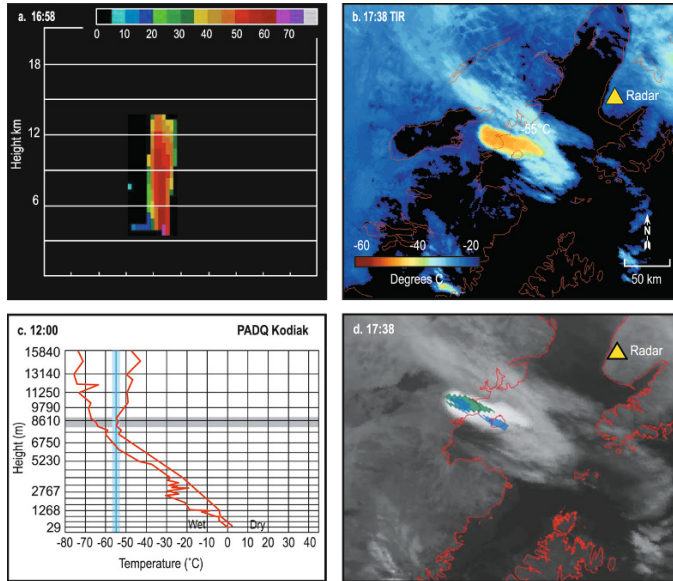


Figure 5.17. A wide range of plume heights were measured for the eruption of Augustine Volcano on January 17, 2006 at 16:58 UTC. A height of 14 km was measured by ground-based radar as shown in a profile view of the plume (a) at 16:58 UTC. An AVHRR satellite image (TIR, B4) recorded an hour later (b) shows a minimum plume temperature of -55°C which correlates to an altitude of 8 km based on the atmosphere profile, the intersection of the blue and gray line in (c). The tropopause height, the gray line in (c), equals 8 km. The height of ash particles detected on the plan view of radar (d) coincides with height estimates from radar data (a), 3.8 km (green) and 7.2 km (blue).

located at many cities in Washington, Oregon, Idaho, and California, providing coverage of most volcanoes in the region. In the Kamchatka Peninsula and the Kurile Island regions there are no civilian radars available for coverage of volcanoes at this time (pers. comm., P. Izbekov, UAF AVO).

One of the earliest applications of ground-based radar for volcanic eruptions was in Iceland at the 1970 eruption of Hekla Volcano (Marzano *et al.*, 2006). Others include Mt. St. Helens, 1980 (Harris and Rose, 1983; Harris *et al.*, 1981); Mt. Spurr, 1992 (Rose *et al.*, 1995); Hekla Volcano, 2000 (Lacasse *et al.*, 2004); Mt. Augustine, 2006 (pers. comm., D. Schneider, USGS, AVO); and Mt. Redoubt, 2009. Radar has been used to detect ash for at least 24 eruptions worldwide (Marzano *et al.*, 2006). These and other studies suggest that radar plume height estimates appear to be more reliable and consistent than the other methods described above, but some dilemmas were encountered. Radar provides discrete estimates even in the tropopause where the cloud temperature method has problems. For example, height estimates from

satellite images of the first eruption on January 11, 2006 at Augustine Volcano were not definitive (Figure 5.16) because the plume penetrated the tropopause but the radar showed 9 km. Height could not be estimated for the second eruption since the satellite temperature of the plume was colder than the radiosonde profile (Figures 5.16b,c). Radar measurements were not available for this second eruption. However, using a wet adiabatic lapse rate of $-4.5^{\circ}\text{C}/\text{km}$, based on a lapse rate calculated from the radiosonde and a base temperature of -10°C also from the radiosonde profile (Figure 5.16b), the height was estimated to be 10 km. A plan view derived from the composite radar images over this period corresponds in space and time with the satellite images. During the Augustine eruption on January 17, 2006 at 16:58 UTC, the plumes penetrated the tropopause, which resulted in height estimates ranging from 6.5 to 13.5 km. Radar showed 14 km, which was close to the upper temperature estimates (Figure 5.17). For the many explosive events at Augustine 2006, the height estimates were both higher and lower than the satellite estimates but

usually within a few kilometers (Bailey *et al.*, 2010). During the Redoubt 2009 eruption preliminary radar estimates showed some cloud tops over 18 km while satellite temperatures indicate heights near the tropopause (9.5 km). Moreover, movement of the ash clouds is consistent with dispersion model predictions at the lower altitudes. Perhaps the bulk of the Redoubt ash is near the tropopause boundary, which is what the satellite detects but the concentration of the higher material may be below satellite detection limits for $\sim 1 \text{ km}^2$ pixels. Another dilemma is the rapid rise rate of these very high cloud tops, 400 m s^{-1} at Mt. Pinatubo (Oswalt *et al.*, 1996), which exceeds the typical rate of a few tens to 200 m s^{-1} (Sparks *et al.*, 1997). Similar or even higher rise rates were calculated at Redoubt (2009). Perhaps the high rise rate is related to a pressure wave caused by the eruption and to condensing clouds behind the wave, which is what radar may be detecting (pers. comm., C. Cahill, UAFGI). Resolution of the large height discrepancies between radar and satellite measurements is critical for accurate hazard warning and assessment and will require further study.

Ground-based radar offers significant advantages over other techniques for measuring plume height and collecting additional information about an eruption, but there are limitations. Advantages include accurate height and position estimates in near-real time, high temporal resolution measurements of ash rise and fall rates, ash retrieval (mass), and gas cloud penetration. All of these advantages are critical measurements for hazard assessments. Disadvantages include the limited number of volcanoes within radar range, detection limited to coarse particles or high concentrations of fine particles, and detection limited to ash near the vent where larger particles are still airborne compared with distal volcanic clouds that contain finer particles. Radar is most sensitive to large particles; the returned power is proportional to r^6 . The thermal BTDR signal arises from small-sized ash particles ($r < 16 \mu\text{m}$). Radars are also expensive to purchase and maintain, requiring significant manpower. These limit availability in many parts of the world.

5.8.5 Stereoscopic methods

Several satellite sensors include the capability to image the same scene from multiple view angles simultaneously, or from different view angles within a short time, or from different view angles using two or more platforms. Among these are MISR, the

ATSR family, and by using two or more geosynchronous satellites. The principle of stereoscopic imaging is well established (Hasler, 1981; Wylie *et al.*, 1998; Glenkova *et al.*, 2007) and needs no further discussion here. A recent study by Scollo *et al.* (2010) employed MISR imagery to estimate plume tomography for the 2001 Etna eruption. Prata and Turner (1997) have shown how the conical scan of the ATSR instrument can be used to determine cloud top height by combining two views, one at 22° and the other near 55° , in either infrared or visible channels. Since these methods are essentially geometrical, the limitation is largely due to the pixel size (1 km in the case of the ATSRs) and to the skill and sophistication of the pattern-matching techniques employed. The method is not restricted to daytime-only use as pattern-matching can be done using the infrared channels. For the NOPAC region stereoscopic height estimation can be done using data from two geosynchronous measurements (see Hasler, 1981 for details on the methodology), giving the possibility of high temporal resolution cloud height estimates.

5.8.6 Pilot reports

Reports from pilots (PIREPS) or ground observers are a qualitative observation but still an important contribution to height estimation. Often these are the first estimates, especially in remote areas, where satellite and radar data are limited or not available. Because of their qualitative nature the variance can be large, depending on the experience and thoroughness of the pilot. (Examples of two of these eruptions are shown in Figures 5.16 and 5.17; see Chapter 9 for more details.)

5.8.7 Comparing height estimates

Plume height estimates can be quite variable between different techniques and may differ by many kilometers. Height estimates from the eruptions of Augustine Volcano, 2006 (Bailey *et al.*, 2010) exemplify variations in the different techniques (Table 5.3). These eruptions emitted plumes that ascended to heights less than, equal to, or above the tropopause. Height estimates were analyzed using polar-orbiting and geostationary satellite data, ground-based radar data, and reports from pilots (PIREPS) and ground observers. All these data were approximately concurrent in time for each eruption event.

Table 5.3. Examples of the variation in height estimates for the 2006 eruptions of Augustine Volcano. Generally, ground-based radar is considered more accurate and provides a discrete estimate compared with satellite techniques. Usually, satellite temperatures and trajectories are in general agreement and are often expressed as a range rather than a discrete value. However, during the recent Redoubt eruption some radar height estimates were often much higher (by a factor of 2) than those from other techniques.

Date	Time (UTC)	BT D (K)	Plume T (°C)	Height estimate model (km)				
				Radar	Temperature	Trajectory	PIREP	Comments
11-Jan-06	13:44	0		9		>8	—	
	13:48		−46		7–12			
	14:12	0	−45		7–12	9		
	14:25	0	−55		8.5	—		
13-Jan-06	13:24	0		10.5			14.5–16	Supercooled
	13:28	0	< −54			8		
	13:56	0	−52.5					
	17:47							
	19:24	0	−44		6.5			
	20:41	−1.4	−54	11	9.5		16	Ash on rim
	21:03	−4	−51.5	11	7.5			Ash on rim
14-Jan-06	01:45	−1.9	−55	10.5	8–8.5			Ash on rim
17-Jan-06	16:58			14				
	17:38	0	−55			8	8–9	

The eruption of Augustine Volcano on January 14, 2006 at 01:45 UTC is a good example of height estimates and how they may relate to the morphological structure of the plume (Figure 5.18). The volcano erupted at 01:40 UTC. Satellite data, radar, and an oblique photograph were recorded within minutes of each other. The photograph shows a central peak at a higher altitude (Figure 5.18a) surrounded by what appears to be a relatively flat plume at a lower altitude.

The satellite image shows a circular plume approximately 10 km across with a minimum temperature of -55°C for the central peak and -52°C for the surrounding plume top. The temperature of the central peak correlates to a height of about 8 km (Figure 5.18c) and, since the central peak temperature is not colder than the surrounding atmosphere, this shows that it is not supercooled. The temperature of the lower portion of the plume translates to atmospheric heights between 7.5 and 10 km while radar suggests a height of approximately 10 km. If height estimates were based solely on plume temperature a single definitive value could not be given but limits could be provided, such as greater than 7.5 km. One PIREP estimates the plume height to between 9 and 10.5 km which agrees with other

estimates. The January 14 eruption is also a good example of how temperature is related to the structure of the plume. Comparing the photograph (Figure 5.18a) with the satellite image (Figure 5.18b) the thin edges of the plume (circles in the figure) have warmer temperatures (-25°C , blue) than regions closer to the center and, hence, are semi-transparent allowing background radiation to penetrate the cloud resulting in a warmer signal detected by the satellite sensors. In this example the semi-transparent edges are estimated to be less than 1 km thick based on comparing the dimensions of the plume width and plume height on satellite data with the perspective photography.

The structure of a volcanic cloud and its height are very dynamic, especially when the cloud is still attached to the volcanic vent. The dynamics are affected by variations in the heat and emissions from the volcano, structure of the atmosphere, entrainment of moisture, composition of the cloud (ash-rich, water-rich), presence of ice (Rose *et al.*, 1995), and the injection of aerosols. These conditions change in time as the cloud evolves (Tupper *et al.*, 2003, 2004, 2007). Moreover, these conditions impact the electromagnetic signal as a function of wavelength measured in satellite data, which might

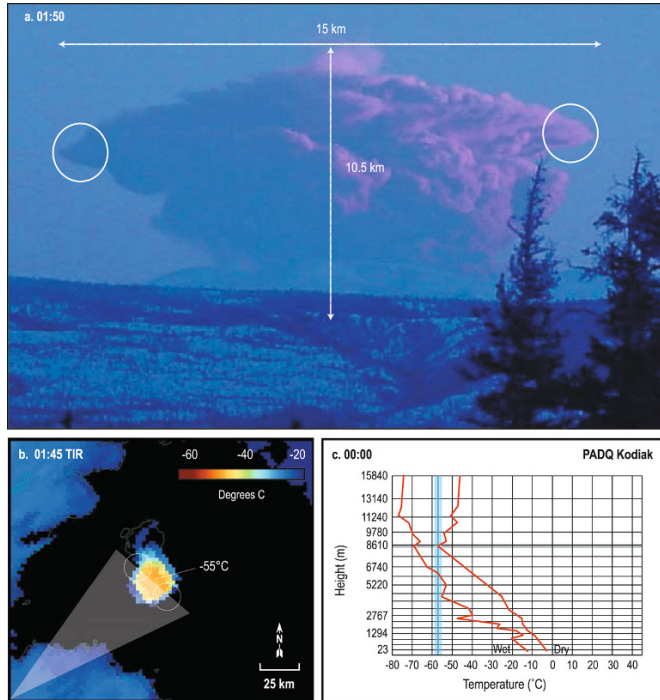


Figure 5.18. An oblique photograph of an eruption plume at Augustine taken on January 14, 2006, 01:50 UTC (a) shows a profile view of the plume recorded on a satellite image at 01:45 UTC (b). The satellite image shows the coldest part of the plume (yellow and orange) to be elliptical, 10×15 km in size, and 10.5 km high according to radar. The coldest temperature is -55°C near the center of the satellite image and decreases to -24°C (light blue) along the edges. Comparing the photograph with the satellite image shows that the thickest part of the plume coincides with the coldest regions (yellow and orange) and is presumably opaque. The warm edge of the plume (light blue) coincides with the thin edge in the photograph and is presumably semi-transparent as seen on the satellite image (open circles). The thin edge is estimated to be less than 1 km thick. The viewing direction of the photograph, the gray area in (b), is NE (modified from Bailey, 2010).

also help to explain some of the variations in height estimates.

A conceptual model of a plume (based on Turco *et al.*, 1983) shows gas and water vapor capping the plume with ash in the lower parts of the umbrella region of the plume (Figure 5.19). The boundary between the ash and gas-rich components is not an impenetrable barrier—but a transition. Pilots viewing the cloud are looking in the visible wavelengths and see Rayleigh scattering of light by gases at the very top of the cloud and, so, the viewing geometry greatly affects the accuracy of height estimates (Tupper *et al.*, 2003). Thermal infrared wavelengths used by satellite sensors record radiated energy that is emitted from a range of heights near the top of the cloud although it is assumed that most of the energy is radiated at the point where the

plume is opaque (Sparks *et al.*, 1997). Therefore, the temperature measurement is an integrated value over a pixel area (spatial and depth) somewhere within the upper portion of the cloud. Thus, the cloud temperature and derived height is not solely from the cloud top. At radar wavelengths gas clouds are mostly transparent, but particles within clouds reflect microwave energy back to the sensor. The size of the particles detected by radar depends upon the wavelength used. The AVO and NEXRAD radars are sensitive to 1 to 0.01 mm size particles. Radar instruments detect particles that might be composed of ash or ice crystals or condensed droplets. Radar is probably more sensitive to fewer particles than satellite sensors.

From the perspective of satellite sensors alone one might expect height estimates from PIREPS to

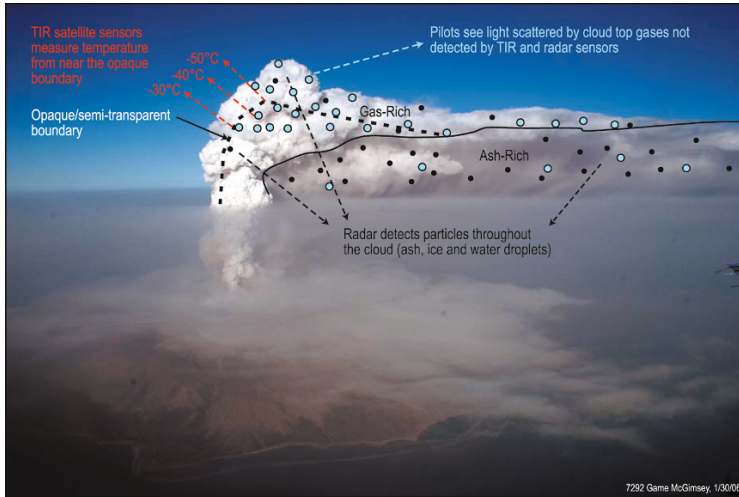


Figure 5.19. A conceptual model of a plume showing a gas-rich region capping the ash-rich region (modified from Lane *et al.*, 1995 and Turco, 1992). Pilots observe scattered light in the visible from volcanic aerosol layers (H_2SO_4 , SO_2 , and some ash). TIR satellite sensors detect radiated energy from multiple levels but near the opaque/semi-transparent boundary and measure an integrated temperature over a pixel but below the cloud top. Radar detects reflected energy from particles throughout the cloud as a function of its wavelength but gases are mostly transparent.

be higher than other methods (even if geometry was accounted for) and TIR satellite sensors somewhat lower than the visual cloud top due to cloud penetration. Radar data may provide a more accurate height estimate of ash particles but the signal may be from particles other than ash, be sensitive to particle concentrations below satellite detection limits, and will ignore gas components. The height of a plume, particularly during its initial stages, changes rapidly (on the order of minutes) and the timing of observations is critical for these estimates. Even if the observations are coincident in time they are affected by different conditions, so plume height estimates will vary between techniques.

5.9 PHYSICAL PRINCIPLES OF ASH DETECTION IN THE INFRARED

5.9.1 Volcanic ash detection

Volcanic ash is a hazard to aircraft and, therefore, needs to be detected and its movement tracked (Casadevall, 1994; Casadevall *et al.*, 1996; Miller and Casadevall, 1999). The problem of detecting volcanic clouds using satellite data is really a problem of discrimination. Ash clouds absorb, emit, and

scatter radiation in the visible, infrared, and microwave regions of the electromagnetic spectrum. At visible wavelengths, depending on the geometry of illumination (by the Sun or using a laser light source) and the geometry of observation, clouds may appear bright or dark. This is true of clouds of water, ice, silicates (volcanic ash), wind-blown dust (desert dust), smoke (e.g., from a large forest fire) or any other naturally or anthropogenically generated cloud of particles. It is sometimes very clear that a particular cloud is meteorological in origin (e.g., a cloud of water droplets or ice particles, or a mixed phase cloud), but often not so clear that it is not a meteorological cloud. Figure 5.20a–h shows some satellite images of anomalous clouds in the atmosphere. These are daytime MODIS images that have been enhanced to provide a true-color rendition of the scene. In all of these scenes there are meteorological clouds and clouds due to other sources: (a) a thick ash column rising above Ruang Volcano (Sangihie Islands, Indonesia, 125.37°E , 2.30°N), (b) a drifting ash and gas plume recently emitted from Karthala Volcano (Comoros, 11.75°S , 43.38°E), (c) a low-level gas (predominantly SO_2 and H_2O) plume from Ambrym Volcano (Vanuatu, 16.25°S , 168.12°E), (d) an ash and gas plume over snow-covered terrain from

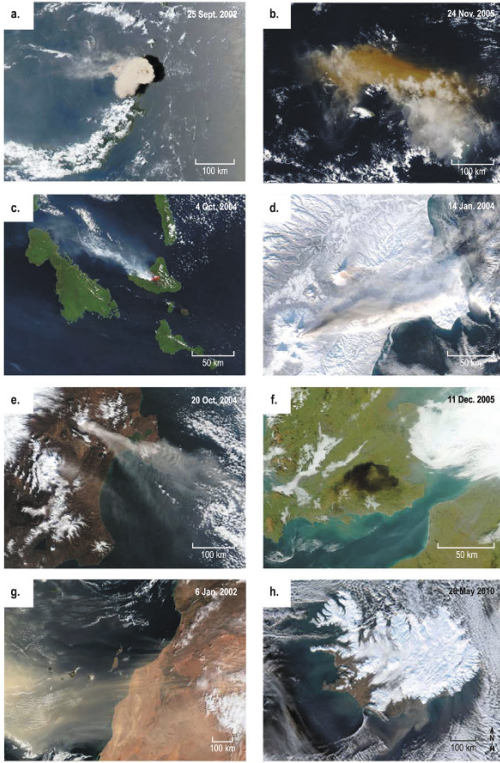


Figure 5.20. Daytime MODIS scenes showing anomalous clouds: (a) thick ash column from Ruang Volcano; (b) drifting ash and gas plumes from Karthala Volcano; (c) low-level gas cloud plume from Ambrym Volcano; (d) ash and gas plume over snow-covered terrain (Kliuchevskoi Volcano); (e) ash and gas plume from Shiveluch Volcano; (f) a noxious gas cloud from an industrial fire in southern England; (g) a dust outbreak over the Canary Islands; and (h) surface ash resuspended by wind streaming off the southern coast of Iceland (images are courtesy of NASA Earth Observing website).

Kliuchevskoi Volcano (Kamchatka, 56.057°N , 160.638°E), (e) an ash and gas plume from Shiveluch but in summer, (f) a noxious cloud generated from an industrial accident in southern England, (g) a dust outbreak traveling westwards over the Canary Islands (28.00°N , 15.58°W), and (h) wind-blown ash off the coast of Iceland. These examples illustrate some of the variability found in anomalous clouds when viewed by satellites during the day. Some clouds appear almost black (Figure 5.20f) or dark gray (Figure 5.20h), some are as white as water/ice clouds (Figure 5.20c, d), while

others take various sandy shades with brown and yellow hues (Figure 5.20a, b, e, g). By using objective analysis of daytime visible imagery alone, it has been very difficult to unambiguously discriminate ash clouds from other clouds. During the nighttime, the task is made even more difficult because there is no sunlight available and, hence, the visible satellite channels cannot be used. This is the main reason researchers have turned their attention to using infrared data (e.g., Hanstrum and Watson, 1983; Prata, 1989a, b; Barton *et al.*, 1992; Ellrod *et al.*, 2003).

5.9.2 Transmission of EM energy through a cloud

Satellite-borne infrared radiometers are used to measure atmospheric radiation in narrow ($0.5\text{--}1.0\ \mu\text{m}$) wavelength bands, collecting energy from all components of the scene within the field of view of the instrument. In general terms, it is possible to write down the radiative transfer equation (RTE) governing this kind of measurement, with some suitable approximations to make the problem tractable. A useful starting point is to consider a directional (downwards) measurement of the upwelling radiation from a cloud-less atmosphere over a narrow band of infrared wavelengths, where the contributions from solar radiation are negligible, ignore infrared scattering, and adopt plane-parallel geometry. With these conditions, we may write:

$$I_{\lambda}(\varphi, \theta) = I_{s,\lambda}(\varphi, \theta)\tau_{s,\lambda}(\varphi, \theta) + \int_0^{\infty} B_{\lambda}[T(z)] \frac{\partial \tau_{\lambda}(z; \varphi, \theta)}{\partial z} dz \quad (5.2)$$

where I is the directional radiance measured at the sensor; I_s is the radiation from the surface; B is the Planck function; T is temperature; $T(z)$ is the vertical temperature profile; λ is wavelength; z is height; τ is the atmospheric transmittance; φ is the azimuth angle; and θ is the zenith angle.

All quantities are to be considered as averages over a narrow band; for notational convenience the band is designated by a single wavelength that represents the band-averaged central wavelength. The radiance measured consists of two terms: the first term represents radiation from the surface and the second term represents radiation (emission and absorption) from the atmosphere. The surface term can be divided further into surface emission and radiation from the atmosphere reflected back off

the surface:

$$I_{s,\lambda} = \varepsilon_{s,\lambda}(\varphi, \theta) B_\lambda[T_s] + \frac{1}{2\pi} \int_{\Omega} I_{a,\lambda}(\varphi, \theta) \rho_{s,\lambda}(\varphi, \theta) \cos \theta \sin \theta d\Omega \quad (5.3)$$

where W is the solid angle; $\varepsilon_{s,\lambda}$ is the surface emissivity; ρ is the bi-directional reflectance distribution function; and T_s is the surface temperature. An assumption often made, and one that will be made here, is to take:

$$\varepsilon_{s,\lambda} = 1 - \rho_{s,\lambda} \quad (5.4)$$

which assumes that the surface is Lambertian (i.e., there is no preferred direction for reflected radiation). Let us now introduce a plane-parallel cloud into this plane-parallel model¹ and adjust the RTE to include this layer:

$$I = I_s + I_a + I_c + I_\uparrow \quad (5.5)$$

where I_a is the atmospheric radiance but with the upper limit of the integral terminated at the base of the cloud (z_b); and I_c is the cloud radiance. We have omitted the notation for wavenumber and angular dependence for convenience. The term I_\uparrow represents atmospheric radiation above the cloud top (z_t) and can often be ignored for window channels and when the cloud is high. There is also radiation from above the cloud that is reflected off the cloud back towards the sensor, but this is a very small contribution and can be safely neglected. An idealized depiction of the model is shown in Figure 5.21. While scattering has been ignored in the atmosphere, it cannot be ignored in the cloud. In fact, without including the effects of scattering, the foundations for detecting ash clouds using infrared instruments would be flawed. The RTE for scattering by a layer of particles can be written:

$$\mu \frac{\partial I}{\partial t}(t, \mu) = I(t, \mu) - (1 - \varpi_0) B(T) - \frac{\varpi_0}{2} \int_{-1}^1 P(\mu; \mu') I(\tau, \mu') d\mu' \quad (5.6)$$

where $t = -\ln(\tau)$ is the optical depth; μ is the cosine of the zenith angle; ϖ_0 is the single-scattering albedo; and P is the axially symmetric phase function. The cloud layer has an optical depth t_1 and we

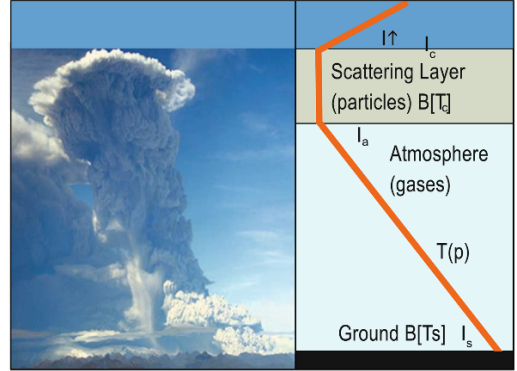


Figure 5.21. Idealized radiative transfer model for calculating radiation propagation through an absorbing atmosphere and scattering layer of cloud particles (see text for the meaning of the various terms).

are only concerned with the upwelling radiance in the direction μ at the cloud top ($\tau = 0$). This equation can be solved using boundary conditions of no downward radiance incident on the cloud top:

$$I(0, -\mu) = 0 \quad (5.7)$$

and the upward radiance incident on the cloud base is due only to that emitted from the ground:

$$I(t_1, +\mu) = I_v \quad (5.8)$$

The plus and minus signs signify upward and downward directions, respectively. Thus, to model radiative transfer it is necessary to calculate (or measure) the radiance emitted by the surface and atmosphere beneath the cloud and be able to characterize the optical properties of the scatterers inside the cloud as a function of wavelength. Given that the RTE described above is quite complex it is informative to use a highly simplified model that still captures the important features of infrared sensing of volcanic ash clouds. Such a model is described next and we will return to the more complex treatment in Section 5.10.2.

5.10 MODELING RADIATIVE TRANSFER IN ASH CLOUDS

5.10.1 A simplified model

In order to isolate the important factors affecting the RT inside an ash cloud, some simplifying assumptions are made. First, the atmosphere below the cloud layer is assumed to be totally transparent:

¹ The assumption of plane-parallel conditions is not particularly limiting, but simplifies the mathematical treatment. These equations can be re-cast for a spherical shell atmosphere and an arbitrarily shaped cloud.

$I_a = 0$. Second, the Earth's surface below the cloud is assumed to be a blackbody: $I_s = B[T_s]$. Third, we consider nadir viewing only: $\varphi = 0, \theta = 0$. Fourth, we consider the cloud to consist of homogeneous particles at a single temperature, T_c . Finally, rather than consider a broad spectrum of narrow bands, we take just two:

$$I_{\lambda_1} = B_{\lambda_1}[T_s] \exp(-t_1) + (1 - \exp(-t_1)) B_{\lambda_1}[T_c] \quad (5.9)$$

$$I_{\lambda_2} = B_{\lambda_2}[T_s] \exp(-t_2) + (1 - \exp(-t_2)) B_{\lambda_2}[T_c] \quad (5.10)$$

These two equations can be linearized (see Prata and Grant, 2001 for details) and, noting that the cloud emissivity is $1 - \exp(-t)$, we may write:

$$T_1 = T_s(1 - \varepsilon_1) + \varepsilon_1 T_c \quad (5.11)$$

$$T_2 = T_s(1 - \varepsilon_2) + \varepsilon_2 T_c \quad (5.12)$$

$$\varepsilon_i = 1 - \exp(-t_i) \quad (5.13)$$

$$t_i = k_i L \quad (5.14)$$

where k_i is the absorption coefficient of the particles at wavelength i ; and L is the geometric thickness of the cloud. These equations can be solved to obtain:

$$\Delta T = \Delta T_c (X - X^\beta) \quad (5.15)$$

$$X = 1 - \frac{\Delta T_1}{\Delta T_2} \quad (5.16)$$

$$\beta = \frac{k_1}{k_2} \quad (5.17)$$

where $\Delta T = T_1 - T_2$; $\Delta T_c = T_s - T_c$; and $\Delta T_1 = T_s - T_1$. The important physics is captured in the parameter β , which represents the ratio of extinction coefficients at two wavelengths, λ_1 and λ_2 . It is possible to explore the parameter range of β , guided by typical values for the extinction coeffi-

cients. Since the two wavelengths are usually close together the extinction coefficients are not very different and $\beta \approx 1$.

Figure 5.22 shows the variation of ΔT with T_1 for $\beta < 1$, $\beta > 1$, and $\beta = 1$. When $\beta < 1$, the extinction coefficient at $k_{\lambda_1} > k_{\lambda_2}$ leads to a U-shaped curve, while for the opposite case $\beta > 1$ an arch-shaped curve results. If $\beta = 1$ then ΔT has no variation with T_1 and no information can be retrieved from this analysis. It turns out that for $\lambda_1 \approx 11 \mu\text{m}$ and $\lambda_2 \approx 12 \mu\text{m}$, typical of channels on many satellite sensors, $\beta < 1$ for silicates (ash particles) and $\beta > 1$ for water molecules and ice particles. If one were free to design a sensor solely for ash detection, it would be sensible to select channels that optimize the U-shaped curve.

One of the main problems with identifying ash in a cloud arises because often the ash is in a mixture with liquid water droplets or ice particles. Liquid water and ice clouds have $\beta > 1$ and therefore cause an opposite effect to that brought about by ash clouds on the ΔT vs. T_1 diagram. The simple model can be examined further to correct for water vapor effects, or at least understand how these effects manifest themselves. Assuming that the temperature difference observed arises from a linear combination of the signal from ash (ΔT_{ash}) and the signal due to water vapor (ΔT_{wv}), a two-component model can be developed. If the fraction of ash in the mixture is F , then we may write the observed temperature difference as:

$$\Delta T = F \Delta T_s [Z - Z^\beta] \quad (5.18)$$

where

$$Z = 1 - \frac{1}{F} \frac{\Delta T_1}{\Delta T_s} \quad (5.19)$$

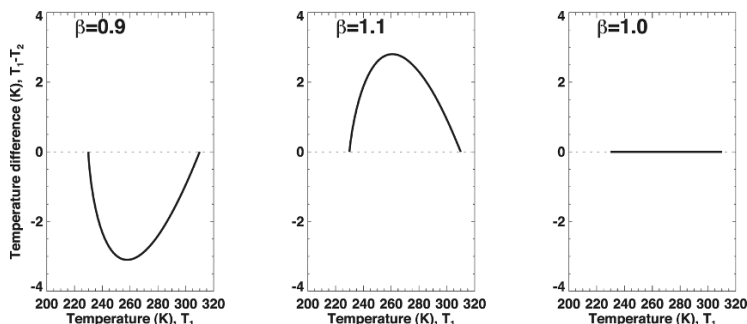


Figure 5.22. Variation of $rT = T_1 - T_2$ with T_1 for three values of the parameter β . When $\beta = 0.9$ (left panel) a characteristic U-shaped curve is found, indicative of silicate particles. Conversely, when $\beta = 1.1$ (middle panel) the curve is arch-shaped and indicates liquid water droplets or ice particles. When $\beta = 1$, there is no variation with T_1 .

The other parameters are defined as before. Ideally, this procedure needs to be automated. There are several parameters that can be determined from the image data. These are:

- (1) the clear sky surface temperature T_s ;
- (2) the cloud top temperature T_c ;
- (3) the clear sky value of the water vapor correction; and
- (4) the ratio of extinction coefficients β that governs the magnitude of the U-shaped distribution of negative differences.

A procedure for estimating these parameters from image data has been developed. A brief outline is given below:

1. T_s —this is easily estimated by finding the maximum value of T_1 occurring in the data. If the scene is too cloudy then an estimate from a climatology or from analysis data can be used.
2. T_c —this is more difficult to estimate from the data, because the lowest value may not necessarily correspond to the volcanic cloud. However, provided an area in close proximity to the suspect cloud can be delineated it may be reasonable to assume that the lowest value is the cloud top temperature. As the cloud top height can vary the use of a single T_c may introduce errors.
3. *Water vapor correction*—an empirical relation (Yu *et al.*, 2002) between the precipitable water in an atmospheric column and the brightness temperature difference ($T_1 - T_2$) is used to estimate the water vapor effect:

$$\Delta T_{\text{wv}} = \exp[6T_* - b] \quad (5.20)$$

where $T_* = T_1/T_{\text{max}}$; and T_{max} is an arbitrary normalization constant assigned a value of 320 K. The free parameter b essentially determines the value of the water vapor effect on $T_1 - T_2$ at the maximum value of T_1 . Hence, b can be determined directly from the image data, allowing realistic flexibility on the size of the water vapor correction determined by this semi-empirical approach. Values of b between 3 to 5 appear to be acceptable.

4. b —theoretical estimates of β suggest a value of around 0.7. A method for estimating β , T_s , and T_c simultaneously has been developed by using the distribution of T_1 vs. $T_1 - T_2$. The distribution is first histogrammed (or binned) into intervals of 0.5 K in T_1 . Then, the lowest values

in each bin are found and a curve is generated giving the outline of the distribution. The curve is smoothed and fitted using a nonlinear least squares model. The model has three parameters— T_s , $T_s - T_c$, and β —that can be estimated from the fit.

The curve-fitting procedure uses the model developed earlier with $F = 1$ and the partial derivatives of the model, which are analytic. Writing:

$$Y = \alpha(X - X^\beta) \quad (5.21)$$

where $Y = T_1 - T_2$, $\alpha = T_s - T_c$, $X = 1 - (\gamma/\alpha)$, $\gamma = T_s - T_1$. The partial derivatives are:

$$\frac{\partial Y}{\partial \alpha} = (X - X^\beta) + \frac{\gamma}{\alpha} + \beta \frac{\gamma}{\alpha} \left(1 - \frac{\gamma}{\alpha}\right)^{\beta-1} \quad (5.22)$$

$$\frac{\partial Y}{\partial \beta} = \alpha X^\beta \log \beta \quad (5.23)$$

$$\frac{\partial Y}{\partial \gamma} = 1 - \beta X^{\beta-1} \quad (5.24)$$

An example of the correction procedure is shown in Figure 5.23. The characteristic U-shaped curve indicating ash is apparent in the uncorrected (black dots) and water vapor corrected (red dots) data. The solid line is determined from the simple model using a suitable value of β and values for T_s and T_c . The important point to note is that the water vapor correction does not simply decrease all the values uniformly, rather the correction rotates the points in a clockwise direction about a point close to $\Delta T = 0$ and $T_{11\mu\text{m}} = T_s$. This gives larger correction to points closer to T_s ; points that are nearer the surface and hence expected to be affected greater by water vapor. The simple model considers only absorption as the process for extinction of IR radiation. In reality, scattering is also important and, unfortunately, this requires more complex modeling and the use of numerical methods.

5.10.2 Complex RT model

Prata (1989a, b), Wen and Rose (1994), Prata and Grant (2001), and Watson *et al.* (2004) have proposed RT models to solve the IR absorption/scattering processes for a volcanic ash cloud. The models essentially follow the theory outlined above, but the methods of solution differ in detail.

Wen and Rose (1994) and Prata and Grant (2001) have shown that, by including a micro-physical model of the ash particles with a detailed

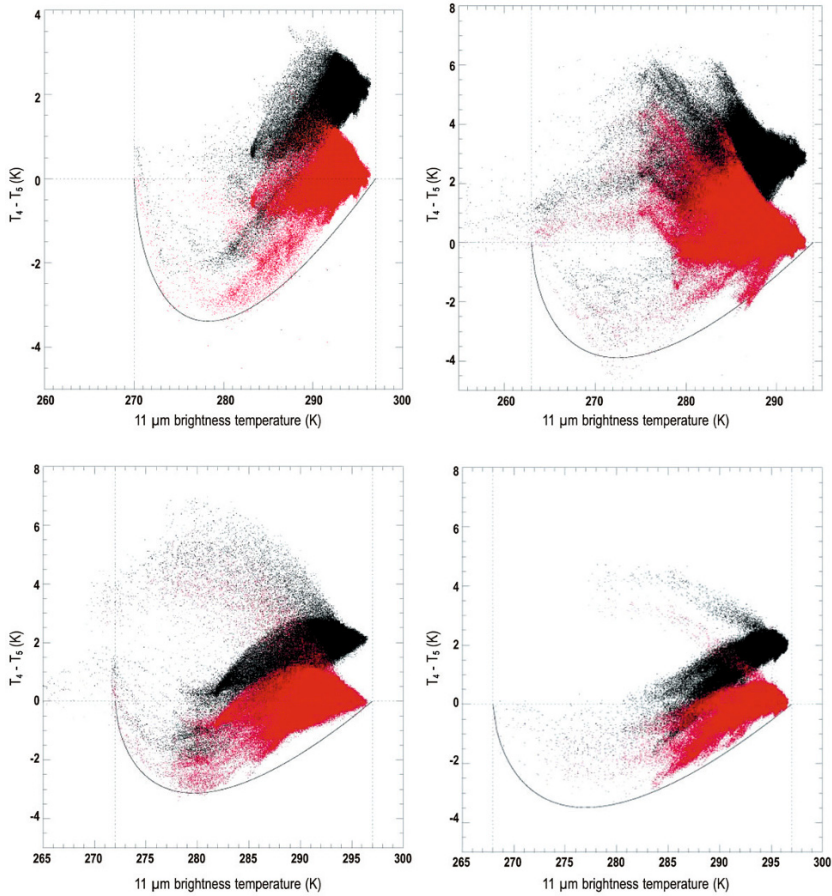


Figure 5.23. Temperature difference distributions without water vapor corrections (black dots) and with corrections (red dots). The water to vapor correction was applied to four different volcanic clouds using AVHRR data. T_4 and T_5 are AVHRR channel 4 (11 μm) and 5 (12 μm) brightness temperatures that correspond to T_1 and T_2 used in the theory here.

radiative transfer model, infrared data can be inverted to reveal mean particle size and cloud opacity. When these parameters are integrated over the area covered by the cloud, the total mass and mass loading can be inferred from the data. These are quantifiable products that may be incorporated in dispersion models to generate risk maps for use by the aviation industry. An example of this kind of retrieval is given in Figure 5.24 for the Karthala eruption.

There are many satellites (polar and geosynchronous) that carry these infrared channels, so this product can be delivered globally. Table 5.4 gives details of some of the satellite instruments capable of providing ash mass loadings.

5.10.3 Retrieval method

The radiative transfer required to extract quantitative information from infrared window radiances (8–12 μm) employs Mie theory and plane-parallel radiative transfer in an absorbing and scattering cloud. Given the real and imaginary parts of the index of refraction of the ash cloud particle as a function of wavelength, as well as the particle shape and size distribution, then the efficiencies for scattering, absorption, and extinction can be calculated using a Mie scattering program. There is scant information on particle shapes in real ash clouds and only approximate methods exist for calculating efficiencies for particles of arbitrary shapes. We

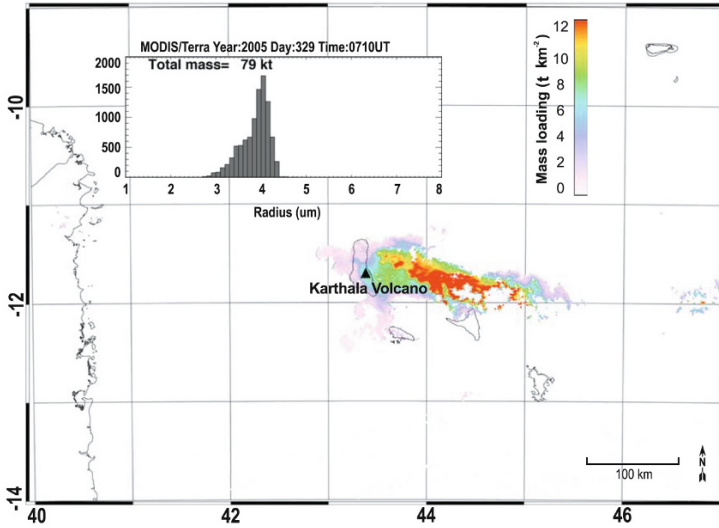


Figure 5.24. MODIS ash mass concentrations in t km^{-2} (or g m^{-2}) for an eruption of Karthala Volcano, November 2005.

Table 5.4. Details of past and current satellite instruments that can be used to detect ash and generate ash mass loading maps from infrared measurements.

<i>Satellite</i>	<i>Instrument</i>	<i>Spatial resolution</i> (km × km)	<i>Temporal resolution</i> (per day)	<i>Time period covered</i>
NOAA	AVHRR-2, -3	1 × 1	2	1981–present
NOAA	HIRS-2, -3, -4	10 × 10 ^a	2	1979–present
GOES	VISSR/VAS	5 × 5	24	1980–present
ENVISAT	ATSR family	1 × 1	2 ^b	1991–present
GMS-5	VISSR	5 × 5	24	1995–present
Terra/Aqua	MODIS	1 × 1	4 ^c	1999–present
Aqua	AIRS	14 × 14	2	2002–present
MetOp	IASI	12 × 12	2	2007–present
MSG	SEVIRI	3 × 3	96	2006–present

^a Earlier HIRS (1–3) instruments had a larger field of view of $18 \times 18 \text{ km}^2$.

^b These satellites are in a 3-day repeat cycle such that the same point imaged twice in one day will not be imaged again until 3 days later.

^c Assuming two satellites in orbit at any given time.

assume that the particles are spherical and the exact Mie theory computer program of Evans (1988) is employed to calculate the efficiencies. Some measurements exist for the particle size distribution at the edges of the Mt. St. Helens ash cloud (see the papers in Newell and Deepak, 1982). These data

indicate that a log-normal (or ZOLD) size distribution gives a reasonable fit to the distribution. The measurements reported by King *et al.* (1984) and Hofmann and Rosen (1984) of the El Chichón stratospheric aerosol layer (King *et al.*, 1984; Matson, 1984) fit a modified- γ size distribution

quite well. These data generally pertain to volcanic aerosol layers that are relatively old and high in the atmosphere. Only the fine particles can be detected in nascent and low (tropospheric) volcanic plumes, and it is assumed that the size distributions would be similar to those reported for El Chichón (Hofmann and Rosen, 1984) and Mt. St. Helens. Both size distributions have been used to perform radiative transfer calculations and, although there were differences in detail between the results for the two distributions (see also Wen and Rose, 1994), the basic results and mass loadings were essentially the same.

The parameters used in the Mie program are described in Prata (1989b). Once the Mie program has been run for each value of the size parameter (mean particle size and monochromatic wavelength), scattering parameters are then fed into a plane-parallel discrete ordinates radiative transfer program (Stamnes and Swanson, 1981). Given the single-scattering albedo, asymmetry parameter, extinction and scattering efficiencies as a function of monochromatic wavelength, and the cloud top and surface temperatures, radiances emerging from the top of the cloud along n distinct streams (zenith angles) can be computed. These radiances are calculated for cloud optical depths ranging from 0 to 20 at wavelengths corresponding to the thermal IR channels of the sensor (e.g., AVHRR, MODIS, SEVIRI, etc.) for atmospheres that contain no water. On completion of these calculations, a large two-dimensional (corresponding to the 11 and 12 μm channels) look-up table exists with entries at prescribed values of the mean particle size r_m and optical depth τ . Each entry in the table consists of pairs of brightness temperatures $T_{11\mu\text{m}}$ and $T_{12\mu\text{m}}$. The retrieval then consists of locating the (r_m, τ) pairs within the look-up table that best match $(T_{11\mu\text{m}}, T_{12\mu\text{m}})$ measurements at each image pixel.

The calculations were performed assuming that there is no absorption of infrared radiation by water vapor. The effects of atmospheric water vapor absorption on satellite brightness temperatures can be assessed by performing radiative transfer calculations. The radiative transfer model Modtran 3 (Berk *et al.*, 1989) was used to calculate the temperature difference between satellite-measured brightness temperatures at the 11 and 12 μm wavelengths, at each vertical level using the temperature and moisture structure from a nearby radiosonde profile. The results of this analysis show that the effect of water vapor is greatest at the lowest levels,

where it typically exceeds 1 K. At higher levels, near the location of the plume, the effect is less than 0.2 K. In the tropics and under high-humidity conditions, the effect of water vapor absorption can mask out the “reverse” absorption effect of volcanic ash clouds. This can lead to misidentification of volcanic clouds and is a limitation of the current thermal detection method.

5.10.4 Size distributions, scattering parameters, and mass loading

The modified- γ distribution has the functional form:

$$n(r) = N_0 \frac{r^\alpha}{\Gamma\left[\frac{\alpha+1}{\gamma}\right]} b^{(\alpha+1)/\gamma} \exp(-br^\gamma) \quad (5.25)$$

where $n(r)$ is the number of particles per unit volume; r is the particle radius; Γ is the Gamma function (see Press *et al.*, 1986, p. 156); N_0 , b , α , and γ are parameters of the distribution. The size parameter x is related to the particle radius and the wavelength λ through:

$$x = \frac{2\pi r}{\lambda} \quad (5.26)$$

where $\gamma = 1$; $\alpha = 6$; $b = 6/r_0$. Equation (5.25) reduces to:

$$n(x) = Cx^6 \exp\left(-\frac{6x}{x_0}\right) \quad (5.27)$$

where C is a constant replacing the other parameters. Within a distribution of sizes, the mode radius r_0 corresponds to the mode size parameter x_0 .

The log-normal distribution is described by:

$$n(x) = N_0 \frac{1}{\sigma_x} \exp\left[-\frac{(\ln(x) - \ln(x_0))^2}{2\sigma_x^2}\right] \quad (5.28)$$

where, as before, x is the size parameter. The parameter $\sigma_x = 2\pi\sigma_r/l$ is related to the standard deviation (σ_r) of the distribution and is a measure of its spread. In the calculations performed with this distribution, σ_r was set to 0.5, 0.75, 1.0, and 1.25 μm and results were reported for $\sigma_r = 1.0 \mu\text{m}$.

The inputs to the Mie program are the real and imaginary parts of the refractive index (m), the size parameter, and the size distribution. The outputs are the extinction efficiency (\hat{Q}_{EXT}), scattering efficiency (\hat{Q}_{SCA}), and phase function ($P(\theta)$). For polydispersions these efficiency factors are related to the

single-particle efficiencies (\hat{Q}_f) by:

$$\hat{Q}_f = \frac{\int_0^\infty \pi r^2 Q_f \left(\frac{2\pi r}{\lambda}, m \right) \frac{dn(r)}{dr} dr}{\int_0^\infty \pi r^2 \frac{dn(r)}{dr} dr} \quad (5.29)$$

The absorption efficiency is then:

$$\hat{Q}_{\text{ABS}} = \hat{Q}_{\text{EXT}} - \hat{Q}_{\text{SCA}} \quad (5.30)$$

The remaining parameters needed to perform radiative transfer calculations which relate to the cloud microphysical structure are the single-scattering albedo:

$$\varpi = \frac{\hat{Q}_{\text{EXT}}}{\hat{Q}_{\text{SCA}}} \quad (5.31)$$

and the asymmetry parameter:

$$g = \frac{1}{2} \int_{-1}^1 P(\theta) \cos \theta d \cos \theta \quad (5.32)$$

where θ is the scattering angle. The number of particles per unit volume in the cloud is:

$$N = \int_0^\infty \frac{dn}{dr} dr \quad (5.33)$$

The optical depth of the cloud is:

$$\tau_\lambda = \pi L \int_0^\infty r^2 Q_{\text{EXT}}(r, \lambda) n(r) dr \quad (5.34)$$

where L is the geometrical thickness of the cloud. The mass loading (kg m^{-2} , mg mm^{-2} or kt km^{-2})² is

$$M = \frac{4}{3} \pi \rho L \int_0^\infty r^3 n(r) dr \quad (5.35)$$

where ρ is the density of the ash.

5.10.5 Mass loadings

The U.S. Military consider mass concentrations $>50 \text{ mg m}^{-3}$ a potential hazard to their aircraft operations. Przedpelski and Casadevall (1994) estimated a mass concentration of $\approx 2,000 \text{ mg m}^{-3}$ at 25,000 ft ($\approx 7.5 \text{ km}$) for the December 15, 1989 Redoubt eruption cloud that caused significant damage to a KLM Boeing 747-400 jet aircraft. Mass loadings include all particles with radii $<50 \mu\text{m}$ which have atmospheric residence times of the order of at least a few hours. Having determined the particle size distribution, the geometrical thickness of the cloud, and its areal extent, it is

² $1 \text{ mg mm}^{-2} = 1 \text{ kt km}^{-2}$.

possible to estimate the mass loading of fine particles in an ash plume. The density of the ash is taken to be $2,600 \text{ kg m}^{-3}$ and the area of a pixel is typically taken as $\sim 1 \text{ km}^2$ —this is a mean area for pixels for both the AVHRR-2 and MODIS; pixels near the scan edges will be somewhat larger (several km^2). Pixels are counted if they satisfy the criterion $DT < T_{\text{cut}}$, where T_{cut} is a threshold usually taken as 0 K and the retrieved particle size is in the range $1 < r_m < 8 \mu\text{m}$. An estimate of the cloud thickness is crucial to the evaluation of mass concentrations. Data on cloud thicknesses are not available so they must be estimated by other means. Studies of plume rise in stable stratified atmospheres (e.g., Briggs, 1975) suggest that, to a reasonable approximation, the vertical extent of a plume can be estimated from the cloud top height. For example, Manins (1985) has calculated the heights and vertical extents of stabilized smoke plumes as a function of power release and, following Briggs (1975), suggests that the vertical extent (cloud thickness) Δz of these plumes is given by:

$$\Delta z = 0.4 z_{\text{top}} \quad (5.36)$$

where z_{top} is the height of the plume top. New measurements from the CALIOP lidar (Winker *et al.*, 2007) on board CALIPSO suggest that drifting volcanic plumes are no more than 1–3 km thick, but variable. The variability of cloud thickness along the plumes and the problem of not having simultaneous plume top height and plume base height data for each of the plumes means that we cannot estimate plume thickness to any greater accuracy. The total mass can be calculated by multiplying (5.36) by the area of a pixel.

5.10.6 Retrieval procedure

In the $(T_{11\mu\text{m}}, T_{11\mu\text{m}} - T_{12\mu\text{m}})$ plane there exist isolines of constant mean particle radius r_m^j . Each point on the isoline r_m^j corresponds to particular values of the optical depth $\tau^{j,i}$. Lines connecting equal values of $\tau^{j,i}$ also exist. Given the measured values $(T_{11\mu\text{m}}^*, T_{12\mu\text{m}}^*)$, the retrieval procedure requires us to find the best values of (τ, r_m) . Linear interpolation is adopted:

- Find values of $T_{11\mu\text{m}}(\tau^{j,i}, r_m^j)$ that bracket $T_{11\mu\text{m}}^*$. Label these:

$$T_{11\mu\text{m}}^1(r_m^j), T_{11\mu\text{m}}^2(r_m^j), T_{11\mu\text{m}}^1(r_m^{j+1}), T_{11\mu\text{m}}^2(r_m^{j+1})$$

- Interpolate on the r_m^j isolines to find the appropriate $\Delta T(r_m^j) = T_{11\mu\text{m}}(r_m^j) - T_{12\mu\text{m}}(r_m^j)$:

$$\Delta T(r_m^j) = w_1 \Delta T_2(r_m^j) + (1 - w_1) \Delta T_1(r_m^j) \quad (5.37)$$

$$w_1 = \frac{T_{11\mu\text{m}}^1(r_m^j) - T_{11\mu\text{m}}^*(r_m^j)}{T_{11\mu\text{m}}^1(r_m^j) - T_{11\mu\text{m}}^2(r_m^j)} \quad (5.38)$$

Similarly for $\Delta T(r_m^{j+1})$:

$$\Delta T(r_m^{j+1}) = w_2 \Delta T_2(r_m^{j+1}) + (1 - w_2) \Delta T_1(r_m^{j+1}) \quad (5.39)$$

and the weight w_2 is defined in an analogous way to w_1 .

- The required mean particle radius is obtained using linear interpolation:

$$r_m^* = w_r r_m^j + (1 - w_r) r_m^{j+1} \quad (5.40)$$

$$w_r = \frac{\Delta T(r_m^{j+1}) - \Delta T^*}{\Delta T(r_m^{j+1}) - \Delta T(r_m^j)} \quad (5.41)$$

- In practice there are n isolines of r_m^j ($j = 1, n$), n is small ($n = 18$), and there are many more values of $\tau^{j,l}$ ($i = 1, k$) ($k = 100$ is used in the current software). Thus, $2n \times k$ values of ΔT are precomputed.

In summary the solution process for determining mass loadings from two-channel IR sensors entails:

- specifying the cloud geometry;
- specifying the viewing geometry;
- determining boundary conditions at the cloud;
- specifying the refractive indices of ash as a function of wavelength;
- specifying the size distribution and particle shape; and
- solving for cloud optical depth, particle size

(radius), and mass using multi-scattering radiative transfer code.

Studies (e.g., Wen and Rose, 1994) have shown that the calculation is sensitive to the size distribution, particle shape, and refractive indices used, and errors as large as 40% can arise from inaccurate knowledge of these parameters.

5.11 MICROPHYSICAL VOLCANIC CLOUD MODEL

The new (e.g., MODIS) and proposed advanced multispectral sensors (e.g., GLI, SEVIRI, AIRS, IASI) include many channels capable of providing detection and discrimination of volcanic ash clouds. A model of an ash cloud has been developed in order to exploit these new sensors. We include information from the visible to infrared—although most of the discussion has centered on infrared window radiances, it seems likely that visible and near-infrared data may also provide a means for ash cloud detection.

At near-infrared wavelengths ($\lambda = 1.61 \mu\text{m}$, for example) ice clouds appear much darker than clouds of water droplets, because the imaginary part of the refractive index of ice is larger than that of water at this wavelength and, consequently, ice absorbs more strongly at this wavelength. A comparison of the refractive indices of water, ice, and andesite (a common constituent of ash clouds) is given in Table 5.5.

Pollack *et al.* (1973) list refractive indices of andesite (and some other minerals) over a large range of wavelengths from the UV to the infrared.

Table 5.5. Refractive indices for water, ice, and andesite (a silica-rich volcanic rock). The last column gives the reference to the origin of the data shown.

Wavelength (μm)	n_r	n_i	Reference
Ice			
0.63	1.309	1.04×10^{-8}	Masuda and Takashima (1990)
1.61	1.289	3.41×10^{-4}	Masuda and Takashima (1990)
Water			
0.63	1.332	1.44×10^{-8}	Masuda and Takashima (1990)
1.61	1.317	0.87×10^{-4}	Masuda and Takashima (1990)
Andesite			
0.68	1.470	1.70×10^{-3}	Pollack <i>et al.</i> (1973)
1.61	1.470	3.30×10^{-3}	Pollack <i>et al.</i> (1973)

These data are not the only source of refractive index values for minerals (see, for example, Ivlev and Popova, 1973; Volz, 1973; Sokolik and Toon, 1999). We have used the Pollack *et al.* values as a starting point to provide the input optical parameters required for more detailed radiative transfer calculations, and we propose a model of a volcanic ash cloud based on the Pollack *et al.* refractive indices of andesite. The ash cloud model consists of spherical andesite particles in a log-normal size distribution with a mean particle radius of 3 μm . The single-scattering albedo, asymmetry parameter, as well as the coefficients of absorption, scattering, and extinction are calculated for the polydisperse particle size distribution using the Mie program discussed earlier. Prata and Grant (2001) provides a listing of the the variation of single-scattering albedo (ω), extinction coefficient (Q_{EXT}), and asymmetry parameter (g) for wavelengths ranging from 0.3 to 14.5 μm —the range most commonly used in remote sensing of the Earth's atmosphere. Also shown are the results for a model ash cloud with mean particle radii of 1 and 5 μm .

5.11.1 Volcanic ash products

The main operational use for volcanic ash detection and retrieval is to assist aviation in the avoidance of hazardous ash clouds. The research and development for these algorithms has taken place at many different universities and research agencies and transferred for use at Volcanic Ash Advisory Centers (VAACs). There are nine VAACs (see Table 5.6) that cover almost all of the global flight regions, and these are sited at national meteorological centers and tend to utilize local R&D. This has led to a diversity of ash detection schemes and products, but nearly all are based on the reverse absorption method or an improvement to it. Some schemes utilize the 3.7 μm channel (see Table 5.7), and VAACs that rely on geosynchronous data tend to use single-channel visible and/or infrared temporal information. Several of the VAACs have posted case studies on their websites (see Table 5.6): the Washington VAAC studies can be found at <http://www.ssd.noaa.gov/PS/SAMPLES/> and the Darwin VAAC studies at <http://www.bom.gov.au/info/vaac/images.shtml>

Table 5.6. Locations of the nine Volcanic Ash Advisory Centers (VAACs), satellites used to generate ash products, and the principal dispersion model(s) utilized. The current URL is also given where available.

VAAC	Region		Satellites	Dispersion model
	Longitude (°E)	Latitude (°N)		
Anchorage ^a	(150, -135)	(50, 90)	GOES, POES, MODIS	Puff, HYSPLIT, CanERM
Buenos Aires ^b	(-90, -10)	(-90, -10)		
Darwin ^c	(75, 160)	(-90, 10)	MTSAT, POES, MODIS	HYSPLIT
London ^d	(-30, 60)	(45, 90)	MSG, MODIS, MetOp	NAME
Montreal ^e	(-135, 0)	(45, 90)	GOES-E, GOES-W	CanERM
Tokyo ^f	(90, 165)	(15, 60)	MTSAT, POES	Puff
Toulouse ^g	(-30, 90)	(-90, 70)	MSG, MetOp, MODIS	Media, MOCAGE
Washington ^h	(-150, -40)	(-10, 45)	GOES, POES, OMI	HYSPLIT
Wellington ⁱ	(160, -140)	(-90, 0)	MTSAT, POES	HYSPLIT

^a <http://vaac.arh.noaa.gov/>

^b <http://www.meteoia.mil.ar/vaac/vaac.htm>

^c <http://www.bom.gov.au/info/vaac/>

^d <http://www.metoffice.gov.uk/aviation/vaac/index.html>

^e http://meteo.gc.ca/eer/vaac/index_e.html

^f <http://ds.data.jma.go.jp/svd/vaac/data/index.html>

^g <http://ds.data.jma.go.jp/svd/vaac/data/index.html>

^h <http://www.ssd.noaa.gov/VAAC/washington.html>

ⁱ <http://vaac.metservice.com/vaac/>

Table 5.7. Summary of ash detection algorithms and techniques used with satellite infrared (IR) and visible channel data (RA = reverse absorption; TVAP = Three-channel volcanic ash product; PCI = principal component image; RAT = ratio method; WVC = water vapor correction method).

<i>Name</i>	<i>Principle</i>	<i>Reference</i>
RA	Two-band IR (11 and 12 μm)	Prata (1989a, b)
Ratio	Two-band IR (11 and 12 μm)	Holasek and Rose (1991)
Four-band	IR + visible	Mosher (2000)
TVAP	Three-band IR (3.9, 11, and 12 μm)	Ellrod <i>et al.</i> (2003)
PCI	Multi-band principal components	Hillger and Clark (2002a, b)
WVC	Two-band IR + water vapor correction	Yu <i>et al.</i> (2002)
RAT	Three-band IR (3.5, 11, and 12 μm)	Pergola <i>et al.</i> (2004)
Three-band	Three-band (IR and visible)	Pavolonis <i>et al.</i> (2006)

5.11.2 Ash measurements from geosynchronous platforms

Polar-orbiting instruments are much better suited for remote sensing at high latitudes, and some sophisticated systems have been developed utilizing AVHRR and MODIS data. For AVHRR and MODIS measurements it is possible to obtain up to six images per day from each satellite in the polar regions. With two satellites this gives hourly coverage compared with four times daily at low latitudes. Geosynchronous satellites, on the other hand, provide very high temporal frequency (15 min sampling in some cases) but, with a total field of view of 70° centered at the equator, coverage at high latitudes is limited. Nevertheless, geosynchronous sensors offer some interesting possibilities for ash cloud sensing at high latitudes by exploiting the oblique views offered. Gu *et al.* (2005) have shown that oblique viewing enhances the ash signal due to the longer path lengths obtained through the cloud. They demonstrated the effect for measurements of the 2001 Cleveland eruption and showed that enhancements of -8 K were evident compared with -3 K for measurements from MODIS. Prata and Barton (1994) showed through RT modeling that some quite complex behavior is possible for oblique viewing with the possibility of the reverse absorption effect disappearing (this will almost certainly occur as the opacity of the cloud gets larger) or even giving an opposite effect, similar to the arch shape observed for semi-transparent ice clouds. Another related aspect of using oblique viewing combined with high temporal resolution was demonstrated

for the Kasatochi eruption that started on August 7, 2008. In this case, oblique viewing clearly showed the emergence of an erupting ash cloud through an extensive layer of meteorological cloud. This is shown in the panels of Figure 5.25, which are separated in time by 10–30 min. Cloud shadows thrown onto the meteorological deck of clouds below the emerging ash column can be used to calculate the height of the ash column. After 2 hours the ash cloud disperses in a southeasterly direction and becomes indistinguishable from meteorological clouds.

At low latitudes geosynchronous sensors have already proven to be extremely useful for monitoring ash clouds (e.g., Malingreau and Kaswanda, 1986; Sawada, 1987, 1996; Tupper *et al.*, 2004, 2007; Prata and Kerkmann, 2007), but their use at high latitudes has not been fully appreciated or exploited.

5.11.3 Examples of ash discrimination at high latitudes

The detection of ash clouds in the atmosphere using IR measurements is often confounded by the presence of water vapor, ice, and water clouds. There is a strong latitudinal dependence of water vapor in the atmosphere, with highest amounts near the equator and smallest amounts near the poles. From this we anticipate that, in general, it is easier to detect ash clouds in the polar (drier) regions. However, water vapor can be spatially and temporally quite variable and this is why robust ash detection

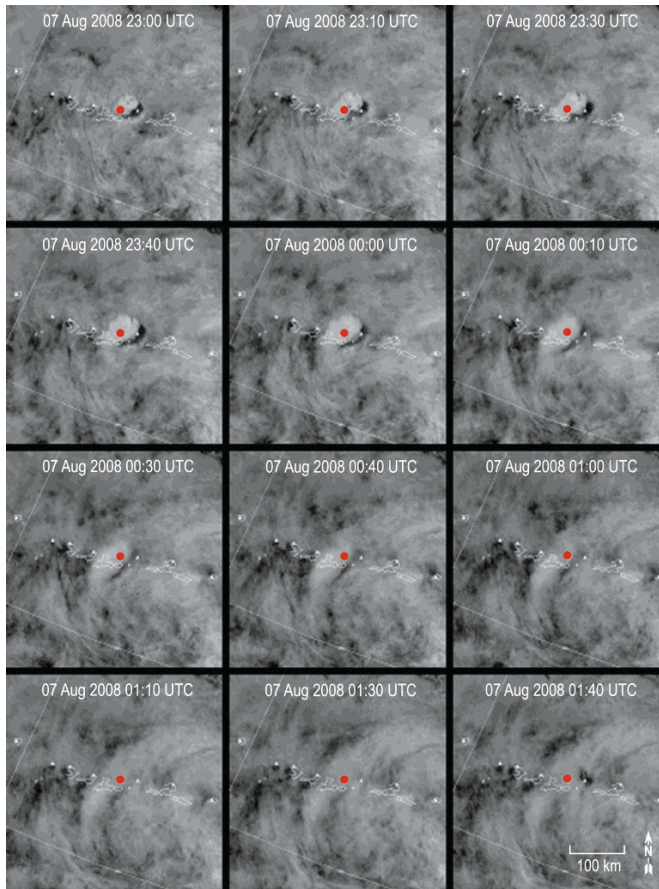


Figure 5.25. Sequence of GOES geosynchronous images of the eruption from Kasatochi Volcano, 2008. The oblique view of the sensor provides an excellent means for observing the ash column as it penetrates an existing cloud deck, and the subsequent dispersal of the ash cloud can be tracked using these high temporal resolution images. The red dot shows the location of the volcano.

schemes attempt to correct for water vapor (e.g., Gu *et al.*, 2003). Water and ice clouds are ubiquitous throughout the atmosphere but, within the moist tropics near strong convective regions, towering cumulonimbus clouds can form. These are ice rich with mixed-phase clouds and can spread over large areas. Persistent cloudiness is associated with mid-latitude baroclinic zones and frontal systems, and these can cause problems for ash detection, as was observed during the 2001 eruptions of Cleveland among others (Simpson *et al.*, 2002; Webley *et al.*, 2008). Cloudiness can also form around volcanoes generated by thermal heat or during the ascent of the eruption column through entrainment, nucleation, and cloud condensation. Although

there do not appear to be any algorithms designed to operate in specific geographical regions,³ it is useful to provide examples separately for high-latitude and low-latitude regions.

Holasek *et al.* (1996) described the use of satellite data for studying the eruptions of Augustine in 1986, a high-latitude volcanic eruption. For the example, we choose a more recent event, the eruption of Kasatochi in 2008, which also provides some

³ The algorithms developed by Pergola *et al.* (2004) utilize climatological data and are geographically dependent, but have only been tested for the Mediterranean region around Sicily. Gu *et al.* (2005) have shown certain advantages when using GOES data at high latitudes for ash detection.

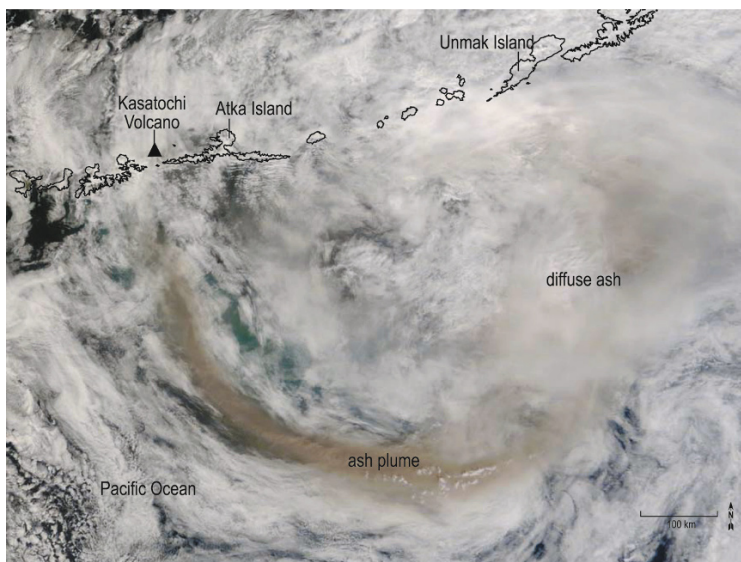


Figure 5.26. True-color MODIS image of the ash plume from Kasatochi Volcano on August 8, 2008.

salient features of ash detection. Kasatochi erupted on August 7, 2008 (http://www.volcano.si.edu/world/volcano.cfm?vnum=1101-13-&volpage=var#bgvn_3307) sending ash and SO₂ up to 15 km and spreading ash some 1,200 km in a SE direction, while the SO₂ was dispersed across Canada, the continental U.S.A., and on to Europe and Russia. A true-color MODIS image of the ash plume on August 8 is shown in Figure 5.26. The ash is seen as a discolored filamental cloud overlying other meteorological clouds, displayed in shades of gray to white. Any ash below these meteorological clouds is not detectable using visible or infrared measurements. Some parts of the ash cloud are quite diffuse and can be discriminated from other clouds through context and continuity with thicker, brown-colored filaments. By using the ash retrieval scheme described earlier, the distribution of the mass of fine ash ($r < 10 \mu\text{m}$) can be determined (Figure 5.27). The ash density has values as high as 10 t km^{-2} (10 g m^{-2}), and the total mass in the cloud is about 220 kt. A feature of this eruption was that it emitted a significant amount of SO₂, and this was tracked for much longer and over much greater distances than the ash.

There is a strong indication that the ash and SO₂ were collocated in the Kasatochi volcanic clouds, and this is demonstrated in Figure 5.27, where SO₂ column amounts (in DU) are plotted

with the ash concentrations. The SO₂ columns were determined using AIRS 7.3 μm measurements obtained at the same time but from a different instrument and a different spectral region and, so, may be considered as independent of the MODIS measurements. There is a clear indication that the SO₂ and ash are collocated and traveling together. Unfortunately, ash detection sensitivities are not as good as SO₂ sensitivities, so it is not possible to estimate for how long the ash persisted with the SO₂. In this instance there is a strong case to be made for using SO₂ measurements as a surrogate for ash, but this is by no means a universal assumption.

5.11.4 Examples of ash discrimination at low latitudes

For completeness we show how it is still possible, under favorable conditions, to determine geophysical parameters for ash clouds using infrared satellite data in the moist tropics. The eruption of Ruang, situated at the tip of Sulawesi in Indonesia, on September 25, 2002 was captured by several satellite sensors and has been discussed by Tupper *et al.* (2004) and Prata and Bernardo (2007). The initial eruption formed a tall, light-colored ash-rich column that rose over the Sangihe Islands (2.28°N , 125.43°E , 725 m) and, subsequently, dispersed west-

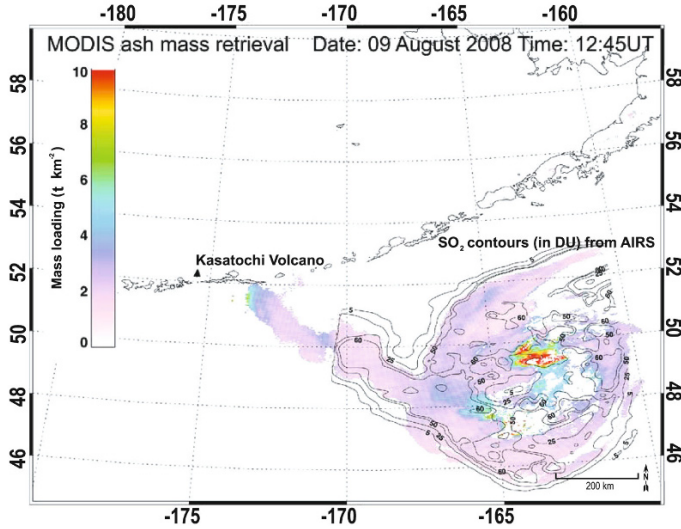


Figure 5.27. MODIS ash mass retrieval for an eruption from Kasatochi. Also shown are SO_2 contours (partial column in DU) derived from the AIRS sensor (see Prata and Bernardo, 2007).

wards, southwards, and eastwards (Figure 5.20a). It is likely that branches moving in different directions were at different heights and contained different volcanic material. The westward and southwestward-moving branches probably contained the majority of ash and some SO_2 and reached heights of up to 10–15 km. The faster moving eastward branch was at about 20 km and contained mostly SO_2 . Unlike the previous example, this case shows that relying on SO_2 as a marker for ash would be unreliable, although it would still be advisable to avoid the SO_2 cloud, which may or may not have contained sufficient ash to be a hazard to aircraft. Figure 5.28 shows MODIS ash masses determined during the night-time overpass of the Aqua satellite, together with concurrent AIRS SO_2 retrievals. Note that AIRS suggests a significant SO_2 cloud traveling southwards, while the MODIS retrievals indicate little ash in this portion of the cloud, indicating that ash–gas separation has occurred (Holasek *et al.*, 1996).

5.11.5 Extensions

There are now several ash detection algorithms in use or proposed, based on IR and visible satellite data. Table 5.7 shows a summary of ash detection schemes (with original references), based mostly on using infrared channels. Several of these techniques show great promise for detecting volcanic ash, but

there are important nuances and caveats associated with all of these techniques (including the two-channel, reverse absorption method) and we strongly recommend that the interested reader examine the original papers (listed in Table 5.7) carefully.

The two-channel, reverse absorption technique is very useful in cases where the ash is not too thick and not too dispersed; it is used at the VAACs (Watkin, 2003). The problems and pitfalls of using the reverse absorption technique have been discussed in the research literature (e.g., Simpson *et al.*, 2000; Prata *et al.*, 2001) and are well known to experienced meteorological analysts. Context is a key element in determining whether a particular cloud is an ash hazard or not, and trained meteorologists tasked with identifying ash clouds will use multiple sources of information including satellite imagery, pilot reports, ground observer reports, wind trajectories, and background information regarding regional volcanic activity and prior behavior.

Two of the instruments listed in Table 5.4 are capable of measuring much more than ash mass loadings. These instruments, AIRS and IASI, have high spectral resolution and, by utilizing more measurement channels, it may be possible to infer something about the mineralogy of the ash. Indeed, it may also be possible to discriminate dust (Figure 5.20g) and wind-blown ash (Figure 5.20h) out-

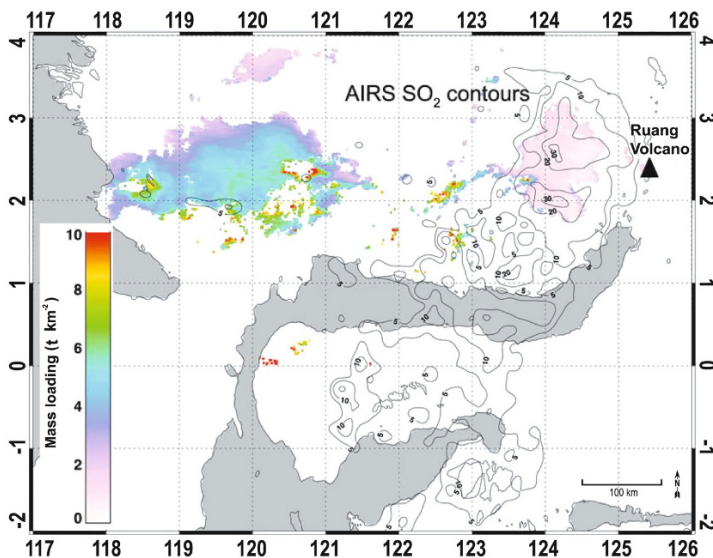


Figure 5.28. Ash mass concentrations in t km^{-2} (or g m^{-2}) for an eruption cloud from the eruption of Ruang, September 25, 2002. Also shown are contours of SO_2 amount (partial column in DU) derived from the AIRS spectrometer.

breaks from volcanic ash eruption clouds and plumes. Clerbaux *et al.* (2007) have shown the potential of IASI for measuring volcanic SO_2 .

The analysis described above was predicated on the assumption that just a few (typically two) channels are available in the IR to discriminate ash from other airborne substances and perform retrievals. With AIRS and IASI, more than 2,000 channels are available, and this opens up possibilities for doing more elaborate retrievals and also providing more constraints of the retrieval which usually leads to more accurate solutions. The same theory may be used in the case of high spectral resolution IR data.

Figure 5.29 shows a spectral transect (all AIRS lines along a single AIRS column) as a function of wavenumber and contains a daunting amount of information. We may extend the ideas developed earlier to this high spectral domain in a simple manner. The reverse absorption or two-channel technique can be seen as a special case of sampling from a continuous spectral signature due to ash or water/ice clouds, now amenable to analysis from AIRS and IASI measurements. To illustrate how these signatures can be used in AIRS data, Figure

5.30 shows the ratio between the spectral brightness temperature (BT) and a reference brightness temperature at $1,000\text{ cm}^{-1}$ (BT_{ref}^4) for six scene elements. The idea behind dividing by a reference brightness temperature is to approximate the emissivity variation of the spectra; the choice of $1,000\text{ cm}^{-1}$ is arbitrary, but it is necessary to avoid absorption regions and the region around $1,000\text{ cm}^{-1}$ is quite transparent. Within the region between 850 and $1,000\text{ cm}^{-1}$, the ratio for ice (blue line) increases with wavenumber, whereas for ash and desert dust it decreases. For a clear atmosphere there is a slight increase with wavenumber due to water vapor absorption. Water clouds generally have a slope between that of the ice cloud and the clear scene. Ice and water clouds behave this way because the radiance spectra for ice and water over this region decrease with increasing wavenumber, which is a consequence of the decrease in cloud emissivity with increasing wavenumber, which in turn is related to the spectral variation of the refractive indices of ice and water. This change of slope of the spectral ratio with wavenumber can be used to discriminate ash from ice, water clouds, and clear scenes. The slopes are also sensitive to the optical depth of the cloud as well as the microphysics of the particles (refractive index, size, size distribution, and shape).

⁴The use of wavenumber ν (in cm^{-1}) instead of wavelength λ (in μm) is deliberate here because AIRS and IASI use this unit: $\nu(\text{cm}^{-1}) = 10,000/\lambda(\mu\text{m})$.

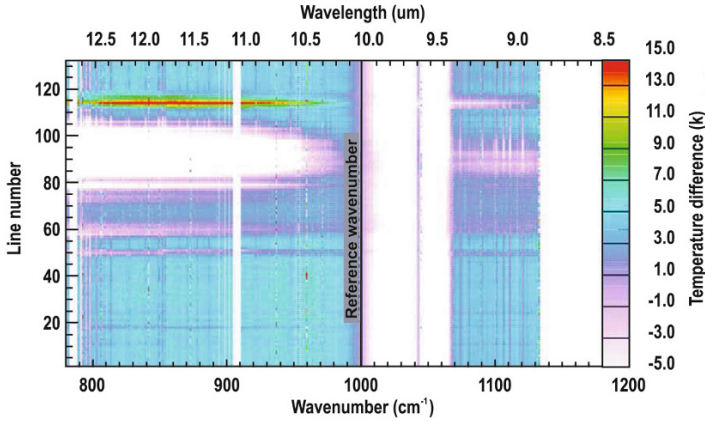


Figure 5.29. AIRS spectrum shown as a transect along a constant pixel number. The brightness temperature at $1,000\text{ cm}^{-1}$ has been subtracted from the spectra and plotted as brightness temperature differences (BTDs).

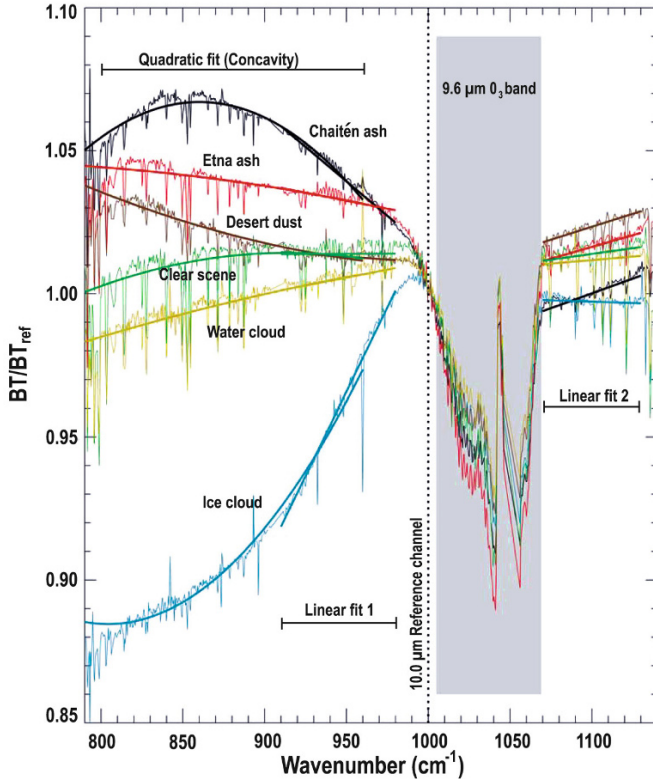


Figure 5.30. Spectral ratio of the top-of-atmosphere brightness temperature for a single AIRS pixel and for six different scenes: (1) a pixel containing a semi-transparent ice cloud (blue line), (2) a water cloud (yellow line), (3) a clear pixel (green line), (4) desert dust (brown line), (5) a pixel affected by ash from an eruption of Etna (red line), and (6) a Chaitén ash-affected pixel (black line). The grayed-out region includes the strong O_3 absorption and is not used in the analyses. The spectral regions where linear and quadratic fits are performed are also indicated on the plot.

Spectral fits (rather than channel differences) can be performed to obtain objective parameters for discriminating ash, water, ice, and other airborne substances. These fits are shown in Figure 5.30, labeled as “the concavity” (a quadratic fit) and two linear fits. Furthermore, the shape or signature of the spectral variation is sensitive to many parameters, including particle size and composition. By using a detailed RT model it may be possible to infer, for the first time, the composition of ash in the atmosphere providing useful insights into processes occurring in the interior of a volcano.

5.12 DIFFICULTIES AND FUTURE RESEARCH

Perhaps the greatest hindrance to detection and discrimination of volcanic ash clouds arises from interference effects from liquid water droplets and ice particles. Simpson *et al.* (2001) drew attention to the issue of water vapor absorption effects on the reverse absorption algorithm, but the analyses in that paper contained numerous errors and lacked rigor (Prata *et al.*, 2001). Many of the problems with ash detection have been described in the literature (Prata, 1989a, b; Rose *et al.*, 1995; Schneider *et al.*, 1995, 1999; Prata and Grant, 2001; Prata *et al.*, 2001; Dean *et al.*, 2002, 2004; Webley *et al.*, 2008) and at various workshops, symposia, and conferences. A further issue, still not fully resolved and of some importance, is the difficulties surrounding separation of ash and SO₂ in dispersing volcanic clouds. It had been thought that there is often significant (detectable) SO₂ emitted with ash during an explosive eruption. The eruption of Chaitén Volcano in southern Chile (Carn *et al.*, 2009) showed the opposite, as large amounts of ash were transported over significant distances with just minor SO₂ emissions. These observations reinforce the need to have robust ash detection algorithms together with SO₂ algorithms and indicate that research into improved ash retrieval schemes using a variety of satellite tools is warranted.

It seems possible, with sufficient spectral information, to isolate the main effects due to the various airborne volcanic substances. If ash particles are encased by ice then the characteristic infrared signature cannot be detected and some other means of detection is warranted. Rose *et al.* (2004) have elucidated the times and places when ice is likely to be present in volcanic clouds. Combinations of sensors and techniques will be required if further

advances are to be made in volcanic ash detection. The recent use of active methodologies (e.g., ground-based radar and the space-borne lidar Calipso; Winker *et al.*, 2007) provides new insights into the properties of volcanic clouds. Active sensors also provide range information, sadly lacking from the current operational suite of instruments. The way forward will utilize a multitude of sensors (passive and active), wavelengths (ultraviolet, visible, infrared, and microwave; Constantine *et al.*, 2000), and platforms (e.g., satellite and ground-based) and combine these measurements with dispersion models, models of ash column generation (e.g., ATHAM; Oberhuber *et al.*, 1998), and knowledge gained from geophysical data derived from seismic and other more traditional volcanological tools. Recent work by Pavolonis (2010) has extended the reverse absorption method demonstrating a robust scheme that gives fewer false alarms and that has the potential to be fully automated. The scheme can be used with any of the satellite sensors with the appropriate infrared bands and utilities independent of meteorological data. The scheme also includes a method for estimating cloud top height.

5.13 REFERENCES

- Bailey, J.E.; Dean, K.; Dehn, J.; Webley, P. (2010). Integrated satellite observations of the 2006 eruption of Augustine Volcano, in J.A. Power, M.L. Coombs, and J.T. Freymueller (Eds.), *The 2006 Eruption of Augustine Volcano, Alaska* (USGS Professional Paper 1769), U.S. Geological Survey, Reston, VA, pp. 481–506.
- Barton, I.J.; Prata, A.J.; Watterson, I.G.; Young, S.A. (1992). Identification of the Mount Hudson volcanic cloud over SE Australia, *Geophys. Res. Lett.*, **19**, 1211–1214.
- Berk, A.; Bernstein, L.S.; Robertson, D.C. (1989). *MODTRAN: A Moderate Resolution Model for LOW-TRAN 7* (AFGL-TR-89-0122), U.S. Air Force Phillips Laboratory, Nascom Air Force Base, MA.
- Bluth, G.J.S.; Doiron, S.D.; Krueger, A.J.; Walter, L.S.; Schetzler C.C. (1992). Global tracking of the SO₂ clouds from the June, 1991 Mount Pinatubo eruptions, *Geophys. Res. Lett.*, **19**, 151–154.
- Briggs, G.A. (1975). Plume rise predictions, in *Lectures on Air Pollution and Environmental Impact Analyses*, American Meteorological Society, Boston, pp. 59–111.
- Carn, S.A.; Pallister, J.S.; Lara, L.; Ewert, J.W.; Watt, S.; Prata, A.J., Thomas, R.J.; Villarosa, G. (2009). The

- unexpected awakening of Chaitén Volcano, Chile, *EOS Trans.*, **90**(24), 205–206.
- Casadevall, T.J. (1994). The 1989/1990 eruption of Redoubt Volcano Alaska: Impacts on aircraft operations, *J. Volcanol. Geothermal Res.*, **62**(30), 301–316.
- Casadevall, T.J.; Delos Reyes, P.J.; Schneider, D.J. (1996). The 1991 Pinatubo eruptions and their effects on aircraft operations, in C.G. Newhall and R.S. Punongbayan (Eds.), *Fire and Mud: Eruptions and Lahars of Mount Pinatubo, Philippines*, Philippines Institute of Volcanology and Seismology/University of Washington Press, Quezon City/Seattle, WA, pp. 625–636.
- Clerbaux, C.; Turquety, S.; Hadji-Lazaro, J.; George, M.; Boynard, A.; Pommier, M.; Coheur, P.-F.; Hurtmans, D.; Wespes, C.; Razavi, A. (2007). Monitoring of volcanic SO₂ using thermal infrared IASI/METOP sounders (TES, IASI), paper presented at the *Support to Aviation Control Service Meeting, Toulouse, France, November 26–27, 2007*.
- Constantine, E.K.; Bluth, G.J.S.; Rose, W.I. (2000). TOMS and AVHRR sensors applied to drifting volcanic clouds from the August 1991 eruptions of Cerro Hudson, in P. Mougini-Mark, J. Crisp, and J. Fink (Eds.), *Remote Sensing of Active Volcanism* (AGU Monograph 116), American Geophysical Union, Washington, D.C., pp. 45–64.
- Dean, K.; Bowling, S.A.; Shaw, G.; Tanaka, H. (1994). Satellite analyses of movement and characteristics of the Redoubt volcano plume, January 8, 1990, *J. Volcanol. Geothermal Res.*, **62**, 339–352.
- Dean, K.; Dehn, J.; Engle, K.; Izbekov, P.; Papp, K.; Patrick, M. (2002). Operational satellite monitoring of volcanoes at the Alaska Volcano Observatory, *Adv. Environ. Monit. Model.*, **1**, 3–35.
- Dean, K.G.; Dehn, J.; Papp, K.R.; Smith, S.; Izbekov, P.; Peterson, R.; Kearney, C.; Steffke, A. (2004). Integrated satellite observations of the 2001 eruption of Mt. Cleveland, Alaska, *J. Volcanol. Geothermal Res.*, **135**, 51–73.
- Ellrod, G.P.; Connell, B.H.; Hillger, D.W. (2003). Improved detection of airborne volcanic ash using multispectral infrared satellite data, *J. Geophys. Res.*, **108**(D12), 4356, doi: 10.1029/2002JD002802.
- Evans, B.T.N. (1988). *An Interactive Program for Estimating Extinction and Scattering Properties of Moist Particulate Clouds* (Department of Defence Report MRL-R-1123), Defence Science & Technology Organisation, Materials Research Laboratory, Ascot Vale, Victoria, Australia.
- Fierstein, J. (2007). Explosive eruptive record in the Katmai region, Alaska Peninsula: An overview, *Bull. Volcanol.*, **69**, 469–509.
- Glenkova, I.; Seiz, G.; Zuidema, P.; Zhao, G.; Di Girolamo, L. (2007). Cloud top height comparisons from ASTER, MISR and MODIS for trade wind cumuli, *Rem. Sensing Env.*, **107**, 211–222.
- Gu, Y.; Rose, W.I.; Bluth, G.J.S. (2003). Retrieval of mass and sizes of particles in sandstorms using two MODIS IR bands: A case study of April 7 2001 sandstorm in China, *Geophys. Res. Lett.*, **30**(15), 1805, doi: 10.1029/2003GL017405.
- Gu, Y.; Rose, W.I.; Schneider, D.J.; Bluth, G.J.S.; and Watson, I.M. (2005). Advantageous GOES IR results for ash mapping at high latitudes: Cleveland eruptions 2001, *Geophys. Res. Lett.*, **32**, L02305, doi: 10.1029/2004GL021651.
- Hanstrum, B.N.; Watson, A.S. (1983). A case study of two eruptions of Mount Galunggung and an investigation of volcanic eruption cloud characteristics using remote sensing techniques, *Aust. Met. Mag.*, **31**, 131–177.
- Harris, D.M.; Rose, W. (1983). Estimating particle sizes, concentration, and total mass of volcanic ash clouds using weather radar, *J. Geophys. Res.*, **88**, 10969–10983.
- Harris, D.M.; Rose, W.; Roe, R.; Thompson, M.R. (1981). Radar observations of ash eruptions, in P.W. Lipman and D.R. Mullineaux (Eds.), *The 1980 Eruptions of Mount St. Helens, Washington* (USGS Circular 1250), U.S. Geological Survey, Reston, VA, pp. 323–333.
- Hasler, A.F. (1981). Stereographic observations from geosynchronous satellites: An important new tool for the atmospheric sciences, *Bull. Amer. Meteorol. Soc.*, **62**(2), 194–212.
- Hillger, D.W.; Clark, J.D. (2002a). Principal component image analysis of MODIS for volcanic ash, Part I: Most important bands and implications for future GOES imagers, *J. Appl. Meteorol.*, **41**, 985–1001.
- Hillger, D.W.; Clark, J.D. (2002b). Principal component image analysis of MODIS for volcanic ash, Part II: Simulation of current GOES and GOES-M imagers, *J. Appl. Meteorol.*, **41**, 1003–1010.
- Hofmann, D.J.; Rosen, J.M. (1984). On the temporal variation of stratospheric aerosol size and mass during the first 18 months following the 1982 eruptions of El Chichón, *J. Geophys. Res.*, **89**(D3), 4883–4890, doi: 10.1029/JD089iD03p04883.
- Holasek, R.E.; Rose, W.I. (1991). Anatomy of 1986 Augustine Volcano eruptions as recorded by multispectral image processing of digital AVHRR weather satellite data, *Bull. Volcanol.*, **53**, 420–435.
- Holasek, R.; Self, S. (1995). GOES weather satellite observations and measurements of the May 18, 1980, Mt. St. Helens eruption, *J. Geophys. Res.*, **100**, 8469–8487.
- Holasek, R.E.; Woods, A.W.; Self, S. (1996). Experiments on gas–ash separation processes in volcanic umbrella clouds, *J. Volcanol. Geothermal Res.*, **70**, 169–181.
- Holton, J. (2004). *An introduction to Dynamic Meteorology*, Academic Press, San Diego, CA, pp. 116–117.

- Ivlev, L.S.; Popova, S.I. (1973). The complex refractive indices of substances in the atmospheric aerosol dispersed phase, *Atmospheric Oceanic Physics*, **9**(10), 587–591.
- Kearney, C. (2010). The effects of silicate ash on thermal infrared sulfur dioxide retrievals, Unpublished doctoral dissertation, University of Bristol, Bristol, U.K.
- Kennedy, B.; Spieler, O.; Scheu, B.; Kueppers, U.; Taddeucci, J.; Dingwell, D.B. (2005). Conduit implosion during Vulcanian eruptions, *Geology*, **33**, 581–584, doi: 10.1130/G21488.1.
- King, M.D., Harshvardhan; Arking, A. (1984). A model of the radiative properties of the El Chichón stratospheric layer, *J. Climate Appl. Meteorol.*, **23**, 1121–1137.
- Lacasse, C.; Karlsdóttir, S.; Larsen, G.; Soosalu, H.; Rose, W.I.; Ernst, G.G.J. (2004). Weather radar observations of the Hekla 2000 eruption cloud, Iceland. *Bull. Volcanol.*, **66**, 457–473.
- Lane, S.J.; Gilbert, J.S.; Kemp, A.J. (1995). Electrical and chemical properties of eruption plumes at Sakurajima volcano, Japan. In: *Eighth Report of Geophysical and Geochemical Observations at Sakurajima Volcano*, Sakurajima Volcano Research Center, Sakurajima, Japan, pp. 105–127.
- Lutgens, F.K.; Tarbuck, E.J. (1986). *The Atmosphere: An Introduction to Meteorology*, Prentice-Hall, Englewood Cliffs, NJ, pp. 154–160.
- Lutgens, F.K.; Tarbuck, E.J. (1995). *The Atmosphere*, Prentice-Hall, Englewood Cliffs, NJ, 462 pp.
- Lynch, J.S.; Stephens, G. (1996). Mount Pinatubo: A satellite perspective of the June 1991 eruptions, in C. Newhall and R.S. Punongbayan (Eds.), *Fire and Mud*, University of Washington Press, Seattle, WA, pp. 637–646.
- Malingreau, J.-P.; Kaswanda (1986). Monitoring volcanic eruptions in Indonesia using weather satellite data: The Colo eruption of July 28, 1983, *J. Volcanol. Geothermal Res.*, **27**(1/2), 179–194.
- Manins, P.C. (1985). Cloud heights and stratospheric injections resulting from a thermonuclear war, *Atmos. Environ.*, **19**(8), 1245–1255.
- Marzano, F.S.; Vulpiani, G.; Rose, W.I. (2006). Microphysical characterization of microwave radar reflectivity due to volcanic ash clouds, *IEEE Trans. Geosci. Remote Sens.*, **44**, 313–327.
- Masuda, K.; Takashima, T. (1990). Deriving cirrus information using the visible and near-ir channels of the future NOAA-AVHRR radiometer, *Remote Sens. Environ.*, **31**, 65–81.
- Matson, M. (1984). The 1982 El Chichón volcano eruptions: A satellite perspective, *J. Volcanol. Geothermal Res.*, **23**, 1–10.
- Miller, T.P.; Casadevall, T.J. (1999). Volcanic ash hazards to aviation, in H. Sigurdsson, B. Houghton, S.R. McNutt, H. Ryman, and J. Stix (Eds.), *Encyclopedia of Volcanoes*, Academic Press, San Diego, CA, pp. 915–930.
- Miller, T.P., Chouet, B.A. (1994). The 1989–1990 eruptions of Redoubt Volcano: An introduction, *J. Volcanol. Geothermal Res.*, **62**, 1–10, doi: 10.1016/0377-0273(94)90025-6.
- Mosher, F.R. (2000). Four channel volcanic ash detection algorithm, *Preprint Volume: 10th Conference on Satellite Meteorology and Oceanography, January 9–14, 2000, Long Beach, California*, pp. 457–460.
- Newell, R.E.; Deepak, A. (Eds.) (1982). *Mount St. Helens Eruptions of 1980: Atmospheric Effects and Potential Climate Impact* (NASA Workshop Report, NASA SP-458), Scientific and Technical Information Branch, NASA, Washington, D.C., 119 pp.
- Oberhuber, J.M.; Herzog, M.; Graf, H.; Schwanke, K. (1998). Volcanic plume simulation on large scales, *J. Volcanol. Geothermal Res.*, **87**(1/4), 29–53.
- Oswalt, J.S.; Nichols, W.; O'Hara, J.F. (1996). Meteorological observations of the 1991 Mount Pinatubo eruption, in C. Newhall and R.S. Punongbayan (Eds.), *Fire and Mud: Eruption and Lahars of Mount Pinatubo, Philippines*, University of Washington Press, Seattle, WA, pp. 625–636.
- Pavlonis, M.J. (2010). Advances in extracting cloud composition information from spaceborne infrared radiances: A robust alternative to brightness temperatures, Part I: Theory, *J. Applied Meteorology and Climatology*, **49**, 1992–2012.
- Pavlonis, M.J.; Feltz, W.F.; Heidinger, A.K.; Gallina, G.M. (2006). A daytime complement to the reverse absorption technique for improved automated detection of volcanic ash, *J. Atmos. Oceanic Technol.*, **23**, 1422–1444.
- Pergola, N.; Tramutoli, V.; Marchese, F.; Scaffidi, I.; Lacav, T. (2004). Improving volcanic ash cloud detection by a robust satellite technique, *Remote Sens. Environ.*, **90**, 1–22.
- Pollack, J.B.; Toon, O.B.; Khare, B.K. (1973). Optical properties of some terrestrial rocks and glasses, *Icarus*, **19**, 372–389.
- Prata, A. J. (1989a). Observations of volcanic ash clouds using AVHRR-2 radiances, *Int. J. Remote Sensing*, **10**(4/5), 751–761.
- Prata, A.J. (1989b). Radiative transfer calculations for volcanic ash clouds, *Geophys. Res. Lett.*, **16**(11), 1293–1296.
- Prata, A.J.; Barton, I.J. (1994). Detection and discrimination of volcanic ash clouds by infrared radiometry, I: theory, in T.J. Casadevall (Ed.), *Volcanic Ash and Aviation Safety: Proceedings of the First International Symposium on Volcanic Ash and Aviation Safety, Seattle, WA* (USGS Bulletin 2047), U.S. Geological Survey, Reston, VA, pp. 305–311.
- Prata, A.J.; Bernardo, C. (2007). Retrieval of volcanic SO₂ column abundance from Atmospheric Infrared

- Sounder data, *J. Geophys. Res.*, **112**, D20204, doi: 10.1029/2006JD007955.
- Prata, A.J.; Grant, I.F. (2001). Retrieval of microphysical and morphological properties of volcanic ash plumes from satellite data: Application to Mt. Ruapehu, New Zealand., *Quart. J. Roy. Meteorol. Soc.*, **127**(576B), 2153–2179.
- Prata, A.J.; Kerkmann, J. (2007). Simultaneous retrieval of volcanic ash and SO₂ using MSG-SEVIRI measurements, *Geophys. Res. Lett.*, **34**, L05813, doi: 10.1029/2006GL028691.
- Prata, A.J.; Turner, P.J. (1997). Cloud-top height determination using ATSR data, *Remote Sens. Environ.*, **59**(1), 1–13.
- Prata, A.J.; Bluth, G.J.S.; Rose, W.I.; Schneider, D.J.; Tupper, A.C. (2001). Comments on failures in detecting volcanic ash from a satellite-based technique. *Remote Sens. Environ.*, **78**, 341–346.
- Press, W.H.; Flannery, B.P.; Teukolsky, S.A.; Vetterling, W.T. (1986). *Numerical Recipes*, Cambridge University Press, Cambridge, U.K., 818 pp.
- Przedpelski, Z.J.; Casadevall, T.J. (1994). Impact of volcanic ash from 15 December 1989 Redoubt volcano eruption on GE CF6-80C2 turbofan engines, in *Volcanic Ash and Aviation Safety: Proceedings of the First International Symposium on Volcanic Ash and Aviation Safety, Seattle, WA, July 1991* (USGS Bulletin 2047), U.S. Geological Survey, Reston, VA, pp. 129–135.
- Pyle, D.M. (1989). The thickness, volume and grain size of tephra fall deposits. *Bull. Volcanol.*, **51**(1), 1–15.
- Rose, W.I.; Kostinski, A.B.; Kelly, L. (1995a). *Real-Time C-Band Radar Observations of 1992 Eruption Clouds from Crater Peak, Mount Spurr Volcano, Alaska* (USGS Bull. 2139), U.S. Geological Survey, Reston, VA, pp. 19–26.
- Rose, W.I.; Delene, D.J.; Schneider, D.J.; Bluth, G.J.S.; Kruger, A.J.; Sprod, I.; McKee, C.; Davies, H.L.; and Ernst, G.J. (1995b). Ice in the 1994 Rabaul eruption: Implications for volcanic hazard and atmospheric effects, *Nature*, **375**, 477–479.
- Rose, W.I.; Bluth, G.J.S.; Ernst, G.G.J. (2000). Integrating retrievals of volcanic cloud characteristics from satellite remote sensors: A summary, *Phil. Trans. Roy. Soc. Lond., Ser. A: Mathematical, Physical, and Engineering Sciences*, **358**(1770), 1585–1606, doi: 10.1098/rsta.2000.0605.
- Rose, W.I.; Bluth, G.J.S.; Watson I.M. (2004). Ice in volcanic clouds: When and where? *Proceedings of the Second International Conference on Volcanic Ash and Aviation Safety*, Office of the Federal Coordinator for Meteorological Services and Supporting Research, Washington, D.C., Session 3, p. 61.
- Sawada, Y. (1987). *Study on Analysis of Volcanic Eruptions Based on Eruption Cloud Image Data Obtained by the Geostationary Meteorological Satellite (GMS)* (Technical Report 22), Meteorological Research Institute, Tsukuba, Japan, 335 pp.
- Sawada, Y. (1996). Detection of explosive eruptions and regional tracking of volcanic ash clouds with geostationary meteorological satellites (GMS), in R. Scarpa and R.I. Tilling (Eds.), *Monitoring and Mitigation of Volcano Hazards*, Springer-Verlag, Berlin, pp. 299–314.
- Schneider, D.J.; Rose, W.I.; Kelley, L. (1995). *Tracking of 1992 Eruption Clouds from Crater Peak of Mount Spurr Volcano, Alaska, Using AVHRR* (USGS Bulletin 2139), U.S. Geological Survey, Reston, VA, pp. 27–36.
- Schneider, D.J.; Rose, W.I.; Coke, L.R.; Bluth, G.J.S. (1999). Early evolution of a stratospheric volcanic eruption cloud as observed with TOMS and AVHRR, *J. Geophys. Res.*, **104**(D4), 4037–4050.
- Scollo, S.; Folch, A.; Coltelli, M.; Realmuto, V.J. (2010). Three-dimensional volcanic aerosol dispersal: A comparison between Multiangle Imaging Spectro-Radiometer (MISR) data and numerical simulations, *J. Geophys. Res.*, **115**, D24210, doi: 10.1029/2009JD013162.
- Searcy, C.; Dean, K.; Stringer, W. (1998). PUFF: A high-resolution volcanic ash tracking model, *J. Volcanol. Geothermal Res.*, **80**, 1–16.
- Simpson, J.J.; Hufford, G.; Pieri, D.; Berg, J. (2000). Failures in detecting volcanic ash from a satellite-based technique, *Remote Sens. Environ.*, **72**, 191–217.
- Simpson, J.J.; Berg, J.S.; Koblinsky, C.J.; Hufford, G.L.; Beckley, B. (2001). The NVAP Global Water Vapor Data Set: Independent cross-comparison and multi-year variability, *Remote Sensing of Environment*, **76**(1), 112–129, doi: 10.1016/S0034-4257(00)00199-1.
- Simpson, J.J.; Hufford, G.; Pieri, D.; Servranckx, R.; Berg, J. (2002). The February 2001 Eruption of Mount Cleveland, Alaska: Case study of an aviation hazard, *Weather and Forecasting*, **17**, 691–704.
- Sokolik, I.N.; Toon, O.B. (1999). Incorporation of mineralogical composition into models of the radiative properties of mineral aerosol from UV to IR wavelengths, *J. Geophys. Res.*, **104**(D8), 9423–9444.
- Sparks, R.S.J.; Bursik, M.I.; Carey, S.N.; Gilbert, R.S.; Glaze, L.S.; Sigurdsson, H.; Woods, A.W. (1997). *Volcanic Plumes*, John Wiley & Sons, New York, 574 pp.
- Stamnes, K.; Swanson, R.A. (1981). A new look at the discrete ordinates method for radiative transfer calculations in anisotropically scattering atmospheres, *J. Atmos. Sci.*, **38**, 387–399.
- Stohl, A.; Prata, A.J.; Eckhardt, S.; Clarisse, L.; Durant, A.; Henne, S.; Kristiansen, N.I.; Minikin, A.; Schumann, U.; Seibert, P. *et al.* (2011). Determination of time- and height-resolved volcanic ash emissions for quantitative ash dispersion modeling: The

- 2010 Eyjafjallajökull eruption, *Atmos. Chem. Phys. Discuss.*, **11**, 5541–5588.
- Tupper, A.; Oswalt, J.S. (2005). Satellite and radar analysis of the volcanic cumulonimbi at Mount Pinatubo, Philippines, 1991, *J. Geophys. Res.*, **110**(D09204), 1–15.
- Tupper, A.; Kinoshita, K.; Kanagaki, C. (2003). Observations of volcanic cloud heights and ash–atmosphere interactions, *WMO/ICAO Third Workshop on Volcanic Ash, Toulouse, France, September 29–October 3*.
- Tupper, A.; Carn, S.A.; Davey, J.; Kamada, Y.; Potts, R.J.; Prata, A.J.; Tokuno, M. (2004). An evaluation of volcanic cloud detection techniques during recent significant eruptions in the western Ring of Fire, *Remote Sens. Environ.*, **91**, 27–46.
- Tupper, A.; Itikarai, I.; Richards, M.; Prata, F.; Carn, S.; Rosenfeld, D. (2007). Facing the challenges of the International Airways Volcano Watch: The 2004/05 eruptions of Manam, Papua New Guinea, *Weather and Forecasting*, **22**(1), 175–191.
- Turco, R.P., Toon, O.B., Whitten, R.C., Hamill, P., and Keesee, R.G. (1983). The 1980 eruptions of Mt. St. Helens: Physical and chemical processes in the stratospheric clouds, *J. Geophys. Res.*, **88**, 5299–5319.
- Turco, R.P. (1992). Physical and chemical processes of volcanic interactions with the atmosphere, in L.T. Simarski (Ed.), *Volcanism and Climate Change* (AGU Special Report), American Geophysical Union, Washington, D.C., p. 5.
- Volz, F.E. (1973). Infrared optical constants of ammonium sulfate, Sahara dust, volcanic pumice, and fly ash, *Appl. Opt.*, **12**(3), 564–568.
- Walker, G.P.L. (1971). Grain-size characteristics of pyroclastic deposits, *J. Geology*, **79**, 696–714.
- Watkin, S.C. (2003). The application of AVHRR data for the detection of volcanic ash in a Volcanic Ash Advisory Center, *Meteorol. Appl.*, **10**, 301–311.
- Watson, I.M.; Realmuto, V.J.; Rose, W.I.; Prata, A.J.; Bluth, G.J.S.; Gu, Y.; Bader, C.E.; Yu, T. (2004). Thermal infrared remote sensing of volcanic emissions using the moderate resolution imaging spectroradiometer, *J. Volcanol. Geothermal Res.*, **135**, 75–89.
- Webley, P.W.; Atkinson, D.; Collins, R.L.; Dean, K.; Fochesatto, J.; Sassen, K.; Cahill, C.F.; Prata, A.J.; Flynn, C.J.; Mizutani, K. (2008). Predicting and validating the tracking of a volcanic ash cloud during the 2006 eruption of Mt. Augustine volcano, *Bull. Amer. Meteorol. Soc.*, 1647–1657, doi: 10.1175/2008BAMS2579.1, .
- Wen, S.; Rose, W.I. (1994). Retrieval of sizes and total masses of particles in volcanic clouds using AVHRR bands 4 and 5, *J. Geophys. Res.*, **99**(D3), 5421–5431.
- Winker, D.M.; Hunt, W.H.; McGill, M.J. (2007). Initial performance assessment of CALIOP, *Geophys. Res. Lett.*, **34**, L19803, doi: 10.1029/2007GL030135.
- Wood, J.; Scott, C.; Schneider, D. (2007). WSR-88D radar observations of volcanic ash, *Fourth International Workshop on Volcanic Ash*, World Meteorological Organization (WMO) in close collaboration with the International Civil Aviation Organization (ICAO) and the Civil Aviation Authority of New Zealand, Rotorua, New Zealand.
- Woods, A.W.; Self, S. (1992). Thermal disequilibrium at the top of volcanic clouds and its effect on estimates of the column height, *Nature*, **355**, 628–630.
- Wylie, D.P.; Santek, D.; O’Starr, D. (1998). Cloud-top heights from GOES-8 and GOES-9 stereoscopic imagery, *J. Appl. Meteorol.*, **37**, 405–413.
- Yu, T.; Rose, W.I.; Prata, A.J. (2002). Atmospheric correction for satellite-based volcanic ash mapping and retrievals using split window IR data from GOES and AVHRR, *J. Geophys. Res.*, **107**(D16), 4311, doi: 10.1029/2001JD000706.
- Zobin, V.M.; Jiménez, M. (2008). Some regularity in the process of re-awakening of andesite and dacite volcanoes: Specific features of the 1982 El Chichón volcano, México reactivation, *J. Volcanol. Geothermal Res.*, **175**(4), 482–487

Remote sensing of gas emissions from volcanoes

Fred Prata, Gregg Bluth, Cynthia Werner, Vince Realmuto, Simon Carn, Matt Watson

6.1 INTRODUCTION

There are many good reasons to study and observe gaseous emissions from volcanoes. Quantitative measurements provide insights into volcanic processes occurring deep within a volcano, at more shallow levels where gases exsolve from magma and escape via fissures and cracks, into eruption processes at the surface and within the atmosphere. Emission rate monitoring of reawakening volcanoes helps constrain forecasts of eruption timing and magnitude. Once in the atmosphere these gases can be hazardous to life and the environment and have global consequences by affecting the radiative balance and chemistry of the atmosphere. Eruptive gaseous emissions from North Pacific volcanoes enter the atmosphere where the tropopause is low (~6–8 km) and hence have a greater chance of reaching the stable stratosphere (Halmer and Schmincke, 2003) where the gases, particles, and aerosols can reside for months to years and have a local or global climate impact. In the last 10 years there have been enormous advances in the technology used for remotely detecting volcanic gases. Many of the advances have come through clever use of satellite-borne sensors not originally intended for monitoring volcanic gases. Other advances have come through deliberate planning and updating of older satellite technology; for example, with the development of the Ozone Monitoring Instrument (OMI), improved using experience with the Total Ozone Mapping Spectrometer (TOMS) and the change in specification of a channel on the Ad-

vanced Baseline Imager (ABI) on the Geostationary Operational Environmental Satellite (GOES-R) for SO₂ monitoring. Still other advances have come from unexpected quarters: the development and now widespread use of ground-based mini-DOAS ultraviolet (UV) spectrometers and the development of thermal infrared and UV camera systems are two examples. The volcanoes of the North Pacific (NOPAC) are prime examples of where the use of remote sensing is having a large impact. While the need for consistent, long-term evaluations of volcanic emissions is great, the difficulties associated with making routine field measurements at these volcanoes, the climatic conditions, potential aviation hazards, logistical and economical constraints, and the high number of volcanoes that need monitoring increase the appeal of remote sensing as a measurement tool for the NOPAC.

This chapter is intended to provide an introductory level discourse on the remote-sensing techniques and instruments used to detect and quantify volcanic gases, with an emphasis on NOPAC region volcanoes. We describe both satellite and ground-based technologies from the ultraviolet to the infrared. The evolution of the techniques is portrayed through examples based mostly on satellite retrievals, and we provide an assessment of what advances are likely in the near future. A discussion of ground-based remote-sensing systems is included as well; although this field is evolving rapidly, there have already been some compelling developments and we suggest this is an area of study that is likely to become increasingly important for monitoring

gases in remote volcanic regions. Each of the technologies and retrieval schemes has disadvantages and advantages and these are discussed in separate subsections of this chapter and in more detail in Chapter 5.

This chapter is organized as follows: we begin by describing volcanic gases from the perspective of Earth history. This is followed by a brief discussion of three important areas where volcanic gas measurements can make a contribution to understanding volcanic processes, volcanic hazards, and volcanic effects on climate. The remainder of the chapter discusses the instruments used to remotely sense volcanic gases and describes the principles of the most commonly used retrieval algorithms. Special emphasis is given to measuring SO₂ from space and from the ground, because this gas is preponderant in volcanic emissions and amenable to detection in the UV and thermal IR. We conclude with some comments concerning advances in remote-sensing technology and how these are likely to lead to better constraints on volcanic emissions and improved inventories of volcanic gas species.

6.1.1 The origin of gases in the Earth's atmosphere

The atmosphere consists primarily of nitrogen and oxygen gases with small amounts of the principal trace gases: argon, carbon dioxide, neon, helium, krypton, xenon, hydrogen, methane, nitrous oxide, and carbon monoxide. The gaseous composition of the Earth's atmosphere has changed over long (~Gyr) time scales and the primordial atmosphere was probably formed by a process of accretion of volatiles from large impacts (so-called "ingassing"). Oxygen is thought to have arisen, perhaps ~2.3 Gyr ago, through the action of life; before that, the planet was warmed by methane, some 100 times more abundant than today's levels. Volcanic gases have played a role in the cycling of important elements between the atmosphere, land, and ocean. Oxidation of volcanic gases affects the levels of atmospheric O₂, and volcanic outgassing of SO₂/H₂S and CO₂ contribute to the important sulfur cycle and carbonate-silicate cycle. Volcanic gases therefore have important implications for the composition of the atmosphere and remain the major source of gaseous input to the atmosphere, although individually other sources account for greater input (e.g., CO₂ from burning fossil fuels). There have been many measurements of gas emission rates at individual volcanoes which demon-

strate the high variability of emissions between different volcanoes and the high variability with time at particular volcanoes (e.g., Malinconico, 1979; Stoiber *et al.*, 1986; Marty and Giggenbach, 1990; Casadevall *et al.*, 1994; Oppenheimer *et al.*, 1998a; Burton *et al.*, 2000). Most of these gas emission rate estimates contain large errors and variabilities, and new measurement techniques are undergoing continual refinement to improve the estimates. Table 6.1 shows the emission rates for the main gases emitted from volcanic sources (eruptions, fumaroles, lava lakes, etc.), into the atmosphere. These are the current best estimates of the global input of volcanic gases to the atmosphere.

Generally speaking, H₂O is by far the largest component of volcanic gas emissions but, because of the large background atmospheric abundance, other numerous large sources, and high variability, volcanoes are not regarded as an important atmospheric source. The presence or release of H₂O from magmas affects the explosiveness of eruptions through thermodynamical considerations of the change of phase of H₂O. Its presence also affects important chemical transformations involving SO₂. Thus, it is of some interest to have knowledge of the water vapor budget in eruptions. The next largest gaseous component is CO₂. There are several volcanoes that emit copious amounts of CO₂ (e.g., Mt. Etna, Popocatepetl, Yellowstone) (e.g., Gerlach, 1991; Werner and Brantley, 2003), but the total global emissions from volcanoes (~145–255 Tg yr⁻¹ according to some estimates) are negligible compared with other sources, such as anthropogenic and biotic (~22 Pg yr⁻¹). However, knowledge of the volcanogenic CO₂ emission rate is important for understanding volcanic processes and diagnosing the likely course of volcanic unrest. The volcanic sulfur-bearing gases, SO₂ and H₂S, represent some 15% of all volcanic emissions to the atmosphere and, because volcanoes can inject these gases high into the atmosphere at stratospheric levels, the volcanic source is dominant over other natural sources. Pyle *et al.* (1996) have estimated that the annual input of SO₂ to the stratosphere from explosive eruptions is ~1 Tg yr⁻¹, while the literature provides estimates ranging from 120 Tg yr⁻¹ (see the references in Table 6.1). Interannual variability is high, because the input from one large eruption can dominate the average and there is significant short-term variability in major eruption frequency. For example, Pinatubo emitted approximately 18 Tg of SO₂ into the atmosphere in June 1991

Table 6.1. Current best estimates of the major volcanic gas emission rates to the atmosphere.

Gas	Emission rate (Tgyr ⁻¹)	Reference
H ₂	0.24	Cadle (1980)
H ₂ O	~700*	Stoiber (1995)
HF	0.7–8.6 0.06–6	Halmer <i>et al.</i> (2002) Symonds <i>et al.</i> (1988)
HBr	$2.6\text{--}43.2 \times 10^{-3}$ 3.3×10^{-3}	Halmer <i>et al.</i> (2002) Stoiber <i>et al.</i> (1983)
HCl	1.2–170 0.4–11	Halmer <i>et al.</i> (2002) Stoiber <i>et al.</i> (1987)
H ₂ S	1.5–37.1 0.21 2.8	Halmer <i>et al.</i> (2002) Bandy <i>et al.</i> (1982) Andres and Kasgnoc (1998)
SO ₂	7.5–10.5 7.8 10.0 13.0 13.4 15.2 18.7 20.0	Halmer <i>et al.</i> (2002) Cadle (1975) Stoiber and Jepsen (1973) Bluth <i>et al.</i> (1993) Andres and Kasgnoc (1998) Berresheim and Jaeschke (1983) Stoiber <i>et al.</i> (1987) Graf <i>et al.</i> (1997)
OCS	10^{-4} –0.3 0.022 6×10^{-3} –0.09 0.3	Halmer <i>et al.</i> (2002) Bandy <i>et al.</i> (1982) Belviso <i>et al.</i> (1986) Andres and Kasgnoc (1998)
CS ₂	10^{-5} – 4×10^{-2} 0.022 0.3	Halmer <i>et al.</i> (2002) Bandy <i>et al.</i> (1982) Andres and Kasgnoc (1998)
CO ₂	100–500 65	Gerlach (1991) Williams <i>et al.</i> (1992)
CO	0.02	Cadle (1980)
CH ₄	0.34	Cadle (1980)
BrO	0.03 (Br)	Bobrowski <i>et al.</i> (2003)

* Best approximation.

and the major portion was stratospheric. SO₂ converts to sulfate aerosol (H₂SO₄) with a stratospheric e-folding time of approximately 3 weeks. The aerosol resides in stratospheric layers at altitudes of 20–30 km and has an effect on the radiative balance of the Earth–atmosphere system. Pinatubo aerosols are thought to have cooled the Earth’s surface by

~0.5 K on average between 1991 and 1993. In comparison, Nyamuragira Volcano is estimated to have emitted at least 25 Tg between 1979 and 2005 but, as the majority of these effusive emissions remained in the troposphere, little atmospheric impact was registered. When compared with the warming trend observed over the last 30 years of ~0.01 K yr⁻¹, the volcanic effect is transient but large. Figure 6.1 shows the cumulative net forcing of climate from four different mechanisms, based on the data from Crowley (2000). The steadily increasing trend in net forcing is the “enhanced greenhouse effect”, principally due to increases in CO₂, while the rapid excursions from this trend (negative net forcing) are due to stratospheric aerosols from volcanic eruptions. Tropospheric aerosols (non-volcanic) and solar irradiance also affect climate, while changes in stratospheric H₂O and ozone (not shown) have much smaller effects on the net forcing of climate.

Other volcanic gases may also affect the Earth’s atmosphere. HCl is a less common component of overall volcanic emissions but can be significant at some volcanoes (e.g., White Island in New Zealand and Erebus in Antarctica). There has been some suggestion that volcanic HCl may contribute to ozone depletion by increasing stratospheric Cl content, and this may be a bigger issue for high-latitude (low-tropopause) volcanoes. However, as indicated earlier, the dominance of H₂O in volcanic gas emissions and particularly in the ice phase would cause the HCl to be scavenged on a time scale of a few days (Textor *et al.*, 2003, 2004). Some relevant aspects of the atmospheric chemistry of volcanic gases and their impact on climate are discussed by McKeen *et al.* (1984), Seinfeld and Pandis (1998), and Pitari *et al.* (2002). CH₄, HF, and N₂ are quite minor components of volcanic emissions and have little enduring atmospheric effects. H₂ is the most abundant reduced gas in volcanic surface emissions and over long time scales is involved in the Earth’s oxygen and hydrogen balance.

Volcanic gases also have important local environmental impacts and hazardous effects on health. SO₂ is responsible for acid rain, and vegetation close to a volcanic source of SO₂ suffers stunted growth and greater susceptibility to diseases. Exposure to large amounts of CO₂ can cause unconsciousness and possible death in humans. The large, near-instantaneous outgassing of CO₂ from Lake Nyos, Cameroon in 1986 was reported to have caused about 1,700 deaths. Other deaths at volcanoes have been reported due to CO₂ asphyxiation, making CO₂ the most dangerous vol-

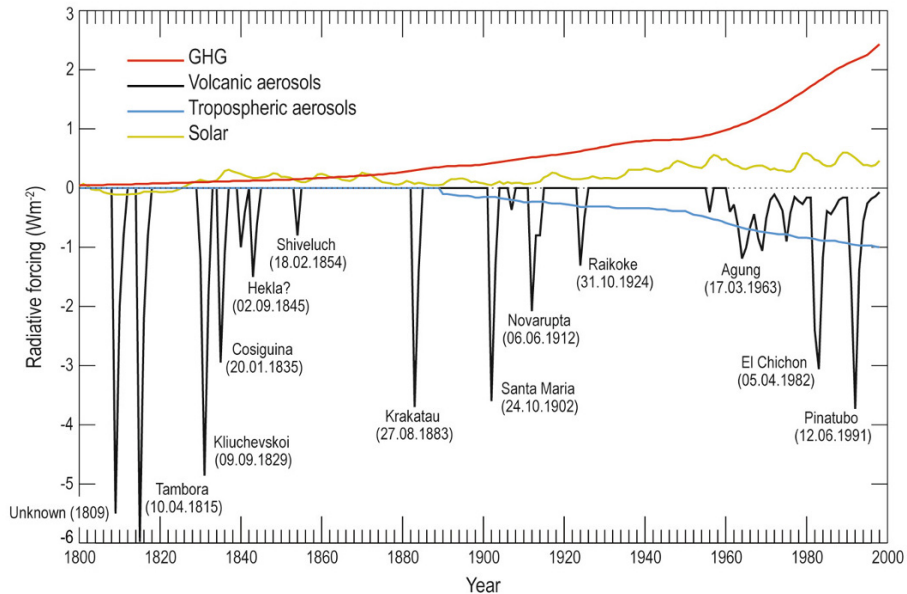


Figure 6.1. Radiative forcings due to four different mechanisms. The largest negative forcing is that due to stratospheric aerosols, largely volcanic aerosol forcing. The data are plotted at yearly intervals and the volcanic eruption thought most likely to have caused the spike in stratospheric sulfate loading is indicated on the plot. In some cases more than one eruption may have been responsible and, in one case (1809 eruption), the volcano responsible is not known (drawn from data reported by Crowley, 2000).

canic gas. High concentrations of H_2S can cause poisoning, while SO_2 has been linked with asthma and some other respiratory problems in humans. Continuous outgassing of SO_2 , HCl , HF from Laki fissure eruptions in 1783 are believed to have caused continental-scale environmental and health effects and possibly altered the local climate for several years (Thordarson and Self, 2003) and caused a significant climate perturbation in the northern hemisphere north of 30°N (Oman *et al.*, 2005).

6.2 VOLCANIC GASES

6.2.1 Volcanic processes

The emission rates and ratios of certain volcanic gases (e.g., CO_2 , SO_2 , and CO_2/SO_2 ratios) provide useful insights into volcanic processes occurring deep within volcanoes. Volcanic gas emission data provide a means for anticipating possible eruptive scenarios. The CO_2 emission rate and its change with time can be used to forecast volcanic unrest or at least a change in the volcano's current eruptive state. Ground-based and aircraft-based measure-

ments of CO_2 at volcanoes have been made but measurements from satellites, while highly desirable, are not yet feasible. Future CO_2 space-based instruments such as OCO and ASCENDS (NRC, 2007) will not provide sufficient sampling resolution (spatial or temporal) to have significant value for volcano research and there is a need for a dedicated instrument. The situation is quite different for another important volcanic gas: SO_2 . SO_2 is a key species since it is the stable S-bearing gas at high temperatures and low pressures. Increases in SO_2 emissions may therefore signal the ascent of fresh magma to shallow depths within a volcano. Conversely, decreasing SO_2 and other gas emissions from an active system sometimes indicate plugging or sealing of the volcanic conduit and an increased potential for explosive eruption or, alternatively, a waning eruption. Interpretation of SO_2 emission data must also take into account the potential action of hydrothermal and other subsurface processes prior to emission, such as "scrubbing" (dissolution) of water-soluble gases such as SO_2 by groundwater or a hydrothermal system and the modulation of measured SO_2 emissions by meteorological and atmospheric processes (e.g.,

Oppenheimer *et al.*, 1998b). Measurement of volcanic gas ratios can be a powerful tool for diagnosing volcanic processes and the source of volcanic emissions. For example, the ratios of CO_2/He and $\text{H}_2\text{O}/\text{CO}_2$ in volcanic gases tend to have characteristic values in convergent plate, divergent plate, and hot-spot settings (Delmelle and Stix, 2000). Over the last decade, ground-based Fourier transform infrared (FT-IR) spectroscopy has been developed for simultaneous retrieval of IR-active gas species and the determination of gas ratios. Using FT-IR spectroscopy, Love *et al.* (1998) measured an increase in the ratio of SiF_4/SO_2 just prior to an explosive eruption of Popocatepetl. Measurements of ratios of HCl/SO_2 have been used to infer lava dome growth rates at Soufrière Hills Volcano, Montserrat (Oppenheimer *et al.*, 2002). In addition to these applications to volcano monitoring, FT-IR measurements are providing constraints on the volcanic contribution to global budgets of several gases (e.g., HCl , HF).

6.2.2 Volcanic hazards

Volcanic gases pose a hazard to health and a potential hazard to aviation. The hazard to aviation is discussed in Chapters 1, 5, 7, and 9 in the context of volcanic ash, while here we consider the measurement of volcanic gases from the viewpoint of the potential impact of an aircraft encounter with SO_2 gas and sulfate acid aerosol. First, we briefly discuss the health effects of volcanic gases.

Volcanic gases can affect human, animal, and environmental health (Allen *et al.*, 2000; Delmelle *et al.*, 2002; Horwell and Baxter, 2006). SO_2 can affect the respiratory system and has been linked to asthma, is toxic at mixing ratios above 10 ppm,¹ and can cause death at concentrations >20 ppm. Typical downwind concentrations at surface level seldom exceed a few parts per million in dilute volcanic plumes, but concentrations well in excess of this may be experienced close to the source or during violent degassing episodes. Remote-sensing methods can easily detect concentrations of 10 ppm*m; in fact, the satellite-based OMI is able to detect concentrations as low as 10^{-1} ppm*m if the gas is distributed over a large area.

CO_2 is also a toxic gas at high concentrations. It is heavier than air and will displace air in confined

places, which can lead to asphyxiation and death. Gas concentrations are expressed as a percentage of the gas in air by volume ($1\% = 10^4$ ppmv). At $\sim 3\%$ concentration, CO_2 causes noticeable effects (breathing difficulties, headaches), with worsening effects up to 10% concentration. Beyond 15%, death is possible and loss of consciousness can occur within 10–15 minutes. A concentration of 10% corresponds to 10^5 ppmv which exceeds ambient levels by a factor of ~ 300 . There is now great interest in detecting leaks, both large and small, from geosequestered CO_2 experiments designed to reduce CO_2 emissions to the atmosphere. Remote-sensing technologies are being developed for monitoring leaks (e.g., Etheridge *et al.*, 2005) and these are focusing on laser and infrared systems; thus, these methods will certainly soon be applied towards detecting volcanogenic CO_2 . Large CO_2 emissions (e.g., from Etna with an estimated $13 \pm 3 \text{ Tg yr}^{-1}$; Allard *et al.*, 1991) are currently detectable from space (e.g., from AIRS, Chahine *et al.*, 2006 or SCIAMACHY, Bovensmann *et al.*, 1999).

Other important gases that have effects on health include H_2S , HCl , and HF . An excellent discussion of the health effects of these gases and health guidelines is provided on the International Volcanic Health Hazard Network website (see <http://www.ivhnn.org/>).

As most of the NOPAC volcanoes are distant from population centers, the direct health effects from volcanic gases are not considered of utmost importance for the region. The hazards to aircraft and the ability to forecast unrest, eruption intensity, and subsequent plume movement are important for the region. This topic is dealt with in Chapters 1, 5, 7, and 9, but a brief mention is made here for completeness.

During explosive volcanic activity, the particulates and gases emitted can reach heights that intersect typical cruise altitudes for jet aircraft. Ash is known to cause turbine jet engines to stall and its abrasive nature damages turbine blades, windows, and onboard avionics equipment (e.g., pitot-static tubes) and can be detected using satellite sensors (see Chapter 5) and ground-based instruments (Prata *et al.*, 1993). Under some circumstances it is difficult to detect airborne volcanic ash using remote-sensing techniques, while for the reasons mentioned above it is crucial to know its whereabouts both in the horizontal and vertical domains. Whenever ash and SO_2 erupt together it is natural to assume that by detecting the presence of one

¹ 1 ppm*m = 10.76 DU (at STP); 1 DU = 2.687×10^{16} mol cm^{-2} ; 1 ppm*m = 2.5×10^{15} mol cm^{-2} ; 1 DU = 1 matm-cm.

substance it is possible to infer the presence of the other. When there is little or no vertical wind shear the detection of SO₂ can be used as a surrogate for the detection of the greatly more hazardous ash. This has motivated researchers to develop satellite-based SO₂ detection schemes to assist aviation authorities locate volcanic ash hazards. These schemes often do not require much accuracy, although it is desirable to have a low minimum detection threshold. SO₂ in itself may not be a hazard to aviation (little is known about this at the time of writing), but once converted to sulfate aerosol the acid can cause degradation of external surfaces, most notably etching of windows. Because the human sensory system can detect SO₂ and H₂S at quite low levels of concentration, advice to pilots includes alertness to sulfur odors that might suggest an encounter with a volcanic ash cloud. Unfortunately, the turbulent atmosphere often ensures that volcanic gases and ash (particles) separate in the vertical and any wind shear will then cause the gas and ash to move in different directions and destroy the underlying assumption of collocation.

Measurements of precursor activity (e.g., change in the emission rate or change in the ratio of important gases) can give important early indications of subsequent volcanic activity. Remote sensing, especially ground based, can play a role in providing these measurements. When coupled with other data (e.g., seismic) a great deal can be inferred about the likelihood and severity of subsequent activity and, hence, more reliable aviation warnings can be made.

6.2.3 Volcanic gases and climate effects

The atmosphere can be divided into several distinct parts based primarily on the way that temperature varies with altitude. The troposphere is the region where most of the weather resides and is characterized by decreasing temperature with height at a mean adiabatic rate of about 7 K km⁻¹. The “free” troposphere is a region of the troposphere where air motions are less restricted by the effects of the surface (e.g., friction) and where transport over long distances (thousands of kilometers) and long time scales (days) can occur. At some point in the troposphere the temperature stops decreasing and a stable region is reached where the temperature reaches a minimum or stays constant with height. This is the tropopause and its height is variable in space and time. The tropopause is generally highest near the equator and at low latitudes where heights

of 15–18 km are common. At high latitudes the tropopause can be much lower, in the region of 5–8 km. Above the tropopause temperatures start to rise again and this part of the atmosphere is quite stable as rising air experiences warmer temperatures. The main cause of the temperature increase in this part of the atmosphere is due to absorption of solar ultraviolet radiation by ozone. This region, called the stratosphere, extends from the tropopause to about 50 km, where once again temperatures start to decrease. Beyond the stratosphere is the mesosphere which is not considered to be important in the discussion of volcanic gases and climate effects. Because of this vertical temperature structure, which strongly affects the ability of air to rise or fall, there is a clear distinction between climate-perturbing volcanic eruptions; namely, those that inject gases and particles that penetrate the tropopause and enter the stratosphere where these substances can have long residence times, and those that remain in the troposphere which may create local or perhaps regional consequences. Stratospheric injections have the greatest effect on global climate.

As Figure 6.1 illustrates, there are significant radiative perturbations and climate effects following large eruptions. The largest known eruptions (e.g., Krakatau, 1883, Tambora, 1815, and Toba, ~75 kyr) occurred before direct measurements of stratospheric aerosols were available. This has limited our knowledge of climate sensitivity to large-scale volcanic forcing and has demonstrated the need for quantitative, long-term measurements of volcanic gas emissions. The main cause for the reduction of surface temperature is reflection of incoming shortwave (solar) radiation by sulfuric acid aerosol (sulfate aerosol). This aerosol exists in stratospheric layers (above ~17 km) and is the product of chemical conversion of SO₂ to H₂SO₄. The sulfate aerosol layers are chemically quite stable, but diminish in concentration with time, and are replenished sporadically by injection of volcanic SO₂. The climate effect is quite complex (e.g., Bluth *et al.*, 1997; Robock, 2000), depending not only on the stratospheric loading of SO₂ but also on the timing and location of the eruption event. The most important factor is the delivery of SO₂ into the stratosphere. Lower-tropospheric SO₂ is quickly removed by wet and dry deposition processes and has a relatively small impact on climate. Stratospheric SO₂ converts to sulfate aerosol on time scales of weeks, depending on temperature and the availability of moisture, and can remain in the

stratosphere for 1–2 years. Volcanic SO₂ emissions to the free troposphere (>5 km) have intermediate lifetimes and are believed to contribute significantly to the tropospheric sulfate burden (e.g., Graf *et al.*, 1997) and, hence, may play a role in climate forcing.

High-latitude (>50° of latitude) volcanic eruptions have a greater chance of causing a climatic impact because the height of the tropopause is lower (e.g., 6–8 km) or not much higher than Kamchatkan volcanic summits at high latitudes, and so SO₂ has a greater chance of penetrating the tropopause and reaching the stratosphere. However, as Oman *et al.* (2005) have shown, high-latitude eruptions cause a different global pattern of climate change than low-latitude eruptions. The principle reason for this is the confinement of high-latitude eruptions to the hemisphere in which they occur, whereas low-latitude eruptions can spread sulfates to ±60° latitude. Oman *et al.* (2005) found that a model simulation of the 1912 Katmai (~58.3°N) eruption caused a decrease in the intensity of the Asian summer monsoon. The complex dynamical response of the climate system to volcanic forcing makes it difficult to predict the detailed climate impact of stratospheric eruptions. The local effects are more predictable, particularly for long-lived eruptions with large amounts of degassing.

6.3 REMOTE-SENSING DETECTION TECHNIQUES

The previous discussion has shown that volcanic gases have important impacts on the Earth system and that SO₂ gas is of particular importance. Not surprisingly, scientists have concentrated on developing safe and accurate methods for measuring SO₂, and remote sensing is well suited to this task. The main volcanic gas measured by many remote-sensing instruments is SO₂ and this is justified on the basis of the importance of this gas in volcanic and atmospheric processes. CO₂ and H₂O can both be measured with remote-sensing techniques, but as indicated previously these gases are already abundant in the atmosphere and better accuracies are obtainable currently by *direct* gas-sampling methods from the ground and airborne (Gerlach *et al.*, 1997; McGee *et al.*, 2001; Werner *et al.*, 2006a, 2008).

In the following sections we describe the remote-sensing techniques and retrieval schemes used for monitoring volcanic gases from space and from the ground.

Figure 6.2 shows a schematic of the electromagnetic spectrum from the far UV (0.2 μm) to the infrared (15 μm) illustrating the regions that have been exploited by satellite, ground-based, and airborne remote-sensing technologies to measure volcanic gases. The figure covers three wavelength ranges: (a) 0.2–1.2 μm, (b) 1–5 μm, and (c) 4–20 μm. Figure 6.2a shows the locations of the TOMS, OMI, GOME, and SCIAMACHY channels and the region usually covered by ground-based mini-DOAS instruments. These all cover the strong SO₂ absorption region near 300 nm. MODIS has a set of discrete bands (or channels) extending from the near UV (~400 nm) up to the near IR (~900 nm). The figure also shows where some of the principal atmospheric processes occur (e.g., aerosol scattering and Rayleigh scattering) and indicates the major gaseous absorption features in this part of the spectrum (e.g., the Hartley–Huggins and Chappuis ozone bands). Figure 6.2b shows three panels: the upper two show the line strengths of some important volcanic gases. These simply indicate the regions where these gases are active (i.e., they have an absorption/emission band) and no attempt has been made to consider line-broadening effects or interference effects from other gases. The lower panel includes more MODIS bands, AVHRR and ATSR channels, and the regions covered by the ASTER, MOPITT, and AIRS channels. FT-IR is also used in this spectral region, mostly to measure absorption in the 3–5 μm region. As before, the main absorption regions of some important volcanic gases are indicated on the plot. Figure 6.2c extends the spectral region out to 20 μm. The main part of this region used for atmospheric remote sensing lies between 8 and 14 μm, the so-called “dirty window”. MODIS, AVHRR, and ATSR all have channels in this window, principally for surface viewing, but the channels at 11 μm and 12 μm have proved to be very useful for studying volcanic ash. Channels near to 8.6 μm can be used to measure SO₂ and, as shown in Section 6.4.1, channels near 7.3 μm can be used to measure upper-troposphere/lower-stratosphere (UTLS) SO₂. It seems also likely that high spectral resolution spectrometers and interferometers can measure SO₂, H₂SO₄, CO₂ and perhaps H₂S, OCS, and CH₄ within the region 6–15 μm. Beyond 15 μm, the atmosphere is quite opaque, largely due to CO₂ and H₂O absorption, but several gases (O₂ and SO₂) can also be measured at microwave frequencies (e.g., using the Microwave Limb Sounder or MLS). We will refer to this figure later in relation

to some of the techniques used to measure volcanic gases.

6.4 MONITORING VOLCANIC GASES

As we have seen, many volcanic gases have absorption features in the IR region of the electromagnetic spectrum (Figure 6.2a–c). Water vapor has a large number of bands, lines, and continuum features throughout the IR region from 1 to 30 μm . Between 3–4 μm and 8–12 μm there are atmospheric windows that are less affected by water vapor absorption and can be exploited to study other gases. The choice of spectral region or band, for measuring gas concentrations, is done by careful study of the absorption band, minimization of the interference from other gas species, signal-to-noise considerations, and the availability of technology to make accurate measurements. There is no shortage of choice for measuring water vapor concentrations but, because of its abundance and variability as explained previously, volcanic water vapor has not been extensively measured. There are also alternative technologies for measuring many volcanic gases, including water vapor. The next most abundant volcanic gas, CO_2 , also has many absorption bands (see Figure 6.2a–c) but, like water vapor, CO_2 is abundant in the background atmosphere. Above-ambient CO_2 has been measured at several Cook inlet volcanoes using an IR spectrometer (MIRAN) and the 4.3 μm CO_2 absorption band (Doukas, 1995). Interferometers are well suited to the task of measuring volcanic CO_2 as these instruments have sufficient precision and versatility to permit both emission and absorption measurements and can be adapted to avoid interference from other gaseous species. FT-IR interferometry may be able to measure isotopic compositions of CO_2 (Cambaliza *et al.*, 2005), which can provide information on the origin of volcanically degassed CO_2 and distinguish this source from background ambient sources.

Satellite monitoring of both CO_2 and SO_2 is possible. For CO_2 the major goal over the next several decades will be to characterize the sources and sinks of this important gas for climate studies. There is a less urgent need to measure SO_2 for climate (although this gas does play an important role in climate) but, as it turns out, SO_2 is much easier to measure than CO_2 and current sensors can be used for volcanic studies. This is not the case for CO_2 , and it is unlikely that the planned dedicated

CO_2 sensors (e.g., OCO and ASCENDS) will be able to provide the information needed to improve volcanic process studies and volcanic eruption forecasting. For this reason discussion of satellite sensing is restricted to SO_2 and only brief mention of CO_2 satellite sensing is made.

Gas concentrations can also be measured using a combination of remote sensing and *in situ* sampling. In some recent research, measurements of passive degassing at volcanoes have been obtained by using COSPEC for SO_2 , Interscan electrochemical sensor-based instruments for SO_2 and H_2S , and LI-COR infrared analyzers for CO_2 , all mounted in an aircraft (Gerlach *et al.*, 1997; McGee *et al.*, 2001; Werner *et al.*, 2006b, 2008). The movement of the aircraft provides a means to obtain two-dimensional (height–horizontal distance) concentration maps of the gases. FT-IR and other types of IR spectrometers must employ scanning or be used from a moving platform in order to acquire two-dimensional concentration maps (McGee and Gerlach, 1998). Imaging devices are not yet in common use.

Ground-based and airborne imaging IR spectrometers and thermal cameras have been used in the field and show great promise for doing quantitative gas concentration measurements. The Phoenix thermal imaging system (Prata and Bernardo, 2007) uses a modified thermal imaging camera to image SO_2 and particulates. The generic form of this instrument includes an uncooled microbolometer detector array, filter wheel, and blackbody shutter. The use of a blackbody allows the camera to be calibrated and for thermal images acquired at different wavelengths to be compared, differenced, and used in sophisticated retrieval schemes to derive the microphysical properties of particulates and SO_2 gas concentrations.

Image sampling at 30–60 Hz is possible, and with multiple filters and frame averaging image data can be acquired at several wavelengths at intervals of a few tens of seconds.

6.4.1 Space-based monitoring

Space-based monitoring of the atmosphere, mainly by instruments on board orbiting satellites, has a long and successful history in meteorology and the atmospheric sciences. Instruments have been designed for specific purposes, such as measuring the temperature and moisture profiles in the atmosphere, or for looking through the atmosphere at the surface to measure, for example, the tempera-

ture of the sea or the amount of vegetation on the land. There are many considerations needed when designing satellite instruments. These might include optimizing viewing times, instrument scan geometry, spatial resolution (field-of-view size and scan swath dimensions) and temporal resolution (repeat cycles or acquisition frequency from a geosynchronous platform), instrumental signal-to-noise performance, power and data management (bandwidth), among others. Polar-orbiters fly much closer to the Earth's surface (~700–900 km above the Earth's surface) than geosynchronous satellites (~6,000 km), are cheaper to launch, and can carry heavier payloads. However, depending on the scan swath of the instrument, they may have as little as just two views of the same point on the Earth each 24 hours. If the instrument relies on solar radiation as a source for the measurement, then this may be one view in 24 hours (e.g., the OMI instrument, p. 160). Geosynchronous satellites view the same face of the Earth (a circle of about 70°) continuously, or at least at frequent intervals—15 minutes is common. But from their much higher altitude the field of view (pixel size) is generally much bigger than for an equivalent instrument in polar orbit and the signal to noise tends to be smaller. They also have poorer coverage at high latitudes and no coverage of the poles at all. At polar latitudes many more observations are possible from a polar-orbiter as the traces of the orbit lines converge near the poles. Many of the considerations mentioned above are driven by the satellite's scientific purpose (e.g., measuring ozone). To date there has not been a satellite remote-sensing instrument designed specifically for the purpose of measuring volcanic gases, and so ingenious and sometimes fortuitous use of existing instrument capabilities has been the main route to measure volcanic gases from space.

Since late 1978, TOMS has been providing global SO₂ estimates from space. TOMS uses reflected solar UV radiation and, although originally designed to measure ozone, it has proven to be very useful for mapping SO₂ emissions. The TOMS technology and measurement principle has been extended and improved by a new generation of UV spectrometers that include GOME (and GOME-2), SCIAMACHY, and OMI (see the book's prelims for the meaning of the acronyms). Table 6.2 lists the major (current) instruments that are capable of providing SO₂ column (total or partial) amount.

From Table 6.2 it can be seen that space-based methods can be broadly divided into instruments

that use the UV part of the electromagnetic (EM) spectrum and those that use the infrared part. (The MLS uses microwave radiation and has not been employed in studies of volcanic gases to any large extent and so we will not discuss this technology in detail.) Thus, it is convenient to compare and contrast these technologies, describe the instruments and algorithms (retrieval schemes), and give examples of SO₂ retrievals from each of the main space-based instruments. This section is subdivided into two parts: ultraviolet monitoring and infrared monitoring.

Satellite measurement capabilities for CO₂ have been omitted from Table 6.2 as it seems unlikely that current or planned missions will contribute significantly to volcanic CO₂ monitoring. The Orbiting Carbon Observatory (OCO) due for launch in 2014 will be primarily used to provide global (daytime only) CO₂ maps at regional scale suitable for inverse modeling with the goal of characterizing CO₂ sources and sinks. The limited spatial (regional) and temporal (high-Sun, daytime-only) sampling of OCO mean that it is highly unlikely the data could provide measurements suitable for volcanic CO₂ monitoring. The active sensing of CO₂ emissions over nights, days, and seasons (ASCENDS) mission used a laser to actively sense the CO₂ column. This mission is planned for deployment in the 2013–2016 time-frame and the goal is to characterize the carbon budget. Space scales will be roughly 100 km over land and 200 km over the oceans and the desired temporal sampling is weekly. These goals are not compatible with those for studying volcanic behavior; however, it may be possible to use the laser returns from fortuitous coincidences with active volcanoes or perhaps through special processing of the data over well-known, frequent volcanic CO₂ emitters (e.g., Etna). For now the use of these data for volcanic CO₂ is too uncertain.

Ultraviolet monitoring

Measurements of reflected solar radiation at UV wavelengths (280–320 nm, often referred to as the UVB region) can be used to detect and quantify SO₂ in the atmosphere. This is possible because SO₂ has some strong absorption bands between about 300 to about 320 nm. The dominant process affecting the distribution of radiation in this region of the EM spectrum is scattering, mostly by molecules but also by aerosols. Since the amount of molecular scattering varies approximately as λ^{-4} , it becomes

Table 6.2. Satellite and terrestrial (ground-based and airborne) instruments capable of detecting and determining SO₂ and other volcanic gases.

<i>Instrument</i>	<i>Platform</i>	<i>Bands</i>	<i>Gases</i>	<i>Spatial resolution (FOV size, km)</i>
<i>Infrared</i>				
HIRS	NOAA series	7.3 μm	SO ₂	~15–30
VISSR	GOES	7.2 μm	SO ₂	~5
MODIS	Terra/Aqua	4.0, 7.3, 8.6 μm	SO ₂ , ash	~1
ASTER	Terra	8.6 μm	SO ₂ , ash	~0.09
SEVIRI	MSG	4.0, 7.3, 8.6 μm	SO ₂ , ash	~4
AIRS	Aqua	4.0, 7.3, 8.6 μm	SO ₂ , CO ₂ , HCl, H ₂ S, CO, O ₃	~15
TES	Aura	4.0, 7.3, 8.6 μm	SO ₂ , CO ₂ , HCl, H ₂ S	~5
IASI	MetOp-A	4.0, 7.3, 8.6 μm	SO ₂ , CO ₂ , HCl, H ₂ S, CO, O ₃	~15
<i>Ultraviolet</i>				
TOMS	Various	300–360 nm	SO ₂ , O ₃	~50
OMI	Aura	270–310 nm 310–500 nm	SO ₂ , BrO, OClO, NO ₂ , O ₃	~12–48
OMPS	JPSS	250–1,000 nm	O ₃ , SO ₂ , NO ₂	50
GOME	ERS-2	240–790 nm	SO ₂ , BrO, OClO, NO ₂ , O ₃	~40–320
GOME-2	MetOp-A	240–790 nm	SO ₂ , BrO, OClO, NO ₂ , O ₃	40–80
SCIAMACHY	ENVISAT	240–1,700 nm, 2–2.4 μm	SO ₂ , BrO, OClO, NO ₂ , CO ₂	~32–215
<i>Microwave</i>				
MLS	Aura	118 GHz–2.5 THz	SO ₂ , BrO, HCl, NO ₂ , H ₂ O, O ₃ , CO, ClO	~2–17
<i>Ground-based</i>				
COSPEC	Ground-based	300–315 nm	SO ₂ , NO ₂	Variable
FT-IR	Ground-based	3–15 μm	CO ₂ , CO, HF, SO ₂ , HCl, H ₂ SO ₄	Variable
UV spectrometers	Ground-based	300–315 nm ^a	SO ₂ , HCl, BrO, NO ₂	Variable
IR cameras	Ground-based	7–14 μm	SO ₂ , H ₂ O, CO ₂ , H ₂ SO ₄ , ash	Variable

^a Depends on device: FlySpec (300–315 nm); DOASIS (303–313 nm).

increasingly important at shorter wavelengths. Water vapor does not absorb at these UV wavelengths so interference is not expected nor observed. Aerosols scatter light with a power law dependence (Angstrom coefficient) varying from about 0.5 to

about 2 (i.e., significantly less than for molecular scattering). Clouds also scatter UV radiation and can enhance the amount of UV reaching the ground compared with a clear-sky day. Some gases absorb UV radiation with a known spectral behavior that

permits determination of the amount of gas from inversion of a multiwavelength measurement set. The main gases that absorb in the UV between 280 and 330 nm are O₃, SO₂, and NO₂.

Space-based quantitative SO₂ measurements using UV backscattered solar radiation have been made from several instruments (see Table 6.2) with significant success, by developing algorithms or retrieval procedures that account for the interfering effects of molecular scattering and the presence of other absorbers (e.g., O₃). Since UV measurements from space include backscattered radiation from all targets within the field of view of the instrument, corrections must also be made for the UV reflected off the underlying surface. The amount of UV reflected off the surface depends on the surface type and its structure. A measure of the ability to reflect UV is given by the ratio of upwelling UV irradiance to downwelling UV irradiance and is referred to as albedo. Rough, visibly dark surfaces have a low UV albedo (e.g., grass), while smooth, visibly bright surfaces have a high UV albedo (e.g., fresh, dry snow). UV albedos of natural surfaces can vary from as low as 0.005 to almost 1. The structure of the surface also plays a role in the way UV light is reflected. The reflection can be the same in all directions (regardless of the direction of the incoming light) and such surfaces are often referred to as Lambertian. In extreme cases, specular reflection can occur, as if the surface is behaving as a mirror. In most cases, natural surfaces behave somewhere between Lambertian and specular reflection. There may also be a spectrally dependent albedo effect for some surfaces, which needs to be taken into account when analyzing multispectral measurements (e.g., GOME and OMI) using backscattered light. The path the UV radiation takes on its journey downwards through the atmosphere and back towards the sensor is also important in UV measurements. Longer paths imply greater opportunity for scattering. Since most of the UV instruments on satellites use scanning as a means to generate an image, different atmospheric paths are traversed depending on the pixel being sampled in the image. This can lead to so-called “limb effects”, whereby observed radiances are expected to be lower as the scan angle increases for a homogeneous scene. These confounding influences on the retrieval of SO₂ using UV measurements are often treated together. The retrieval algorithm simultaneously accounts for the effects of O₃, surface reflectivity, scan angle, and wavelength dependences when deriving the column abundance of SO₂. More detail on the

retrieval methods can be found in Krueger *et al.* (1995, 2000), Krotkov *et al.* (2006), and Yang *et al.* (2007).

TOMS SO₂ UV instrument

TOMS is a single-grating Ebert–Fastie-type spectrometer with multiple slits centered on six different wavelengths in the region 300–360 nm (Kramer, 2002). It owes its heritage to the backscatter ultraviolet (BUV, later the solar BUV or SBUV) instruments that flew on the Nimbus series of research satellites and utilized the Hartley–Huggins (see Figure 6.2a) bands to retrieve ozone. The wavelengths were chosen for ozone retrieval (see Krueger *et al.*, 1980) but, as SO₂ absorbs within this wavelength region, it was soon realized that volcanic SO₂ could also be retrieved (Krueger, 1983). TOMS has been deployed on four polar-orbiting satellites since late 1978 and an archive of volcanic SO₂ measurements has been developed (<http://toms.umbc.edu/intro.html>). The final TOMS mission (Earth Probe) stopped collecting operational data at the end of 2005.

TOMS measures the solar UV flux scattered by the atmosphere, clouds, and the surface, and retrieval schemes must account for scattering and other effects not related to the gas under study. The principle of the method relies on selecting pairs of wavelengths where absorption by the gas (e.g., ozone) is higher at one wavelength than at the other, and because the wavelengths are close together the reflectance differences can be assumed to be small. (This is not the case for absorption processes, where absorption can change rapidly with wavelength.) Since the measurements contain solar flux reflected off the surface it is necessary to include a third measurement, or several pairs of measurements to account for surface and cloud reflection. For ozone retrieval, meteorological clouds present no problems because the ozone lies many kilometers above clouds but, for tropospheric SO₂, meteorological clouds can cause difficulties. TOMS wavelengths were not optimal for SO₂ retrieval but, by simultaneously accounting for the effects of O₃ and SO₂, retrieval precisions of ~4 DU (or 4 matm-cm) can be achieved (Krueger *et al.*, 1995).

An example of TOMS SO₂ retrievals is given in Figure 6.3 for the Spurr eruption of 1992. The Mt. Spurr SO₂ cloud was observed traveling eastwards over a period of 5 days from September 16 to 21, 1992. The inset panel shows an inter-

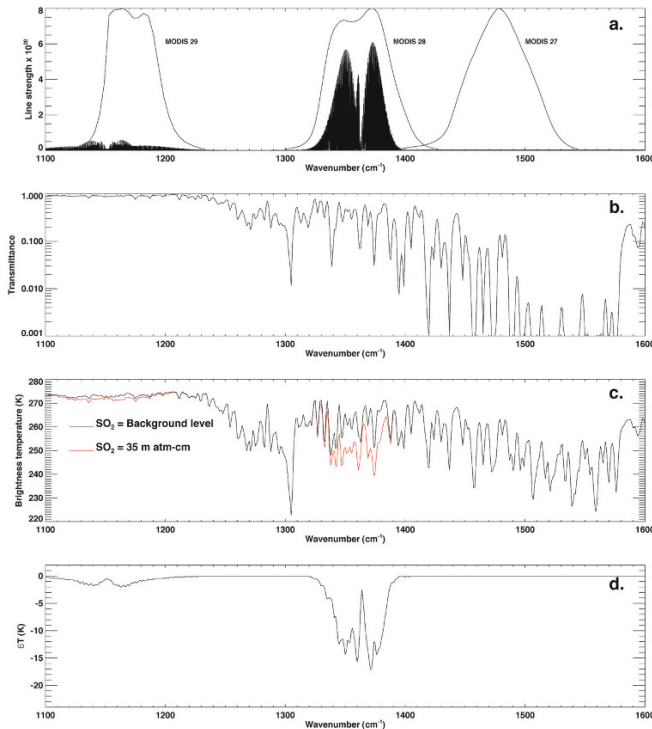


Figure 6.3. TOMS SO₂ total column for the September 1992 eruption of Mt. Spurr.

comparison of TOMS column SO₂ amounts with some ground-based measurements made with a Brewer spectrometer (see Krueger *et al.*, 2000 for more details). Several studies have used TOMS to determine SO₂ emission rates (Carn and Bluth, 2003) and, because of the long-term nature of the measurements (now almost 26 years; e.g., Carn *et al.*, 2003), budget studies and estimates of annual SO₂ emissions to the atmosphere (troposphere and stratosphere) have been possible (Bluth *et al.*, 1992).

TOMS will be replaced by the OMPS (Ozone Mapping and Profiler Suite) instrument that owes its heritage to TOMS and SBUV. OMPS, as the name suggests, will be capable of measuring column amounts as well as profiles. It was to be launched on the NPOESS (National Polar-orbiting Operational Environmental Satellite System), but has been moved to the JPSS (Joint Polar Satellite System) to be launched in 2016.

GOME

The Global Ozone Monitoring Experiment (GOME) was launched on board the ERS-2 satel-

lite on April 21, 1995. The double spectrometer is split into four channels that cover the spectral range 240–790 nm, with a spectral resolution of 0.2 nm–0.4 nm. The instrument is designed to measure solar reflected radiation to determine the vertical columns of O₂, O₃, NO₂, NO₃, HCHO, OClO, H₂O, and SO₂, using the DOAS (Differential Optical Absorption Spectroscopy) technique (Platt, 1994). In this method gas concentrations are inferred by separating absorption and scattering effects by optical filtering; typically, two or more passbands are carefully selected so that the gas of interest absorbs in one passband and does not in another. The pixel size for the GOME instrument is 40 × 320 km² (smaller pixel sizes of 40 × 40 km² are possible with a smaller swath width) and the swath width is 960 km. Further details can be found in Eisinger and Burrows (1998), Burrows *et al.* (1999), and online (<http://earth.esa.int/ers/gome/> and <http://www.iup.physik.uni-bremen.de>). The GOME swath width and repeat cycle of ERS-2 make global coverage possible in 3 days. Figure 6.4a shows the monthly average slant-column SO₂ GOME retrieval for May 2003 when both the Nyiragongo (Congo, central Africa) and

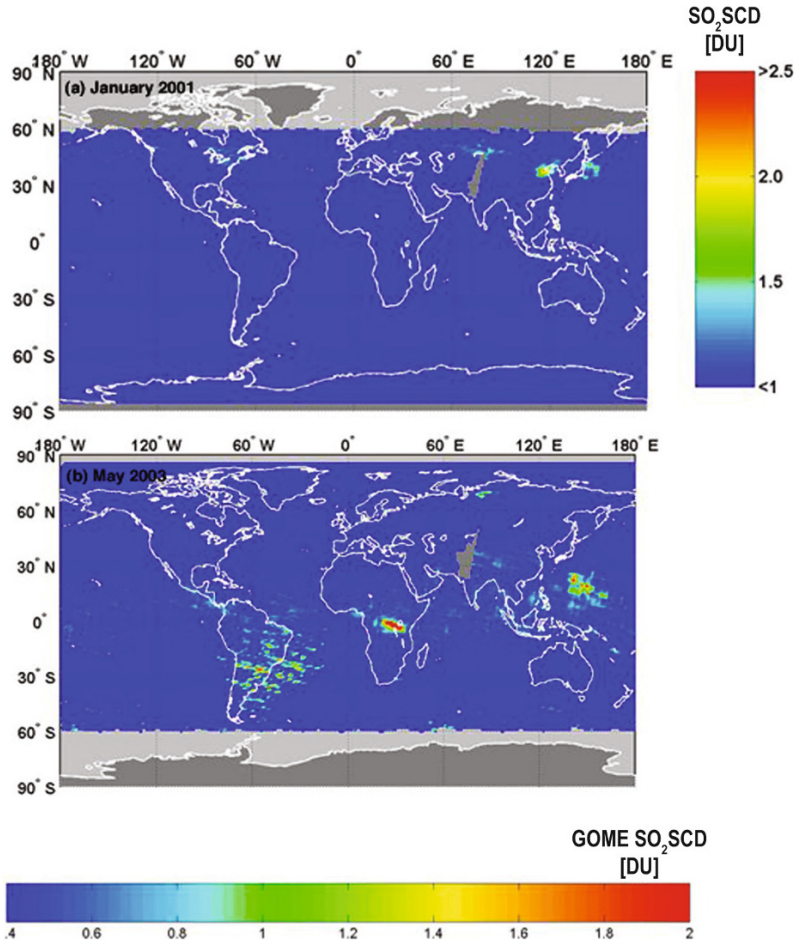


Figure 6.4. GOME SO₂ retrievals: (a) January 2001; (b) May 2003. The SO₂ anomalies seen in the January 2001 data are probably due to eruptions from Miyakijima, whilst those shown in the May 2003 measurements are due to Anatahan (over the Philippine Sea) and Nyamuragira over central Africa. The anomalies over Argentina and Chile may be due to noise induced by the satellite passing through the South Atlantic Anomaly, a stream of very intense radiation that affects the satellite's electronic systems.

Anatahan (Mariana Islands) Volcanoes were active. Figure 6.4b shows the GOME SO₂ retrievals for January 2001. In this example SO₂ emissions from Miyakejima are observable but, because of low light conditions, any emissions north of about 60°N cannot be detected. Failure of GOME's on-board data recorder in June 2003 curtailed collection of global data, with subsequent data only available from ground stations. GOME-2, a successor to GOME with better spatial resolution (40 × 80 km²) and a wider swath (1,920 km), was launched on the polar-orbiting MetOp-A satellite on October 19, 2006.

SCIAMACHY

SCIAMACHY (Bovensmann *et al.*, 1999) is a joint project between Germany, the Netherlands, and Belgium on board the ENVISAT satellite platform (3-day orbital repeat cycle). SCIAMACHY is an imaging spectrometer with a spectral resolution of 0.2–1.5 nm operating over the spectral range 240–1,700 nm, a pixel size of 30 × 60 km² in the forward and 30 × 240 km² in the backward scan, and a swath width of ~1,000 km. This scan geometry and orbital configuration allow global coverage in

6 days. Its principal goal is to measure tropospheric trace gases, including NO_2 , O_3 , CO , SO_2 , and others, as well as some stratospheric species, such as BrO (Richter *et al.*, 2005). Volcanic SO_2 emissions have been monitored by SCIAMACHY since August 2002 (see http://www.oma.be/BIRA-IASB/Molecules/SO2/SO2_volc.php, <http://www.temis.nl/aviation/so2.php>, and http://www.iup.uni-bremen.de/does/scia_data_browser.htm). The retrieval scheme also uses the DOAS technique to determine the slant-column amount, which is then converted to a vertical column by applying airmass factors (AMFs). The AMFs account for the enhancement of absorption due to the path traveled by the light, and this depends on the scan geometry, the wavelength of the light, and the trace gas profiles (Bovensmann *et al.*, 1999). SCIAMACHY has many common features with GOME and relies heavily on experience gained with GOME processing algorithms and data-processing methods. No distinction is made between volcanic and non-volcanic sources and tropospheric and stratospheric loadings. Since the spectrometer uses reflected solar radiation, no measurements are available at night. Despite these limitations the precision of SO_2

retrievals is ~ 0.5 DU, equivalent to a single-pixel SO_2 mass loading of 25 and 100 t for the forward and backward scan, respectively.

Given the paucity of global SO_2 measurements SCIAMACHY is also useful to estimate annual SO_2 emissions from volcanoes, with around 4 years of data available to date. This has been calculated using monthly averaged data from September 2004 to April 2006 and the results are provided in Figure 6.5. The emissions have been calculated for each of 19 volcanic regions (Simkin and Siebert, 1994), summed over the 20-month time period and given as an annual emission rate for each region in Mg yr^{-1} . The global annual emission for the period is $\sim 3.5 \text{ Tg yr}^{-1}$ (SO_2), which is on the low side of global emission estimates; Graf *et al.* (1997) estimate $4 \pm 2 \text{ Tg yr}^{-1}$ (S) for explosive volcanism. For NOPAC volcanoes (sum of regions 9–12) the total annual emission is $\sim 417 \text{ Mg yr}^{-1}$ or $\sim 12\%$ of total global emissions and the third largest contribution after Indonesia and South America.

There are several possible reasons for the low emission estimates. The incomplete coverage of SCIAMACHY is likely to cause an underestimate of SO_2 emissions because many short-duration SO_2

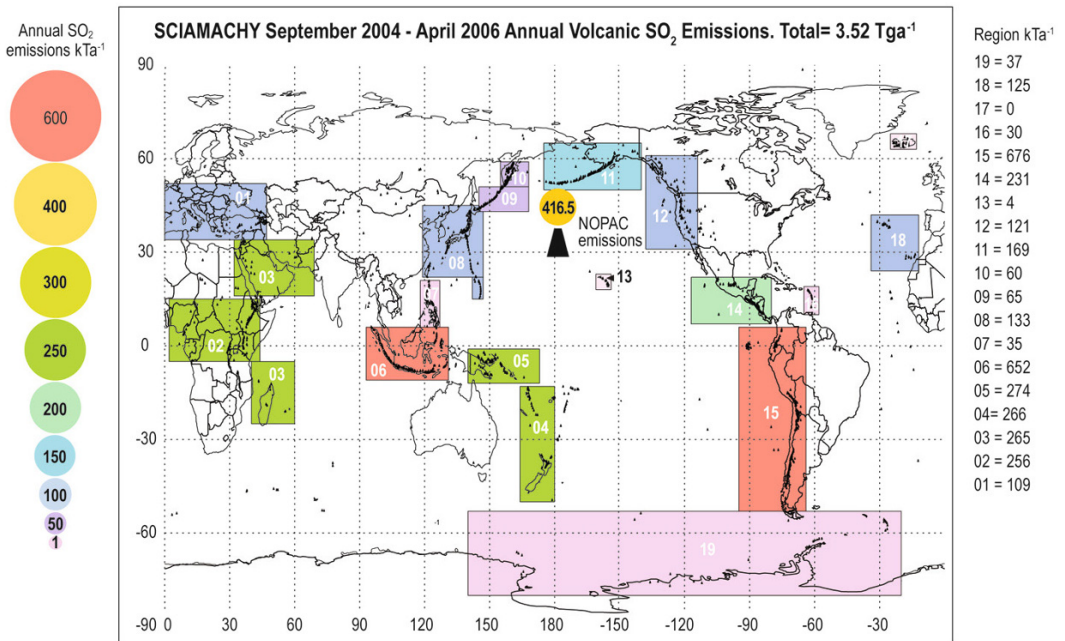


Figure 6.5. Global annual SO_2 emissions derived from SCIAMACHY monthly averages for 20 months starting in September 2004 and ending in April 2006. Annual emission from the NOPAC region is $\sim 417 \text{ Mg yr}^{-1}$.

emission episodes will be missed. The eruption of Grimsvötn (Iceland) in November 2004 was detected by OMI but appears not to have been detected by SCIAMACHY. Daytime-only measurements will also cause an underestimate. The analysis only calculates SO₂ within each volcanic region and makes no allowance for SO₂ that has moved out of the region, and so there is some error in attributing volcano sources by region. Thus, emissions from volcanoes located in region 11 may be contributing to the emission rate estimate for region 12, for example. It is also not clear whether SCIAMACHY (or GOME) can detect passively degassing sources and, hence, this estimate may only apply to significant eruptions. Finally, the estimate covers just 20 months, during which the global emissions may have been quite low in any case. Care must be taken in making annual emission estimates because of the very high variability in volcanic emissions coupled with the fact that the annual budget is often dominated by large emissions from a few sources. Counterbalancing these considerations, the analysis does not distinguish between volcanic and non-volcanic sources, so that any other natural or man-made SO₂ emissions will be captured in the budget, provided these emissions fall within one of the 19 volcanic regions.

Measurements of volcanic BrO employing SCIAMACHY and GOME have also been recently studied by Afe *et al.* (2004), who report no correlation between SO₂ and BrO emissions from volcanoes and a detection limit of 20 ppt for BrO from a single GOME or SCIAMACHY pixel.

OMI

OMI (Levelt *et al.*, 2006) is a hyperspectral UV/visible spectrometer incorporating a two-dimensional CCD, developed by a consortium of Dutch and Finnish research laboratories. OMI was launched in July 2004 on the Aura platform in NASA's A-Train series of polar-orbiting satellites and began collecting science data in September 2004. It is a natural progression from TOMS and also relies on knowledge gained from the GOME and SCIAMACHY instruments. Spectral resolution varies with wavelength, but in the UV-2 band (310–365 nm) used for SO₂ retrieval it is ~0.45 nm. Although OMI and TOMS have about the same noise figure, the availability of better wavelengths to discriminate SO₂ from O₃ and the smaller field of view lead to a factor-of-10 improvement in measurement precision (~0.5 DU). For

volcanic processes these improvements make measurements of passive degassing realizable from OMI.

OMI has a nadir pixel reaching a size of about 13 × 24 km which progressively gets larger towards the scan edges, reaching a size of 13 × 128 km at the extreme edges of the scan. The wide swath of the scan (~2,600 km) permits global coverage at a frequency of once per day, with a local equator crossing time of 13:45 LT. OMI SO₂ retrievals have a standard deviation of ±0.5 DU or less (Krotkov *et al.*, 2006) but there is also a variable bias error of 0.2–0.5 DU, which depends on the reflectivity of meteorological clouds. Of course, no measurements can be made during the night because the instrument relies on backscattered solar radiation, which also means there is a seasonality to OMI SO₂ measurements at high latitudes of both hemispheres. Deep, optically thick clouds can also be a hindrance to SO₂ retrievals from OMI, but generally speaking clouds are much less troublesome for SO₂ retrieval in the UV than in the IR. There is also some sensitivity of the measurements to height, with a better OMI sensitivity to SO₂ in the mid and upper troposphere.

Details of the OMI SO₂ retrieval schemes are provided by Chance (2002), Krotkov *et al.* (2006), and Yang *et al.* (2007). The SO₂ algorithm will be updated for production of publicly released SO₂ data, which is now available (<http://daac.gsfc.nasa.gov/data/datapool/OMI/>). Use of these data for routine and for specific volcanic eruption case studies is just beginning (see Carn *et al.*, 2007a) and the potential of these data to measure passive degassing from volcanoes as well as from anthropogenic sources has been highlighted in some recent work by Carn *et al.* (2004, 2007b, 2009) and Thomas and Prata (2011).

Several NASA Earth Observatory featured stories have illustrated the use of OMI data for monitoring volcanic SO₂ and for detecting low-level SO₂ plumes (e.g., from passively degassing volcanoes; http://earthobservatory.nasa.gov/NaturalHazards/natural_hazards_v2.php?img_id=13253). OMI's ability to track stratospheric SO₂ clouds for great distances from the source was demonstrated during atmospheric residence of the SO₂ cloud emitted by Soufrière Hills Volcano (Montserrat) on May 20, 2006 (see animation at http://earthobservatory.nasa.gov/Newsroom/NewImages/images.php?img_id=17334). Figure 6.6 shows some examples of OMI SO₂ retrievals for eruptions and degassing of NOPAC volcanoes.

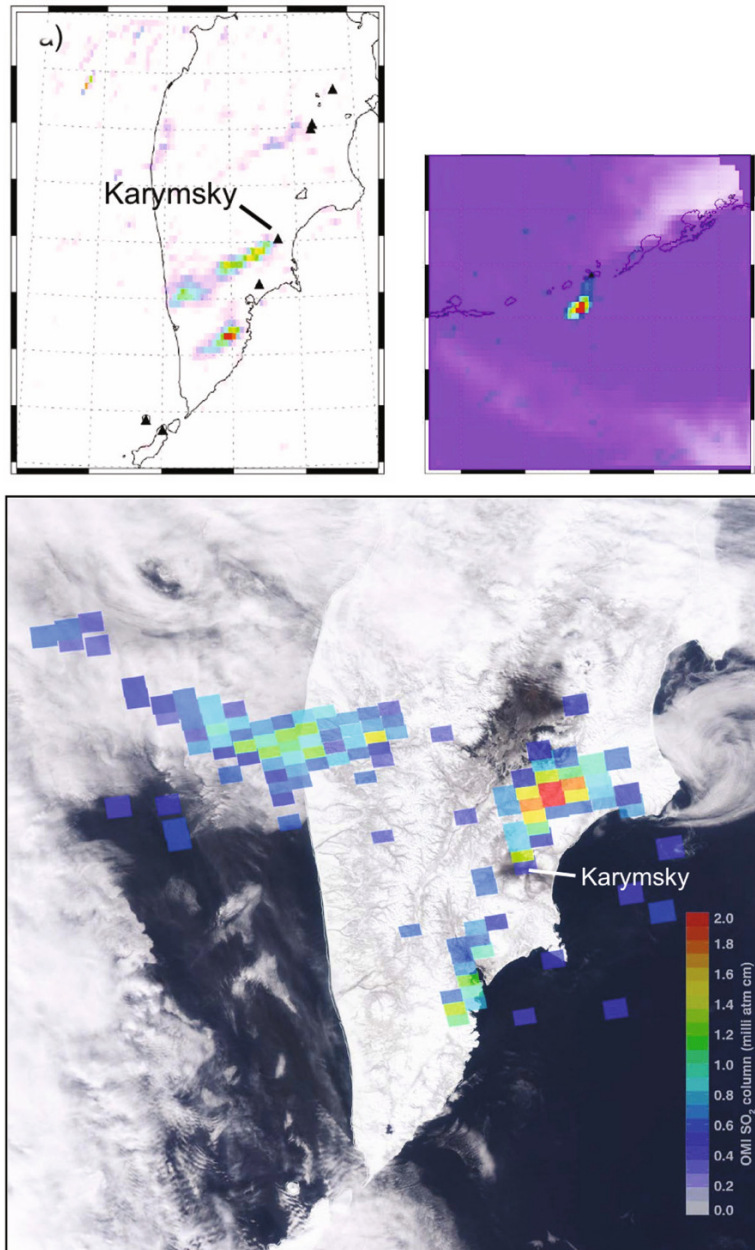


Figure 6.6. OMI SO₂ retrievals for NOPAC volcanoes. (a) Weak eruptive or passive SO₂ emissions from Karymsky Volcano (Kamchatka) on May 4, 2006. The origin of the SO₂ anomaly detected in southern Kamchatka is uncertain; two historically active volcanoes, Mutnovsky and Gorely, are located in this region, and there have been reports of degassing at the former in recent years. (b) A small SO₂ cloud from a minor eruption of Cleveland Volcano (Aleutian Islands) on May 23, 2006. The estimated SO₂ mass in the cloud is 100–200 t. Meteorological clouds are shown in shades of white on this map. (c) SO₂ emissions from an eruption of Karymsky on April 25, 2006. In this image, color-coded OMI pixels showing SO₂ concentrations are plotted over a coincident Aqua MODIS visible image of the Kamchatka Peninsula.

6.4.2 Infrared monitoring

Studies by Realmuto *et al.* (1994, 1997, 2000), Prata *et al.* (2003), Watson *et al.* (2004), Campion *et al.* (2010), and Urai and Pieri (2011) have shown that it is possible to detect and quantify the column SO₂ amount from measurements of the thermal IR emission within particular bands. The SO₂ molecule has several strong absorption features in the IR, the principal IR band centers being at 4, 7.3, and 8.6 μm. In response to the need for detailed knowledge of the infrared properties of the atmosphere, the HITRAN (high-resolution transmission molecular absorption database) compilation of spectroscopic parameters was developed by the Air Force Cambridge Research Laboratories (AFCRL) in the late 1960s. The current version of HITRAN contains more than 1.7 million spectral lines covering 37 molecules and is therefore very useful for investigating all of the important volcanic gases. Figure 6.7 shows the HITRAN line strengths for two of the three major SO₂ bands (a). The MODIS filter response functions covering this region are also shown. The strongest of the bands is the 7.3 μm anti-symmetric stretch. Panel (b) shows the vertical transmittance due to water vapor; the rapid variations in transmittance and low values show how water vapor interferes strongly at 7.3 μm, but much less so at 8.6 μm. Panels (c) and (d) show the effect on top-of-atmosphere brightness temperature² for a background atmosphere and one with a moderate (35 DU) loading of SO₂. Interference from several other trace gases is also included, but none of these (apart from water vapor) causes any significant interference. The change in brightness temperature due to this moderate loading of SO₂ demonstrates that thermal IR satellite measurements can be used to determine global SO₂ total column amounts.

Realmuto *et al.* (2000) has described methods for exploiting the 8.6 μm band to determine column SO₂ amounts. The retrieval scheme relies on having several bands available within and outside the 8.6 μm band and uses detailed radiative transfer calculations to account for the effects of water vapor and other absorbing gases. The scheme also accounts for spectral emission from the surface below the SO₂ cloud. Prata *et al.* (2003) have described a method for determining SO₂ column amounts from TOVS/HIRS measure-

ments, and Guo *et al.* (2004) have used TOVS/HIRS data to derive SO₂ loadings from the June 1991 Pinatubo eruptions. The method utilizes the 7.3 μm band and accounts for water vapor absorption below the cloud by an ad hoc procedure that relies on synthesizing radiances from two neighboring bands. The retrieval scheme appears to work quite well for SO₂ clouds above ~3 km or so (i.e., once the cloud is above most of the atmospheric water vapor). Water/ice clouds and in-cloud water vapor are partially accounted for in the method, but tests are applied to eliminate the gross effects of high cloud and very cold surfaces. The 4.0 μm band has not been utilized to any extent for SO₂ retrieval but, as Figure 6.4 shows, the absorption feature is certainly seen in AIRS data. A potential problem with using this band is that during the day the effects of solar scattered radiation need to be taken into account. The major advantage of this band is that it is relatively free of absorption by other gases and is the least affected of all three bands by interference from water vapor.

Infrared methods suffer from a number of drawbacks including

- (1) thermal contrast
- (2) interference from other absorbers, principally water vapor and ash
- (3) interference from clouds
- (4) spectroscopy of SO₂
- (5) the noise-equivalent temperature difference (NEAT, a measure of sensitivity) limitations.

Of these, (1) and (2) are more important. Cloud effects can be handled by a variety of means and, as long as they are detected, the retrieval scheme can flag the effect. Detector noise is a fundamental limit imposed by the design constraints and operation of the instrument. Typically, NEAT at 300 K for current satellite infrared instruments is in the region of ±0.1 to ±0.5 K. At mid-troposphere temperatures (~240 K), these NEATs are larger by a factor of 1.5 or so and get progressively worse as the target temperature decreases.

Thermal contrast limits the retrieval scheme by reducing the absorption signal whenever the radiating temperature of the SO₂ cloud is close to that of the radiating surface below the cloud. Thus, for thin SO₂ veils over cold surfaces, the infrared techniques suffer from poor signal-to-noise ratios. Likewise, for optically thick SO₂ clouds, the emitting surface below the cloud may be completely

²The temperature corresponding to the measured radiance integrated over the filter response function of the instrument and used with the Planck function.

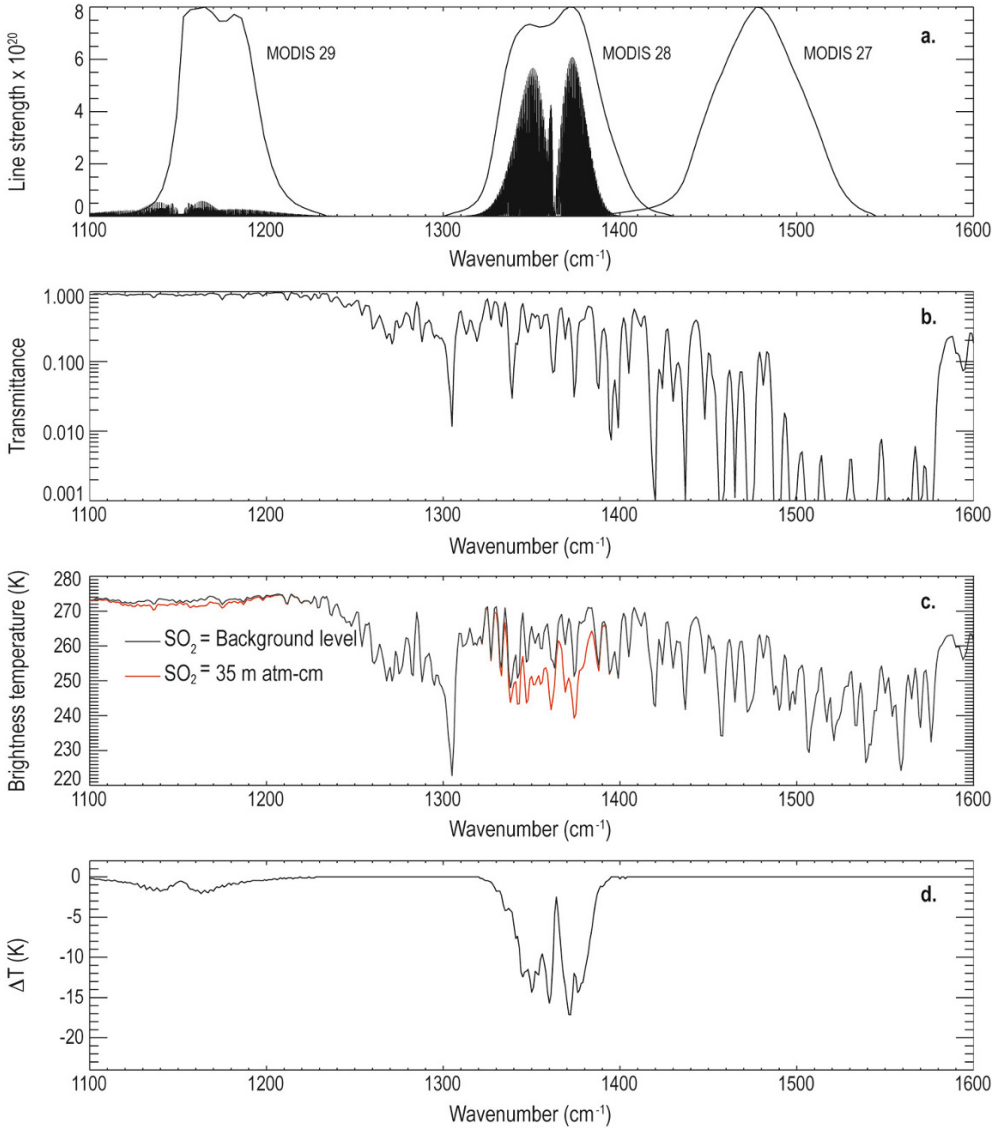


Figure 6.7. Radiative transfer calculations for the 7.3 and 8.6 μm bands of SO_2 . (a) Line strengths and MODIS bands 27–29. (b) Vertical transmittance through the atmosphere (from space looking at the surface). (c) As for (b) but with 35 matm-cm (DU) of SO_2 (red line). (d) Brightness temperature difference (background – SO_2 atmosphere).

obscured and only emission from the SO_2 cloud is observed. In this case the basic assumptions concerning the radiative exchange process are violated and the retrieval is invalidated. (The scheme could be adapted to account for emission and absorption.) Tests can be included to limit the retrieval

to operate between acceptable optical depth ranges. TOVS/HIRS retrieval actually models the radiative exchange as if the radiating surface were a graybody below the active SO_2 cloud. The graybody is assumed to be water vapor (its precise location in the vertical and radiating temperature is not

required to be known in the retrieval, but the height of the SO₂ cloud is needed to properly model the properties of the atmosphere beneath the cloud). At the current time, infrared retrievals from broad-band sensors (such as MODIS and TOVS/HIRS) suffer from a number of difficulties (e.g., lack of sensitivity to boundary layer gases, interference from clouds and water vapor) which make these data problematic for use in operational SO₂ estimation. New algorithms and incorporation of ancillary atmospheric data are needed to make improvements, and combining the IR data with UV data will help to overcome some of the difficulties.

Retrievals using high spectral resolution data (e.g., AIRS) model the radiative exchange process in a spectrally dependent manner and make use of the band shape and magnitude. In this case, knowledge of the spectroscopy of SO₂ becomes a limiting factor in the retrieval. Other retrieval schemes that utilize detailed radiative transfer calculations (e.g., Carn *et al.*, 2005) also require knowledge of the spectroscopic parameters of SO₂ and, specifically, the height of the cloud. The difficulty with all of these methods arises because of the ubiquity of water vapor and its inherent variability; greater retrieval accuracy can only be obtained by retrieving water vapor simultaneously. Fortunately, gases other than water vapor do not absorb strongly in the SO₂ bands being exploited. CO₂, H₂S, CH₄, and a few other trace gases do have effects in these spectral intervals (Figure 6.8), but all are second order compared with the drawbacks listed above.

ASTER SO₂ and the 8.6 μm band

The Advanced Spaceborne Thermal Emission and Reflection Radiometer (ASTER) is a multispectral visible and infrared imaging radiometer on board the EOS Terra polar-orbiting satellite. The instrument was designed for geological remote-sensing applications and has a high spatial resolution of 90 m in the infrared channels. Realmuto *et al.* (1994, 1997) and Realmuto (2000) have pioneered the use of ASTER for determining SO₂ from infrared measurements. The scheme proposed makes use of the TIR bands of the ASTER scanner to simultaneously correct for water vapor (atmospheric) effects and surface effects (emissivities). The methodology relies on an iterative radiative transfer calculation that converges to a solution that minimizes the differences between modeled and measured radiances in up to five bands. The altitude of the

SO₂ and surface must be specified. Opaque plumes and plumes with copious amounts of ash can cause retrieval scheme problems. Realmuto (2000) estimates that amounts of ~0.5 g m⁻² (~17 DU) can be detected by ASTER. Pugnaghi *et al.* (2002) have used a similar approach to estimate SO₂ total column from airborne MIVIS (Multispectral Infrared and Visible Imaging Spectrometer) data.

Realmuto (1995) has also developed software and analysis methods for using ASTER, MASTER, and TIMS (airborne scanning radiometers with similar spectral characteristics to ASTER) data to retrieve SO₂ from volcanic plumes. Extensive use of detailed radiative transfer calculations is made and optimal use of the data is a hallmark of the retrieval scheme. Figure 6.9 contains the results of a preliminary MAP_SO2 and De-stretch³ analysis of ASTER image data depicting the quiescent degassing of SO₂ from Augustine Volcano. The ASTER data were acquired on January 25, 2006, during a pause between explosive eruptions of Augustine on January 17 and 27. During this period SO₂ emission rates were on the order of 2,000–5,000 t/day (Power *et al.*, 2006), suggesting quite high passive degassing rates. The yellow display color of the plume in the De-stretch color-composite (Figure 6.9a) indicates that the plume was free of ash and ice crystals. The lack of any expression of the plume in the maps of maximum brightness temperature (Figure 6.9b) and estimated surface temperature (Figure 6.9d) indicates that the plume was transparent to radiance in at least one of the ASTER channels and that the surface temperature estimates were not adulterated by plume absorption.

The high spatial resolution (~90 m pixels) of ASTER in the TIR provides high sensitivity to SO₂ without the benefit of a channel centered on the ν₃ (or 7.3 μm) band, which has much greater sensitivity to SO₂ than the 8.6 μm band of the ASTER instrument. The majority of the SO₂ estimates for the Augustine plume (Figure 6.9c) were on the order of 1.0 g m⁻² (35 DU), although the De-stretch composite (Figure 6.9a) indicates that ASTER is sensitive to SO₂ at lower concentrations than were detected by MAP_SO2 (Figure 6.9c). This discrepancy is attributed to the inability to characterize cloudy atmospheric conditions. The surface temperature and misfit maps (Figures

³ MAP_SO2 is a graphic user interface to the MODTRAN radiative transfer model. De-stretch is an image-processing technique which attempts to optimize image information for visualization.

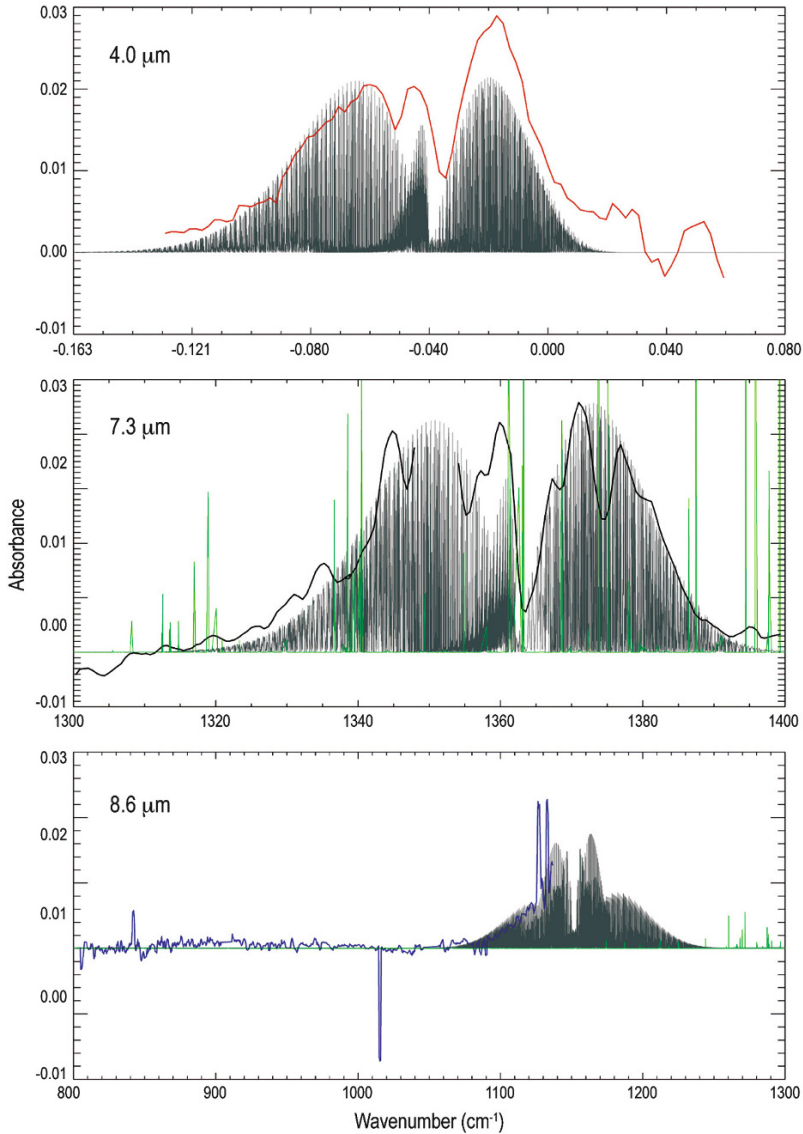


Figure 6.8. Absorbance vs. wavenumber for three SO_2 absorption bands: 4.0, 7.3, and 8.6 μm . The gray lines show *scaled* line strengths. The red line shows the 4.0 μm envelope of AIRS measurements for an eruption of Anatahan Volcano in May 2003. The black line shows the 7.3 μm envelope of AIRS measurements for the same eruption. The green lines show water vapor lines, and the blue line shows the 8.6 μm envelope of AIRS measurements. Note that there is a spectral gap in the AIRS measurements between $\sim 1,130$ and $\sim 1,300 \text{ cm}^{-1}$.

6.9d, e) indicate that clouds are the primary source of error in the estimation procedure. Despite these minor shortcomings, the results of the Augustine study demonstrate that monitoring of “non-explosive” passive degassing of SO_2 with satellite-

based remote sensing is possible. The Augustine event warrants further study, as COSPEC measurements (see Section 6.4.3, p. 173) and other satellite sensor measurements were available for comparison.

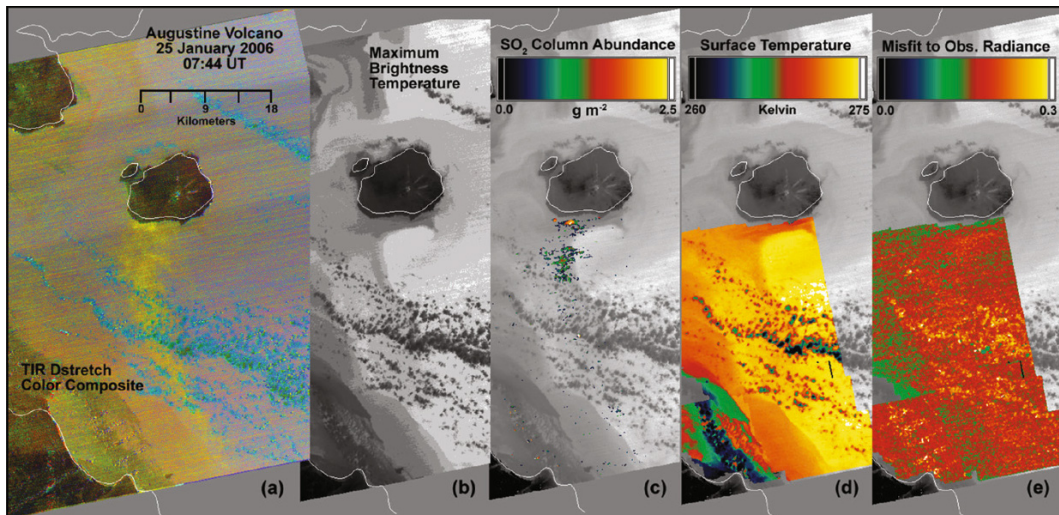


Figure 6.9. Results of MAP_SO2 analysis of ASTER data acquired over Augustine Volcano on January 25, 2006.

TOVS/HIRS SO₂ and the 7.3 μm band

The TIROS Operational Vertical Sounder (TOVS) comprises a suite of instruments, including the High-resolution InfraRed Sounder (HIRS), a scanning multichannel radiometer developed specifically for the purpose of improving weather forecasts and studying meteorological processes (e.g., water vapor impacts). TOVS is in a polar orbit on board NOAA operational weather satellites, and during most of the ~28-year period of operation there have been at least two satellites in orbit at any given time. Determining SO₂ from HIRS relies on infrared channels, and thus the temporal frequency is twice that of TOMS, OMI, GOME, or SCIAMACHY sensors, which rely on solar radiation. HIRS was not designed to measure SO₂, and it was serendipitous that a HIRS channel designed for water vapor sounding overlapped a very strong SO₂ absorption band. Even so, it is not straightforward to determine SO₂ from the HIRS data because of interference from clouds and water vapor. A brief description of a HIRS SO₂ retrieval algorithm (or scheme) is provided here and more detail can be found in Prata *et al.* (2003).

The retrieval scheme relies on the assumption that there is an almost linear relation between the radiances at 6.7 and 11 μm in a SO₂-free atmosphere. The radiance at 7.3 μm is estimated by interpolation and is then assumed to be the radiance that would be measured (with some error) in the absence

of SO₂. When SO₂ is present the measured 7.3 μm radiance is smaller (due to absorption by SO₂); the difference between the synthesized radiance and the observed radiance is a measure of the SO₂ total column. The temperature (or radiance) difference determined in this way is related to the SO₂ column through a series of detailed radiative transfer calculations (GENLN 2 is used; Edwards, 1992) that provide a look-up table indexed by altitude. The overall precision of the scheme is estimated to be 5–20 DU. Clouds, low thermal contrast, and water vapor effects cause problems for the scheme. The retrieval works best for SO₂ clouds that are high (upper troposphere/lower stratosphere or UTLS) and not opaque in the infrared. The great advantage of using TOVS/HIRS data is that the sensor has been on board the NOAA series of operational satellites since 1979, thus providing an uninterrupted global record of SO₂ emissions for 27 years, with a great deal of additional coverage when multiple NOAA instruments were simultaneously operational. Polar-orbiting measurements are also better suited for the NOPAC region. Figure 6.10 shows the eastward progress of an SO₂ cloud from the Mt. Spurr eruptions between September 17 and 20, 1992. The same clouds were monitored by TOMS (Bluth *et al.*, 1995), and there is general agreement between the IR and UV retrievals in this case. The cloud moved rapidly in the upper-level winds, crossing into the U.S.A. before curving northwards and decaying over Greenland. A very similar trajectory

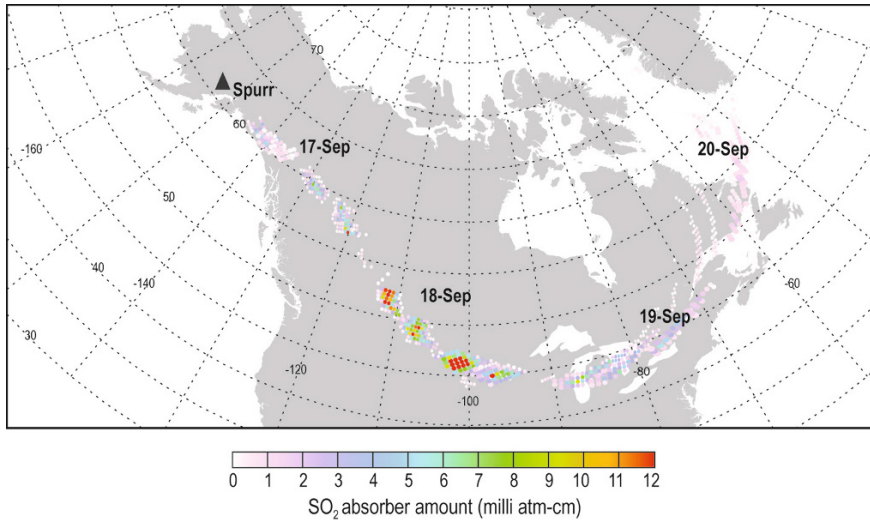


Figure 6.10. TOVS/HIRS retrievals of upper-troposphere/lower-stratosphere (UTLS) SO_2 total column for the September 1992 Mt. Spurr eruption.

was taken by the ash clouds from this eruption (Schneider *et al.*, 1995). It should be noted that the $7.3\ \mu\text{m}$ SO_2 retrieval scheme is much less sensitive to ash than the scheme relying on $8.6\ \mu\text{m}$ data. Two further examples for NOPAC eruptions (Cleveland in 2001 and Augustine in 1992) are shown in Figure 6.11, where the data have been re-sampled and accumulated over a few days to show the spatial distribution of SO_2 emissions. Since TOVS/HIRS has quite low sensitivity, this kind of analysis improves the coherence of the retrievals.

The TOVS/HIRS SO_2 retrieval scheme is being made into an operational SO_2 watch system (S-watch); currently there are two operational HIRS (HIRS-3) instruments in orbit, providing up to four measurements per day anywhere on Earth, and many more at polar latitudes. The data from S-watch are expected to be useful in climate studies, since the SO_2 measured by TOVS/HIRS is mostly UTLS and therefore more likely to affect climate and, as illustrated in Figure 6.12, the data provide global coverage.

MODIS SO_2 and the $7.3\ \mu\text{m}$ band

The Moderate Resolution Imaging Spectroradiometer (MODIS) is a multichannel visible and infrared scanning radiometer in polar orbit on the EOS Terra and Aqua platforms. The Terra

MODIS has been in operation since late 1999, while the Aqua MODIS began operations in 2002. These instruments have infrared channels (see Figure 6.2c) that are sensitive to SO_2 with spatial resolutions of $\sim 1 \times 1\ \text{km}$ at nadir. Such high spatial resolution data with global coverage on a 2-day time scale offer new possibilities for studying SO_2 emissions. The principal channels used are the $7.3\ \mu\text{m}$ channel (similar to the HIRS instrument, but at finer spatial resolution) and the $8.6\ \mu\text{m}$ channel (similar to the ASTER instrument, but at coarser spatial resolution). The retrieval methods for the 7.3 and $8.6\ \mu\text{m}$ channels are different and described separately here.

Retrieval using the $7.3\ \mu\text{m}$ MODIS channel uses essentially the same scheme as that proposed for HIRS (Prata *et al.*, 2003, 2007; Watson *et al.*, 2004). Separate look-up tables are generated for MODIS and better account of clouds can be taken because of the much better spatial resolution of the sensor compared with HIRS (~ 1 vs. $\sim 20\ \text{km}$). The main difficulties associated with using this channel for SO_2 retrieval stem from interference effects due to water vapor. Indeed, the channel was selected for the purpose of measuring mid-troposphere water vapor. That SO_2 can be determined from measurements using this channel can be understood by considering the measurement principle of a sounding channel and through the concept of a weighting function. The contribution to the radiation reach-

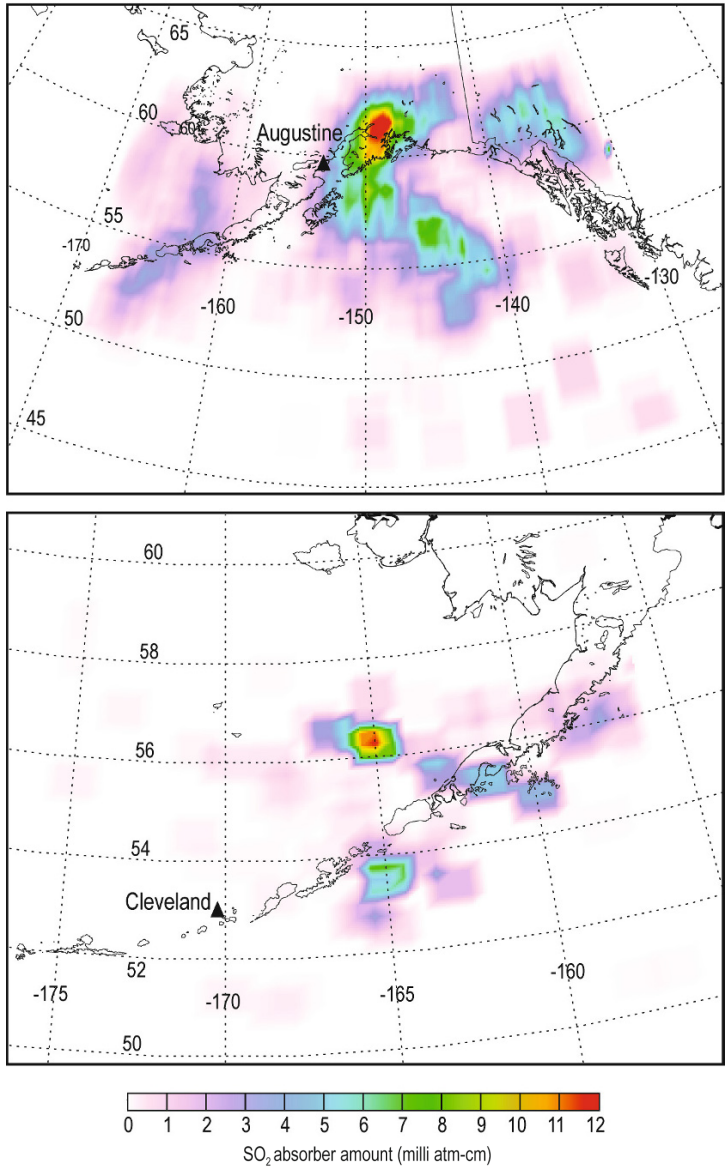


Figure 6.11. TOVS/HIRS SO₂ retrievals for Augustine, 1996 (top) and Cleveland, 2001 (bottom). In these plots the cumulative SO₂ is shown.

ing a narrowband radiometer viewing the atmosphere from above from different portions of the atmosphere can be described mathematically by a weighting function. Denoting the Planck function by $B[T(p), \nu]$, where $T(p)$ is the vertical temperature profile, $\tau(\nu, p)$ is the vertical transmittance profile,

and p_s is the surface pressure, the monochromatic atmospheric radiance $R_{\nu,p}$ can be calculated from

$$R_{\nu,p} = \int_{p_s}^p B[T(p), \nu] \frac{\partial \tau(\nu, p)}{\partial p} dp$$

The weighting functions ($\partial \tau / \partial p$) for three MODIS

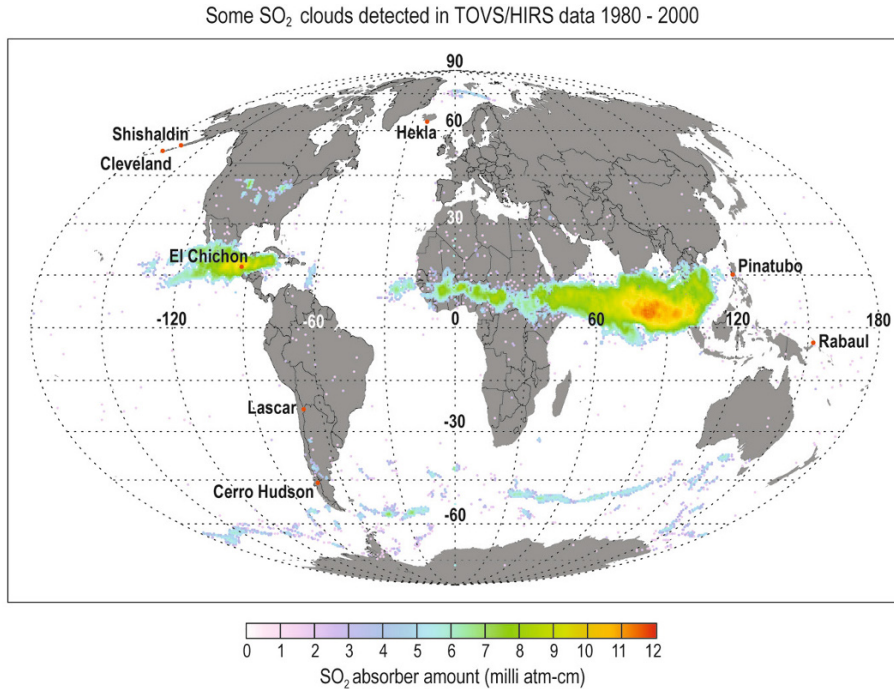


Figure 6.12. Cumulative TOVS/HIRS SO₂ for the largest eruptions sending SO₂ into the UTLS in the period 1980–2000.

channels (centered at 908, 1,362, and 1,477 cm⁻¹) for typical mid-latitude water vapor and temperature profiles indicate that radiation from the 908 cm⁻¹ channel mostly emanates from the surface (this is also true for the 1,172 and 831 cm⁻¹ channels); radiation from the 1,362 cm⁻¹ emanates from the mid-troposphere (~700 hPa) and radiation from the 1,477 cm⁻¹ emanates from the upper troposphere (~450 hPa). The 1,362 cm⁻¹ weighting function for an atmosphere perturbed by an SO₂ cloud centered at ~250 hPa has the location of the peak radiance contribution close to the location of the peak SO₂ concentration and occurs above the location of the peak water vapor concentration. Thus, when the SO₂ cloud is high and separated from water vapor, the 1,362 cm⁻¹ channel can unambiguously identify SO₂. To make quantitative estimates of the amount of SO₂ requires an estimate of the brightness temperature difference between a measurement from this channel with and without SO₂. Since there is only one measurement, the brightness temperature of the unperturbed (SO₂-free) channel must be obtained by some other means. This is done

by assuming a linear relationship between radiance and wavenumber across the region 1,100–1,600 cm⁻¹, which covers three of the MODIS channels. By linearly interpolating the radiance from a channel below 1,362 cm⁻¹ and a channel above 1,362 cm⁻¹, an estimated 1,362 cm⁻¹ brightness temperature can be obtained. The difference between this estimate and the measurement is a quantitative measure of the absorption of radiation by SO₂ and can be related to transmittance. Offline radiative transfer calculations may then be used to relate transmittance to an absorber amount. Transmittance does depend on the location of the SO₂ cloud in the vertical and offline radiative transfer calculations being performed for different altitudes, and the retrieval then requires an independent estimate of the SO₂ cloud height. Under cloud-free conditions, theoretical estimate of the errors suggest that the retrieval procedure has a precision of ~2–6 DU.

The Cleveland, 2001 eruption was detected quite well using MODIS 7.3 μm retrievals as illustrated in Figure 6.13.

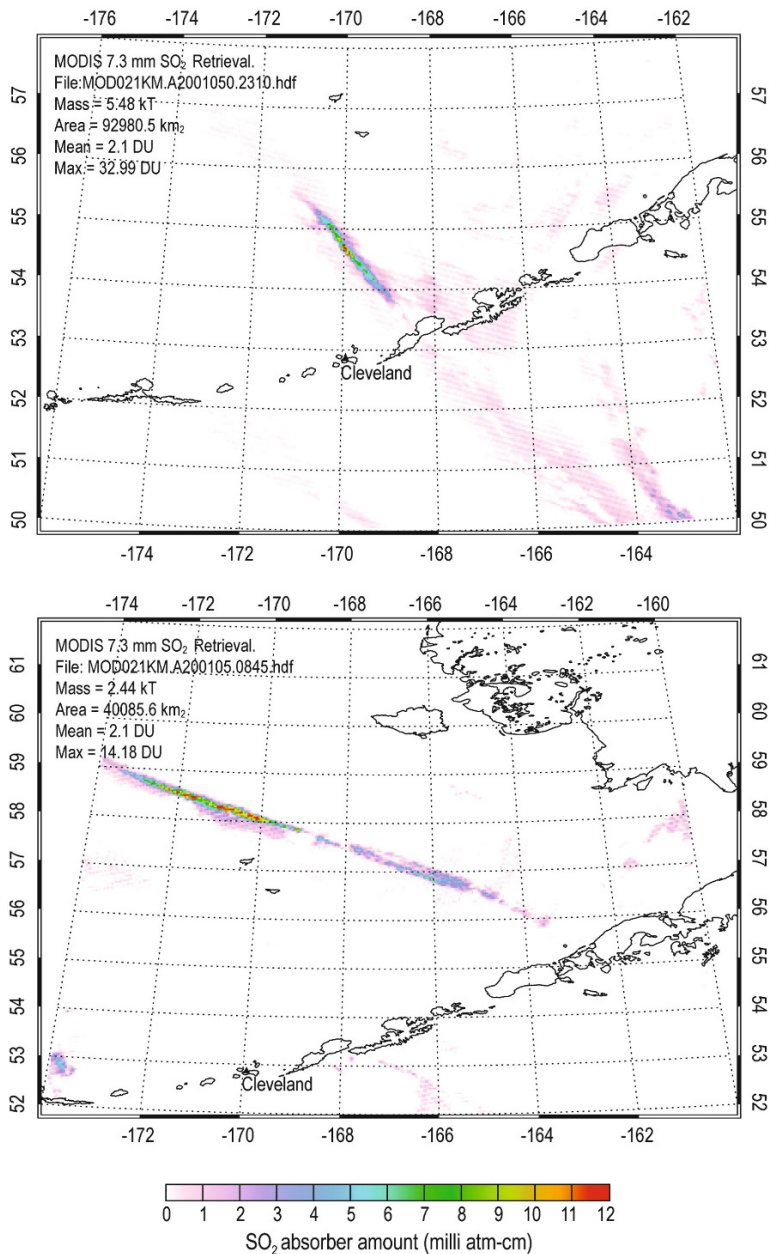


Figure 6.13. MODIS 7.3 μm SO₂ retrievals for the Cleveland eruption of February 19–20, 2001.

MODIS SO₂ and the 8.6 μm band

The scheme for this retrieval is described by Watson *et al.* (2004) and is essentially the same as the ASTER retrieval. The method employed here is different from that for the 7.3 μm channel essen-

tially because this is a window channel that is much less influenced by water vapor. Thus, rather than employing the constraint that SO₂ and water vapor must reside at different heights in the atmosphere, the principle is to account for its presence using other channels and radiative transfer calculations.

Realmuto (2000) has described the basic ideas behind the retrieval scheme for airborne scanner and ASTER data. The main difference for MODIS is that there are fewer channels between 8 and 13 μm to constrain the retrieval and, hence, the retrieval is likely to be less robust. There are two further effects that must be accounted for: (1) the influence of volcanic ash and (2) the effect of varying emissivity of the underlying surface. The first effect is rather difficult to take into account as ash has a similar effect on the 8–13 μm brightness temperatures as SO_2 . Fortunately, it seems that ash and SO_2 are frequently separated in the vertical and the problem is not so severe, especially for moderate to large eruptions. The second effect is accounted for by utilizing independent estimates of the wavelength-dependent emissivity of the surface. For SO_2 clouds over the sea surface this approach works very well as the sea surface has high infrared emissivity and low spectral dependence. There is also a possibility of interference from H_2SO_4 aerosols as these form from SO_2 hydration and oxidation, and H_2SO_4 has absorption features between 8 and 11 μm . None of these effects is significant for 7.3 μm measurements.

As MODIS has fewer channels available compared with ASTER, the retrieval is less well determined while the problems with ash and water vapor variability are still present, as discussed on p. 167. Watson *et al.* (2004) provide some examples of 8.6 μm MODIS data retrievals for eruptions from Hekla in 2000 and Cleveland in 2001.

AIRS SO_2 and the 7.3 μm band

AIRS is an echelle grating spectrometer operating in the infrared at wavenumbers between 650 and 2,700 cm^{-1} . There are more than 2,000 channels available, with each channel having 90 across-track pixels with $15 \times 15 \text{ km}^2$ spatial resolution at nadir. This information-rich cube of data requires a different approach from geophysical retrieval.

Two independent schemes have been proposed to determine SO_2 from the high spectral resolution data from AIRS. Carn *et al.* (2005) propose a method that uses a radiative transfer model (SARTA) that was specifically designed for the AIRS instrument and that uses a minimization procedure between modeled and measured radiances. The second method proposed by Prata and Bernardo (2007) uses the shape of the 7.3 μm band to identify SO_2 and, by comparison with a reference spectrum and a radiative transfer model, to determine column abundance. Both methods must

account for water vapor absorption. Prata and Bernardo (2007) estimate a precision of $\sim 5 \text{ DU}$ and suggest that vertical profile information (three levels: boundary layer, lower troposphere, and UTLS) may be retrieved by including information from the 4, 7.3, and 8.6 μm regions.

The Kliuchevskoi February/March 2005 eruptions were monitored by AIRS as were the recent (January 2006) Augustine eruptions. Figure 6.14 illustrates AIRS retrievals for Kliuchevskoi and the mean daily emission rate ($\sim 1 \text{ Mg day}^{-1}$) of SO_2 during this eruption episode.

GOES-VISSR, MSG-SEVIRI SO_2 and the 7.3 μm band

Prata *et al.* (2004) and Ackermann *et al.* (2008) have described a method for estimating SO_2 from the GOES sounder. The scheme relies on using information from a reference channel (as in the HIRS retrieval) and works best for upper-troposphere/lower-stratosphere SO_2 . The GOES VISSR 7.3 μm channel is not optimally placed for SO_2 and, consequently, retrievals are always likely to be inaccurate: mainly due to greater water vapor interference effects. However, the temporal resolution (15 min to 1 h) of the GOES provides extra information not usually available from polar sensors; specifically, the ability to obtain spatially coherent images of SO_2 clouds at frequent time intervals. The SEVIRI instrument on MSG is likely to provide even better SO_2 estimates because the channel is better positioned for SO_2 determination and the temporal resolution can be every 15 min. Prata and Kerkmann (2007) have shown that the MSG SEVIRI can determine SO_2 and ash by using channels at 7.3, 8.6, 11, and 12 μm . The new ABI (Advanced Baseline Imager) has a channel specifically selected for SO_2 studies (Schmit *et al.*, 2006). Geosynchronous satellites are much less useful for studying the NOPAC region because the nadir point is over the equator and there is some loss of spatial resolution, distortion of the cloud, and additional retrieval uncertainty due to the extreme look angle. Nevertheless, Gu *et al.* (2005) have exploited certain aspects of the slant-viewing geometry for polar regions to study volcanic clouds.

MLS

The Microwave Limb Sounder (MLS) is included briefly here for completeness. The MLS measures naturally occurring microwave thermal emission from the edge (or limb) of the Earth's atmosphere.

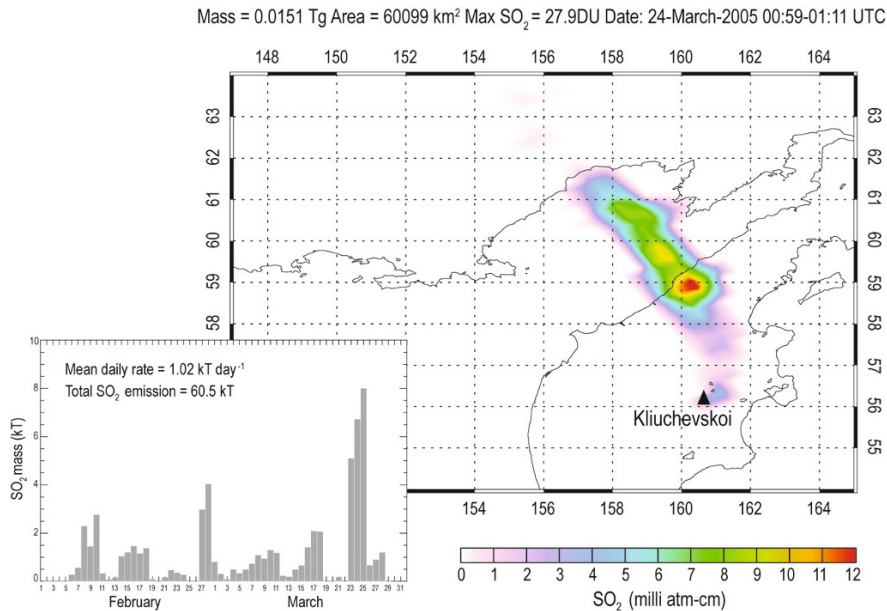


Figure 6.14. AIRS SO₂ total column retrievals for an eruption of Kliuchevskoi, March 24, 2005. *Inset:* SO₂ mass loading as a function of time for February–March 2005. Average flux is ~ 1 Mg day⁻¹.

By looking towards the limb, relatively high vertical resolution can be obtained and vertical profiles of various chemical species that are microwave active can be inferred. MLS instruments have been in space since 1991 and currently there is one in orbit on board the EOS Aura platform. Data from the MLS have been used to determine volcanic SO₂ and have the potential to measure several other volcanic gases (e.g., HCl and BrO). The MLS measures passive microwave emissions from the Earth's limb at several discrete frequency intervals ranging from 118 GHz to 2.5 THz. The Aura MLS has been providing atmospheric vertical retrievals above 10 hPa of several gas species and is a follow-on instrument from the UARS MLS which observed the Pinatubo SO₂ cloud (Read *et al.*, 1993). Waters *et al.* (2006) provide further detail of the MLS, its measurement principle, example retrievals, and accuracies. They also mention an observation of HCl and SO₂ injected into the stratosphere from the January 27 Manam eruption. Prata *et al.* (2007) discuss MLS HCl retrievals and compare the concentrations in the stratosphere from the May 2006 Soufrière Hills (Montserrat) eruption with SO₂ retrievals from OMI and AIRS. These are the first satellite-derived ratios of HCl:SO₂ in an evolving volcanic cloud. The maximum HCl vmr (volume mixing ratio)

occurred later than the maximum SO₂ vmr and gas ratios HCl:SO₂ varied from 0.03 to 0.1. This ratio is smaller than that inferred for Pinatubo and El Chichón of ~ 0.2 – 0.25 (Westrich and Gerlach, 1992), but similar to that found for the stratospheric portion from Pinatubo of ~ 0.1 (Mankin *et al.*, 1992) and for the Hekla 2000 volcanic plume of ~ 0.07 (Rose *et al.*, 2006). By using a combination of sensors from different satellite platforms to measure gases and particulates it is likely that satellites will provide new information on the chemistry and dynamics of volcanic clouds.

Ultraviolet vs. infrared summary

Currently, there are several UV and IR instruments in space that are capable of providing estimates of SO₂ gas emissions from volcanoes. At the time of writing, UV instruments provide better accuracies and precisions than IR instruments. IR instruments have in their favor generally better spatial and temporal sampling, and the development of retrieval techniques is at an early stage. For boundary layer studies of gas emissions it is likely that UV instruments will always be superior as the thermal contrast of IR measurements near the surface will be a fundamental limitation. So far, none of the instru-

ments have demonstrated a capability to provide vertical profile information. This will likely come from interferometric data in the IR or from limb-scanning solar absorption IR and UV measurements. Rose *et al.* (2003, 2006) have shown the value of using data from several sensors (remote and in situ) synergistically to better understand the microphysical, dynamical, and chemical interactions within evolving volcanic clouds and plumes. An ideal space-based system that would minimize the disadvantages of UV and IR systems would be to develop a geosynchronous combined UV and IR imager. The IR imager would provide information on SO₂, ash, and clouds at higher spatial resolution ($1 \times 1 \text{ km}^2$ is possible) during day and night, while the UV imager would provide accurate daytime-only SO₂ column amounts down to the boundary layer.

IR techniques have several advantages over UV methods which include

- (1) day and night use
- (2) currently, greater spatial resolution
- (3) better temporal resolution (there are no geo-UV sensors)
- (4) potential for vertically resolved SO₂ (e.g., profiles from AIRS).

The advantages of UV techniques include

- (1) higher sensitivity to lower-tropospheric SO₂ (enabling detection of passive degassing)
- (2) no susceptibility to water vapor interference
- (3) ability to measure SO₂ in fresh, opaque eruption clouds
- (4) smaller data volume (primarily due to lower spatial resolution).

The best spatial resolution achieved so far for UV sensors (OMI) is $\sim 13 \times 24 \text{ km}^2$, while ASTER retrievals can achieve spatial resolutions as small as $90 \times 90 \text{ m}^2$ and MODIS provides global 2-day resolution at $1 \times 1 \text{ km}^2$ resolution. The geosynchronous sensors on GOES and MSG can achieve temporal sampling frequencies as rapid as once every 15 minutes while, to date, there are no plans for a geostationary UV sensor and temporal frequency is limited to once per day at equatorial latitudes, with more frequent coverage possible at high latitudes where polar orbits converge. The spectrally resolved SO₂ band structure contains information on the vertical distribution of the absorber. AIRS and TES have sufficient spectral

resolution across the 4.0 and 7.3 μm SO₂ bands to provide some vertical resolution. UV sensors may have this capability too, but currently only total column data products are being developed (e.g., Chance, 2002).

6.4.3 Ground-based monitoring

Ground-based monitoring of volcanic emissions using remote sensing is particularly attractive at volcanoes that are restless and inaccessible for safety reasons and for cost-effectiveness. Early warning of volcanic unrest for aviation hazard awareness and for diagnosing future volcanic activity are two areas where ground-based sensing can play a key role. In the past, the main instrument used for measuring gases remotely was the COSPEC. With recent technology advances the COSPEC is now being replaced by mini-spectrometers operating at UV wavelengths, by portable FT-IRs, and by cameras operating in the UV and IR. Sun photometers and other optical devices traditionally used to measure aerosols have also been used to monitor volcanic gases and particulates (Watson and Oppenheimer, 2000; Porter *et al.*, 2002). Visible (webcams) and near-infrared cameras have also been deployed at volcanoes for routine plume surveillance (Kinoshita *et al.*, 2003). We briefly summarize the principal methods used and progress made with ground-based instruments for volcanic gas remote sensing, starting with IR techniques and finishing with the very successful UV techniques.

FT-IR

Fourier transform infrared (FT-IR) interferometers have been used by physical scientists and spectroscopists for decades to study atmospheric gases in laboratory and field settings. The measurement principle consists of an infrared detector, telescope, and a means for splitting and re-combining a beam of light. The beam splitter is usually a mirror (or corner cube reflector) although any device that introduces a path difference into one of the beams will do. The re-combined beams create an interference pattern on the infrared detector, and information (amplitude and phase as a function of wavenumber) on the spectrum is captured all at once. This multiplexing nature of an interferometric device is a major advantage over other radiometric measurement devices. The instruments have quite broad applications. Their first application to vol-

canic gas measurements was in 1991 at Asama Volcano, Japan (Notsu *et al.*, 1993), and they have since been adopted by several research groups (e.g., Francis *et al.*, 1998; Love *et al.*, 1998). Horrocks *et al.* (2001) provide a comprehensive error budget for volcanic SO₂ measurements using FT-IR, and Duffell *et al.* (2001) report on FT-IR volcanic gas flux measurements. Their great advantage over other instruments is their ability to “multiplex”; that is, the measured signal contains information about all parts of the sampled electromagnetic spectrum at once. Thus, a variety of gases including CO, CO₂, SO₂, HCl, and HF that have spectral features within the sampled band can be straightforwardly measured at the same time, allowing gas ratios to be determined. Originally cumbersome and difficult to operate, these instruments have been adapted for field use for work on volcanoes. Several different mobile FT-IRs are now commercially available and, given the right field conditions, measurements can use IR energy emitted directly from hot lava as an emission source. Gases present in the open path between the infrared source and the instrument can be detected and quantified. An additional advantage of these instruments is that they are capable of great precision and accuracy where the open pathlength is known. Combining the ratios of the major species quantified allows computation of a complete gas analysis. Disadvantages include the cost (although this is reducing), the need to sometimes operate in absorption mode requiring an IR source (e.g., a globar and retroreflector, hot lava, or the Sun), instrument operability (the need for detector cooling; e.g., liquid N₂), and the complexity of data analysis. Some great advances in volcanic gas measurements have been made through interpretation of FT-IR data (see the review by McGonigle, 2005 for a discussion).

Thermal radiometry

Infrared radiometers have been deployed at volcanoes, mostly for inferring gas/lava temperatures and for monitoring purposes (e.g., Chapter 3; Harris and Ripepe, 2007; Ripepe *et al.*, 2009). To study gas compositions these radiometers must be modified to include bandpass filters, in accordance with the principal gas absorption features illustrated in Figure 6.2b–c. The easiest gas to measure in this way is SO₂. The 8.6 μm SO₂ absorption feature sits neatly within the atmospheric window, often exploited for surface temperature measurements

using IR radiometers. The basic idea is to measure the temperature of the gas plume using either a broadband (7–14 μm) radiometer or filtered (10–12 μm) IR radiometer, and simultaneously measure the temperature at 8.6 μm, using a filtered (8.3–8.9 μm) IR radiometer. By using radiative transfer analysis it is possible to estimate the effective SO₂ absorption at 8.6 μm and hence infer SO₂ concentration. Greater accuracy and the need for fewer assumptions can be achieved by using a multispectral (multifilter) radiometer. Prata *et al.* (1993) were the first to report ground-based measurements using a multifilter radiometer at Sakurajima Volcano, where they identified ash and SO₂ gas. More progress has been made using these kinds of radiometers from space (e.g., Realmuto *et al.*, 1994) or from an airborne platform (Pugnaghi *et al.*, 2002).

Thermal cameras

The obvious extension of the single-view IR radiometer (the simplest type of radiometer) is to develop it into an imaging system. This can be achieved either by increasing the number of detectors, by scanning, or by a combination of these. The latter option is used for satellite and airborne systems, although a staring array (fixed view) thermal IR camera has been operated from space (IRAS). The superior option for ground-based systems is to use uncooled microbolometer detectors as a staring array. Sizes of up to 240 × 320 detectors are commercially available, with claimed broadband NEΔTs of ~50 mK. By adding filters, improving instrument temperature stabilization through the use of a blackbody shutter, and developing good calibration methodologies, a multispectral thermal imaging camera can be developed. Prata *et al.* (2004) reported some measurements of ash and gases at volcanoes using a modified thermal IR camera. While preliminary results looked promising, several major improvements were needed in design, particularly in the radiative transfer modeling of the system. These improvements have been made in camera development. With this design and algorithms the camera is capable of quantitative SO₂ gas measurements. An example SO₂ gas retrieval at a known industrial SO₂ source is shown in Figure 6.15. The rapid sampling rate from this camera permits emission rate calculations; an example for this industrial source is shown in Figure 6.16. The reported emission rate from the industrial operator is ~1.8 kg s⁻¹, which agrees quite well with the

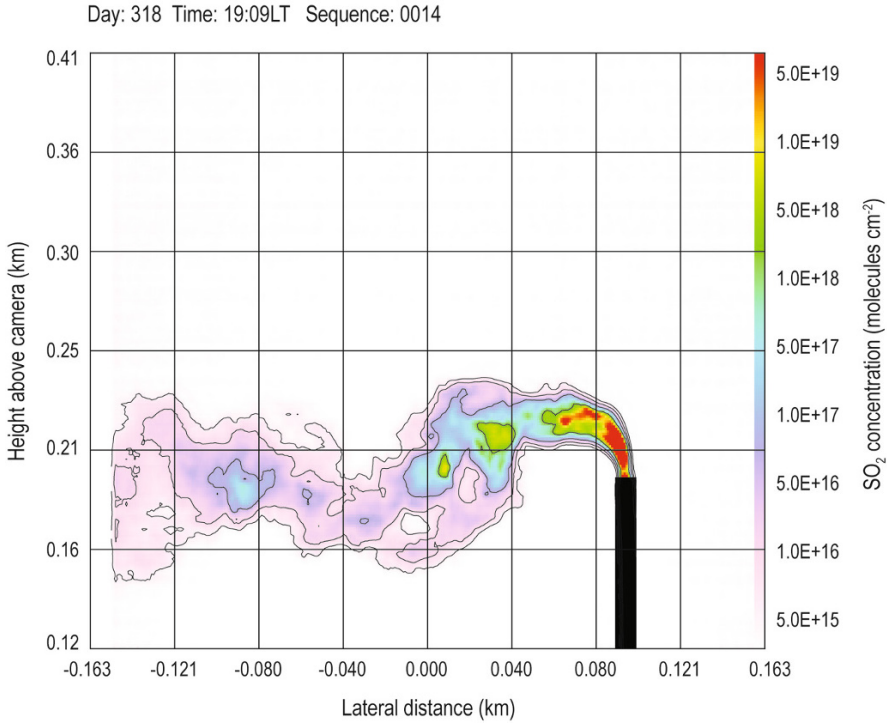


Figure 6.15. Concentrations of an industrial SO₂ plume derived from a ground-based thermal imaging camera system.

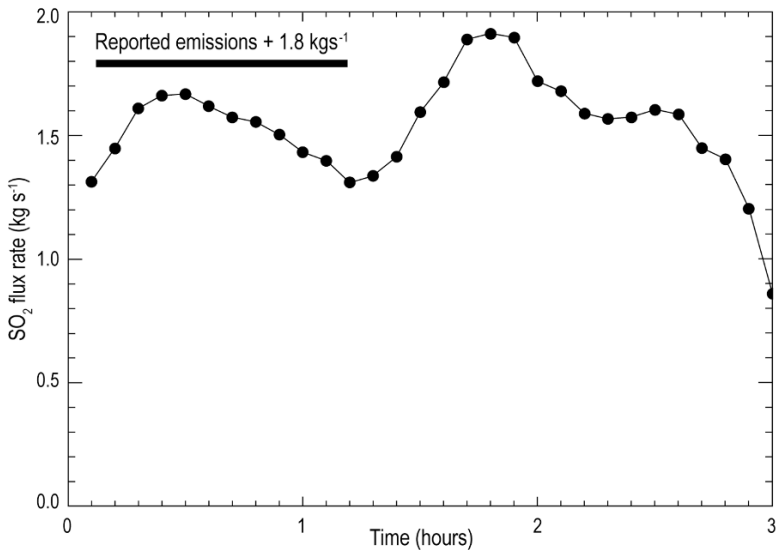


Figure 6.16. SO₂ flux derived from sequential thermal images from a ground-based thermal imaging camera. The reported average flux is $\sim 1.8 \text{ kg s}^{-1}$.

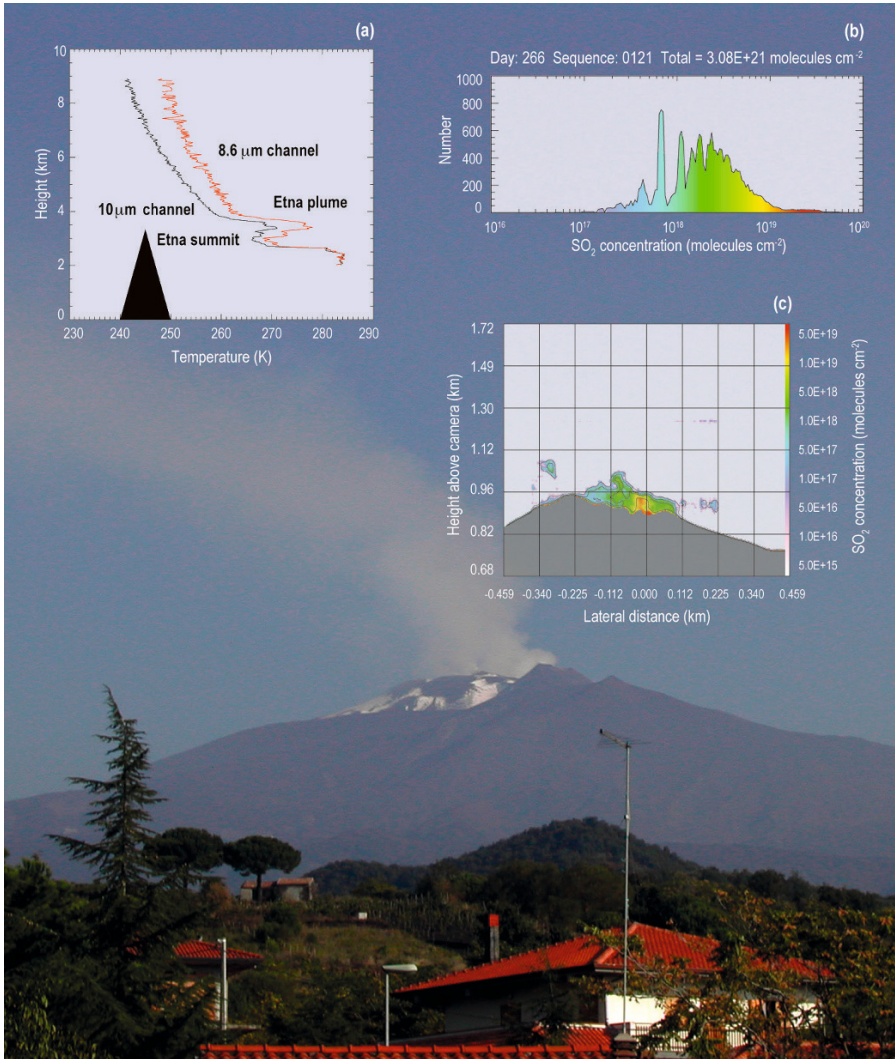


Figure 6.17. Thermal camera SO₂ retrieval for a plume from Mt Etna, Sicily. The plume contains water vapor (hence its white appearance) which must be corrected for by using radiative transfer calculations. The top left inset panel (a) shows the profile of temperature vs. height for two channels of the imager, indicating the presence of SO₂ and water vapor in the plume. Panel (b) shows the distribution of SO₂ concentration (mol m⁻²) within the plume. Panel (c) shows the SO₂ concentration image.

measurements, although there are some noticeable temporal variations about this value. Measurements of SO₂ have also been made at Etna and Stromboli and some results are shown in Figure 6.17. Retrieval requires at least three spectral measurements: an estimate of the water vapor profile, angular and background atmosphere corrections, and careful camera calibrations. Full details of

the camera design, calibration, and retrieval algorithms for both SO₂ and ash are described in Prata and Bernardo (2009).

The use of ground-based IR thermometry (radiometers and cameras) at volcanoes is still in its infancy. While some tests of these systems have occurred at various volcanoes, the widespread use of these systems has not happened. With costs

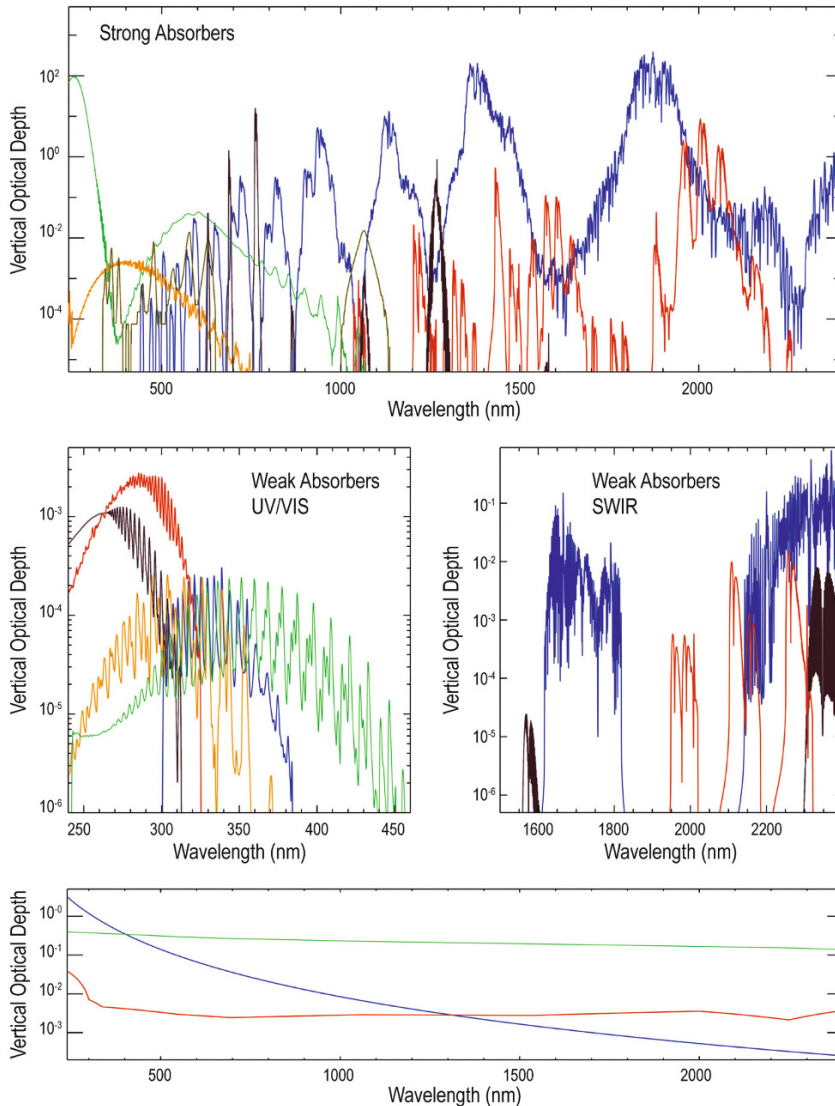


Figure 6.18. Vertical optical depth for various atmospheric gases calculated for 55°N at 10:00 local time. Strong absorbers (top-right panel), weak absorbers (middle panels), and the wavelength variation of Rayleigh scattering, aerosol extinction, and absorption are shown (bottom panel) (reproduced from Gottwald *et al.*, 2006).

decreasing and instrument performance increasing through validation studies and algorithm improvements, this situation will change. The major advantage of ground-based IR systems over UV systems (see the “UV cameras” section on p. 178) is their ability to detect at night, and hence these are the only systems capable of continuous volcanic monitoring. For NOPAC (high-latitude) volcanoes this

advantage is accentuated, and it is anticipated that thermal IR cameras and radiometers are likely to be increasingly used at these locations.

Figure 6.18 shows that SO₂ and other volcanic gases (e.g., BrO) have significant interactions at UV wavelengths. A brief discussion of the main developments and principles in UV sensing of volcanic gases follows.

COSPEC

The Correlation Spectrometer (COSPEC) has been the mainstay instrument for volcanic SO₂ measurements since its introduction for volcanic use in the 1970s (Moffat and Millan, 1971). Stix and Gonac'h (2000) provide a brief historical perspective on the COSPEC and its value to volcanic gas measurements. There are numerous papers that describe the use of the COSPEC for volcanological studies (e.g., Rose *et al.*, 1988). The COSPEC measurement principle utilizes an optical “mask” which is placed between the UV light entering the instrument and the photodetector to produce a modulated signal that depends on the slant, or vertical column, of SO₂ in the line of sight. A cell containing a known quantity of SO₂ is used to provide a calibration point for converting the UV signal to ppm*m of SO₂. By moving the instrument perpendicularly to the SO₂ plume and with an estimate of the plume speed (e.g., wind speed at plume height) the SO₂ emission rate (kg s⁻¹ or t day⁻¹) can be calculated. There are large uncertainties in this measurement technique because the plume speed is difficult to estimate accurately; only some parts of a heterogeneous, moving plume are sampled and there are inherent instrument uncertainties. However, with the introduction of wind circles (Doukas, 2002), the accuracy of airborne COSPEC measurements has increased greatly. Typically, overall variability is about 25% due to plume dispersion dynamics. Because emission rates at volcanoes can vary on a scale of several orders of magnitude, the uncertainties are not so serious and it is often the change in gas emission rate that is most important. Being able to detect changes using routine COSPEC measurements has proved highly effective. The COSPEC technology is now being rapidly overtaken by cheaper and easier-to-use UV CCD spectrometers.

Mini-DOAS

The mini-DOAS approach, based on the standard DOAS technique (e.g., Weibring *et al.*, 1998), has attracted great interest due to the availability of low-cost UV spectrometers. These lightweight spectrometers, combined with versatile fore-optics and a subnotebook computer, can be assembled from off-the-shelf components and are easily adapted for use in quantitative remote sensing of several gases, most frequently SO₂ though (Galle *et al.*, 2002; Edmonds

et al., 2003). Systems can be used to derive emission rates in the same way that COSPEC instruments are used. They are subject to the same uncertainties with respect to wind speed: for example, by scanning from a fixed station or moving vehicle, or multiple spectrometers can be deployed where each case has unique wind conditions (McGonigle *et al.*, 2002, 2003, 2005; Edmonds *et al.*, 2003; Miller *et al.*, 2006; Werner *et al.*, 2006b). The accuracy and versatility of the retrieval methods, portability, and ease of use of these economical instruments have caused them to gain wide acceptance for volcano emission monitoring. Mini-DOAS systems employing in situ calibration cells compare favorably with those using retrievals based on values calibrated using laboratory spectra; both are comparable with the COSPEC (Elias *et al.*, 2006). Many volcanic gases have been observed using mini-DOAS systems, including SO₂ (Galle *et al.*, 2002; McGonigle *et al.*, 2004) and many others such as BrO (Bobrowski *et al.*, 2003), ClO (Lee *et al.*, 2005), and H₂S and HCl (O'Dwyer *et al.*, 2003). A good synopsis and assessment of future prospects for UV spectroscopy in volcano remote sensing is given by McGonigle (2005).

UV cameras

An extension of the mini-DOAS system to an imaging system has been proposed by Bluth *et al.* (2006) and by Mori and Burton (2006). The development involves the construction and testing of a UV camera with a bandpass filter covering the UV SO₂ absorption band. By using calibration cells and correcting for stray light and Rayleigh scattered light, it has been shown that it is feasible to image SO₂ plumes and calculate SO₂ emission rates from volcanoes. Figure 6.19 is an example from some field work undertaken at Villarrica Volcano in Chile. The great utility of a UV camera is its ability to image the whole plume and simultaneously provide SO₂ emission rates by feature tracking to directly calculate plume speed (Kyle *et al.*, 1994). The camera could be used as a quantitative SO₂ webcam. The main restrictions of the system are the need to apply scattered light corrections and, as with all UV systems, the need for sunlight. For NOPAC volcanoes, UV systems may be less attractive than IR systems because of lighting constraints.

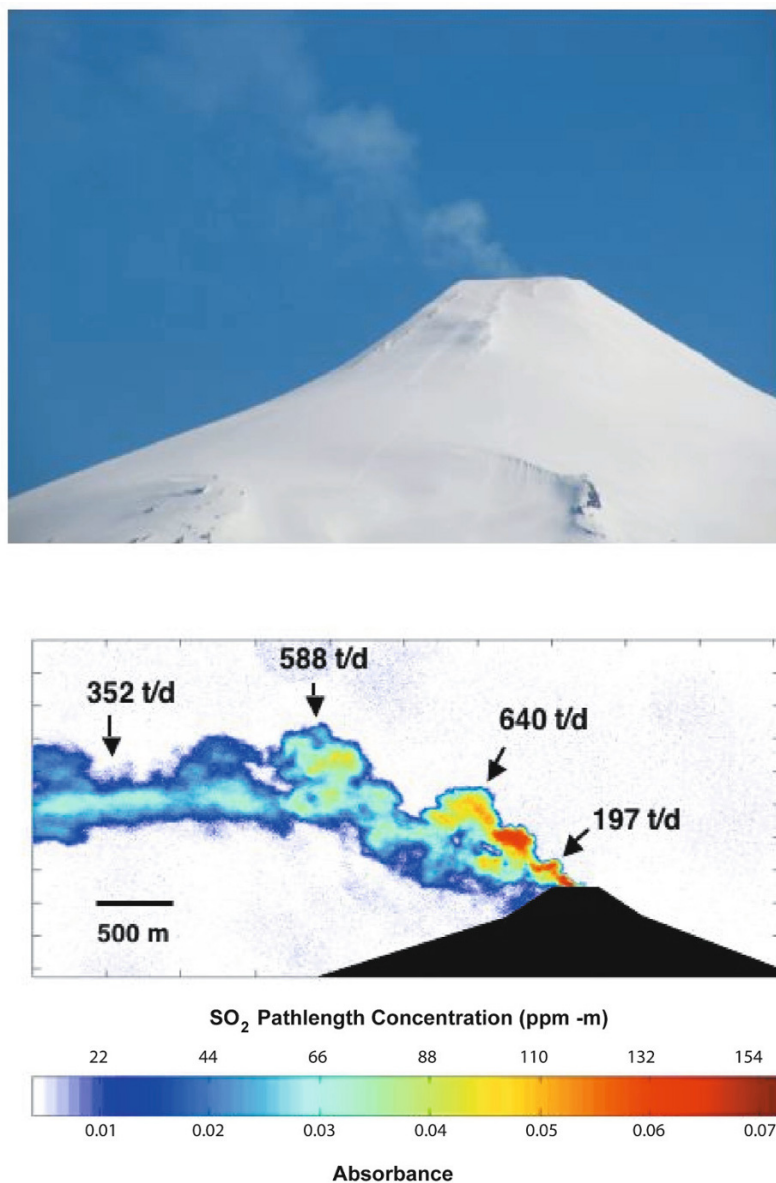


Figure 6.19. UV camera, SO₂ retrieval and fluxes for Villarrica Volcano, Chile (Bluth *et al.*, 2006).

6.5 CONCLUSIONS

There is great scope for measuring and monitoring a variety of volcanic gases using remote-sensing techniques. Many advances have been made in the use of ground-based UV mini-DOAS systems and also micro-bolometer thermal imaging systems.

These have mirrored the development of spaceborne systems, such as OMI and AIRS, both well suited to measure atmospheric SO₂. The use of these techniques and instruments is generic to all volcanoes, with some important caveats. Instruments that make use of reflected sunlight (UV instruments) are better suited to mid-latitude and

tropical volcanoes. AIRS and other infrared instruments have advantages for polar night and low-light conditions but suffer from problems associated with thermal contrast and have greater difficulty measuring gases close to the surface.

Polar-orbiting satellite systems generally have better coverage for high-latitude volcanoes due to overlapping orbits and so are better suited for NOPAC volcanoes. A polar-orbiting satellite can provide 6–10 views of a high-latitude ($>50^{\circ}\text{N}$) volcano per day. Geosynchronous satellites view a cone with a total viewing angle of $\sim 70^{\circ}$, giving reasonable coverage to roughly 60°N . Ground-based sensors suffer similar limitations to those of satellites, except that viewing conditions can be tailored to each volcano and therefore can be minimized. An ideal suite of ground-based instruments would include a scanning or imaging mini-DOAS/UV camera, a thermal imaging camera, and a webcam. The thermal camera can be used at night, either to make quantitative gas measurements or simply as a night camera. Combining ground-based measurements with satellite measurements seems a natural future direction and it might even be possible to use ground-based information to direct a satellite instrument to begin intensive monitoring.

With the advent of OMI and its ability to detect passively degassing and explosive events, coupled with several other sensors capable of providing quantitative SO_2 , there is now a need to develop validation methods. Ground-based measurements will play a key role in this; however, it is not yet clear how validation can best be done. COSPEC, mini-DOAS, and UV/IR cameras have been designed to make emission rate measurements (e.g., in tonnes per day) while satellite sensors make column (total or partial) column measurements. The infrequency of satellite measurements means that converting these column measurements to emission rates will be problematic. Furthermore, there are spatial sampling issues yet to be resolved. Satellite sensors sample large areas (on the order of tens of square kilometers) while ground-based measurements often cover much smaller areas (on the order of tens of square meters). Carefully planned validation experiments at well-instrumented volcanoes are needed. Airborne remote-sensing measurements would also be extremely valuable for satellite validation studies, but to date there are no airborne remote-sensing instruments specifically designed for volcanic gas studies. An airborne instrument (e.g., an FT-IR) capable of measuring

multiple gases (SO_2 , CO_2 , H_2S , and others) and particulates would clearly be of great value. Eventually, it would be desirable to be able to use quantitative satellite remote sensing of volcanic gases in a routine and perhaps operational manner for volcanic process studies and for early warning of activity.

Active systems (e.g., lidar) have not been discussed in any detail here because they are only just beginning to be deployed from satellites (e.g., CALIPSO). These systems add the ability to determine the height of volcanic particulates in the atmosphere. This information is of prime importance for aviation hazard warnings and also for assessing the impact of volcanic SO_2 on climate. High-resolution spatial data from ASTER have proven to be of value for measuring low-level SO_2 degassing and, although cloud cover can be a problem, the data have been used for studying NOPAC volcanoes. The temporal frequency of gas measurements at volcanoes from satellites is restricted for the NOPAC region by the frequency of overpasses of the polar-orbiters. The alignment of several (currently five) Earth-observing NASA satellites along a common orbit, spaced a few minutes apart (the A-Train), provide views of the same point on the Earth's surface using sensors in the optical and microwave domains. These data can be combined and used in new synergistic ways to study gaseous emissions and perhaps provide gas budgets and emission rates from restless volcanoes. Remote sensing as a technique offers great potential, but its greatest value comes when it is combined with other types of measurements or by assimilating data into models. The use of trajectory models (e.g., PUFF, HYSPLIT, or FLEXPART) in combination with remote sensing provides constraints for retrieval schemes and checks on the dispersion of volcanic gases. There is likely to be increasing use of remote-sensing data in "chemical" modeling activities and for forecasting "chemical weather" (transport of pollutants, particularly in urban environments), with an increasing focus on using remote sensing to measure tropospheric gases. It is possible in the future to see remote-sensing measurements used to provide health hazard warnings at degassing volcanoes. Finally, the large range of ground-based and satellite-based instruments able to detect global, passively degassing, and explosive SO_2 volcanic emissions can form the basis for an accurate and timely volcano-monitoring service for the research, aviation, and emergency planning communities.

6.6 ACKNOWLEDGMENTS

We are grateful to Arlin Krueger, Jeff Sutton, and John Ewert for providing thorough and helpful reviews of this chapter. Their expertise and critical advice has helped to improve this chapter greatly.

6.7 REFERENCES

- Ackerman, S.A.; Schreiner, A.J.; Schmit, T.J.; Woolf, H.M.; Li, J.; Pavolonis, M. (2008). Using the GOES sounder to monitor upper level SO₂ from volcanic eruptions, *J. Geophys. Res.*, **113**, D14S11, doi: 10.1029/2007JD009622.
- Afe, O.T.; Richter, A.; Sierk, B.; Wittrock, F.; Burrows, J.P. (2004). BrO emission from volcanoes: A survey using GOME and SCIAMACHY measurements, *Geophys. Res. Lett.*, **31**, L24113, doi: 10.1029/2004GL020994.
- Allard, P.; Carbonnelle, J.; Dajčević, D.; Le Bronec, J.; Morel, P.; Robe, M.C.; Maurenas, J.M.; Faivre-Pierrat, R.; Martin, D.; Sabroux, J.C.; Zettwoog, P. (1991). Eruptive and diffuse emissions of CO₂ from Mount Etna, *Nature*, **351**, 387–391.
- Allen, A.G.; Baxter, P.J.; Ottley, C.J. (2000). Gas and particle emissions from Soufrière Hills volcano, Montserrat, West Indies: Characterization and health hazard assessment, *Bull. Volcanol.*, **62**, 8–19.
- Andres, R.J.; Kasgnoc, A.D. (1998). A time-averaged inventory of subaerial volcanic sulfur emissions, *J. Geophys. Res.*, **103**(D19), 25251–25261.
- Bandy, A.R.; Maroulis, P.J.; Wilner, L.A.; Torres, A.L. (1982). Estimates of the fluxes of NO, SO₂, H₂S, CS₂, and OCS from Mt. St. Helens deduced from in situ plume concentration measurements, *Geophys. Res. Lett.*, **9**, 1097–1100.
- Belviso, S.; Nguyen, B.C.; Allard, P. (1986). Estimate of carbonyl sulfide (OCS) volcanic source strength deduced from OCS/CO₂ ratios in volcanic gases, *Geophys. Res. Lett.*, **13**(2), 133–136, doi: 10.1029/GL013i002p00133.
- Berresheim, H.; Jaeschke, W. (1983). The contribution of volcanoes to the global atmospheric sulfur budget, *J. Geophys. Res.*, **88**, 3732–3740.
- Bluth, G.J.S.; Doiron, S.D.; Schnetzler, C.C.; Krueger, A.J.; Walter, L.S. (1992). Global tracking of the SO₂ clouds from the June 1991 Mount Pinatubo eruptions, *Geophys. Res. Lett.*, **19**, 151–154.
- Bluth, G.J.S.; Schnetzler, C.C.; Krueger, A.J.; Walter, L.S. (1993). The contribution of explosive volcanism to global sulphur dioxide concentrations, *Nature*, **366**, 327–329.
- Bluth, G.J.S.; Scott, C.J.; Sprod, I.E.; Schnetzler, C.C.; Krueger, A.J.; Walter, L.S. (1995). Explosive SO₂ emissions from the 1992 eruptions of Mount Spurr, Alaska, *U.S. Geological Survey Bulletin*, **2139**, 37–45.
- Bluth, G.J.S.; Rose, W.I.; Sprod, I.E.; Krueger, A.J. (1997). Stratospheric loading of sulfur from explosive volcanic eruptions, *J. Geol.*, **105**, 671–684.
- Bluth, G.J.S.; Shannon, J.M.; Watson, I.M.; Prata, A.J.; Realmuto, V.J. (2007). Development of an ultraviolet digital camera for volcanic SO₂ imaging, *J. Volcanol. Geothermal Res.*, **161**(1/2), 47–56, doi: 10.1016/j.volgeores.2006.11.004.
- Bobrowski, N.; Honninger, G.; Galle, B.; Platt, U. (2003). Detection of bromine monoxide in a volcanic plume, *Nature*, **423**, 273–276.
- Bovensmann, H.; Burrows, J.P.; Buchwitz, M.; Frerick, J.; Noël, S.; Rozanov, V.V.; Chance, K.V.; Goede, A.P.H. (1999). SCIAMACHY: Mission objectives and measurement modes, *J. Atmos. Sci.*, **56**, 127–150, doi: 10.1175/1520-0469(1999)056<0127:SMOAMM>2.0.CO;2.
- Burrows, J.P.; Weber, M.; Buchwitz, M.; Rozanov, V.; Ladstätter-Weissenmayer, A.; Richter, A.; DeBeek, R.; Hoogen, R.; Branstedt, K.; Eichmann, K.-U.; Eisinger, M.; Perner, D. (1999). The Global Ozone Monitoring Experiment (GOME): Mission concept and first scientific results, *J. Atmos. Sci.*, **56**, 151–175, doi: 10.1175/1520-0469(1999)056<0515:TGOMEG>2.0.CO;2.
- Burton, M.R.; Oppenheimer, C.; Horrocks, L.A.; Francis, P.W. (2000). Remote sensing of CO₂ and H₂O emission rates from Masaya volcano, Nicaragua, *Geology*, **28**(10), 915–918, doi: 10.1130/0091-7613.
- Cadle, R.D. (1975). Volcanic emissions of halides and sulfur compounds to the troposphere and stratosphere, *J. Geophys. Res.*, **80**, 1650–1652.
- Cadle, R.D. (1980). A comparison of volcanic with other fluxes of atmospheric trace gas constituents, *Rev. Geophys. Space Phys.*, **18**(4), 746–752.
- Cambaliza, M.O.; Mount, G.; Lamb, B.; Westberg, H.; Gibson R. (2005). *Measurement of Ecosystem–Atmosphere Exchange of Isotopic CO₂ using Fourier Transform Infrared (FTIR) Spectroscopy*, American Geophysical Union, Washington, D.C., Fall Meeting Abstracts.
- Campion, R.; Salerno, G.G.; Coheur, P.-F.; Hurtmans, D.; Clarisse, L.; Kazahaya, K.; Burton, M.; Caltabiano, T.; Clerbaux, C.; Bernard, A. (2010). Measuring volcanic degassing of SO₂ in the lower troposphere with Aster band ratios, *J. Volcanol. Geotherm. Res.*, **194**, 42–54, doi: 10.1016/j.volgeores.2010.04.010.
- Carn, S.A.; Bluth, G.J.S. (2003). Prodigious sulfur dioxide emissions from Nyamuragira volcano, D.R. Congo, *Geophys. Res. Lett.*, **30**(23), 2211, doi: 10.1029/2003GL018465.
- Carn, S.A.; Krueger, A.J.; Bluth, G.J.S.; Schaefer, S.J.; Krotkov, N.A.; Watson, I.M.; Datta, S. (2003).

- Volcanic eruption detection by the Total Ozone Mapping Spectrometer (TOMS) instruments: A 22-year record of sulfur dioxide and ash emissions, in C. Oppenheimer, D.M. Pyle, and J. Barclay (Eds.), *Volcanic Degassing*, Special Publication 213, Geological Society, London, pp. 177–202.
- Carn, S.A.; Krueger, A.J.; Krotkov, N.A.; Gray, M.A. (2004). Fire at Iraqi sulfur plant emits SO₂ clouds detected by Earth Probe TOMS, *Geophys. Res. Lett.*, **31**(19), L19105, doi: 10.1029/2004GL020719.
- Carn, S.A.; Strow, L.L.; de Souza-Machado, S.; Edmonds, Y.; Hannon S. (2005). Quantifying tropospheric volcanic emissions with AIRS: The 2002 eruption of Mt. Etna (Italy), *Geophys. Res. Lett.*, **32**.
- Carn, S.A.; Krotkov, N.A.; Yang, K.; Hoff, R.M.; Prata, A.J.; Krueger, A.J.; Loughlin, S.C.; Levelt, P.F. (2007a). Extended observations of volcanic SO₂ and sulphate aerosol in the stratosphere, *Atmos. Chem. Phys. Discuss.*, **7**, 2857–2871.
- Carn, S.A.; Krueger, A.J.; Krotkov, N.A.; Yang, K.; Levelt, P.F. (2007b). Sulfur dioxide emissions from Peruvian copper smelters detected by the Ozone Monitoring Instrument, *Geophys. Res. Lett.*, **34**, L09801, doi: 10.1029/2006GL029020.
- Carn, S.A.; Pallister, J.S.; Lara, L.; Ewert, J.W.; Watt, S.; Prata, A.J.; Thomas, R.J.; Villarosa, G. (2009). The unexpected awakening of Chaitén Volcano, Chile, *EOS, Transactions American Geophysical Union*, **90**(24), 205, doi: 10.1029/2009EO240001.
- Casadevall, T.J.; Doukas, M.P.; Neal, C.A.; McGimsey, R.G.; Gardner, C.A. (1994). Emission rates of sulfur dioxide and carbon dioxide from Redoubt Volcano, Alaska during the 1989–1990 eruptions, *J. Volcanol. Geothermal Res.*, **62**, 519–530.
- Chahine, M.T.; Pagano, T.S.; Aumann, H.H.; Atlas, R.; Barnett, C.; Blaisdell, J.; Chen, L.; Divakarla, M.; Fetzer, E.J.; Goldberg, M. *et al.* (2006). AIRS: Improving weather forecasting and providing new data on greenhouse gases, *Bull. Amer. Meteorol. Soc.*, **87**(7), 911–926, <http://hdl.handle.net/2014/40298>.
- Chance, K. (Ed.) (2002). OMI Algorithm Theoretical Basis Document (Volume IV): OMI Trace Gas Algorithms, ATBD-OMI-04, Version 2.0, 78 pp, available at http://www.knmi.nl/omi/research/documents/algorithm_docs.html
- Crowley, T.J. (2000). Causes of climate change over the past 1000 years, *Science*, **289**, 270–277.
- Delmelle, P.; Stix, J. (2000). Volcanic gases, in H. Sigurdsson, B.F. Houghton, S.R. McNutt, H. Rymer, and J. Stix (Eds.), *Encyclopedia of Volcanoes*, Academic Press, San Diego, CA, pp. 803–816.
- Delmelle, P.; Stix, J.; Baxter, P.J.; Garcia-Alvarez, J.; Barquero, J. (2002). Atmospheric dispersion, environmental effects and potential health hazard associated with the low-altitude gas plume of Masaya volcano, Nicaragua, *Bull. Volcanol.*, **64**(6), 423–434.
- Doukas, M.P. (2002). *A New Method for GPS-based Wind Speed Determinations during Airborne Volcanic Plume Measurements*, USGS Open-File Report 02-395, U.S. Geological Survey, Reston, VA, 13 pp.
- Doukas, M.P. (1995). *A Compilation of Sulfur Dioxide and Carbon Dioxide Emission-rate Data from Cook Inlet Volcanoes (Redoubt, Spurr, Iliamna, and Augustine)*, Alaska during the Period from 1990 to 1994, USGS Open-File Report 95-55, U.S. Geological Survey, Reston, VA, 15 pp.
- Duffell, H.; Oppenheimer, C.; Burton, M. (2001). Volcanic gas emission rates measured by solar occultation spectroscopy, *Geophys. Res. Lett.*, **28**(16), 3131–3134.
- Edmonds, M.; Herd, R.A.; Galle, B.; Oppenheimer, C.M. (2003). Automated, high time-resolution measurements of SO₂ flux at Soufrière Hills volcano, Montserrat, *Bull. Volcanol.*, **65**, 578–586, doi: 10.1007/s00445-003-0286-x.
- Edwards, D.P. (1992). *GENLN2: A General Line-by-line Atmospheric Transmittance and Radiance Model—Version 3.0, Description and User's Guide* (NCAR Technical Note, NCAR/TN-367+STR), National Center for Atmospheric Research, Boulder, CO, 157 pp.
- Eisinger, M.; Burrows, J.P. (1998). Tropospheric sulfur dioxide observed by ERS-2 GOME instrument, *Geophys. Res. Lett.*, **25**, 4177–4180.
- Elias, T.; Sutton, A.J.; Oppenheimer, C.; Horton, K.A.; Garbeil, H.; Tsanev, V.; McGonigle A.J.S.; and Williams-Jones, G. (2006). Comparison of COSPEC and two miniature ultraviolet spectrometer systems for SO₂ measurements using scattered sunlight, *Bull. Volcanol.*, **68**, 313–322, doi: 10.1007/s00445-005-0026-5.
- Etheridge, D.M.; Leuning, R.; De Vries, D.; Dodds, K. (2005). *Atmospheric Monitoring and Verification Technologies for CO₂ Storage at Geosequestration Sites in Australia*, C/1032, Report No. RPT05-0134, ii, 81 pp., CO₂CRC, Canberra.
- Francis, P.; Burton, M.R.; Oppenheimer, C. (1998). Remote measurements of volcanic gas compositions by solar occultation spectroscopy, *Nature*, **396**, 567–570.
- Galle, B.; Oppenheimer, C.; Geyer, A.; McGonigle, A.J.S.; Edmonds, M.; Horrocks, L. (2002). A miniaturised ultraviolet spectrometer for remote sensing of SO₂ fluxes: A new tool for volcano surveillance, *J. Volcanol. Geothermal Res.*, **119**, 241–254.
- Gerlach, T.M. (1991). Present-day CO₂ emissions from volcanos, *EOS, Transactions American Geophysical Union*, **72**(23), 249, doi: 10.1029/90EO10192.
- Gerlach, T.M.; Delgado, H.; McGee, K.A.; Doukas, M.P.; Venegas, J.J.; Cardenas, L. (1997). Application of the LI-COR CO₂ analyzer to volcanic plumes: A case study, volcán Popocatepetl, Mexico,

- June 7 and 10, 1995, *J. Geophys. Res.*, **102**(B4), 8005–8019.
- Gottwald, M.; Bovensmann, H.; Lichtenberg, G.; Noel, S.; von Bargaen, A.; Slijkhuis, S.; Piters, A.; Hoogeveen, R.; von Savigny, C.; Buchwitz, M. *et al.* (2006). *SCIAMACHY: Monitoring the Changing Earth's Atmosphere*, Deutsche Forschungsanstalt für Luft und Raumfahrt, Oberpfaffenhofen, Germany.
- Graf, H.-F.; Feichter, J.; Langmann, B. (1997). Volcanic sulfur emissions: Estimates of source strength and its contribution to the global sulfate distribution. *J. Geophys. Res.*, **102**, 10727–10738.
- Gu, Y.; Rose, W.I.; Schneider, D.J.; Bluth, G.J.S.; Watson, I.M. (2005). Advantageous GOES IR results for ash mapping at high latitudes: Cleveland eruptions 2001, *Geophys. Res. Lett.*, **32**, L02305, doi: 10.1029/2004GL021651.
- Guo, S.; Bluth, G.J.S.; Rose, W.I.; Watson, I.M.; Prata, A.J. (2004). Re-evaluation of SO₂ release of the 15 June 1991 Pinatubo eruption using ultraviolet and infrared satellite sensors, *Geochem. Geophys. Geosyst.*, **5**(4), Q04001, doi: 10.1029/2003GC000654.
- Halmer, M.M.; Schmincke, H.-U. (2003). The impact of moderate-scale explosive eruptions on stratospheric gas injections, *Bull. Volcanol.*, **65**, 433–440, doi: 10.1007/s00445-002-0270-x.
- Halmer, M.M.; Schmincke, H.-U.; Graf, H.-U. (2002). The annual volcanic gas input into the atmosphere, in particular into the stratosphere: A global data set for the past 100 years, *J. Volcanol. Geothermal Res.*, **115**, 511–528.
- Harris, A.J.L.; Ripepe, M. (2007). Synergy of multiple geophysical approaches to unravel explosive eruption conduit and source dynamics: A case study from Stromboli, *Chemie der Erde*, **67**(1), 1–35, doi: 10.1016/j.chemer.2007.01.003.
- Harris, D.M.; Sato, M.; Casadevall, T.J.; Rose, Jr., W.I.; Bornhorst, T.J. (1981). Emission rates of CO₂ from plume measurements, in P.W. Lipman and D.R. Mullineaux (Eds.), *The 1980 Eruptions of Mount St. Helens*, USGS Professional Paper 1250, U.S. Geological Survey, Reston, VA, pp. 201–207.
- Horrocks, L.; Oppenheimer, C.; Burton, M.; Duffell, H.J. (2001). Open-path Fourier transform infrared spectroscopy of SO₂: An empirical error budget analysis, with implications for volcano monitoring, *J. Geophys. Res.*, **106**(D21), 27647–27659, .
- Horton, K.A.; Williams-Jones, G.; Garbeil, H.; Elias, T.; Sutton, A.J.; Mouginiis-Mark, P.; Porter, J.N.; Clegg, S. (2006). Real-time measurement of volcanic SO₂ emissions: Validation of a new UV correlation spectrometer (FLYSPEC), *Bull. Volcanol.*, **68**, 313–322, doi: 10.1007/s00445-005-0026-5.
- Horwell, C.J.; Baxter, P.J. (2006). The respiratory health hazards of volcanic ash: a review for volcanic risk mitigation, *Bull. Volcanol.*, **69**, 124, doi: 10.1007/s00445-006-0052-y.
- Kinoshita, K.; Kanagaki, C.; Minaka, A.; Tsuchida, S.; Matsui, T.; Tupper, A.; Yakiwara, H.; Iino, N. (2003). Ground and satellite monitoring of volcanic aerosols in visible and infrared bands, *CERES Int. Symp. on Remote Sensing: Monitoring of Environmental Change in Asia, Chiba, Japan, December 16–17, 2003*.
- Kramer, H.J. (2002). *Observations of the Earth and Its Environment: Survey of Missions and Sensors* (Fourth Edition), Springer-Verlag, New York, 1,510 pp.
- Krotkov, N.A.; Carn, S.A.; Krueger, A.J.; Bhartia, P.K.; Yang, K. (2006). Band residual difference algorithm for retrieval of SO₂ from the Aura Ozone Monitoring Instrument (OMI), *IEEE Trans. Geosci. Remote Sensing*, **44**(5), 1259–1266.
- Krueger, A.J. (1983). Sighting of El Chichón sulfur dioxide clouds with the Nimbus 7 Total Ozone Mapping Spectrometer, *Science*, **220**, 1377–1379.
- Krueger, A.J.; Guenther, B.; Flieg, A.J.; Heath, D.F.; Hilsenrath, E.; McPeters, R.; Prabhakara, C. (1980). Satellite ozone measurements, *Philosophical Trans. Royal Society London*, **A296**, 191–293.
- Krueger, A.J.; Walter, L.S.; Bhartia, P.K.; Schnetzler, C.C.; Krotkov, N.A.; Sprod, I.; Bluth, G.J.S. (1995). Volcanic sulfur dioxide measurements from the total ozone mapping spectrometer instruments, *J. Geophys. Res.*, **100**(D7), 14057–14076.
- Krueger, A.J.; Schaefer, S.J.; Krotkov, N.; Bluth, G.; Baker, S. (2000). Ultraviolet remote sensing of volcanic emissions, in P.J. Mouginiis-Marks, J.A. Crisp, and J.H. Fink (eds), *Remote Sensing of Active Volcanism*, AGU Monograph Series 116, American Geophysical Union, Washington, D.C., pp. 25–43.
- Kyle, P.R.; Sybeldon, L.M.; McIntosh, W.C.; Meeker, K.; Symonds, R. (1994). Sulfur dioxide emission rates from Mount Erebus, Antarctica, *Volcanological and Environmental Studies of Mount Erebus, Antarctica*, **66**, 69–82.
- Lee, C.; Kim, Y.J.; Tanimoto, H.; Bobrowski, N.; Platt, U.; Mori, T.; Yamamoto, K.; Hong, C.S. (2005). High ClO and ozone depletion observed in the plume of Sakurajima volcano, Japan, *Geophys. Res. Lett.*, **32**, L21809, doi: 10.1029/2005GL023785.
- Levelt, P.F.; van den Oord, G.H.J.; Dobber, M.R.; Mälkki, A.; Visser, H.; de Vries, J.; Stammes, P.; Lundell, J.; Saari, H. (2006). The Ozone Monitoring Instrument, *IEEE Trans. Geosci. Remote Sensing*, **44**(5), 1093–1101, doi: 10.1109/TGRS.2006.872333.
- Love, S.P.; Goff, F.; Counce, D.; Siebe, C.; Delgado, H. (1998). Passive infrared spectroscopy of the eruption plume at Popocatepetl volcano, Mexico, *Nature*, **396**, 563–566.
- Malinconico, L.L. (1979). Fluctuations in SO₂ emission during recent eruptions of Etna, *Nature*, **278**, 43–45.
- Mankin, W.G.; Coffey, M.T.; Goldman, A. (1992). Airborne observations of SO₂, HCl, and O₃ in the

- stratospheric plume of the Pinatubo volcano in July 1991, *Geophys. Res. Lett.*, **19**(2), 179–182.
- Marty, B.; Giggenbach, W.F. (1990). Major and rare gases at White Island volcano, New Zealand: Origin and flux of volatiles, *Geophys. Res. Lett.*, **17**(3), 247–250.
- McGee, K.A.; Gerlach, T.M. (1998). Airborne volcanic plume measurements using a FT-IR spectrometer, Kīlauea volcano, Hawaii, *Geophys. Res. Lett.*, **25**(5), 615–618.
- McGee, K.A.; Doukas, M.P.; Gerlach, T.M. (2001). Quiescent hydrogen sulfide and carbon dioxide degassing from Mount Baker, Washington, *Geophys. Res. Lett.*, **28**(23), 4479–4482.
- McGonigle, A.J.S. (2005). Volcano remote sensing with ground-based spectroscopy, *Philosophical Trans. Royal Society London*, **A363**, 2915–2929.
- McGonigle, A.J.S.; Oppenheimer, C.; Galle, B.; Mather, T.A.; Pyle, D.M. (2002). Walking traverse and scanning DOAS measurements of volcanic gas emission rates, *Geophys. Res. Lett.*, **29**, 1985–1989, doi: 10.1029/2002GL015827.
- McGonigle, A.J.S.; Oppenheimer, C.; Galle, B.; Edmonds, M.; Caltabiano, T.; Salerno, G.; Burton, M.; Mather, T.A. (2003). Volcanic sulphur dioxide flux measurements at Etna, Vulcano and Stromboli obtained using an automated scanning static ultraviolet spectrometer, *J. Geophys. Res.*, **108**, 2455, doi: 10.1029/2002JB002261.
- McGonigle, A.J.S.; Oppenheimer, C.; Tsanev, V.I. (2004). Sulphur dioxide fluxes from Papua New Guinea's volcanoes, *Geophys. Res. Lett.*, **31**, L08606, doi: 10.1029/2004GL019568.
- McGonigle, A.J.S.; Inguaggiato, S.; Aiuppa, A.; Hayes, A.R.; Oppenheimer, C. (2005). Accurate measurement of volcanic SO₂ flux: Determination of plume transport speed and integrated SO₂ concentration with a single device, *Geochem. Geophys. Geosyst.*, **6**, Q02003.
- McKeen, S.A.; Liu, S.C.; Kiang, C.S. (1984). On the chemistry of stratospheric SO₂ from volcanic eruptions, *J. Geophys. Res.*, **89**(D3), 4873–4881.
- Miller, C.A.; Werner, C.A.; Herd, R.; Edmonds, M. (2006). A remotely operated, automatic scanning DOAS system at White Island, New Zealand, *EOS, Trans. Am. Geophys. Union*, **87**(52), Fall Meeting Suppl., Abstract V53A-1722.
- Moffat, A.J.; Millan, M.M. (1971). The application of optical correlation techniques to the remote sensing of SO₂ plumes using skylight, *Atmos. Environ.*, **5**, 677–690.
- Mori, T.; Burton, M. (2006). The SO₂ camera: A simple, fast and cheap method for ground-based imaging of SO₂ in volcanic plumes, *Geophys. Res. Lett.*, **33**, L24804, doi: 10.1029/2006GL027916.
- Notsu, K.; Mori, T.; Igarashi, G.; Tohjima, Y.; Wakita, H. (2003). Infrared spectral radiometer: A new tool for remote measurement of SO₂ of volcanic gas, *Geochem. J.*, **27**, 361–366.
- NRC (2005). *Earth Science and Applications from Space: Urgent Needs and Opportunities to Serve the Nation*, National Academies Press, Washington, D.C., 456 pp. [National Research Council].
- O'Dwyer, M.; McGonigle, A.J.S.; Padgett, M.J.; Oppenheimer, C.; Inguaggiato, S. (2003). Real time measurements of volcanic H₂S/SO₂ ratios by UV spectroscopy, *Geophys. Res. Lett.*, **30**, 1652–1655, doi: 10.1029/2003GL017246.
- Oman, L.; Robock, A.; Stenchikov, G. (2005). Climatic response to high-latitude volcanic eruptions, *J. Geophys. Res.*, **110**, D13103, doi: 1029/2004JD 005487.
- Oppenheimer, C.; Francis, P.; Burton, M.; Maciejewski, A.; Boardman L. (1998a). Remote measurement of volcanic gases by Fourier transform infrared spectroscopy, *Applied Physics*, **B67**, 505–515.
- Oppenheimer, C.; Francis, P.; Stix, J. (1998b). Depletion rates of sulfur dioxide in tropospheric volcanic plumes, *Geophys. Res. Lett.*, **25**(14), 2671–2674.
- Oppenheimer, C.; Edmonds, M.; Francis, P.; Burton, M.R. (2002). Variation in HCl/SO₂ gas ratios observed by Fourier transform spectroscopy at Soufrière Hills volcano, Montserrat, in T.H. Druitt and P. Kokelaar (Eds.), *The Eruption of Soufrière Hills Volcano, Montserrat, from 1995 to 1999*, Memorandum 21, Geological Society, London, pp. 621–639.
- Pitari, G.; Mancini, E.; Rizi, V.; Shindell, D.T. (2002). Impact of future climate and emission changes on stratospheric aerosols and ozone, *J. Atmos. Sci.*, **59**, 414–440.
- Platt, U. (1994). Differential optical absorption spectroscopy (DOAS), *Chem. Anal. Series*, **127**, 27–83.
- Porter, J.N.; Horton, K.A.; Mouginis-Mark, P.J.; Lienert, B.; Sharma, S.K.; Lau, E. (2002). Sun photometer and lidar measurements of the plume from the Hawaii Kilauea volcano Pu'u O'o vent: Aerosol and SO₂ lifetime, *Geophys. Res. Lett.*, **29**(16), doi: 10.1029/2002GL014744.
- Power, J.A.; Nye, C.J.; Coombs, M.L.; Wessels, R.L.; Cervelli, P.F.; Dehn, J.; Wallace, K.L.; Freymueller, J.T.; Doukas, M.P. (2006). The reawakening of Alaska's Augustine Volcano, *EOS, Transactions American Geophysical Union*, **87**(37), 373–377.
- Prata, A.J.; Bernardo, C. (2007). Retrieval of volcanic ash particle size, mass and optical depth from a ground-based thermal infrared camera, *J. Volcanol. Geotherm. Res.*, **186**(1/2), 91–107, doi: 10.1016/j.volgeores.2009.02.07.
- Prata, A.J.; Kerkmann, J. (2007). Simultaneous retrieval of volcanic ash and SO₂ using MSG-SEVIRI measurements, *Geophys. Res. Lett.*, **34**, L05813, doi: 10.1029/2006GL028691.
- Prata, A.J.; Barton, I.J.; Kingwell, J. (1993). Aircraft hazard from volcanoes, *Nature*, **366**, 199.

- Prata, A.J.; Rose, W.I.; Self, S.; O'Brien, D.M. (2003). Global, long-term sulphur dioxide measurements from TOVS data: A new tool for studying explosive volcanism and climate, in A. Robock and C. Oppenheimer (Eds.), *Volcanism and the Earth's Atmosphere*, Geophysical Monograph 139, American Geophysical Union, Washington, D.C., pp. 75–92.
- Prata, A.J.; Schreiner, A.; Schmit, A.; Ellrod, G. (2004). First measurements of volcanic sulphur dioxide from the GOES sounder: Implications for improved aviation safety, *Proc. Int. Conf. on Volcanic Ash and Aviation Safety, Alexandria, VA, June 21–24, 2004*.
- Prata, A.J.; Carn, S.A.; Stohl, A.; Kerkmann, J. (2007). Long range transport and fate of a stratospheric volcanic cloud from Soufrière Hills volcano, Montserrat, *Atmos. Chem. Phys.*, **7**, 5093–5103.
- Pugnaghi, S.; Teggi, S.; Corradini, S.; Buongiorno, M.F.; Merucci, L.; Bogliolo, M.P. (2002). Estimation of SO₂ abundance in the eruption plume of Mt Etna using two MIVIS thermal infrared channels: A case study from the Sicily-1997 campaign, *Bull. Volcanol.*, **64**, 328–337, doi: 10.1007/s00445-002-0211-8.
- Pyle, D.M.; Beattie, P.D.; Bluth, G.J.S. (1996). Sulphur emissions to the stratosphere from explosive volcanic eruptions, *Bull. Volcanol.*, **57**, 663–671.
- Read, W.G.; Froidevaux, L.; Waters, J.W. (1993). Microwave limb sounder measurement of stratospheric SO₂ from the Mt. Pinatubo volcano, *Geophys. Res. Lett.*, **20**(12), 1299–1302.
- Realmuto, V.J. (1995). *Volcanic SO₂: High and Moderate Spatial Resolution*, EOS IDS Volcanology Team Data Product Document #3289, v3.0, Jet Propulsion Laboratory, Pasadena, CA, 16 pp.
- Realmuto, V.J. (2000). The potential use of earth observing system data to monitor the passive emission of sulfur dioxide from volcanoes, in P. Mouginis-Marks, J. Crisp, and J. Fink (Eds.), *Remote Sensing of Active Volcanism*, AGU Monograph 116, American Geophysical Union, Washington, D.C., pp. 101–115.
- Realmuto V.J.; Abrams M.J.; Buongiorno, M.F.; Pieri, D.C. (1994). The use of multispectral thermal infrared image data to estimate the sulfur-dioxide flux from volcanoes: A case-study from Mount Etna, Sicily, July 29, 1986, *J. Geophys. Res.—Solid Earth*, **99**(B1), 481–488.
- Realmuto, V.J.; Sutton, A.J.; Elias, T. (1997). Multispectral thermal infrared mapping of sulfur dioxide plumes: A case study from the East Rift Zone of Kīlauea, Hawaii, *J. Geophys. Res.*, **102**, 15057–15072.
- Richter, A.; Burrows, J.P.; Nuss, H.; Granier, C.; Niemeier, U. (2005). Increase in tropospheric nitrogen dioxide over China observed from space, *Nature*, **437**, 129–132, doi: 10.1038/nature04092.
- Ripepe, M.; Delle Donne, D.; Lacanna, G.; Marchetti, E.; Ulivieri, G. (2009). The onset of the 2007 Stromboli effusive eruption recorded by an integrated geophysical network, *J. Volcanol. Geotherm. Res.*, **182**(3/4), 131–136, doi: 10.1016/j.jvolgeores.2009.02.011.
- Robock, A. (2000). Volcanic eruptions and climate, *Rev. of Geophys.*, **38**(2), 191–219.
- Rose, W.I.; Heiken, G.; Wohletz, K.; Eppler, D.; Barr, S.; Miller, T.; Chuan, R.L.; Symonds, R.B. (1988). Direct rate measurements of eruption plumes at Augustine volcano: A problem of scaling and uncontrolled variables, *J. Geophys. Res.*, **93**(B5), 4485–4499.
- Rose, W.I.; Gu, Y.; Watson, I.M.; Yu, T.; Bluth, G.J.S.; Prata, A.J.; Krueger, A.J.; Krotkov, N.; Carn, S.; Fromm, M.D. et al. (2003). *The February–March 2000 Eruption of Hekla, Iceland from a Satellite Perspective*, in A. Robock and C. Oppenheimer (Eds.), *Volcanism and the Earth's Atmosphere*, AGU Monograph 139, American Geophysical Union, Washington, D.C., pp. 107–130.
- Rose, W.I.; Millard, G.A.; Mather, T.A.; Hunton, D.E.; Anderson, B.; Oppenheimer, C.; Thornton, B.F.; Gerlach, T.M.; Viggiano, A.A.; Kondo, Y. et al. (2006). Atmospheric chemistry of a 33–34 hour old volcanic cloud from Hekla Volcano (Iceland): Insights from direct sampling and the application of chemical box modeling, *J. Geophys. Res.*, **111**, D20206, doi: 10.1029/2005JD006872.
- Schmit, T.; Gunshor, M.M.; Menzel, P.W.; Gurka, J.J.; Li, J.; Backmeier, A.S. (2006). Introducing the next-generation advanced baseline imager on GOES-R, *Bull. Amer. Meteorol. Society*, **86**(8), 1079–1096, doi: 10.1175/BAMS-86-8-1079.
- Schneider, D.J.; Rose, W.I.; Kelly, L. (1995). Tracking of 1992 eruption clouds from Crater Peak vent on Mount Spurr Volcano, Alaska, in T.E.C. Keith (Ed.), *The 1992 Eruptions of Crater Peak Vent, Mt. Spurr Volcano, Alaska* (USGS Bulletin 2139), U.S. Geological Survey, Reston, VA, 220 pp.
- Seinfeld, J.H.; Pandis, S.N. (1998). *Atmospheric Chemistry and Physics: From Air Pollution to Climate Change*, John Wiley & Sons, New York, 1,326 pp..
- Simkin, T.; Siebert, L. (1994). *Volcanoes of the World* (Second Edition), Geoscience Press, Tucson, AZ, 349 pp.
- Stix, J.; Gaonac'h, H. (2000). Gas, plume, and thermal monitoring, in H. Sigurdsson, B.F. Houghton, S.R. McNutt, H. Rymer, and J. Stix (Eds.), *Encyclopedia of Volcanoes*, Academic Press, San Diego, CA, pp. 1141–1163.
- Stoiber, R.E. (1995). Volcanic gases from subaerial volcanoes on Earth, *Global Earth Physics: A Handbook of Physical Constants*, AGU Reference Shelf 1, American Geophysical Union, Washington, D.C., pp. 308–319.

- Stoiber, R.E.; Jepsen, A. (1973). Sulfur dioxide contributions to the atmosphere by volcanoes, *Science*, **182**, 577–578.
- Stoiber, R.E.; Malinconico, Jr., L.L.; Williams, S.N. (1983). Use of the Correlation Spectrometer at volcanoes, in H. Tazieff and J.-C. Sabroux (Eds.), *Forecasting Volcanic Events*, Elsevier, Amsterdam, pp. 425–444.
- Stoiber, R.E.; Williams, S.N.; Huebert, B.J. (1986). Sulfur and halogen gases at Masaya Caldera Complex, Nicaragua: Total flux and variations with time. *J. Geophys. Res.*, **91**, 12215–12231.
- Stoiber, R.E.; Williams, S.N.; Huebert, B. (1987). Annual contribution of sulfur dioxide to the atmosphere by volcanoes, *J. Volcanol. Geothermal Res.*, **33**, 1–8.
- Symonds, R.; Rose, W.I.; Reed, M. (1988). Contributions of Cl and F bearing gases to the atmosphere, *Nature*, **344**, 415–418.
- Textor, C.; Graf, H.-F.; Herzog, M.; Oberhuber, J.M. (2003). Injection of gases into the stratosphere by explosive volcanic eruptions, *J. Geophys. Res.*, **108**(D19), D4606, doi: 10.1029/2002JD002987.
- Textor, C.; Graf, H.-F.; Timmrick, C.; Robock, A. (2004). Emissions from volcanoes, in C. Granier, P. Artaxo, and C.E. Reeves (Eds.), *Emissions of Atmospheric Trace Compounds*, Kluwer Academic, Dordrecht, The Netherlands, pp. 269–303.
- Thomas, H.E.; Prata, A.J. (2011). Sulphur dioxide as a volcanic ash proxy during the April–May 2010 eruption of Eyjafjallajökull Volcano, Iceland, *Atmos. Chem. Phys. Discuss.*, **11**, 7757–7780, doi: 10.5194/acpd-11-7757-2011.
- Thordarson, H.; Self, S. (2003). Atmospheric and environmental effects of the 1783–1784 Laki eruption: A review and reassessment, *J. Geophys. Res.*, **108**(D1), 4011, doi: 10.1029/2001JD002042.
- Urai, M.; Pieri, D. (2011). ASTER applications in volcanology, in B. Ramachandran, C.O. Justice, and M.J. Abrams (Eds.), *Land Remote Sensing and Global Environmental Change*, Springer, New York, pp. 245–272.
- Waters, J.W. et al. (2006). The Earth Observing System Microwave Limb Sounder (EOS MLS) on the Aura Satellite, *IEEE Trans. Geosci. Remote Sensing*, **44**(5), 1075–1091.
- Watson, I.M.; Oppenheimer, C. (2000). Particle size distribution of Mount Etna's aerosol plume constrained by sun photometry, *J. Geophys. Res.*, **105**(D8), 9823–9829.
- Watson, I.M.; Oppenheimer, C.; Voight, B.; Francis, P.W.; Clarke, A.; Stix, J.; Miller, A.; Pyle, D.M.; Burton, M.R.; Young, S.R.; Norton, G.; Loughlin, S.; Darroux B.; MVO Staff (2000). The relationship between degassing and ground deformation at Soufrière Hills Volcano, Montserrat, *J. Volcanol. Geothermal Res.*, **98**(1–4), 117–126.
- Watson, I.M.; Realmuto, V.J.; Rose, W.I.; Prata, A.J.; Bluth, G.J.S.; Gu, Y.; Bader, C.E.; Yu, T. (2004). Thermal infrared remote sensing of volcanic emissions using the moderate resolution imaging spectroradiometer, *J. Volcanol. Geothermal Res.*, **135**, 75–89.
- Weibring, P.; Edner, H.; Svanberg, S.; Cecchi, G.; Pantani, L.; Ferrara, R.; Caltabiano, T. (1998). Monitoring of volcanic sulphur dioxide emissions using differential absorption lidar (DIAL), differential optical absorption spectroscopy (DOAS), and correlation spectroscopy (COSPEC), *Appl. Phys.*, **B67**, 419–426.
- Werner, C.; Brantley, S. (2003). CO₂ emissions from the Yellowstone volcanic system, *Geochem. Geophys. Geosyst.*, **4**(7), 1061, doi: 10.1029/2002GC000473.
- Werner, C.; Miller, C.A.; Edmonds, M.; Herd, R. (2006a). Short-term temporal variability of SO₂ emissions at White Island, New Zealand, *EOS, Trans. Am. Geophys. Union*, **87**(52), Fall Meeting Suppl., Abstract V43E-02.
- Werner, C.; Christenson, B.W.; Hagerty, M.; Britten K. (2006b). Variability of volcanic emissions during a crater lake heating cycle at Ruapehu Volcano, New Zealand, *J. Volcanol. Geothermal Res.*, **106**, 291–302.
- Werner, C.; Hurst, A.W.; Scott, B.; Sherburn, S.; Christenson, B.W.; Britten, K.; Cole-Baker, J.; Mullan, B. (2008). Variability of passive gas emissions and seismicity during crater lake growth at White Island Volcano, New Zealand, 2002–2006, *J. Geophys. Res.*, **113**, B01204, doi: 10.1029/2007JB005094.
- Westrich, H.R.; Gerlach, T.M. (1992). Magmatic gas source for the stratospheric SO₂ cloud from the June 15, 1991 eruption of Mount Pinatubo, *Geology*, **20**(10), doi: 10.1130/0091-7613.
- Williams, S.N.; Schaefer, S.J.; Calvache, V.; Lopez, D. (1992). Global carbon dioxide emission to the atmosphere by volcanoes, *Geochim. Cosmochim. Acta*, **36**, 1765–1770.
- Yang, K.; Krotkov, N.A.; Krueger, A.J.; Carn, S.A.; Bhartia, P.K.; Levelt, P.F. (2007). Retrieval of large volcanic SO₂ columns from the Aura Ozone Monitoring Instrument: Comparison and limitations, *J. Geophys. Res.*, **112**, D24S43, doi: 10.1029/2007JD008825.

Volcanic ash transport and dispersion models

*Rorik Peterson, Peter Webley, Réal D'Amours, René Servranckx,
Barbara Stunder, Ken Papp*

7.1 INTRODUCTION

A volcanic eruption is an amazing event. The associated earthquakes, lava flows, and ash clouds are both intriguing yet potentially dangerous features that can cause enormous changes to the landscape, damage to infrastructure, and even loss of life. Obviously, the ability to predict the occurrence and dynamics of an eruption is both desirable and necessary for public safety. Despite many advances in the understanding of what leads to volcanic eruptions, predicting the commencement of an eruption remains difficult. Once an eruption has begun, predicting its behavior is equally if not more important in order to minimize the potential financial and human costs. The airborne ash cloud is the one eruptive feature that can have very long ranging impacts. Once ash is ejected into the atmosphere, it can be transported over great distances, even circumnavigating the entire planet, such as the catastrophic eruption of Mt. Pinatubo in 1991 (Self *et al.*, 1996). Fortunately, many satellite remote-sensing platforms are capable of detecting ash clouds and tracking them over these great distances. However, there are limitations to all remote-sensing techniques, as discussed throughout this book, and they cannot be solely relied upon to provide all necessary information. Furthermore, no remote-sensing technique provides a forecast for the ash cloud trajectory. To help fill this void, volcanic ash transport and dispersion (VATD) models have been developed as an additional tool

in the arsenal to comprehensively monitor volcanic ash clouds.

The primary users of a VATD model are those involved in the operational forecasting of potential volcanic hazards because they wish to know the future trajectory of an ash cloud. These include the Volcanic Ash Advisory Centers (VAACs) around the world and those agencies involved in the International Airways Volcano Watch (IAVW), to name a few. A more detailed description of the role these groups play in the complex, multi-tiered task of volcano monitoring, and the flow of information between them, is given in Chapter 9. Obviously VATD models play an important role in forecasting the movement of volcanic ash clouds. The model forecasts complement remote-sensing data and visual observations from the ground and aircraft. They also can provide unique information that is otherwise difficult or impossible to collect from these other data sources. For example, a model simulation can provide the concentration of ash, the size distribution of particles and aggregates, or the cloud age since the eruption commenced. The limitations in the accuracy of this information will be discussed throughout this chapter. Most of these limitations stem from both inherent design principles and uncertainties in the parameters used to describe the model physics, input meteorology, and source term. Lastly, VATD models are important for reanalyzing data after a volcanic eruption in an attempt to better understand the event and for help-

ing to determine methods for improving the capabilities of the model for future use.

The major goals of this chapter are the following. First, a more detailed background into the role that VATD models play in volcano monitoring is provided. A discussion of who the users are, what information they require, and the necessary trade-offs is provided. Second, a description of the primary physical processes that are modeled is given. Mathematical equations are only provided to give a flavor for how some processes are modeled, and they are not intended as part of a comprehensive survey. Third, the modeling of four historic eruptions in the North Pacific (NOPAC) region is discussed, and the forecasts from three different VATD models (Puff, HYSPLIT, and CanERM) are compared and contrasted. While the three models discussed are only a subset of those used around the world, they do constitute the primary ones used in the NOPAC region.

There are over 100 active volcanoes in the NOPAC region, most of which are located in uninhabited areas along the Aleutian Islands, the Russian Kamchatkan Peninsula, and extending into the Kurile Islands. The region is often defined as 120°E to 120°W longitude and 30°N to 80°N latitude. Some of these volcanoes erupt explosively with frequencies as high as several times per year and have the capability of sending ash and aerosols up to altitudes greater than 10 km into air traffic routes. The importance of tracking and understanding the dispersion of recently emitted volcanic ash clouds in the NOPAC region is crucial because ash concentrations are at a maximum (Rose *et al.*, 1995), which can cause severe damage to jet aircraft engines, fuel lines, abrade internal and external surfaces, and shut down major airports (Blong, 1984; Casadevall, 1993; Casadevall and Krohn, 1995; Miller and Casadevall, 2000).

In an operational setting where the potential or ongoing activity of volcanoes is continuously monitored, satellite data provide observations while VATD models provide forecasts. In a research setting where investigators are attempting to recreate a past eruption, satellite data can identify the plume “footprint” (horizontal size and location) and possibly total ash content (Wen and Rose, 1994). VATD models estimate more detailed information, even when there is no satellite data, such as vertical dimensions of the ash cloud, spatial extent of ash particles of different sizes, future trajectories, and even the distribution of different chemical species assuming there is source term information on the

chemical species. Here the term “plume” will be generically used to denote a distinct group of particles that is still “attached” to the volcano, while the term “volcanic cloud” will be used to denote a discrete group of particles no longer attached to its source. Satellite data are generally limited to time intervals of several hours, with some higher temporal resolution data being available at intervals of about 15 min. VATD models generally provide output at intervals within the range of one to several hours, but more frequent data can be generated depending on the specific application. Accuracy and reliability are obviously more important than temporal resolution. Satellite-derived volcanic ash analyses are sometimes not possible because of meteorological cloud cover, lack of daylight, or a number of other reasons. Both satellite and forecast systems require a hierarchy of data acquisition, assimilation, and distribution, often using sophisticated computers and other hardware. Operations centers require timely satellite analyses and dispersion forecasts.

Satellite images of volcanic ash clouds provide a two-dimensional view of the ash cloud as seen from above. Different analysis techniques can provide information about the height of the cloud top (e.g., Holasek and Self, 1995) and sometimes relative density within the cloud (e.g., Wen and Rose, 1994). However, it is generally not possible to obtain detailed quantitative information about the three-dimensional structure, including thickness of the cloud and ash concentrations within the cloud. VATD models can estimate a complete description of the ash cloud at an instant in time including the upper, lower, and lateral extent of the cloud, relative concentration of ash within the cloud, and possibly particle size and distribution of the ash. This is dependent upon the accuracy of the wind field data used by the VATD model. Perhaps the most important attribute of VATD models is their ability to provide a forecast for the trajectory and developing morphology of the volcanic ash cloud. Furthermore, models can continually provide updated forecasts as new data become available, maintaining a several day outlook.

All VATD models require some level of user interaction. Some procedures are “turnkey”, simply requiring a volcano name or location and beginning time of the eruption. Others are more detailed involving the physical characteristics of the initial eruption column, composition of the ash, and type of meteorological wind field model to be used as initialization. Any uncertainties or errors in these

specifications will adversely affect the results generated by the VATD model. Therefore, a form of training is required both by users who run the model and for those who will interpret the model results. Models are also limited to describing only processes for which they are designed, which is usually limited to those few primary processes that are reasonably well understood such as advection, sedimentation, and diffusion. Particle aggregation and chemical reactions with the atmosphere are still poorly integrated into current operational VATD models. These processes are more complicated to describe mathematically and are being studied by researchers as further developments that could be made to operational VATD models. However, the time for a prediction to be made needs to be weighed against the number of parameters that the model is able to account for in the prediction. Furthermore, VATD model results are strongly dependent on the input meteorology. In most cases, advection is the primary process for ash cloud movement. Three-dimensional wind field data are needed due to the high spatial variability in wind speed and direction at any given time. Furthermore, even small uncertainties or errors in these initial meteorological conditions can be magnified with time, making longer term forecasts less certain in terms of their accuracy.

VATD models play a pivotal role in describing the details of an eruption well after the event has occurred. In this instance, model data work in conjunction with remote-sensing information (providing a means of reciprocal validation) and observations from the air (pilot reports or "PIREPS") and ground. It is during post-event analyses that techniques and methods for improving the VATD model forecast capability are identified and eventually implemented. Much research needs to be done before VATD models simulate the exact position, spatial extent, and composition details of an evolving ash cloud. Current simulations can range from exceptionally good to quite inaccurate. Model simulation ability can be assessed by comparisons of VATD model output using meteorology and remote-sensing data that have been carefully analyzed in order to extract the most useful and detailed information from the data. When VATD model output appears to agree well with observational data, some insight into the physical processes that occurred during the event is achievable. It is possible to assume that accurate model simulations indicate that the modeled physical processes correspond to the actual physical processes that

occurred, although other physical processes may exist and hence need to be added to the model, such as atmospheric reaction or wet removal (particle scavenging).

Sometimes model simulations do not agree with observational data. All remote-sensing techniques have their own limitations (such as an ash cloud obscured by local meteorological clouds or no ash signal yet detectable) and model simulations may be providing some of the most accurate information of the ash cloud's location. At other times, improvements in how to best mathematically describe the model physics may be required. If observational data can provide sufficient and accurate information about when, why, and how the model failed, modifications to the model may be possible. For example, if a particular type of meteorological condition appears to affect the diffusion rate of an ash cloud in a "regular" and consistent fashion, which the model is not currently capable of describing, then this behavior can be added in an attempt to properly describe it and model the ash cloud more accurately in the future. However, sometimes disagreement may occur due to factors beyond the ability of the model itself, such as inaccurate input parameters (initial height or eruption duration) or errors in the meteorological data. Little can be done in these cases and exemplifies the importance of good judgment by qualified personnel in volcanic advisory roles.

Three VATD models (Puff, HYSPLIT, and CanERM) are used operationally in the NOPAC to provide forecast ash location/movement information in Volcanic Ash Advisories and SIGMETs (significant meteorological information). Puff is used as an operational tool by the AVO, AFWA, and Anchorage and Washington VAAC. HYSPLIT is used for volcanic ash forecasting by the Anchorage and Washington VAAC. CanERM is similarly used for volcanic ash forecasting by the Montreal VAAC. The Anchorage VAAC is operated by the NOAA NWS. The Washington VAAC is operated by the NOAA National Environmental Satellite, Data, and Information Service and the NWS National Centers for Environmental Prediction. The Montreal VAAC is operated by the Canadian Meteorological Centre.

7.2 MODELING TECHNIQUES

There is a wide array of VATD models used throughout the world. Use of a particular model

is often associated with a geographical region or personal preference, although some models are used worldwide. There are several different ways to categorize the various VATD models. Some models are classified as *runtime* or *operational*, while others are *research*, and some may be used for both purposes. The distinction can be drawn based on the time frame in which results are generated and the input meteorology used. In order for a runtime model to be useful during an eruptive event, it must be capable of producing forecasts quickly enough to be used for hazard mitigation. Aircraft cruising at 500 mph (approx. $800 \text{ km} \cdot \text{h}^{-1}$) require information quickly and, in general, this means results should be available to make decisions within minutes—not hours or days. Also, runtime model results need to be based on the current and forecast weather in the proximity of the erupting volcano, in contrast to time-averaged or climatological conditions. Research models, on the other hand, may take much longer to generate results and can use time-averaged climatic conditions. For example, seasonally averaged meteorological conditions may be used to determine the most likely trajectory and dispersion of an ash cloud in the event of a future eruption; for example, see Papp *et al* (2005) and Sections 7.10 and 7.11 of this chapter.

An alternative distinction between models is based on the model coordinate framework, which is usually either eulerian or lagrangian. Models using a eulerian coordinate system superimpose a regular grid over the domain in both the three-spatial and temporal dimensions. The model equations are placed in differential form and the differentials are approximated using Euler's method. To approximate the derivative of the parameter u with coordinate variable x , Euler's method results in Equation (7.1) where the subscripts indicate the grid location from which the parameter values are taken; therefore, u_x is read as "the value of u at location x_1 ". Derivatives with respect to all dimensions can all be approximated in this manner, and the parameter u can itself be a differential quantity, giving rise to a second-order derivative, which is useful for the diffusion equation

$$\frac{\partial u}{\partial x} \approx \frac{u_{x_1} - u_{x_0}}{x_1 - x_0} \quad (7.1)$$

In contrast, a lagrangian model specifies how individual entities (such as ash particles) behave in space and time, and does not necessarily operate on

a predefined regular grid. A eulerian model may define an ash cloud as a region of space with a minimum concentration of ash. A lagrangian model, however, uses representative "tracer" particles, each having an individual location in space and time. The concentration is backed out of this formulation by counting the number of particles in a defined volume of the atmosphere. Lagrangian models require a large number of particles to obtain meaningful concentration values and for discriminating between areas of high and low concentrations. The number of required particles can vary depending on the length of simulation and degree of dispersion among other factors, and can be difficult to know ahead of time. However, each particle may operate with a different and possibly varying time step. Optimization of the time steps helps to reduce the computational requirement of large particle arrays.

Perhaps the most important way that differing VATD models are distinguished from each other is in the physical processes they do or do not attempt to model, and the way the processes are described mathematically. There are three primary processes that all VATD models describe: *advection*, *diffusion*, and *sedimentation*. There are many secondary processes that may also be modeled, some of which include aggregation, atmospheric chemical reaction, or wet deposition. In general, runtime models do not attempt to describe generation of the initial ash column, which is a very complicated process itself and covered by *eruption column models* (see Chapter 4 of Sparks *et al.*, 1997). Instead, a set of parameters are used as initial conditions to describe the eruption column, which may include the initial column shape, height, particle distribution, temperature, or other physical attributes of the volcanic eruption plume. There is no straightforward way to define the exact time during an eruption at which the initial column has formed and the VATD model becomes applicable. A good approximation is the time at which the ash cloud has approached thermal equilibrium with its surroundings and is no longer buoyantly ascending. At this point, motion of the ash cloud is predominantly due to the three primary dispersion processes, and is no longer driven by buoyancy and vent-driven convection. In addition, any seismically based data of the volcanic event, if available, can provide information on the start time for VATD models and help to accurately predict ash cloud movement, given an accurate eruption start time.

7.3 MODELING THE MAIN PHYSICS PROCESSES IN VOLCANIC ASH TRANSPORT AND DISPERSION

Volcanic ash transport and dispersion is modeled by mathematically describing each relevant process where possible, but not necessarily all that may occur during an event. In this chapter, *dispersion* will refer to the overall movement of an ash cloud, while *diffusion* will refer only to the single process of net particle movement from an area of high to low concentration due to eddy turbulence. All processes acting collectively and often nonlinearly result in ash cloud dispersion. Processes may act independently or be interdependent to varying degrees. Figure 7.1 is a schematic showing the three primary processes that affect volcanic ash dispersion. Some VATD models may use different formulations or choose not to describe a particular process, and may also include additional processes. This is dependent on the model's use, operationally or in research, and the forecast that it is intended to provide, quickly or time-averaged.

7.3.1 Advection

Advection is the most dominant process that affects the movement of volcanic ash clouds. In a meteorological context, advection is defined as “the process of transport on an atmospheric property solely by the mass motion (velocity field) of the atmosphere” (AMS, 2000). In other words, advection of volcanic ash is caused by the wind where a parcel of ash is transported simultaneously and unchanged with the

air parcel surrounding it. Advection is a vector quantity, so it has a magnitude and direction associated with it. Although the description of advection is relatively simple, generation of the three-dimensional wind field is complicated; hence, VATD models rely on external data for this term. Wind field data may come from either meteorological model output on regular grid or point radiosonde/rawinsonde data. In eulerian terms, advection affects the concentration of ash, c , in proportion to the wind velocity, V (Equation 7.2). In a lagrangian context, a forward Euler integration specifies that a particle changes its position, R , in proportion to the wind velocity (Equation 7.3):

$$\frac{\partial c}{\partial t} = -v \cdot \nabla c \quad (7.2)$$

$$R(t + \Delta t) = R(t) + V(t) \Delta t \quad (7.3)$$

A more accurate value for the left-hand side of Equation (7.3) can be obtained by re-evaluating R using the average of $V(t)$ and $V(t + \Delta t)$ (Draxler and Hess, 1998). When gridded model data provide the wind velocity in the lagrangian formulation, interpolation is generally performed to determine an approximate velocity at the exact particle location R . Linear interpolation is very quick and fairly accurate for higher resolution grids, while a non-linear spline interpolation may yield better precision at greater computation cost (Chapra and Canale, 2001).

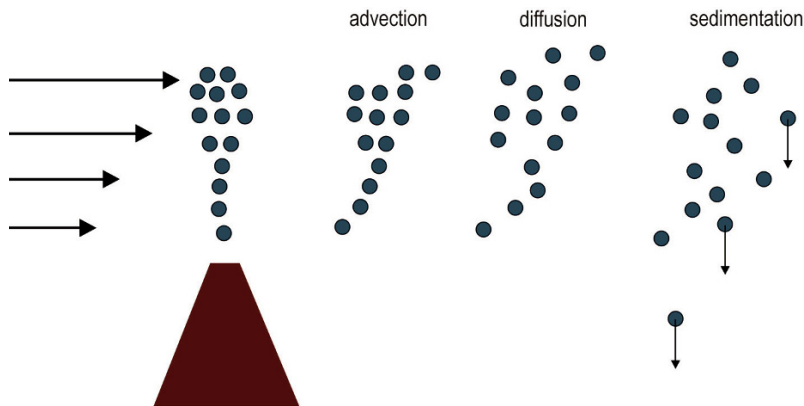


Figure 7.1. Primary processes of advection, diffusion, and sedimentation involved in particle dispersion.

7.3.2 Diffusion

Diffusion is the movement of particles due to random motion, which almost always results in net migration from areas of high to low concentration (temperature gradient and pressure gradient effects on diffusion are negligible). On the size scale of volcanic ash dispersion, diffusion is primarily due to turbulence and the formation of eddies of varying length scales. Classical diffusion in three dimensions can be modeled in eulerian terms by Fick's law:

$$\frac{\partial c}{\partial t} = \nabla \cdot (K \nabla c) \quad (7.4)$$

The diffusion coefficient, K , may depend on parameters such as temperature, atmospheric stability, spatial location, or time. Fick's law is based on random *brownian* molecular motion and is not strictly applicable to multi-scale atmospheric dispersion. However, atmospheric turbulence will cause net particle migration from areas of high to low concentration analogous to the behavior described by Fick's law. Therefore, this classical description can be used if an appropriate value for the diffusion coefficient can be determined. When using this formulation, diffusion coefficients for both the horizontal and the vertical direction are used and, generally, vary greatly with the horizontal value exceeding the vertical by perhaps three orders of magnitude (Suzuki, 1983). This large difference in horizontal and vertical diffusion is due to the relatively small vertical scale of the atmosphere compared with its horizontal extent. A falling particle will continually enter and leave individual eddies, thereby reducing their vertical contribution relative to pure gas diffusivity values (Armienti *et al.*, 1988). Diffusion coefficients may be based on atmospheric stability (Draxler and Hess, 1998) where the formulation can be complex, requiring heat and momentum fluxes in the boundary layer provided by meteorological models. In this case, diffusion coefficients may vary in space and time.

Another approach is to use an empirical constant for K based on fitting VATD model predictions to satellite imagery from previous eruptions (Searcy *et al.*, 1998). For a lagrangian model, net particle movement due to diffusion can be calculated and added linearly to the other dispersion terms such as advection. For each particle, a random value g is drawn from a gaussian distribution with a zero mean. The velocity due to diffusion, 7.5, where τ is the time duration over which diffusion

has occurred (Searcy *et al.*, 1998):

$$v_d = \sqrt{\frac{2K}{\tau}} \quad (7.5)$$

The value of τ often used is the lagrangian time step. Hypothetical examples of discrete cloud and sustained plume growth rates are shown in Figure 7.2 (after Slade, 1968). The rate of growth for a discrete cloud release is directly related to the size of the cloud (Richardson, 1926), which is illustrated in Figures 7.2a–c. When the discrete cloud is small relative to the spatial scale of the dominant surrounding motions of the flow field, the cloud is often transported *en masse* undergoing only slight deformations at its edges (Figure 7.2a). A second case (Figure 7.2b) describes the situation when the spatial scale of the flow field is similar to that of the cloud, which results in rapid deformation, mixing, growth, and dilution. Third, when the cloud is much larger than the spatial scale of the dominant flow field, the discrete cloud will typically experience slow dilution and growth at its boundaries (Figure 7.2c). In contrast, for a continuous plume flow field, motions larger than the dimensions of the plume often transport the plume intact, known as meander (Figure 7.2d), while smaller motions

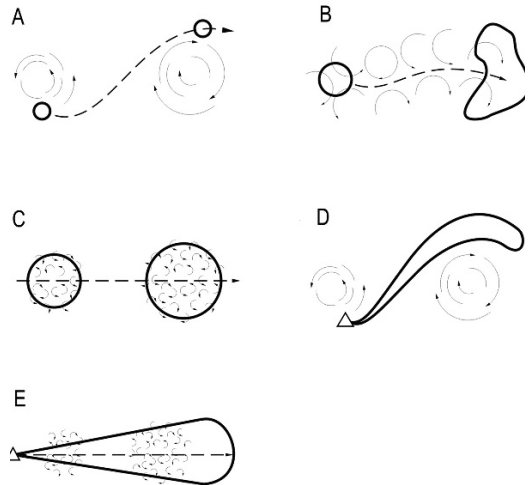


Figure 7.2. Cloud and plume growth rates: (A–C) the rate of growth for a discrete cloud release is directly related to the size of that puff; (D, E) diffusion of a sustained plume acts in the vertical and cross-wind directions. The triangles are the source for sustained plumes. Map views shown (modified from Slade, 1968).

simply act at the boundaries causing further mixing and dilution to occur (Figure 7.2e).

Diffusion of these two release types acts quite differently. For the discrete cloud, diffusion is allowed to act about its center of mass diluting the plume along the cross-wind, along-wind, and vertical directions. Diffusion of a continuous plume case is a two-dimensional process in the cross-wind and vertical directions, with along-wind expansion becoming negligible (Batchelor, 1949, 1950; Boybeyi, 2000).

7.3.3 Settling

Settling is the downward movement of ash particles due to gravity. Fluid dynamics of solid particles traveling through a fluid describes three different regimes based on the Reynolds number, Re , in Equation (7.6), where u is the particle velocity relative to the fluid, d is the particle diameter, and ν is the kinematic viscosity. The laminar region is defined for small values of the Reynolds number ($Re < 0.1$), and Stokes' settling law is generally applicable for determining terminal velocities using Equation (7.7), where g is the gravitational constant:

$$Re = u \frac{d}{\nu} \quad (7.6)$$

$$v_s = \frac{gd^2}{18\nu} \quad (7.7)$$

At a Reynolds number of 1, Stokes' law predicts a drag force that is about 10% too low (Bird *et al.*, 1960, p. 59). Stokes' settling law is derived for spherical particles, which is generally not true of volcanic particles. Therefore, a shape factor C , to account for shape and/or slip, may be introduced and used such that the true settling velocity v is defined by Equation (7.8). For large particles where the Reynolds number is greater than 1, turbulent fallout occurs and the terminal velocity may be approximated by Equation (7.9) where σ is the air density (Bonadonna and Phillips, 2003). Between the laminar and turbulent regimes is the transition region where a hybrid fallout equation is applicable (Equation 7.10) (Bonadonna and Phillips, 2003). Shape factors are usually defined as some function of the three linear dimensions of the particle and may be used with all three settling equations. It is possible for a single ash particle to travel through all three regions during descent from high elevations. Long-term forecasts often use only a modified form of Stokes' settling law since most large par-

ticles fall out rather quickly and are not relevant to cloud trajectory forecasts:

$$v = Cv_s \quad (7.8)$$

$$v_s = \sqrt{\frac{3.1gd}{\sigma}} \quad (7.9)$$

$$v_s = d(4\rho^2g^2/225\mu\sigma)^{(1/3)} \quad (7.10)$$

Equations (7.7), (7.9), and (7.10) are based on analytic expressions of the drag coefficient from the work of Kunii and Levenspiel (1969). An alternative method for determining the settling velocity is to curve-fit experimental data. Suzuki (1983) proposed the following equation for the settling velocity based on experimental data of Wilson and Huang (1979)

$$v_s = \frac{\rho g d^2}{9\mu F^{-0.32} + \sqrt{81\mu^2 F^{-0.64} + 1.5\rho_a \rho d^3 \sqrt{1.09 - F}}} \quad (7.11)$$

where the shape factor, $F = (b + c)/2a$, is based on the three orthogonal particle dimensions. Equation (7.11) fits experimental data for the terminal fall velocity of particles in the size range 0.01–10 μm with a shape factor range of 0.4–0.6 (Suzuki, 1983).

Ash may be deposited when it contacts the ground surface. In some cases resuspension is possible due to high surface winds (Hadley *et al.*, 2004). In that case, a resuspension factor that relates the concentration of ash in the air to that on the ground can be used at each time step to determine the amount of ash that becomes resuspended (Draxler and Hess, 1998). Resuspension is not typically used operationally in volcanic ash models but is an important factor for volcanic ash hazard mitigation for local populations and low-level aircraft.

7.3.4 Aggregation

An aggregate is a cluster of one or more ash particles often bound by liquid or frozen water (Textor *et al.*, 2006). Aggregation occurs when an existing aggregate or single particle collides with another aggregate or particle and subsequently binds together. The result is an increase in mass and size of the aggregate, which directly affects fall velocity. Aggregation in dry conditions can occur by electrostatic attraction and forms a weaker bond than wet aggregates (Textor *et al.*, 2006). Experimental data on electrostatic aggregation indicate that particles less than 180 μm begin to aggregate, and nearly

90% of particles smaller than 45 μm form aggregates (Schumacher, 1994). In more humid conditions where particles and aggregates may have an outer liquid film, surface tension forces may cause particles to stick together. In particularly wet conditions of near-100% humidity where water droplets are present, particles can be engulfed in the falling droplets forming a *mud rain* (Sparks *et al.*, 1997).

The rate of aggregation is a function of humidity, temperature, particle size distribution, and ash concentration (Textor *et al.*, 2006). Relative humidity is perhaps most important since it affects the mode by which it occurs: mechanical, surface tension, or droplet scavenging. Temperature is also important since it will determine whether a liquid water or ice film will develop on the surface of existing aggregates. Two aggregates or particles must first collide, which is usually the result of disparate fall velocities. Very small particles may not collide at all with larger ones since they will tend to follow stream lines around the faster moving, larger particle (Sparks *et al.*, 1997). Therefore, particle size distribution and ash concentration are interrelated with aggregation rates.

Due to the current limited understanding of how volcanic ash aggregates in the atmosphere, most VATD models do not directly account for the process. Furthermore, aggregation may not occur at a significant rate at moderate distances from the vent where lower concentrations preclude aggregation by any process. A direct method to include this fairly complex process into VATD models is to use an empirical relation (Equation 7.12) for the change in mass, m , of individual ash particles with age of the plume where R is the aggregate radius, c is the ash concentration, u is the relative velocity between the colliding entities, and A is an empirical aggregation parameter (Sparks *et al.*, 1997):

$$\frac{dm}{dt} = AuR^2c \quad (7.12)$$

The collision or aggregation parameter, A , is a function of atmospheric humidity and temperature, and possibly aggregate size. Studies of fall deposits with secondary maxima, such as at Mt. St. Helens in 1980 (Sarna-Wojcicki *et al.*, 1981) and Mt. Spurr in 1992 (McGimsey *et al.*, 2001), have indicated that some meteorological conditions such as increased atmospheric instability may cause an increase in the rate of aggregation. Therefore, the aggregation

parameter may also be a function of local weather conditions.

Another technique for modeling aggregation that has been more widely implemented is not time dependent, but instead assumes the smaller particles will aggregate early enough in the formation of the eruption cloud to be immaterial to the transport model. Using this technique, Carey and Sigurdsson (1982) successfully modeled the secondary thickness maximum observed in the ash fallout from the 1980 Mt. St. Helens eruption. Bonadonna and Phillips (2003) have explored variations of this method when modeling six different historic eruptions. The basic premise of this technique is the following. An initial particle size distribution is specified, and then some fraction of the smaller particles (e.g., 50, 75, or 100%) is formed into aggregates of a larger size. Based on the data of Schumacher (1994), Bonadonna and Phillips (2003) assumed that particles smaller than 125 μm are formed into aggregates of a larger size. Carey and Sigurdsson (1982) found an optimum match with fallout data assuming particles smaller than 63 μm formed aggregates several hundred microns in diameter. The size of the aggregate is a function of the constituent particles' size and density, mass loading of the cloud, and final aggregate porosity (Bonadonna and Phillips, 2003). An earlier model by Cornell *et al.* (1983) assumed all aggregates were 250 μm , while the model of Bonadonna and Phillips led to aggregates in the range of 2–8 mm.

7.4 INITIAL CONDITIONS

The solutions to model equations, whether numeric or analytic, must satisfy initial conditions. For VATD models, the initial conditions describe the young eruption column. This description may come from a separate eruption column model that describes the multi-phase flow and thermodynamic disequilibrium of volcanic ejecta (Oberhuber *et al.*, 1998). Alternatively, a simpler user-specified characterization of the initial column may be used. This specification usually entails the approximate eruption plume shape, maximum and minimum height, and rate of mass generation. When VATD models are used operationally, there is usually not sufficient time or resources to generate an initial description using an eruption column model. In this case, the conditions are specified through a set of parameters that describe the ash column.

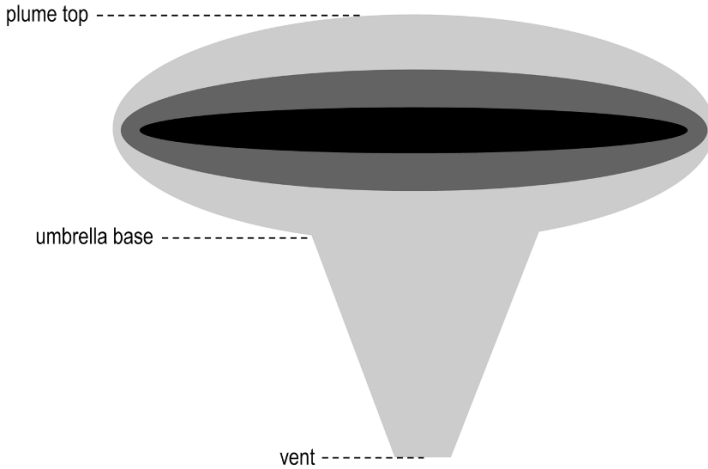


Figure 7.3. Schematic of an idealized initial ash cloud.

Figure 7.3 is a schematic of a potential initial volcanic ash column, shown here as an umbrella shape. The cloud top specifies the initial maximum height of ash, and this value can sometimes be estimated from near-real time satellite data. Given that the thermal signature from the cloud top correlates with atmospheric temperature, the elevation can then be determined by assuming thermal equilibrium between the ash cloud and the atmosphere. Often, meteorological data can provide the temperature as a function of height for the region near the volcano such as radiosonde or numerical weather prediction (NWP) data. Alternatively, the height can be estimated by matching the observed ash cloud motion with the meteorological model's wind velocity vertical profile near the volcano. When meteorological model data or radiosondes are not available within close proximity to the volcano, the *standard atmosphere* approximation can be used with the temperature in the troposphere dropping by a so-called "lapse rate" as a function of altitude. This is sometimes a poor approximation, particularly away from mid-latitudes. The ash cloud bottom/base cannot in general be obtained from satellite data, as satellite data detect the signal off the top of the ash cloud if it is opaque and through the ash cloud if it is translucent.

For low-intensity plumes with low cloud tops, the bottom of the plume may simply be at the volcano vent elevation. For more intense eruptions, the cloud top, H_t , is related to the cloud bottom, H_b , by the approximation in Equation (7.12) where b_0 is the vent radius (Sparks *et al.*, 1997). Both heights

are measured relative to the vent elevation:

$$H_t = 1.32(H_b + 8b_0) \quad (7.13)$$

The intensity of the eruption is intrinsic to the cloud bottom, H_b , as more vigorous eruptions will have larger H_b values. The cloud bottom still remains a qualitative label since ash fallout of larger pyroclasts often occurs very close to the vent in even the largest eruptions, blurring the line between the bottom of the cloud and the ground surface. However, the smallest particles and water vapor can often be observed occupying a space of finite thickness such as shown in Figure 7.3, from which the cloud bottom can be estimated. The shape of the column in the horizontal direction depends on the intensity of the local winds relative to the eruption rate. For low-intensity wind, high eruption rate situations, the horizontal shape is generally circular and axisymmetric. However, strong winds can cause low-intensity eruption columns to become asymmetric and "bent over" in the direction of the prevailing wind. The initial distribution of particles within the column may be concentrated at some location within the cloud (as shown by the darker regions in Figure 7.3). A log-normal distribution may be applicable, where the highest concentration is slightly below the cloud top. When not using an eruption column model for initiation, the initial particle size distribution will be specified at all elevations. It is often more applicable to weight lower elevations with larger particles (e.g., $>500 \mu\text{m}$), particularly for low-intensity eruptions or columns with high cloud tops, because early

sedimentation should not be neglected and can be an important factor in operational VATD modeling.

7.5 WIND FIELDS

In addition to initial volcanic ash column conditions, the horizontal and vertical advection by wind is essential information that must be specified by an outside source. The domain of wind fields may be global, regional, or simply a point such as a radiosonde measurement. The wind field domain defines the limits for which the model is applicable and is usually provided by either meteorological models or direct radiosonde/rawinsonde data. Most VATD models utilize meteorological model data since the desired forecast usually extends beyond the immediate domain of a single, nearby, radiosonde station. Meteorological models use radiosonde/rawinsonde (commonly known as radiosondes) data as one source of initial and boundary conditions but also include other observations, such as from satellite analyses, and mathematical data assimilation and initialization schemes to provide a more accurate description of the conditions at, and between, the measurement locations.

Radiosondes refer to a direct measurement of wind speed and direction, temperature, relative humidity, and pressure using radar or other telemetry equipment at many altitudes. Typically, radiosonde data are obtained at locations worldwide twice a day at 00:00 UTC and 12:00 UTC. Global coverage is non-uniform and sparse in less densely populated areas such as parts of the NOPAC region. Vertical resolution is sometimes better than that in meteorological models. Radiosonde data are collected at set altitudes (e.g., 1,000, 925, 850, 700 mb, etc.) during ascent through the atmosphere as well as at “levels” when there are significant changes in the data. Their horizontal coverage is inferior to models, and sometimes only a single vertical profile is available in a region of interest. When only radiosonde data are used in a VATD model, it is assumed that the point measurements are representative of an entire region, which becomes less valid as the lateral domains used by VATD models increase in size. For these reasons, most VATD models do not use radiosonde data directly.

Numerical weather analyses and forecasts are produced by numerous agencies such as the National Oceanic and Atmospheric Administration’s (NOAA) National Centers for Environmental Prediction (NCEP), U.S. Navy, Canadian

Meteorological Centre (CMC), U.K. Met Office, Météo France, Australian Government Bureau of Meteorology, and the European Centre for Medium Range Weather Forecasts (ECWMF), among others. Each of these centers provides forecasts over a number of forecast time and space time scales (e.g., global, local short term <1 day, long term >7 days). Global models are particularly important for long-term forecasting, given that ash clouds can travel thousands of kilometers from their source. Global grid spacing is necessarily larger than that of regional models because of computer resource constraints. For example, global models output data typically on a 0.5 to 1.0° grid spacing, although the internal model may run at a greater resolution (40–50 km). In comparison, regional models may have a finer resolution of perhaps an order of magnitude in the lateral directions. Regional models are usually cast on a regular grid projected onto the globe. A polar stereographic projection is typical for the NOPAC region. There are lateral boundaries to these models, and ash clouds cannot be tracked beyond them unless the VATD model also inputs meteorological data on a larger domain. Global model data are often used as initial conditions for regional models, resulting in nested sets with improved resolution.

There are a wide variety of models currently used by different agencies. Numerical meteorological forecast output is typically produced at intervals of 1 to 12 h, depending on the model. The total length of the forecast also varies, with some providing only 12 h forecasts (Rapid Update Cycle model by NOAA–RUC) while others extend over a week such as NOGAPS (Navy Operational Global Atmospheric Prediction System–US Navy) and GFS (Global Forecast System–NCEP). Since some models are aimed at capturing specific atmospheric characteristics, forecast variability may increase with increasing forecast time as the models are true forecasts. To account for some model uncertainties, some centers (e.g., NOAA, CMC) produce ensemble forecasts that may be used in VATD models. Another ensemble of possible scenarios may be provided if VATD models simulate the same eruption, but utilize different meteorological model data. In these instances, it is the job of the analyst to create a single forecast, possibly including probabilities, using the ensemble members in a style that can be employed operationally.

Wind fields are the critical components for producing a *back trajectory*, another useful product from some VATD models. A back trajectory is used

when the source of an existing ash cloud (or report of an ash cloud) needs to be identified. Beginning at the current cloud location, the transport model is basically run backwards causing a tracer particle to retrace the steps required to get there. The diffusion component is removed, and transport only occurs by reverse advection and sedimentation. Similar to the standard forward trajectory, any uncertainty in location at the beginning of the simulation will lead to a range of source locations (i.e., final positions in the back trajectory).

A good example of the use of back trajectory analysis is discussed by Tupper *et al.* (2007), who attempt to identify the source of probable volcanic ash made in pilot reports over Micronesia in 2002–2003. In both of the two separate incidents discussed, satellite data analysis failed to conclusively identify any volcanic ash in the vicinity of the reports. Back trajectories were then generated from the location of the reports to see if ash could have originated from any potentially active volcanoes in the region. In one case, the analysis indicated the likely source to be Rabaul Volcano in Papua New Guinea, where strong convective motion quickly lofted ash from a low-level eruption (2–3 km) to flight altitudes (~10 km). In the second case, the most likely source turns out to be a large eruption of El Reventador in South America which occurred about 20 days prior and over 14,000 km away. Although it is impossible to definitively conclude that El Reventador was indeed the source in the

second case, their analysis demonstrates another useful application of VATD models.

7.6 LIMITATIONS AND UNCERTAINTIES

There are three general areas of uncertainty that all VATD models must address: the volcanic ash source term, the meteorology, and the transport and dispersion description (Servranckx and Chen, 2004). The VATD model should obviously attempt to minimize the uncertainty in each area, but also clearly identify the level of uncertainty in each area. Only with a proper measure of how accurate a particular forecast may be, given the level of uncertainty in each area, can that forecast be safely used for hazard mitigation.

One of the most important applications of VATD models is as an aid to the aviation industry. An encounter between an aircraft and an ash cloud can have serious consequences (Casadevall *et al.*, 1991), such as occurred during the 1989 jet encounter with an ash cloud originating from Mt. Redoubt, Alaska and described in Casadevall (1993, 1994). Ash particles can melt and deposit inside the hot turbine section of a jet engine causing damage and possibly failure (Kim *et al.*, 1993; Dunn *et al.*, 1996). Jet aircraft travel at several hundred kilometers per hour along very precise routes such as those shown in Figure 7.4, and therefore require timely and accurate ash cloud forecasts.

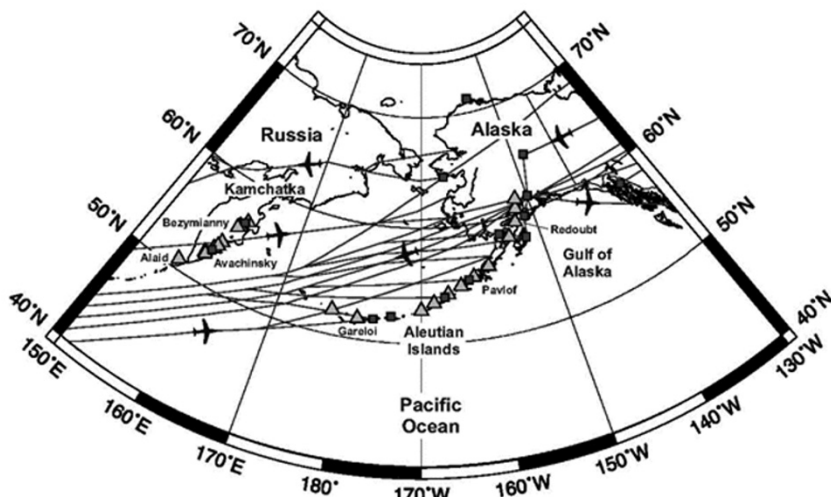


Figure 7.4. Major North Pacific air traffic routes, towns/airports (squares), and volcanoes (triangles) that have erupted in the past 100 years.

These forecasts need to identify both where ash is as well as where ash is absent, so airlines can continue to operate during the days, weeks, or even months that a volcano is active. These requirements pose the greatest challenge for VATD models.

Producing fast yet accurate predictions tends to be at odds for numerical models because increased precision and representation of other atmospheric parameters comes at the expense of increased computation. Furthermore, there are several sources of uncertainty in the input parameters used in the VATD models, including the meteorology and details of the ash source. It is often difficult to quickly know details of the “source term”, which includes the amount of ash erupted, time and duration of the eruption, and maximum height, among others. In fact, sometimes these parameters may never be known with much accuracy. However, many of the details in the source emission term have profound effects on VATD model forecasts and research model simulations.

Operationally, a quick forecast based on any sparse information initially available is complemented with a set of default parameters. As more information becomes available, updated forecasts can be produced. Moreover, after an initial forecast is made, a higher precision but computationally more intensive simulation can be performed as time permits. The degree of variation in model forecasts with increasing computational detail (i.e., decreased grid spacing or increased time resolution) varies between models and is also a function of the current meteorology and input parameters. A sensitivity analysis of the uncertainties is required to quantify this variation, as has been done with other particle tracer models (Manomaiphiboon and Russell, 2004).

The volcanic ash source term is probably the most difficult to quantify accurately, particularly during the early hours of an eruption. The duration of the eruption is largely unknown at this point, as is the rate of mass production. The initial vertical or horizontal extent of the cloud may be difficult to know for a variety of reasons including water or ice cloud cover. An approximation of the eruption start time is often limited to available remote-sensing data or pilot reports, especially for volcanoes that are located in sparsely populated areas of the world. Useful remote-sensing coverage in the NOPAC may be limited to the relatively infrequent polar-orbiting platforms with the next pass occurring in a few hours. To address this problem, many recently active volcanoes in the NOPAC region are being

instrumented with other monitoring systems such as infrasound and seismic detection which have greater temporal resolution. In even the best cases, the vertical distribution of ash within the initial plume is unknown and must be approximated, perhaps using eruption column models (if time permits) or a standard plume with defined characteristics that can be refined once additional remote-sensing data are available, which could be from additional passes of the polar-orbiting platforms or from ground-based data from radar (example for Mt. Spurr in Rose *et al.*, 1995) and lidar (example for Mt. Augustine in Sassen *et al.*, 2007 and Webley *et al.*, 2007).

Uncertainties in the meteorology are also a limiting factor for VATD models. If the meteorological forecast is incorrect, then the VATD forecast will subsequently be of limited utility. An example of this occurred during the November 23, 2004 eruption of Manam Volcano in Papua New Guinea, where an incorrect meteorological forecast led to a VATD forecast that failed to capture the dynamics of a bifurcating cloud (Tupper *et al.*, 2007). Although some meteorological models are run at the relatively high horizontal resolution of 50 km or less, their forecasts are output on a coarser grid to maintain a more manageable amount of data. The time and space resolution of the models and the interpolation schemes often employed by VATD models can lead to substantial uncertainty, particularly under complex weather conditions, such as vertical wind shear. The units of the vertical coordinate are generally pressure (eta or sigma coordinates) and must be converted to an absolute elevation (meters or feet) to be useful for aircraft that operate and communicate in terms of flight levels (100-foot increments). Conversion of pressure to vertical height requires knowledge of the geopotential height distribution, which can vary considerably and may also not be accurately known at the time.

The Earth's topology also affects local meteorology and, therefore, VATD model predictions. However, because of smoothing algorithms related to grid spacing, the effects of some geographic features such as steep mountain ranges and extreme elevations, are reduced. For example, in the 2004 version of CMC's regional model with 24 km horizontal resolution, Mt. McKinley (Denali) in Alaska is represented as a 2,640 m bump instead of its true 6,194 m extremity (Servranckx and Chen, 2004). Although there are many limitations to current VATD models due to these uncertainties, they are

still a vital tool for the aviation industry, if for no other reason lack of another alternative. Operating aircraft during a volcanic event is an instance where some information is definitely better than no information. As VATD models continue to improve, so will the ability of airlines to operate safely and confidently in areas of volcanic activity.

7.7 EXAMPLE MODELS

There are many different VATD models used around the world for predicting and tracking the movement of volcanic ash clouds. The basic principles of each are similar, and the differences are usually limited to things such as: (1) the meteorological models used, (2) the layout of the graphical output generated, and (3) the choice of mathematical description of certain processes, such as diffusion. There are three VATD models often used for forecasting ash cloud motion in the NOPAC region: Canadian Emergency Response Model (CanERM), Hybrid Single-Particle Lagrangian Integrated Trajectory (HYSPLIT), and Puff. In order to convey a general idea of the similarities and differences between these models without being overly verbose, brief descriptions of these three models follow. Table 7.1 is a summary that highlights some important features of the different models. Both CanERM and HYSPLIT are general transport and dispersion models not restricted to volcanic ash, and can accommodate many different types of airborne material, including aerosols and radioactive particles or gases. Puff is primarily focused on forecasting volcanic ash transport and dispersion. Each of these VATD models has developed over several years in response to changes in

application. Some of these model details are continually evolving due to the dynamic nature of volcanic ash modeling, and updated versions of these models are always being developed.

7.7.1 CanERM

The Canadian Emergency Response Model (CanERM) is the operational transport dispersion model used for environmental emergency response at the Canadian Meteorological Centre (CMC). CanERM is a fully three-dimensional eulerian grid model for medium-range and long-range transport of pollutants in the atmosphere. A detailed description of the model is found in Pudykiewicz (1988, 1989). The CanERM model was developed by Environment Canada's Atmospheric Environment Service (now known as the Meteorological Service of Canada) in response to the Chernobyl nuclear power plant accident. The first Canadian simulation of the Chernobyl dispersion was performed in real time with a simple two-dimensional hemispheric model quickly adapted for the situation (Pudykiewicz, 1988). Following the emergency simulation, extensive development work with a three-dimensional tracer model was conducted and new simulations were made using objectively analyzed meteorological fields over a period of one month (Pudykiewicz, 1989).

In 1993, the CMC was designated by the World Meteorological Organization (WMO) as a Regional Specialized Meteorological Center (RSMC) for the provision of atmospheric transport modeling advice for nuclear and radiological emergencies in WMO Regions III (South America) and IV (North and Central America). CanERM was modified in the early 1990s to address the emerging threat posed

Table 7.1. Dispersion models often used in the NOPAC region for volcanic ash forecasting.

	<i>CanERM</i>	<i>HYSPLIT</i>	<i>Puff</i>
Material	Volcanic and other	Volcanic and other	Volcanic
Framework	Eulerian	Eulerian/Lagrangian	Lagrangian
Dispersion coefficient	Variable	Variable	Constant
Approx. particle size range	Not applicable	Microns	Microns to millimeters
Settling types	Constant	Variable	Variable
Ash particle height	Not applicable	Calculated externally	Calculated externally
Multiple volcanic events	No	Yes	Yes

by airborne volcanic ash to aircraft safety. The model was customized for prediction of the volcanic ash and input parameters defined (visual ash cloud criteria, default eruption scenario, etc.) through the use of archived meteorological, satellite, and eruption databases; in particular, the well-documented eruptions of Mt. Spurr, Alaska in 1992. The CMC was designated as the Montreal Volcanic Ash Advisory Center (VAAC) by the International Civil Aviation Organization (ICAO) in 1993.

In the model, the advection terms are calculated using a semi-lagrangian scheme (Robert, 1982), both in the horizontal and in the vertical. Horizontal diffusion is modeled according to the K -theory. Diffusivity coefficients depend on the state of the boundary layer at low levels and are constant in the free atmosphere. The vertical diffusion coefficient is calculated in terms of a mixing length and a function of the Richardson number, according to a formulation similar to the one proposed by Louis (1979). The model simulates wet and dry scavenging and provides estimates of wet and dry deposition. CanERM uses the concept of virtual source (Pudykiewicz, 1988) to model unresolved subgrid-scale effects of emission and dispersion processes near the point of release. The virtual source is expressed according to a Gaussian function in the horizontal, whereas for the vertical the user chooses the function (gaussian, constant, or empirical). Because of the gaussian function used for the horizontal distribution of ash near the source, CanERM is not designed to evaluate dispersion near the source but rather at some distance from the volcano. The model operates on a polar stereographic grid of 229 by 299 points and can be run for any location on the globe. The horizontal spacing of the grid points is selected by the user (5 to 150 km) according to the situation and forecast duration. A 25 km grid is suitable for most situations. In the vertical, 25 levels are used (eta coordinates).

CanERM uses meteorological fields provided by the CMC global data assimilation and forecast system. In diagnostic mode, the last seven days of analyzed meteorological fields are kept online. In forecast mode, the model uses the results of a number of regional and global numerical weather prediction forecast models on grids ranging from 10 to 100 km and forecast periods of 72 h twice a day and 240 h once a day. Servranckx *et al* (1996) provide a good description of CanERM and its application for volcanic ash forecasting at the CMC and Montreal VAAC. The CanERM model also requires the input of the following: latitude and

longitude of the volcano, time and date of the eruption, duration of the eruption, ash release time function (constant, exponential, or gaussian), the amount of ash erupted, and the plume height. Since detailed information about eruption characteristics is often not available, accepted default values for ash volume, eruption duration, and release function are used to initially run the model until information is updated. Comparisons have been done between the model results and databases obtained from field experiments (D'Amours, 1998) as well as qualitative information from volcanic eruptions and Asian dust events (e.g., Simpson *et al.*, 2002, 2003). These show that CanERM provides useful guidance, which is quite remarkable (Servranckx and Chen, 2004) considering the uncertainties associated with the many parameters that act as input to the model (e.g., eruption parameters).

7.7.2 HYSPLIT

HYSPLIT, initially developed at the NOAA Air Resources Laboratory (ARL) with the last major upgrade developed in collaboration with the Australian Bureau of Meteorology, supports a wide range of simulations related to the transport, dispersion, and deposition of substances in the air such as volcanic ash or radioactive species as well as dust storms (Draxler *et al.*, 2001). Simulation results can vary from simple trajectories to more complex air concentration contour patterns. The modeling system is available online at and can be downloaded (<http://www.arl.noaa.gov/ready/hysplit4.html>). Draxler and Hess (1997, 1998) provide an overview of the HYSPLIT-4 system and its use for trajectories, dispersion, and deposition. Draxler (1999) provides the user guide for those wanting to run HYSPLIT locally. In the guide they compare model predictions for pollutant transportation with balloon trajectories, air concentrations from tracer experiments, and satellite photographs of a volcanic eruption at Rabaul Volcano, Papua New Guinea. Draxler and Hess (1998) find that for this volcanic explosion HYSPLIT does show a good qualitative agreement for the shape and size of the volcanic cloud when compared with a geostationary meteorological satellite (GMS) visible satellite image.

Calculations can be performed with gridded archival or forecast meteorological data, or a combination of both. Archived data since 1948 are available directly from ARL online via their archive system. With archived data, HYSPLIT can be run

in dispersion model mode or as a forward/backward trajectory model, with initialization models such as the Global Data Assimilation System (GDAS), NCEP Final Analyses (FNL), Eta Data Assimilation System (EDAS), Nested Grid Model (NGM), and NCEP reanalysis depending on the time scale required for the model run. HYSPLIT may be applied on a variety of computer platforms. In addition to the main part of the code that calculates trajectories and concentrations, the HYSPLIT system contains meteorological utility programs and post-processing programs that convert several kinds of meteorological model output into HYSPLIT-compatible format or convert HYSPLIT model output to GIS (Geographic Information Systems) shapefile format. Dispersion output may be displayed as contoured concentration patterns or plots of the model particles. Ensemble and matrix simulations may also be run. A graphical user interface (GUI) is included with the PC version. The HYSPLIT trajectory and dispersion codes may be run online via ARL but some model inputs are either pre-set or limited because of computer resources. More information on HYSPLIT and a link to the PC version is found via the ARL home page.

In HYSPLIT, dispersion is calculated by assuming either single puff or particle dispersion, or a combination of both. In the Puff model, individual puffs expand until they are greater than the size of the meteorological grid cell and then split into several new puffs. In the particle model, a fixed number of initial particles are advected about the model domain by the mean wind field and a turbulent component. The model's default configuration assumes puff distribution in the horizontal and particle dispersion in the vertical. Turbulence is computed using a diffusivity approach based on vertical stability estimates and horizontal wind field deformation. In some cases, typically with high-level volcanic ash simulations, turbulent velocities are computed directly from the stability parameters. Winds are linearly interpolated in both time and space. Model time steps are calculated based on the grid size of the meteorological data and the wind speed.

Volcanic ash particles are defined initially as a set of discrete "pollutants", each with a given particle size, density, shape, and mass emission rate. Gravitational settling includes the Cunningham slip correction (for details see Draxler and Hess, 1998) and accounts for nonspherical particles. Wet deposition in-cloud and below-cloud constants

may be chosen, though NCEP does not include wet deposition in their volcanic ash dispersion forecasts. Aggregation is not modeled. Model particles may be output at given time intervals. The concentration grid (i.e., the grid on which concentrations are calculated) is set independently of the input meteorological grid. Values include horizontal grid spacing, vertical levels, and output time interval. Display programs include utilities to display the particle contours or concentration contours.

HYSPLIT trajectories or dispersion may be run in ensemble mode (Draxler, 2003). In the ensemble configuration, instead of having a point or line source an array of sources around and including the point source are defined. The ensemble approach provides a method to account for some of the uncertainty in the source height and input gridded meteorology. Ensemble trajectory output is shown as one plot showing all the ensemble members' trajectories. Ensemble concentration output can be shown as a plot of the number count of the spatial distribution of ensemble members that have a nonzero concentration, a plot giving the probability of exceeding a given concentration, and a plot of the concentrations at a given probability level. The U.S. NOAA National Weather Service (NCEP) runs HYSPLIT operationally to support the Washington Regional Specialized Meteorological Center (RSMC) for Environmental Emergency Response (EER) and added the capability of modeling volcanic ash in 2004 to support the Washington and Anchorage Volcanic Ash Advisory Centers (VAACs). HYSPLIT is the operational VATD model for the Australian Bureau of Meteorology in support of the Melbourne RSMC and the Darwin VAAC.

7.7.3 Puff

The Puff model is specifically tailored for volcanic ash and is maintained by the Geophysical Institute at the University of Alaska, Fairbanks (UAF). Puff was initially conceived and developed by Prof. H. Tanaka, University of Tsukuba, Japan, as a method for simulating ash cloud trajectories during the eruption of Mt. Redoubt in 1989. The numerical code was modified and a graphical user interface added by C. Searcy of the NWS in the late 1990s so the program could be used operationally for volcano ash cloud modeling and assist in AVO volcanic ash cloud monitoring. Improvement and refinement of the model continue as new resources and techniques are utilized. Several universities and

institutions continue to use the Puff model for both research and operational activities, including AVO in the NOPAC region (see <http://puff.images.alaska.edu/>). Recently, Puff has been used to predict forest fire smoke trajectories as well (Tanaka *et al.*, 2004).

Perhaps the most unique feature of the Puff model is its focus on providing forecasts for volcanic ash clouds only, compared with CanERM and HYSPLIT which additionally address dispersion of other materials and trajectory analysis. While this is restrictive for more general purposes, it has allowed streamlining of the model architecture. Model simulations can be performed in 30 s to a few minutes using 1 GHz desktop computers. The numerical code is also fairly portable and requires no network connectivity as long as the meteorological wind fields are stored locally, which allows for its straightforward use worldwide. Puff is a lagrangian model and uses an adjustable number of tracer particles to represent a volcanic ash cloud. Meteorological model data on a regular grid are used to define the advective term. Linear interpolation is used in the space and time dimensions for advection at particle locations between grid points. The diffusion rate is defined by adjustable constants for the horizontal and vertical directions, and the two generally differ by orders of magnitude due to the anisotropy in turbulent eddies (Armenti *et al.*, 1988). Gravitational settling assumes spherical particles with different fall velocities based on the flow regime defined by the fluid dynamic Reynolds number. There is no aggregation or resuspension physics defined in the model.

Puff uses either a constant value for the diffusion coefficient or variable diffusion coefficients based on turbulent airflow. Diffusion describes the random mixing of a fluid within a spatial scale much smaller than the scale of the mean flow. Since the spatial resolution of wind field models is not high enough to include this motion, the diffusion term becomes an additional component when describing the overall path of the particle. Fluctuations in the wind field, the drifting of a high-pressure or low-pressure system, plume interaction with tropospheric winds, and the removal of particles within the plume via fallout can all play a major role in the diffusion rate over time. Using turbulent diffusion allows for a more accurate representation of “real” atmospheric diffusion, which varies throughout the turbulent atmosphere. The amount of diffusion within a plume is a function of the spatial scale of the plume, the spatial scale of the

eddies within the overall wind pattern, the magnitude of directional and speed shear, the particle density of the plume, and the time scale over which the plume travels.

The initial number distribution of tracer particles in the vertical dimension is adjustable depending on the strength of the eruption. Low-altitude plumes commonly are linearly distributed while more powerful events begin with some type of “umbrella” shape with a higher concentration of particles near the top. Particle size is specified using either a log-normal distribution with an adjustable mean value, or can be explicitly specified using a φ -distribution. Utilities for running simulations and viewing the data afterwards are independent of the main model and included with the entire package. The model can be installed and run locally or simulations can be performed using Puff online. Tracer particle distributions can be displayed by height or concentration, and fallout by relative or absolute concentration. Relative ash concentration can be calculated on an adjustable grid, and absolute values are possible if the total eruption mass or volume is known. Results are output using an adjustable time interval with a default of 6 h.

Within the online interface, there are several options that can be specified for each eruption, such as eruption length, plume shape, plume size, plume width, plume height, initialization wind model, start time, and length of simulation. The plume shape can be defined as linear, Poisson, or exponential with respect to the vertical number distribution of particles. Cell size and altitude are important factors that must be taken into consideration when these data are used for hazard assessments. The GFS, NAM, and WRF data summarized in Table 7.2 are all forecast data and are available online with a one-week archive. For model predictions one week after the event, NCEP reanalysis data are required. The model can be run with or without a digital elevation model (DEM) to define the ground surface elevation. Use of a DEM can significantly affect forecast results when ground elevations are far from sea level or highly variable, which is important for accurately tracking low-level ash clouds and potential ashfall.

In recent years, Puff has been linked with the Bent model (Bursik, 2001; Bursik *et al.*, 2012) to provide a better set of initial conditions (as noted in Section 7.4). Originally designed for small bent-over plumes, Bent can begin with a series of eruption source parameters and create a more plausible input for the initial plume conditions in Puff. By perform-

Table 7.2. Gridded wind fields used by the Puff model in the NOPAC region.

<i>Wind fields</i>	<i>Cell size</i>	<i>Model top pressure (mbar)</i>	<i>Approx. maximum altitude (based on std. atm.) (km)</i>	<i>Region</i>
BADC	$2.5 \times 5^\circ$	0.1	65	Global
GFS	$1.25 \times 1.25^\circ$	70	20	Global
NOGAPS	$1 \times 1^\circ$	10	34	Global
NAM	45×45 km	50	22	Regional
WRF	10×10 km	200	16	Regional

BADC: British Atmospheric Data Center; GFS: NOAA NCEP Global Forecast System; NOGAPS: Navy Operational Global Atmospheric Prediction System; NAM: North American Mesoscale Model; and WRF: Weather Research and Forecast Model (derivative of Mesoscale Model v. 5).

ing many runs (thousands or more) and creating an ensemble of eruption conditions and models, a probabilistic map can be generated in a relatively short time (hours) to create very good forecasts of ash position (Bursik *et al.*, 2012).

The Puff model has the ability to display volcanic ash dispersion predictions in a variety of forms. Data can be displayed in JPEG, PNG, or GIF file format and can include airborne ash color-coded by altitude, airborne ash concentration, or ash fall. Optional map projections include polar stereographic, Mercator, or Lambert. Multiple eruptions can be tracked simultaneously. While the scenario in which two volcanoes erupt simultaneously in the same region is somewhat rare, intermittent eruptions from the same volcano are relatively more common. From a modeling perspective, each of these events can be treated as a separate eruption and tracked simultaneously. There is no inherent limit to the number of events that can be tracked at one time. Furthermore, an existing ash cloud can begin to be tracked even when it is far from its origin, or the origin is unknown. The Puff model accomplishes this by allowing the user to input basic geographic information about an existing ash cloud, such as its depth and mean altitude, lateral extent, and even relative densities between different parts of the cloud.

7.8 EXAMPLES OF VATD MODELING DERIVED ASH CLOUD TRACKING

CanERM, HYSPLIT, and Puff model predictions will be compared using volcanic eruptions from Mt. Spurr (September 17, 1992) (example reference: Eichelberger *et al.*, 1995), Kliuchevskoi (September

30, 1994), Mt. Cleveland (February 19, 2001) (example reference: Dean *et al.*, 2004), and Mt. Augustine (January 13, 2006) (example reference: Power *et al.*, 2006). Table 7.3 summarizes the source parameters for these four events. These volcanoes are all monitored as part of the Alaska Volcano Observatory (AVO) system across the NOPAC. In addition, model simulations are compared with the Advanced Very High Resolution Radiometer (AVHRR) satellite data used operationally by AVO.

Quantitative comparisons are beyond the scope of this effort. A more thorough comparison among the models and between the models and satellite analyses could include statistical measures such as threat score (TS) (i.e., the ratio between the overlap area of two model output areas to the total area of the two models), the Pearson chi-square test, or the Kolmogorov–Smirnov test. The threat score (e.g., Wilks, 2006) is a common meteorological verification measure and is applied by Stunder *et al.* (in press). Other statistical techniques are discussed in Conner and Conner (2006) and have been applied in the analysis of tephra fallout models.

All three VATD models have the option of using forecast or analysis meteorological data. Comparison of forecast VATD model output includes uncertainties in the meteorological forecast model as well as in the VATD model, whereas use of analysis meteorology eliminates the forecast meteorology component. Stunder *et al.* (2007) estimate forecast area reliability for several volcanoes using forecast and analysis meteorology.

For three of these examples (Mt. Spurr, Kliuchevskoi, and Mt. Cleveland), analysis data (either NCEP/NCAR or FNL) have been used. For the Augustine 2006 eruptive event, however, output

Table 7.3. VATD model source parameters for the four volcanic eruption cases.

<i>Eruption parameter</i>	<i>Mt. Spurr Volcano (September 19, 1992)</i>	<i>Kliuchevskoi Volcano (September 30, 1994)</i>	<i>Mt. Cleveland Volcano (February 19, 2001)</i>	<i>Mt. Augustine Volcano (January 13, 2006)</i>
Start time	08:00 UTC	15:00 UTC	14:30 UTC	13:24/17:47/20:22 UTC
End time	11:40 UTC	17:00 UTC	17:30 UTC	13:35/17:51/20:25 UTC
Duration	3 h 40 min	2 h	3 h	0.1833/0.0714/0.0567 h
Plume height	14 km	10 km	10 km	11/10/10 km
Wind field	Reanalysis	Reanalysis	Reanalysis	Reanalysis/NAM216
Mass distribution by height	Poisson/Umbrella shape	Poisson/Umbrella shape	Poisson/Umbrella shape	Poisson/Umbrella shape
Simulation length	48 h	48 h	48 h	24 h
GSD	$10 \mu\text{m} \pm 1\sigma$	$10 \mu\text{m} \pm 1\sigma$	$10 \mu\text{m} \pm 1\sigma$	$10 \mu\text{m} \pm 1\sigma$

using both forecast and analysis data will be shown. During the eruption of Mt. Augustine, AVO used forecast input data to Puff for near-real time predictions of the volcanic ash clouds. These will be shown and compared with HYSPLIT and CanERM output using analysis meteorology since forecasts are not available.

7.8.1 Mount Spurr Volcano: September 1992

The eruption of Mt. Spurr on September 17, 1992 started at 08:03 UTC and ended at 11:39 UTC. A volcanic ash plume rose to 10.7 km, as reported by PIREPS (pilot reports) and U.S. National Weather Service (NWS) radar. By 08:48 UTC, the volcanic plume had risen to 12.2 km as determined by NWS radar and 13.9 km by 10:21 UTC. By 13:45 UTC, NWS radar showed no plume at Crater Peak, a vent at Mt. Spurr. The subsequent ash cloud moved eastward, dusted the north edge of Anchorage, and deposited about 1.5 mm of ash north of Anchorage. This Spurr eruption is a good example showing that VATD models can be reasonably accurate over a 3-day period and a 7,500 km distance. Details of the eruption are provided in Eichelberger *et al.* (1995) and other papers in USGS Bulletin No. 2139. Figure 7.5 shows the AVHRR split-window ash detection (Prata, 1989) from this September 1992 event. The images show a combination of the data collected at AVO/UAF from September 17–20, 1992. The ash cloud moves away to the east across eastern Alaska and into northern

Canada. By 11:00 UTC on September 18, the AVHRR-detected ash cloud can be seen extending over portions of Alberta and Saskatchewan (Canada) and Montana (U.S.A.). By 20:45 UTC, the ash cloud is situated over North and South Dakota and the ash signal has not reduced in strength. The ash cloud then proceeds to travel across the northern continental U.S./Canada border and over Quebec and is detected over Greenland at 17:00 UTC on September 20, 1992, a full 80 h after the eruption began. For this event at Mt. Spurr, HYSPLIT, CanERM, and Puff were used to compare their abilities to accurately track the ash cloud seen in Figure 7.5.

Figure 7.6 shows the CanERM forecast predictions for the September 1992 event at Mt. Spurr, displaying the airborne ash concentrations at 17:00 UTC on September 17 (7.6a), 11:00 UTC on September 18 (7.6b), and 19:00 UTC on September 19, 1992 (7.6c). The CanERM prediction on September 17 shows the highest ash concentration matching the location of the satellite-derived ash cloud in Figure 7.5. However, the CanERM predictions show a section of the ash cloud to be north and northwest of the volcano (see the inset in Figure 7.6a). Preliminary analysis suggests that this feature (not seen in Figure 7.5 or HYSPLIT and Puff predictions later in this section) is a result of the initial conditions of the plume shape and associated distribution of ash in the plume used for the CanERM prediction. Further analysis of this feature with respect to the other models and satellite data is required. At 11:00 UTC on September 18, the

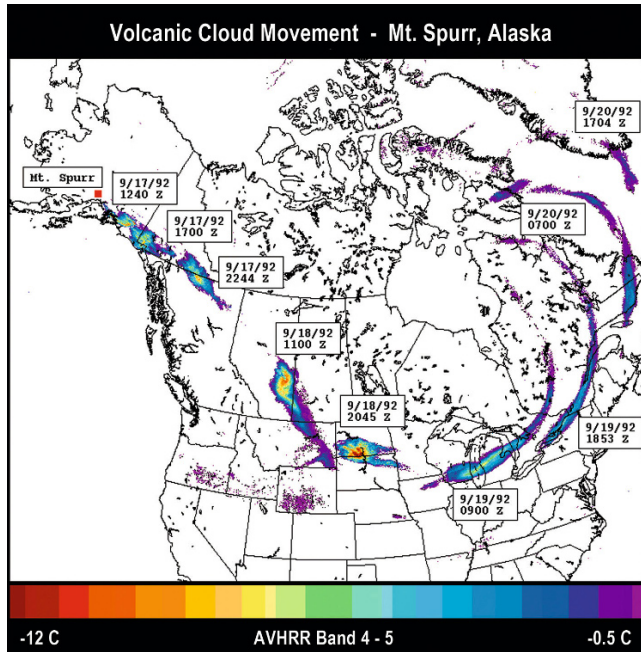


Figure 7.5. AVHRR split-window detection (from Schneider *et al.*, 1995).

CanERM prediction shows the highest ash concentration to be farther downwind of the position of the ash cloud observed in the satellite data. CanERM shows the tail of the ash cloud to extend all the way to Alaska, and the prediction matches the HYSPLIT and Puff predictions. This ash concentration may be below the detection limits of the satellite sensor. By 19:00 UTC on September 19, CanERM predicts the ash to be extending from northeastern U.S.A. into Canada and beyond. The concentrations predicted by this time are much lower than in the previous two images, indicating that the cloud is dispersing. The prediction is relatively close (displaced somewhat to the southeast) to the ash cloud observed in the satellite data and the cloud location predicted by the HYSPLIT and Puff models.

Figure 7.7 shows the HYSPLIT trajectory analysis starting at the beginning of the Mt. Spurr 1992 eruption and three simulated locations of the ash clouds and airborne ash concentrations. Figure 7.7a shows that the 5 and 10 km trajectories match the AVHRR detected ash signal well, with the initial 10 km trajectory eventually reaching an 8 km elevation after 48 h (06:00 UTC on September 19). The trajectories at 2 and 5 km do not mimic the ash cloud observed in the AVHRR image, which

implies the ash is likely at higher elevations, a hypothesis supported by the results of the CanERM model simulations in Figure 7.6. The HYSPLIT airborne ash concentrations are shown in Figure 7.7b–d, integrated over one hour. Figure 7.7b shows the HYSPLIT simulation closely matches the position of the ash cloud observed in the 17:00 UTC satellite image. These figures are scaled according to the Washington VAAC “visual ash” level, such that the unitless concentrations greater than 1.0 correspond to “visual ash”. By 10:00–11:00 UTC on September 18, HYSPLIT simulations show the ash cloud extending across the Canadian/U.S. border with the highest concentration (blue region in Figure 7.7c) coinciding with the location of the ash cloud observed in the AVHRR image. By 18:00–19:00 UTC on September 19, HYSPLIT simulates the ash cloud to extend over the northeastern U.S.A. almost matching the ash detected by AVHRR at 18:53 UTC (Figure 7.7d).

The Puff model simulated an eruption cloud initially 14 km above sea level (a.s.l.) with an eruption duration of 3.5 h (Figure 7.8). In Figure 7.8 the ash cloud location is shown color-coded by altitude and relative airborne concentration. Figures 7.8a, d show a snapshot at 17:00 UTC for September 17, corresponding to the ash cloud east-southeast in

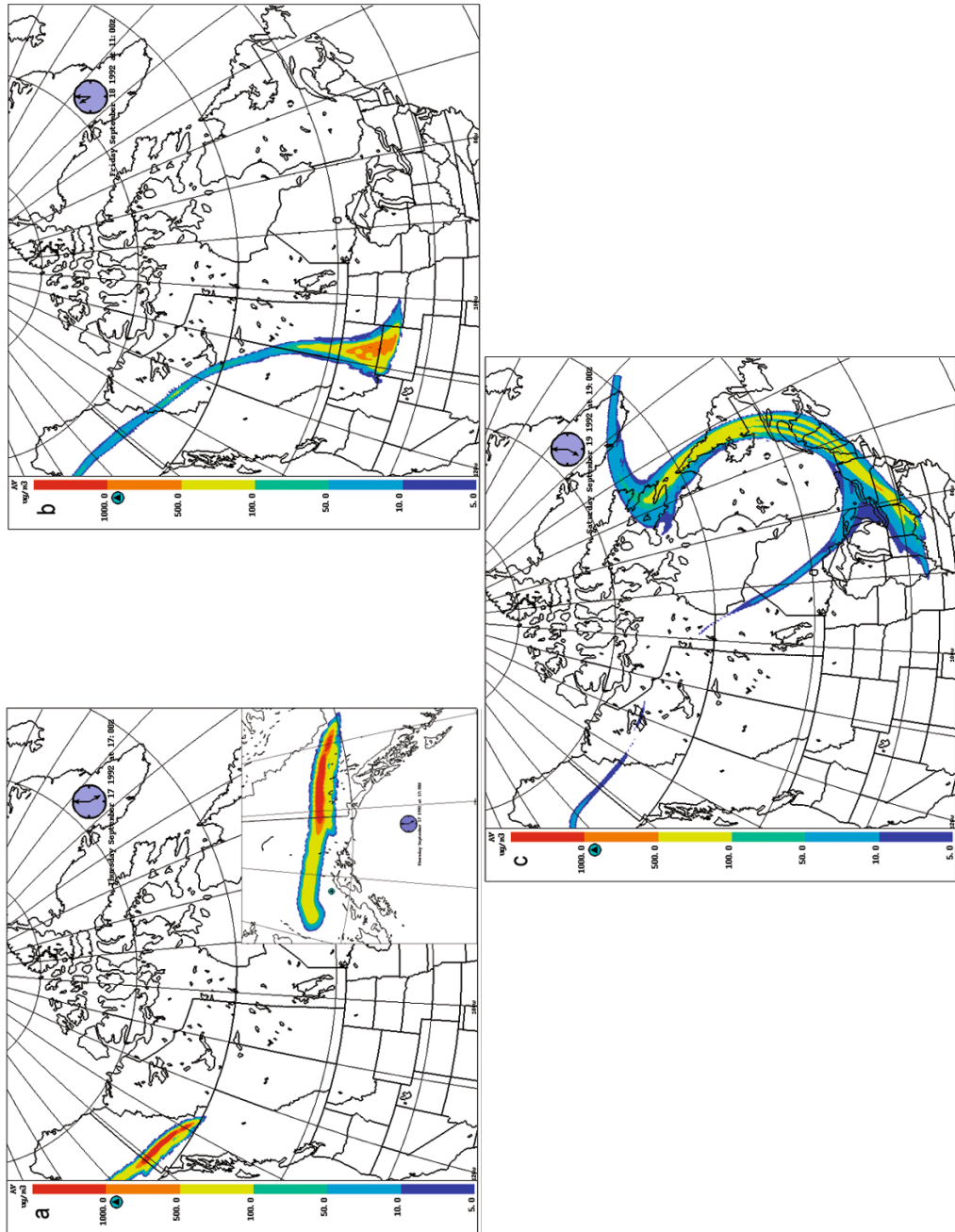


Figure 7.6. CanERM model airborne ash concentration predictions from Mt. Spurr's September 1992 eruption: (a) 17:00 UTC on September 17 (with inset zoomed in on the ash cloud); (b) 11:00 UTC on September 18; and (c) 19:00 UTC on September 19, 1992.

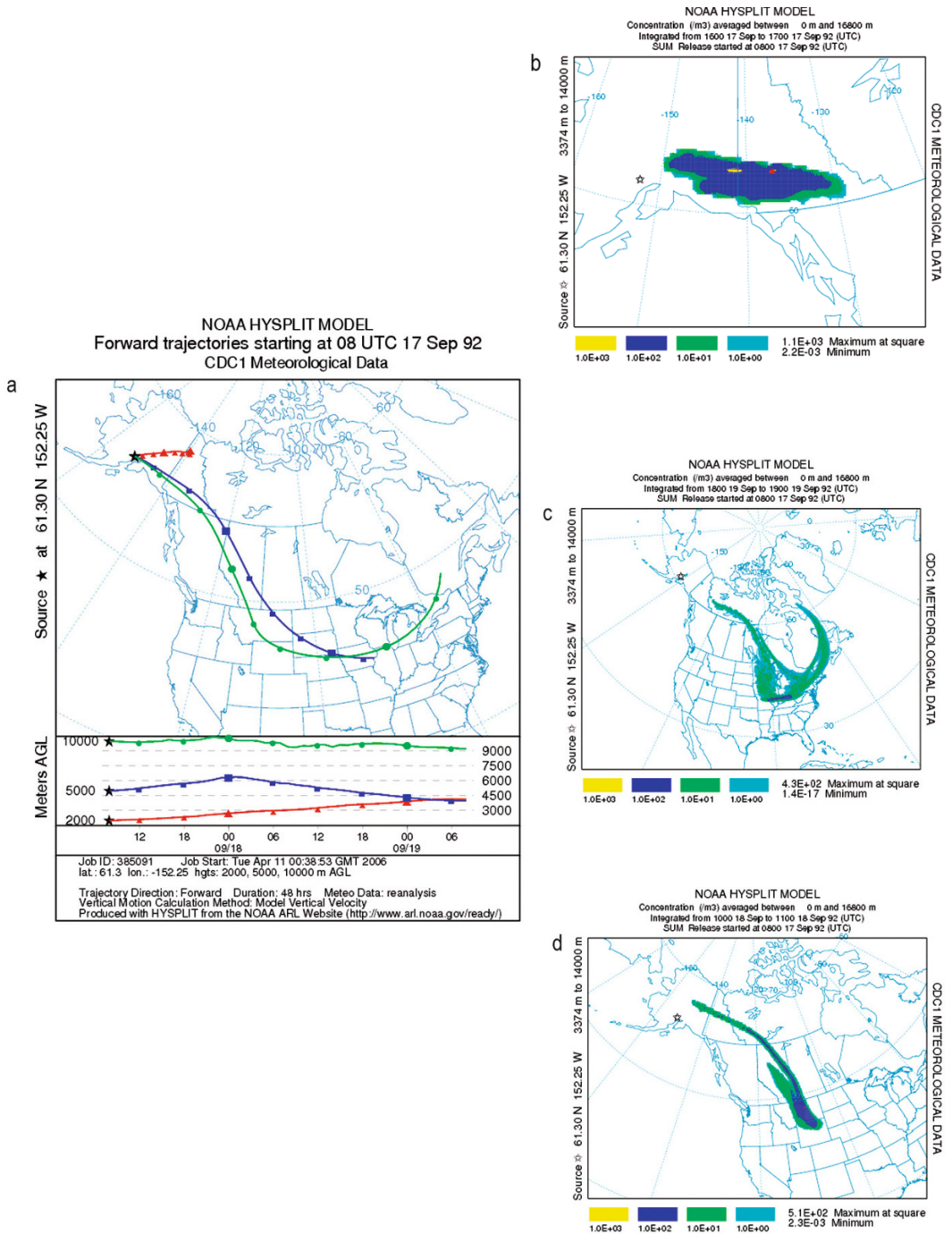


Figure 7.7. (a) HYSPLIT model trajectories from Mt. Spurr beginning September 17, 1992. HYSPLIT model-simulated airborne ash relative concentration from the Mt. Spurr September 1992 eruption: (b) 16:00–17:00 UTC September 17, 1992; (c) 10:00–11:00 UTC September 18, 1992; and (d) 18:00–19:00 UTC September 19, 1992.

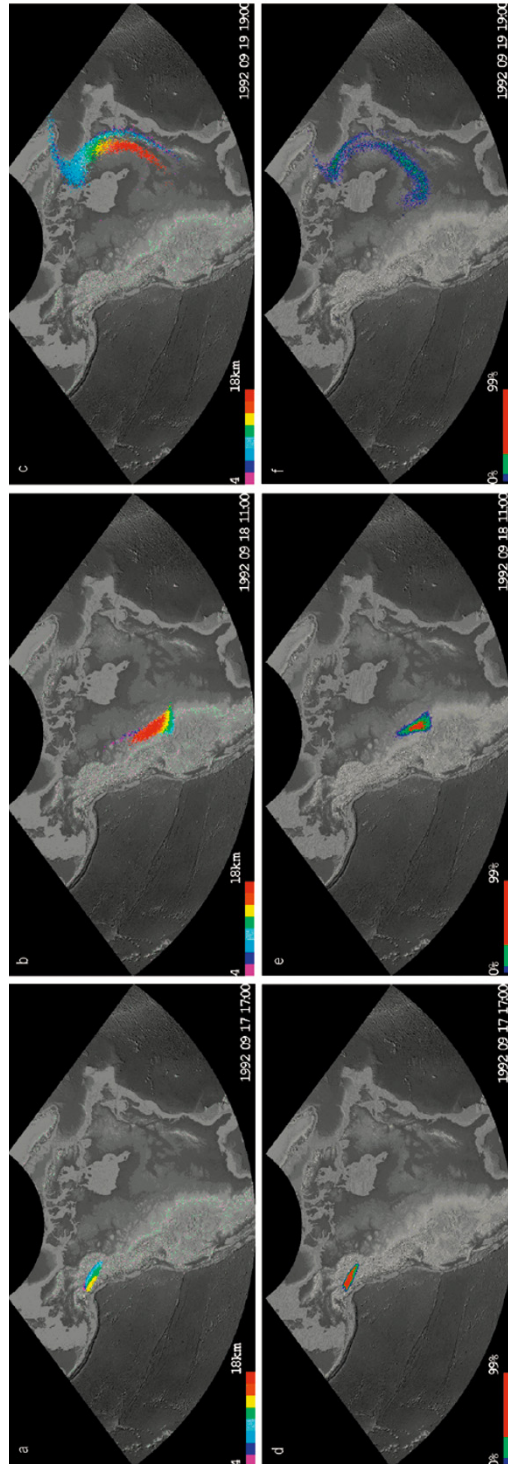


Figure 7.8. Puff model predictions for volcanic ash from Mt. Spurr at 17:00 UTC on September 17, 1992, 11:00 UTC on September 18, 1992, and 19:00 UTC on September 19, 1992 for airborne ash colored by height (a, b, c) and ash concentrations (d, e, f), respectively.

Figure 7.5. By 11:00 UTC on September 18 (Figure 7.8b,e), the Puff prediction shows the ash over southern Canada near the U.S. border, matching the AVHRR ash detection. By 19:00 UTC on September 19 (Figures 7.8c,f), the ash cloud is now over the Great Lakes region with the high-altitude portions of the ash cloud matching the AVHRR data. The Puff simulation indicates the expected decrease in ash concentration as the ash cloud becomes more disperse. For the September 17, 1992 event at Mt. Spurr, all three models agree well and are able to track the ash cloud as it moves east-southeast across Alaska and Canada and across into the northern U.S.A. All three VATD models predicted the ash cloud's movement with a high degree of accuracy and provided insight regarding the height of the ash cloud and wind shear over the course of its movement.

From this September 1992 eruption, the ash cloud moved in the direction of the contiguous U.S. As Schneider *et al.* (1995) stated, this raised the issue of whether Alaskan eruptions could pose hazards to the principal domestic air routes within the contiguous U.S. The model results from CanERM, HYSPLIT, and Puff all showed evidence of this transport into the contiguous U.S. and so illustrate the utility that VATD modeling has in simulating ash cloud movement over a several-day period and distances of approximately 7,000 km. The most important feature of this model-to-satellite data comparison is that the ash cloud was detected in the satellite data for approx. 3 days after the eruption (Schneider *et al.*, 1995) and the tracking models were able to accurately simulate the movement of this cloud.

7.8.2 Kliuchevskoi Volcano: October 1994

Kamchatkan volcanoes can produce volcanic ash clouds at jet aircraft altitudes (>20,000 ft or FL200) which can move across and parallel to the shoreline of the Kamchatka Peninsula, due to westerly and northwesterly winds spreading across the whole NOPAC region, and hence present a serious threat to aircraft in the region. Kliuchevskoi Volcano (56.06°N, 160.64°E) on the Kamchatka Peninsula about 135 km north of Petropavlovsk is a basaltic stratovolcano with a summit elevation of 4,835 m. The eruption that commenced on September 8, 1994 had a volcanic explosivity index (VEI) of 3 with a lava volume approaching $\sim 30 \pm 10$ million m^3 and tephra volume near 50 million m^3 by the time it ended (GVP, 1994). During mid-September

1994, ash bursts rose 500–700 m above the crater and an eruption column extended 50 km southeast of the volcano. By the last week of September, this had increased to a 2 km plume above the crater and 100 km to the southeast. Eruptive activity increased on the afternoon of September 30, 1994, and by October 1, 1994 at 06:00 UTC the eruption entered a paroxysmal stage with eruptive bursts rising 4.5 km above the crater. The ash column top was estimated at 15–20 km altitude and extended more than 100 km to the southeast (GVP, 1994).

Between 09:00 and 11:00 UTC on October 1, 1994, ash and lava bursts produced a dark, ash-laden plume rising to a height of 15–18 km and moving east-southeast. Wind speeds at altitudes between 10 and 15 km were 40 to 50 $m s^{-1}$ (120 mph) and generally from the east-southeast (Searcy *et al.*, 1998). GMS satellite images showed ash ~ 565 km southeast of the volcano and moving at ~ 140 km/h. Lava and ash explosions continued from the central crater at 15:00 UTC, when the ash column rose to 12–14 km a.s.l. (above sea level) and moved east-southeast at an altitude of 10–11 km. Pilot reports indicated that the ash was at 9–11 km (FL300–370, $\sim 30,000$ – $37,000$ ft). A 747 aircraft reported an ash encounter at 11 km altitude, but avoided the cloud by climbing to ~ 12 km (FL390). The eruption appeared to reach its maximum intensity between 06:00 and 16:30 UTC. By 17:00 UTC on October 1, 1994, the eruption began to subside and was no longer considered a hazard to aviation, as ash clouds were not predicted along aviation flight routes at the time. It should be noted, however, that this event was relatively recent to the formation of the International Airway Volcano Watch in 1987 and that information was scarce. Figure 7.9 shows the AVHRR split-window signal for the Kliuchevskoi Volcano eruption at 06:40 UTC on October 1, 1994. This is just after the start of the paroxysmal stage and shows the ash cloud resulting from both this event and the activity on September 30, 1994, starting at 15:00 UTC. This ash cloud extends to the southeast from the volcano across the Kamchatkan Peninsula into the Bering Sea.

All three VATD models (HYSPLIT, CanERM, and Puff) were applied to ascertain their ability to track this eruption from Kliuchevskoi Volcano in September/October 1994. Figure 7.10 shows the CanERM model simulations from the eruption in 1994. Figure 7.10a shows the simulated location of the ash cloud at 03:00 UTC on October 1, matching the shape of the ash cloud observed in the AVHRR

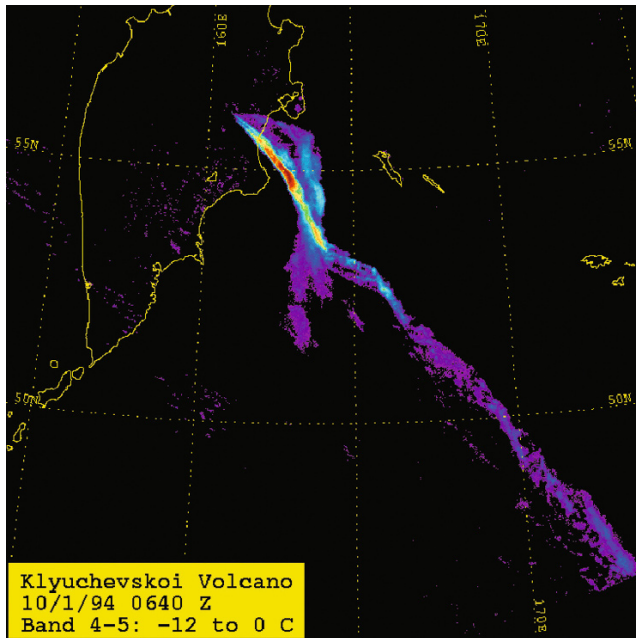


Figure 7.9. AVHRR split-window detection at 06:40 UTC on October 1, 1994 from the September/October 1994 eruption. Figure courtesy of Dave Schneider.

split-window image shown in Figure 7.9 and the HYSPLIT and Puff predictions in Figures 7.11a and 7.12a, respectively. Figure 7.10b at 15:00 UTC on October 2 shows that CanERM simulated the ash cloud traversing the whole North Pacific and passing into Alaska. This matches the ash cloud predictions from HYSPLIT (Figure 7.11c) and Puff (Figure 7.12b).

Figure 7.11a shows the HYSPLIT trajectories beginning at 15:00 UTC September 30, 1994 from Klyuchevskoi Volcano starting at 2, 5, and 10 km altitudes. The 10 km trajectory (green line) follows the ash cloud (as seen in Figure 7.9) in the early part of the simulation and follows CanERM-simulated movement from 18:00 UTC as well. By the end of the 10 km HYSPLIT trajectory simulation at 15:00 UTC on October 2, 1994 the ash cloud reached Alaska and northwest Canada at an altitude greater than 10 km. The 2 and 5 km trajectory simulations from HYSPLIT suggest that the ash cloud would have been much closer to the volcano and would have moved in a more southerly direction. Figure 7.11b, c show two one-hour averages of HYSPLIT airborne ash concentrations. These figures are scaled to the Washington VAAC “visual ash” practice (unitless concentration of 1.0 defines the ash cloud edge). Figure 7.11b from 06:00 to 07:00 UTC

on October 1, 1994 shows the HYSPLIT simulation matching the AVHRR-detected ash cloud (Figure 7.9) from 06:40 UTC. By 14:00–15:00 UTC on October 2, the simulation shows the ash across the Aleutian Islands and extending to the mainland. This agrees well with the 10 km trajectory analysis, the CanERM simulations in Figure 7.10, and the Puff model simulations in Figure 7.12.

The Puff model run began at 15:00 UTC on September 30, 1994 with an initial 10 km plume and lasted until 06:00 UTC on October 1, 1994 when it changed to a 14 km ash column and erupted for an additional 5 h ending at 11:00 UTC on October 1, 1994. The model was then run for 72 h ending on October 4, 1995 at 06:00 UTC. Figure 7.12a, c show the airborne ash colored by altitude and ash concentration, respectively, at 06:40 UTC on October 1, 1994, equivalent in time to the AVHRR data in Figure 7.8. Here, the highest relative ash concentration from Puff matches the strongest signal in the AVHRR data and shows a significant ash cloud extending into the Bering Sea and northern Pacific. The AVHRR data in Figure 7.9 show a weak and more disperse signal to the east-southeast of the brightness temperature difference (BTD) maxima region but follows the same path. By 15:00 UTC on October 2, 1994, both Puff and CanERM show

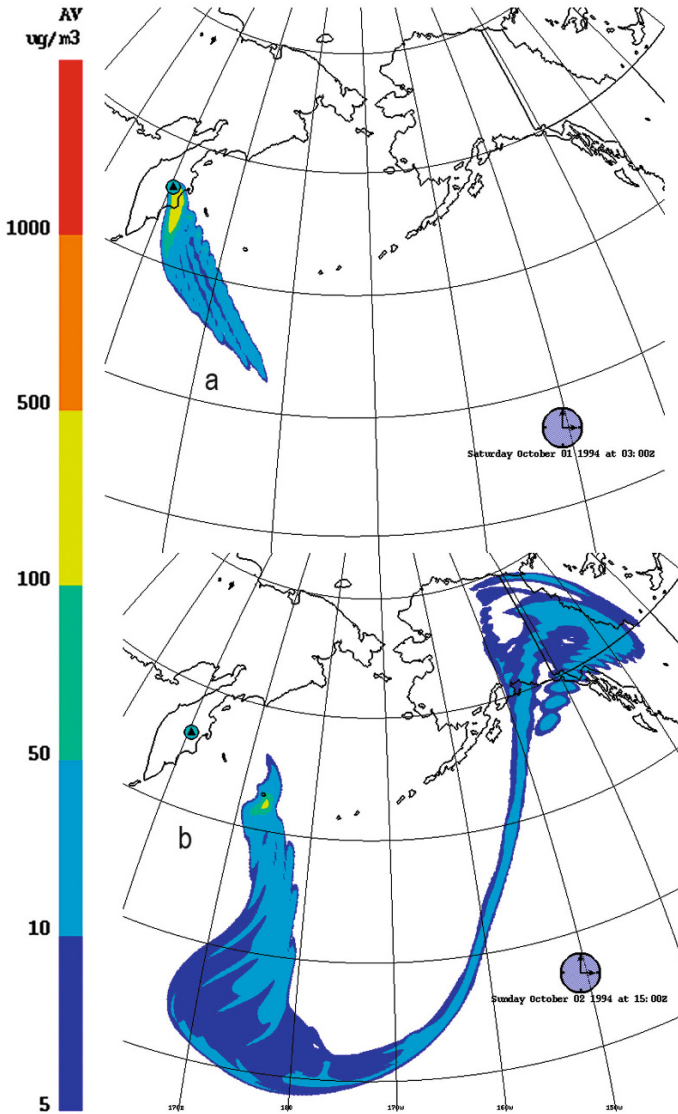


Figure 7.10. CanERM model airborne ash concentration predictions from the Kliuchevskoi September/October 1994 eruption: (a) 03:00 UTC on October 1 and (b) 15:00 UTC on October 2, 1994.

the ash cloud extending south of Alaska, following regional wind patterns. The highest ash concentrations as predicted by Puff occur close to the volcano and the Kamchatka Peninsula. This agrees with the CanERM prediction which suggested ash at both low elevations and mid-elevations.

The shape and trajectory of the high-altitude ash cloud shown in the Puff prediction agrees with the HYSPLIT 10 km trajectory. The concentrations

of ash that reach Alaska are very low when compared with the emitted ash concentrations during the eruptive event at the volcano based on the low signal strength of the split-window (BTD) AVHRR images. The 2 and 5 km trajectories from HYSPLIT, by the end of the simulation, have dropped to much lower altitudes and correspond to the 2–4 km region in the Puff prediction situated in the North Pacific to the east-southeast

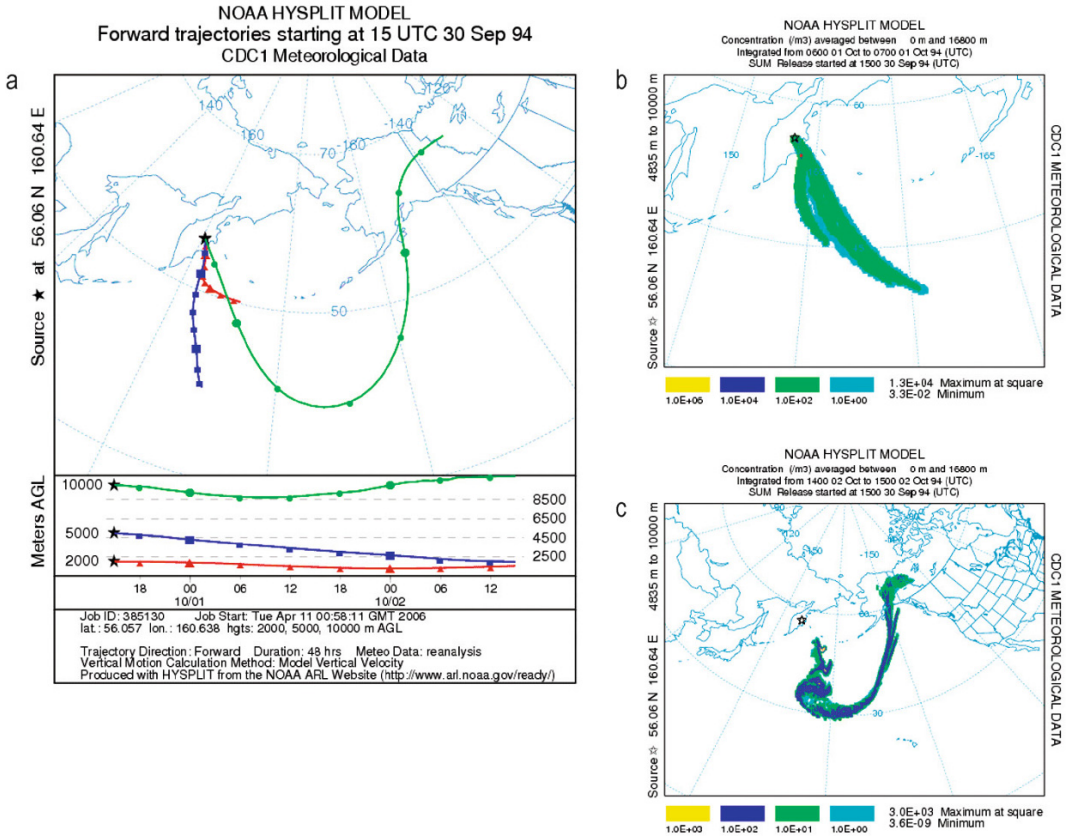


Figure 7.11. (a) HYSPLIT model trajectories from Klyuchevskoi beginning September 30, 1994. HYSPLIT-simulated airborne ash relative concentration from the Klyuchevskoi 1994 eruption; (b) 06:00–07:00 UTC October 1, 1994; and (c) 14:00–15:50 UTC October 2, 1994.

of Kamchatka. The Puff output in Figure 7.12d shows the relative airborne ash concentration. Comparison with the CanERM prediction at the same time, 15:00 UTC on October 2, in Figure 7.10b shows an identical shape to the ash cloud and the highest concentrations (red in Puff and green in CanERM) match as well. A quantitative comparison of the measured airborne concentrations depends largely on the initial parameters and would need to be validated by airborne instruments to allow a more detailed assessment of each model.

In general, the results from all three models agree quite well for the September/October 1994 event at Klyuchevskoi Volcano, and are able to track the ash cloud as it moves east-southeast from the volcano out across the Bering Sea into the North Pacific, Alaska, and northwest Canada.

Given that all three models used similar wind fields this is an insightful result showing the models agree with each other as well as the ash signal in the satellite data. The movement of the ash clouds from these simulations showed the extent to which volcanic ash clouds can affect the North Pacific. The Kamchatkan Volcanic Eruption Response Team (KVERT) and AVO actively monitor Klyuchevskoi Volcano operationally by satellite remote sensing and seismic data. Since Kamchatkan eruptions can generate ash clouds that extend across major air transport routes, accurate wind field model predictions in the event of a major eruption become very important for hazard mitigation and operational monitoring. Not only do the predictions assist volcanologists but they also provide information for the VAACs and local air authorities (such as NWS/FAA in the U.S.) responsible for issuing

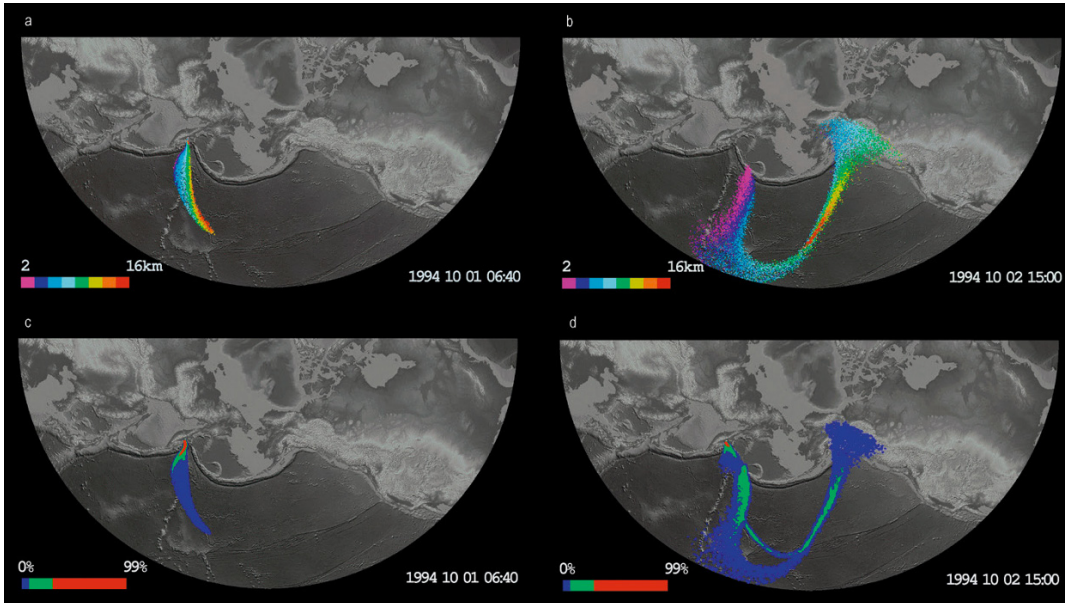


Figure 7.12. Puff model predictions for volcanic ash colored by altitude (a and b) and airborne concentration (c and d) from Kliuchevskoi Volcano from the September/October 1994 eruptions at 06:40 UTC on October 1 and 15:00 UTC on October 2, 1994.

NOTAMs (notices to airmen) and SIGMETs. Kamchatkan eruptions are obviously of interest to the Airport Meteorological Center (AMC) at Yelizovo Airport in Petropavlovsk-Kamchatsky and the Kamchatka Department of Civil Emergency (Kirianov *et al.*, 2002).

7.8.3 Mt. Cleveland Volcano: February 2001

The Mt. Cleveland example shows that VATD models can produce accurate results during complex weather conditions and provides a possible validation point for a potential aircraft–ash encounter. This report is particularly significant because of the lack of satellite-detected volcanic ash in the area at the time of the encounter. Mt. Cleveland (52.82°N, 169.85°W, 1,730 m a.s.l.) is located on the western half of Chuginadak Island, which is part of the Islands of Four Mountains group located in the east central Aleutian Islands, Alaska. Chuginadak Island is uninhabited and remote, located 1,526 km southwest of Anchorage. The closest inhabited community, Nikolski, is 75 km to the east on Umnak Island. The volcano is a distinctively conical, young stratovolcano, and

at sea level the base of the cone is approximately 8 km across, suggesting a volcanic cone volume above sea level of about 29 km³. References for the Mt. Cleveland eruption include Dean *et al.* (2002, 2004) and Simpson *et al.* (2002).

On February 19, 2001, Mt. Cleveland erupted explosively at approximately 14:30 UTC (Dean *et al.*, 2002). Pilot reports indicate that the altitude of the plume increased with time from 7.5 km a few hours after the start of the eruption, and up to 12 km a.s.l. 8 h later. The ash cloud dispersion was complex due to speed and directional wind shear. The ash cloud extended in two directions: 40 km northwest and 60 km southeast of the volcano within 2 h of the eruption. Figure 7.13a shows the satellite-detected ash cloud at this time. The northwest portion of the cloud was at 8 km a.s.l., while the southeast portion was at 5 km a.s.l. based on cloud/atmospheric temperature correlations. From the satellite analysis in Figure 7.13a, the southeast portion of the cloud had a strong ash signal that was detected using the split-window technique, but the northwest portion was not detected at this time due to its high opacity. Moreover, wind field data indicated shear at approximately 6 km, which caused the bi-directional flow of the plume. This is illustrated in Figure

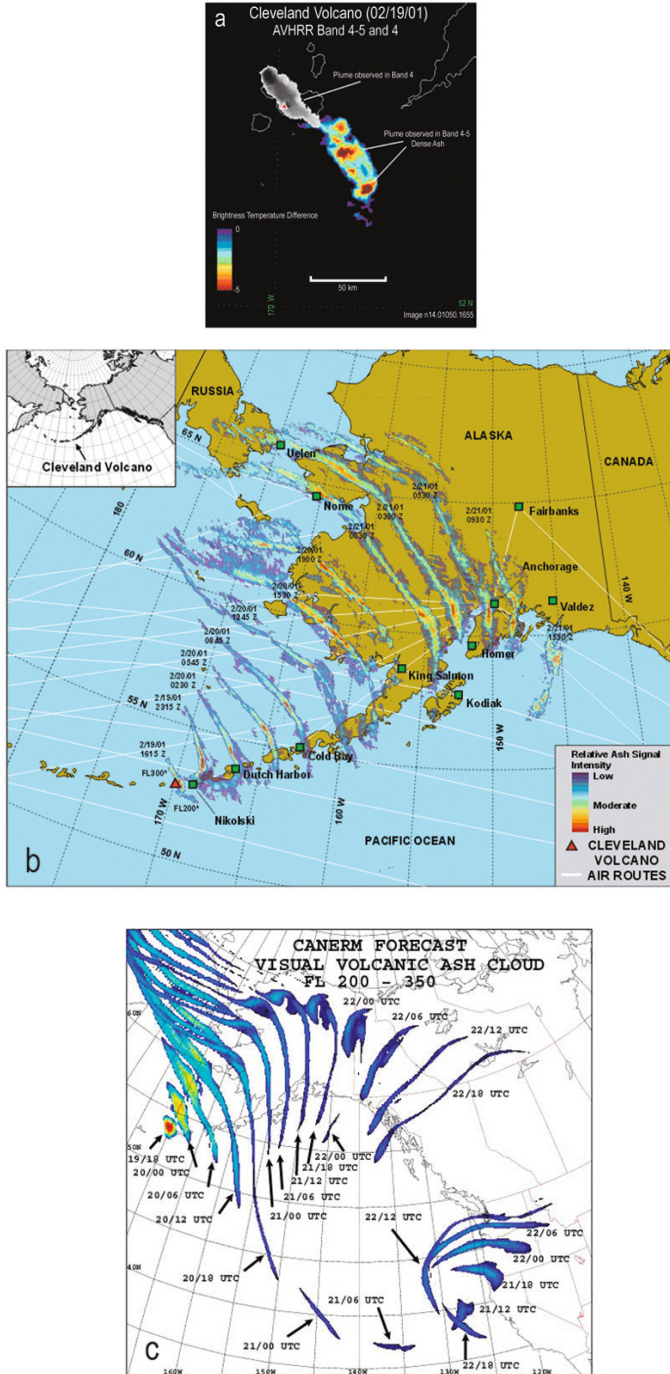


Figure 7.13. (a) Volcanic ash cloud from AVHRR at 16:55 UTC on February 19, 2001 showing the split-window to the southeast and AVHRR band 4 to the northwest. (b) Time-sequential composite of GOES split-window data. (c) CanERM time-sequential model forecast of the February 19, 2001 volcanic eruption at Mt. Cleveland.

7.13a by the split-window section to the southeast and the AVHRR band 4 ($\sim 10\ \mu\text{m}$ channel) to the northwest.

Satellite analysis suggests that volcanic ash production was more or less continuous for approximately 8 h. The volcano erupted into an atmospheric deformation zone formed by a low-pressure system to the south and east, and a front moving to the north. As a result the ash cloud became an elongated arc moving to the northeast over the Alaska Peninsula and across the Alaskan mainland. Figure 7.13b illustrates a time-sequential composite of the volcanic ash cloud detected from the satellite data. The air traffic routes (white lines in Figure 7.13b) show how the ash cloud passed over the routes and affected some Alaskan airports. By February 21, 2001 at 03:00 UTC, 35 h after the eruption, the ash cloud was over 1,000 km long and extended from Cook Inlet (Alaska) to Chukotsk Peninsula (Russia). Eventually this long, arcing cloud split into three segments: one that drifted north over the Arctic Ocean, one over Fairbanks near the center of the state, and one south into the Gulf of Alaska. After 19:30 UTC on February 21, 2001, the Fairbanks and Gulf of Alaska segments were pulled into a low-pressure system in the southern Gulf of Alaska and became too diffuse or masked by weather clouds to be detected in the GOES data.

Figure 7.13c shows the combined ash prediction from CanERM for the February 2001 eruption of Cleveland. Model predictions show the ash cloud moving across Alaska to the northeast of the volcano. In addition, CanERM predicts a portion of the ash cloud moving southeast across the Gulf of Alaska (not seen in the satellite data presumably due to low ash concentrations or particular environmental conditions that limit split-window detection), and this resultant cloud is predicted to arrive at the northwest U.S. coast at around 12:00 UTC on February 21, 2001 and to last until 18:00 UTC on February 22, 2001. During the eruption, the southeastern portion of the ash cloud moved into a low-pressure system. Simpson *et al.* (2002) state that there was a tropical storm that passed eastward from Japan to the Aleutian Islands and into the Gulf of Alaska. The ash cloud to the southeast of Mount Cleveland that passed into this “storm” cloud was probably not detected by the satellite data. The cloud cover and frontal weather conditions would have meant the split window was not able to detect any ash moving to the southeast.

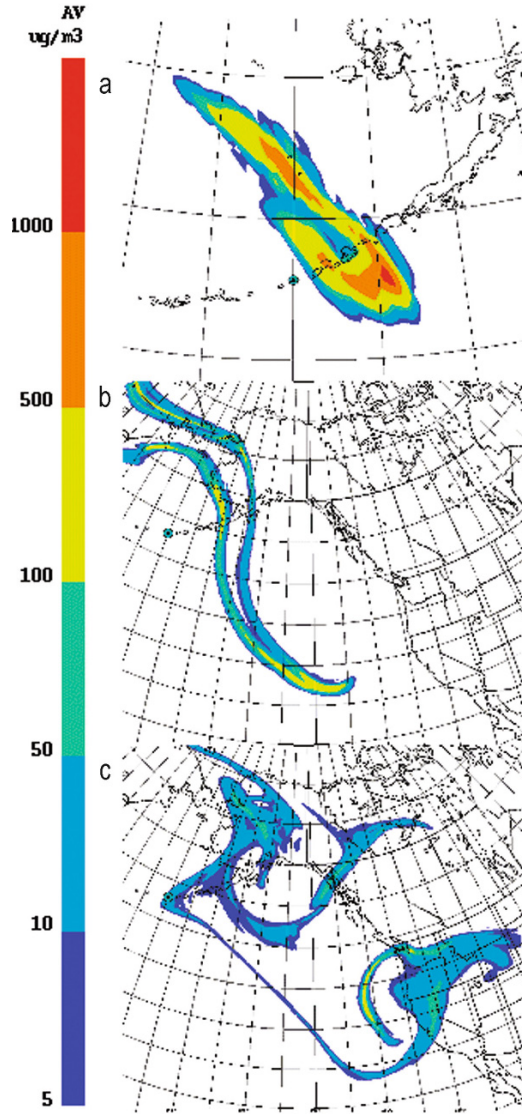


Figure 7.14. CanERM model airborne ash concentration predictions from the Mt. Cleveland February 2001 eruption: (a) 03:00 UTC on February 20; (b) 04:00 UTC on February 21; and (c) 14:00 UTC on February 22, 2001.

Figure 7.14 shows the CanERM model predictions for the February 2001 event. Figure 7.14a shows the ash cloud at 03:00 UTC on February 20, 2001, matching the early GOES data and the HYSPLIT and Puff model predictions (Figures 7.16 and 7.17, respectively). The CanERM predic-

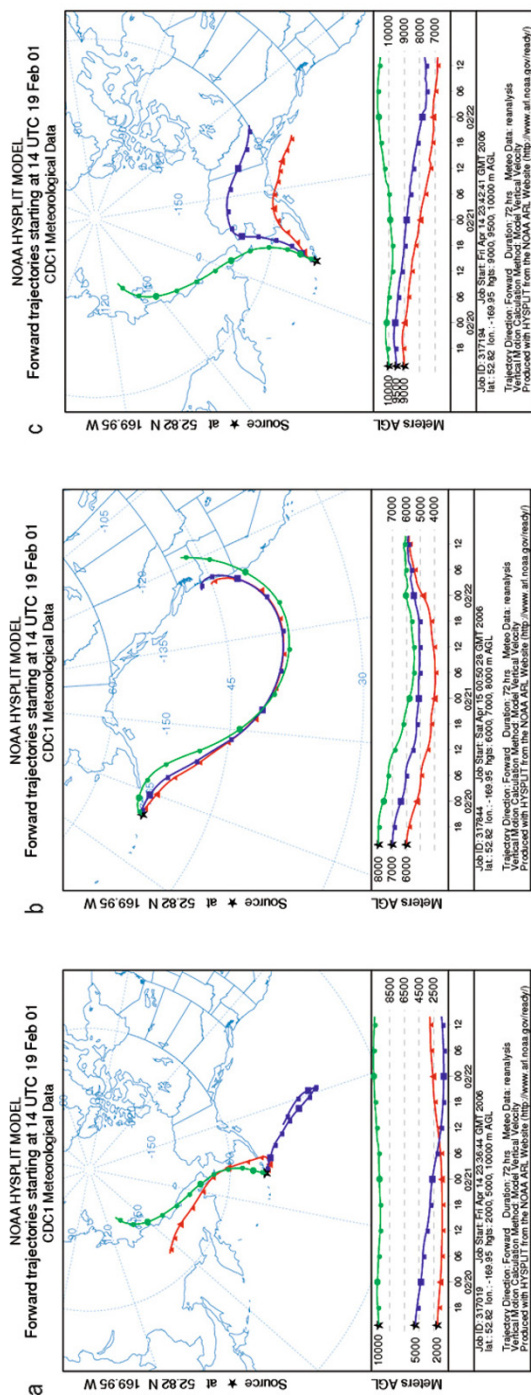


Figure 7.15. (a) HYSPLIT model trajectories from Mt. Cleveland beginning February 19, 2001: (a) 2, 5, and 10 km; (b) 6, 7, and 8 km; and (c) 9, 9.5, and 10 km.

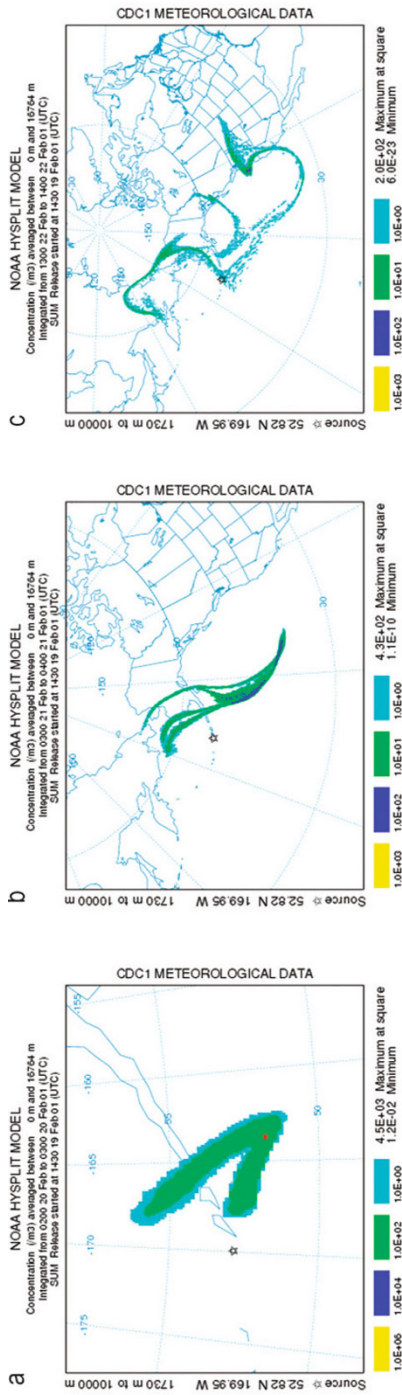


Figure 7.16. HYSPLIT-simulated airborne ash relative concentration from the Mt. Cleveland February 2001 eruption. (a) 02:00-03:00 UTC February 20; (b) 03:00-04:00 UTC February 21; and (c) 13:00-14:00 UTC February 22, 2001.

tions show the highest relative ash concentrations at the head of the plume, corresponding to the thickest portion of the ash cloud, given the predictions of ash throughout the atmospheric column. By 04:00 UTC on February 21, the ash cloud has become more disperse with lower concentrations throughout. Figure 7.14c shows the extent of the ash cloud agrees with the HYSPLIT results shown in Figure 7.16 and the Puff results in Figures 7.17 and 7.18. Of particular note is potential ash off the coast of California, which corresponds with a possible aircraft–ash encounter.

Figure 7.15 shows three sets of HYSPLIT trajectory analyses (reanalysis data were used) for the beginning of the eruption at Mt. Cleveland (14:00 UTC on February 19, 2001). Figure 7.15a shows the trajectories starting at 2, 5, and 10 km a.s.l. The 5 km trajectory travels southeast from the volcano and reverses direction into a low-pressure system as it falls to below 2.5 km at the end of the simulation. The 2 km trajectory follows the 5 km trajectory path for a short period of time. It then diverges sharply to the northwest when it is “caught” in the local weather system (the tropical storm in the Gulf of Alaska discussed earlier) causing it to diverge sharply to the northwest. Conversely, the 10 km trajectory path is to the north-northwest for the full timelength of the trajectory.

These trajectories don’t quite match with the CanERM predictions or the satellite data derived ash signal but they do indicate transport to the north and northwest. Trajectories starting at 6, 7, and 8 km a.s.l. (Figure 7.15b) show a different pattern. This matches the southeast movement of the CanERM pattern and the ash cloud reaching the northwest corner of the U.S. on February 22, 2001. For trajectories between 9 and 10 km (Figure 7.15c), the simulations show the ash cloud movement from the beginning of the eruption across the Alaskan interior and follows the southern coastline of Alaska, which agrees well with the satellite data. The effect of the weather system on the movement of the ash cloud becomes apparent when analyzing the 6–8 km and 9–10 km trajectories. All trajectories from the start of the Cleveland eruption don’t fully agree with concentration patterns because the trajectories start only at one instant in time and one vertical location, and they don’t include dispersion. The trajectories from 9–10 km agree with the highest concentration of ash. The trajectories follow the wind field conditions and give a representation of the movement that an

ash particle would have undertaken at those starting conditions.

Figure 7.16 shows the HYSPLIT airborne ash concentration predictions for the February 2001 eruption at Mt. Cleveland. Figure 7.16a at 02:00–03:00 UTC on February 20, 2001 shows the ash cloud moving away from Mt. Cleveland in east-southeast and northeast directions, which agrees well with the early GOES data in Figure 7.13b, the CanERM predictions in Figure 7.14a, and the Puff results in Figure 7.17a, c. By 03:00–04:00 UTC on February 21, the HYSPLIT model simulations (Figure 7.16b) show the ash cloud has moved across the Aleutian Islands as seen in the GOES data but also has a southeasterly movement as simulated by CanERM (Figure 7.14b) and Puff (Figure 7.17b, d). HYSPLIT simulates the highest ash concentration to have been in this southeasterly tail. By 13:00–14:00 UTC on February 22, 2001, the HYSPLIT simulations show a very disperse ash cloud and suggest the ash cloud has drifted to northern California, as also illustrated by the CanERM (Figure 7.14c) and Puff (Figure 7.18) results.

Figure 7.17 shows the ash cloud color-coded by altitude and relative ash concentration, respectively, as simulated by Puff. Puff accurately simulated the first day’s arc of ash drifting to the northeast across Alaska. The model predicted the expansion of the ash cloud to the northwest and southeast that was caused by wind shear at approximately 5 km a.s.l. during the first few hours of the eruption. Puff was able to predict two “waves” of ash that moved across the interior of Alaska, one at low level and one much higher. HYSPLIT and CanERM also have two waves, indicating the level of concentration and matching in geographical location of the Puff simulations. Puff was also able to track the ash that traveled to the southeast, across the Gulf of Alaska, and reached the northwest corner of the contiguous U.S. This agrees with the results of the HYSPLIT and CanERM predictions, but was not detected by the split-window technique due to this portion of the cloud traveling into more cloudy and humid weather conditions when compared with the ash of the “northern” wave, thus showing one of the limitations to the split-window detection technique (Simpson *et al.*, 2002).

After the first 10 h of the eruption, the Puff simulation showed that the ash cloud would have continued to drift to the northeast and that the length of the ash cloud arc would continue to expand to the northwest and southeast (15:00 UTC

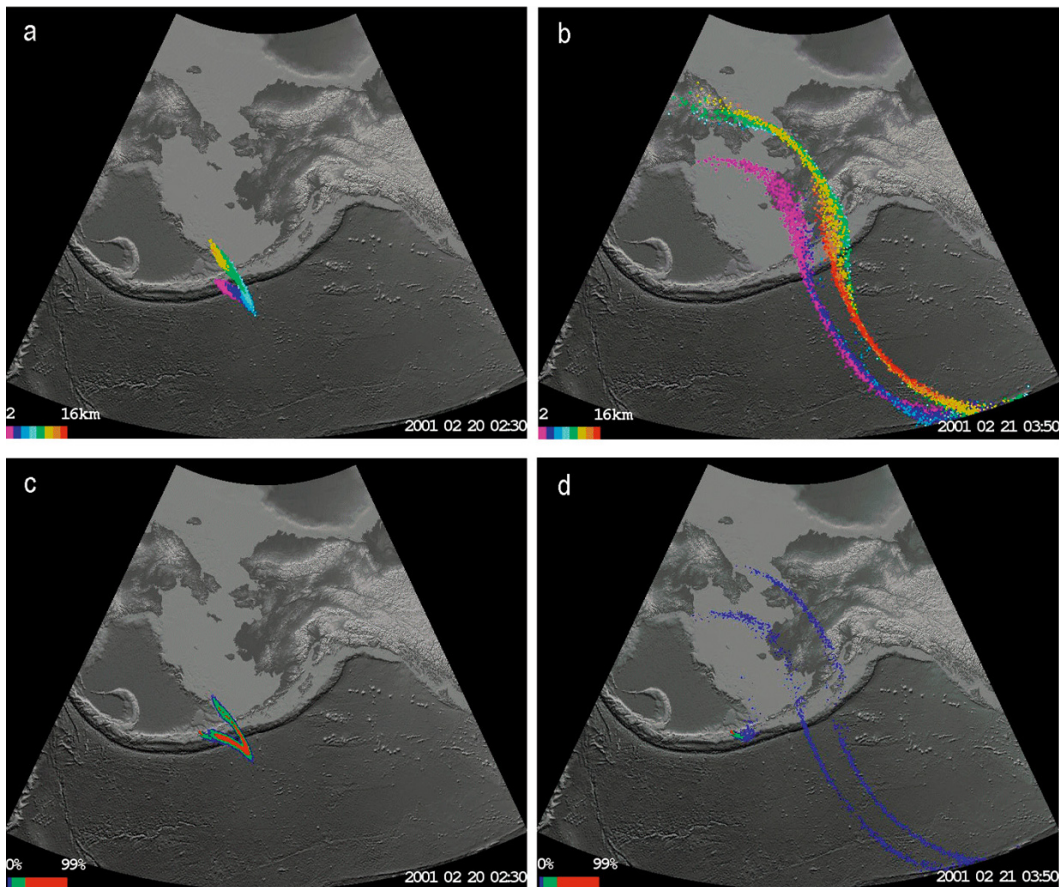


Figure 7.17. Puff model predictions for volcanic ash (colored by altitude) from Mt. Cleveland at 02:30 UTC on February 20 and 03:50 UTC on February 21, 2001 for airborne ash colored by height (a, b) and ash concentrations (c, d), respectively.

on February 20, 2001). Simpson *et al* (2002) state that there was a “probable” ash encounter of a Boeing 747 off the coast of California at 12:00 UTC on February 22, 2001. The prediction results from HYSPLIT, CanERM, and Puff all indicate potential ash at this location and time. Figure 7.18 shows the Puff prediction at 14:00 UTC on February 22 with potential ash off the coast of California, which corresponds with the probable ash encounter. In Figure 7.18, the red stars represent the aircraft reports of ash clouds as well as any potential aircraft–ash encounters, with the potential encounter in California in the bottom right corner of the figure. Simpson *et al* (2002) indicate that there is some debate regarding the reported aircraft elevation (FL300 or 30,000 ft) for the time of exposure,

which is corroborated by CanERM concentration predictions, HYSPLIT concentrations, and the Puff 6 km region for the location and time in question.

All three models similarly predict the dispersion of ash for the Mt. Cleveland February 2001 eruption ash cloud over the Alaskan mainland (as seen in the satellite data) and the ash cloud that traveled southeast from the volcano eventually reaching the northwest corner of the contiguous U.S. Analyses of the southeast portion of the volcanic cloud shown in the model output highlight the usefulness of ash dispersion simulation/prediction models to track ash clouds that exist beyond the detection limits of the split-window technique and those where local environmental and meteorological conditions prevent detection. The VATD models not

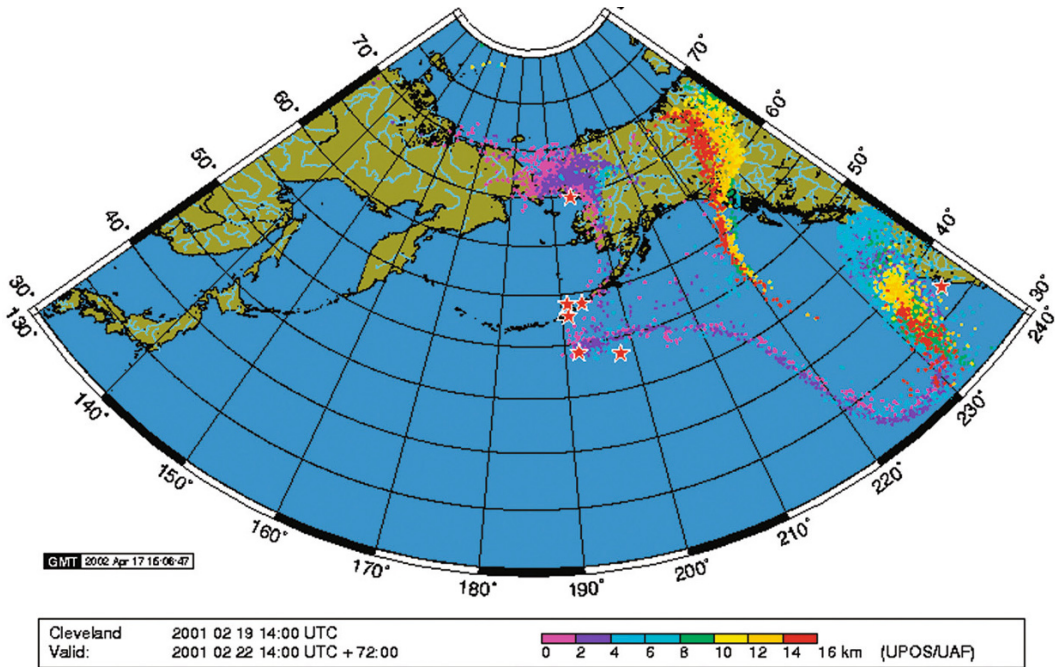


Figure 7.18. Puff model prediction of volcanic ash cloud position at 14:00 UTC on February 22, 2001 from the February 19 event at Mt. Cleveland. The red stars represent aircraft reports of ash clouds as well as any potential aircraft–ash encounters.

only predicted this low-concentration ash cloud but were also able to predict its movement in a very complex wind field (Dean *et al.*, 2004).

7.8.4 Mt. Augustine Volcano: January 2006

The example from Mt. Augustine shows results from the modeling of an eruption that consists of multiple events within a 24 h period. Mt. Augustine (59.37°N, 153.42°W, 1,252 m a.s.l.) and its deposits comprise almost the entire 8 × 11 km volcanic island. It is located in the Lower Cook Inlet of Alaska (Miller *et al.*, 1998) about 290 km southwest of Anchorage. Mt. Augustine is the most active volcano of the eastern Aleutian Arc, with past activity in 1812, 1883, 1935, 1963–1964, 1976, and 1986. Eruptions of Mt. Augustine typically consist of multiple phases spanning several months. During each phase, explosive ash eruptions are often accompanied by mudflows and pyroclastic flows (Miller *et al.*, 1998). The eruption of Mt. Augustine in early 2006 was preceded by increased seismicity in May 2005, dome inflation, and rockfalls later in

the fall of 2005. Approximately 68 earthquakes were detected on November 25, 2005, and by 21:15 UTC on November 29 the AVO alert status had changed to yellow, meaning the volcano is exhibiting signs of elevated unrest above known background levels.

There was a significant thermal anomaly seen in remote-sensing data on January 11, 2006. Soon after, there were two explosive events lasting up to 3 min, the second producing a plume up to 10 km a.s.l. On January 13 and 14, 2006, six explosive events occurred with some lasting up to 11 min. Additional eruptive events occurred on January 17 and January 28, 2006 with some lasting for up to 9 min, producing ash clouds as high as 30,000–40,000 ft or 10–12 km a.s.l. The AVHRR split-window data shows three ash clouds resulting from three explosive events on January 13, 2006 in Figure 7.19. The first ash cloud is to the west of Port Graham and southwest of Homer (Figure 7.19a). Figure 7.19b shows the first ash cloud has moved to the northeast over the Kenai Peninsula while the second cloud has moved to the southwest of Port Graham. Figure 7.19c shows the three ash clouds,

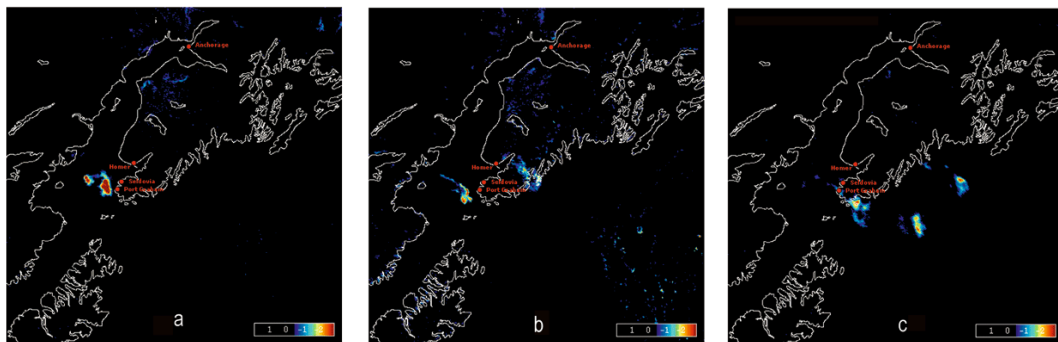


Figure 7.19. AVHRR split-window detection of volcanic ash clouds during January 13, 2006 from the ongoing eruption of Mt. Augustine Volcano: (a) 15:37 UTC; (b) 19:24 UTC; and (c) 22:21 UTC.

with the third one southeast of Port Graham, the second one now moving into the Gulf of Alaska, and the first one moving off to the northeast. Power *et al* (2006) provide a summary of the Augustine eruption.

Figure 7.20 shows the CanERM predictions from each of the three ash clouds on January 13, 2006. HYSPLIT results are shown in Figures 7.21 and 7.22 while the Puff results are shown in Figures 7.23 and 7.24 using the multiple eruption cloud option. CanERM model analysis provides the predictions for each event separately: Figure 7.20a, d, g for the first event, Figure 7.20b, e, h for the second event, and Figure 7.20c, f, i for the third event. These three predictions agree with the Puff and HYSPLIT runs showing the ash clouds moving away from Mt. Augustine to the southeast across the Gulf of Alaska. The CanERM prediction for each event shows the highest concentrations to be at the head of the ash cloud but with moderate to high concentrations behind it.

Figure 7.21 shows the HYSPLIT trajectories for the three events at (a) 13:00 UTC, (b) 18:00 UTC, and (c) 20:00 UTC at starting altitudes of 2, 5, and 10 km using the NCEP FNL data. Figure 7.21 indicates that the ash clouds would move in a southeast direction from the volcano which matches satellite observations. The 5 and 10 km trajectories diverge from each other over time, which illustrates the ash cloud dispersion. The low-level trajectory at 2 km, however, is confined to the Gulf of Alaska. Figure 7.22 shows the HYSPLIT airborne ash concentration simulation for the three events at Mt. Augustine on January 13, 2006. These figures are again scaled using the Washington VAAC “visual ash”

scale. Figure 7.22a at 22:00–23:00 UTC on January 13 agrees with the location of the three ash clouds observed in the AVHRR data in Figure 7.19c and the Puff results shown in Figure 7.24. Figure 7.22b indicates the ash cloud (as predicted by HYSPLIT) became more dispersed (lower concentrations in green for each subsequent image in Figure 7.20) which agrees with the CanERM and Puff predictions for the same time period. By 23:00–00:00 UTC on January 14/15, the HYSPLIT ash concentration simulations show the three ash clouds to have “merged”, an effect also observed in the Puff predictions seen in Figure 7.24b, d, f and the geographical location of the CanERM predictions shown in Figure 7.20.

Puff ash dispersion predictions in Figure 7.23 are shown in three different formats that were available for the AVO remote-sensing group to monitor and track the ash clouds under operational conditions in January 2006. Puff shows similar dispersion to the HYSPLIT trajectories and ash concentrations in Figures 7.21 and 7.22, respectively. Figure 7.23a shows the three ash clouds for 22:20 UTC, which corresponds to the 22:21 UTC AVHRR split-window image in Figure 7.19c. Puff was initialized using information from the onset of significant seismic events, and with an initial 10 km plume a.s.l. Analysis of the Puff prediction for the 8–10 km a.s.l. region suggests the results are in good agreement with the AVHRR data. This allowed an assessment of the relative height of the ash cloud, and a similar height was determined from the satellite data using the cloud temperature method (see Chapter 5) and radiosonde data. Figure 7.23b, c shows the ash concentration in the 8–10 km region

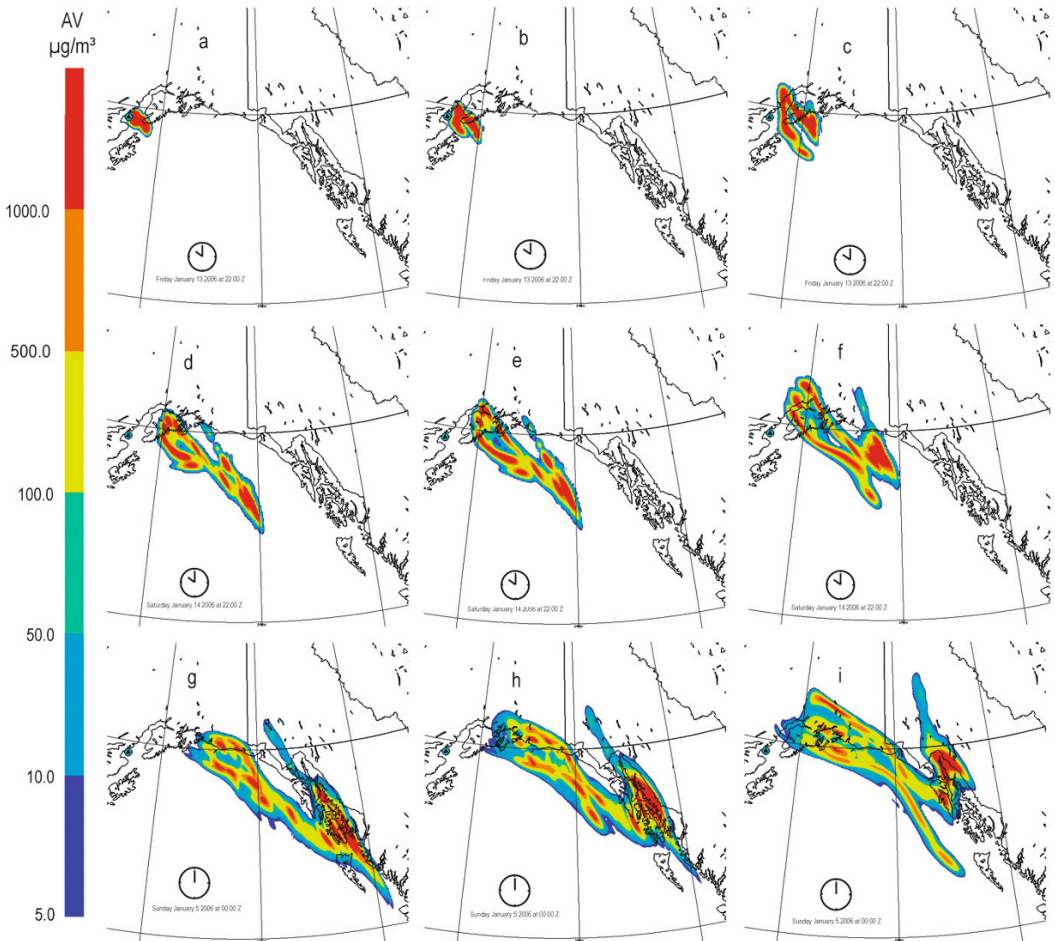


Figure 7.20. CanERM model airborne ash concentration predictions from the Mt. Augustine January 2006 eruption. Displays show the three events separately at (a–c) 22:00 UTC on January 13; (d–f) 10:00 UTC on January 14; and (g–i) 00:00 UTC on January 15, 2006.

of the atmosphere and the airborne ash colored by altitude, respectively. Ground surface topography is also color-coded by elevation.

Figure 7.24a,c,e shows examples of the ash cloud predictions for the six explosive events on January 13 and 14, 2006. The relative position of the low-level (purple and blue), mid-level (greens), and upper-level (yellow and orange) portions of the ash cloud agree well with the HYSPLIT trajectories at 2, 5, and 10 km a.s.l. The most recent event had just occurred and can be seen near the volcano. At 23:30 UTC on January 14, 2006, the ash clouds from the six events move farther east and become more

dispersed resulting in lower ash concentrations (Figure 7.24f). By now, the most recent event's ash cloud has merged into the other ash clouds, all of which show the same morphology. Comparisons of Puff ash cloud predictions with CanERM and HYSPLIT concentrations and trajectories indicate that all three models suggest the high-altitude ash moved across southwest Canada. The mid-altitude ash remains farther south and closer to the Canada/U.S.A. border, while the low-altitude ash remains closer to Alaska and in the Gulf of Alaska. Logically, the ash concentrations are much lower at the end of the model predictions than when the ash

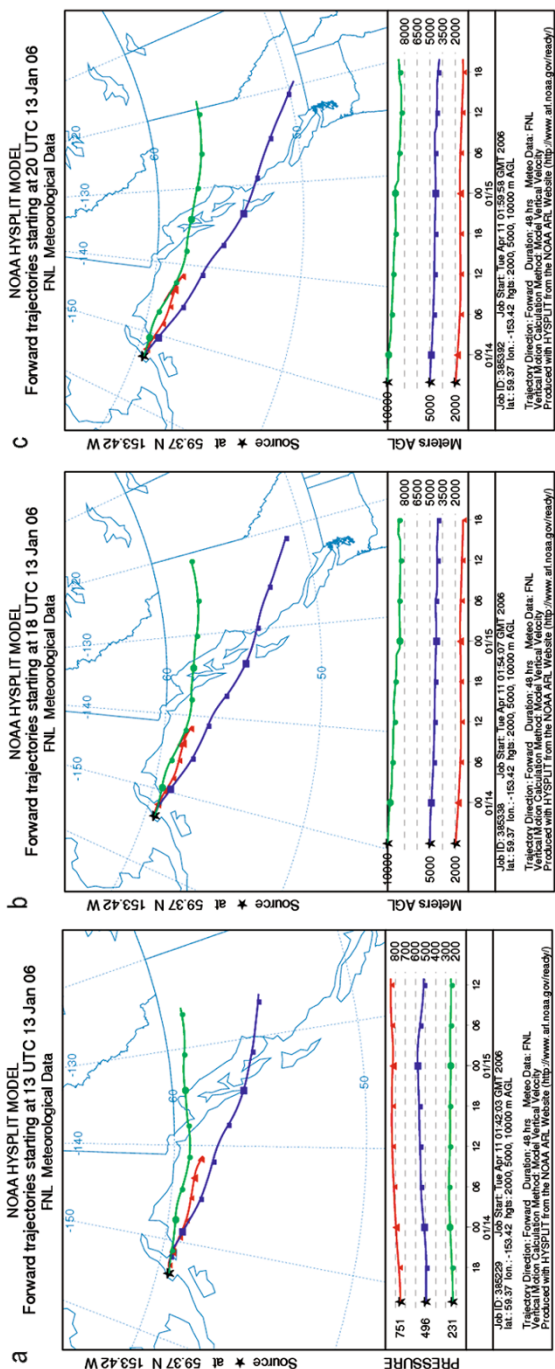


Figure 7.21. HYSPLIT model trajectories of 48 h duration from Mt. Augustine beginning: (a) 13:00 UTC; (b) 18:00 UTC; and (c) 20:00 UTC January 13, 2006.

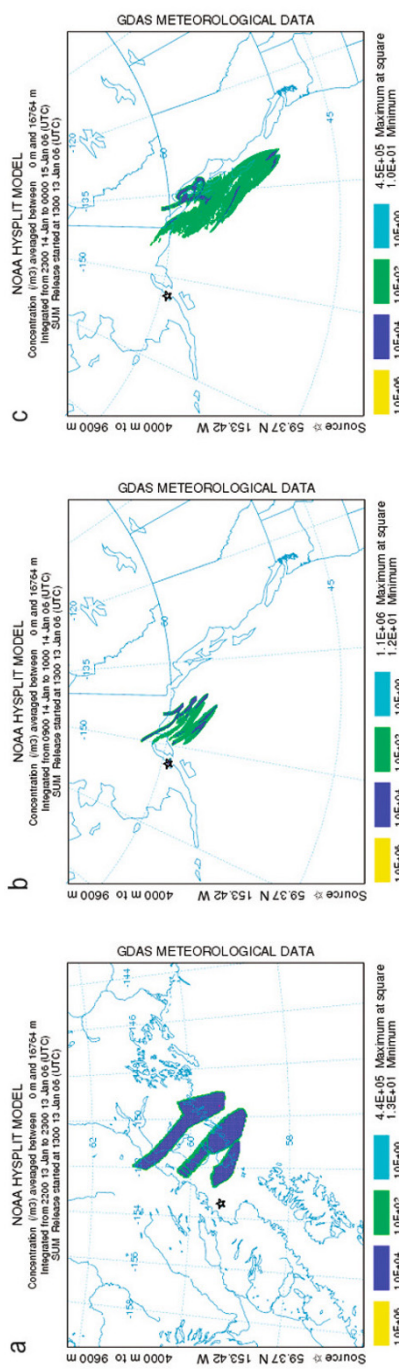


Figure 7.22. HYSPLIT-simulated airborne ash relative concentration from the Mt. Augustine January 2006 eruption: (a) 22:00–23:00 UTC January 13; (b) 09:00–10:00 UTC January 14; and (c) 23:00–00:00 UTC January 14–15, 2006.

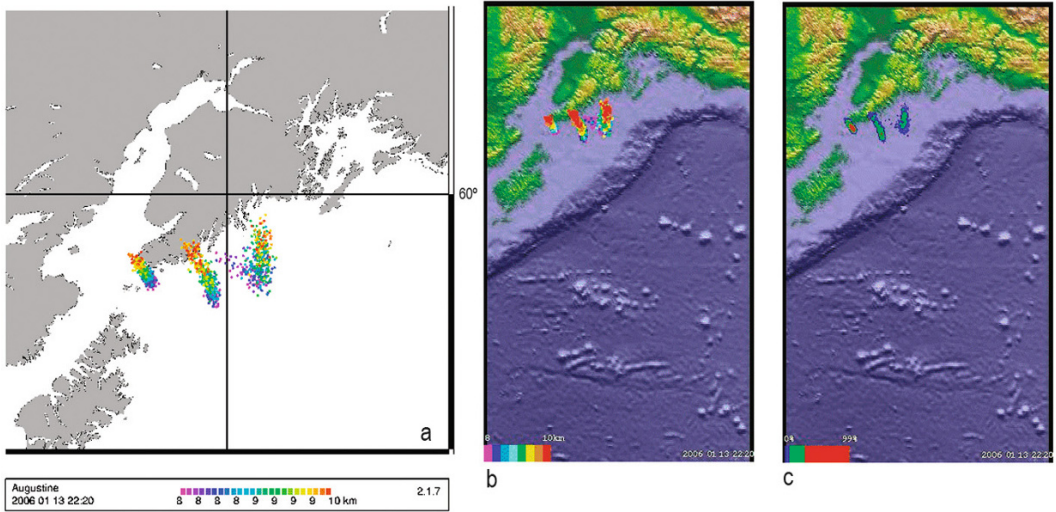


Figure 7.23. Puff model predictions of the three events at 22:20 UTC on January 13, 2006 for the Mt. Augustine Volcano. Panels (a) and (b) show the ash particles color-coded by height but displayed using different map backgrounds. Panel (c) shows particles color-coded by concentration. These model runs are focused on modeling the clouds observed in satellite data.

clouds were closer to the volcano. Ash concentration and location are the two most important factors in making assessments of the hazard to aviation, and assessments need to be made as to the location and as to whether the concentrations are at levels harmful to aircraft.

The Puff, CanERM, and HYSPLIT VATD model results for the Augustine eruption of January 2006 agree well with the location and movement of the ash clouds observed in the remote-sensing data. The three models all provide information of the relative concentrations of the ash cloud. During the operational monitoring of Mt. Augustine by AVO, the combination of remote-sensing data and VATD models provided updates on the location, extent, and movement of the ash clouds as well as ash cloud height estimates. VATD model predictions provided information on projected ash cloud movement, allowing assessments to be made on aircraft trajectories to avoid the ash clouds. During the eruptive events, AVO and NWS (responsible for the Anchorage VAAC) were in constant contact to allow SIGMETs (significant meteorological information) to be released. Such insight from VATD models of the future location of ash clouds allows the assessment of ash cloud potential effect on local populations and local and international air traffic.

7.8.5 Summary of VATD modeling comparison

The CanERM, HYSPLIT, and Puff models were qualitatively compared for simulations of volcanic eruptions at Mt. Spurr, Kliuchevskoi, Mt. Cleveland, and Mt. Augustine Volcanoes. Differences in model output displays are clearly evident but, overall, the results from all three models were in general agreement and compared well with the remote-sensing data available at the time of the eruptions or soon after. The good agreement among the models gives confidence in their simulations, but may also indicate similar deficiencies in the models. The good qualitative agreement between model simulations and satellite analyses suggest the simulations are reasonably accurate. The use of remote-sensing observational data and VATD model output is essential for post-analysis of volcanic ash clouds.

Analyses of the February 2001 Mt. Cleveland eruption discussed in Section 7.8.3 and by Dean *et al.* (2004) show that the VATD models were capable of qualitatively predicting the shape and movement of eruption clouds in a very complex wind field. The detection of the southeast portion of the volcanic cloud showed the usefulness of VATD models to track ash clouds whose concentration may have

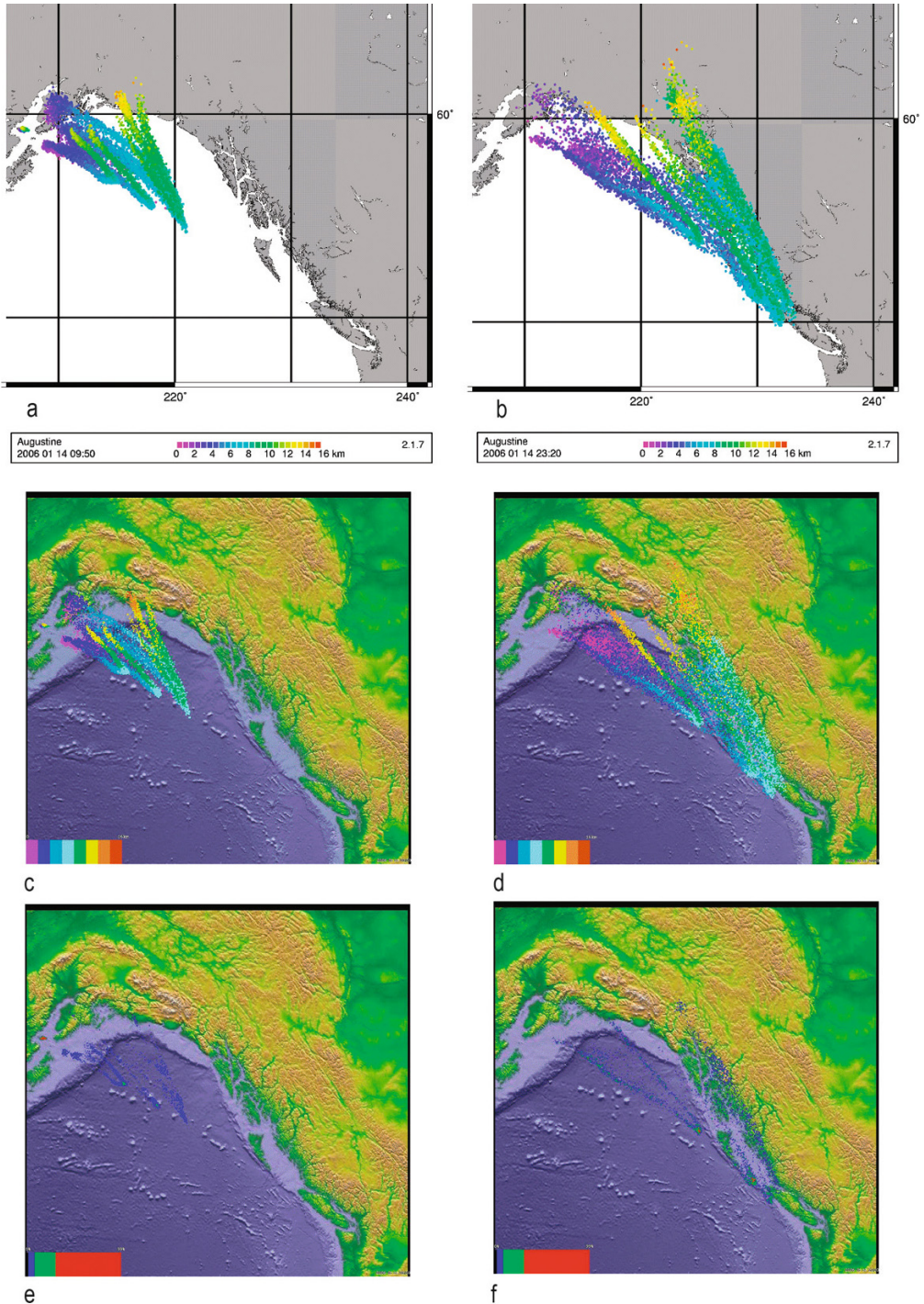


Figure 7.24. Multiple eruptions of six volcanic clouds using Puff for the Mt. Augustine events on January 13–14, 2006 showing the three possible display outputs at 09:50 UTC (a, c, e) and 23:20 UTC (b, d, f) on January 14, 2006.

been below the limits of remote-sensing techniques. Tuning VATD models to match satellite observations may eliminate invalid predictions, but may also remove valid ones. Therefore, satellite observations are still critical in validating overall model predictions. Analysis of the September 1992 Mt. Spurr eruption highlighted in Section 7.8.1 and discussed by Schneider *et al* (1995) points out that this eruption cloud is noteworthy because it traveled as a coherent mass for 5 days after the eruption and disrupted commercial air traffic in Canada and the United States. The October 1994 ash cloud at Kliuchevskoi Volcano (Section 7.8.2) shows how ash can easily reach the main aircraft routes across the North Pacific. Although a volcano's location may be thousands of kilometers from Alaska and the contiguous U.S., it is important for monitoring personnel in the North Pacific to monitor the eruptions at these relatively distant volcanoes for hazard mitigation. Section 7.8.4 illustrates how the Puff model was used operationally in multiple eruption mode for the Mt. Augustine events in January 2006, a feature not available operationally from the other two models at the time.

7.9 AIRBORNE ASH PROBABILITY DISTRIBUTION MAPS

A recent goal at the University of Alaska Fairbanks (UAF) has been to investigate the possibility that VATD models can be used to identify upper-atmospheric regions that may potentially contain high concentrations of airborne ash from volcanic eruptions in the NOPAC region. This work is described in detail in Papp *et al.* (2005). The distribution of airborne ash was analyzed by running daily Puff model eruption simulations at several volcanoes during 1994–1995 and 1997–2001. Each simulation was recorded after 24 h, representing the distribution of airborne ash at that time. Each record contains the latitude, longitude, height, and age of all particles tracked during the simulation. Summing the number of times each horizontal position contained ash for all simulations over the time period analyzed (i.e., winter, October to April, or summer, May to September) produced a two-dimensional grid, with each grid value representing the total number of ash clouds that moved over a 1° latitude/longitude column, in this case separated between the low and high altitudes of 3–8 km and 8–16 km. The seasonal probability distribution percentage was then calculated for each location by

dividing by the total number of (winter or summer) simulations. The X, Y, Z (longitude, latitude, percentage) data are then contoured and mapped using a polar stereographic projection. The resulting conditional probability contours are referred to as airborne ash probability distribution (AAPD) maps and show the likelihood that a given map region will contain ash for a given hypothetical eruption.

Most volcanoes are known to have a unique eruption style that strongly influences the height of an initial eruption column and the frequency that the volcano erupts. To include “realistic” components in ash distribution analyses, these factors were included in the study. The key volcanological criterion utilized was eruption column height because of the significant wind speed variation observed with altitude. One of the products generated from this project includes an AAPD map for the entire NOPAC region, which consists of a summation of simulations from 22 active volcanoes (see Papp *et al.*, 2005 for the list). A weighting factor, based on each volcano's eruption frequency over the last 100 years, was developed in order to more accurately display the regional areas that are most susceptible to volcanic ash input. Although volcanoes may have a repose period much longer than 100 years, accurate information about activity is only available for this shorter period. Eruption frequency was calculated by dividing 100 by the total number of eruption events during 1900–2000, which gives the average value of the elapsed time between eruptions in years per eruption.

The AAPD maps indicate the likelihood that a given map region will contain a volcanic ash cloud emitted by a volcano 24 h after the start of an eruption (Figures 7.25–7.27). The maps are compiled for the winter (October–April), summer (May–September), low altitude (3–8 km) and high altitude (8–12.5 km). In general, the maps show large, circular- to elliptical-shaped contours with, in most cases, the region most susceptible to contain airborne ash located east of the volcano. The shape, extent of the region, and location of areas with the highest probabilities of ash vary for each volcano, season, and altitude. Probability distribution contours for AAPD maps showing individual volcanoes have been quantitatively scaled for comparison. In contrast, regional NOPAC AAPD maps are qualitatively scaled, due to the arbitrary nature of the actual probability values, a result of regional NOPAC maps being a composite of the airborne ash distribution from 22 volcanoes.

7.9.1 Mt. Redoubt, Alaska

The AAPD maps for Mt. Redoubt, Alaska (Figure 7.25) suggest that most of Alaska and north-northwest Canada lie beneath the affected zone, which is centered northeast of the volcano. The contour morphology and extent of this zone are similar for both altitudes and seasons shown. The range of probability distribution values is equally large for both high and low altitudes due to the eruption characteristics of the volcano (Simkin and Siebert, 1994 and Miller *et al.*, 1998). These patterns suggest ash clouds from Mt. Redoubt are capable of reaching as far southeast as the Pacific Northwest in the contiguous United States within a 24 h period, regardless of season or altitude. The most likely upper-atmospheric region to contain airborne ash from Mt. Redoubt after 24 h, however, is over the Alaskan interior, near Fairbanks, the state's second largest city. According to the results, this region has airborne ash probabilities as high as 18% for low

altitudes during winter (Figure 7.25a), which is a result of prevailing southwesterly winds and Mt. Redoubt's eruption characteristics.

7.9.2 Bezymianny Volcano, Kamchatka

The 24 h AAPD maps for Bezymianny Volcano, Kamchatka (Figure 7.26) suggest that the highest airborne ash distribution probabilities (15%) occur over and to the south of the Komandorsky Islands, which are located off the east coast of the central Kamchatka Peninsula between the peninsula and the westernmost Aleutian Islands. According to the results, maximum ash distribution probabilities occur over this region during both summer and winter, a result of prevailing northwesterly winds over the region. The contour morphologies indicate a significant number of ash clouds are capable of drifting to the northwest of the volcano during winter (Figure 7.26a, c), when

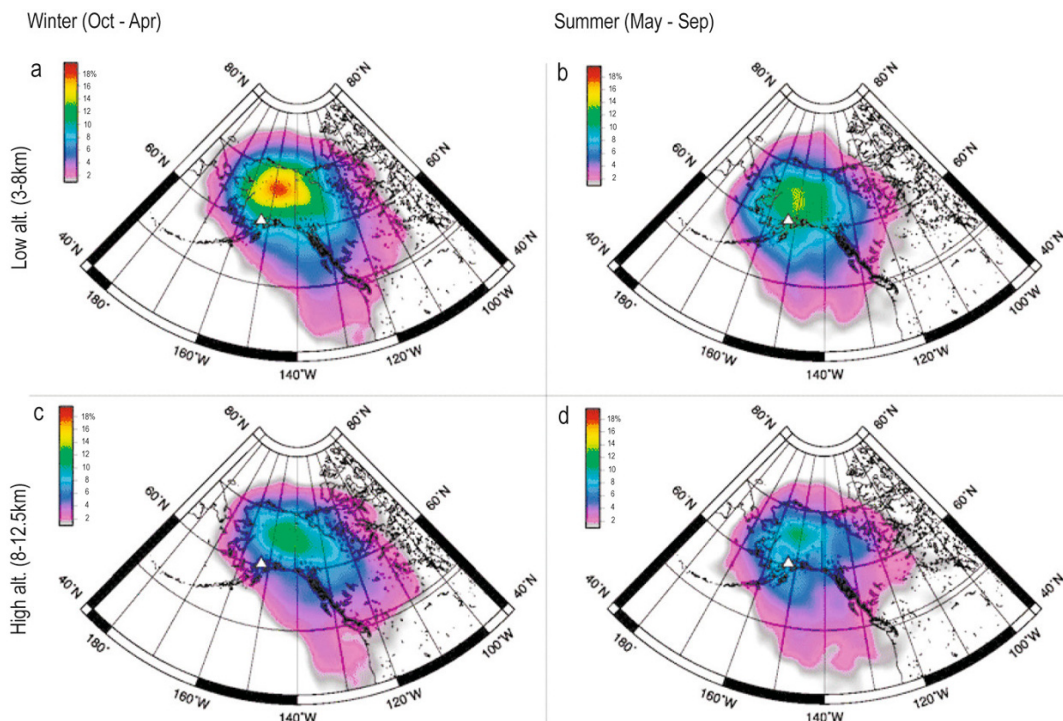


Figure 7.25. Airborne ash probability distribution (AAPD) maps for Mt. Redoubt Volcano, Alaska. The location and magnitude (in %) of these regions is based on cumulative 24 h eruption simulations using the Puff ash dispersion model, 100-year eruption statistics, and wind field data from 1994–1995 and 1997–2001: (a) low-altitude winter; (b) low-altitude summer; (c) high-altitude winter; and (d) high-altitude summer. Volcano shown as white triangle (from Papp *et al.*, 2005).

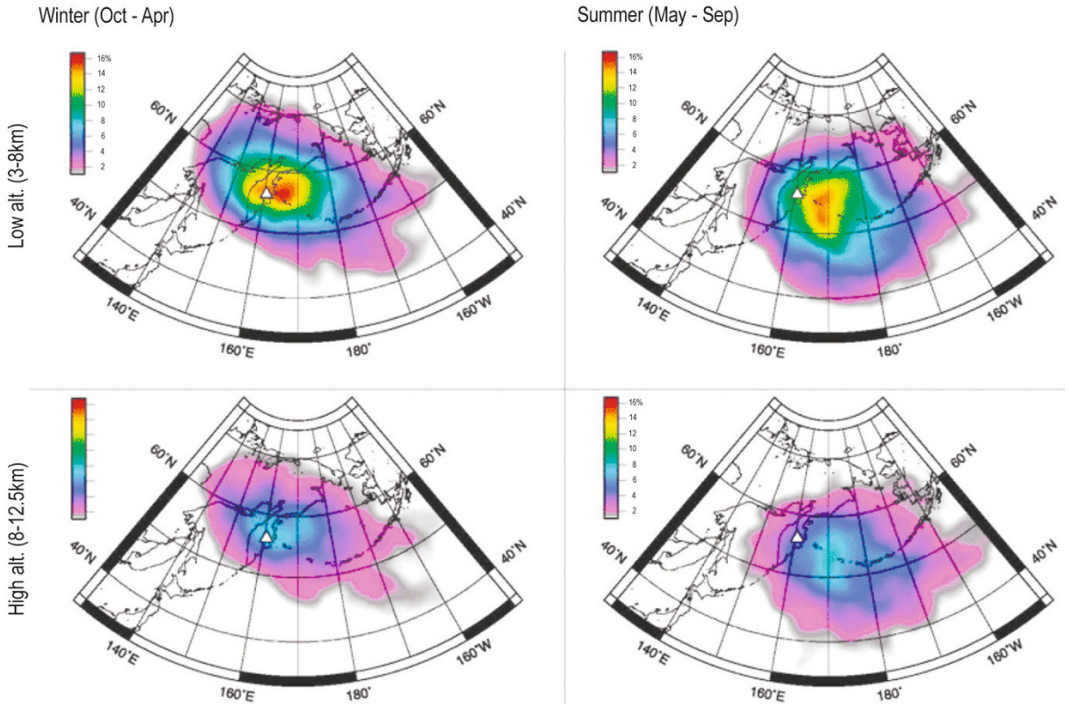


Figure 7.26. Airborne ash probability distribution (AAPD) maps for Bezymianny Volcano, Kamchatka. The location and magnitude (in %) of these regions is based upon cumulative 24 h eruption simulations using the Puff ash dispersion model, 100-year eruption statistics, and wind field data from 1994–1995 and 1997–2001: (a) low-altitude winter; (b) low-altitude summer; (c) high-altitude winter; and (d) high-altitude summer. Volcano shown as white triangle (from Papp *et al.*, 2005).

compared with summer. The affected region is smaller compared with the previous Alaskan AAPD map, implying lower wind speeds over northern Kamchatka.

7.9.3 North Pacific region

The 24 h AAPD maps for the NOPAC region (Figure 7.27) include the cumulative distribution of airborne ash from 22 historically active volcanoes. The low-altitude distributions (Figure 7.27a, b) suggest airborne ash distribution probabilities are highest over (1) the entire Kamchatkan Peninsula and regions east, (2) south central Alaska during winter, and (3) the Alaskan Peninsula during winter and summer, respectively. This is a result of high eruption frequencies for the volcanoes located along the Kamchatkan and Alaskan Peninsulas (i.e., Kliuchevskoi, Karymsky, Bezymianny, Shiveluch, Pavlof, Akutan, and Shishaldin). Only 35% of total

erupted ash clouds in the NOPAC, as calculated here using meteorological data between 1994 and 2001, characteristic eruption height, and other eruption parameters, within the past 100 years reached a height above 8 km. As a result, the high-altitude distribution maps (Figure 7.27c, d) show airborne ash distribution probabilities that are relatively lower when compared with the low-altitude maps. High-altitude distribution probability maxima are concentrated in regions east of the Kamchatkan Peninsula and the central Aleutian Islands.

7.10 RAMIFICATIONS OF AIRBORNE ASH PROBABILITY DISTRIBUTION MAPS

The probabilities shown in AAPD maps are conditional, based on the chosen volcano(es), the number

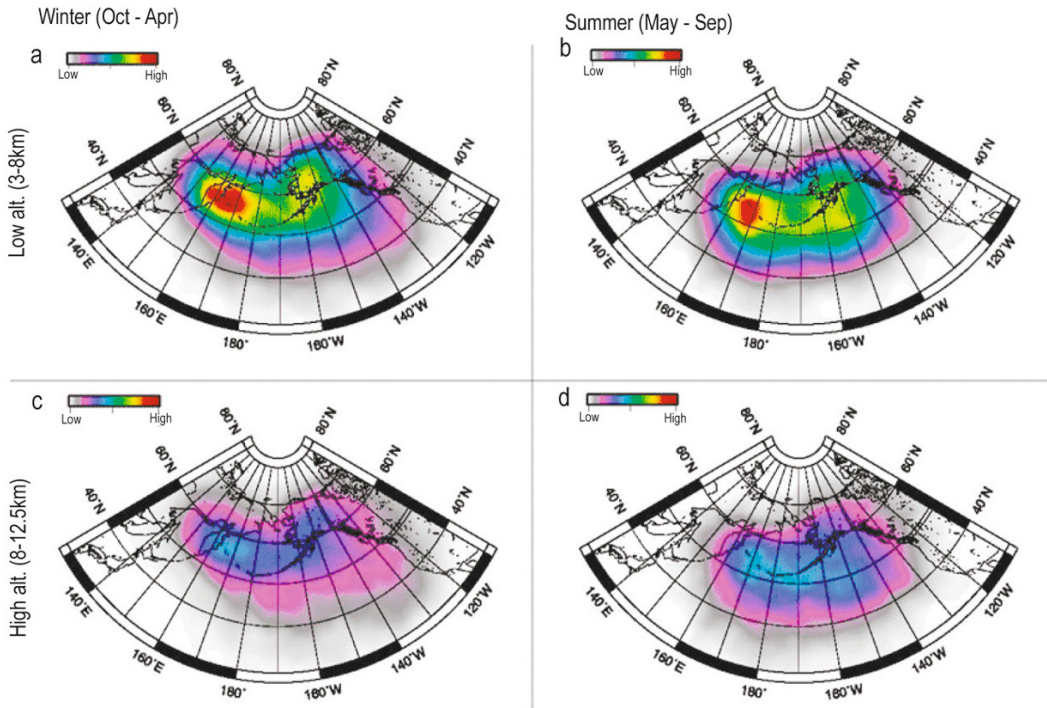


Figure 7.27. Airborne ash probability distribution (AAPD) maps for 22 active volcanoes. The location and magnitude (in %) of these regions is based upon cumulative 24 h eruption simulations from 22 historically active volcanoes using the Puff ash dispersion model, 100-year eruption statistics, and wind field data from 1994–1995 and 1997–2001: (a) low-altitude winter; (b) low-altitude summer; (c) high-altitude winter; and (d) high-altitude summer (from Papp *et al.*, 2005).

of simulations modeled, the eruption characteristics of each of the volcanoes, regional wind characteristics, the initial Puff model parameters chosen (i.e., diffusion coefficient and grain size distribution), and the time after which the distribution is viewed. Quantitative values are shown for single-volcano AAPD maps for logistical reasons only and simply allow comparisons to be made between the seasons, altitude levels, and other volcanoes. The regional AAPD map (Figure 7.27), however, shows a qualitative scale bar, as the map is a cumulative result of 24 h ash cloud simulations from 22 active volcanoes. The number of simulations run to produce the regional map is in the tens of thousands, and therefore a quantitative scale would show very low probability percentages, when compared with single-volcano maps. AAPD maps do not suggest the probability of encountering airborne ash by aircraft. In order to show aircraft encounter probability, the number and frequency of aircraft flying

along each route through the region would have to be known.

The AAPD maps for Mt. Redoubt (Figure 7.25) indicate that after 24 h the upper atmosphere over Fairbanks, Alaska is more susceptible to airborne volcanic ash from an eruption of Mt. Redoubt when compared with other areas. The maps do not indicate the relative probabilities of ash fall, which may be higher at more proximal locations to the volcano (i.e., Anchorage, Alaska). The eruption characteristics, geographic locations, and ash distribution of the volcanoes relative to the North Pacific air traffic routes suggest that eruptions from volcanoes along the Kamchatkan Peninsula are potentially more hazardous to aircraft when compared with other NOPAC volcanoes. The results suggest that low-altitude atmospheric regions (3–8 km a.s.l.) are more susceptible to airborne volcanic ash when compared with regions above 8 km a.s.l. This may be attributed to the

low-level, strombolian-type eruptions characteristic of volcanoes in the North Pacific (Miller *et al.*, 1998, table 2) and the effect of the region's distinct atmospheric profile on eruption column ascent rates (Woods, 1995). The upper-atmospheric region most likely to contain airborne ash, according to the results, is located off the eastern coast of the Kamchatkan Peninsula, and is generally centered over the heavy air traffic flight corridor of the NOPAC. This is due to the fact that 6 of the top 10 most frequently erupting volcanoes in the North Pacific are located in the Kamchatkan Peninsula. The results also indicate that some of the active Alaskan volcanoes are potentially more hazardous to aircraft when compared with other Alaskan volcanoes due to the wind patterns near these volcanoes. Schneider *et al.* (1995), however, have shown that the eruption cloud from an Alaskan volcano is capable of disrupting air traffic well outside the geographic boundaries of the North Pacific. The dangers a volcanic eruption may pose to aircraft may be a function of (1) the height of the eruption, (2) the eruption duration, (3) the grain size distribution, (4) the wind characteristics at the time of the eruption, and (5) the geographic location of the volcano relative to air traffic routes.

The regions most susceptible to airborne volcanic ash in the North Pacific were predicted using the Puff model and gridded meteorological data. The Puff model is not only utilized operationally during an eruption crisis, but can also be used as an effective research tool. The results from this study provide additional airborne ash hazard awareness to airlines and towns/airports within the NOPAC region. The AAPD maps show the extent of ash from a given volcano can encompass all of Alaska, most of the North Pacific Ocean, portions of northwestern North America, regions as far south as 35°N, regions over the western Arctic Ocean, and portions of eastern Russia. The mapping technique shows a very different and more complete picture of ash distribution than a wind-rose diagram. Parameters that were critical in this analysis include height of the initial eruption and volcano eruption frequency. Many NOPAC air traffic routes are located directly over many of the active volcanoes within the region (see Figure 7.4). In addition, the paths of many NOPAC air traffic routes coincide with airborne ash distribution probability maxima suggested by this technique. The results from this work may provide a means to establish more efficient, and less hazardous, air traffic routes and perhaps reveal more logical locations

for new airports and runways. Using similar gridded meteorological data and volcanic VATD models, the techniques utilized herein could be applied to other regions where aircraft along heavily traveled routes may encounter airborne volcanic ash, such as the airspace over Japan, Malaysia, the Philippines, and Papua New Guinea.

7.11 FUTURE ADVANCES IN VATD MODELS

Research and further development of VATD models continues in an effort to create more accurate and timely forecasts. Models must adapt to take advantage of advances in computer hardware and software. Moreover, improvements in satellite analysis techniques combined with improvements in data dissemination and interpretation need to be addressed. This will provide assistance for real-time analysis by operational forecasters and for improvements in analyses for model verification. Improving the physical description of ash dispersion as well as the numerical techniques used is the most direct way to improve model forecasts. A physical description of how ash particles aggregate is an active area of research and has yet to be implemented in most VATD models. Recent research into turbulence effects on particle collisions in clouds (Raymond and Shaw, 2003) appears to have potential applications for ash aggregation. Changes in meteorological models are providing new and improved information relating to humidity and turbulence, which may provide the necessary information for more detailed aggregation models (Textor *et al.*, 2006).

An additional development in VATD models is the prediction of volcanic ash fall, which requires knowledge of the amount of ash in the eruption for quantitative results. However, to be able to accomplish this there is a need for high-resolution meteorological data. The spatial accuracy of VATD forecasts is directly related to the accuracy of the meteorological data. Recently, higher resolution meteorological model data have become available for VATD initialization from NWP models such as the MM5 (Fifth Generation Mesoscale Model) and WRF (Weather Research and Forecast) models. Byrne *et al.* (2007) used MM5 with the sedimentation model of Suzuki (1983) to model the dispersion and fallout from the 1995 eruption of Cerro Negro Volcano in Nicaragua. As an NWP model, WRF is routinely used within the contiguous U.S. at 9.8 km

resolution and the NWS in Alaska uses a grid at 7 km resolution. This higher resolution may not only be a benefit for airborne ash tracking but also improve the operational mapping of ash fall, as demonstrated by Byrne *et al.* (2007). Assessment of a VATD model's ability to accurately predict ash fall requires comparison with isopach maps as well as other dedicated ashfall models, such as ASHFALL described by Hurst and Turner (1999).

The increasingly widespread use of computers from desktops to hand-held devices will probably influence the way people interface with VATD models and their forecast data. While ash forecasts are usually relayed to aircraft pilots via a Volcanic Ash Advisory Center (VAAC) or similar institute, newer planes are being equipped with the ability to access a wide variety of information in near-real time. It is conceivable they may access VATD predictions directly from one or more sources. Greater network connectivity and speed are providing VATD models with a wider range of forecast meteorological models from various sources around the world to be used on locally based computers to improve operational forecasts. Following the success of using ensemble forecasts in meteorology, a similar technique was investigated for VATD models (Stunder and Heffter, 2004). By running a series of model simulations while varying the input parameters slightly, a range of potential outcomes are possible. The sensitivity of VATD models to these slight changes in input parameters is also being quantified. For example, slight changes in diffusivity constants may have a greater influence on the forecast than changes in average particle size, which also helps point to the best direction for further research. A formal sensitivity analysis of VATD models is warranted due to likely nonlinear interactions between different variables.

7.12 REFERENCES

- AMS (2000). *Glossary of Meteorology*, Second Edition, American Meteorological Society, Boston, MA, 850 pp.
- Armenti, P.; Macedonio, G.; Pareschi, M.T. (1988). Air traffic risk evaluation in volcanic ash clouds, *International Journal of Modeling and Simulation*, **8**(1), 29–32.
- Batchelor, G. (1949). Diffusion in a field of homogeneous turbulence, *Australian Journal of Scientific Research*, **A2**, 437–450.
- Batchelor, G. (1950). The application of the similarity theory of turbulence to atmospheric diffusion, *Q. J. Royal Meteorological Society*, **76**, 133–146.
- Bird, R.; Steward, W.; Lightfoot E. (1960). *Transport Phenomena*, John Wiley & Sons, New York.
- Blong, R.J. (1984). *Volcanic Hazards: A Sourcebook on the Effects of Eruptions*, Academic Press, Sydney.
- Bonadonna, C.; Phillips, J.C. (2003). Sedimentation from strong volcanic plumes, *J. Geophys. Res.*, **108**(B7), 2340, doi: 10.1029/2002JB002034.
- Boybeyi, Z. (2000). *Mesoscale Atmospheric Dispersion*, WIT Press, Southampton, U.K., 448 pp.
- Bursik, M. (2001). Effect of wind in the rise of volcanic plumes, *Geophys. Res. Lett.*, **28**(18), 3621–3624, doi: 10.1029/2001GL013393.
- Bursik, M.; Jones, M.; Carn, S.; Dean, K.; Patra, A.; Pavolonis, M.; Pitman, E.B.; Singh, T.; Singla, P.; Webley, P. *et al.* (2012). Estimation and propagation of volcanic source parameter uncertainty in an ash transport and dispersal model: Application to the Eyjafjallajökull plume of 14–16 April 2010, *Bull. Volcanol.*, **74**(10), 2321–2338.
- Byrne, M.A.; Laing, A.G.; Conner C. (2007). Predicting tephra dispersal with a mesoscale atmospheric model and a particle fall model: Application to Cerro Negro Volcano, *J. Appl. Meteorol. Climatol.*, **46**, 121–135.
- Carey, S.N.; Sigurdsson, H. (1982). Influence of particle aggregation on deposition of distal tephra from the May 18, 1980, eruption of Mount St. Helens volcano. *J. Geophys. Res.*, **87**(B8), 7061–7072.
- Casadevall, T.J. (1993). Volcanic hazards and aviation safety: Lessons of the past decade, *FAA Aviation Safety J.*, **2**, 1–11.
- Casadevall, T.J. (1994). The 1989–1990 eruption of Redoubt Volcano Alaska: Impacts on aircraft operations, *J. Volcanol. Geothermal Res.*, **62**(30), 1–316.
- Casadevall, T.J.; Krohn, D. (1995). *Effects of the 1992 Crater Peak Eruptions on Airports and Aviation Operations in the United States and Canada*, USGS Bulletin 2139, U.S. Geological Survey, Reston, VA, pp. 205–220.
- Casadevall, T.J.; Meeker, G.P.; Przedpelski, Z.J. (1991). Volcanic ash ingested by jet engines, *First Int. Symp. on Volcanic Ash and Aviation Safety*, p. 15.
- Chapra, S.C.; Canale, R. (2001). *Numerical Methods for Engineers*, McGraw-Hill, New York.
- Conner, C.; Conner, L.J. (2006). Inversion is the key to dispersion: Understanding eruption dynamics by inverting tephra fallout, in H.M. Mader, S.G. Coles, C.B. Conner, and L.J. Conner (Eds.), *Statistics in Volcanology*, Geological Society, London, pp. 231–242.
- Cornell, W.; Carey, S.; Sigurdsson, H. (1983). Computer simulation of transport and deposition of the Campanian Y-5 ash, *J. Volcanol. Geothermal Res.*, **17**, 89–109.

- D'Amours, R. (1998). Modeling the ETEX plume dispersion with the Canadian Emergency Response Model, *Atmospheric Environment*, **32**, 4335–4341.
- Dean, K.; Dehn, J.; McNutt, S.; Neal, C.; Moore, R.; Schneider, D. (2002). Satellite imagery proves essential for monitoring erupting Aleutian volcano, *EOS, Trans. Am. Geophys. Union*, **83**(22), 241, 246–247.
- Dean, K.G.; Dehn, J.; Papp, K.R.; Smith, S.; Izbekov, P.; Peterson, R.; Kearney, C.; Steffke, A. (2004). Integrated satellite observations of the 2001 eruption of Mt. Cleveland, Alaska, *J. Volcanol. Geothermal Res.*, **135**, 51–73.
- Draxler, R.R. (1999). *HYSPLIT_4 User's Guide*, Tech Memo ERL ARL-230, June, National Oceanic and Atmospheric Administration, Camp Springs, MD, 35 pp.
- Draxler, R.R. (2003). Evaluation of an ensemble dispersion calculation, *J. Appl. Meteorol.*, **42**, 308–317.
- Draxler, R.R.; Hess, G.D. (1997). *Description of the HYSPLIT_4 Modeling System*, Tech Memo ERL ARL-224, December, National Oceanic and Atmospheric Administration, Camp Springs, MD, 24 pp.
- Draxler, R.R.; Hess, G.D. (1998). An overview of the Hysplit_4 modeling system for trajectories, dispersion and deposition, *Australian Meteorological Magazine*, **47**, 295–308.
- Draxler, R.R.; Gillette, D.A.; Kirkpatrick, J.S.; Heller, J. (2001). Estimating PM10 air concentrations from dust storm in Iraq, Kuwait, and Saudi Arabia, *Atmospheric Environment*, **35**, 4315–4330.
- Dunn, M.G.; Baran A.J.; Miatchej J. (1996). Operation of gas turbine engines in volcanic ash clouds, *J. of Engineering for Gas Turbines and Power*, **118**, 724.
- Eichelberger, J.C.; Keith, T.E.C.; Miller, T.P.; Nye, C.J. (1995). The 1992 eruptions of Crater Peak Vent, Mount Spurr volcano, Alaska: Chronology and summary, in T.E.C. Keith (Ed.), *The 1992 Eruptions of Crater Peak Vent, Mount Spurr volcano, Alaska*, USGS Bulletin B 2139, U.S. Geological Survey, Reston, VA, pp. 1–18.
- GVP (1994). *Kliuchevskoi Volcano Activity Monthly Report* (Bull. Global Volc. Network Vol. 19 No. 09), Global Volcanism Program, Smithsonian National Museum of Natural History, Washington, D.C.
- Hadley, D.; Hufford, G.L.; Simpson, J.J. (2004). Resuspension of relic volcanic ash and dust from Katmai: Still an aviation hazard, *Weather and Forecasting*, **19**(5), 829.
- Holasek, R.E.; Self, S. (1995). GOES weather satellite observations and measurements of the May 18, 1980, Mount St. Helens eruption, *J. Geophys. Res.*, **100**(B5), 8469–8487.
- Hurst, A.W.; Turner, R. (1999). Performance of the program ASHFALL for forecasting ashfall during the 1995 and 1996 eruptions of Ruapehu volcano, *N.Z. J. Geology and Geophysics*, **42**, 615–622.
- Keith, T.E.C. (Ed.) (1995). *The 1992 Eruptions of Crater Peak Vent, Mount Spurr Volcano, Alaska*, USGS Bulletin B 2139, U.S. Geological Survey, Reston, VA, 220 pp.
- Kim, J.; Dunn, M.G.; Baran, A.J.; Wade D.P.; Tremba, E.L. (1993). Deposition of volcanic materials in the hot sections of two gas turbine engines, *J. of Engineering for Gas Turbines and Power*, **115**, 641–651.
- Kirianov, V.Y.; Neal, C.A.; Gordeev, E.I.; Miller, R.P. (2002). *The Kamchatkan Volcanic Eruption Response Team (KVERT): Reducing the Risk from Volcano Hazards*, USGS Fact Sheet 064-02, U.S. Geological Survey, Reston, VA, 2 pp.
- Kunii, D.; Levenspiel, O. (1969). *Fluidization Engineering*, John Wiley & Sons, New York.
- Louis, J.F. (1979). A parametric model of vertical eddy fluxes in the atmosphere, *Boundary-Layer Meteorology*, **17**, 187–202.
- Manomaiphiboon, K.; Russell, A.G. (2004). Effects of uncertainties in parameters of a Lagrangian particle model on mean ground-level concentrations under stable conditions, *Atmospheric Environment*, **38**, 5529–5543.
- McGimsey, R.G.; Neal, C.A.; Riley, C.M. (2001). *Areal Distribution, Thickness, Mass, Volume, and Grain Size of Tephra-fall Deposits from the 1992 Eruptions of Crater Peak Vent, Mt. Spurr Volcano, Alaska*, USGS Open-File Report 2001-370, U.S. Geological Survey, Reston, VA, 38 pp.
- Miller, T.P.; Casadevall, T.J. (2000). Volcanic ash hazards to aviation, in H. Sigurdsson (Ed.), *Encyclopedia of Volcanoes*, Academic Press, San Diego, pp. 915–930.
- Miller, T.P.; McGimsey, R.G.; Richter, D.H.; Riehle, J.R.; Nye, C.J.; Yount, M.E.; Dumoulin, J.A. (1998). *Catalog of the Historically Active Volcanoes of Alaska*, USGS Open-File Report 98-0582, U.S. Geological Survey, Reston, VA, 104 pp.
- Oberhuber, J.M.; Herzog, M.; Graf, H.F.; Schwanke, K. (1998). Volcanic plume simulation on large scales, *J. Volcanol. Geothermal Res.*, **87**, 29–53.
- Papp, K.R.; Dean, K.G.; Dehn, J. (2005). Predicting regions susceptible to high concentrations of airborne volcanic ash in the North Pacific region, *J. Volcanol. Geothermal Res.*, **148**, 295–314.
- Power, J.A.; Nye, C.J.; Coombs, M.L.; Wessels, R.L.; Cervelli, P.F.; Dehn, J.; Wallace, K.L.; Freymueller, J.T.; Doukas, M.P. (2006). The reawakening of Alaska's Augustine Volcano, *EOS, Trans. Am. Geophys. Union*, **87**(37), 373, 377.
- Prata, A.J. (1989). Observations of volcanic ash clouds in the 10–12 μm window using AVHRR/2 data, *Int. J. Remote Sensing*, **10**, 751–761.
- Pudykiewicz, J. (1988). Numerical simulation of the transport of radioactive cloud from the Chernobyl nuclear accident, *Tellus*, **40B**, 241–259.

- Pudykiewicz, J. (1989). Simulation of the Chernobyl dispersion with a 3-D hemispheric tracer model, *Tellus*, **41B**, 391–412.
- Raymond, A.; Shaw, R.A. (2003). Particle–turbulence interactions in atmospheric clouds, *Ann. Rev. Fluid Mechanics*, **35**, 183–227.
- Richardson, L. (1926). Atmospheric diffusion on a distance-neighbor graph, *Proc. Royal Society London*, **A110**, 709–737.
- Robert, A. (1982). A semi-Lagrangian and semi-implicit numerical integration scheme for the primitive meteorological equations, *J. Meteorol. Society Japan*, **60**, 319–325.
- Rose, W.I.; Kostinski, A.B.; Kelley, L. (1995). *Real-time C-Band Radar Observations of 1992 Eruption Clouds from Mt. Spurr Volcano, Alaska*, USGS Bulletin 2139, U.S. Geological Survey, Reston, VA, pp. 19–26.
- Sarna-Wojcicki, A.M.; Shipley, S.; Waitt, Jr. R.B.; Dzurisin, D.; Wood, S.H.; Lipman, P.W.; Mullineaux, D.R. (1981). Areal distribution, thickness, mass, volume, and grain size of air-fall ash from the six major eruptions of 1980, in P.W. Lipman and D.R. Mullineaux (Eds.), *The 1980 Eruptions of Mount St. Helens, Washington* (USGS Professional Paper 1250), U.S. Geological Survey, Reston, VA, pp. 577–600.
- Sassen, K.; Zhu, J.; Webley, P.W.; Dean, K.; Cobb, P. (2007). Volcanic ash plume identification using polarization lidar: Augustine eruption, Alaska, *Geophys. Res. Lett.*, **34**(8), doi: 10.1029/2006GL027237.
- Schneider, D.J.; Rose, W.I.; Kelley, L. (1995). *Tracking of 1992 Eruption Clouds from Crater Peak Vent of Mount Spurr Volcano, Alaska, Using AVHRR*, USGS Bulletin 2139, U.S. Geological Survey, Reston, VA, pp. 27–36.
- Schumacher, R. (1994). A reappraisal of Mount St Helens ash clusters: Depositional model from experimental observation, *J. Volcanol. Geothermal. Res.*, **59**(3), 253–260.
- Searcy, C.; Dean, K.G.; Stringer, W. (1998). PUFF: A volcanic ash tracking and prediction model, *J. Volcanol. Geothermal Res.*, **80**, 1–16.
- Self, S.; Zhao, Jing-Xia; Holasek, R.E.; Torres, R.C.; King, A.J. (1996). The atmospheric impact of the 1991 Mount Pinatubo eruption, in C.G. Newhall and R.S. Punongbayan (Eds.), *Fire and Mud: Eruptions and Lahars of Mount Pinatubo, Philippines*, Philippine Institute of Volcanology and Seismology, Quezon City, Philippines/University of Washington Press, Seattle, WA, pp. 1089–1115.
- Servranckx, R.; Chen, P. (2004). Modeling volcanic ash transport and dispersion: Expectations and reality, *Proc. Second Int. Conf. on Volcanic Ash and Aviation Safety, June 21–24, 2004, Alexandria, VA*.
- Servranckx, R.; D'Amours, R.; Jean, M.; Toviss, J.-P.; Trudel, S. (1996). Volcanic ash forecasting at the Canadian Meteorological Centre, paper presented at *Pan Pacific Hazards '96, July 29–August 2, 1996*, Environmental Emergency Response Division, Environment Canada, Vancouver, BC.
- Simkin, T.; Siebert, L. (1994). *Volcanoes of the World*, Global Volcanism Program, Smithsonian Institution, Washington, D.C./Geoscience Press, Tucson, AZ.
- Simpson, J.J.; Hufford, G.L.; Pieri, D.; Servranckx, R.; Berg, J.; Bauer, C. (2002). The February 2001 eruption of Mount Cleveland, Alaska: Case study of an aviation hazard, *Weather and Forecasting*, **17**(4), 691–704.
- Simpson, J.J.; Hufford, G.L.; Servranckx, R.; Berg, J.; Pieri, D. (2003). Airborne Asian dust: Case study of long-range transport and implications for the detection of volcanic ash, *Weather and Forecasting*, **18**(2), 121–141.
- Slade, D. (1968). *Meteorology and Atomic Energy*, U.S. Department of Commerce, Springfield, VA.
- Sparks, R.S.J.; Bursik, M.I.; Carey, S.N.; Gilbert, J.S.; Glaze, L.S.; Sigurdsson, H.; Woods, A.W. (1997). *Volcanic Plumes*, John Wiley & Sons, Chichester, U.K., 574 pp.
- Stunder, B.; Heffter, J. (2004). Volcanic ash dispersion modeling research at NOAA Air Resources Laboratory, *Proc. Second Int. Conf. Volcanic Ash and Aviation Safety, Alexandria, VA*.
- Stunder, B.J.B.; Heffter, J.L.; Draxler R.R. (2007). Airborne volcanic ash forecast area reliability, *Weather and Forecasting*, **22**, 1132–1139.
- Suzuki, T. (1983). A theoretical model for dispersion of tephra, in D. Shimozuru and I. Yokoyama (Eds.), *Arc Volcanism: Physics and Tectonics*, Terra Scientific, Tokyo, pp. 95–113.
- Tanaka, H.L.; Kanetaka, M. (2004). Real time prediction system of forest-fire smoke using satellite data and the PUFF Model, *Proc. Fifth Int. Workshop on Global Change: Connection to the Arctic, November 15–16, 2004, Tsukuba, Japan*, pp. 103–106.
- Textor, C.; Graf, H.F.; Herzog, M.; Oberhuber, J.M.; Rose, W.I.; Ernst, G.G.J. (2006). Volcanic particle aggregation in explosive eruption columns. Part I: Parameterization of the microphysics of hydrometeors and ash, *J. Volcanol. Geothermal Res.*, **150**, 359–377.
- Tupper, A.; Davey, J.; Stewart, P.; Stunder, B.; Servranckx, R.; Prata, F. (2006). Aircraft encounters with volcanic clouds over Micronesia, Oceania, 2002–03, *Australian Meteorological Magazine*, **55**, 289–299.
- Tupper, A.; Itikarai, I.; Richards, M.; Prata, F.; Carn, S.; Rosenfield, D. (2007). Facing the challenges of the International Airways Volcano Watch: The 2004/2005 eruptions of Manam, Papua New Guinea, *Weather and Forecasting*, **22**, 175–191.

- Webley, P.W.; Dean K.; Collins, R.; Fochesatto, J.; Sassen, K.; Atkinson, D.; Cahill, C.; Prata, A. (2008). Validation of a volcanic ash dispersion model during late January/early February 2006 eruption of Mount Augustine Volcano, *Bull. Amer. Meteorol. Society*, 1647–1658, doi: 10.1175/2008BAMS2579.1.
- Wen, S.; Rose, W.I. (1994). Retrieval of particle sizes and masses in volcanic clouds using AVHRR bands 4 and 5, *J. Geophys. Res.*, **99**, 5421–5431.
- Wilks, D.S. (2006). *2006 Statistical Methods in the Atmospheric Sciences*, Second Edition (International Geophysics Series), Academic Press, St. Louis, MO, 627 pp.
- Wilson, L.; Huang, T.C. (1979). The influence of shape on the atmospheric settling velocity of volcanic ash particles, *Earth Planet Science Lett.*, **44**, 311–324.
- Woods, A.W. (1995). The dynamics of explosive volcanic eruptions, *Rev. Geophysics*, **33**, 495–530.

Interferometric synthetic aperture radar (InSAR): A long-term monitoring tool

Zhong Lu, Daniel Dzurisin, Charles Wicks Jr., John Power

8.1 PRINCIPLES OF INTERFEROMETRIC SYNTHETIC APERTURE RADAR

8.1.1 Introduction

Interferometric synthetic aperture radar (InSAR) imaging is a growing remote-sensing technique. The term “interferometry” draws its meaning from two root words: interfere and measure. The interaction of electromagnetic waves, referred to as interference, is used to precisely measure distances and angles. The interference of electromagnetic waves that are transmitted and received by a synthetic aperture radar (SAR), an advanced imaging radar instrument, is called interferometric SAR (InSAR). Very simply, InSAR involves the use of two or more SAR images of the same area to extract the land surface topography and its deformation patterns.

InSAR is formed by interfering signals from two spatially or temporally separated antennas. The spatial separation of the two antennas is called the baseline. The two antennas may be mounted on a single platform for simultaneous interferometry, the usual implementation for aircraft and spaceborne systems such as the Topography SAR (TOPSAR) and Shuttle Radar Topography Mission (SRTM) systems (Zebker *et al.*, 1992; Farr and Kobrick, 2000). Alternatively, InSAR can be created by utilizing a single antenna on an airborne or spaceborne platform in nearly identical repeating orbits for repeat pass interferometry (Gray and Farris-Manning, 1993; Massonnet and Feigl,

1998). For the latter case, even though the antennas do not illuminate the same area at the same time, the two sets of signals recorded during the two passes will be highly correlated if the scattering properties of the ground surface are undisturbed between viewings. This is the typical implementation for spaceborne sensors such as the U.S. Seasat, European Remote-sensing Satellites (ERS-1 and ERS-2), Shuttle Imaging Radar-C/L (SIR-C/L), Canadian Radar Satellite (Radarsat-1), Japanese Earth Resources Satellite (JERS-1), European Environmental Satellite (Envisat), all of which operate at wavelengths ranging from a few centimeters (C-band) to tens of centimeters (L-band) (Table 8.1). It is this configuration that makes InSAR capable of measuring ground surface deformation with centimeter to subcentimeter precision at a spatial resolution of tens of meters over a relatively large region ($\sim 10^4$ km²).

The capability of measuring land surface deformation using repeat pass InSAR data was first demonstrated by Gabriel *et al.* (1989). However, it was not until 1993 when Massonnet *et al.* (1993) detected earthquake displacements from ERS-1 InSAR data that the science community enthusiastically began to embrace InSAR technology. Two years later, Massonnet *et al.* (1995) also were the first to apply ERS-1 InSAR imagery to map the volcanic deformation associated with the eruption of Mt. Etna. Today, scientists use InSAR data to study volcanoes worldwide (Lu and Dzurisin, 2014). In this chapter, we review the InSAR technique, illustrate how it works, and discuss

Table 8.1. Spaceborne SAR sensors capable of deformation mapping.

<i>Mission</i>	<i>Agency</i>	<i>Period of operation^a</i>	<i>Orbit repeat cycle</i>	<i>Frequency</i>	<i>Wavelength</i> (cm)	<i>Incidence angle at swath center</i> (°)	<i>Resolution</i> (m)
Seasat	NASA ^b	06/27–10/10, 1978	17 days	L-band 1.2 GHz	25	20–26	25
ERS-1	ESA ^c	07/1991 to 03/2000	3, 168, and 35 days ^d	C-band 5.3 GHz	5.66	23	30
SIR-C/ X-SAR	NASA, DLR, ^e and ASI ^f	04/09–04/20, 1994, and 09/30 to 10/11, 1994	6-month, 1-, 2-, 3-day ^g	L-band 1.249 GHz C-band 5.298 GHz X-band 9.6 GHz	24.0 5.66 3.1	17–63 (L- and C-band) 54 (X-band)	10–200 (30 typical)
JERS-1	JAXA ^h	02/1992 to 10/1998	44 days	L-band 1.275 GHz	23.5	39	20
ERS-2	ESA	04/1995 to 05/2011	35 days	C-band 5.3 GHz	5.66	23	30
Radarsat-1	CSA ⁱ	11/1995 to 03/2013	24 days	C-band 5.3 GHz	5.66	10–59	10–100
Radarsat-2	CSA	12/2007 to present					
Envisat	ESA	03/2002 to present	35 days	C-band 5.331 GHz	5.63	14–45	20–100
ALOS	JAXA	01/2006 to 05/2011	46 days	L-band 1.270 GHz	23.6	8–60	10–100

^a Information was current in December 2013.

^b National Aeronautics and Space Agency.

^c European Space Agency.

^d To accomplish various mission objectives, the ERS-1 repeat cycle was 3 days from July 25, 1991 to April 1, 1992 and from December 23, 1993 to April 9, 1994; 168 days from April 10, 1994 to March 20, 1995; and 35 days at other times.

^e German Space Agency.

^f Italian Space Agency.

^g During days 3–4 of the second mission, SIR-C/X was commanded to retrace the flight path of the first mission to acquire repeat pass InSAR data with a 6-month time separation. From day 7 to the end of the second flight, the shuttle was commanded to repeat the flight path of the previous days to acquire 1, 2, and 3-day repeat pass InSAR data.

^h Japan Aerospace Exploration Agency.

ⁱ Canadian Space Agency.

issues on InSAR deformation mapping. We then present a few examples to illustrate the use of InSAR to study Alaskan volcanoes.

8.1.2 Basics of interferometric SAR (InSAR)

A SAR transmits electromagnetic waves at a wavelength ranging from a few millimeters to a few meters. The radar wave propagates through the

atmosphere and interacts with the Earth surface. Part of the energy is returned back to and recorded by the SAR. Using a sophisticated image-processing technique, called SAR processing (Curlander and McDonough, 1991; Bamler and Hartl, 1998; Henderson and Lewis, 1998), both the intensity and phase of the reflected (or backscattered) signal of each ground resolution element (a few meters to tens of meters) can be calculated in the form of a complex-valued SAR image representing the reflec-

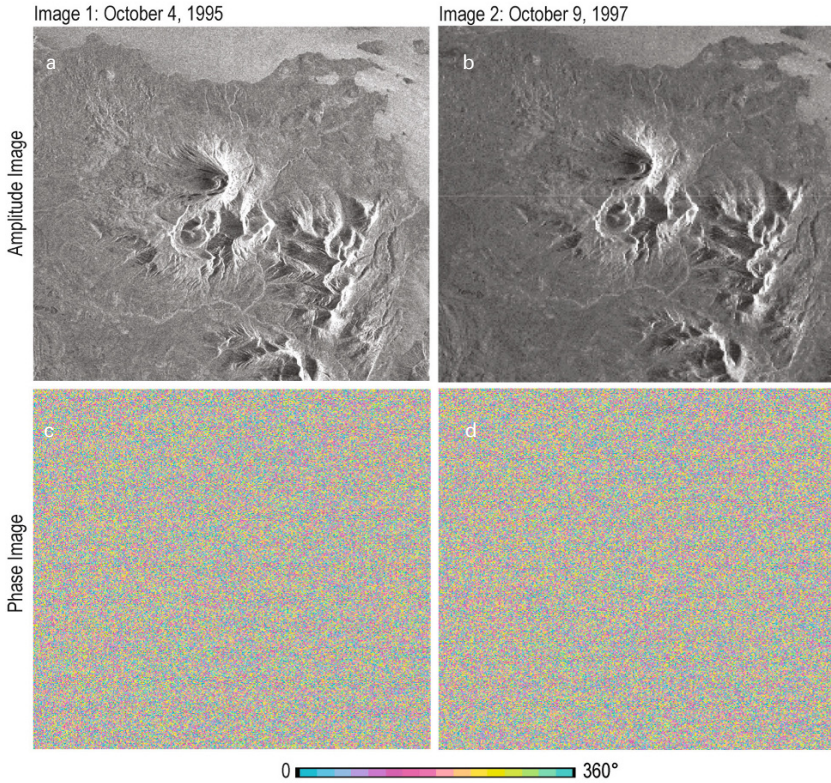


Figure 8.1. Two SLC SAR images acquired on October 4, 1995 by the ERS-1 satellite and on October 9, 1997 by the ERS-2 satellite over the Mt. Peulik Volcano, Alaska. The amplitude and phase of each SAR image are shown separately. The amplitude of a SAR image is primarily controlled by terrain slope, surface roughness, and dielectric constants whereas the phase value of each pixel is related to the apparent distance from the satellite to the ground target.

tivity of the ground surface. The amplitude or intensity of the SAR image (Figure 8.1a) is primarily controlled by terrain slope, surface roughness, and dielectric constants, whereas the phase of the SAR image (Figure 8.1b) is primarily controlled by the distance from the satellite antenna to ground targets, the variable rate of propagation through the atmosphere (or delay), and the interaction of electromagnetic waves with the ground surface (Figure 8.1).

Generation of an interferogram requires two single-look complex (SLC) SAR images. Neglecting phase shifts induced by the transmitting/receiving antenna and SAR-processing algorithms, the phase value of a pixel in an SLC SAR image (Figure 8.1b) can be represented as

$$\phi_1 = -\frac{4\pi}{\lambda} r_1 + \varepsilon_1 \quad (8.1)$$

where r_1 is the apparent range distance (including possible atmospheric delay) from the antenna to the ground target; λ is the wavelength of radar; and ε_1 is the sum of phase shift due to the interaction between the incident radar wave and scatterers within the resolution cell. Because the backscattering phase (ε_1) is a randomly distributed (unknown) variable, the phase value (ϕ_1) in a single SAR image cannot be used to calculate the range (r_1) and is of no practical use. However, a second SLC SAR image (Figure 8.1c,d) could be obtained over the same area at a different time with a phase value of

$$\phi_2 = -\frac{4\pi}{\lambda} r_2 + \varepsilon_2 \quad (8.2)$$

Note that phase values in the second SAR image cannot provide range information (r_2) either.

An interferogram is created by co-registering two SAR images and differencing the correspond-

ing phase values of the two SAR images on a pixel-by-pixel basis (Figure 8.2). The phase value of the resulting interferogram is

$$\phi = \phi_1 - \phi_2 = -\frac{4\pi(r_1 - r_2)}{\lambda} + (\varepsilon_1 - \varepsilon_2) \quad (8.3)$$

The fundamental assumption in repeat pass InSAR is that the scattering characteristics of the ground surface remain undisturbed. The degree of change in backscattering characteristics can be quantified by interferometric coherence, which is discussed further in Section 8.1.4.1. Assuming that the interactions between the radar waves and scatterers remain the same when the two SAR images were acquired (i.e., $\varepsilon_1 = \varepsilon_2$), the interferometric phase value can be expressed

$$\phi = -\frac{4\pi(r_1 - r_2)}{\lambda} \quad (8.4)$$

Nominal values for the range difference ($r_1 - r_2$) extend from a few meters to several hundred meters. The SAR wavelength (λ) is of the order of several centimeters. Because the measured interferometric phase value (ϕ) ranges from $-\pi$ to π , there is an ambiguity of many cycles (i.e., numerous 2π values) in the interferometric phase value. Therefore, the phase value of a single pixel in an interferogram is of no practical use. However, the change in range difference $\delta(r_1 - r_2)$ between two neighboring pixels that are a few meters apart is normally much smaller than the SAR wavelength.

So the phase difference between two nearby pixels, $\delta\phi$, can be used to infer the range distance difference ($r_1 - r_2$) to subwavelength precision. This explains how InSAR uses the phase difference to infer the change in range distance to an accuracy of centimeters or millimeters.

The phase (or range distance difference) in the interferogram represented by Equation (8.4) and exemplified by Figure 8.2 contains contributions from both the topography and any possible ground surface deformation. Therefore, the topographic contribution needs to be removed to derive a deformation map. The most common procedure is to use an existing digital elevation model (DEM) and the InSAR imaging geometry to produce a synthetic interferogram and subtract it from the interferogram to be studied (Massonnet and Feigl, 1998; Rosen *et al.*, 2000). This is the so-called two-pass InSAR. Alternatively, the synthetic interferogram that represents topographic contribution can come from a different interferogram of the same area. The procedures are then called three-pass or four-pass InSAR (Zebker *et al.*, 1994). We now briefly explain how to simulate the topographic effect based on an existing DEM to derive a deformation map in two-pass InSAR.

Two steps are required to simulate a topography-only interferogram based on a DEM. First, the DEM needs to be resampled to project heights from a map coordinate into the appropriate radar geometry via geometric simulation of the imaging

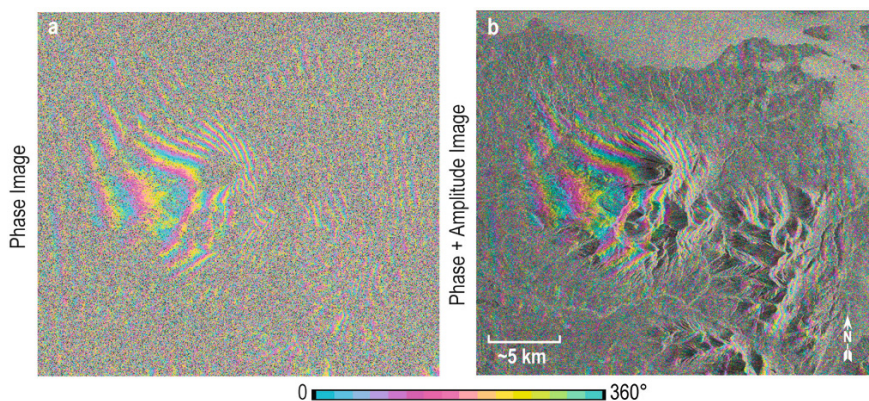


Figure 8.2. An interferogram is formed by differencing the phase values of two SAR images (Figure 8.1b, d) that have been co-registered. The resulting interferogram contains fringes produced by the differing viewing geometries, topography, any atmospheric delays, and surface deformation. The perpendicular component of the baseline is 35 m. Each interferometric fringe (full-color cycle) represents 360° of phase change (or 2.83 cm of range change between the ground and the satellite). The color change from red to yellow, blue, and red in a fringe represents a relative increase in satellite-to-ground distance or an away-from-satellite ground motion.

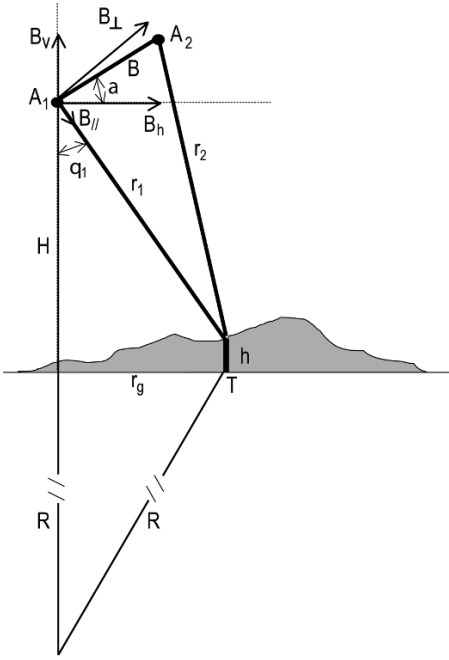


Figure 8.3. InSAR imaging geometry. The InSAR system acquires two images of the same scene with SARs located at A_1 and A_2 . The spatial distance between A_1 and A_2 is called the baseline, which has length B , and is tilted with respect to the horizontal by α . The baseline B can be expressed by a pair of horizontal (B_h) and vertical (B_v) components, or a pair of parallel (B_{\parallel}) and perpendicular (B_{\perp}) components. The range distances from the SARs to a ground target T with elevation h are r_1 and r_2 , respectively. The look angle from A_1 to the ground point T is θ_1 .

process. The InSAR imaging geometry is shown in Figure 8.3. The InSAR system acquires two images of the same scene with SAR platforms located at A_1 and A_2 . The baseline, defined as the vector from A_1 to A_2 , has a length B and is tilted with respect to the horizontal by an angle α . The slant range r from the SAR to a ground target T with an elevation value h is linearly related to the measured phase values in the SAR images by Equations (8.1) and (8.2). The look angle from A_1 to the ground point T is θ_1 . For each ground resolution cell at ground range r_g with elevation h , the slant range value (r_1) should satisfy (Joughin, 1995)

$$r_1 = \sqrt{(H+R)^2 + (R+h)^2 - 2(H+R)(R+h) \cos\left(\frac{r_g}{R}\right)} \quad (8.5)$$

where H is the satellite altitude above a reference Earth surface which is assumed to be a sphere with a radius R . The radar slant range and azimuth coordinates are calculated for each point in the DEM. This set of coordinates forms a nonuniformly sampled grid in the SAR coordinate space. The DEM height data are then resampled into a uniform grid in the radar coordinates using the values over the nonuniform grid.

Second, the precise look angle from A_1 to ground target T at ground range r_g , slant range r_1 , and elevation h is calculated:

$$\theta_1 = \arccos\left[\frac{(H+R)^2 + r_1^2 - (R+h)^2}{2(H+R)r_1}\right] \quad (8.6)$$

By knowing θ_1 , the interferometric phase value due to the topographic effect at target T can be calculated,

$$\begin{aligned} \phi_{\text{dem}} &= -\frac{4\pi}{\lambda}(r_1 - r_2) \\ &= \frac{4\pi}{\lambda}(\sqrt{r_1^2 - 2(B_h \sin \theta_1 - B_v \cos \theta_1)r_1 + B^2} - r_1) \end{aligned} \quad (8.7)$$

where B_h and B_v are horizontal and vertical components of the baseline B (Figure 8.3).

Figure 8.4 shows the simulated topographic effect in the original interferogram (Figure 8.2), using an existing DEM and the InSAR imaging geometry for the interferometric pair (Figure 8.2). Removing the topographic effects (Figure 8.4a, b) from the original one (Figure 8.2) results in an interferogram containing the ground surface deformation during the time duration and the measurement noise (Figure 8.4c, d), with the phase value given as

$$\phi_{\text{def}} = \phi - \phi_{\text{dem}} \quad (8.8)$$

In practice, an ellipsoidal Earth surface, characterized by its major axis, e_{maj} , and minor axis, e_{min} , is used to replace the spherical Earth. The radius of the Earth over the imaged area is then

$$R = \sqrt{(e_{\text{min}} \sin \beta)^2 + (e_{\text{maj}} \cos \beta)^2} \quad (8.9)$$

where β is the latitude of the center of the imaged region.

If h is taken as zero, the procedure outlined in Equations (8.5)–(8.9) will remove the effect of an ellipsoidal Earth surface on the interferogram. This results in a flattened interferogram, whose phase

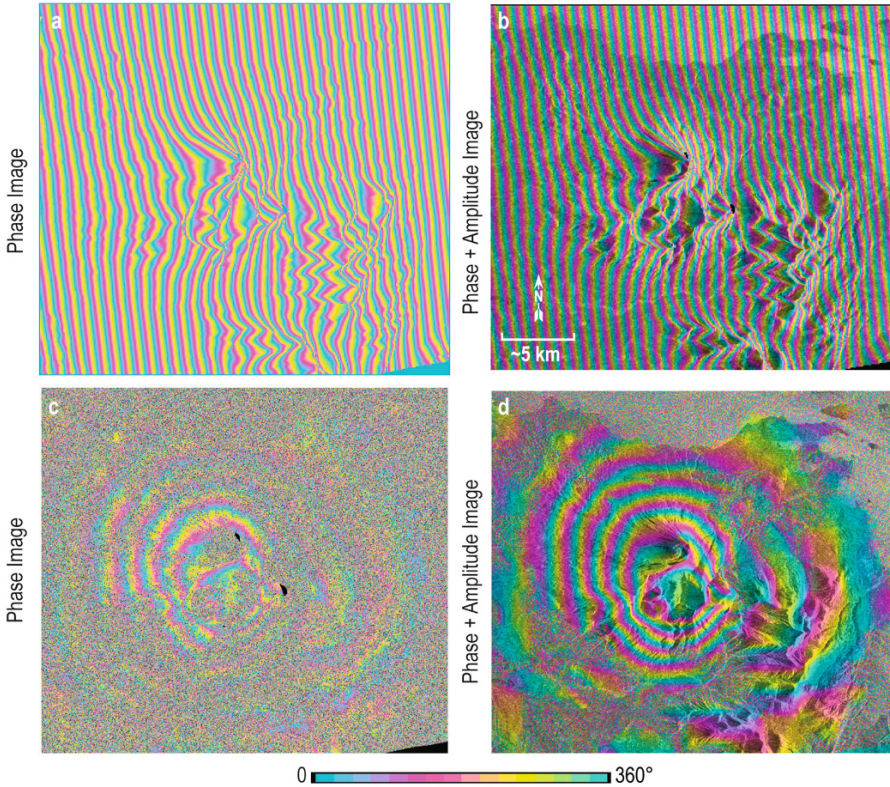


Figure 8.4. (a, b) An interferogram simulated to represent contributions from the topography and the orbital geometry in the original interferogram (Figure 8.2). (c, d) Topography-removed interferogram by subtracting the interferograms in (a, b) from the original interferogram in Figure 8.2. Each interferometric fringe (full-color cycle) represents 360° of phase change (or 2.83 cm of range change between the ground and the satellite). The color change from red to yellow, blue, and red in a fringe represents a relative increase in satellite-to-ground distance or an away-from-satellite ground motion.

values can be approximated mathematically as

$$\begin{aligned} \phi_{\text{flat}} &= -\frac{4\pi B \cos(\theta_1 - \alpha)}{\lambda r_1 \sin \theta_1} h + \phi_{\text{def}} \\ &= -\frac{4\pi B_{\perp}}{\lambda H \tan \theta_1} h + \phi_{\text{def}} \end{aligned} \quad (8.10)$$

where B_{\perp} is the perpendicular component of the baseline with respect to the incidence angle θ_1 (Figure 8.3). If ϕ_{def} is negligible, the phase value in Equation (8.10) can be used to calculate height h . This explains how InSAR can be used to produce an accurate, high-resolution DEM over a large region (Farr and Kobrick, 2000). For the ERS-1/2 satellites, H is about 800 km, θ_1 is about $23 \pm 3^\circ$, λ is 5.66 cm, and B_{\perp} should be less than 1,100 m for a

coherent interferogram. Therefore, Equation (8.10) can be approximated as

$$\phi_{\text{flat}} \approx -\frac{2\pi}{9,600} B_{\perp} h + \phi_{\text{def}} \quad (8.11)$$

For an interferogram with a B_{\perp} of 100 m, one meter of topographic relief produces a phase value of about 4° . However, producing the same phase value requires only 0.3 mm of surface deformation. Therefore, it is evident that the interferogram phase value can be much more sensitive to changes in topography (i.e., surface deformation ϕ_{def}) than to the topography itself (i.e., h). That explains why repeat pass InSAR is capable of detecting surface deformation at a subcentimeter theoretical accuracy.

An important step in InSAR processing is called phase unwrapping. The InSAR phase value as expressed in Equations (8.1)–(8.4), (8.8), and (8.10) is still only known modulo 2π . In other words, the observed InSAR phase value is mathematically limited to the interval $(-\pi, \pi]$ corresponding to the principal value of the arctangent function, even though the true phase may range over an interval greater than 2π . Therefore, a phase-unwrapped algorithm (e.g., Goldstein *et al.*, 1988; Costantini, 1998) is needed to remove the modulo 2π ambiguity. A simple way to do this is to first difference the phase at each pixel, and then to integrate the result (Goldstein *et al.*, 1988). Direct application of this approach allows local errors to propagate, causing global errors. The branch cut method by Goldstein *et al.* (1988) chooses the paths of integration that lead to a correct solution. This implies that in the error-free case the integral of the differenced phase about a closed path should equal zero and that nonzero results are caused by errors. Thus, inconsistencies (local errors) are detected by summing the phase difference clockwise around the closed paths formed by each set of four pixels that are mutual neighbors. An inconsistency is found when summation yields a value of a multiple of 2π rather than 0. These points, called residues, are referred to as positively or negatively charged, depending on their sign (Goldstein *et al.*, 1988). Integration of the differenced phase about a closed path yields a value equal to the sum of residues contained within the path. In order to obtain a correct solution, paths of integration that encircle a net charge must be avoided. This is done by connecting opposite-charged residues to branch cuts, which are lines that the path of integration is restricted from crossing. When all the residues are connected by branch cuts, phase unwrapping can be completed by integrating the differenced phase subject into the rule that paths of integration cannot cross branch cuts.

A more robust algorithm, called minimum cost flow (MCF), is used to minimize the total cost associated with phase discontinuities in the scene associated with noise and layover. MCF formulates phase unwrapping as a global minimization problem by establishing a network structure. For example, triangulation is used to generate a network for phase integration. Each triangle is a node in the network. If integration of the phase around a triangle indicates a positive phase discontinuity, the node is marked as contributing flow to the network. A negative phase discontinuity at a node is marked

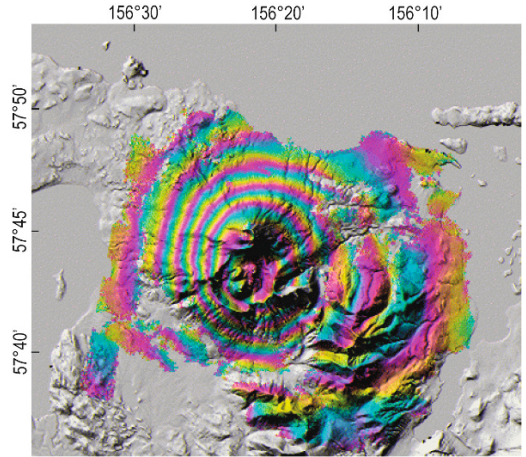


Figure 8.5. A georeferenced interferogram overlaid on a shaded relief image produced from a DEM. Each fringe corresponds to 2.8 cm of range change. The concentric pattern indicates ~ 17 cm of uplift centered on the southwest flank of Mt. Peulik, Alaska, which occurred during an aseismic inflation episode from October 1996 to September 1998 (Lu *et al.*, 2002b). The color change from red to yellow, blue, and red in a fringe represents a relative increase in satellite-to-ground distance or an away-from-satellite ground motion.

as accepting flow from the network. The MCF problem solution gives the optimum flow in each of the arcs that minimize the total cost (Costantini, 1998).

The final procedure in two-pass InSAR is to rectify the SAR images and interferograms into map coordinates, which is a backward transformation of Equation (8.5). The georeferenced interferogram (Figure 8.5) and derived products can be readily overlaid with other data layers to enhance the utility of the interferograms and facilitate data interpretation. Figure 8.5 shows six concentric fringes that represent about 17 cm of range decrease (mostly uplift) centered on the southwest flank of Mt. Peulik, Alaska. The volcano inflated aseismically from October 1996 to September 1998, a period that included an intense earthquake swarm that started in May 1998 near Becharof Lake, 30 km northwest of Mt. Peulik (Lu *et al.*, 2002b).

In-depth description of InSAR processing can be found in Rodriguez and Martin (1992), Zebker *et al.* (1994), Bamler and Hartl (1998), Henderson and Lewis (1998), Massonnet and Feigl (1998), Rosen *et al.* (2000), Zebker *et al.* (2000), Hanssen (2001),

Hensley *et al.* (2001), and Lu and Dzurisin (2014). Interested readers should consult these references for further reading.

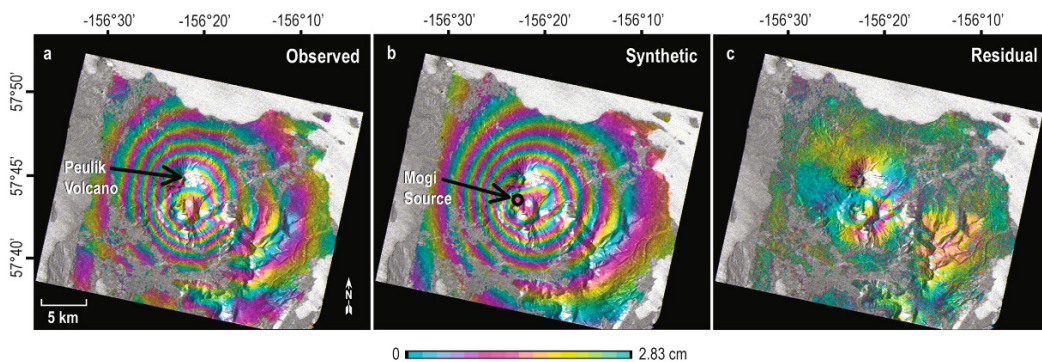
8.1.3 Interferogram interpretation and modeling

To understand magmatic processes, numerical models are often employed to estimate the physical parameters based on the observed deformation (unwrapped InSAR images). By establishing a mathematical model of the deformation process, the deformation data are then used in an inversion process to estimate the parameters of the model. The spatial resolution of surface displacement data provided by InSAR makes it possible to constrain models of volcanic deformation with a variety of source geometries such as the spherical point pressure source (Mogi source) (Mogi, 1958), the dislocation source (sill or dike source) (Okada, 1985), the ellipsoid source (Davis, 1986; Yang *et al.*, 1988), the penny crack source (Fialko *et al.*, 2001), and others. Among the physical parameters, location and volume change of the magma reservoir are the most important.

The most widely used source in volcano deformation modeling is the spherical point pressure source (also called the Mogi source) embedded in an elastic homogeneous half-space (Mogi, 1958).

Even though a Mogi source is the simplest and not physically meaningful, it can fit observed deformation data remarkably well. The four parameters used to describe the point source are horizontal location coordinates, depth, and volume change of a presumed magma body. The magma is assumed to have the same elastic properties as the country rock (Delaney and McTigue, 1994; Johnson *et al.*, 2000). The point source approximation is valid if the size of the source is much smaller than its depth. A limitation of the half-space formulation is its neglect of topographic effects. To account for topographic effects, a simple approach proposed by Williams and Wadge (1998), in which the elevation of the reference surface varies according to the elevation of each computation point in the model, is normally adopted.

A nonlinear least-squares inversion approach is often used to optimize the source parameters (Press *et al.*, 1992; Cervelli *et al.*, 2001). Inverting the observed interferogram in Figure 8.5 using a Mogi source results in a best-fit source located at a depth of 6.5 ± 0.2 km. The calculated volume change is 0.043 ± 0.002 km³. Figure 8.6b shows the modeled interferogram based on best-fit source parameters, and Figure 8.6c is a residual interferogram that is the difference between the observed deformation (Figure 8.6a) and modeled deformation (Figure 8.6b). It is obvious that the Mogi source fits the observed deformation very well.



Best-fit source parameters:

- The model source is located at a depth of 6.5 ± 0.2 km
- The calculated volume change of magma reservoir is 0.043 ± 0.002 km³

Figure 8.6. Deformation interferograms (observed, modeled, and residual) for Mt. Peulik Volcano. Each fringe (full-color cycle) represents 2.83 cm of range change between the ground and the satellite. Synthetic interferograms were produced using a best-fit inflationary point source at about 6.5 km depth with a volume change of 0.043 km³. The residual interferogram is the difference between the observed and modeled interferograms. Areas of loss of radar coherence are uncolored. The color change from red to yellow, blue, and red in a fringe represents a relative increase in satellite-to-ground distance or an away-from-satellite ground motion.

8.1.4 Miscellaneous issues of InSAR processing

8.1.4.1 InSAR coherence

Interferometric coherence is a qualitative assessment of the correlation of SAR images acquired at different times. It determines the amount of phase error and thus the accuracy of deformation estimates or DEM products. Constructing a coherent interferogram requires that SAR images must correlate with each other; that is, the backscattering spectra of the SAR images must be substantially similar over the observation period. Physically, this translates to a requirement that the ground scattering surface be relatively undisturbed at the radar wavelength scale between measurements (Li and Goldstein, 1990; Zebker and Villasenor, 1992). Loss of InSAR coherence is also referred to as decorrelation. There are three primary sources of decorrelation: (a) thermal decorrelation, caused by the presence of uncorrelated noise sources in radar instruments; (b) spatial decorrelation, which results when the target is viewed from different positions; and (c) temporal decorrelation, which is due to environmental changes such as vegetation growth and snow accumulation or melt.

Reduction of interferometric coherence is the major obstacle to applying InSAR to Alaskan volcanoes. At these volcanoes, processes that reduce interferometric coherence include snow/ice melting and accumulation, freezing/thawing of surface material, erosion/deposition of volcanic lava and ash, and growth and movement of vegetation. Past studies have demonstrated that interferometric coherence at the C-band is found to persist for 3 years or more on lava flow and other rocky surfaces covered with short grass and sparsely distributed tall grass, and for at least one year on most pyroclastic deposits (Lu and Freymueller, 1998; Lu *et al.*, 2002c). Interferometric coherence lasts for a few months on lava and rocky surfaces with dense tall grass, and for a few months on alluvium. Snow and ice surfaces lose coherence within a few days. The comparison of L-band and C-band interferometric coherence at Alaskan volcanoes also indicates that the L-band is far superior to the C-band when studying volcanic surfaces covered with thick vegetation or loose material (Lu *et al.*, 2005a, b). Therefore, the chances of producing coherent interferograms increase by using images acquired during summer or early fall, separated in time by a few months (in the same summer/fall) or by one to a few years (Lu and Freymueller, 1998; Lu *et al.*,

2002c), and by using L-band imagery over surfaces with thick vegetation or loose material (Lu *et al.*, 2005a, b).

8.1.4.2 InSAR baseline

A significant error source in InSAR deformation mapping is the baseline uncertainty due to inaccurate determination of SAR antenna positions. For ERS-1/2 satellites, the refined precision orbit data provided by the German Processing and Archiving Facility (D-PAF) (Massmann, 1995) or Delft University in the Netherlands (Scharroo and Visser, 1998) should be used for InSAR processing. The accuracy of the satellite position vectors provided in Radarsat-1 and JERS-1 metadata is much poorer than that for ERS-1 and ERS-2. Therefore, baseline refinement is required for Radarsat-1 and JERS-1 interferogram processing. One of the approaches is to refine the baseline vector based on the two-dimensional offsets of two SAR images. Another method is to determine the baseline vector based on an existing DEM via a least-squares approach (Rosen *et al.*, 1996). In the latter approach, areas of the interferogram that are used to refine the baseline should have negligible deformation or known deformation from an independent source.

8.1.4.3 Atmospheric artifacts

Another critical error source in repeat pass InSAR deformation measurement is due to atmospheric delay anomalies caused by small variations in the index of refraction along the line of propagation. Changes in the total electron content of the ionosphere and water vapor content in the troposphere from one radar acquisition to the other of the pair will result in variations in the phase of signals, which introduces errors in the observed interferogram. The range change caused by atmospheric delays is significant for interferograms over the Aleutian volcanoes. For example, range changes of several centimeters have been found over many Alaskan volcanoes (e.g., Lu *et al.*, 2000c, 2003b). Therefore, multiple observations from independent interferograms for similar time intervals should be used to verify any apparent deformation (Zebker *et al.*, 1997; Lu *et al.*, 2000c). Because atmospheric artifacts do not correlate in time, stacking multiple interferograms will reduce atmospheric noise and enhance the signal-to-noise ratio of the deformation signal (Kwoun *et al.*, 2005).

8.2 InSAR MONITORING OF DEFORMATION OF ALEUTIAN VOLCANOES: CASE STUDIES

8.2.1 Introduction

Many volcanic eruptions are preceded by pronounced ground deformation in response to increasing pressure from magma chambers or to the upward intrusion of magma. Therefore, surface deformation patterns can provide important insights into the structure, plumbing, and state of restless volcanoes (Dvorak and Dzurisin, 1997; Dzurisin, 2003). By analogy with the earthquake cycle in seismology, an “eruption cycle” can be conceptualized as a continuum from deep magma generation through surface eruption, including such stages as partial melting, initial ascent through the upper mantle and lower crust, crustal assimilation, magma mixing, degassing, shallow storage, and final ascent to the surface (Dzurisin, 2003). Not all stages are represented in every event. For example, some eruptions apparently are fed from shallow magma bodies that might not be replenished before every eruption, and others produce primitive lavas that show no evidence of storage, assimilation, or mixing. Some intrusions crystallize before they reach the surface and, therefore, might not advance the cycle toward the next eruption. The time scale for magma generation, ascent, and storage is poorly constrained and variable from one eruption to the next. In some cases, the early part of the cycle is relatively brief (e.g., rapid ascent of magma from a deep source directly to the surface), or the latter part is protracted (e.g., long periods of storage, assimilation, and crystallization between eruptions of large silicic caldera systems). As a result of such complexities, deformation patterns vary considerably both during the eruption cycle and between different volcanoes (Dvorak and Dzurisin, 1997). In addition, magma accumulation at shallow reservoirs typically occurs below the brittle–ductile transition (~5 km beneath volcanoes), so the slow ascent of magma to that depth generally is not marked by earthquakes (e.g., Sibson, 1982). Hence, the induced surface deformation is subtle, especially if the intrusion occurs episodically in a series of small events or gradually over a long time period. Therefore, understanding the dynamic processes of varied magma systems requires an imaging system capable of characterizing complex and dynamic volcano deformation patterns associated with different volcanic processes

(Dzurisin, 2003). The chance for success in meeting this requirement has increased substantially since the recent advent of InSAR-aided volcano monitoring (e.g., Zebker *et al.*, 2000; Dzurisin, 2003; Lu *et al.*, 2003a; Pritchard and Simons, 2004).

The Alaskan volcanoes comprise roughly 10% of the world’s active volcanoes. Major volcanic eruptions are annual events in the Aleutian Arc. More than 170 eruptions were recorded in this area during the last 100 years. Although the rate of eruptive activities in the Aleutian Arc is very high, these volcanoes remain relatively poorly studied due to their remote locations, difficult logistics, high cost of field measurement, and persistent cloud cover. Therefore, all-weather radar satellite images with the capability of measuring subtle ground surface deformation can substantially improve our understanding of the dynamics of these volcanoes (Lu *et al.*, 1997, 1998, 2000a–c, 2002a–c, 2003a–c, 2004, 2005a–b).

In the next five sections, we showcase five examples of how InSAR was used to study five Alaskan volcanoes (Figure 8.7) with SAR images collected by the European ERS-1/2, Canadian Radarsat-1, and Japanese JERS-1 satellites. To understand the magmatic processes, the elastic deformation models of Mogi and dislocation sources (e.g., Mogi, 1958; Okada, 1985) were used to estimate physical parameters based on the observed deformation. For Okmok and Westdahl Volcanoes, InSAR images mapped volcanic deformation before, during, and after the recent eruptions and were used to infer the magma plumbing systems. In the case of Akutan Volcano, InSAR images captured the complex deformation patterns associated with magma intrusion and intense seismic swarms without an eruption. InSAR imagery detected an episodic inflation at Mt. Peulik with a long-repose period. For Shishaldin, InSAR images provided insights into the eruption mechanism of the most active volcano in Alaska.

8.2.2 Okmok Volcano

Okmok is a dominantly basaltic central volcanic complex that occupies most of the northeastern end of Umnak Island, Alaska (Figure 8.7). Catastrophic pyroclastic eruptions ~12.0 and 2.05 kyr resulted in the formation of two overlapping summit calderas. Subsequent eruptions produced a field of small cones and lava flows, including several historically active vents within the younger caldera (Miller *et al.*, 1998; Grey, 2003). Most of the vol-

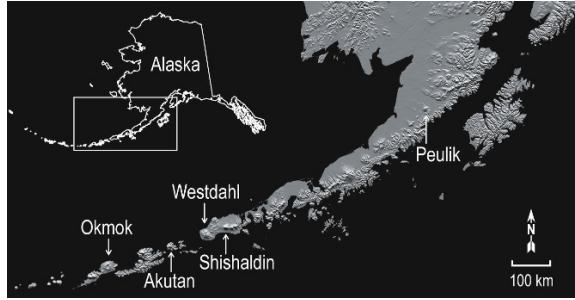


Figure 8.7. Map of Alaska and the five volcanoes presented in this chapter. There are over 40 additional historically active volcanoes in the Aleutian Arc.

cano's historical eruptions are poorly documented because it is so remote. Minor explosive eruptions occurred in 1931, 1936, 1938, 1943, 1960–1961, 1981, 1983, and 1986–1988; blocky basaltic flows were extruded during relatively large effusive eruptions in 1945, 1958, and 1997 (Miller *et al.*, 1998; Grey, 2003). All these eruptions originated from Cone A, located on the southern edge of the caldera floor (Figure 8.8), which formed almost entirely

during the 20th century (Grey, 2003). In 2008 Okmok erupted unexpectedly, breaking its pattern of small eruptions with a large phreatomagmatic event (Larsen *et al.*, 2009).

InSAR images constructed from ERS-1/2, JERS-1, and Radarsat-1 SAR data depict volcanic deformation before, during, and after the February–April 1997 eruption (Lu *et al.*, 1998, 2000c, 2003c, 2005a). Figure 8.9 shows interferograms that

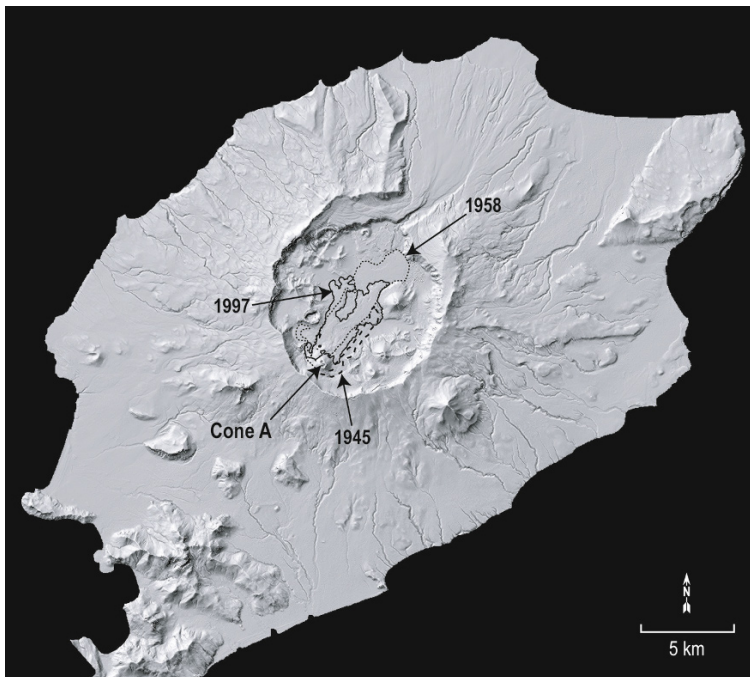


Figure 8.8. Shaded relief image of Okmok Volcano, with outlines marking the extents of lava flows from eruptions in 1945, 1958, and 1997. The 1997 flows overrode parts of the 1945 flows and most of the 1958 flows. The 1997 lava covers an area of 8.9 km^2 and has a volume of about 0.15 km^3 (Lu *et al.*, 2003c).

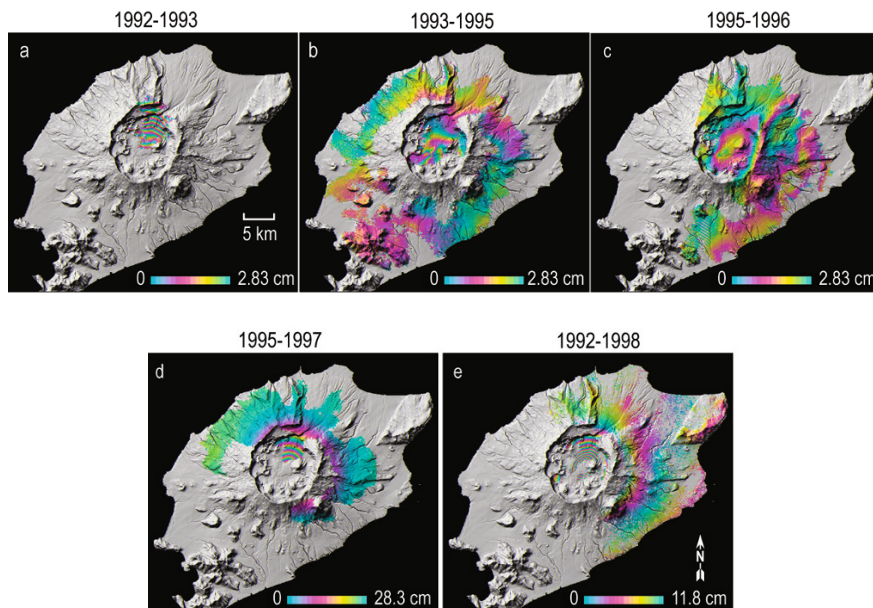


Figure 8.9. Deformation interferograms of Okmok Volcano for the periods before (a–c) and during (d, e) the February–April 1997 eruption. Areas of loss of radar coherence are uncolored. The color change from red to yellow, blue, and red in a fringe represents a relative increase in satellite-to-ground distance or an away-from-satellite ground motion.

map patterns of deformation before and during the 1997 eruption. More than five fringes appear inside the caldera in the 1992–1993 interferogram (Figure 8.9a), but only two appear in the 1993–1995 interferogram (Figure 8.9b). It can be inferred from these two interferograms that the center of the caldera rose more than 14 cm during 1992–1993 and about 6 cm during 1993–1995. The 1995–1996 interferogram (Figure 8.9c) indicates that the caldera subsided 1–2 cm between 1.5 and 0.5 years before the 1997 eruption. Therefore, the pre-eruption inflation rate decreased with time during 1992–1995 and inflation stopped sometime during 1995–1996. More than 140 cm of surface deflation associated with the 1997 eruption can be inferred from the ERS interferogram (Figure 8.9d) and the JERS-1 InSAR image (Figure 8.9e). The deflation presumably is due to the withdrawal of magma (Lu *et al.*, 1998, 2000c, 2005a).

Progressive post-eruptive inflation from 1997 to 2003 is shown in Figure 8.10. The post-eruption inflation rate generally decreased with time during 1997–2001. However, the inflation rate increased again during 2001–2003 to a value greater than that during 1997–1998. The inflation rate during 2002–

2003 was the highest observed since the 1997 eruption.

Based on the shape and radial pattern of the displacement field, Lu *et al.* (2005a) assumed that deformation was caused by a volume change in a spherical magma reservoir, and modeled the surface displacement field using a point source within a homogeneous isotropic elastic half-space (Mogi, 1958). Point source models indicate that a magma reservoir at a depth of 3.2 km below sea level, located beneath the center of the caldera, and about 5 km northeast of the 1997 vent, is responsible for the observed volcano-wide deformation. The deformation source inferred from InSAR data matches well with independent observations from GPS data (Miyagi *et al.*, 2004). Based on about 80 interferograms and modeling results, Lu *et al.* (2005a) derived the annual magma flux as a function of time during 1992–2003 (Figure 8.11), and proposed a plumbing system for Okmok Volcano.

A magma reservoir beneath the center of the caldera, about 3 km below sea level, was responsible for volcano-wide deformation before, during, and after the eruption. Magma filled this reservoir at a rate that varied both before and after the eruption,

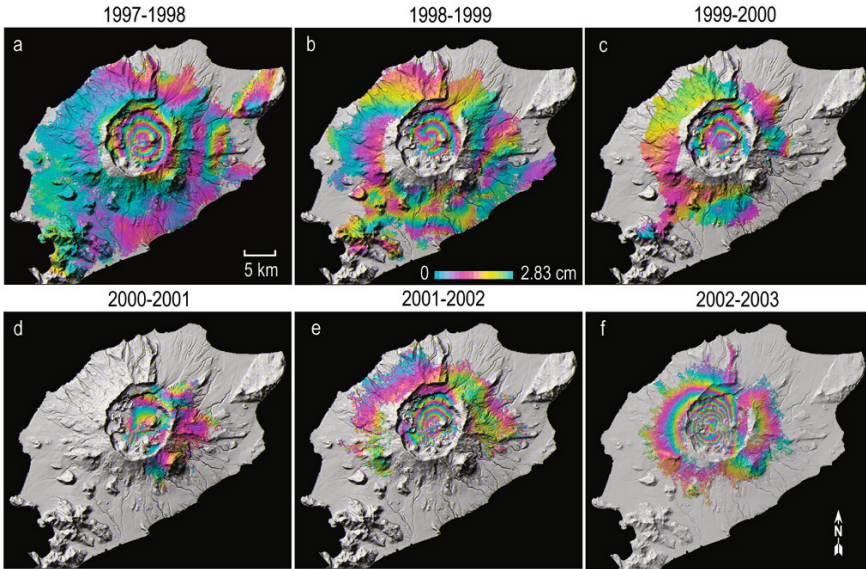


Figure 8.10. Deformation interferograms of Okmok Volcano for six annual periods after the February–April 1997 eruption. Each fringe (full-color cycle) represents 2.83 cm of range change between the ground and the satellite. Areas of loss of radar coherence are uncolored. The color change from red to yellow, blue, and red in a fringe represents a relative increase in satellite-to-ground distance or an away-from-satellite ground motion.

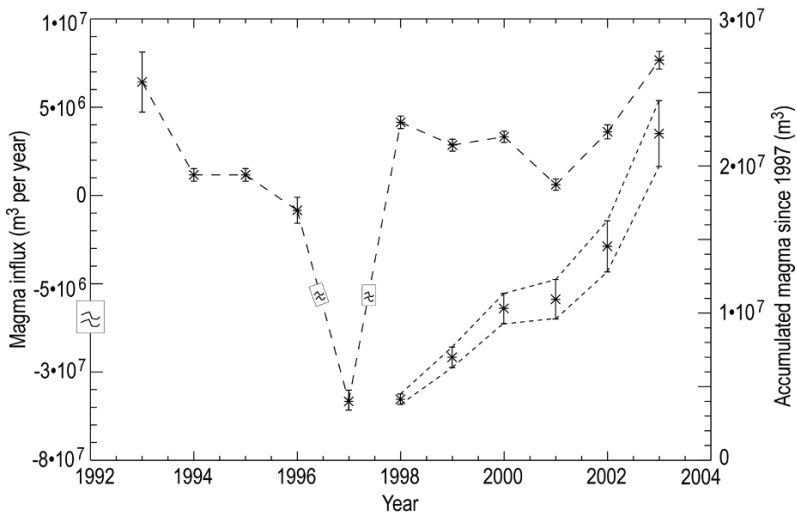


Figure 8.11. Estimated magma supply for the shallow reservoir as a function of time from 1992 to 2003. Incremental magma flux estimates (connected with dashed line) reveal annual supply dynamics. The vertical axis on the left applies to this curve. Error bars are 1σ . Cumulative magma storage following the 1997 eruption (with 1σ bounds) is shown in the lower right portion of the plot. The vertical axis on the right applies to the cumulative curve, which suggests that 30–60% of the volume that erupted in 1997 (based on co-eruption interferograms) has been replenished.

causing volcano-wide inflation. When the magma pressure within the reservoir reached a certain threshold, an eruption ensued. Withdrawal of magma via an eruption depressurized the reservoir, causing volcano-wide deflation, and fed surface lava flows. Magma started to accumulate in the reservoir soon after the eruption stopped, initiating a new inter-eruption strain cycle. By the summer of 2003, 30–60% of the magma volume lost from the reservoir in the 1997 eruption had been replenished. This case study for Okmok Volcano has demonstrated that InSAR is capable of measuring pre-eruptive, co-eruptive, and post-eruptive deformation in the subarctic environment.

8.2.3 Westdahl Volcano

Westdahl is a young glacier-clad shield volcano located on the central Aleutian Arc (Figure 8.7). The edifice is composed of a thick sequence of pre-glacial basalt lava flows. The volcano was frequently active during the latter half of the 20th century, with documented eruptions in 1964, 1978–1979, and 1991–1992 (Miller *et al.*, 1998). The volcanic explosivity index of these last three eruptions was 2 or 3, which corresponds to a “moderate” or “moderate–large” explosive event with 10^6 to 10^8 m³ of erupted products. The most recent

eruption at Westdahl began on November 30, 1991 with a fissure eruption through ice. The fissure extended from near the summit of Westdahl Peak eastward for about 8 km. Ash venting occurred discontinuously along most of the fissure. Dramatic lava fountaining was observed along the lower portion of the fissure, feeding several streams of lava that descended the east flank (Figure 8.12). Fountaining and phreatic activity produced ash plumes that rose to an altitude of 7 km, prompting the U.S. Federal Aviation Agency to divert air traffic. The activity declined in mid-December 1991 and ceased by mid-January 1992 (Miller *et al.*, 1998). By combining information from SAR images, multispectral Landsat-7 data, and DEMs acquired during the 1970s to 1980s and in 2000 by the SRTM, Lu *et al.* (2004) estimated the areal extent of the 1991–1992 flow as 8.4 km², with an average thickness of 13 m (Figure 8.12).

Using ERS-1/2 interferograms, Lu *et al.* (2000b, 2003b) produced interferograms of Westdahl that revealed surface deformation before, during, and after the most recent eruption in 1991–1992 (Figures 8.13 and 8.14). They modeled the deformation using a Mogi source and made four important observations and inferences.

First, volcano-wide deformation before the 1991 eruption is insignificant. Figure 8.13a shows

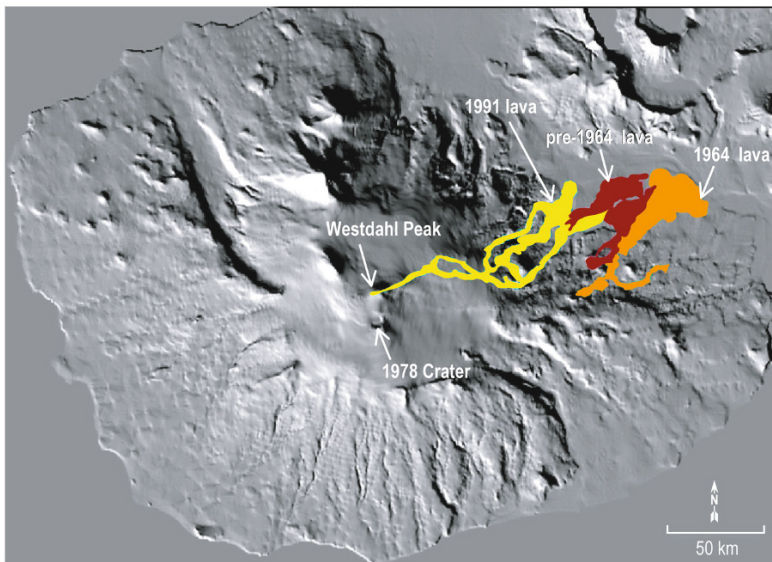


Figure 8.12. Shaded relief image of Westdahl Volcano. The 1978 crater, Westdahl Peak (1991–1992 vent), and three recent lava flows are labeled.

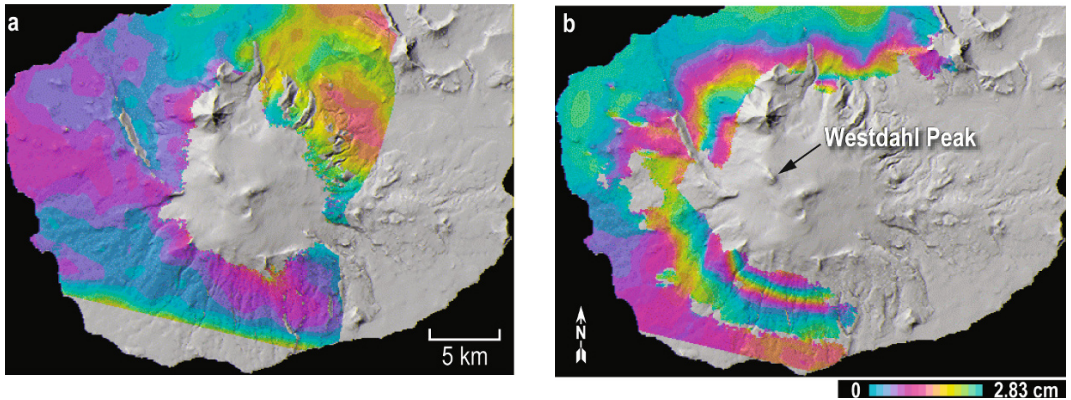


Figure 8.13. (a) Pre-1991 eruption interferogram of Westdahl Volcano during September 7 and November 21, 1991. The latter image was acquired about 8 days before the 1991 eruption. No significant deformation was observed. (b) Interferogram showing the deflation of Westdahl Volcano during the first 20 hours of the 1991 eruption. Each fringe (full-color cycle) represents 2.83 cm of range change between the ground and the satellite. Areas that lack interferometric coherence are uncolored. The color change from red to yellow, blue, and red in a fringe represents a relative increase in satellite-to-ground distance or an away-from-satellite ground motion.

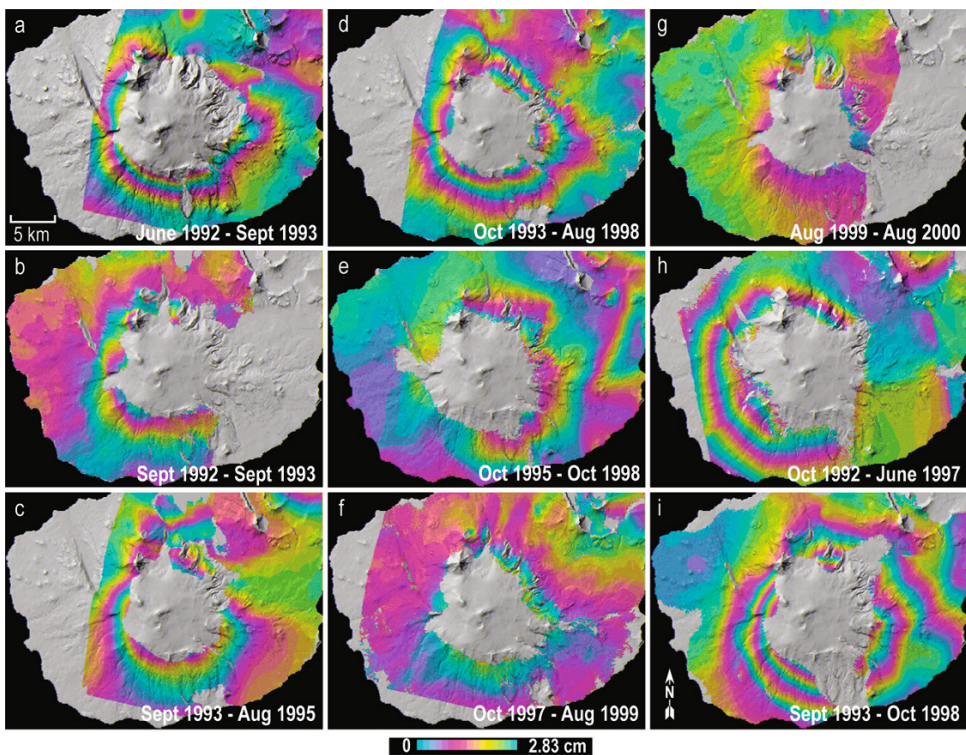


Figure 8.14. Observed interferograms showing progressive inflation for various time windows during 1991–2000 starting after the 1991–1992 eruption. Each fringe (full-color cycle) represents 2.83 cm of range change between the ground and the satellite. Areas that lack interferometric coherence are uncolored. The color change from red to yellow, blue, and red in a fringe represents a relative increase in satellite-to-ground distance or an away-from-satellite ground motion.

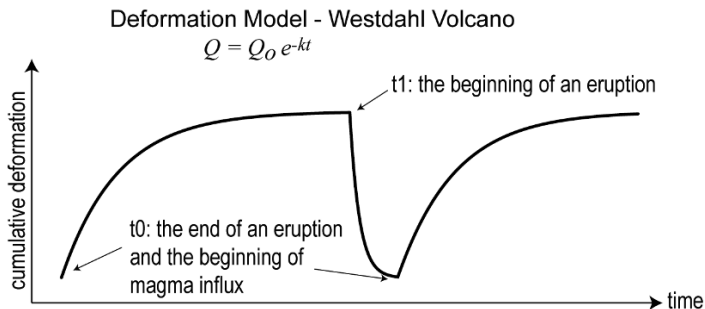


Figure 8.15. A model for the eruption cycle at Westdahl Volcano. The model is based on observed deformation rates and principles of fluid flow from a constant pressure source through a conduit to an elastic reservoir (Lu *et al.*, 2003b). The model predicts that the inflation and deflation rates decay exponentially with time constants being ~ 6 years and a few days, respectively.

an interferogram bracketing a ~ 75 -day time window that ended less than 8 days before the start of the 1991–1992 eruption. The interferogram indicates that the ground deformation which might have occurred during this period was too small to measure. It is also possible that the deformation during this time period came from a source that was very shallow, so that significant displacements were confined to the “hole” in the data where coherence was lost high on the flanks of the volcano.

Second, most of the volcanic deflation associated with magma withdrawal occurred in the first few days during the 45-day eruption from November 29, 1991 to mid-February 1992. The interferogram shown in Figure 8.13b includes the volcano-wide subsidence that occurred within the first 20 hr of the 1991–1992 eruption (Lu *et al.*, 2003b). Two fringes are observed on Westdahl’s flanks, indicating that the upper part of the volcano deflated by more than 5.7 cm. Even though the eruption lasted for about 45 days, including 5 days of strong lava extrusion from November 29 to December 4, 1991 (GVN, 1991), the interferogram indicates that about half of the extruded volume from the 1991–1992 eruption was lost during the first day of eruption. This suggests that the deflation rate must have decreased exponentially with time (with a time constant of a few days). This estimate agrees with the exponentially decreasing deflation rates observed during eruptions at other basaltic shield volcanoes, including Kīlauea, Mauna Loa, and Krafla (Dvorak and Dzurisin, 1997).

Third, post-eruptive inflation resumed as soon as the 1991–1992 eruption stopped and progressed with an inflation rate that decreased with time (Lu *et al.*, 2003b). Figure 8.14 includes nine interfero-

grams that collectively span the time from summer 1992 to summer 2000, showing the progressive inflation of Westdahl following its 1991–1992 eruption. The deformation source inferred from InSAR data matches well with independent observations from GPS data (Mann and Freymueller, 2003). Inspection suggests that the inflation rate decreased with time. Using estimates for volume change from multiple interferograms that span different but overlapping time intervals, Lu *et al.* (2003b) suggested that the rate of inflation can be approximated by an exponential decay function with a time constant of ~ 6 yr.

Fourth, incorporating deformations before, during, and after the 1991–1992 eruption, Lu *et al.* (2003b) inferred a plumbing system model to explain the dynamics of reservoir filling of Westdahl Volcano (Figure 8.15). The deformation behavior of Westdahl is consistent with a deep, constant pressure magma source connected to a shallow reservoir (~ 6 km deep) via a conduit. A magma reservoir ~ 6 km below sea level inflates at an exponentially declining rate for several years before an eruption (or intrusion) ruptures when some unspecified threshold is attained, then deflates at an exponentially declining rate for a few days during the eruption. This cycle then repeats, producing a series of eruptions or intrusions with similar repose intervals and volumes. Eventually, the pattern is broken by some change in the plumbing system, local stress field, or other factors that change the rupture threshold. Magma accumulation occurs mainly below the brittle–ductile transition, which typically occurs ~ 5 km beneath volcanoes (e.g., Sibson, 1982), so the slow ascent of magma to that depth generally is not marked by earthquakes.

In summary, this study of Westdahl Volcano has demonstrated that InSAR can detect deep aseismic magma accumulation by measuring broad, subtle deformation of the ground surface which can be used to identify restless volcanoes long before they become active and to characterize their eruption cycle dynamics. Multiple temporal interferograms enable constructing an inferred magma plumbing system that can be used to constrain magma accumulation at the shallow reservoir and shed light on the projected time window of the next eruption.

8.2.4 Akutan Volcano

Akutan, one of the most active volcanoes in the Aleutian Arc with more than 27 eruptive episodes in the last two centuries, is located in the west central part of Akutan Island in the eastern Aleutian Volcanic Arc. It is a composite stratovolcano with a circular summit caldera about 2 km across (Miller *et al.*, 1998) (Figure 8.7). Lava flows, pyroclastic flows, and other types of volcanic deposits cover much of the west portion of the island including Akutan Volcano. The east half of the island, on the other hand, consists mainly of older, relatively loose deposits (tephra and ash) and undifferentiated volcanic rocks (Miller *et al.*, 1998; Richter *et al.*, 1998). In general, vegetation is denser in the east half of the island than in the west half (Figure 8.16).

Akutan Island was shaken by an intense swarm of volcano-tectonic earthquakes that peaked between March 11 and 16, 1996 and then slowly declined over the next several months. More than 3,000 earthquakes were located using four temporary seismic stations on the island. The estimated cumulative seismic moment of the swarm is 2.7×10^{18} N·m, which is approximately equivalent to a single magnitude-6.0 earthquake (Lu *et al.*, 2000a, 2005b). Fresh ground cracks were observed and extended discontinuously from near Lava Point at the northwest end of the island to the southeast tip a few kilometers south of Akutan Village (Richter *et al.*, 1998) (Figure 8.16). The cracks broke snowfields, and their sides showed little evidence of erosion, suggesting that they had formed recently, almost surely during the March 1996 swarm. The most extensive cracks occurred in a zone roughly 500 m wide and 3 km long between Lava Point and the summit of Akutan Volcano. Local graben structures with vertical displacements of 30–80 cm suggest that the cracks formed in response to extensional stress perpendicular to the

cracks. The cracks on the east side of the island are only a few centimeters wide and apparently represent reactivation of mapped normal faults (Richter *et al.*, 1998).

Two deformation interferograms that bracket the March 1996 swarm are shown in Figure 8.17. The interferogram in Figure 8.17a was produced from C-band (wavelength = 5.66 cm) ERS images acquired on August 20, 1993 and October 7, 1996, whereas the interferogram in Figure 8.17b is an L-band (wavelength = 23.5 cm) JERS-1 deformation interferogram that spans the time interval from October 28, 1994 to June 22, 1997. It is obvious that interferometric coherence is significantly higher at the L-band than at the C-band over similar time intervals. Both the ERS and JERS-1 interferograms show that the western part of the island was uplifted about 60 cm during the 1996 seismic swarm. The JERS-1 interferogram (Figure 8.17c) also shows localized subsidence in the zone of intense ground cracking associated with the swarm on the northwest flank of Akutan Volcano. The subsidence is not observable in the ERS interferograms owing to loss of interferometric coherence. Wholesale uplift of the volcanic edifice combined with localized ground cracking and graben formation has been attributed to magma accumulation and intrusion at other volcanoes (e.g., Rubin, 1992). In addition, the JERS-1 interferogram reveals displacement on two normal faults that were re-activated during the 1996 seismic swarm (Figure 8.17d, e). Displacement profiles across the faults show that the magnitude of displacement was about 5 cm (Figure 8.17d, e), which is consistent with the observed ground breakage of several centimeters (Richter *et al.*, 1998). Portions of faults, which cannot be readily identified in the field because they are obscured by erosion or vegetation, can nonetheless be traced in the JERS-1 interferogram.

The complexity of the deformation field revealed by the interferograms makes it difficult to identify a unique model for the deformation sources. Lu *et al.* (2000b, 2005b) explored a range of possible models using as constraints the asymmetric uplift of Akutan Volcano, the geometry of surface fractures on its northwest flank, the orientation of reactivated faults on the eastern part of the island, and the distribution of well-located 1996–2000 earthquake epicenters (Figure 8.16). The interferograms were modeled with elastic Mogi sources (Mogi, 1958) and dislocation sources (Okada, 1985). Figure 8.18 illustrates a model, composed

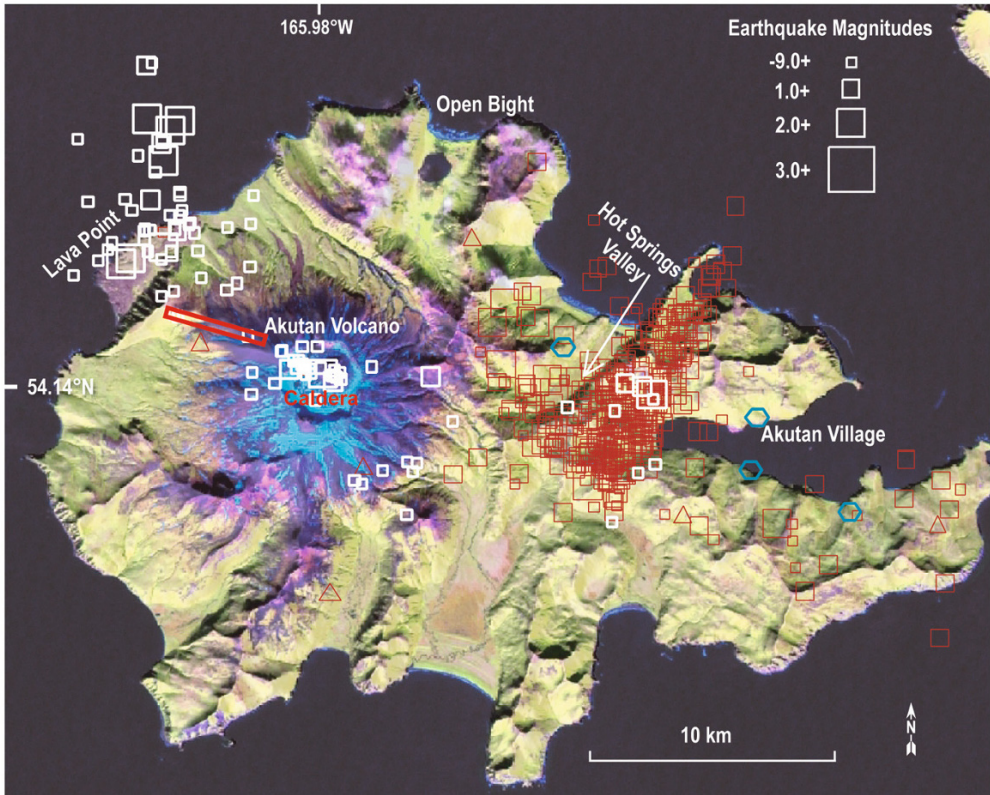


Figure 8.16. A Landsat-7 color-composite image (acquired in August 2002) draped over a DEM of Akutan Island. The Landsat-7 image was created by assigning bands 5, 4, and 3 to red, green, and blue, respectively. Bright blue areas represent ice and snow. Sparsely vegetated areas such as young lava flows and rocky high alpine areas are shown in purple. More densely vegetated areas appear as shades of green. Sparsely vegetated alluvium deposits appear pink. Red squares represent earthquakes located using four temporary seismic stations (hexagons) between March 18 and July 26, 1996. The north-northeast trend of the epicenters, roughly perpendicular to the alignment of the four seismic stations, is probably an artifact of poor network geometry. Earthquakes located using both temporary stations (hexagons) and permanent stations (triangles) from August 1, 1996 to December 31, 1998 are represented by white squares. The overall west-northwest trend of these better located events is roughly parallel to mapped normal faults on the island. The upper right inset shows the earthquake magnitude scale. The red rectangle on the northwest flank of Akutan Volcano represents a zone of ground cracks and graben structures that formed during the March 1996 earthquake swarm.

of four dislocation sources, to fit the observed deformation field (Lu *et al.*, 2005b). Source b1 is a shallow expanding source that strikes N82°W, dips 75°, with its top 0.4 km beneath the surface. This source represents an intruding dike that accounts for the uplift of the west part of the island, including Akutan Volcano. Sources b2 and b3 are contracting sources with horizontal dislocation planes at depths of 3.6 and 16.5 km, respectively. Together, they account for observed subsidence of the eastern part of the island. Their physical mean-

ing is unclear, but depressurization of a hydrothermal system by normal faulting might be a possibility. Source b4 beneath the western part of Akutan Island is also a contracting source, in this case with a steeply dipping dislocation plane and a top at 6.7 km depth. This fourth source accounts for intense ground cracking and graben subsidence on the northwest flank of Akutan Volcano. It might represent the combined effects of magma withdrawal from depth and surface extension caused by shallow dike intrusion.

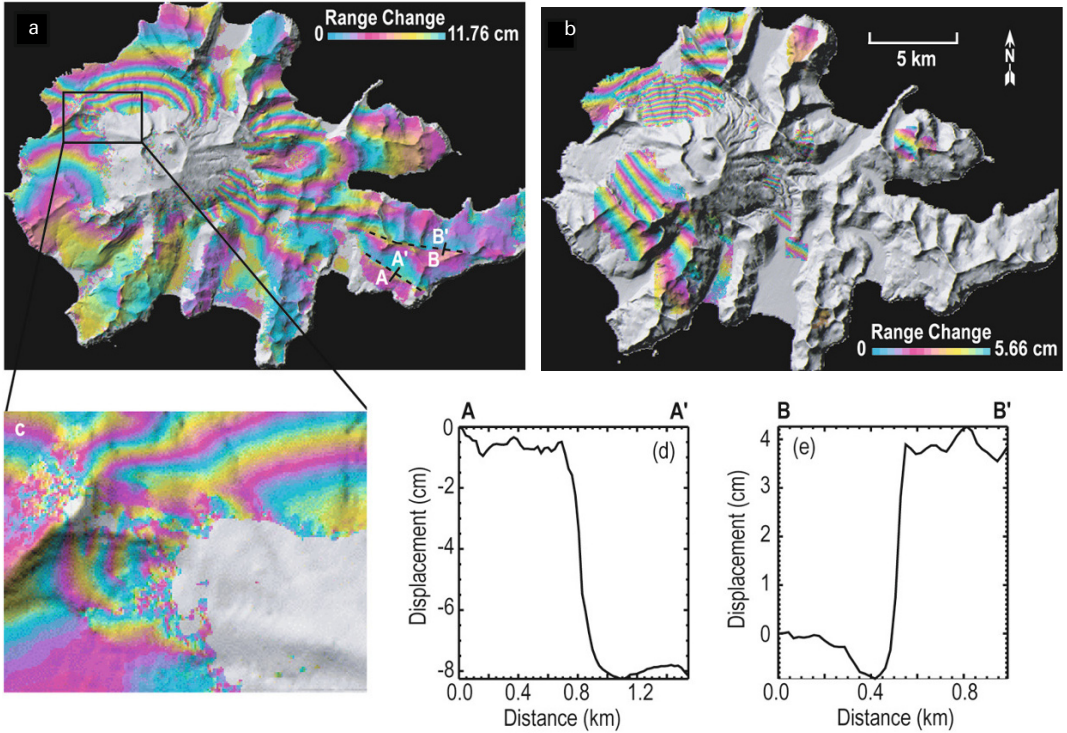


Figure 8.17. Deformation of Akutan Island during the 1996 seismic swarm mapped from (a) JERS-1 SAR images and (b) C-band ERS-1/2 SAR images, showing uplift of the west half of the island and subsidence of the east half. (c) Localized subsidence on the northwest flank of Akutan Volcano, where numerous ground cracks formed during the 1996 seismic swarm. (d, e) Deformation profiles across two faults that were activated during the March 1996 seismic swarm. Locations of the profiles are shown in (b). The color change from red to yellow, blue, and red in a fringe represents a relative increase in satellite-to-ground distance or an away-from-satellite ground motion.

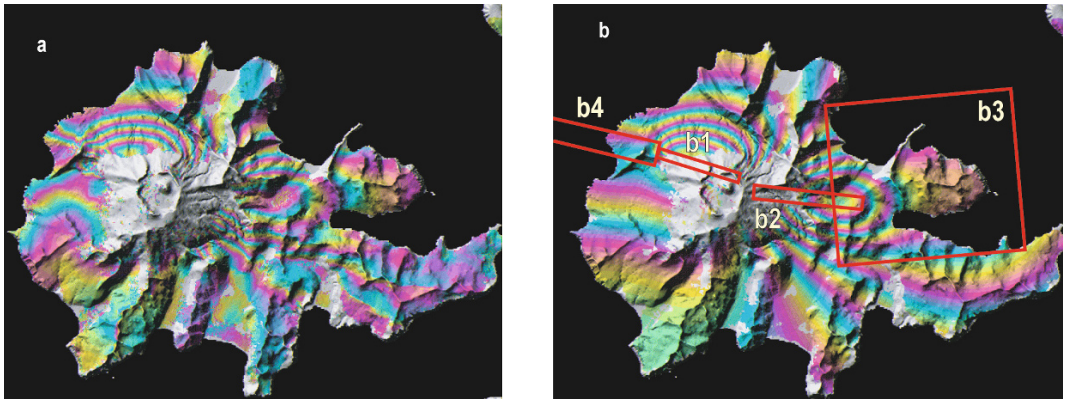


Figure 8.18. Observed and modeled interferograms associated with the March 1996 seismic swarm of Akutan Island: (a) observed JERS-1 interferogram; (b) synthetic interferogram showing the deformation produced by four best-fitting dislocation sources. Each fringe (full-color cycle) represents 11.76 cm range change in the satellite look direction. Areas that lack interferometric coherence are uncolored. The color change from red to yellow, blue, and red in a fringe represents a relative increase in satellite-to-ground distance or an away-from-satellite ground motion.

InSAR study of Akutan Volcano has demonstrated that L-band InSAR is far superior to the C-band for studying volcanic surfaces covered with thick vegetation or loose material. The ability to map surface deformation at high spatial resolution with InSAR makes it an especially useful tool for studying complex deformation patterns, such as those associated with the March 1996 seismic swarm at Akutan Island. These interferograms provide a rare glimpse of surface deformation associated with magma intrusion beneath an island arc volcano. Such effects are often obscured by subsequent eruptive activity, including syn-eruption and post-eruption deformation that might not be distinguishable from pre-eruption effects. This example demonstrates that InSAR can provide a basis not only for interpreting and modeling the movement of shallow magma bodies that feed eruptions, but also for detecting intrusive activities that do not result in an eruption (Lu *et al.*, 2000a, 2005b). The two-dimensional imaging capability of InSAR facilitates characterizing the complex deformation field at Akutan Volcano and, thereby, improves our understanding of its dynamics.

8.2.5 Mt. Peulik Volcano

The Ugashik caldera–Mt. Peulik volcanic system, part of the 2,500 km long Aleutian Volcanic Arc, is located on the Alaska Peninsula approximately 550 km southwest of Anchorage (Figure 8.7). Mt. Peulik is a small, truncated stratovolcano that partially overlaps the north flank of Ugashik caldera, an island arc collapse caldera, roughly 5 km in diameter, of probable Late Pleistocene age (Miller *et al.*, 1998) (Figure 8.19a). Eruptions in 1814 and 1870 are the only two reports of historical activity at Mt. Peulik, and no unusual activity of any kind has been noted in the area since 1977 when Ukinrek Maars was formed about 15 km northwest of Mt. Peulik. During May and October 1998, an intense swarm of earthquakes, led by an $M_L = 5.2$ event, occurred about 30 km northwest of Mt. Peulik, near the western shoreline of Becharof Lake (Figure 8.19a). The cumulative seismic moment of the swarm was 7.15×10^{17} N m, which is approximately equivalent to a single magnitude-5.8 earthquake (Lu *et al.*, 2002b).

A series of ERS interferograms that collectively span the time interval from July 1992 to August 2000 reveal that Mt. Peulik Volcano inflated about

20 cm from 1996 to 1998 (Lu *et al.*, 2002b) (Figure 8.19b–d). Mogi models that fit the observed deformation interferograms suggested that a presumed magma body located 6.6 km beneath the Mt. Peulik volcano inflated by 0.051 km^3 between October 1996 and September 1998 (Lu *et al.*, 2002a) (Figure 8.19). The average inflation rate of the magma body was about $0.003 \text{ km}^3/\text{month}$ from October 1996 to September 1997 (Figure 8.19b), peaked at $0.005 \text{ km}^3/\text{month}$ from June to October 1997 (Figure 8.19c), and dropped to $0.001 \text{ km}^3/\text{month}$ from October 1997 to September 1998 (Figure 8.19d). Deformation before October 1996 or after September 1998 was not significant (Figure 8.19e, f).

The relative timing of the Peulik inflation episode (October 1996 to September 1998) and the Becharof Lake earthquake swarm (May to October 1998) suggests that the swarm might have been triggered by a magmatic intrusion beneath the volcano (Figure 8.20). However, calculated static stress changes beneath the epicentral area due to inflation of 0.05 km^3 in a point source beneath Mt. Peulik appear too small to provide a causal link (Lu *et al.*, 2002b). The 1996–1998 inflation episode was probably the latest in a series of events that cumulatively produced a stress perturbation large enough to trigger the 1998 swarm.

The 1996–1998 inflation episode at Mt. Peulik Volcano has important implications for the eruption cycle at long-dormant stratovolcanoes and, thus, for hazard assessment and eruption forecasting. At arc volcanoes that seldom erupt, volcanologists have been mostly frustrated in their attempts to anticipate the beginning of new cycles of activity. Such volcanoes are quiescent for decades or centuries before unrest is recognized, typically a few days to months prior to eruptions. Detection of the 1996–1998 inflation episode at Mt. Peulik Volcano is important because: (1) it confirms that satellite radar interferometry can detect magma accumulation beneath dormant volcanoes at least several months before other signs of unrest are apparent and perhaps years before an eventual eruption; (2) it includes a possible case of earthquake stress triggering by a magmatic intrusion that might otherwise have gone unnoticed; and (3) it represents a first step toward understanding the eruption cycle at Mt. Peulik and other stratovolcanoes with characteristically long repose periods. Similar studies at other dormant volcanoes where magma might be accumulating episodically, and in some cases aseismically, could lead to improved eruption forecasting and hazard mitigation.

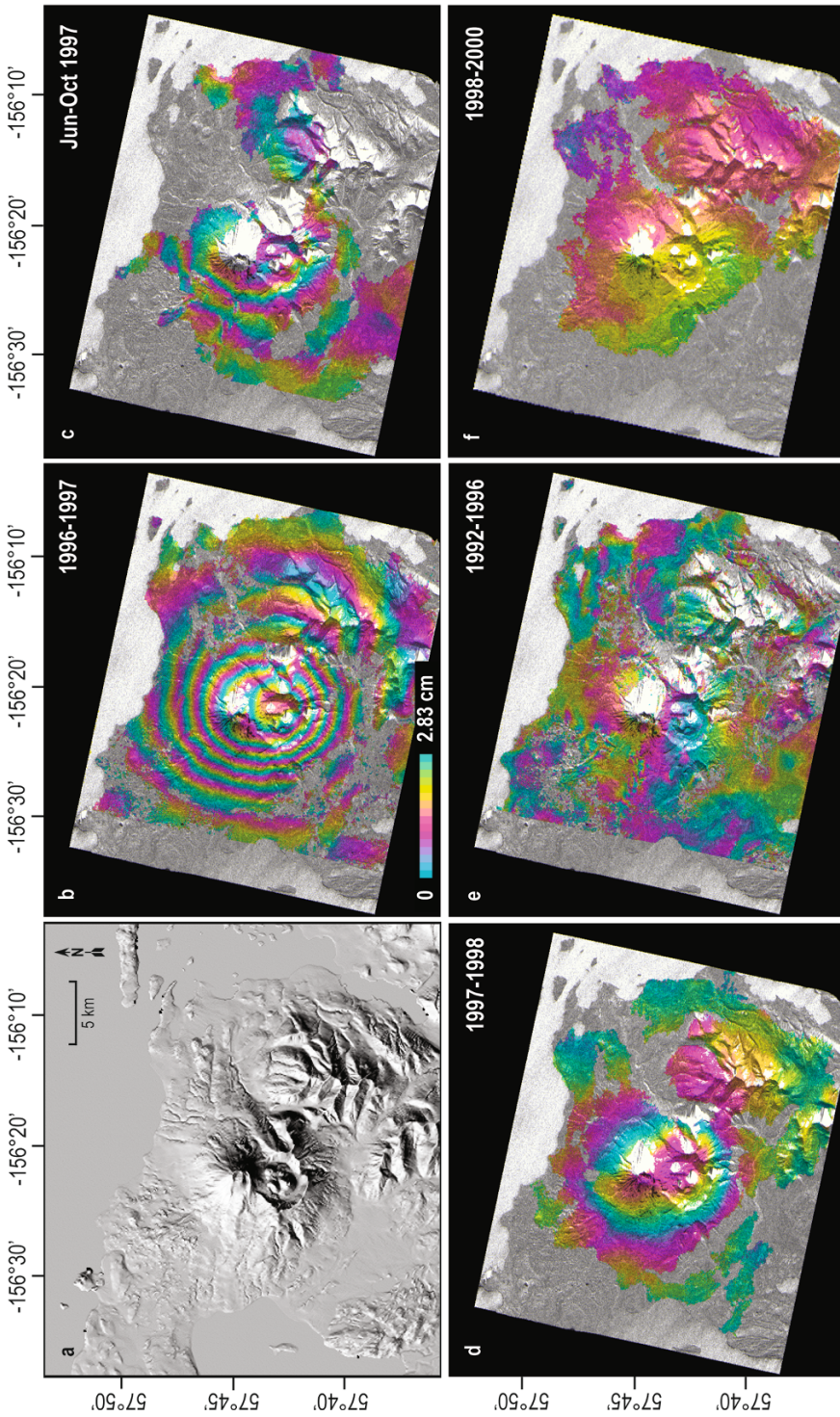


Figure 8.19. (a) A shaded relief image of Mt. Peulik Volcano. (b–f) Topography-removed interferograms of Mt. Peulik Volcano that span several different time intervals. Each fringe (full-color cycle) represents 1.76 cm range change in the satellite look direction. Areas that lack interferometric coherence are uncolored. The color change from red to yellow, blue, and red in a fringe represents a relative increase in satellite-to-ground distance or an away-from-satellite ground motion.

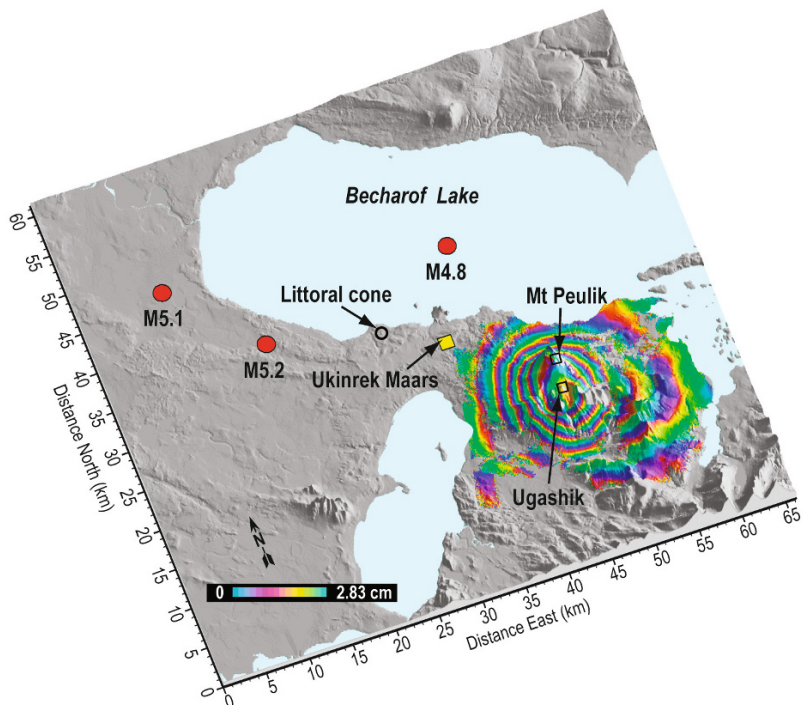


Figure 8.20. A perspective view of topography near Mt. Peulik Volcano. Superimposed on the topography is an interferogram for the period from October 1996 to September 1997, which shows ~17 cm of uplift centered beneath the volcano’s southwest flank. Each interferometric fringe (full-color cycle) represents 2.83 cm of range change between the ground and the satellite. The three largest earthquakes (red circles) occurred from May 8 to October 19, 1998, which is approximately when inflation beneath Mt. Peulik Volcano stopped. The color change from red to yellow, green, blue, and red in a fringe represents a relative increase in satellite-to-ground distance or an away-from-satellite ground motion.

8.2.6 Shishaldin Volcano

Shishaldin is a stratovolcano located near the center of Unimak Island in the eastern Aleutians (Figure 8.7). The spectacular symmetric cone has a base diameter of approximately 16 km and a small summit crater that typically emits a steam plume with occasional small amounts of ash. Shishaldin is the third most active volcano in the Aleutian Arc, having erupted at least 28 times since 1775 and most recently from December 1995 to May 1996 and in April 1999 (Miller *et al.*, 1998). The summit area (~5 km radius) is covered by snow and ice most of the year and, therefore, does not maintain coherence for C-band ERS interferograms with time separation of more than a few days.

Figure 8.21 shows six interferograms produced from ERS-1/2 SAR images with time spans of one year or more. Except for the displacement due to a

magnitude-5.2 earthquake (March 1999) located about 15 km west of the volcano’s peak (Figure 8.21c, d), no significant volcanic deformation was observed in the coherent areas before, during, and after the 1995–1996 and 1999 eruptions, using interferograms with one-year or multiple-year intervals.

These observations suggest four possible scenarios: (1) pre-eruptive inflation was balanced by co-eruptive deflation and no net displacement could be observed; (2) the magma source is deeper than 10 km, so that induced deformation over the coherent areas is negligible during magma accumulation and withdrawal (Moran *et al.*, 2006); (3) no significant pre-eruptive and co-eruptive deformation was associated with these eruptions; and (4) the magma source is very shallow and its strength so small that deformation could only occur over the summit area where coherence is lost. Accepting the third interpretation is difficult as deformation has been

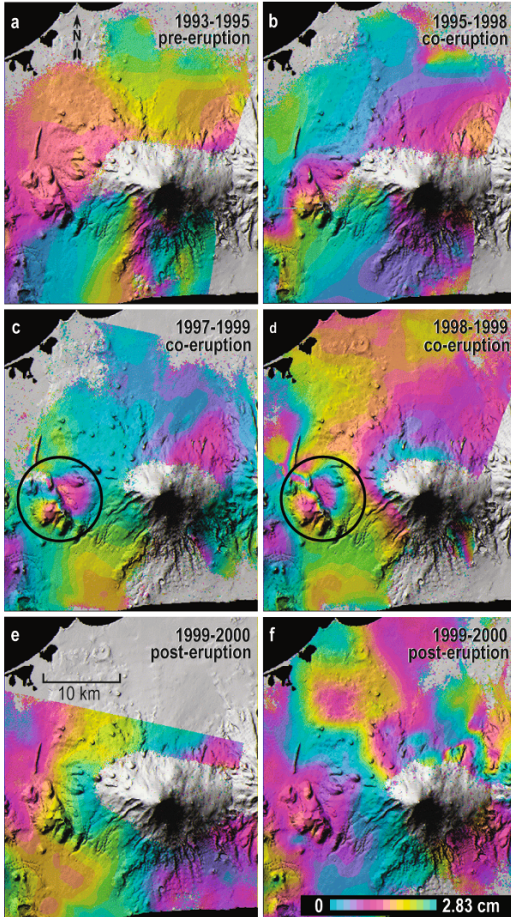


Figure 8.21. Topography-removed interferograms of Shishaldin Volcano that span several different time intervals: (a) from 1993 to 1995 before the 1995–1996 eruption; (b) from 1995 to 1998, including the 1995–1996 eruption; (c) from 1997 to 1999, including the 1999 eruption; (d) from 1998 to 1999, including the 1999 eruption; (e) from 1999 to 2000 after the 1999 eruption; and (f) from 1999 to 2000 after the 1999 eruption. Any volcanic deformation over coherent areas is insignificant. The deformation over the area marked with the circle in (c) and (d) is due to a magnitude-5.2 earthquake that occurred before the 1999 eruption. Interferograms are draped over DEM shaded relief images, and areas that lack interferometric coherence are uncolored.

observed via InSAR in association with similar-sized eruptions and intrusions at other Aleutian Arc volcanoes (e.g., Lu *et al.*, 2002c). Given the size of the 1995–1996 and 1999 eruptions, the last inter-

pretation is also unlikely (Moran *et al.*, 2006). The lack of observed deformation in coherent interferograms that span one year or multiple years may indicate that any pre-eruption inflation may be compensated by subsequent withdrawal of a roughly equivalent volume of magma, leaving no net deformation field. The InSAR study over this active volcano suggests that magma intrusion and transport might occur relatively quickly. This demands a better temporal sampling of SAR images than currently available and an L-band sensor to defeat interferometric decorrelation. Better monitoring of this type of volcano also requires observations from continuous global positioning systems (GPS) and seismometers.

8.3 CONCLUDING REMARKS

The satellite InSAR technique has proven to be a powerful spaceborne geodetic tool for studying a variety of volcanic processes by analyzing surface deformation patterns (Lu *et al.*, 1997, 1998, 2000a–c, 2002a–c, 2003a–c, 2004, 2005a–b). However, the InSAR images presented in this chapter are after-the-event (hindcasting) studies, but what we need for forecasting is a different, better data collection approach. For InSAR to become an effective volcano hazard mitigation tool, an L-band SAR with shorter imaging repeat times, on the order of a few days rather than weeks, is essential. The spatial baseline length should be as small as possible to reduce decorrelation effects and yield more usable image pairs. Satellite positions should be determined with an accuracy of a few millimeters to reduce artifacts due to baseline errors.

With the implementation of InSAR technology, volcano monitoring has entered an exciting phase wherein magma accumulation in the middle to upper crust can be observed long before the onset of short-term precursors to an eruption. Ultimately, more widespread use of InSAR for volcano monitoring could shed light on the inter-eruption part of the eruption cycle—the time period between eruptions when a volcano appears quiet. This makes InSAR an excellent space-based, long-term volcano-monitoring tool. Combining InSAR applications with observations from continuous GPS, gravity meters, strain meters, tilt meters, seismometers, and volcanic gas studies will substantially improve our capability to forecast future eruptions and lead to improved volcano hazard assessments and better eruption preparedness.

8.4 ACKNOWLEDGMENTS

ERS-1/2, Radarsat-1, and JERS-1 SAR images are copyrighted ©1991–2003 European Space Agency (ESA), Canadian Space Agency (CSA), and Japan Aerospace Exploration Agency (JAXA), respectively, and were provided by ASF, ESA, and JAXA. The research summarized in this chapter was supported by funding from the NASA Radarsat Program and Solid Earth & Natural Hazards Program, USGS Volcano Hazards Program, USGS Land Remote Sensing Program, and USGS contracts O3CRCN0001. We thank the ASF, JAXA, and ESA staff members for their special efforts in making the SAR data available to us on a timely basis. We thank J. Freymueller, O. Kwoun, D. Mann, T. Masterlark, V. McConnell, D. Meyer, S. Moran, R. Rykhus, W. Thatcher, and many other colleagues for contributions to this research. We also thank G. Wadge, J. Freymueller, B. Ramachandran, and O. Kwoun for critical reviews and constructive comments.

8.5 REFERENCES

- Bamler, R.; Hartl, P. (1998). Synthetic aperture radar interferometry, *Inverse Problems*, **14**, R1–54.
- Cervelli, P.; Murray, M.H.; Segall, P.; Aoki, Y.; Kato, T. (2001). Estimating source parameters from deformation data, with an application to the March 1997 earthquake swarm of the Izu Peninsula, Japan, *J. Geophys. Res.*, **106**, 11217–11237.
- Costantini, M. (1998). A novel phase unwrapping method based on network programming, *IEEE Trans. Geosci. Remote Sensing*, **36**, 813–821.
- Curlander, J.; McDonough, R. (1991). *Synthetic Aperture Radar Systems and Signal Processing*, John Wiley & Sons, New York.
- Davis, P.M. (1986). Surface deformation due to inflation of an arbitrarily oriented triaxial ellipsoidal cavity in an elastic half-space, with reference to Kīlauea Volcano, Hawaii, *J. Geophys. Res.*, **91**, 7429–7438.
- Delaney, P.T.; McTigue, D.F. (1994). Volume of magma accumulation or withdrawal estimated from surface uplift or subsidence, with application to the 1960 collapse of Kīlauea Volcano, *Bull. Volcanol.*, **56**, 417–424.
- Dvorak, J.; Dzurisin, D. (1997). Volcano geodesy: The search for magma reservoirs and the formation of eruptive vents, *Rev. Geophys.*, **35**, 343–384.
- Dzurisin, D. (2003). A comprehensive approach to monitoring volcano deformation as a window on eruption cycle, *Rev. Geophys.*, **41**, doi: 10.1029/2001RG000107.
- Farr T.G.; Kobrick, M. (2000). Shuttle Radar Topography Mission produces a wealth of data, *EOS, Trans. Am. Geophys. Union*, **81**, 583–585.
- Fialko, Y.; Khazan, Y.; Simons, M. (2001). Deformation due to a pressurized horizontal circular crack in an elastic half-space, with applications to volcano geodesy, *Geophys. J. Int.*, **146**, 181–190.
- Gabriel, A.K.; Goldstein, R.M.; Zebker, H.A. (1989). Mapping small elevation changes over large areas: Differential radar interferometry, *J. Geophys. Res.*, **94**, 9183–9191.
- Goldstein, R.; Zebker, H.; Werner, C. (1988). Satellite radar interferometry: Two-dimensional phase unwrapping, *Radio Science*, **23**, 713–720.
- Gray, A.L.; Farris-Manning, P.J. (1993). Repeat-pass interferometry with airborne synthetic aperture radar, *IEEE Trans. Geosci. Remote Sensing*, **31**, 180–191.
- Grey, D. (2003). Post-caldera eruptions at Okmok volcano, Umnak Island, Alaska, with emphasis on recent eruptions from Cone A, MS thesis, University of Alaska, Fairbanks, December.
- GVN (1991). Global Volcanism Network, *Smithsonian Inst. Bull.*, available at <http://www.volcano.si.edu>
- Hanssen, R. (2001). *Radar Interferometry: Data Interpretation and Error Analysis*, Kluwer Academic, Dordrecht, The Netherlands.
- Henderson, F.; Lewis, A. (1998). Principles and applications of imaging radar, *Manual of Remote Sensing*, Vol. 2, John Wiley & Sons, New York.
- Hensley, S.; Munjy, R.; Rosen, P. (2001). Interferometric synthetic aperture radar (InSAR), in D. F. Maune (Ed.), *Digital Elevation Model Technologies and Applications: The DEM User's Manual*, American Society for Photogrammetry and Remote Sensing, Bethesda, MD, pp. 143–206.
- Johnson, D.J.; Sigmundsson, F.; Delaney, P.T. (2000). Comment on “Volume of magma accumulation or withdrawal estimated from surface uplift or subsidence, with application to the 1960 collapse of Kīlauea volcano” by P.T. Delaney and D.F. McTigue, *Bull. Volcanol.*, **61**, 491–493.
- Joughin, J. (1995). Estimation of ice-sheet topography and motion using interferometric synthetic aperture radar, Ph.D. thesis, University of Washington, pp. 182.
- Kwoun, O.; Lu, Z.; Neal, C.; Wicks, C. (2006). Quiescent deformation of the Aniakchak Caldera, Alaska, mapped by InSAR, *Geology*, **34**, 5–8.
- Larsen, J.; Webley, P.; Freymueller, J.; Haney, M.; McNutt, S.; Scheider, D.; Prejean, S. (2009). Eruption of Alaska volcano breaks historic pattern, *EOS, Transactions American Geophysical Union*, **90**(20), 173–174.
- Li, F.K.; Goldstein, R.M. (1990). Studies of multibaseline spaceborne interferometric synthetic aperture radars, *IEEE Trans. Geosci. Remote Sensing*, **28**, 88–96.

- Lu, Z.; Freymueller, J. (1998). Synthetic aperture radar interferometry coherence analysis over Katmai volcano group, Alaska, *J. Geophys. Res.*, **103**, 29887–29894.
- Lu, Z.; Dzurisin, D. (2014). *InSAR Imaging of Aleutian Volcanoes: Monitoring a Volcanic Arc from Space*, Springer/Praxis, Heidelberg, Germany/Chichester, U.K., 388 pp.
- Lu, Z.; Fatland, R.; Wyss, M.; Li, S.; Eichelberger, J.; Dean, K.; Freymueller, J. (1997). Deformation of New Trident volcano measured by ERS-1 SAR interferometry, Katmai National Park, Alaska, *Geophys. Res. Lett.*, **24**, 695–698.
- Lu, Z.; Mann, D.; Freymueller, J. (1998). Satellite radar interferometry measures deformation at Okmok volcano, *EOS, Trans. Am. Geophys. Union*, **79**, 461–468.
- Lu, Z.; Wicks, C.; Power, J.; Dzurisin, D. (2000a). Ground deformation associated with the March 1996 earthquake swarm at Akutan volcano, Alaska, revealed by satellite radar interferometry, *J. Geophys. Res.*, **105**, 21483–21496.
- Lu, Z.; Wicks, C.; Dzurisin, D.; Thatcher, W.; Freymueller, J.; McNutt, S.; Mann, D. (2000b). Aseismic inflation of Westdahl volcano, Alaska, revealed by satellite radar interferometry, *Geophys. Res. Lett.*, **27**, 1567–1570.
- Lu, Z.; Mann, D.; Freymueller, J.; Meyer, D. (2000c). Synthetic aperture radar interferometry of Okmok volcano, Alaska: Radar observations, *J. Geophys. Res.*, **105**, 10791–10806.
- Lu, Z.; Masterlark, T.; Power, J.; Dzurisin, D.; Wicks, C. (2002a). Subsidence at Kiska volcano, Western Aleutians, detected by satellite radar interferometry, *Geophys. Res. Lett.*, **29**(18), 1855, doi: 10.1029/2002GL014948.
- Lu, Z.; Wicks, C.; Dzurisin, D.; Power, J.; Moran, S.; Thatcher, W. (2002b). Magmatic inflation at a dormant stratovolcano: 1996–98 activity at Mount Peulik Volcano, Alaska, revealed by satellite radar interferometry, *J. Geophys. Res.*, **107**(B7), 2134, doi: 10.1029/2001JB000471.
- Lu, Z.; Power, J.; McConnell, V.; Wicks, C.; Dzurisin, D. (2002c). Pre-eruptive inflation and surface interferometric coherence characteristics revealed by satellite radar interferometry at Makushin Volcano, Alaska: 1993–2000, *J. Geophys. Res.*, **107**(B11), 2266, doi: 10.1029/2001JB000970.
- Lu, Z.; Wicks, C.; Dzurisin, D.; Power, J.; Thatcher, W.; Masterlark, T. (2003a). Interferometric synthetic aperture radar studies of Alaska volcanoes, *Earth Observation Magazine (EOM)*, **12**(3), 8–18.
- Lu, Z.; Masterlark, T.; Dzurisin, D.; Rykhus, R.; Wicks, C. (2003b). Magma supply dynamics at Westdahl Volcano, Alaska, modeled from satellite radar interferometry, *J. Geophys. Res.*, **108**(B7), 2354, doi: 10.1029/2002JB002311.
- Lu, Z.; Fielding, E.; Patrick, M.; Trautwein, C. (2003c). Estimating lava volume by precision combination of multiple baseline spaceborne and airborne interferometric synthetic aperture radar: The 1997 eruption of Okmok Volcano, Alaska, *IEEE Trans. Geosci. Remote Sensing*, **41**(6), 1428–1436.
- Lu, Z.; Rykhus, R.; Masterlark, T.; Dean, K. (2004). Mapping recent lava flows at Westdahl volcano, Alaska, using radar and optical satellite imagery, *Remote Sensing of Environment*, **91**, 345–353.
- Lu, Z.; Masterlark, T.; Dzurisin, D. (2005a). Interferometric Synthetic Aperture Radar (InSAR) study of Okmok Volcano, Alaska, 1992–2003: Magma supply dynamics and post-placement lava flow deformation, *J. Geophys. Res.*, **110**, B02403, doi: 10.1029/2004JB003148.
- Lu, Z.; Wicks, C.; Kwoun, O.; Power, J.; Dzurisin, D. (2005b). Surface deformation associated with the March 1996 earthquake swarm at Akutan Island, Alaska, revealed by C-band ERS and L-band JERS radar interferometry, *Can. J. Remote Sensing*, **31**, 7–20.
- Mann, D.; Freymueller, J. (2003). Volcanic and tectonic deformation on Unimak Island in the Aleutian Arc, Alaska, *J. Geophys. Res.*, **108**(B2), 2108, doi: 10.1029/2002JB001925.
- Massmann, F.H. (1995). *Information for ERS PRL/PRC Users*, Technical Note, GeoForschungsZentrum, Potsdam, Germany.
- Massonnet, D.; Feigl, K. (1998). Radar interferometry and its application to changes in the Earth's surface, *Rev. Geophys.*, **36**, 441–500.
- Massonnet, D.; Rossi, M.; Carmona, C.; Adragna, F.; Peltzer, G.; Feigl, K.; Rabaute, T. (1993). The displacement field of the Landers earthquake mapped by radar interferometry, *Nature*, **364**, 138–142.
- Massonnet, D.; Briole, P.; Arnaud, A. (1995). Deflation of Mount Etna monitored by spaceborne radar interferometry, *Nature*, **375**, 567–570.
- Miller, T.M.; McGimsey, R.G.; Richter, D.H.; Riehle, J.R.; Nye, C.J.; Yount, M.E.; Dumoulin, J.A. (1998). *Catalog of the Historically Active Volcanoes of Alaska*, USGS Open-File Report 98-582, U.S. Geological Survey, Reston, VA.
- Miyagi, Y.; Freymueller, J.T.; Kimata, F.; Sato, T.; Mann, D. (2004). Surface deformation caused by shallow magmatic activity at Okmok Volcano, Alaska, detected by GPS campaigns 2000–2002, *Earth Planets and Space*, **56**, e29–e32.
- Mogi, K. (1958). Relations between the eruptions of various volcanoes and the deformation of the ground surface around them, *Bull. Earthquake Res. Inst. Univ. Tokyo*, **36**, 99–134.
- Moran, S.; Kwoun, O.; Masterlark, T.; Lu, Z. (2006). On the absence of deformation signals from InSAR interferograms bracketing the 1995–1996 and 1999

- eruptions of Shishaldin Volcano, Alaska, *J. Volcanol. Geothermal Res.*, **150**, 119–131.
- Okada, Y. (1985) Surface deformation due to shear and tensile faults in a half-space, *Bull. Seismol. Society Am.*, **75**, 1135–1154.
- Press, W.; Teukolsky, S.; Vetterling, W.; Flannery, B. (1992). *Numerical Recipes in C: The Art of Scientific Computing*, Cambridge University Press, Cambridge, U.K., 994 pp.
- Pritchard, M.; Simons, M. (2004). Surveying volcanic arcs with satellite radar interferometry: The central Andes, Kamchatka, and beyond, *Geological Society of America (GSA) Today*, **14**(8), 4–11.
- Richter, D.H.; Waythomas, C.F.; McGimsey, R.G.; Stelling, P.L. (1998). *Geologic Map of Akutan Island, Alaska*, USGS Open-File Report 98-135, U.S. Geological Survey, Reston, VA.
- Rodriguez, E.; Martin, J.M. (1992). Theory and design of interferometric synthetic aperture radars, *Proc. IEEE*, **139**, 147–159.
- Rosen, P.; Hensley, S.; Zebker, H.; Webb, F.H.; Fielding, E.J. (1996). Surface deformation and coherence measurements of Kīlauea volcano, Hawaii, from SIR-C radar interferometry, *J. Geophys. Res.*, **101**, 23109–23125.
- Rosen, P.; Hensley, S.; Joughin, I.R.; Li, F.K.; Madsen, S.N.; Rodriguez, E.; Goldstein, R.M. (2000). Synthetic aperture radar interferometry, *Proc. IEEE*, **88**, 333–380.
- Rubin, A.M. (1992). Dike-induced faulting and graben subsidence in the volcanic rift zones. *J. Geophys. Res.*, **97**, 1839–1858.
- Scharroo, R.; Visser, P. (1998). Precise orbit determination and gravity field improvement for the ERS satellites, *J. Geophys. Res.*, **103**(C4), 8113–8127.
- Sibson, R. (1982). Fault zone models, heat flow, and the depth distribution of seismicity in the continental crust of the United States, *Bull. Seismol. Society Am.*, **72**, 151–163.
- Williams, C.A.; Wadge, G. (1998). The effects of topography on magma chamber deformation models: Application to Mt. Etna and radar interferometry, *Geophys. Res. Lett.*, **25**, 1549–1552.
- Yang, X.-M.; Davis, P.M.; Dieterich, J.H. (1988). Deformation from inflation of a dipping finite prolate spheroid in an elastic half-space as a model for volcanic stressing, *J. Geophys. Res.*, **93**, 4249–4257.
- Zebker, H.A.; Villasenor, J. (1992). Decorrelation in interferometric radar echoes, *IEEE Trans. Geosci. Remote Sensing*, **30**, 950–959.
- Zebker, H.A.; Madsen, S.N.; Martin, J.; Wheeler, K.B.; Miller, T.; Yunling Lou; Alberti, G.; Vetrilla, S.; Cucci, A. (1992). The TOPSAR interferometric radar topographic mapping instrument, *IEEE Trans. Geosci. Remote Sensing*, **30**, 933–940.
- Zebker, H.A.; Rosen, P.A.; Goldstein, R.M.; Gabriel, A.; Werner, C.L. (1994). On the derivation of coseismic displacement fields using differential radar interferometry: The Landers earthquake, *J. Geophys. Res.*, **99**, 19617–19634.
- Zebker, H.; Rosen, P.; Hensley, S. (1997). Atmospheric effects in interferometric synthetic aperture radar surface deformation and topographic maps, *J. Geophys. Res.*, **102**, 7547–7563.
- Zebker, H.; Amelung, F.; Jonsson, S. (2000). Remote sensing of volcano surface and internal processes using radar interferometry, in P.J. Mouginiis-Mark, J.A. Crisp, and J.H. Fink (Eds.), *Remote Sensing of Active Volcanism* (AGU Monograph), American Geophysical Union, Washington, D.C., pp. 179–205.

An overview of satellite monitoring of volcanoes

Kenneson G. Dean, Jeff Osiensky, Evgenii Gordeev, Sergey Senyukov, Alexander V. Rybin, Yury V. Karagusov, Nikolay S. Terentyev, Vyacheslav B. Guryanov

9.1 INTRODUCTION

9.1.1 Why use satellite data to monitor volcanoes

The North Pacific region is remote and vast (5,000 by 2,000 km), and includes several hundred volcanoes in Kamchatka, the Kurile Islands, Alaska, and the northwestern U.S.A. (Figure 9.1). Within this region, approximately 100 volcanoes are considered active (the exact count depends upon how the term is defined) with an almost daily occurrence of some level of activity, including emission of ash and gas resulting in a volcanic cloud, effusion of lava domes, lava flows, pyroclastic flows, and debris flows. These processes result in elevated temperatures at the volcano (thermal anomalies), distinct signatures from airborne volcanic ash and gas resulting in a volcanic cloud, or distinct changes in landforms, all of which can be detected by satellite data. Many eruptions are explosive and capable of sending ash clouds many kilometers vertically and dispersing many thousands of kilometers downwind. Satellite data provide a synoptic view that covers this vast region and are able to detect or track these clouds.

Most of the volcanoes in the region are difficult and expensive to access, and field work is often limited to the summer season at these northern latitudes. In addition, transmission of data from ground-based instruments and voice communication is limited. Satellite data do not have these geographic, seasonal, or infrastructure limitations,

although the coverage is episodic within a 24-hour period. For these reasons, satellite data are an excellent source of information for monitoring volcanic activity in the Northern Pacific region and supplement other geophysical techniques. The Alaska Volcano Observatory (AVO) was the first U.S. observatory where remote sensing is used as a daily, routine monitoring tool due to geography, logistics, expense, and eruption styles and frequency in the region.

The large number of volcanoes and high frequency of activity are hazardous to communities in the region. The Kamchatka Peninsula, the northern Kurile Islands, and the Aleutians are historically the most active areas but have relatively low population densities. The northwestern U.S.A. (Washington and Oregon) has a low frequency of activity but eruptions from these volcanoes pose a greater threat due to the higher population density and the large number of cultural centers near the volcanoes.

Explosive eruptions from volcanoes in this region also pose a serious threat to domestic and international transportation and commerce. These volcanoes have some form of eruptive activity almost monthly that can eject ash to low or high altitudes, which can damage or destroy jet aircraft engines or airframes, either during landing and takeoff or at high altitude. Airfreight is a primary source of commerce in the region, and access to local airports is crucial. Moreover, the North Pacific is a major global air traffic route (Figure 9.1). In 1999, an estimated 200 flights carrying

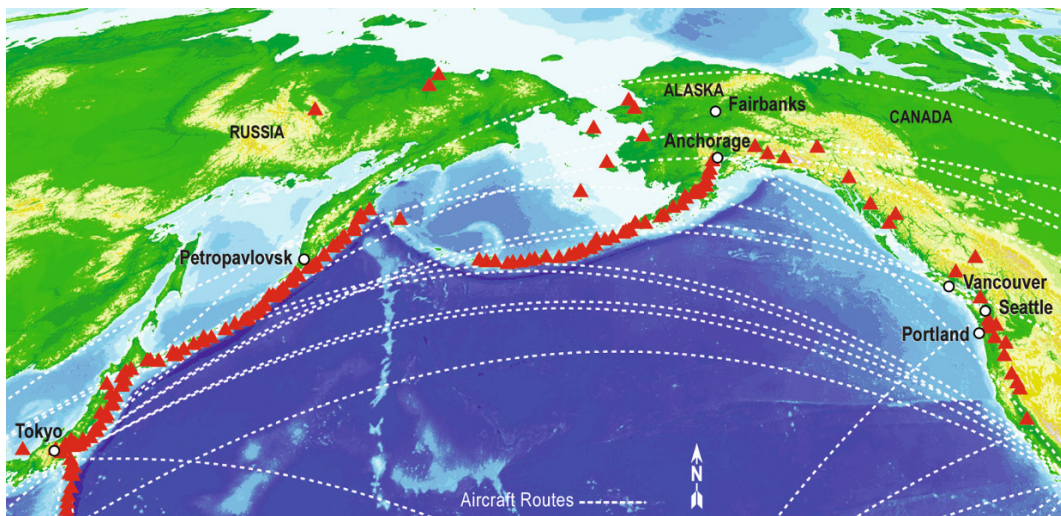


Figure 9.1. Location diagram of the North Pacific region. Major cities, volcanoes, and selected air traffic routes are shown (Casadevall *et al.*, 1999). Historically active volcanoes are located on the Kamchatka Peninsula, Alaska, and the northwestern U.S.A. The predominant wind direction is to the east which transports volcanic clouds across the Pacific Ocean into air traffic routes and over North America.

20,000 passengers and more than 12 million pounds of cargo per day transited this region. More recent estimates suggest this daily average is now over 200 flights per day (2007, pers. commun., G. Ferguson, FAA). In addition, the predominant winds are from the west and erupted volcanic ash from volcanoes in the region can be transported into heavily populated areas in North America as shown by the eruption of Mt. Spurr, Alaska (Schneider *et al.*, 1995).

9.1.2 Types of satellite monitoring

The purpose of monitoring volcanoes is to detect and analyze data that indicate current or possible eruptive activity, and inform agencies and the public of the potential hazard. Satellite monitoring can be short term or long term. Short-term monitoring uses data that are recorded multiple times per day and detects changes in volcanic activity over a relatively short time interval, hours to days. Volcanic activity observed in these data includes sudden increases in ground temperature, and flowage or the presence of volcanic clouds or ash deposits. To provide warnings of eruptions these data must be received, recorded, processed, and analyzed immediately after a satellite pass. Short-term monitoring is often referred to as operational monitoring, and data received immediately after they are recorded are referred to as near-real time data. True

real-time satellite monitoring is not possible due to processing delays inherent in the system. This chapter is primarily focused on short-term monitoring operations and analysis at AVO and sister observatories in Kamchatka and the Kurile Islands, Russia.

Long-term monitoring utilizes data that record volcanic activity over a longer period of time (e.g., monthly or annually). Long-term observations, such as increased deformation or thermal flux, may indicate that short-term monitoring frequency should be increased. Long-term data are also used to define background trends, which can then be used for comparison with short-term analysis. Typically, high spatial resolution data are required, but the frequency of data coverage is lower, weekly to monthly.

9.2 BACKGROUND

One of the reasons for monitoring explosive eruptions is their potential for serious impact on aircraft. Well over 20 aircraft have encountered airborne volcanic ash in the North Pacific region since 1953. The severity of these encounters include contamination of air handling systems and fluids, exterior and engine abrasion, frosting or breaking of windows, engine damage, and temporary engine failure. The most serious incident in the region

occurred in 1989 when KLM Flight 867, a 747 jet aircraft, traveling from Amsterdam to Tokyo, encountered ash from the eruption of Redoubt Volcano. The plane flew into ash at an altitude of approximately 7.5 km (25,000 ft) above south central Alaska near Anchorage. The plane climbed to 8.5 km (27,900 ft) trying to escape the ash when all four engines failed. It then glided without power and descended to 4 km (13,300 ft) before the pilots were able to restart all four engines and make an emergency landing at Anchorage International Airport. The plane was within 0.6 km (2,300 ft) of the highest peaks in the area or 1 or 2 min from impact (Zygmunt and Casadevall, 1994; Casadevall, 1994; Miller and Casadevall, 2000) (see DVD for animation and the voice recording of this incident).

Satellite-based monitoring of volcanoes focuses on two primary phenomena: thermal anomalies before, during, and after eruptions, and volcanic clouds produced by eruptions. Recent studies of the thermal characteristics of volcanoes using satellite data have demonstrated the utility of thermal monitoring in detecting unrest (Francis and Rothery, 1987; Harris *et al.*, 1997a, b, 1999; Harris and Thornber, 1999; Harris *et al.*, 2000). Ground temperature and heat flux have been calculated for a target volcano and a model developed to automatically detect hot ground (Higgins and Harris, 1997). Techniques to estimate changes in thermal energy using assumed parameters, such as physical properties of the rocks, volcano geometry, satellite calibration, known atmospheric conditions, and physical constants, have also been developed (Harris *et al.*, 2000). These studies primarily concentrated on mafic volcanoes, with relatively constant flux of hot material such as lava lakes and flows. For daily near-real time monitoring of volcanoes in the North Pacific, many of these inputs are more complex and often not available due to variability of the types of volcanism and environmental conditions. In these cases, relative change is important, and understanding the long-term variability of thermal anomalies for individual volcanoes provides the basis for detecting small changes that may presage an eruption.

Image data from the Geostationary Operational Environmental Satellite (GOES) imager, Advanced Very High Resolution Radiometer (AVHRR) sensor, and the Moderate Resolution Imaging Spectroradiometer (MODIS) sensor are the primary satellite platforms used to detect and monitor volcanic clouds (Kienle *et al.*, 1990; Schneider *et al.*, 1995, 2000; Dean *et al.*, 1998; Carn

and Oppenheimer, 2000; Hufford *et al.*, 2000). Volcanic clouds consist of ash and gas emitted by the volcano which, if connected to the volcano, is often referred to as a plume. Ash in volcanic clouds can be detected by subtracting or ratioing longwave thermal infrared bands, referred to as the split-window technique (Prata, 1989; Holasek and Rose, 1991). Volcanic sulfur dioxide has been detected using the Total Ozone Mapping Spectrometer (TOMS) sensor (Bluth *et al.*, 1995; Schneider *et al.*, 1999) and more recently with the Ozone Monitoring Instrument (OMI) (Chahine *et al.*, 2006; Carn *et al.*, 2009). Dispersion models are used to predict the movement of airborne ash and SO₂ (Heffter and Stunder, 1993; Servranckx *et al.*, 1996; Searcy *et al.*, 1998). Techniques have been developed to retrieve the sizes and total masses of ash particles in volcanic clouds (Wen and Rose, 1994). However, not all of the detection techniques are 100% successful (Simpson *et al.*, 2000).

Success of the different techniques is often a result of the availability of data with appropriate temporal, spatial, and spectral resolutions to detect eruptions or increased activity that may lead to an explosive event. Temporal resolution is a measure of how frequently the volcano can be observed. The required temporal resolution depends upon the rate of change of the process to be monitored. Ideally, volcanoes should be viewed every few minutes to detect the start of an eruption and monitor its progress. Presently, satellites with the highest temporal resolution are geostationary which means they remain above the same equatorial location on Earth at all times (Sabins, 1997). GOES and Multi-Functional Transport Satellite (MTSAT) are examples of geostationary satellites and record images every 0.25 to 0.5 h depending upon wavelength. However, geostationary satellites view high latitudes obliquely, distorting pixels thereby reducing the spatial resolution. To offset this oblique view, data from polar-orbiting satellites are used in conjunction with data from GOES and MTSAT. Swaths of data from the AVHRR and MODIS sensors on polar-orbiting satellites overlap due to converging satellite orbits which increases temporal resolution from 12 h at the equator to a couple of hours near the poles per satellite (Mouginis-Mark and Domergue-Schmidt, 2000).

Spatial resolution is a measure of a sensor's ability to detect closely spaced objects (Sabins, 1997) and will hereafter be referred to as pixel size for satellite images. Commercially available data have pixels that range in size from <1 m to

kilometers. Data with 1 km pixels have successfully detected thermal anomalies and volcanic clouds during various stages of activity or eruptions. Higher spatial resolution data would improve the detection of subtle increases in thermal flux; however, sensors with high spatial resolution have low temporal resolution (Mouginis-Mark and Domergue-Schmidt, 2000). At this time, sensors on multiple polar-orbiting satellites (AVHRR and MODIS) provide a 1.1 km resolution.

Spectral resolution is a measure of the wavelength range within the electromagnetic spectrum detected by the sensor. The spectrum is segmented into wavelength intervals called bands. A sensor that records a large number of bands with each band recording a relatively narrow spectral range is considered to have high spectral resolution. Of the satellite sensors used for daily volcano monitoring, MODIS has the highest spectral resolution with 36 bands. Another important consideration is the portion of the electromagnetic spectrum detected by the sensor. The wavelength regions and designations discussed in this chapter are

- visible (VIS: 0.4–0.7 μm);
- near-infrared (NIR 0.7–1.3 μm);
- shortwave infrared (SWIR: 1.3–3.0 μm);
- mid-infrared (MIR 3.0–8.0 μm);
- thermal infrared (TIR: 8.0–14 μm).

These wavelengths detect volcanic cloud components including ash, water vapor, and other gases, surface and cloud temperatures, and surface landforms/deposits such as lava flows, ash falls, and lahars (see Chapters 2, 3, 4, 5, and 6).

9.2.1 History of satellite volcano monitoring in the North Pacific region

The use of satellite data by AVO to routinely monitor and analyze eruptions started in 1989 with the eruption of Redoubt Volcano (Dean *et al.*, 1990, 1994). Development of the monitoring system was driven by a need to detect activity at volcanoes that were not monitored with other instruments, verify volcanic activity at the Earth's surface suggested by other instrumental data, and detect and track airborne ash and gas. The story of this development parallels the evolution of satellite sensors, processing speed, electronic communication, and advances in data acquisition and processing techniques.

During the eruption of Redoubt Volcano from 1989 to 1990, AVHRR images were requested from the NOAA National Environmental Satellite Data and Information Services (NESDIS) Command and Data Acquisition Station at Gilmore Creek, Alaska whenever an explosive event occurred. This response was reactive as opposed to proactive. Eight-bit data were limited to three bands at the visible and IR wavelengths, and analysis was mostly limited to single-band volcanic cloud detection and location. The results from the analysis were faxed to others in AVO who consolidated information from various detection systems and shared this information with other agencies. It took 7 h to acquire, process, and distribute these data. This data acquisition and analysis scenario was acceptable for response to events such as the *Exxon Valdez* oil spill (Stringer *et al.*, 1992) where significant changes in hazardous conditions were relatively slow, on the order of a day, but were found to be unacceptable for volcanic eruptions where conditions changed subhourly.

To shorten the response time, in January 1990 a system to access satellite data was developed using a Domestic Communication Satellite (DOMSAT) receiving station at the University of Miami. When eruptions occurred, the DOMSAT station was notified by telephone and data from successive passes were acquired and processed at the University of Miami, then downloaded and analyzed by AVO at the University of Alaska Fairbanks (UAF). The Miami station data provided all five image bands available in AVHRR data. Unlike the Gilmore images, these were geometrically corrected, radiometrically calibrated, and had embedded coastlines for geographic reference. These basic data-processing refinements were critical improvements for analysis capabilities as they now allowed temperature measurements, more accurate volcanic cloud location and size estimates, and response time was reduced to 1 h after a satellite pass. Previously, images were faxed to AVO but, by the end of the Redoubt eruptions, electronic sharing of data via ftp (file transfer protocol) was common. In 1993, UAF acquired an AVHRR receiving station and provided data directly to AVO. This station significantly increased the number of passes acquired, provided capabilities to do more advanced processing such as mathematical analysis of multiband data, and reduced the eruption response time to minutes after a satellite pass under ideal conditions. Thus, from 1993 AVO satellite-monitoring methods became proactive (i.e., volcanoes were observed

daily to search for volcanic activity). Access to GOES data via computer networks began in 1997 which increased the temporal resolution by providing continuous observations every half-hour in IR bands, but at low spatial and spectral resolutions. MODIS data were incorporated into the system in 2001 through an additional receiving station at UAF. The high spectral resolution of the MODIS data further enhanced volcano monitoring and analysis capabilities.

As our understanding of eruption processes and their appearance in satellite data improved, the need for high spatial resolution data to detect more subtle activity such as phreatic explosions, increases in thermal flux and degassing, and identification of the processes behind the volcanic signatures observed in coarse (~ 1 km) satellite data, became apparent. Webcams became a key supplement to satellite data at several volcanoes after they started to be installed in approximately 2003. More importantly, timely access to high spatial resolution satellite data was developed. In 2005, a system was implemented that automatically requests ASTER data based on increased volcanic activity. The data requests alert analysts at the U.S. Geological Survey (USGS) EROS Data Center to schedule coverage, and data are received by AVO within days as opposed to weeks previously. Most recently, Multifunctional Transport Satellite (MTSAT) data became available in 2006 which provide high temporal observations of the Kamchatka region and Kurile Islands.

9.3 SATELLITE SENSORS AND DATA

Currently, daily volcano monitoring for the North Pacific uses data from the following sensors: GOES imager, AVHRR, and MODIS on the Terra and Aqua satellites. These data are recorded multiple times each day providing frequent looks at the volcanoes. Each data swath covers large geographic areas which is helpful in detecting drifting volcanic clouds, at suitable wavelengths and spatial resolution (although perhaps not optimum) to detect thermal anomalies, volcanic clouds, and large changes in surface characteristics that may reflect new volcanic deposits. These data are acquired directly from the satellite as it passes within sight of receiving stations (i.e., direct broadcast), and have no restrictions in their use and distribution, which is important for a volcano-monitoring program where information and data need to be shared.

The sensor characteristics of these satellites are shown in Tables 9.1 and 9.2.

GOES and MTSAT record images in the visible, NIR, MIR, and TIR wavelengths (Table 9.1) with a full or partial view of the Earth. The large field of view provides coverage across two sectors: Kamchatka and the Kurile Islands (GOES-9, pre 2006; MTSAT, starting in 2006) and the west coast of North America (GOES-10). Images from these satellites are recorded every 0.25 h in visible bands and every 0.5 h in TIR bands, with 1 and 4 km spatial resolution at nadir, respectively. The primary strengths of GOES and MTSAT data are their high temporal resolution and large field of view, making them ideal to detect volcanic clouds. Unfortunately, pixels at high latitudes are badly distorted due to the sensors' oblique view of polar regions, which results in larger pixels compared with those at the equator (nadir view). These distorted pixels are 7.5 km N-S and 4.5 km E-W in thermal infrared channels at 60° N latitude. Hence, the area of hot ground required to illuminate a pixel that could clearly be distinguished from the background in most cases would have to be over 10 times larger than that needed for AVHRR in the MIR (3–5 μ m wavelength bands). These data would not be good at detecting small (~ 100 m²) thermal anomalies as precursor signals to explosive events. GOES and MTSAT data have been shown to be good at detecting volcanic clouds that produce a recognizable split-window signal (e.g., $\leq 2^\circ$ C) in several pixels (e.g., ≥ 35 km²) (Schneider *et al.*, 1995, 2000; Dean *et al.*, 2004; Tupper *et al.*, 2004). However, the MTSAT IR channels are badly calibrated, meaning that their effectiveness for ash detection has decreased (Tokuno, 2000; Tupper *et al.*, 2004). A detailed description of GOES and MTSAT can be found at their NOAA and Japan Meteorological Agency (JMA) websites.

The AVHRR sensors on NOAA polar-orbiting satellites record data in the visible, NIR, MIR, and TIR wavelengths (Table 9.1). These data have a swath width of approximately 3,000 km with a spatial resolution of 1.1 km at nadir, but pixels increase in size away from nadir, especially near the edges of each swath (Kidwell, 1998). Data are recorded of the same area once every 12 h per satellite at the equator but at high latitudes the orbits converge, resulting in considerable overlap between swaths, increasing temporal resolution. The time interval between passes may vary from minutes to hours depending on satellite orbits. Small and large volcanic clouds and thermal anomalies are easily

Table 9.1. Characteristics of the GOES imager, AVHRR, and MTSAT MVIRI sensors used for daily monitoring in the North Pacific region. Critical spectral bands used in routine volcano monitoring are in bold.

<i>Satellite/Sensor</i>	<i>Spectral bands (mm)</i>	<i>Pixel size, nadir</i>	<i>Scenes per day</i>	<i>Satellites and coverage</i>	<i>Applications</i>	
GOES/Imager	1 VIS 0.52– 0.72	1–4 km (at 60°N)	48–96	GOES-9 (Kamchatka) GOES-10 and 11 (Alaska and Cascades)	Volcanic clouds	
	2 MIR 3.78– 4.03				2–8 km (at 60°N)	
	3 TIR 6.74– 7.02					Thermal anomalies and volcanic clouds
	4 TIR 10.20–11.20 5 TIR 11.50–12.50					
NOAA/AVHRR	1 VIS 0.58–0.68	1.1 km	20	NOAA-15, 16, 17, 18, 19 (North Pacific)	Volcanic clouds	
	2 NIR –0.73–1.10					
	3 MIR 3.55–3.93					Thermal anomalies
	4 TIR 10.50–11.50 5 TIR 11.50–12.50					Volcanic clouds
MTSAT/MVIRI	1 VIS 0.55– 0.90	1–4 km or 2–8 km (at 60°N)	48 – 96	MTSAT-1 (Kamchatka, Kuriles)	Thermal anomalies and volcanic clouds	
	2 TIR 10.30–11.30					
	3 TIR 11.50–12.50				Volcanic clouds	
	4 MIR 6.50– 7.00					
	5 MIR 3.50– 4.00					

detected in these data. The primary strengths of AVHRR data are their spatial resolution, relatively large field of view, and the large number of passes acquired by multiple satellites, making them the most important data source for volcano monitoring in this region. Their temporal resolution, however, is less than that of geostationary data. A detailed description of AVHRR satellites can be found at NOAA websites.

The MODIS sensors on NASA's Terra and Aqua satellites have the best spectral resolution of the sensors currently used for daily volcano monitoring with data recorded in the visible, NIR, SWIR, MIR, and TIR wavelengths. These polar-orbiting satellites record data with swath widths and lengths similar to the AVHRR sensor, but with 250, 500, and 1,000 m pixel sizes, depending upon wavelengths (Table 9.2). These data are recorded for the same area once every 12 h per satellite at the equator but again, due to orbital convergence near the poles, there is considerable overlap of swaths, which significantly increases repetitive looks at high-latitude volcanoes. As with AVHRR data, small and large volcanic clouds and thermal anomalies are easily detected. Due to the high spec-

tral, radiometric, and spatial resolution relative to GOES and AVHRR data, and geometric accuracy of MODIS data, much more sophisticated analyses can be performed, such as improved automated eruption detection algorithms (Wright *et al.*, 2004; Pavlonis *et al.*, 2006), detection of SO₂ volcanic clouds (Realmuto *et al.*, 1994, 1997; Watson *et al.*, 2004), studies of volcanic cloud composition and structure, and better derivation of thermal flux and effusive rates (Dehn *et al.*, 2000, 2002; Harris *et al.*, 2000; Dean *et al.*, 2002). The primary strengths of MODIS data are their high spatial resolution and geometric accuracy, and the large number of spectral bands. Their weakness is low temporal resolution (fewer repeat looks at volcanoes in a given day) compared with GOES and AVHRR. A detailed description of MODIS can be found at NASA websites.

9.4 ACQUISITION OF SATELLITE DATA IN ALASKA AND RUSSIA

Data from NOAA AVHRR and/or NASA MODIS polar-orbiting satellites are received as direct

Table 9.2. Characteristics of the MODIS sensor used for daily monitoring in the North Pacific region. Critical spectral bands used in routine volcano monitoring are in bold.

<i>Satellite/Sensor</i>	<i>Spectral bands (mm)</i>	<i>Pixel size, nadir</i>	<i>Scenes per day</i>	<i>Satellites and coverage</i>	<i>Applications</i>
Terra and Aqua/ MODIS	1 VIS 0.62–0.67 2 VIS 0.84–0.88	250 m	12	Terra and Aqua (North Pacific)	Volcanic clouds, deposits, and landforms
	3 VIS 0.46–0.48 4 VIS 0.55–0.57 5 NIR 1.23–1.25 6 SWIR 1.63–1.65	500 m			
	7 SWIR 2.11–2.16				
	8 VIS 0.41–0.42 9 VIS 0.44–0.45 10 VIS 0.48–0.49 11 VIS 0.53–0.54 12 VIS 0.55–0.56 13 VIS 0.66–0.67 14 VIS 0.67–0.68 15 NIR 0.74–0.75 16 NIR 0.86–0.88 17 NIR 0.89–0.92 18 NIR 0.93–0.94 19 NIR 0.92–0.97	1,000 m			Volcanic clouds, deposits
	20 MIR 3.66–3.84 21 MIR 3.93–3.99 22 MIR 3.93–3.99 23 MIR 4.02–4.08 24 MIR 4.43–4.50				Deposits, thermal anomalies
	25 MIR 4.48–4.55 26 SWIR 1.36–1.39 27 MIR 6.54–6.90				
	28 MIR 7.18–7.48 29 TIR 8.40–8.70 30 TIR 9.58–9.88 31 TIR 10.78–11.28 32 TIR 11.77–12.27				Volcanic clouds and gases
	33 TIR 13.19–13.49 34 TIR 13.49–13.79 35 FIR 13.79–14.09 36 FIR 14.09–14.39				

downlinks by stations at the University of Alaska, Fairbanks, Alaska (UAF), the Center of Communication and Monitoring, Petropavlovsk, Kamchatka, Russia (KCCM), and the DalInforGeoCenter of the Ministry of Natural Resources (DMNR), Yuzhno-Sakhalinsk, Sakhalin Island, Russia. The UAF stations were built by SeaSpace, U.S.A. The KCCM station was built

by Smartrack, France. The DMNR station was built by ScanEx at the Research and Development Center, Moscow. Each of these stations has its own native format which complicates the sharing of data and algorithms. NOAA AVHRR data are also received from the NOAA Fairbanks Command & Data Acquisition Station, Gilmore Creek, Alaska (near Fairbanks) as a backup to the stations at

UAF. The areal coverage of these stations overlap, providing complete coverage of the region and backup during station failures (Figure 9.2). GOES and MTSAT data are received over computer networks from the Naval Research Laboratory, Monterey, California and NOAA websites (www.ssd.noaa.gov/VAAC/kamchatka.html), respectively.

9.4.1 Data management and analysis: AVO Fairbanks

AVO receives AVHRR and MODIS data from the UAF Geographic Information Network of Alaska (GINA) project which operates and maintains the receiving stations and archives the data. The AVHRR archive starts in 1993 and the MODIS archive starts in 2001. The station mask extends from Greenland in the east, to the Lena River delta (Russia) in the west, and from northern California in the south to just beyond the North Pole in the north (Figure 9.2). The MODIS station mask is a circle approximately 500 km in diameter less than that of AVHRR.

AVHRR data are received from multiple satellites (NOAA-15, 16, 17, 18, and 19 at this time).

MODIS data are received from the Terra and Aqua satellites. The greatest frequency of coverage occurs from passes that cross over or near the receiving station, averaging 10 images per 24 h for the area of Cook Inlet (Figure 9.3). Coverage decreases near the edge of the receiving station mask, averaging four images per 24 h for Kamchatka/Kurile and Cascade volcanoes. The station receives an average of 22 swaths of data per 24 h (Figure 9.3).

GOES data of Alaska and Kamchatka–Kuriles are received from stations outside the North Pacific region. The Alaskan GOES data (presently GOES-10) are received from the Naval Research Laboratory, Monterey, California via computer networks at full radiometric resolution and processed locally within 1 h after a satellite pass. MTSAT data of Kamchatka–Kuriles are accessed via computer networks and are only available as graphic images (e.g., JPEGs). MTSAT data can be viewed at the Anchorage Volcano Ash Advisory Center (VAAC) website.

Once AVHRR and MODIS data are received at AVO, automated processing is performed to expedite volcano monitoring and to decrease the size of data files. Each swath of data is subsectioned to match nine pre-defined sectors (Figure 9.4).

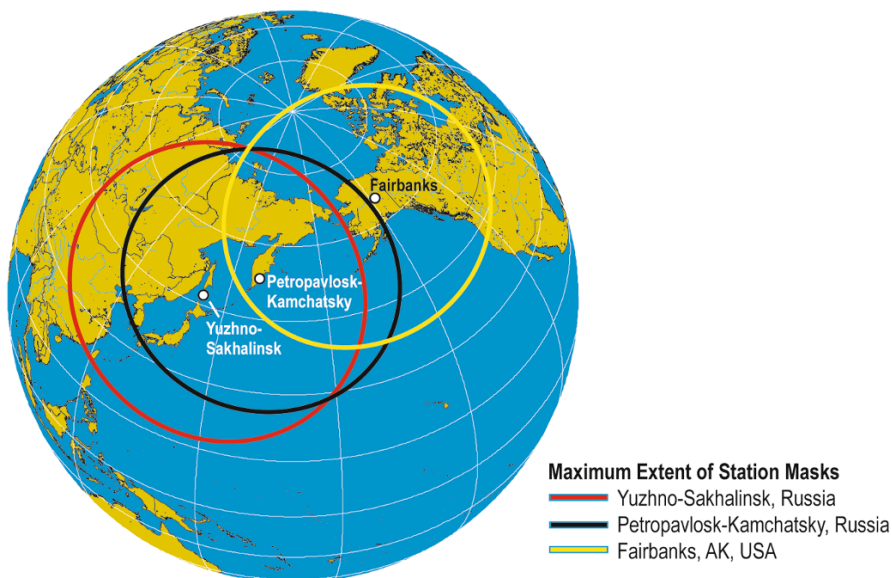


Figure 9.2. The maximum areal extent (station mask) of AVHRR and MODIS data received by stations used for volcano monitoring in the North Pacific region. AVHRR and MODIS data are received by the Yuzhno-Sakhalinsk station. AVHRR data are received by the Petropavlovsk-Kamchatsky station. AVHRR and MODIS data are received by Fairbanks, Alaska stations. The maximum extent of MODIS data is approximately 500 km less than the limits shown.

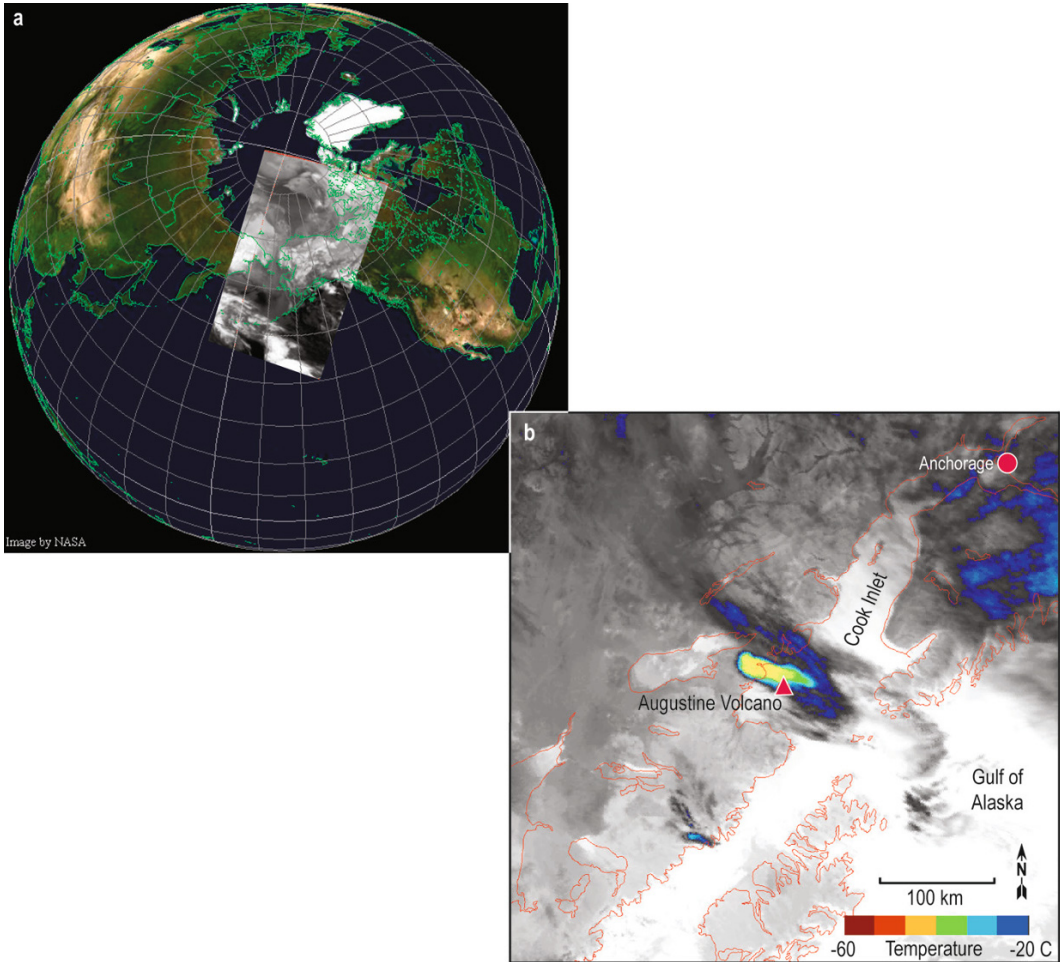


Figure 9.3. A swath of AVHRR data (a) covers $2,000 \times 5,000$ km, and has a typical file size of 100 MB. MODIS data are similar but the file size is 800 MB counting selected bands typically used for monitoring. Subsections, 2.6 or 10.4 MB in size, are extracted from each swath creating a monitoring sector (b) to reduce the file size to be processed and analyzed. This example is the Augustine sector and the image is AVHRR data (n15.06.017.1738), TIR band 4 (10.5 to $11.5 \mu\text{m}$). An opaque plume from an eruption of Augustine Volcano can be seen in the image.

These sectors are 512×512 AVHRR pixels (563×563 km) or $1,024 \times 1,024$ pixels ($1,126 \times 1,126$ km) in size. Each sector is named after a volcano at or near its center. Data for each sector are geometrically corrected and radiometrically calibrated so analysts can locate volcanoes and extract radiance, temperature, and albedo values (Figures 9.5 and 9.6). GIF and JPEG images are generated and sent to a server for remote or web access. This automated processing takes 10 to 20 min (depending upon the size of data files) after the data are

received at the station (Figure 9.6). A web interface (Web Tools) is used to access and view images, webcams, status reports on data ingestion and display, and tables that describe types of volcanic activity that have been reported. Additional processing is done by analysts at workstations, including contrast adjustment, insertion of coastline or volcano location, band manipulations, and reading of pixel temperature values and location (Figures 9.5 and 9.6). Similar processing is done to Alaskan GOES data.

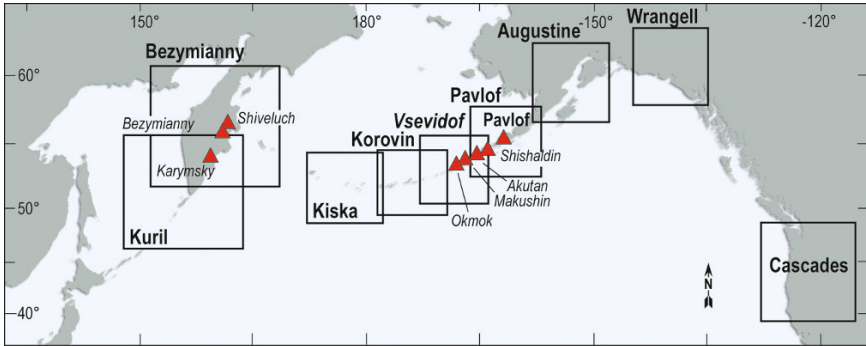


Figure 9.4. Nine sectors have been established containing multiple volcanoes. Only volcanoes discussed in this chapter are shown (red triangles).

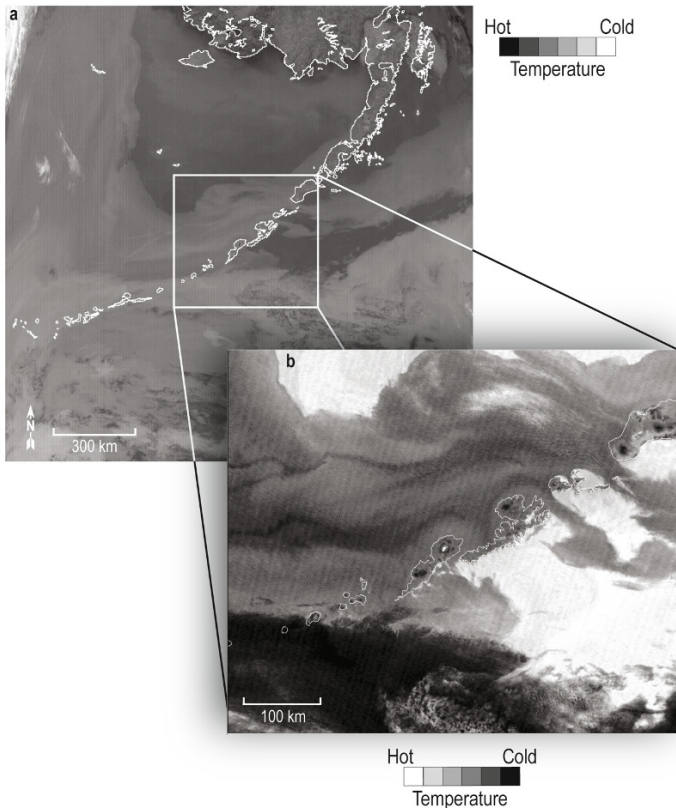


Figure 9.5. A full swath of geometrically and radiometrically uncorrected data (a) is received by AVO and then corrected and subsectioned (b) to facilitate monitoring. In this example, an AVHRR MIR band 3 image of the Vsevidof Sector is shown. Data are further processed by analysts who adjust the contrast, add a coastline, and apply mathematical functions. Manipulation of the sectored images allows analysts to detect critical features such as the thermal anomaly (white) caused by a lava flow at Okmok Volcano at the center of image (b). Small features (e.g., thermal anomalies) are very difficult to detect on the uncorrected swath image (a). In (b) the temperature mapping is reversed, white = hot. The image ID is n14.97.153.1405.

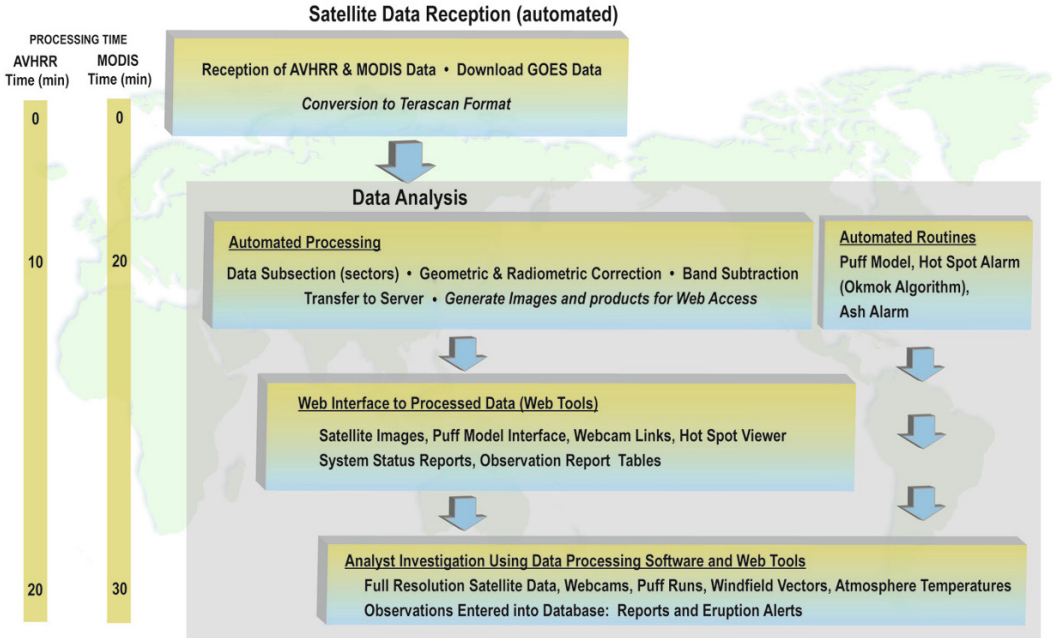


Figure 9.6. Flow chart of AVO data processing and elapsed time from satellite data reception to investigation by analysts. After reception, AVHRR data are available to analysts in approximately 20 min and MODIS in 30 min. MODIS takes longer to process due to the file size.

An increased number of satellite sensors and remote webcams have significantly improved eruption monitoring and analysis capabilities due to better temporal, spatial, and spectral resolution. This has resulted in the detection of thermal anomalies and volcanic clouds that previously were not identified or detected by satellite, such as small explosive events, hot debris flows, fresh ash deposits, and short-lived strombolian and phreatic events. These new and additional sensors have increased data volume and therefore complicated the reporting of activity. In response to these improvements AVO developed a new satellite volcano-monitoring database system to streamline monitoring procedures and to provide consistency in reporting information. This relational database system has been operational since April 2005 at AVO. Previously, a static data-reporting system required five separate steps: data analysis, writing/sending an observation report, manual data entry, and the preparation of both bi-monthly and weekly reports to catalogue activity. Each of these steps was completely independent. The new system has two steps, which may be carried out in parallel: data analysis and data entry. Observations includ-

ing cloud cover conditions and description of volcanic activity (e.g., thermal anomaly and ash cloud signal values, location, size, direction, satellite zenith angle) are entered via a simple web interface (Figures 9.7 and 9.8). The monitoring database requires analysts to record all critical information. There is an option to enter more information and analysis comments. The system then populates the database and automatically generates observation reports as well as tables describing activity as requested. The observation reports describe what the analyst observed in as few words as possible and are distributed throughout AVO.

This new database is a significant improvement over previous systems by ensuring that all entries are consistent and include critical information, thus reducing the time required for monitoring and increasing the standard and quality of reporting. The database has a web-based graphical user interface, simplifies and standardizes contributed information, and automatically ingests some information from the receiving station, such as scene identification numbers, thereby minimizing typing errors, a serious problem in previous systems. The database is fully searchable and used for analysis

Step 3. Report store and send

Base Page	Satellite Observations	Camera Observations	Preview Email	Send and Store
---------------------------	--	-------------------------------------	-------------------------------	--------------------------------

Report is for: AM or PM , yesterday or today

Subject: 9 August 2005 AM satellite report

From: Lovro Valcic <fslv@uaf.edu>

To: avo_ops@eq.giseis.alaska.edu, avo_kvrt@eq.giseis.alaska.edu

AM satellite report for August 9, 2005

SUMMARY:
Thermal anomaly at St. Helens

OBSERVATIONS:
Cleveland (Yellow): Clear at volcano
Spurr (Yellow): Cloudy at volcano
St. Helens (Orange): Clear at volcano
Image a1.05221.1009: mostly clear at volcano, sat zenith angle of 0.8
- ch20b hotspot: 2 anomalous pixels, peak reading of 50.4 C, background of 7 C
Bezymianny (Yellow): Mostly cloudy at volcano
Ebeko (Yellow): Partly cloudy at volcano
Karymsky (Orange): Mostly cloudy at volcano
Kliuchevskoi (Yellow): Mostly cloudy at volcano
Shiveluch (Orange): Mostly cloudy at volcano

CLOUD CONDITIONS:
Wrangells (Wrangell sector): Clear
Cook Inlet (Augustine sector): Cloudy
Alaska Peninsula (Pavlof sector): Mostly Cloudy
Eastern Aleutians (Vsevidof sector): Cloudy
Central Aleutians (Korovin sector): Partly Cloudy
Western Aleutians (Riska sector): Cloudy
Cascades (Cascades sector): Clear
Yellowstone (Yellowstone sector): No Coverage
Kamchatka (Bezymianny sector): Cloudy
Kuriles (Kurile sector): Mostly Clear

LAST IMAGES VIEWED:
AVHRR: 222 03:35 UTC
GOES10: 222 05:30 UTC
GOES9: 222 05:03 UTC
MODIS: 221 23:14 UTC
BezyCam: 222 07:13 UTC
HelensCam: 221 11:56 PDT
KliuCam: 222 07:45 UTC
ShivCam: 222 07:56 UTC
SpurrCam: 221 10:40 ADT
VeniCam: 221 10:18 ADT

Figure 9.8. A report is automatically generated by the database.

Monitoring (KCCM) station acquires AVHRR data that are used by the Kamchatka Branch of the Geophysical Survey (KBGS) of the Russian Academy of Science and the Kamchatka Volcanic Eruption Response Team (KVERT). KCCM automatically posts data at the Internet site <http://www.kccm.ru> (in Russian) in the original format together with preview images and metadata. These data are available online for one month after acquisition and then archived on DVD. GIF images can be acquired at <ftp://emsd.iks.ru/pub/DATA/RTS/Volcanoes/> (English). These data are downloaded via local computer networks which currently take ~20 min to process a single 60 Mb image. Up to six

images are received daily of Kamchatka and the Kurile Islands and two images daily of Alaska and the Aleutians.

The volcanoes are analyzed and monitored daily by scientists at KBGS using techniques similar to those used at AVO but without a database system. The following parameters are determined for thermal anomalies:

- (1) presence or absence of an anomaly and source volcano;
- (2) if an anomaly is present, the size of the anomaly is determined (in pixels);
- (3) the temperature of the anomaly is determined;

For volcanic clouds a similar set of parameters are determined:

- (1) presence or absence of a volcanic cloud;
- (2) if a volcanic cloud is present, the height is estimated based on atmospheric temperature profiles and the presence of ash is evaluated using the split-window technique;
- (3) the length and direction of the cloud is determined.

Since September 16, 2003, the results of these analyses are posted daily at

- <http://emsd.iks.ru/~ssl/monitoring/main.htm>;
- <http://emsd.iks.ru/~ssl/>

If a thermal anomaly and/or a volcanic cloud are observed, the information is transmitted verbally or sent as a priority email to the local Department of the Ministry of Emergency Situations, KVERT, and AVO (in English) and to other interested emergency response groups.

9.4.3 Satellite data management and analysis: Yuzhno-Sakhalinsk

AVHRR and MODIS satellite data have been used for volcano monitoring in the southern Kurile Islands since 2003. Up to 22 swaths of AVHRR data are received daily from four of the satellites, NOAA-14, 15, 16, 17, 18, and 19. Approximately three swaths of MODIS data are received daily, which cover an area from Anadyr to Bratsk (east to west) and from the Arctic Ocean to Taiwan

(north to south). The Department of the Ministry of Natural Resources (DMNR) station provides satellite data to the Sakhalin Volcanic Eruption Emergency Response Team (SVERT) which is part of the Institute of Marine Geology and Geophysics (IMGG) for analysis of volcanic activity.

Most of the data processing is performed at the DMNR station prior to distribution to decrease the large volume of raw MODIS data (~350 Mb), that cover the volcanoes (Figure 9.2). The processing includes (1) ingesting high-resolution picture transmission (HRPT) data, calibration, and georeferencing, (2) generating color composites based on three calibrated bands (Table 9.3), and (3) conversion of images to JPEG format for selected areas of interest (Figure 9.9). The JPEG images are distributed to SVERT. Three color composite images are generated based on spatial resolution (250, 500, and 1,000 m) using various spectral bands (Table 9.3). For example, the 500 m spatial resolution data are used to generate a color composite image using MODIS bands 3, 5, and 7 in the R, G, and B image planes, respectively. This reduces the number of images to three with a total size of 5 Mb that are distributed to SVERT via local RadioEthernet-based networks.

SVERT analyzes these MODIS and AVHRR data to detect volcanic phenomena. Since January 2003 SVERT has reported on the eruptions of Chikurachki, Ebeko, Ekarma, Grozny, Alaid, Chirinkotan, and Sarychev Peak volcanoes, steam plumes at Sinarka and Severgin Volcanoes, and probable mud flows at Tyatya Volcano. Unlike other observatories in the region, SVERT uses JPEG color composite images as opposed to single-band or mathematical-band combinations for

Table 9.3. Examples of image products distributed by the DMNR Receiving Station in Yuzhno-Sakhalinsk.

<i>File name (example)</i>	<i>Ground resolution (m)</i>	<i>Bands</i>	<i>Band width and color assignments for compositing</i>	<i>Typical file size (Mb)</i>	<i>Application</i>
MOD02QKM.A0403040013r	250	1 2	620– 670 μm R, B 811– 876 μm G	3	Ash and steam clouds, ash deposits on snow
MOD02HKM.A0403040013r	500	3 5 7	469– 479 μm B 1,230–1,250 μm G 2,105–2,155 μm R	1.5	Ash clouds, thermal anomalies
MOD021KM.A0403040013r	1,000	20 22 23	3.66– 3.84 μm B 3.929–3.989 μm G 4.020–4.080 μm R	0.6	Thermal anomalies

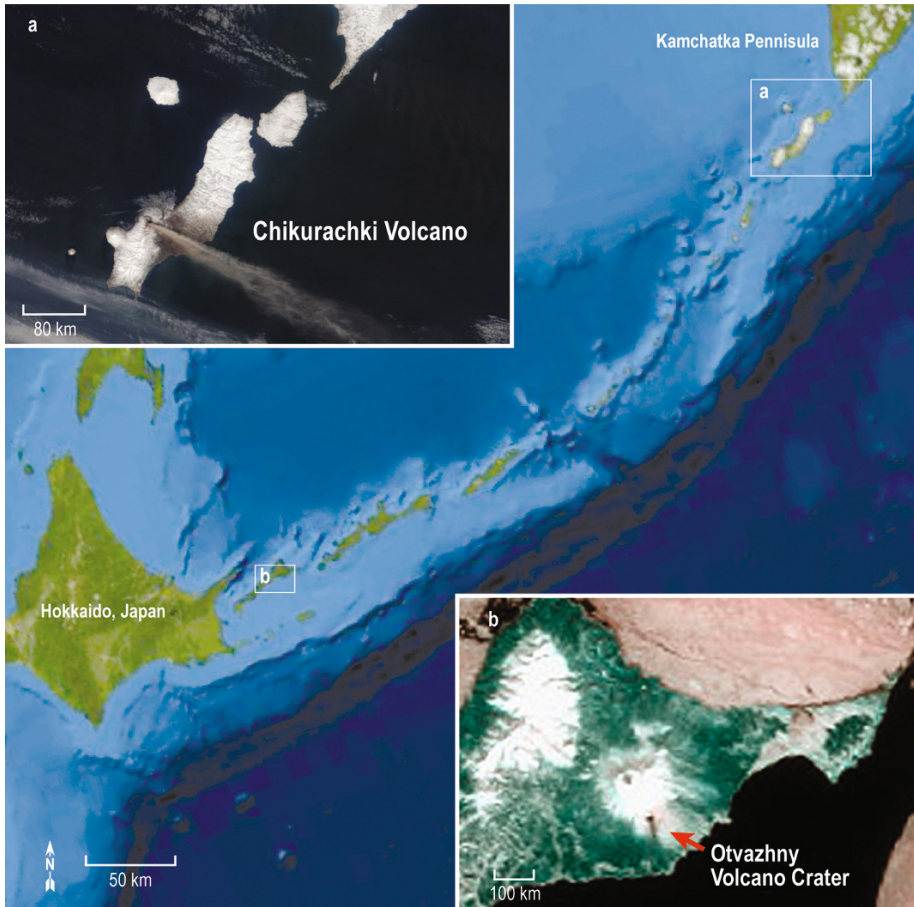


Figure 9.9. Examples of MODIS images distributed by the Yuzhno-Sakhalinsk station. Chikurachki Volcano plume and ash fall are shown on this image of the April 22, 2003 eruption (above left) and mud flows at Tyatya Volcano (above right). Both images are processed using bands 1 and 2 at 250 m spatial resolution.

analysis. In each of the three color composite images the contrast and color balance is adjusted to optimize the detection of volcanic clouds composed of ash and steam, thermal anomalies, and ash deposits on snow (Table 9.3). MODIS images are the primary data analyzed each day, but AVHRR images are used as a secondary data source to track and detect volcanic clouds. Satellite observations, along with reports from two seismic stations in the southern Kuriles and ground observers are then used to produce a daily report, which is sent via email to different organizations. The DMNR satellite station can also receive data from other platforms if needed and augment normal data reception in the event of an eruption.

9.5 DATA ANALYSIS FOR DETECTION OF VOLCANIC ACTIVITY

All data processing is designed to optimize detection of thermal anomalies and volcanic clouds (Figure 9.10). Visible and infrared band data provide valuable information, although some bands are more useful than others for certain phenomena as described below. Selected bands, band combinations, and custom images generated from the metadata are made available through the AVO software interface to expedite monitoring by analysts (Table 9.4).

Band combinations used for daily monitoring are generated for each sector (Figure 9.4) and

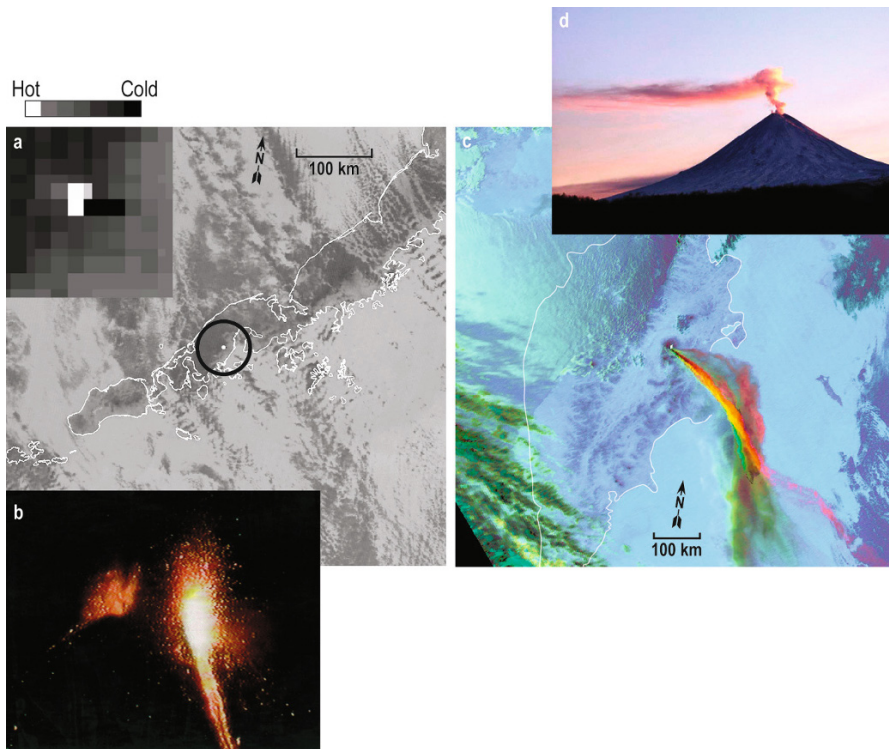


Figure 9.10. Thermal anomalies and plumes are critical features detected in satellite data. The thermal anomaly (left) was detected on TIR B3 AVHRR data (n14.96258.1258) and resulted from a strombolian eruption of Pavlov Volcano, 1996 (as shown in the photographic inset). The photograph was recorded on September 30, 1996, 16 days after the satellite pass (courtesy of G. McGimsey and S. McNutt, AVO). The enlargement shows hot pixels (white) and cold recovery pixels (black). The plume (right) was detected in AVHRR data (n12.94274.0640) of Kliuchevskoi Volcano, 1994. The image is a color composite of band 3 (red), band 4 (green) and band 4 minus 5 (blue). *Inset:* From the October 4, 2003 eruption of Kliuchevskoi Volcano (courtesy of S. Senyukov, KBGS).

reviewed by analysts twice daily (more frequently during heightened alerts). Using the database system, these observations generate reports twice daily. The preferred wavelengths (generalized) for detection of activity and the information derived from these data are (see Chapters 3, 5, and 6):

1. Visible and NIR (0.5 to 1.1 μm): detection of plumes composed of water vapor, ash, and/or gas (sunlit regions only).
2. MIR (3 to 5 μm): detection of thermal anomalies, anomaly temperature, background terrain temperature, size of the thermal anomaly (pixel counts), and detection of plumes.
3. TIR (10 to 12 μm): detection of cold volcanic clouds, as well as their temperature, direction of movement from source vent, length, and occasional thermal anomalies.

4. Split-window technique: subtraction of TIR bands (10 to 11 μm minus 11 to 12 μm) for detection of ash-rich volcanic clouds, signal strength (strongest negative signal), direction of movement from source vent, and length.

Other wavelengths used to analyze activity but not automated in the present AVO interface include 8.5 to 8.7 μm minus 11.7 to 12.3 μm for detection of SO_2 (Realmuto *et al.*, 1994, 1997; Prata *et al.*, 2003) and 3 to 5 μm minus 10 to 11 μm to remove solar heating effects (Harris *et al.*, 1995). Also essential to the reporting process is the satellite’s zenith angle which is the angle at which the satellite sensor views the ground (at nadir this is zero); for example, low angles are critical to look into a vent and large angles result in distortion and oversampling of the pixels near the edge of a swath.

Table 9.4. Selected satellite bands, band combinations, and custom images used for twice-daily monitoring at AVO. These data are automatically generated for viewing by analysts for each sector. Satellite zenith angle images are also available.

<i>Satellite/Wavelength</i>	<i>Visible</i>	<i>NIR</i>	<i>SWIR</i>	<i>MIR</i>	<i>TIR</i>	<i>Split window</i>
AVHRR	B1	B2	B3		B4, 5	B4m5
MODIS	B1, 3, 4	B6, 7	B20 to 25	B28, 29	B31, 32	B31m32
GOES	B1		B2		B4, 5	B4m5

“B” stands for “band” and “m” stands for “minus”; hence, “B4m5” means “band 4 minus band 5”.

9.5.1 Thermal anomalies (see Chapter 3 for detailed description)

A thermal anomaly is an area with a higher surface radiant temperature relative to its neighbors (Figures 9.10 and 9.11). If a thermal anomaly is located at a volcano, the source may be related to volcanic activity. Analysts can detect a pixel that is 5°C warmer than those around it under ideal conditions (i.e., minimal variation in background radiance and a known target area, such as a volcano summit). MIR wavelengths recorded by AVHRR (B3) and MODIS (B20 to B25) sensors are the preferred sensors and bands for detection of thermal anomalies.

The critical characteristics of thermal anomalies for volcano monitoring include location, time, pixel temperature, and number of hot pixels including their shape or orientation. Location and time are needed to constrain the geography and chronology of activity. The temperature and number of hot pixels are required to measure variations in thermal activity. The hottest pixel is reported by analysts but integrated values of several warm pixels could also be reported. Shape and orientation help identify the type of activity represented by the anomaly; for example, heated domes and lava lakes are typically symmetrical while lava flows, pyroclastic flow deposits, and hot/warm debris flows are typically linear (Figure 9.12).

Data recorded by MIR wavelengths (3 to $5\ \mu\text{m}$) or slightly shorter are best used to detect relatively warm or hot ground as described by Wien’s displacement law (Sabins, 1997; Chapter 2). The sensors detect an integrated brightness temperature value that includes cold background and elevated volcano temperatures over the full pixel area of $1,210\ \text{km}^2$ (AVHRR). The integrated pixel temperature value is often only a few degrees above background in the images. For example, background temperatures may be 0°C , but the high-temperature

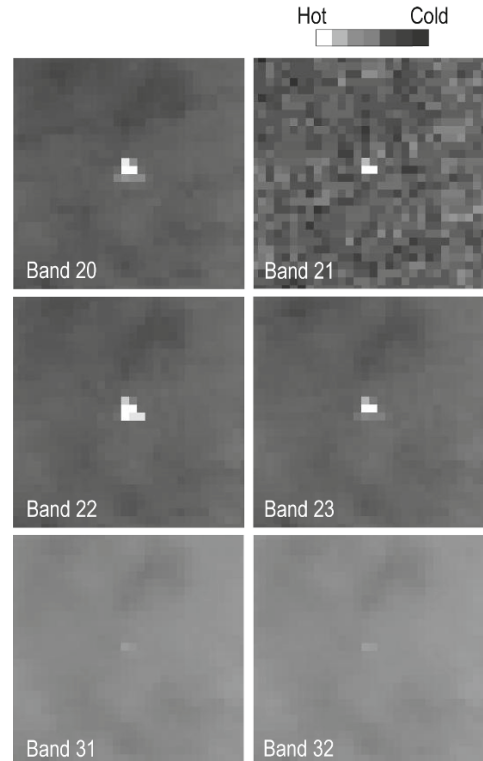


Figure 9.11. Thermal anomalies from the dome at Bezymianny Volcano on the Kamchatka Peninsula detected in MODIS data, October 25, 2000. The number of hot pixels (white) varies from 3 to 6 in the mid-IR (bands 20, 21, 22, and 23) but are barely discernible from background in the TIR (bands 31 and 32). The highest pixel temperature is 34°C (band 20) and the background is approximately -25°C , but this varies between bands due to differences in emissivity and atmospheric absorption as a function of wavelength. Usually, the hottest temperature in band 20 is reported by analysts. The number of hot pixels counted by analysts is somewhat subjective. Each pixel is $1\ \text{km}^2$ and the size of each image is $30 \times 30\ \text{km}$.

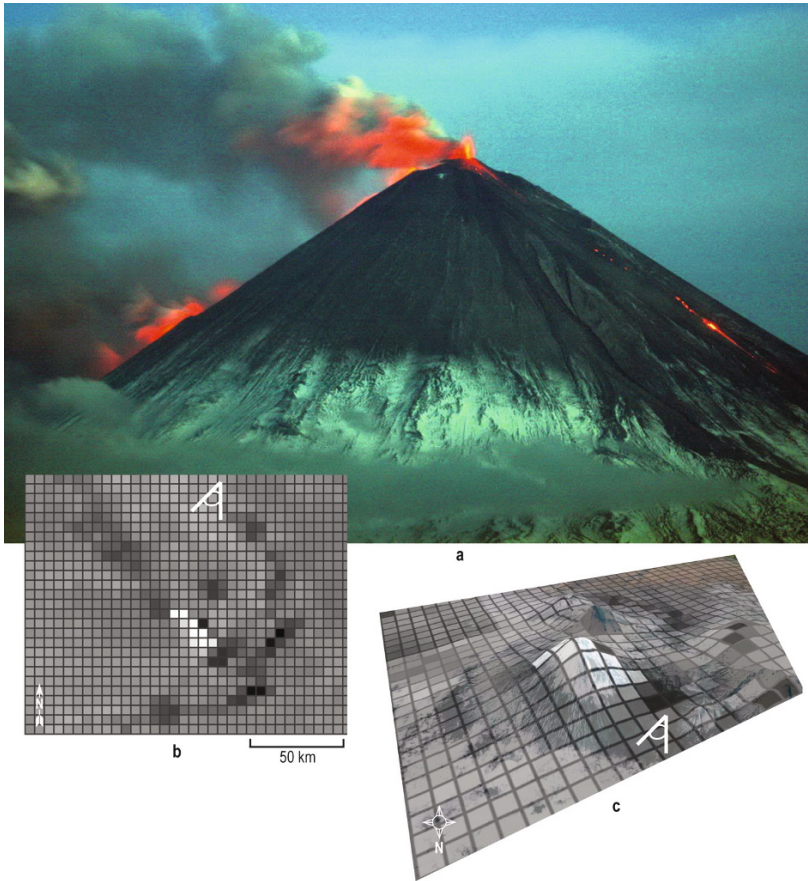


Figure 9.12. Example of validation and characterization of thermal anomalies detected on satellite data used for daily monitoring of volcanoes. Photograph shows lava fountaining and flows at the summit and on the flanks of Kliuchevskoi Volcano (a). An AVHRR satellite image (b) recorded 26 min after the photograph was taken shows eight adjacent warm pixels (white) extending NW and SE of the summit. This coincides with the lava flows in the photograph. The temperature of the pixels ranges from 52 to 57°C which is near or at sensor saturation. Satellite temperatures are much lower than actual lava temperatures due to integration over the 1.21 km² pixel area and sensor range. The plume in the photograph extends SE of the lava pixels. The look direction of the photograph is shown on the image (b). The AVHRR image draped over a DEM from Google Earth[®] shows the position of the thermal anomalies with respect to topography. The photograph was taken at 04:20 UTC, May 31, 2007 and the AVHRR satellite was recorded at 04:46 UTC. Image ID n16.07.151.0446 (photograph courtesy of Yuri Demyanchuk, IVS, and provided by Olga Girina, KVERT).

pixel caused by a small lava flow is significantly less than lava temperatures (e.g., 30°C). Saturation of a pixel occurs when the integrated pixel temperature is above the detection capability of the sensor, which is approximately 50–65°C (AVHRR). At MIR wavelengths, a 121 m² area at 1,000°C will saturate an AVHRR B3 pixel (Harris *et al.*, 1997a, b; Chapter 3). The saturation of pixels limits the temperature and thermal flux information that can be measured. The presence of a saturated pix-

el(s) indicates that there is significant thermal energy being emitted. Occasionally, an increased signal is observed in the NIR or SWIR data at night (e.g., AVHRR B2, MODIS B7) and is usually related to incandescence from vigorous lava fountaining (Harris *et al.*, 1997a, b; Dean *et al.*, 1998; Chapter 3).

To offset the effect of sensor saturation, data from bands with slightly longer wavelengths or decreased sensor sensitivity are used. For AVHRR

data there is a 6.5 μm wavelength increase from B3 to B4 (10.5 μm) band, and this large jump requires a very hot and/or large heat source to be readily detectable at this wavelength. Thus, little to no information can be salvaged from most AVHRR saturated pixels. However, MODIS data include stepwise increases in thermal bands from 3.6 to 14.4 μm , and in some cases the sensor sensitivity changes (Figure 9.11). Thus, saturated pixels in MODIS data are analyzed using slightly longer wavelength bands or less sensitive gain settings to retrieve temperatures.

Thermal anomalies do fluctuate during an eruption, as seen in time-sequential AVHRR and MODIS data. These fluctuations can be caused by weather, changes in ground temperatures, increase in size of the anomaly, changes in the thermal contrast compared with background temperature, and presence and absence of hot pixels at the same location on succeeding passes (Dehn *et al.*, 2000; Harris *et al.*, 2000). Possible explanations of these fluctuations include changes in solar heating or reflections, masking of the signal (e.g., weather or volcanic clouds), variation in the heat flux of the volcanic source, increase in seasonal contrast, atmospheric effects, and orbital geometry (Mouginis-Mark *et al.*, 1994; Harris *et al.*, 1997a,b; Dehn *et al.*, 2000; Chapter 3). Thermal anomalies have been detected at volcanoes prior to or in the early stages of an eruption; for example, Pavlof, 1996 (Figure 9.10); Karymsky, 1996; Okmok, 1997; Bezymianny, 1997; and Shishaldin, 1999 (Dehn *et al.*, 2000; Harris *et al.*, 2000; Chapter 3).

Analysts have identified criteria to distinguish volcanic and nonvolcanic thermal anomalies as well as potential sources of misinterpretations:

1. Solar reflections from clouds, water, and daytime solar heating can appear as thermal anomalies.
2. Solar heating will result in thermal anomalies at many peaks in the area, whereas those related to volcanic activity are restricted to usually one or at most two peaks, as occasionally observed on the Kamchatka Peninsula.
3. Lakes will appear as thermal anomalies in the fall and winter (if not frozen) due to changes in the thermal contrast created when the background temperature decreases below that of lake-water temperature.
4. Wild fires and structural (i.e., man-made) fires can result in a thermal anomaly similar to that

from a volcano but usually they are not located near the volcano summit.

5. Lava lakes, volcanic vents, and domes often result in symmetrical anomalies consisting of one to a few AVHRR or MODIS pixels.
6. Lava flows and hot debris flows tend to generate linear thermal anomalies.

9.5.2 Automated detection of surface temperatures

Subtle increases in the surface temperature of volcanoes can be a precursory signal to explosive eruptions or early stages of activity. The Okmok Algorithm was developed to automate measurement of fluctuations in satellite-derived radiant temperature and to detect subtle changes in temperature that otherwise may go unnoticed (Dean *et al.*, 1998; Dehn *et al.*, 2000, 2002; Chapter 3). The algorithm was developed during the 1996 eruption of Pavlof Volcano and refined during the 1997 Okmok eruption (Dean *et al.*, 1998). As satellite data are received at the station, the algorithm automatically extracts a 40×40 -pixel area surrounding each volcano, scans MIR bands (e.g., AVHRR B3) for the hottest pixel, and then reads temperature and albedo values of that pixel in bands 2, 3, 4, and 5. This information is then plotted on a time vs. temperature/albedo graph (Figure 9.13).

It can be difficult to distinguish volcanic from nonvolcanic signals in the initial Okmok implementation. Manual elimination of solar reflections and clouds by filtering, or using night-time data only, can result in a graph that clearly records an eruption. The addition of graphs of the annual background temperature with the hottest radiant temperatures recorded at the summit of the volcano also help distinguish volcanic signals (Dehn *et al.*, 2000). Only data above background that indicate potential eruption activity are plotted.

The newly upgraded version of the Okmok 2 Algorithm uses the same subsector as the initial version but is based on a series of logical queries designed to eliminate unusable data, select suitable images, detect volcanic signals, and send alerts to analysts, and requests for high-resolution data acquisition (see Chapter 3 for details). This is accomplished by, first, data with excessive noise is eliminated. Second, night-time, cloud-free images are identified that are suitable for detecting potential thermal anomalies based on visible, MIR, and TIR signals. Third, data are analyzed at two thresholds, coarse and fine, to identify a thermal anomaly.

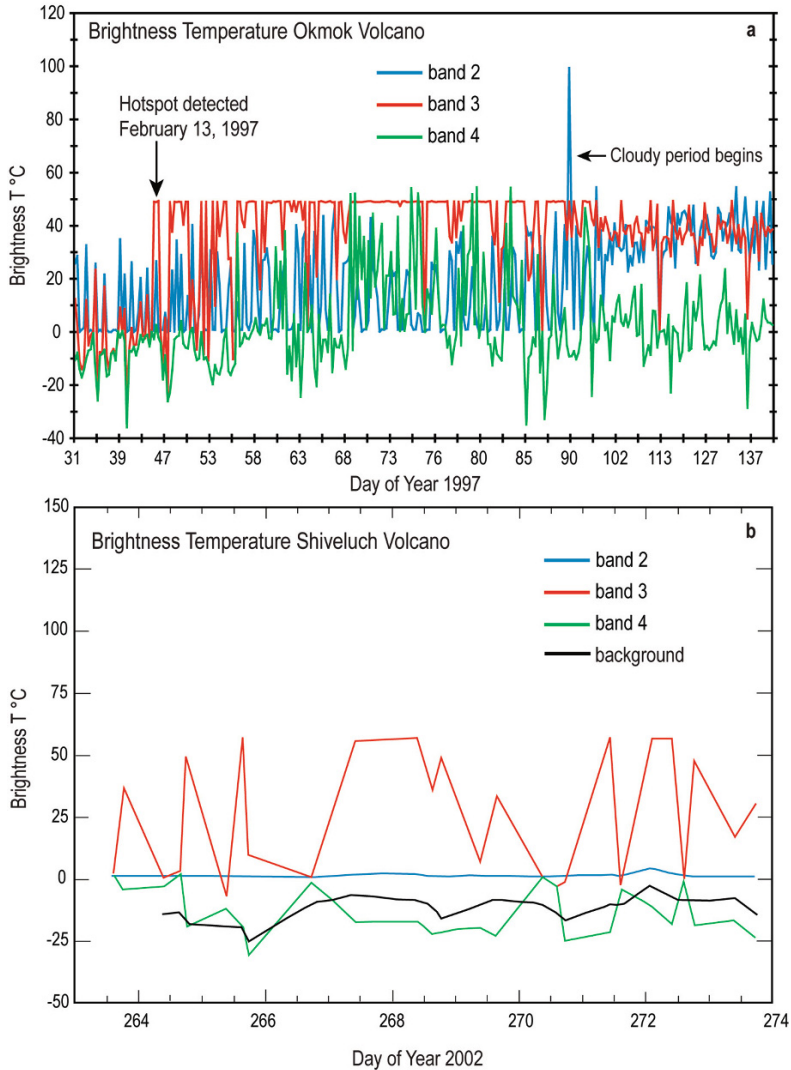


Figure 9.13. Time temperature or albedo graphs of activity at volcanoes are used to monitor temperature as activity changes. The spectral response of AVHRR bands 2, 3, and 4 are shown. Image (a) shows an unfiltered signal over 3 months during lava effusion at Okmok Volcano. The volcanic signal is evident in the saturation of band 3 at approximately 50°C, but obscured by the diurnal cycle and cloudy periods. Image (b) shows filtered data for 2 weeks at Shiveluch Volcano. Only night-time cloud-free images are used, making the volcanic temperature signal from the lava dome easy to recognize.

Coarse-level data have three criteria that identify a potential thermal anomaly and trigger an alarm based on pixel saturation, band addition thresholding, and statistical analysis of temperatures (Harris *et al.*, 1997a, b). Fine-level data have four criteria, two of which must be met before an alarm and automatic data request is submitted. These criteria

are similar to those of the coarse level but have more rigid thresholds. Fine criteria include a temperature value greater than one standard deviation higher than the normal seasonal value (Dehn *et al.*, 2000), elevated brightness temperatures in MIR and TIR bands, and elevated volcanic alert levels (Gardner and Guffanti, 2006). Many of these criteria take

advantage of the thermal properties of lava and other hot volcanic features, as well as the effects on Wien's displacement law where wavelength peak emittance is based on the temperature of the target (Chapter 3).

Okmok 2 also generates a 40×40 -pixel image for every image at every volcano analyzed and stores these subsectors online in a searchable database (even images that did not pass the original criteria). The data can be searched and used with other types of information, such as seismic, geologic, and geodetic for analysis. Software to view and analyze the images is available at UAF/GI.

Automated alarms take several forms. First, emails are sent to analysts containing numerical information on the identified anomaly (location, number of pixels, maximum pixel temperature, background pixel temperature, and satellite zenith angle), with a link to the subsector image stored in the database that is accessible via the World Wide Web. If a volcano has not triggered an alarm in over a week, a cellphone message is also sent to key staff. This works as a rapid response should a new volcano erupt, but will not bother staff members for ongoing eruptions where they would clearly already be on alert. The cellphone trigger also prompts an emergency request for higher resolution data (e.g., ASTER). Since the automated alarm system has been 70% effective in ~ 400 cases, it returns very few false alarms. For the North Pacific, the average number of alarms sent to cellphones is one per day (2007, pers. commun., J. Bailey). Over the 15 years of AVHRR monitoring, the majority of the volcanoes have shown thermal anomalies before (often days) or during early stages of recent activity, such as at Shishaldin, 1999; Pavlof, 1996; Okmok, 1997; Karymsky, 1996; Bezymianny, 1997, 1998, 1999; Kliuchevskoi, 1994; Cleveland, 2001; Augustine, 2006; and Redoubt, 2009.

9.5.3 Volcanic clouds (see Chapter 5 for detailed description)

Volcanic clouds consist of ash, water vapor, CO_2 , SO_2 , and other gases emitted by the volcano but currently only ash, water vapor, and SO_2 are readily detectable using routinely available satellite data. The opacity, composition, height, temperature, age, particle size distribution, particle concentration, temperature of underlying surface (i.e., land or water), and winds are factors that influence how volcanic clouds are detected and appear in satellite data. Volcanic eruption columns can attain heights

of over 20 km but over the past 20 years most eruption columns in the North Pacific have not attained heights over 10 km which is near the tropopause boundary. Most volcanic clouds are opaque near the vent and gradually disperse as they drift downwind. Some clouds are ash rich and others are ash poor (high in magmatic volatiles and/or water vapor plus or minus ice). As volcanic clouds age, their physical composition evolves. Coarser material settles close to the vent and fine material remains suspended in the atmosphere, sometimes for months, eventually settling or dissipating. Further chemical reactions such as SO_2 to H_2SO_4 occur on the scale of hours to days. All of these factors influence the spectral characteristics of a volcanic cloud, many of which can be detected at various wavelength bands (Figure 9.14).

The critical characteristics of volcanic clouds for monitoring include the source volcano, time of observation, location or distance from the source vent, cloud temperature, direction of movement, and composition of the cloud. The source volcano and time are needed to constrain the geography and activity. The temperature is indicative of cloud height, and the direction of movement is critical for developing warning messages. The composition of the cloud—including whether it is ash rich, ash poor, or contains SO_2 —is also critical for hazard mitigation and climatological studies, and holds information about eruption processes. The following is a description of volcanic cloud features detected and analyzed as a function of wavelengths.

Visible NIR and SWIR wavelengths (0.4 to 3 μm)

Visible, NIR, and SWIR data (e.g., GOES B1, AVHRR B1 and B2, MODIS B1 to B19) are used to detect both ash-rich and ash-poor volcanic clouds (Figure 9.14a), provide information on cloud morphology, and often detect small ash-poor clouds not seen in other wavelength bands (Kinoshita *et al.*, 2003; Tupper *et al.*, 2007). Also, cloud heights can be estimated using cloud shadow, satellite zenith angle, and basic geometric principles. The primary strength of these data is the detection of volcanic clouds, especially short, low-altitude ones. The major disadvantages of these data are their requirement for sunlight, which is a critical problem at high latitudes especially during winter months, and their limited capability to distinguish between weather and volcanic clouds (Chapter 5).

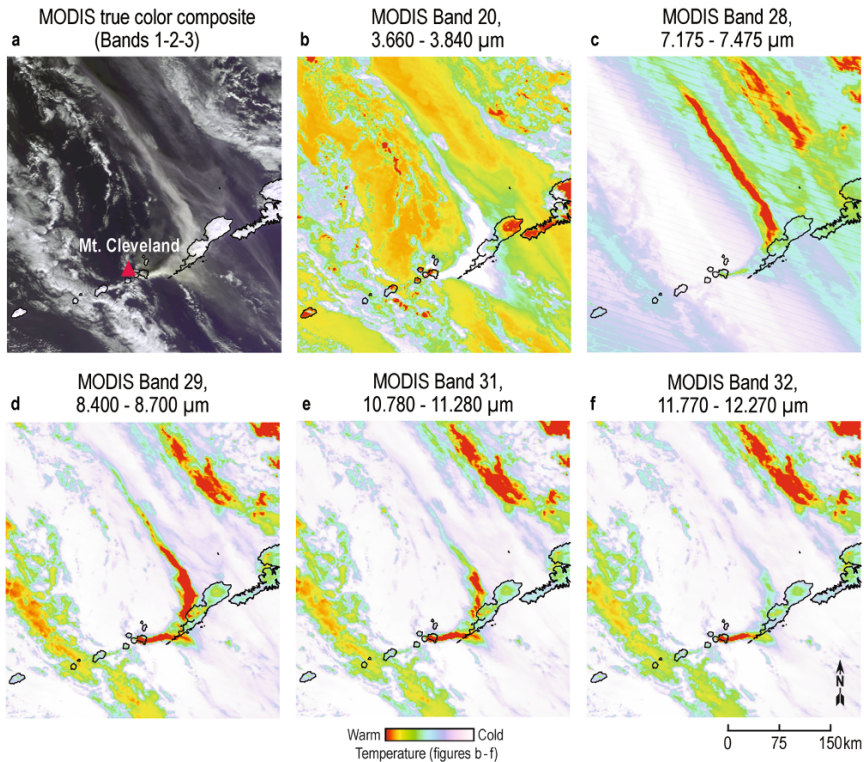


Figure 9.14. MODIS satellite images of the eruption showing Mt. Cleveland, Alaska, February 19, 2001 at wavelengths commonly used to detect volcanic clouds and variations in the structure of the cloud as a function of wavelength—(a) natural color composite, (b) band 20, (c) band 28, (d) band 29, (e) band 31, and (f) band 32. Variations are related to the composition and concentration of material in the plume and atmospheric parameters. The true-color composite image (a) consisting of bands 1, 2, and 3 is for reference. The remaining TIR images have been analyzed using a default contrast linear stretch optimized for each image and a color mapping. The spatial resolution of band 2 is 250 m while the others are 1,000 m. Scene ID is t1.01050.2310.

Intermediate infrared data (MIR, 3 to 8 μm)

MIR data (e.g., AVHRR B3, MODIS B20) can provide unique information about volcanic clouds due to their sensitivity to particle size and solar illumination angle (Figure 9.14b,c). These data are useful for the detection of small, low-altitude volcanic plumes, especially those composed primarily of water vapor, and often reveal plumes that cannot be detected in longer TIR wavelengths in daylight data. These data can be used to discriminate between ash-rich volcanic clouds and weather clouds on daytime data (Tupper *et al.*, 2007) but not at night. Another disadvantage of these wavelengths is that highly reflective, small steam plumes or weather clouds can be mistaken for thermal anomalies in daytime data. There is an absorption peak at 7.3 mm that can be used in conjunction

with TIR wavelengths to detect SO_2 clouds, but abundant water vapor absorption in the lower atmosphere limits its use to high-altitude clouds only (Prata *et al.*, 2003; Chapters 5 and 6).

Thermal infrared data (TIR, 8 to 14 μm)

TIR data (e.g., AVHRR B4 and B5, MODIS B31 and 32) are sensitive to cloud temperatures and the absorption characteristics of ash. Hence, they are the preferred bands to detect and analyze volcanic clouds (Figure 9.13d-f). At these wavelengths, the radiant temperature of opaque volcanic clouds can be measured. However, ash cannot be detected if the cloud is opaque. Ash and weather clouds are detected and distinguished by manipulating different bands over this wavelength range (split-window technique) (Prata, 1989; Simpson *et al.*, 2000; Prata

et al., 2001a, b). However, these data often do not detect small, ash-poor volcanic clouds presumably due to limitations in sensor sensitivity and spatial resolution. Longwave thermal infrared channels are best for detecting volcanic clouds because they do not require solar illumination and are sensitive to cold cloud temperatures and volcanic ash. A weak absorption peak at 8.6 μm permits detection of SO_2 . See Chapters 5 and 6 on volcanic clouds for a more detailed discussion.

9.5.4 Detection of opaque volcanic clouds

Opaque volcanic clouds are often the first satellite observation of the airborne components of an explosive eruption. These clouds can be at very low temperatures (-50°C and below) and, when this cold, are often at altitudes over 10 km. This is higher than many weather clouds. They tend to be circular, elliptical, or v-shaped with the apex of the “v” over the vent. Despite these distinctive shapes, orographic clouds can look very similar and are often mistaken for volcanic clouds. However, orographic clouds usually develop at multiple, surrounding mountain peaks while eruptions occur at one or perhaps two volcanoes simultaneously (Pavolonis, 2010). Moreover, due to reflectivity characteristics in NIR/TIR, the clouds can often be distinguished in true-color images or, for umbrella clouds, by the presence of gravity waves or temperature structures indicating a dynamic convective cloud (Holasek *et al.*, 1996; De Angelis *et al.*, 2011).

9.5.5 Detection of airborne ash

Ash-rich and ash-poor volcanic clouds are best distinguished from weather clouds using the split-window technique (Figure 9.15). The technique is critical in helping to detect volcanic clouds that are translucent (e.g., older clouds removed from the vent) in single-band data (Prata, 1989) but it does not produce a signal from opaque clouds (e.g., dense and near the vent) (Figure 9.16). Typically, the ash signal is between 0 and -20°C with more negative values representing the stronger ash signal. The split-window technique is a significant breakthrough permitting the detection and tracking of ash in volcanic clouds for days after the eruption has ceased, and is critical for hazard mitigation, especially for aircraft warnings. However, some weather clouds, storm fronts, dust clouds (Acker-

man, 1997; Murayama *et al.*, 2001; Simpson *et al.*, 2003) and smoke from fires (Little *et al.*, 1999) produce a signal similar to that of volcanic ash. These often have lower split-window signals than ash clouds. In addition, moisture and ice coating may mask the ash signal (Rose *et al.*, 1995a; Simpson *et al.*, 2000; Prata *et al.*, 2001a, b; Tupper *et al.*, 2004). Knowing that an eruption has occurred, the source volcano and the use of tracking models to predict the location of an ash cloud helps distinguish them from non-ash clouds. Moreover, as mentioned previously, weather clouds can be identified because they form at multiple, surrounding mountain peaks simultaneously while eruptions usually occur at a single peak. A skilled analyst can often identify an ash cloud based on its shape and temperature structure. At AVO and the Anchorage Volcanic Ash Advisory Center (VAAC), split-window images are automatically generated to aid in the detection of ash clouds (e.g., AVHRR B4mB5; MODIS B31mB32).

9.5.6 Estimating volcanic cloud height

Estimating the height of volcanic clouds is a critical component for hazard evaluation and warnings issued in response to an explosive eruption. In addition, height constraints provide input to transport models for estimating cloud location and for assessing climatological impact. Several methods have been developed to estimate cloud height based on measurable parameters: cloud temperature, wind shear, cloud shadow, and seismic tremor amplitude. Estimates can also be made using dispersion models such as Puff (e.g., Dean *et al.*, 2004). The most commonly used methods are described below.

Cloud temperature method

The cloud temperature method incorporates TIR satellite data to measure cloud top temperature and atmospheric sounder data to provide an atmospheric temperature profile (Dean *et al.*, 1994; Holasek *et al.*, 1996). Generally, the higher the cloud the colder the temperature, as long as the cloud does not penetrate the troposphere–stratosphere boundary (tropopause), which usually starts at approximately 9 km at Arctic latitudes (Lutgens and Tarbuck, 1979; Carey and Bursik, 2000). After the initial gas thrust phase, a volcanic

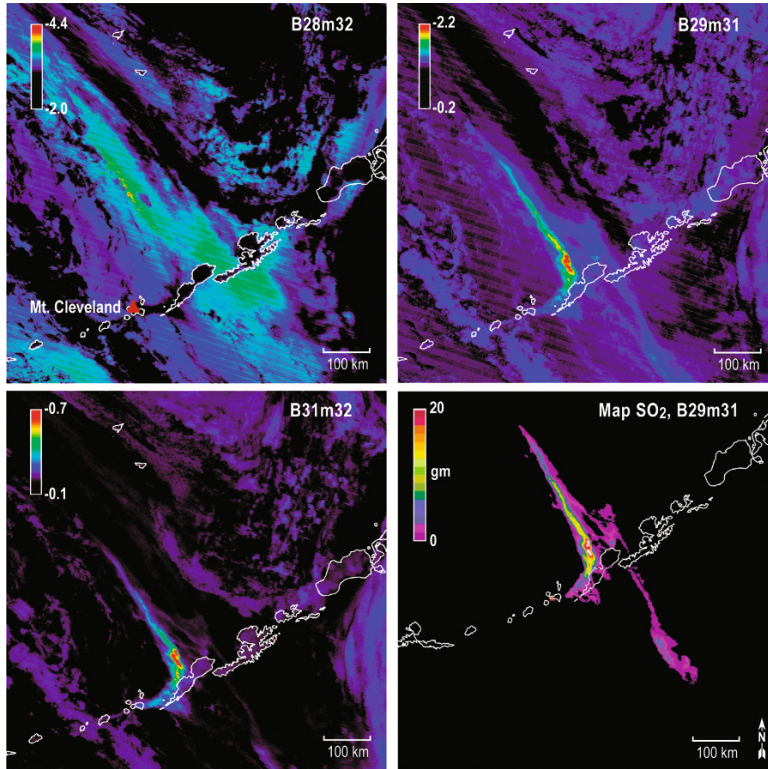


Figure 9.15. MODIS split-window satellite images of the eruption of Mt. Cleveland, Alaska, February 19, 2001. In the North Pacific region, B31m32 (MODIS) or B4m5 (AVHRR & GOES) data are automatically generated to detect translucent volcanic clouds, to ascertain if ash is present and to differentiate volcanic clouds from weather clouds. Other split-window data (e.g., B28m32 and B29m32) detect ash and SO_2 , although B28 is hampered by atmospheric absorption. The MAP SO_2 image is derived from an algorithm designed to detect sulfur dioxide using MODIS data (Realmuto *et al.*, 1994).

cloud ascends to higher altitudes in its convective thrust phase and drifts downwind. Its temperature equilibrates to the surrounding atmosphere, often attaining values of -50°C or colder at altitudes over 10 km (33,000 ft). Often, some parts of the cloud will supercool with respect to the surrounding atmosphere and ascend to higher altitudes than can be sustained by buoyancy (Carey and Bursik, 2000). To estimate the maximum height of an eruption cloud, the cloud must be opaque. Its temperature is measured using satellite imagery at 10–12 μm wavelengths. Cloud temperature is then compared with a vertical atmospheric temperature profile to derive the height (Figure 9.17). The supercooled portions are excluded from cloud measurements and can be identified since they are colder than the atmospheric temperature seen on the profiles.

These profiles are measured by sounding balloons launched twice daily from selected sites (usually airports). In the Alaska, Kamchatka, and Kurile Islands region there are relatively few balloon launch sites compared with more densely populated areas in the world. Further, volcanoes are often far removed from these locations (<http://weather.uwyo.edu/upperair/sounding.html>) and, hence, sounder profiles may not always represent the atmospheric conditions above volcanoes. To compensate for the sparse soundings in the North Pacific region, temperature profiles are generated from global gridded atmospheric model data of the conditions above each volcano using an automated algorithm provided by the University Data (Unidata) System at the National Center for Environmental Prediction (NCEP). These interpolated values have been

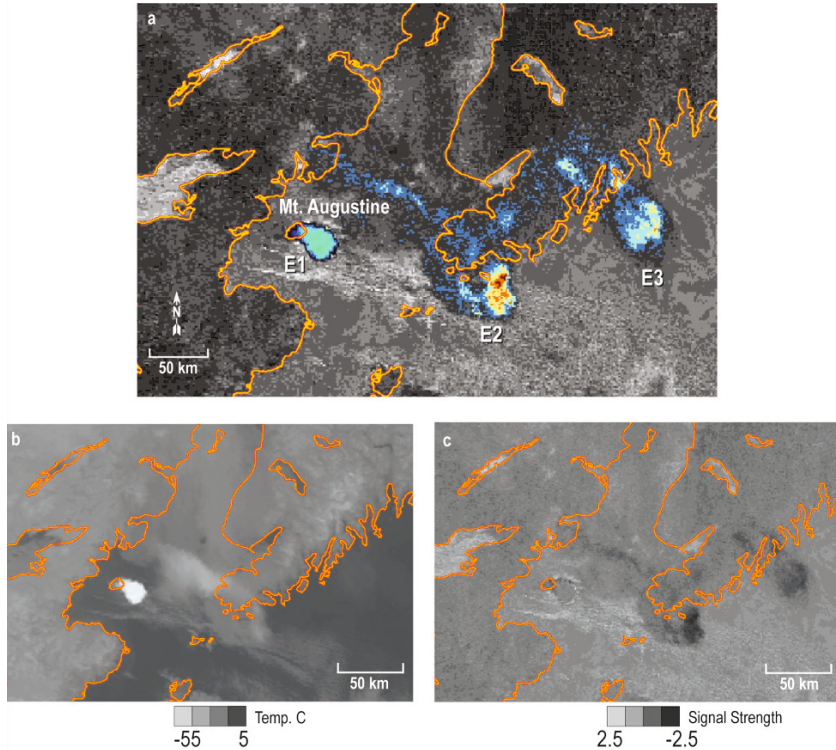


Figure 9.16. Opaque and translucent volcanic clouds at Augustine Volcano, January 13, 2006, seen on AVHRR data (n17.06.013.2042). Image (a) is a color composite of B4 and split-window images showing volcanic clouds from three separate eruptive events which are labeled E1, E2, and E3. The TIR band 4 image (b) clearly detects E1 and faintly E2. The split-window image (c) easily detects E2 and E3, but opaque E1 is barely discernible. The opaque cloud E1 is 0.2 hours old. Translucent cloud E2 is 2.9 hours old and E3 is 18.3 hours old. Detection of volcanic clouds requires the use of TIR for opaque clouds and split-window data for translucent clouds.

known to be more accurate or representative than site-specific sounders. The interpolated profiles are updated every 6 h when new atmospheric data are received. There are potential errors associated with temperature–height derivation (Woods and Self, 1992; Oppenheimer, 1998) but this technique certainly provides a first-order estimate. Several case studies have shown this technique to be reasonably accurate although no statistical studies have been performed. For example, the eruption of Mt. Spurr Volcano on August 19, 1992 at 00:42 UTC resulted in a plume that had a radiant temperature of -65°C . Comparing this temperature with an interpolated atmosphere temperature profile indicates that the cloud reached an altitude of 12 to 14 km (Figure 9.17), which agrees with ground-based weather radar (Rose *et al.*, 1995b). This method can be used for day and night eruptions but can

only be applied to opaque clouds—not translucent clouds.

Wind shear method

Another technique estimates volcanic cloud height using dispersion models and variations in wind direction or velocity with altitude. A dispersion model simulation showing particles color-coded as a function of altitude is compared with the structure of the volcanic cloud seen on a correlative satellite. An example is shown for the March 11, 2001 eruption of Cleveland Volcano (Figure 9.18). The Puff dispersion model (Searcy *et al.*, 1998) shows particles drifting north at >7 km height and particles drifting east at <7 km height. The satellite image shows drifting to the east, indicating that the

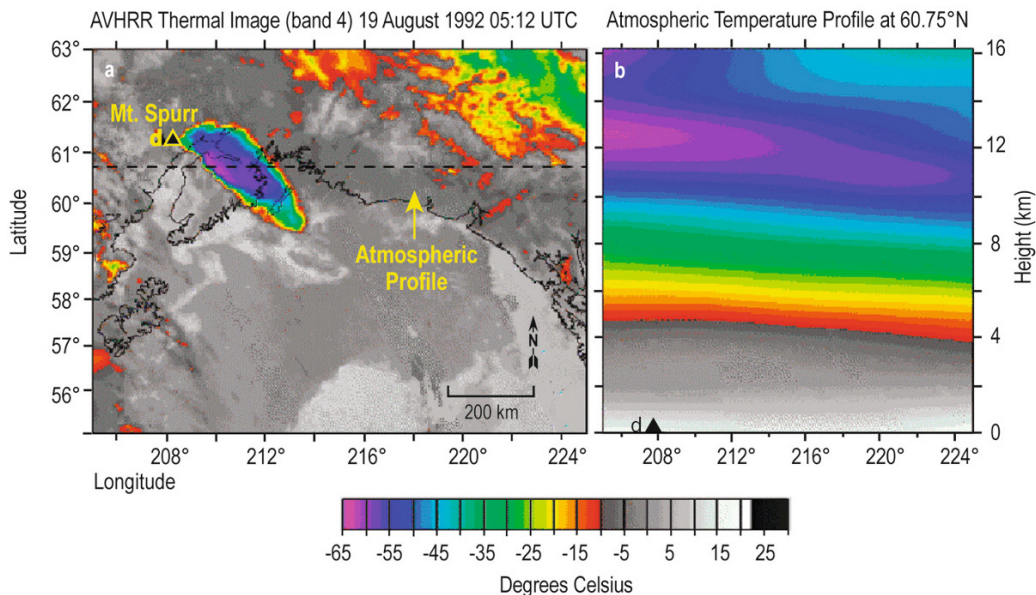


Figure 9.17. Determination of plume height using the cloud top temperature technique. An AVHRR TIR band 4 image (left) shows the coldest temperature of the plume as approximately -65°C which correlates to a height of 12–14 km as shown in the atmospheric profile (right) which agrees with NWS C-band radar (Rose *et al.*, 1995a) (image courtesy of Craig Searcy, NWS).

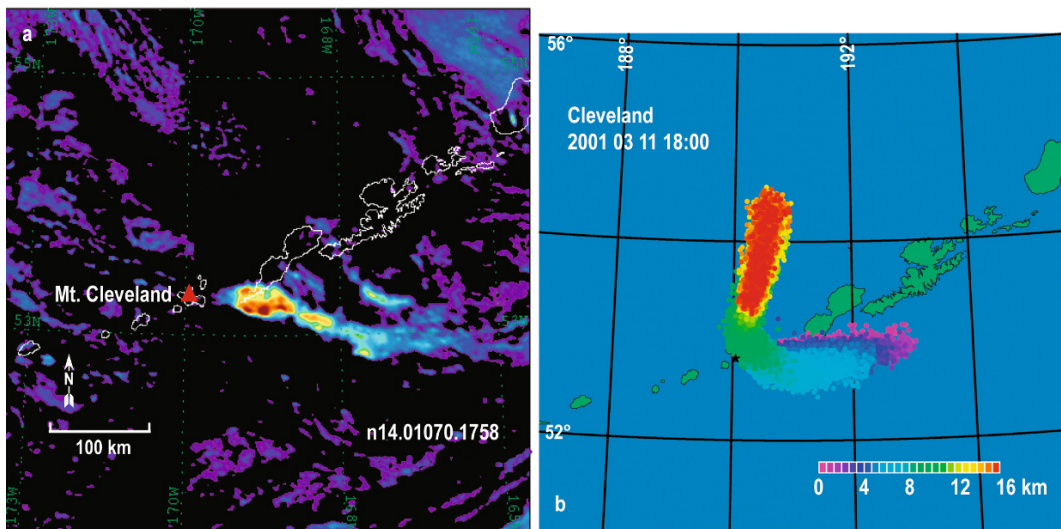


Figure 9.18. Determining the height of the volcanic cloud using satellite images and dispersion models. An AVHRR band 4m5 image (top) shows a plume extending to the east. The Puff dispersion model shows plume particles at <7 km altitude extending to the east and others >7 km extending to the north. Since the satellite image only shows the plume trending eastwards, it must therefore be below the 7 km height. Reanalysis wind fields were used in the dispersion model runs.

cloud is below 7 km. Similar comparisons can be applied when wind velocities differ with altitude.

Cloud shadow method

The cloud shadow method involves using satellite data, solar angle, and basic geometric principles. The length of the shadow produced by a volcanic cloud is measured on visible wavelength satellite data and the solar angle is determined using astronomical tables. Using this information the height can be calculated. This method has limited use since it requires daylight, low Sun angle, the satellite in the correct position, and opaque volcanic clouds. Moreover, one has to make a simplifying assumption that the shadow is projected onto a horizontal surface; however, the shadow start and end points can be ambiguous.

Seismic amplitude method

A final method involves using seismic tremor data to estimate volcanic cloud height and tephra volume (McNutt, 1994, 2004). Tremor data are normalized to their reduced displacement amplitudes and plotted against the Volcanic Explosivity Index (VEI) (Newhall and Self, 1982). These plots are used to estimate ash volume and cloud height, although there is considerable scatter in these graphs due to stochastic variations and other factors such as different atmospheric conditions (Graf *et al.*, 1999), vent size, vent geometry, attenuation, seismic coupling, and possible nonlinearity of volcanic processes. The advantage of this method is that seismic data are useful even during periods of darkness or poor weather. A similar seismic technique has been successfully implemented by scientists at the Kamchatka Branch of the Geophysical Survey (KBGS) (2005, pers. comm., S. Senyukov). Semi-automated coupling of satellite dispersion modeling and seismic techniques for volcano monitoring could potentially become a powerful tool to estimate the critical cloud height value, especially for volcanoes that erupt frequently and repetitively.

Qualitative methods

Two qualitative methods for estimating volcanic cloud heights are pilot reports (PIREPs) and webcams. Pilots frequently estimate cloud heights based on visual observations from the aircraft cockpit. Sometimes it is difficult to make these estimates because pilots do not know the distance to the cloud

nor the angle to the cloud with respect to the flight path of the aircraft.

Webcams have drawbacks similar to pilot reports but with fewer unknowns. In most cases the distance from the webcam to the volcano is known and the field of view is usually constant. The height of the volcano is known and is used as the scale bar in the image. Moreover, the vertical angle from the webcam to the top of the cloud can be measured. However, the distance to the volcanic cloud is still unknown and the cloud could be moving towards or away from the camera. So it is possible to get a reasonable estimate of the height of the cloud in some cases. The webcam method is used at some volcanoes in Kamchatka. Despite these uncertainties, PIREPs and webcams are a valuable source of information for first-order estimates and corroborative observations.

9.5.7 Predicting the movement of volcanic clouds (see Chapter 7 for a detailed description)

Airborne volcanic ash dispersion and tracking models are critical tools for volcano monitoring and hazard mitigation that are used in conjunction with satellite observations. While satellite images provide site-specific and time-specific observations, dispersion models predict the movement of volcanic clouds, their location, and structure. This information is extremely valuable for hazard mitigation in terms of warning aircraft of possible ash encounters and predicting ash deposition and movement. Moreover, these models allow the prediction of areas of ash fall and, hence, could be used to warn of potential health and machinery problems and to estimate structural loads on buildings. Model predictions are validated using satellite images.

Most dispersion models are initiated by releasing a column of hypothetical particles above a volcano which are subsequently transported by advection, diffusion, and gravitational settling in a gridded wind field (Chapter 7). They currently do not model eruption column dynamics as in the Active Tracer High-Resolution Atmospheric Model (ATHAM) (Oberhuber *et al.*, 1998). Dispersion models are used for both operational response to an eruption and for retrospective analysis of eruptions. For operational response, the models must be fast, efficient, and easily configurable for diverse conditions and approximate transport physics

without becoming cumbersome. Output must be clear and easily incorporated into formal warning products.

There are several dispersion models currently used in the North Pacific region, including Hybrid Single-Particle Lagrangian Integrated Trajectories (HYSPLIT) (Draxler and Hess, 1998), Canadian Emergency Response Model (CanERM) (Pudykiewicz, 1988, 1989; Pudykiewicz and Dastoor, 1995), and Puff (Searcy *et al.*, 1998). These models vary in spatial resolution (depending upon wind fields) and implementation of transport mechanisms. Puff differs from the other models in that it is designed specifically for responding to volcanic eruptions, while the other models are used for many applications. Puff is the primary model used at AVO for dispersion analysis of volcanic clouds. At the Anchorage NWS (VAAC and the Center Weather Service Unit, CWSU), where predictions and warnings are the primary concern, Puff is used as the first-look simulation due to its speed and simplicity, but HYSPLIT and CanERM, both federal agency models, are considered the official trajectory analysis tools.

Gridded global or regional wind field data are a basic component of dispersion models. Forecast wind fields are received through computer networks one to four times daily depending upon the model. Wind field forecasts extend out to 72 h, although they are less reliable at the later hours in this range. Access to real-time wind fields can be problematic in areas where computer networks are slow or unreliable and the amount of data is large. The wind fields have various grid cell sizes, extend to various altitudes, and may be global or regional in coverage (Chapter 7).

Dispersion models can be implemented for real-time volcano monitoring either by remote login to existing sites or by installing a dispersion model on a local computer. Puff and HYSPLIT both have a web interface to remotely implement and download results. This is the simplest solution for developing access to dispersion models, but it is not conducive to custom development specific to local conditions and needs. Installing a model on a local computer allows custom development. For example, the source code for Puff can easily be downloaded, implemented, and modified to meet local requirements. However, dispersion models need access to wind fields, which requires a software and hardware commitment to maintain the current wind field data and dispersion model interface; in addition, wind field data sets can be large.

To illustrate the use of dispersion models for ash cloud monitoring, a typical Puff simulation is described. A simple Puff run, which is used when an explosive eruption is first detected or suspected, requires only the volcano name or location and eruption start time. All other input parameters have default values and are left unchanged. It takes minutes to run. Results can be displayed either as particles that are color-coded by height (preferred for immediate height estimates) or as relative concentrations. The simulations are overlaid on a map of the region. Multiple images are generated as a function of time and can be animated. As additional information is received regarding an eruption, input parameters such as volcanic cloud height, eruption column shape, particle size, diffusion rate, simulation length, wind field type can be modified and the model rerun. Ash concentration as a function of height can also be displayed. Predicted relative ash deposition can be overlaid on a digital elevation model (DEM). Puff is able to track ash simultaneously from multiple eruptions from single or multiple volcanoes.

Model simulations are compared with volcanic clouds observed in coincidental satellite data to validate their accuracy, to improve (“tune”) the model to better match a particular eruption, and to help identify the cloud structure as a function of height (Figure 9.19). The portion of volcanic clouds detected in satellite data are assumed to be the highest concentrations and considered to be ground-truth for dispersion models. Un-tuned model runs often predict particle transport that extends beyond satellite observations. By modifying parameters, such as diffusion, dispersion, or cloud height (based on other observations), the models are tuned to match satellite observations.

Numerous comparisons with satellite data have shown these models to be reasonably accurate (Searcy *et al.*, 1998). However, the accuracy of dispersion models depends upon the accuracy of the wind fields used. These can be quite variable among climate models. During the March 19, 2001 eruption of Mt. Cleveland, for example, satellite images showed a bifurcated plume with portions going south and east, but Puff predicted only the southern leg of the plume. The error occurred when interpolated gridded wind field data incorrectly modeled upper-atmospheric conditions. In general, tracking models have been accurate for moderate- to high-altitude plumes (>5 km), and have had variable success with low-altitude plumes (<5 km) and in situations with complex ground relief. This is likely

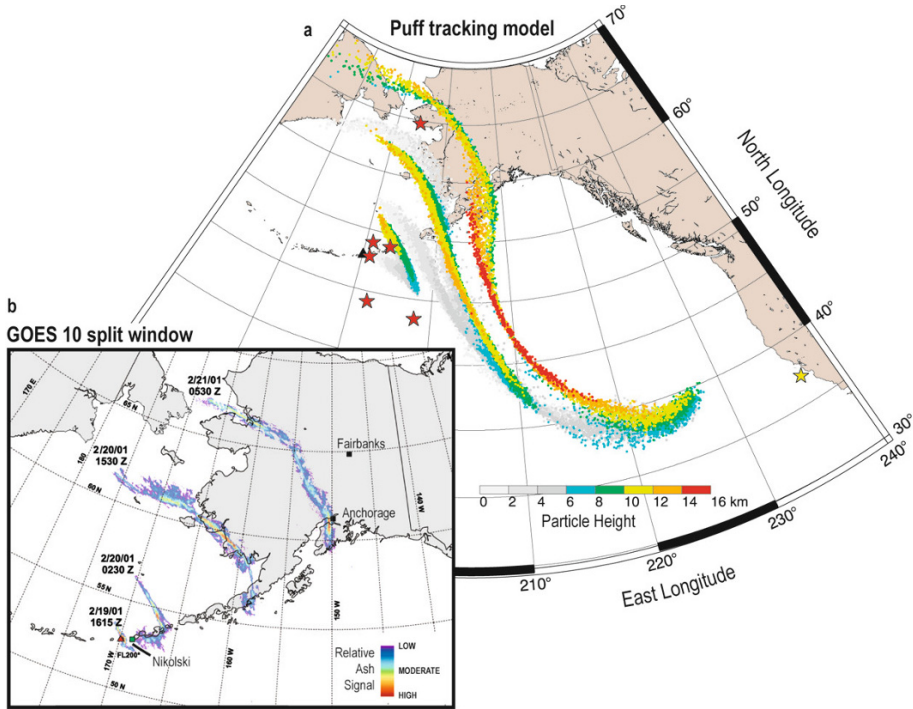


Figure 9.19. Accuracy of dispersion models for the eruption of Mt. Cleveland Volcano, February 19, 2001. The Puff dispersion model predicted that ash extended NW and SE of the volcano as the cloud drifted E, approaching the west coast of the U.S. (a). A multirate composite of GOES split-window images (b) detected ash NE of the volcano as it drifted over the Alaska mainland. The satellite images agree with Puff model predictions over the Aleutian Islands and Alaska. However, satellite images did not detect ash over the Pacific Ocean. Stars represent the location of aircraft that observed or detected the ash cloud. In the Puff animation (see DVD), aircraft are represented by gold stars but turn red at the time they observe or detect the ash cloud. An aircraft near the U.S. west coast (gold star) turns red when this simulated ash cloud encounters the aircraft. The flight crew reported “sulfur and particles” in the cabin (Simpson *et al.*, 2002). Often dispersion models predict ash beyond satellite observations. This is one of the first observations that validated a distal plume prediction (Simpson *et al.*, 2002; Dean *et al.*, 2004). It is likely that the ash and gas cloud in this region was below satellite detection limits. Apparently, the cloud was not dangerous to aircraft since no difficulties were reported.

due to difficulties in accurately modeling atmospheric circulation in the near-surface boundary layer.

Dispersion model predictions of particle transport that extend beyond the cloud detected on satellite data may also be valid. A verbal pilot report associated with the Cleveland Volcano eruption on February 19, 2001 describes particles and strong odor in the cabin (Simpson *et al.*, 2002; Dean *et al.*, 2004) from a region well south of the satellite-detected cloud but in an area that Puff indicated would be impacted (Figure 9.19). A computer animation of this event can be seen on the included DVD. Moreover, back trajectory prediction using

CanERM points to Cleveland Volcano as the source at about the time of the eruption (2007, pers. comm., R. Servranckx, CMC and Montreal VAAC). This single report provided a qualitative observation of ash detection below the lower limit of satellite sensor detection capability.

A critical question is, “Are the low concentrations of ash and aerosols predicted by models and not detected by satellites dangerous to aircraft?” Reports of volcanic cloud encounters with aircraft are few and far between, but are critical for assessing dispersion model accuracy and hazardous conditions. Research comparing aircraft position and dispersion models as a function of time in addition

to satellite observations and pilot reports will help quantify these analyses (Pieri *et al.*, 2002; Dean *et al.*, 2004; Tupper *et al.*, 2006).

9.5.8 Use of dispersion models for hazard mitigation

Dispersion models have been used by AVO, Anchorage VAAC, U.S. Air Force Weather Agency (AFWA), and some airlines to help mitigate potential hazards by predicting volcanic cloud movement and/or estimating cloud height. Although experimental at this time, ash fall can also be predicted using these models. Dispersion models provide useful results for far-field regions ($> \sim 100$ km from the volcano) but, in regions close to a volcano ($< \sim 100$ km), airborne ash is affected by eruption

column dynamics not presently included in the models.

Furthermore, the coarse space and time resolution of commonly available gridded wind fields, both regional and global, are problematic for short-term hazard forecasts for communities within approximately 100 km of a volcano (Figure 9.20). At this distance there may be only a couple of grid cells that provide very limited and possibly misleading information on the direction of cloud movement as well as position and arrival time of the ash cloud. High-velocity winds could place volcanic clouds over these nearby cities within minutes, which is very little time to issue warnings. In these situations dispersion models would provide limited information. Low-velocity winds may allow a few hours of warning for cities 100 km from the volcano, such as in the case of the eruption of Spurr Volcano, 1992.

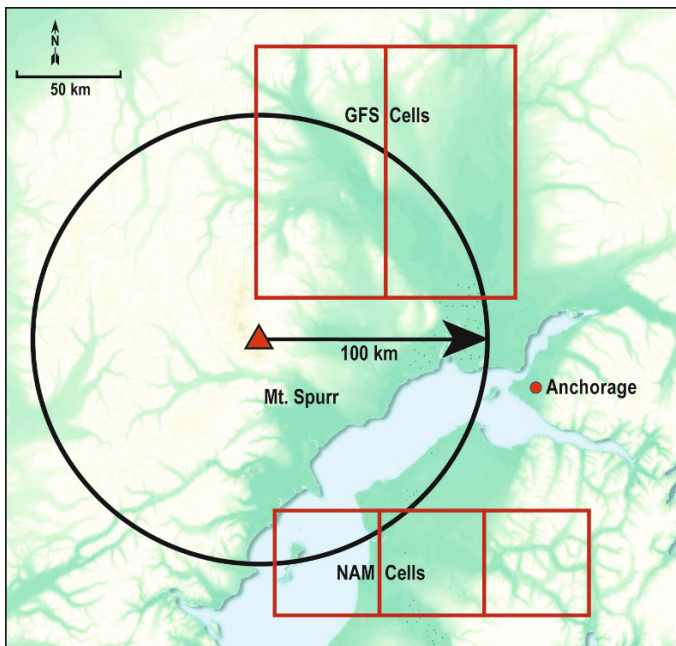


Figure 9.20. Dispersion models have limited use for hazard mitigation for areas within approximately 100 km of a volcano. The two wind field models often used for dispersion modeling are the Global Forecast System (GFS-AVN) and the regional North American Mesoscale (NAM) system, which have typical cell sizes of $1 \times 1^\circ$ or 55×110 km at 60° N and 45×45 km, respectively. In this example, predictions of ash dispersion approaching Anchorage, Alaska from an eruption of Mt. Spurr Volcano would be based on two to three wind field cells, which limits the accuracy of model output. During high-speed winds, ash may be over Anchorage within tens of minutes, which is little time for warnings or hazard mitigation. However, during the eruption of Mt. Spurr, August 19, 1992, ash fell at Anchorage approximately 4 hours after the start of the eruption due to low wind speeds. Despite these model limitations, predictions of the direction of ash movement, its position, and its speed can be critical information for hazard mitigation for the region.

A few hours of warning would permit evacuation of aircraft or the protection of equipment.

Dispersion models may be useful for planning aircraft routes or airport locations by analyzing cloud movement using multiple years of historical wind fields. Hypothetical eruptions of volcanoes in a given area are run using several years of wind field data predicting the distribution of airborne particles. The resulting data from each run are combined and airborne ash probability distribution maps are generated. These maps show where ash will most likely end up in the event of an eruption. Ash probability maps have been generated for representative areas in the North Pacific region (Papp *et al.*, 2005).

9.6 HIGH SPATIAL RESOLUTION DATA FOR MONITORING

High spatial resolution satellite data have a temporal resolution on the order of days to months. These data do not provide sufficient coverage of volcanoes for daily monitoring, but are used to validate and calibrate coarser spatial resolution data (GOES, AVHRR, and MODIS) and are extremely valuable for retrospective studies of eruptions. Examples of these data include Landsat, ASTER, RADARSAT, ERS JERS, and ENVISAT and consist of information in the visible, infrared, and microwave wavelength bands. High spatial resolution data provide detailed observations of volcano morphology, such as location of eruptive vents, deposit characteristics and distribution, and edifice deformation. Applications include relative age dating, landscape change analysis, modeling or mapping of hazardous areas, and generation of digital elevation models. Morphological information can provide insight into volcanic processes such as movement of magma (implied from surface deformation), lava effusion rates, and thermal flux. High spatial resolution data have limited use for volcanic cloud analysis in an operational setting, primarily due to their small field of view, the low probability of recording an explosive event, and available sensor wavelengths. However, high spatial resolution data coupled with daily monitoring data can provide excellent insight into eruption processes.

High spatial resolution satellites can also supplement daily observations by detecting subtle changes over a prolonged period of time, thereby

targeting volcanoes that could potentially erupt in the near future. Three new techniques for long-term monitoring with high-resolution data are increases in surface temperatures and SO₂ discharge using TIR data employing instruments such as ASTER (Chapters 4 and 6), and volcano deformation using interferometric SAR (InSAR) techniques (Chapter 8). This type of monitoring does require that data are routinely acquired and processed in a timely fashion. Coverage by both SAR and ASTER satellites must be requested and scheduled for each target area, which is not conducive to the urgency of monitoring during a crisis. As mentioned previously, techniques have been developed to automatically request high-resolution coverage at areas with increased activity (Chapter 4).

9.7 REPORTING AND COMMUNICATION

Timely reporting and communication, both within the monitoring organization and to other government agencies, industry, and the public, is as critical as the data used to detect an eruption. Satellite data and associated models are good at detecting precursory signals of activity in terms of surface thermal anomalies and deformation, and detecting, tracking, and predicting the movement of volcanic clouds, but they are not good at detecting the subsurface, short-term activity seen in seismic and geodetic data. Satellite data must be coupled with seismic, geodetic, and geologic data for a complete picture of activity. To develop clear and helpful communication and sharing of data must involve all data sources, agencies, industry, and the affected population.

Information must be rapid, accurate, concise, and easily understood. Hazards associated with eruptions are a combination of land-based and airborne conditions, and the communication format may be different and have varied response times depending upon the type of hazard. For example, a Boeing 747 jet aircraft traveling at 14 km (9 miles) per minute or 869 km (540 miles) per hour (see Boeing Specifications webpage) can approach an ash cloud very rapidly, and hence require warnings as soon as possible. On the other hand, most lava flows move slowly, equivalent to a brisk walking pace (Kilburn, 2000) and there is sufficient time to prepare a response and to analyze the path of movement.

Advance warning of explosive eruptions and the presence of volcanic clouds with as much lead time as possible is required to minimize risk to aircraft. The airline industry has requested a target of 5 min warning to the cockpit after the start of an eruption (Hufford *et al.*, 2000). Currently, this is not achievable based solely on routinely available satellite data, since the best repeat coverage is every 15 min (GOES VIS channels) and additional time is required for data processing and distribution. Real-time seismic data can provide the information required within this time limit, but less than a third of potentially active volcanoes in the North Pacific region are instrumented with seismometers. More-

over, seismic signals can be ambiguous regarding ash emissions.

In response to the dangers posed by airborne volcanic ash a system of nine Volcanic Ash Advisory Centers (VAACs) was established worldwide to issue warnings to the international aviation industry of the location and movement of volcanic clouds (ICAO, 2004). There are four VAACs that cover the North Pacific region: Tokyo VAAC, Anchorage VAAC, Washington VAAC, and Montreal VAAC (Figure 9.21). A volcanic cloud from an eruption in Kamchatka and Alaska often drifts across zones covered by multiple VAACs. Volcanoes in the North Pacific region are monitored

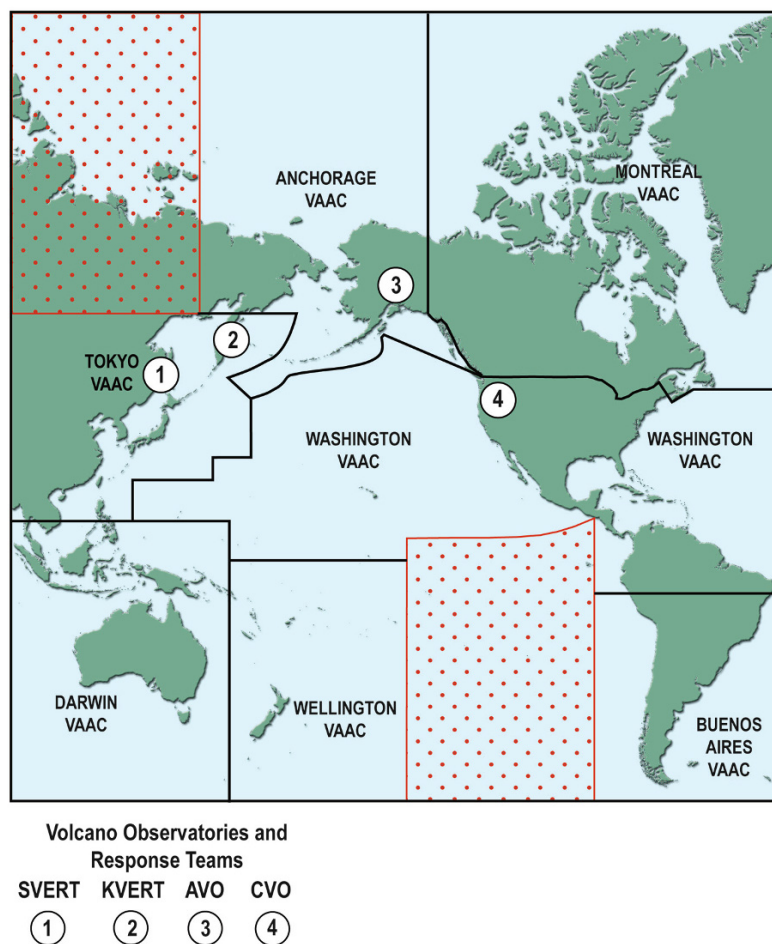


Figure 9.21. Map showing the boundaries of Volcanic Ash Advisory Centers, Volcano Observatories, and Response Teams in the North Pacific region. The stippled red area indicates no VAAC coverage at this time.

by four facilities (Figure 9.21). These are AVO (Alaskan volcanoes), CVO (Cascade volcanoes), KVERT (Kamchatkan volcanoes), and SVERT (Kurile Island volcanoes). These facilities along with several other agencies, such as the National Weather Service (NWS), Federal Aviation Authority (FAA), Department of Defense (DOD), and their counterparts in Russia and Japan (Neal *et al.*, 2007), are responsible for volcano monitoring and/or warnings of eruptions. Each of these agencies provides information to the VAACs in their region, as well as to government response and emergency agencies, industry, and the population in general.

An important communication tool in the U.S.A. is the U.S. Geological Survey's Alert Notification System for Volcanic Activity (Table 9.5) (Gardner and Guffanti, 2006). The alert system consists of an Aviation Color Code system (NOAA, 2011), and a ground-based Volcano Alert Level system. The alert levels defined by this system notify the appropriate federal, state, and local emergency management agencies of volcanic unrest and eruptive activity. The notified agencies then disseminate information outward to other government and public organizations. The Aviation Color Code system is in use by KVERT and SVERT as well.

9.7.1 Alaska Communication Model

Generally, observatories and response agencies use a communication model similar to that in Alaska but with different emphasis depending on eruptive activity and data utilized. In Alaska the frontline agencies involved are AVO, NWS, and FAA. These agencies notify other agencies, industry, and the public of eruptions. These include the Department of Homeland Security and Emergency Management, Department of Defense (DOD), Governor's Office, Canadian Meteorological Center, and NOAA. The flow of information is defined in the Alaska Interagency Operating Plan for Volcanic Ash Episodes (NOAA, 2011).

9.7.2 AVO reporting and communication

AVO is responsible for volcano monitoring, hazard assessments, and eruption notification in Alaska. Internal AVO communication includes technical data displayed on webpages that integrate the multidisciplinary data used for monitoring and a weblog to share data and information. The webpage and weblog are intended to support operational monitoring and thus have restricted access.

Table 9.5. The USGS Alert Notification System for volcanic activity (Gardner *et al.*, 2004).

<i>Volcano alert levels</i>	
<i>Normal</i>	Typical background activity of a volcano in a noneruptive state. Or, after a change from a higher level: volcanic activity considered to have ceased, and volcano reverted to its normal, noneruptive state
<i>Advisory</i>	Elevated unrest above known background activity. Or, after a change from a higher level: volcanic activity has decreased significantly but continues to be closely monitored for possible renewed increase
<i>Watch</i>	Volcano is exhibiting heightened or escalating unrest with increased potential for eruptive activity. Or: a minor eruption is under way that poses limited hazards
<i>Warning</i>	Highly hazardous eruption under way or imminent
<i>Aviation color code</i>	
<i>Green</i>	Volcano is in a normal, noneruptive state. Or, after a change from a higher level: volcanic activity considered to have ceased and volcano reverted to its normal, noneruptive state
<i>Yellow</i>	Volcano is exhibiting signs of elevated unrest above known background levels. Or, after a change from a higher level: volcanic activity has decreased significantly but continues to be closely monitored for possible renewed increase
<i>Orange</i>	Volcano is exhibiting heightened unrest with increased likelihood of eruption. Or: volcanic eruption under way with no or minor ash emission
<i>Red</i>	Eruption is forecast to be imminent with significant emission of ash into the atmosphere likely. Or: eruption is under way with significant emission of ash into the atmosphere

The internal page includes raw preliminary observations that are displayed to optimize eruption-related information and reports of activity in the region. Satellite, seismic, and other observations are included so analysts can cross-reference and view observations and communicate with other AVO components. The latest satellite graphic images

are automatically made available to AVO analysts through this page, as are seismic and other geophysical data. These data can be accessed from any remote computer for monitoring purposes. Graphical images are only used for the monitoring of remote sites or for a rapid review of the region, since they do not have precise radiometric values.

Analysts routinely examine satellite data twice daily for volcanic activity and enter observations into a monitoring database system (Figure 9.7). During periods of increased activity satellite data are reviewed more frequently or, if an eruption is in progress, data are analyzed immediately after the images are received and observations are immediately entered into the monitoring database.

When volcanic activity is observed by any component of AVO, it is immediately reported by telephone to AVO lead scientific personnel in Anchorage and Fairbanks. In the AVO system an attempt is made to confirm the observed activity. For example, if the initial observation is from satellite data, supporting seismic or ground-level observations are sought. If volcanic ash is involved and the observation validated (when possible), the report is immediately relayed to the warning agency, the NWS, and the FAA Air Route Traffic Control Center (ARTCC), via a call-down, who then distribute warnings accordingly. After the call-down, a written statement is distributed to government agencies, directly affected private parties, the media, commercial airlines, the public, and then posted on a webpage. Additional updates are issued as needed.

9.7.3 Communication and hazard assessments: National Weather Service/Anchorage VAAC

The National Weather Service (NWS) operates the Anchorage VAAC, Alaska Aviation Weather Unit (AAWU), Center Weather Service Unit (CWSU), and the Weather Forecast Offices (WFOs). The AAWU is designated to operate the Anchorage VAAC. The role of the Anchorage VAAC is primarily to detect, analyze, and forecast volcanic ash clouds that move through the Anchorage VAAC area of responsibility (NOAA, 2011). An ash cloud may be detected in a number of different ways; however, most typically it would be either through (1) detection by AVO through seismic or satellite signature, (2) detection by VAAC forecaster using satellite, radar, or other information, or (3) detection by pilot and reported to the air traffic control-

ler and transmitted as an urgent pilot report (URGENT PIREP) through the CWSU (ICAO, 2001, 2004).

Upon detection of a volcanic ash cloud, the VAAC notifies the AAWU of a volcanic event, and the AAWU issues a SIGMET (ICAO, 2001, 2004). A SIGMET is a significant meteorological information release containing the height, location, and direction of movement of the ash cloud (Figure 9.22). The SIGMET serves as the warning message to the aviation community of the impending ash hazard and is valid for a period of up to 6 h after issuance time. The VAAC forecaster will then prepare a Volcanic Ash Advisory (VAA) text message which gives specific information about the volcano including location, height, aviation color code, and time of the eruption (Figure 9.22). In addition to this information, the VAA contains a 6, 12, and 18 h forecast of the ash cloud location and direction/speed of movement of the ash. This information provides essential guidance to the SIGMET issuing office as well as air traffic controllers, air traffic managers, airlines, and other agencies. The FAA may issue a NOTAM (Notice To Airmen) which gives specific information about the volcanic ash hazard and will refer users to the SIGMET that is in effect. The FAA may also issue a Temporary Flight Restriction (TFR) to define closed airspace as a result of the volcanic ash hazard.

In Alaska, the NWS, FAA, and AVO work very closely together during volcanic events to ensure that a consistent message is delivered to its customers. Depending upon the scope and impact of the eruption, several other agencies may become involved in the coordination such as the Alaska Department of Homeland Security and Emergency Management, Alaska Department of Environmental Conservation Division of Air Quality, and local municipality emergency managers (NOAA, 2011).

The sudden, explosive eruption of Mt. Cleveland on February 19, 2001 provides an opportunity to outline the flow and timing of communication during an event (Figure 9.23). It also shows the complexity and intricacies of eruption detection and communication, and its strengths and weaknesses. This volcano is not monitored by seismic instruments, so detection was based on satellite data only. Warning agencies and pilots were notified within minutes after AVO detected the eruption. However, since the eruption started at 04:30 AKST, analysts were not on duty and, hence, there was a 4-hour delay between eruption start and detection.

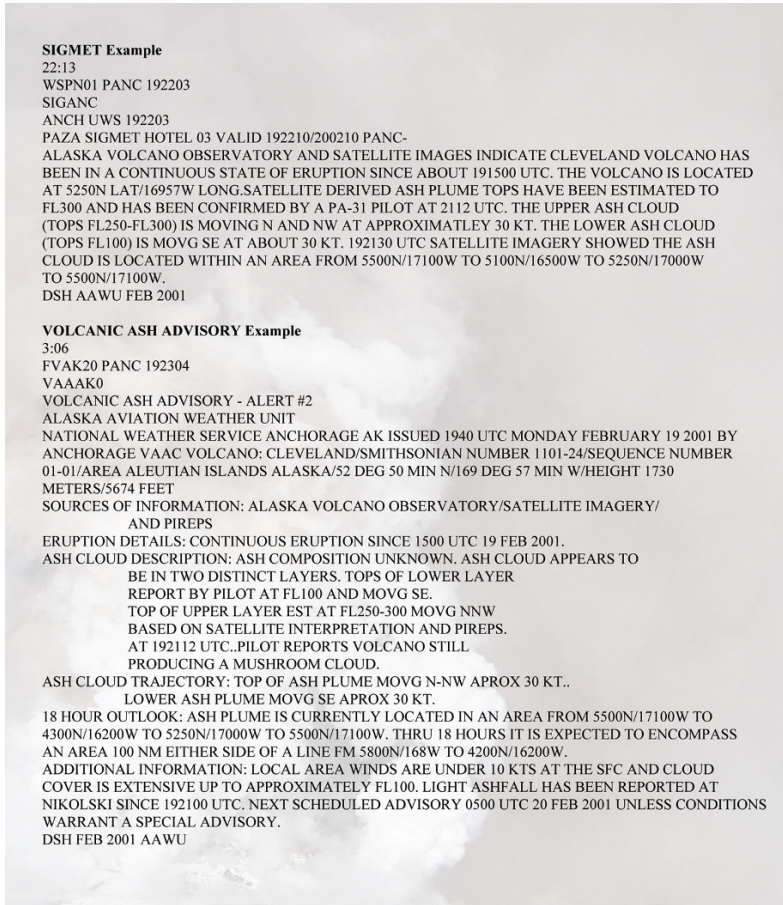


Figure 9.22. Examples of a SIGMET and a Volcanic Ash Advisory for the eruption of Cleveland Volcano on February 19, 2001.

Since this event an automated ash and thermal anomaly detection and alert system has been developed to reduce these time delays.

9.7.4 Volcanic Ash Collaboration Tool (VACT)

VACT is an experimental system that will enable analysts to determine the location, extent, and movement of volcanic ash allowing for more accurate, timely, and consistent forecasts of fallout and dispersion (Rodgers *et al.*, 2004). The system, under development, allows analysts with different expertise and at diverse locations to simultaneously view identical displays of volcanic ash and appropriate related data sets (i.e., shared situational awareness) and collaborate in real time to assess

potential hazardous conditions. From a detection and forecasting perspective, coordination and collaboration will lead to a more efficient and reliable warning and forecast system. The information disseminated from this system will use current approaches and standards to issue societal impact statements but will also be tailored for end user needs in the form of tactical decision aides, such as flagging jet routes or runways affected by ash by color-coding them red. This tool is being tested by the NWS and AVO in Alaska and allows users to view common data sets, chat, and annotate in real time. This tool integrates the meteorological, volcanological, and aviation data into one system that provides an improved shared situational awareness and consistent product suite.

19 February 2001
1430 UTC: Start of Eruption [Note initial estimate of start was 1645 UTC]
1655 UTC: First AVHRR image that recorded the eruption
~1825 UTC: Eruption detected by AVO Satellite Section analyst.
1830 UTC AVO Scientist-In-Charge and Coordinating Scientist were called
1833 UTC First Pilot report regarding the eruption (Simpson et al., 2002). Message sent to Federal Aviation Administration (FAA).
1846 UTC: AVO Satellite Observation Report based on the 1655 AVHRR image
A plume and thermal anomaly over Cleveland were spotted in image n14.01050.1655. The image is night-time. The zenith angle to the summit is about 4.79 degrees. The thermal anomaly is about 6 pixels in size, with maximum temperature at one pixel on the summit of 29.5 degrees. Background was -10 degrees. All data preliminary. The plume is complex. Puff suggests strong wind shear. There is a dark cloud with b4 temperatures of -50 of about 40 km to the NW (bearing 143), and a cloud with strong 4-5 signal (reaching -4.9) for 62 km to the SE (bearing 136). The plume could be as high as 30,000ft, though the NW plume shows no 4-5, it still could contain significant ash. The low plume is estimated at 5 km.
1847 UTC, Sigmet, Anchorage UWS, Indications of a possible eruption at Cleveland Volcano
1924 UTC, Sigmet, Anchorage UWS, Indications of a possible eruption at Cleveland Volcano
1930 UTC AVO USGS: Volcanic Activity Report
AVO detected a volcanic ash cloud emanating from Cleveland Volcano in satellite imagery that began about 1500 Z (0600 AST), in the Islands of the Four Mountains. According to images from 1845 Z (0945 AST), the main part of the cloud was drifting about 120 km (75 mi) southeast of Cleveland and reached about 17,000 feet above sea level. A higher ash cloud extends to the north about 100 km (60 mi) and has reached an estimated altitude of 30,000 ft above sea level.....
52°49'N 169°57'W, Summit Elevation 5,674 ft (1,730 m)
1940 UTC Volcanic Ash Advisory Alert, Alaska Aviation Weather Unit, National Weather Service Anchorage, Ak. by Anchorage VAAC
Volcano: Cleveland/Smithsonian Number 01-01/Area Aleutian Islands, 52 Deg, 50 Min. N/169 Deg. 57 Min. W, Height 1730 Meters/5674 Feet, Source of information AVO/Satellite Imagery, Eruption details: Satellite indication of Feb. 19 1645 UTC Cloud description : Composition unknown, Est. height is FL 30,000 ft. based on information received from NESDIS ash cloud trajectory: Top of ash plume moving NW approx. 25 ks. Lower ash plume moving SE approx. 30 kt. 18 hrs. outlook: Ash plume is expected to stretch out and be located 50 nm either side of a line from 5500 N/1700 W to 4700N/16730 W. This is based on the Puff Model. Additional information: Local area winds are under 10 kts. At the SFC and cloud cover is extensive up to approximately FL 10,000, next scheduled advisory 0200 UTC 20 February unless conditions warrant a special advisory
2020 UTC: Washington VAAC SIGMET (NOAA Archived Volcanic Ash Advisory Statements),
*Volcanic Ash Advisory, Washington VAAC:
 Volcano: Cleveland, 1101-24. Location: S250N 16957W, Area: Aleutian Island Alaska, Summit Elevation: 5675 FT (1730 M), Advisory Number: 2001/02.....*

Figure 9.23. Chronology describing the communication of warnings of the eruption of Mt. Cleveland, February 19, 2001. Approximately 1.5 hours after the eruption was detected by AVO, the Anchorage VAAC alerted pilots. This volcano is remote and monitored using satellite data only and thus there is a time delay in the detection of eruptions due to the temporal resolution of satellite data coverage, data-processing, and observation schedules. Recently implemented automated alerts have decreased the time delay.

9.8 THE FUTURE OF SATELLITE MONITORING OF VOLCANIC ACTIVITY

The future availability of satellite data for real-time daily volcano monitoring looks very promising (Figure 9.24) with the continuation of existing systems and new systems to be launched (Achache *et al.*, 2004). Image data from GOES, NOAA's Polar Orbiting Environmental Satellite (POES), MTSAT, and MODIS sensors will for the most part be available throughout this decade. In addition, data are newly available from the National Polar Orbiting

Environmental Satellite System (NPOESS) Preparatory Project (NPP). In 2015 the GOES R satellite will be launched and, if the current planning holds, in 2017 the Joint Polar Satellite System (JPSS) satellite JPSS-1 will be launched. The GOES-R system is a follow-on to the U.S. GOES missions, and the JPSS system builds on the POES and NPP satellites, both adopting many bands from the MODIS sensor. These new satellites have various strengths and weaknesses regarding their use for volcano monitoring and analysis. In addition, data volume, processing capability, and distribution approaches will be much greater or different

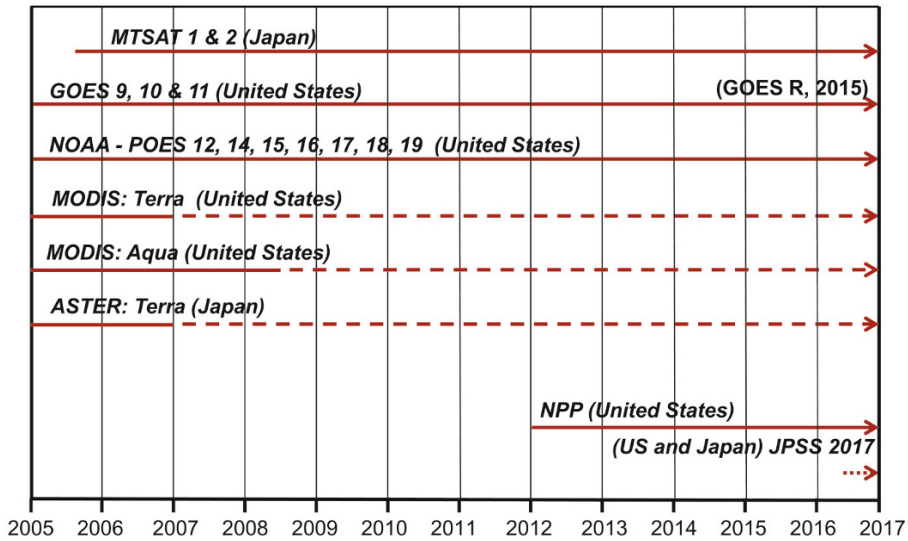


Figure 9.24. Chart showing projected timelines of satellites used for operational volcano monitoring in the North Pacific region. Solid lines are existing satellites, dashed are beyond satellite design life, and dotted are planned satellites starting with estimated launch dates.

than current systems that may require significant upgrades to existing ground stations (e.g., Jones, 2004a, b; Jones *et al.*, 2004; NASA-GSFC and NOAA, 2005).

The GOES sensors will continue to provide data similar to present systems but with higher spatial resolution (double the current abilities) for targets of opportunity and improved image navigation and registration. However, the shifting of a TIR band from 11.5–12.5 μm to 13.00–13.70 μm wavelengths on the most recent GOES satellites limited the ability to detect ash in volcanic clouds using the split-window technique (Ellrod, 2004; NASA-GSFC and NOAA, 2005). The GOES R satellite will provide data with higher spatial, spectral, and temporal resolutions than current systems. Spatial resolution will also be improved by a factor of 2. The Advanced Baseline Imager (ABI) will consist of 16 spectral bands over visible, NIR, and TIR wavelengths. Wavelengths required for ash detection using the split-window technique (NASA, 2005) and those for SO_2 detection will be included (Schmit *et al.*, 2005). The full Earth disk coverage rate will be every 15 minutes compared with 30 minutes (TIR bands) on present satellites.

NPOESS sensors will integrate capabilities currently provided by NASA, NOAA, and DOD Defense Meteorological Satellite Program (DMSP) sensors. Data and associated capabilities developed

for NASA research satellites will become routinely available on NPOESS. Capabilities will include multispectral TIR data for analysis of surface temperatures and improved volcanic, ash cloud, and SO_2 detection (Jones, 2004a, b). The first of these new satellites is the NPOESS Preparatory Project (NPP), which is intended to be a transition from MODIS sensors and algorithms to future systems (Jones *et al.*, 2004; Jones and Nelson, 2005). NPP came online in 2012 and is performing well. Its use in volcano monitoring is growing and it is a valuable addition to polar-orbiting sensors, adding new capabilities and many more views each day. The JPSS system will add to this suite of sensors with the first launch scheduled for 2017.

Planned and proposed satellite sensors will have sufficient resolution to identify subtle fluctuations in background signals that might be related to the early onset of an eruption at levels not presently possible from satellite. Daily measurements of SO_2 degassing, thermal flux, and effusion rates are examples of volcanic processes that will provide precursory signals to explosive activity. Weekly to monthly measurements of ground deformation is another example. However, the 5-minute warning after the start of an eruption, as requested by the airline industry, is still unlikely based on satellites only, even with the new GOES and NPOESS systems.

9.9 CONCLUSIONS

Satellite remote sensing is an invaluable tool for operational volcano monitoring in the vast North Pacific region which complements other geophysical monitoring and geological analyses. Even though satellite data cannot monitor minute-by-minute changes at a volcano, subhourly coverage coupled with immediate processing, analysis, and warnings of activity is sufficient to detect volcanic processes on the scale of hours and days to weeks. Satellite data can be used to detect volcanic clouds, thermal anomalies, and monitor changes in the position, structure, or intensity of these features. No other available technique can monitor these features as well. High temporal resolution satellite data is critical to operational monitoring, and increased spectral resolution has improved detection and analysis capabilities. Techniques have been developed to schedule and acquire some high spatial resolution data in a timely manner in support of daily operational monitoring. High spatial resolution data also provide valuable information on long-term temperature flux and the surface morphology employed to validate and calibrate data used for daily monitoring, and to detect subtle signals that are precursors of eruptive activity.

Processed satellite data must be accessible to analysts within minutes after a satellite pass but, in reality, tens of minutes are required. Automated processing is needed to achieve near-real time capabilities but an analyst is required at some level. Near-infrared and shortwave infrared data can be very useful in detecting opaque and short low-level, ash-free plumes during the day. Mid-infrared data in the 3 to 5 μm range are the best for detection and assessments of hot targets and small ash-free plumes. Thermal infrared data in the 10 to 12 μm range are best for day and night detection and assessments of opaque volcanic clouds and translucent ash-rich clouds (split-window technique). Cloud height is best estimated by cross-referencing cloud temperature to atmospheric temperature profiles, and cloud trajectory to atmospheric wind fields. For optimum detection and analysis, data from the multiple wavelengths described above and using many varied techniques (single-band and multiple-band combinations) must be utilized.

Ash dispersion models are also critical for eruption monitoring to predict the location and direction of movement of volcanic clouds. The models must be easy to implement and produce rapid results, and must have a relatively high spatial reso-

lution to provide useful information for communities near a volcano. Ideally, models should be customizable to account for local conditions and requirements. Dispersion models predict the location and movement of volcanic clouds and provide critical information about the cloud while waiting for a satellite pass or field report. Satellite data are crucial to the validation and “tuning” of the dispersion model. Puff is the locally controlled model used in the North Pacific region, where it is used in conjunction with the HYSPLIT and CanERM models.

Timely communication is as critical as the data used to detect an eruption. At AVO, when volcanic activity is detected, the observations are immediately reviewed internally and, if collaborative evidence supports the observations or if the observations are substantial, warnings are issued to government officials and the general public using voice, fax, and email within tens of minutes after detection. Our goal is to continue to improve our communication between agencies and monitoring techniques for hazard assessment and mitigation.

9.10 ACKNOWLEDGMENTS

This work was supported by the Geophysical Institute, University of Alaska Fairbanks, AVO, and NASA. AVO is part of the U.S. Geological Survey Volcano Hazards Program, which is a collaborative effort of the USGS, UAFGI, and the Alaska Division of the Geological and Geophysical Surveys (ADGGS). Development of the satellite-based volcano-monitoring system at AVO was a collective effort by faculty, staff, and students at UAF and analysts at the USGS. Kevin Engle maintained the satellite stations and data feed and developed many of the initial algorithms used for monitoring. Jon Dehn refined and developed new processing and analysis techniques. Craig Searcy, Rorik Peterson, Peter Webley, Mark Servilla, and Jim Long made the Puff model a powerful eruption response and research tool. John Bailey developed the Google Earth interface as a powerful geographic reference tool. Lovro Valcic, Ray Skoog, and Laura Bickmeier developed and maintained the database monitoring system and new data-processing techniques. Pavel Izbekov provided liaison efforts with Russian scientists at KVERT and SVERT and translated Russian contributions to the manuscript. Great admiration goes to students Ken Papp, Matt Patrick, Steve Smith, Andrea Steffke, Court-

ney Kearney, Joe Lovick, Peter Rinkleff, Gry Andrup-Henriksen, Rachel Wilson Puchrik, Abby Gleason and to all future students for their tireless efforts to monitor volcanoes at all hours, every day of the year. The students are continuously testing and debugging the system and their research provides a basis to develop new techniques. Without student efforts, satellite volcano monitoring in the North Pacific would be difficult and not as dynamic. A special thank-you goes to Ken Papp and John Bailey for proofreading and editing the chapter, to Christina Neal for her amazing editing abilities, and to Andrew Tupper for his insightful editorial comments and references. We would all like to thank our families for not complaining too much about working long hours and weekends during the writing of this chapter and the many late night and early morning phone calls requiring us to respond to eruptions.

9.11 REFERENCES

- Achache, J.; Withee, G.; Erdelen, W. (2004). *For the Monitoring of Our Environment from Space and from Earth* (Geohazards Theme Report), European Space Agency, Noordwijk, The Netherlands, 55 pp.
- Ackerman, S.A. (1997) Remote sensing aerosols using satellite infrared observations, *J. Geophys. Res.*, **102**(D14), 17069–17080.
- Bluth, G.J.S.; Scott, C.J.; Sprod, I.E.; Schnetzler, C.C.; Krueger, A.J.; Walter, L.S. (1995). Explosive emissions of sulfur dioxide from the 1992 Crater Peak eruptions, Mount Spurr Volcano, Alaska, in T.E.C. Keith (Ed.), *The 1992 Eruptions of Crater Peak Vent, Mount Spurr Volcano, Alaska, United States (U.S.A.)* (USGS Bulletin 2139), U.S. Geological Survey, Reston, VA, pp. 37–45.
- Carey, S.A.; Bursik, M. (2000). Volcanic plumes, in H. Sigurdsson, B. Houghton, S.R. McNutt, H. Rymer, and J. Stix (Ed.), *Encyclopedia of Volcanoes*, Academic Press, San Diego, CA, pp. 527–544.
- Carn, S.A.; Oppenheimer, C. (2000). Remote monitoring of Indonesian volcanoes using satellite data from the Internet, *Int. J. Remote Sensing*, **21**(5), 873–910.
- Carn, S.A.; Krueger, A.J.; Krotkov, N.A.; Yang, K.; Evans, K. (2009). Tracking volcanic sulfur dioxide clouds for aviation hazard mitigation, *Nat. Hazards*, **51**, 325–343, doi: 10.1007/s11069-008-9228-4.
- Casadevall, T.J. (1994). The 1989-1990 eruption of Redoubt Volcano, Alaska: Impacts on aircraft operations, *J. Volcanol. Geothermal Res.*, **62**, 301–316.
- Casadevall, T.L.; Thompson, T.B.; Fox, T. (1999). *World Map of Volcanoes and Principal Aeronautical Features*. U.S. Geological Survey, Reston, VA.
- Chahine, M.T.; Pagano, T.S.; Aumann, H.H.; Atlas, R.; Barnett, C.; Blaisdell, J.; Chen, L.; Divakarla, M.; Fetzer, E.J.; Goldberg, M. *et al.* (2006). AIRS: Improving weather forecasting and providing new data on greenhouse gases, *Bull. Am. Meteorol. Soc.*, **87**(7), 911–926.
- De Angelis, S.; McNutt, S.R.; Webley, P.W. (2011). Evidence of atmospheric gravity waves during the 2008 eruption of Okmok volcano from seismic and remote sensing observations, *Geophys. Res. Lett.*, **38**(10), doi: 10.1029/2011GL047144.
- Dean, K.G.; Garbiel, H.; Guritz, R. (1990) Near-real time acquisition and analysis of satellite images of Redoubt Volcano, *EOS, Trans. Am. Geophys. Union*, **71**(43), 1701.
- Dean, K.G.; Bowling, S.A.; Shaw, G.E.; Tanaka, H. (1994). Satellite analyses of movement and characteristics of the Redoubt Volcano plume, January 8, 1990, *J. Volcanol. Geothermal Res.*, **62**, 339–352.
- Dean, K.G.; Servilla, M.; Roach, A. (1998). Satellite monitoring of remote volcanoes improves study efforts in Alaska, *EOS, Trans. Am. Geophys. Union*, **79**(35), 422–423.
- Dean, K.G.; Dehn, J.; McNutt, S.; Neal, C.; Moore, R.; Schneider, D. (2002). Satellite imagery proves essential for monitoring erupting Aleutian Volcano, *EOS, Trans. Am. Geophys. Union*, **83**(22), 246–247.
- Dean, K.G.; Dehn, J.; Papp, K.R.; Smith, S.; Izbekov, P.; Peterson, R.; Kearney, C.; Steffke, A. (2004). Integrated satellite observations of the 2001 eruption of Mt. Cleveland, Alaska, *J. Volcanol. Geothermal Res.*, **135**(1–2), 51–73.
- Dehn, J.; Dean, K.; Engle, K. (2000). Thermal monitoring of North Pacific volcanoes from space, *Geology*, **28**(8), 755–758.
- Dehn, J.; Dean, K.G.; Engle, K.; Izbekov, P. (2002). Thermal precursors in satellite images of the 1999 eruption of Shishaldin Volcano, *Bull. Volcanol.*, **64**(8), 525–534.
- Draxler, R.R.; Hess, G.D. (1998). An overview of the HYSPLIT_4 modelling system for trajectories, dispersion, and deposition, *Australian Meteorological Magazine*, **47**(4), 295–308.
- Ellrod, G.P. (2004). Impact on volcanic ash detection caused by the loss of the 12.0 μm “Split Window” band on GOES imagers, *J. Volcanol. Geothermal Res.*, **135**, 91–103.
- Francis, P.W.; Rothery, D.A. (1987). Using the Landsat Thematic Mapper to detect and monitor active volcanos: An example from Lascar Volcano, northern Chile, *Geology*, **15**(7), 614–617.
- Gardner, C.A.; Guffanti, M.C. (2006). *U.S. Geological Survey’s Alert Notification System for Volcanic Activity*, USGS Fact Sheet 3139, U.S. Geological Survey, Reston, VA, p. 4.
- Gardner, C.A.; Guffanti, M.; Heliker, C.C.; Hill, D.P.; Lowenstern, J.B.; Murray, T.L. (2004). A proposed Alert-Level Notification Scheme for aviation and ground-based hazards at U.S. volcanoes, in *Proceed-*

- ings of the Second International Conference on Volcanic Ash and Aviation Safety, Alexandria, Virginia, pp. 37–41.
- Graf, H.; Herzog, M.; Oberhuber, J.M.; Textor, C. (1999). Effect of environmental conditions on volcanic plume rise, *J. Geophys. Res.*, **104**(D20), 24309–24320.
- Harris, A.J.L.; Thornber, C.R. (1999). Complex effusive events at Kīlauea as documented by the GOES satellite and remote video cameras, *Bull. Volcanol.*, **61**(6), 382–395.
- Harris, A.J.L.; Vaughan, R.A.; Rothery, D.A. (1995). Volcano detection and monitoring using AVHRR data: The Krafla eruption, 1984, *Int. J. Remote Sensing*, **16**(6), 1001–1020.
- Harris, A.J.L.; Blake, S.; Rothery, D.A.; Stevens, N.F. (1997a). A chronology of the 1991 to 1993 Mount Etna eruption using advanced very high resolution radiometer data: Implications for real-time thermal volcano monitoring, *J. Geophys. Res.—Solid Earth*, **102**(B4), 7985–8003.
- Harris, A.J.L.; Butterworth, A.L.; Carlton, R.W.; Downey, I.; Miller, P.; Navarro, P.; Rothery, D.A. (1997b). Low-cost volcano surveillance from space: Case studies from Etna, Krafla, Cerro Negro, Fogo, Lascar and Erebus, *Bull. Volcanol.*, **59**(1), 49–64.
- Harris, A.J.L.; Flynn, L.P.; Rothery, D.A.; Oppenheimer, C.; Sherman, S.B. (1999). Mass flux measurements at active lava lakes: Implications for magma recycling, *J. Geophys. Res.—Solid Earth*, **104**(B4), 7117–7136.
- Harris, A.J.L.; Flynn, L.P.; Dean, K.G.; Pilger, E.; Wooster, M.; Okubo, C.; Mouginiis-Mark, P.J.; Garbeil, H.; Thornber, C.; De la Cruz-Reyna, S.; Rothery, D.A.; Wright, R. (2000). Real-time satellite monitoring of volcanic hot spots, in P. Mouginiis-Mark, J.A. Crisp, and J.H. Fink (Eds.), *Remote Sensing of Active Volcanism*, AGU Monograph 116, American Geophysical Union, Washington, D.C., pp. 139–159.
- Heffter, J.L.; Stunder, B.J.B. (1993). Volcanic ash forecast transport and dispersion (Vaftad) model, *Weather and Forecasting*, **8**(4), 533–541.
- Higgins, J.; Harris, A. (1997). VAST: A program to locate and analyse volcanic thermal anomalies automatically from remotely sensed data, *Computers & Geosciences*, **23**(6), 627–645.
- Holasek, R.E.; Rose, W.I. (1991). Anatomy of 1986 Augustine Volcano eruptions as recorded by multi-spectral image-processing of digital Avhrr weather-satellite data, *Bull. Volcanol.*, **53**(6), 420–435.
- Holasek, R.E.; Self, S.; Woods, A.W. (1996). Satellite observations and interpretation of the 1991 Mount Pinatubo eruption plumes, *J. Geophys. Res.—Solid Earth*, **101**(B12), 27635–27655.
- Hufford, G.L.; Salinas, L.J.; Simpson, J.J.; Barske, E.G.; Pieri, D.C. (2000). Operational implications of airborne volcanic ash, *Bull. Amer. Meteorol. Society*, **81**(4), 745–755.
- ICAO (2001). *Manual on Volcanic Ash, Radioactive Material and Toxic Chemical Clouds*, Doc. 9691-AN/954, First Edition, International Civil Aviation Organization, Quebec, Canada.
- ICAO (2004). *Handbook on the International Airways Volcano Watch (IAVW): Operational Procedures and Contact List*, Doc. 9766-AN/968, International Civil Aviation Organization, Quebec, Canada, p. 46.
- Jones, D. (2004a). The future of earth-sensing from space, *Earth Obs. Mag.*, **13**(1), 4–10.
- Jones, D. (2004b). The next generation earth observation system, *Earth Obs. Mag.*, **13**(2), 8.
- Jones, D.; Nelson, C. (2005). NPOESS: Harvesting the benefits of space technology, *Earth Observation Magazine*, **14**(5), 6.
- Jones, D.; Schneider, S.R.; Wilczynski, P.; Nelson, C. (2004). NPOES Preparatory Project: The bridge between research and operations, *Earth Observation Magazine*, **13**(3), 12–1, 20–22.
- Kidwell, K.B. (1998). *NOAA Polar Orbiter Data User's Guide*, NOAA, NESDIS Climate Services Division, Suitland, MD, <http://www.ncdc.noaa.gov/oa/pod-guide/ncdc/docs/podug/index.htm>.
- Kienle, J.; Dean, K.G.; Garbeil, H.; Rose, W.I. (1990). The 1989–1990 eruption of Redoubt Volcano: Satellite surveillance of volcanic ash plumes, application to aircraft safety [modified], *EOS, Trans. Am. Geophys. Union*, **71**(7), 266.
- Kilburn, C. (2000). Volcanic plumes, in H. Sigurdsson, B. Houghton, S.R. McNutt, H. Rymer, J. Stix (Eds.), *Encyclopedia of Volcanoes*, Academic Press, San Diego, CA, pp. 291–305.
- Kinoshita, K.; Kanagaki, C.; Iino, N.; Koyamada, M.; Terada, A.; Tupper, A. (2003). Volcanic plumes at Miyakejima observed from satellites and from the ground, *Optical Remote Sensing of the Atmosphere and Clouds III*, **4891**, 227–236.
- Krotkov, N.A.; Carn, S.A.; Krueger, A.J.; Bhartia, P.K.; Yang, K. (2006). Band residual difference algorithm for retrieval of SO₂ from the Aura Ozone Monitoring Instrument (OMI), *IEEE Trans. Geosci. Remote Sensing*, **44**(5), 1259–1266.
- Little, K.; Johnson, K.; Servranckx, R. (1999). Volcanic ash forecasting event over Western Canada: Operational response and forensic study, in *Conference on Aviation, Range, and Aerospace Meteorology, Boston, MA*, pp. 269–272.
- Lutgens, F.K.; Tarbuck, E.J. (1979). *The Atmosphere: An Introduction to Meteorology*, Prentice Hall, Englewood Cliffs, NJ, 462 pp.
- McNutt, S.R. (1994). Volcanic tremor amplitude correlated with the volcanic explosivity index and its potential use in determining ash hazards to aviation, *Acta Vulcanologica*, **5**, 193–196.
- McNutt, S.R. (2004). Volcanic tremor and its use in estimating eruption parameters: Conference Booklet, in *Second International Conference on Volcanic Ash and Aviation Safety, Washington D.C.*, pp. 49–50.

- Miller, T.P.; Casadevall, T.J. (2000). Volcanic ash hazards to aviation, in H. Sigurdsson, B. Houghton, S.R. McNutt, H. Rymer, and J. Stix (Eds.), *Encyclopedia of Volcanoes*, Academic Press, San Diego, CA, pp. 915–930.
- Mouginis-Mark, P.J.; Domergue-Schmidt, N. (2000). Acquisition of satellite data for volcano studies, in P. Mouginis-Mark, J.A. Crisp, and J.H. Fink (Eds.), *Remote Sensing of Active Volcanism* (AGU Monograph 116), American Geophysical Union, Washington, D.C., pp. 9–24.
- Mouginis-Mark, P.J.; Garbiel, H.; Flament, P. (1994). Effects of viewing geometry on AVHRR observations of volcanic thermal anomalies, *Remote Sensing of Environment*, **48**, 51–60.
- Murayama, T.; Sugimoto, N.; Uno, I.; Kinoshita, K.; Aoki, K.; Hagiwara, N.; Liu, Z.; Matsui, I.; Sakai, T.; Shibata, T. *et al.* (2001). Ground-based network observation of Asian dust events of April 1998 in east Asia, *J. Geophys. Res.*, **106**, 18345–18339.
- NASA (2005). *NOAA GOES-N, O, P: The Next Generation*, NASA-Goddard Space Flight Center, p. 36.
- NASA-GSFC and NOAA (2005). *NOAA GOES-N, O, P: The Next Generation*, NASA-Goddard Space Flight Center, p. 38.
- NOAA, FAA, and USGS (2011). Alaska Interagency Operating Plan for Volcanic Ash Episodes, 60 pp. <http://www.avo.alaska.edu/downloads/reference.php?cid=3996>.
- Neal, C.; Girina, O.; Senyukov, S.; Rybin, A.; Osiensky, J.; Hall, T.; Nelson, K.; Izbekov, P. (2007). Status report, in *Fourth International Workshop on Volcanic Ash, Rotorua, New Zealand, March 26–20*, p. 8.
- Newhall, C.G.; Self, S. (1982). The volcanic explosivity index (VEI): An estimate of explosive magnitude for historical volcanism, *J. Geophys. Res.*, **87**(C2), 1231–1238.
- Oberhuber, J.M.; Herzog, M.; Graf, H.; Schwanke, K. (1998). Volcanic plume simulation on large scales, *J. Volcanol. Geothermal Res.*, **87**, 29–53.
- Oppenheimer, C. (1998). Volcanological applications of meteorological satellites, *Int. J. Remote Sensing*, **19**(15), 2829–2864.
- Papp, K.R.; Dean, K.G.; Dehn, J. (2005). Predicting regions susceptible to high concentrations of airborne volcanic ash in the North Pacific region, *J. Volcanol. Geothermal Res.*, **148**(3–4), 295–314.
- Pavolonis, M.J. (2010). Advances in extracting cloud composition information from spaceborne infrared radiances: A robust alternative to brightness temperatures. Part I: Theory, *J. Appl. Meteorol. Climatol.*, **49**, 1992–2012.
- Pavolonis, M.J.; Feltz, W.F.; Heidinger, A.K.; Gallina, G.M. (2006). A daytime complement to the reverse absorption technique for improved automated detection of volcanic ash, *J. Atmos. Oceanic Technology*, **23**, 1422–1444.
- Pieri, D.; Ma, C.; Simpson, J.J.; Hufford, G.; Grindle, T.; Grove, C. (2002). Analyses of in-situ airborne volcanic ash from the February 2000 eruption of Hekla Volcano, Iceland, *Geophys. Res. Lett.*, **29**(16), 1767.
- Prata, A.J. (1989). Observations of volcanic ash clouds in the 10–12 μm window using AVHRR/2 data, *Int. J. Remote Sensing*, **10**(4–5), 751–761.
- Prata, F.; Bluth, G.; Rose, B.; Schneider, D. (2001a). Comments on “Failures in detecting volcanic ash from a satellite-based technique,” *Remote Sensing of Environment*, **78**, 347–357.
- Prata, F.; Bluth, G.; Rose, B.; Schneider, D.; Tupper, A. (2001b). Failures in detecting volcanic ash from a satellite-based technique: Comments, *Remote Sensing of Environment*, **78**(3), 341–346.
- Prata, A.J.; O’Brien, D.M.; Rose, W.I.; Self, S. (2003). Global long-term sulphur dioxide measurements from TOVS data: A new tool for studying explosive volcanism and climate, in A. Robock and C. Oppenheimer (Eds.), *Volcanism and the Earth’s Atmosphere*, AGU Monograph, American Geophysical Union, Washington, D.C., p. 360.
- Pudykiewicz, J. (1988). Numerical simulation of the transport of radioactive cloud from the Chernobyl nuclear accident, *Tellus*, **40B**, 241–259.
- Pudykiewicz, J. (1989). Simulation of the Chernobyl dispersion with a 3-D hemispheric tracer model, *Tellus*, **41B**, 391–412.
- Pudykiewicz, J.A.; Dastoor, A.P. (1995). On numerical simulation of the global distribution of sulfate aerosol produced by a large volcanic eruption, *J. Climate*, **8**(3), 464–473.
- Realmuto, V.J.; Abrams, M.J.; Buongiorno, M.F.; Pieri, D.C. (1994). The use of multispectral thermal infrared image data to estimate the sulfur-dioxide flux from volcanos: A case study from Mount Etna, Sicily, July 29, 1986, *J. Geophys. Res.—Solid Earth*, **99**(B1), 481–488.
- Realmuto, V.J.; Sutton, A.J.; Elias, T. (1997). Multispectral thermal infrared mapping of sulfur dioxide plumes: A case study from the East Rift Zone of Kilauea Volcano, Hawaii, *J. Geophys. Res.—Solid Earth*, **102**(B7), 15057–15072.
- Rodgers, D.M.; Pratt, G.; Osiensky, J.M. (2004). Volcanic ash coordination tool (VACT), in *11th Aviation, Range and Aerospace Meteorology Conference, Hyannis Port, MA*.
- Rose, B.; Kostinski, A.; Kelly, L. (1995a). Real-time C-band radar observations of 1992 eruption clouds from Crater Peak, Mount Spurr Volcano, Alaska, *U.S. Geological Survey Bulletin*, **B2139**, 19–26.
- Rose, W.I.; Delene, D.J.; Schneider, D.J.; Bluth, G.J.S.; Krueger, A.J.; Sprod, I.; McKee, C.; Davies, H.L.; and Ernst, G.G.J. (1995b). Ice in the 1994 Rabaul eruption cloud: Implications for volcano hazard and atmospheric effects, *Nature*, **373**, 477–479.
- Sabins, F.F. (1997). *Remote Sensing: Principles and Interpretation*, W.H. Freeman & Co., New York, 494 pp.

- Schmit, T.J.; Gunshor, M.M.; Menzel, P.W.; Gurka, J.J.; Jun, L.; Bachmeier, S.A. (2005). Introducing the next-generation advanced baseline imager on GOES-R, *Bull. Am. Meteorol. Soc.*, **86**(8), 1079–1086.
- Schneider, D.J.; Rose, W.I.; Kelley, L. (1995). Tracking of 1992 eruption clouds from Crater Peak vent of Mount Spurr Volcano, Alaska, using AVHRR, in T.E.C. Keith (Ed.), *The 1992 Eruptions of Crater Peak Vent, Mount Spurr Volcano, Alaska, United States (U.S.A.)* (USGS Bulletin 2139), U.S. Geological Survey, Reston, VA, pp. 27–36.
- Schneider, D.J.; Rose, W.I.; Coke, L.R.; Bluth, G.J.S.; Sprod, I.E.; Krueger, A.J. (1999). Early evolution of a stratospheric volcanic eruption cloud as observed with TOMS and AVHRR, *J. Geophys. Res.—Atmospheres*, **104**(D4), 4037–4050.
- Schneider, D.J.; Dean, K.G.; Dehn, J.; Miller, T.P.; Kirianov, V.Y. (2000). Monitoring and analyses of volcanic activity using remote sensing data at the Alaska Volcano Observatory: Case study for Kamchatka, Russia, December 1997, in P. Mouginiis-Mark, J.A. Crisp, and J.H. Fink (Eds.), *Remote Sensing of Active Volcanism* (AGU Monograph 116), American Geophysical Union, Washington, D.C., pp. 65–85.
- Searcy, C.; Dean, K.; Stringer, W. (1998). PUFF: A high-resolution volcanic ash tracking model, *J. Volcanol. Geothermal Res.*, **80**(1–2), 1–16.
- Servranckx, R.; D'Amours, R.; Jean, M.; Tovissini, J.; Trudel, S. (1996). Volcanic ash forecasting at the Canadian Meteorological Centre, in *Pan Pacific Hazards '96, July 29 to August 2, 1996, Vancouver, BC, Canada*, available at http://www.msc-smc.ec.gc.ca/emc/eer/vaac/pph/index_e.html
- Simpson, J.J.; Hufford, G.; Pieri, D.; Berg, J. (2000). Failures in detecting volcanic ash from satellite-based technique, *Remote Sensing of Environment*, **72**(2), 191–217.
- Simpson, J.J.; Hufford, G.L.; Pieri, D.; Servranckx, R.; Berg, J.S.; Bauer, C. (2002). The February 2001 eruption of Mount Cleveland, Alaska: Case study of an aviation hazard, *Weather and Forecasting*, **17**(4), 691–704.
- Simpson, J.J.; Pieri, D.; Hufford, G.L.; Servranckx, R.; Berg, J. (2003). Airborne Asian dust: Case study of long-range transport and implications for the detection of volcanic ash. *Weather and Forecasting*, **18**(2), 121–141.
- Stringer, W.J.; Dean, K.G.; Guritz, R.M.; Garbeil, H.M.; Groves, J.E.; Ahlhaes, K. (1992). Detection of petroleum spilled from the Mv Exxon-Valdez, *Int. J. Remote Sensing*, **13**(5), 799–824.
- Tokuno, M. (2000). MTSAT window channels (IR1 and IR2) potential for distinguishing volcanic ash clouds, *Meteorological Satellite Center Technical Note*, **38**, 1–10.
- Tupper, A.; Carn, S.; Davey, J.; Kamada, Y.; Potts, R.; Prata, F.; Tokuno, M. (2004). An evaluation of volcanic cloud detection techniques during recent significant eruptions in the western “Ring of Fire”, *Remote Sensing of Environment*, **91**(1), 27–46.
- Tupper, A.; Davey, J.; Stewart, P.; Stunder, B.; Servranckx, R.; Prata, F. (2006). Aircraft encounters with volcanic clouds over Micronesia, Oceania, *Australian Meteorological Magazine*, **55**, 289–299.
- Tupper, A.; Itikarai, I.; Richards, M.S.; Prata, F.; Carn, S.; Rosenfeld, D. (2007). Facing the challenges of the International Airways Volcano Watch: The 2004/05 eruptions of Manam, Papua New Guinea, *Weather and Forecasting*, **22**(1), 175–191.
- Watson, I.M.; Realmuto, V.J.; Rose, W.I.; Prata, A.J.; Bluth, G.J.S.; Gu, Y.; Bader, C.E.; Yu, T. (2004). Thermal infrared remote sensing of volcanic emissions using the moderate resolution imaging spectroradiometer, *J. Volcanol. Geothermal Res.*, **135**(1–2), 75–89.
- Wen, S.; Rose, W. (1994). Retrieval of sizes and total masses of particles in volcanic ash clouds using AVHRR bands 4 and 5, *J. Geophys. Res.*, **99**(D3), 5421–5431.
- Woods, A.W.; Self, S. (1992). Thermal disequilibrium at the top of volcanic clouds and its effect on estimates of the column height, *Nature*, **355**(6361), 628–630.
- Wright, R.; Flynn, L.P.; Garbeil, H.; Harris, A.J.L.; Pilger, E. (2004). MODVOLC: Near-real-time thermal monitoring of global volcanism, *J. Volcanol. Geothermal Res.*, **135**(1–2), 29–49.
- Zygmunt, J.; Casadevall, T. (1994). Impact of volcanic ash from 15 December 1989 Redoubt Volcano eruptions on GE CF6-80C2 turbofan engines, in T.J. Casadevall (Ed.), *Volcanic Ash and Aviation Safety: Proceedings of the First International Symposium on Volcanic Ash and Aviation Safety*, USGS Bulletin 2047, U.S. Government Printing Office, pp. 119–123.

Views of the Kamchatka–Kuriles–Aleutian volcanoes from manned spacecraft

Peter J. Mouginis-Mark, Thomas D. Jones

Abstract. Astronauts and cosmonauts on the International Space Station have unique views of the Earth, and can provide scientifically valuable information on volcanoes in the Kurile Islands, Kamchatka, and the Aleutians. This was, of course, also true of the Space Shuttle before it was decommissioned. Here we describe some of the advantages and operational constraints of hand-held photography for this area, as well as describe first-hand observations from orbit of the 1994 Kliuchevskoi eruption. We also review the radar data sets that were collected from the Space Shuttle. The SIR-C/X-SAR missions in 1994 collected high-quality multi-parameter radar images for parts of Kamchatka. The Shuttle Radar Topography Mission in 2000 collected digital elevation data for almost all the area of interest.

10.1 INTRODUCTION

Since the Gemini space missions in the mid-1960s, photography from space has provided unique views of volcanoes around the world (e.g., Lowman, 1973; Evans *et al.*, 2000). Particularly in such cases as the volcanoes in the Kamchatka–Kuriles–Aleutian (KKA) Arc, images collected from either the Space Shuttle or the International Space Station (ISS) have provided a perspective that cannot be obtained from any unmanned spacecraft. In several instances, eruptions such as those of Rabaul Volcano (Papua New Guinea) in September 1994,

Kliuchevskoi (Kamchatka) in October 1994, and Etna (Sicily) in October 2002 provide striking examples of the way in which hand-held photographs taken from space can provide scientifically valuable information (e.g., Rose *et al.*, 1995).

Photographs and imaging radar data comprise the two principle sets of observations that have been made of the KKA Arc from manned spacecraft. Low-resolution (equivalent to ~ 50 m resolution) color photographs were collected of the KAA from the Space Shuttle since November 1983, when the first mission to fly at an inclination of 57° took place (Table 10.1). The ISS crews have collected natural-color, high-resolution (~ 10 – 40 m/pixel, depending on the lens used) digital photographs of the KKA from December 2000 onwards. Additional constraints also exist for the ISS crews that were not experienced by the Space Shuttle crews, since on the ISS astronauts and cosmonauts have to maintain a permanently operating spacecraft and make numerous trips outside for maintenance and assembly. Despite the long duration of the missions carried out by each crew of the ISS, these constraints mean that only a few dozen images per mission are collected of any specific target; Expedition Crew 6, for instance, collected 25 images of Kamchatkan volcanoes on seven different days during their mission that extended from November 25, 2002 to May 3, 2003. By virtue of the large payload of the Shuttle, it enabled increasingly sophisticated imaging radars to be taken into orbit, so that multi-wavelength, multi-polarization, and interferometric data were collected. However, no multi-spectral or thermal

Table 10.1. Listing of Space Shuttle flights that had the opportunity to photograph the Kuriles, Kamchatka, and the Aleutians.

<i>Name</i>	<i>Launch date</i>	<i>Launch time (EST)</i>	<i>Inclination (deg)</i>	<i>Altitude (km)</i>	<i># orbits</i>	<i>Duration</i>
STS-9	28-Nov-83	11:00 AM	57.0	287	167	10 days, 7 hours
41-G	5-Oct-84	7:03 AM	57	403	133	8 days, 5 hours
51-B	29-Apr-85	12:02 PM	57	411	111	7 days, 0 hours
51-F	29-Jul-85	5:00 PM	49.5	320	127	7 days, 22 hours
61-A	30-Oct-85	12:00 noon	57	383	112	7 days, 0 hours
STS-27	2-Dec-88	9:30 AM	57	Classified	68	4 days, 9 hours
STS-28	8-Aug-89	8:37 AM	57	Classified	81	5 days, 1 hour
STS-36	28-Feb-90	2:50 AM	62	244	72	4 days, 10 hours
STS-39	28-Apr-91	7:33 AM	57	259	134	8 days, 7 hours
STS-42	22-Jan-92	9:52 AM	57	307	129	8 days, 1 hour
STS-45	24-May-92	8:13 AM	57	304	143	8 days, 22 hours
STS-47	12-Sep-92	10:23 AM	57	307	126	7 days, 22 hours
STS-53	2-Dec-92	8:24 AM	57	322	116	7 days, 7 hours
STS-56	8-Apr-93	1:29 AM	57	296	148	9 days, 6 hours
STS-59	9-Apr-94	7:05 AM	57	219	183	11 days, 5 hours
STS-60	3-Feb-94	10:05 AM	57	353	130	8 days, 7 hours
STS-66	3-Nov-94	11:59 AM	57	303	174	10 days, 22 hours
STS-68	30-Sep-94	7:16 AM	57	204	182	11 days, 5 hours
STS-71	27-Jun-95	3:32 PM	51.6	314	153	9 days, 19 hours
STS-74	12-Nov-95	7:30 AM	51.6	394	128	8 days, 4 hours
STS-84	15-May-97	4:07 AM	51.6	340	145	9 days, 5 hours
STS-86	25-Sep-97	10:34 PM	51.6	340	169	10 days, 19 hours
STS-88	4-Dec-98	3:35 AM	51.6	320	185	11 days, 19 hours
STS-89	22-Jan-98	9:48 PM	51.6	296	138	8 days, 19 hours
STS-91	2-Jun-98	6:06 PM	51.6	320	153	9 days, 19 hours
STS-92	11-Oct-00	7:17 PM	51.6	328	203	12 days, 21 hours
STS-96	27-May-99	6:49 AM	51.6	320	153	9 days, 19 hours
STS-97	30-Nov-00	10:06 PM	51.6	320	170	10 days, 19 hours
STS-98	7-Feb-01	6:13 PM	51.6	320	202	12 days, 21 hours
STS-99	11-Feb-00	12:43 PM	57	233	181	11 days, 5 hours
STS-100	19-Apr-01	2:41 PM	51.6	320	185	11 days, 19 hours
STS-101	19-May-00	1:12 AM	51.6	320	155	9 days, 21 hours
STS-102	8-Mar-01	6:42 AM	51.6	226	201	12 days, 19 hours
STS-106	8-Sep-00	8:45 AM	51.6	320	185	11 days, 19 hours
STS-104	12-Jul-01	5:04 AM	51.6	226	200	12 days, 18 hours
STS-105	10-Aug-01	5:10 PM	51.6	226	186	11 days, 21 hours
STS-108	5-Dec-01	5:19 PM	51.6	226	171	10 days, 20 hours
STS-109	8-Apr-02	4:44 PM	51.6	226	170	10 days, 19 hours
STS-11	15-Jun-02	5:22 PM	51.6	226	221	14 days, 1 hour
STS-112	7-Oct-02	3:46 PM	51.6	226	170	10 days, 20 hours
STS-113	23-Nov-02	7:49 PM	51.6	226	216	13 days, 18 hours

imagers have been used during manned missions to study the KKA Arc.

Because of the unique perspective that human observations can provide to our understanding of volcanoes in the KKA, this chapter is focused on some of the highlights and constraints under which these observations have been made since 1983.

10.2 MISSION CONSTRAINTS ON PHOTOGRAPHIC COVERAGE

It was not possible to obtain new images of any part of the Earth during each Space Shuttle flight. Between November 1983 (STS-9) and December 2006 (STS-116) there were 46 flights of the Shuttle that had the opportunity to photograph the KKA (Table 10.1). Several different constraints apply to each mission. Principal among these is the fact that the ISS flies at an altitude of $\sim 205\text{--}410$ km above the Earth's surface and, because it has orbital inclinations that range from 28 to 60° relative to the equator, it is not in Sun-synchronous orbits. These constraints also applied to the Space Shuttle. These orbits allow for a wide range of lighting geometries to be obtained that are not available from unmanned satellites such as Landsat, Terra, or ERS-1. Space Shuttle images have been used for a wide variety of Earth science applications, including oceanography (Yoder *et al.*, 2002), environmental monitoring (Evans *et al.*, 2000), and in the documentation of remote volcanoes (Wood and Kienle, 1990; De Silva and Francis, 1990).

The diversity in the viewing geometry and time of day that image data can be collected is important. In the case of the Space Shuttle, which had a mission duration of at most ~ 16 days, the variable launch times throughout the day or night meant that photographic targets around the globe were viewed at different local times of day on successive missions. The drifting of the Space Shuttle orbit during each mission with respect to the local time of day on the ground meant that both early morning and late afternoon images could be obtained in a single Space Shuttle flight. Furthermore, ISS crews can select optimum targets that are not only directly along the spacecraft's ground track, but also can be imaged at an oblique across-track angle (again, also true of the Space Shuttle).

The Space Shuttle had six windows located at the forward flight deck commander and pilot stations that provided forward, left, and right viewing (Figure 10.1). The two overhead windows and

two payload viewing windows at the aft station location on the flight deck provided rendezvous, docking, and payload viewing. There was also a window in the mid-deck side hatch. The opportunities to photograph the surface depended upon the main objective of the mission, which might be delivering a satellite to orbit, visiting the ISS, or conducting a set of science experiments. In many of these instances, such as the example shown in Figure 10.1, the Space Shuttle was flown with the payload bay facing away from the Earth, precluding clear views of the surface from the windows. The ISS (Figure 10.2) does not have this limitation. A further development in the quality of the photographic coverage from space came with the installation of an optical quality window (Figure 10.3) on the ISS in the U.S. *Destiny* Laboratory. This window became part of the orbiting outpost in February 2001. Until that time, photographs were

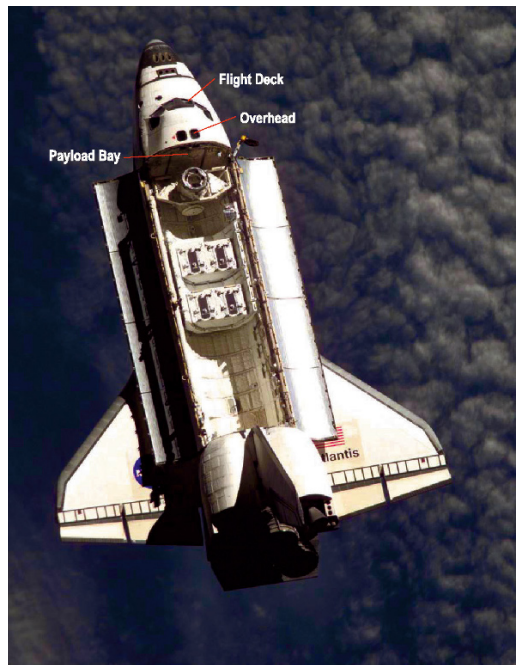


Figure 10.1. View of the Space Shuttle *Atlantis* from the ISS, showing the location of the windows used for orbital photography. The best images were obtained using the two overhead windows but, as can be seen in Figure 10.4, spectacular views of the payload bay, the tail, and the Earth could also be obtained from the two payload bay windows. This is image ISS02E9633, taken on July 22, 2001.

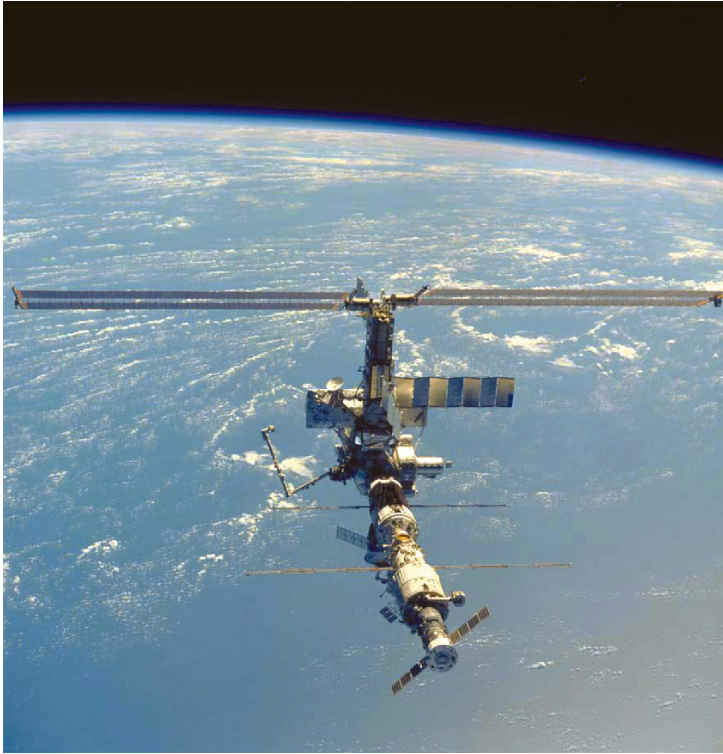


Figure 10.2. This photo of the ISS was taken by an astronaut aboard the Space Shuttle on April 17, 2002. Although its construction is not yet complete, Space Station *Alpha* began operations in November 2000. It now serves as home to three astronauts as well as dozens of already ongoing science experiments. This is image number STS110-717-17.

obtained through one of the Space Shuttle's navigation windows that did not have the excellent transmission qualities of the *Destiny* Laboratory's window.

The camera equipment used by the Space Shuttle astronauts included Hasselblad or Linhof cameras using Kodak natural-color positive film rated at 64 or 100 ASA. Typically, 55, 100, or 250 mm focal length lenses were used. The viewing geometry (tilt) of the camera is highly flexible as the camera is hand-held, and typically ranges from nadir to a highly oblique view at 75° . On the ISS, a Kodak DCS760C electronic still camera is used that has a $3,060 \times 2,036$ -pixel CCD array. This camera (Figure 10.3) has been used with a variety of lenses, including 110, 180, 200, 250, 400, and 800 mm focal lengths, on missions ISS01 to ISS11. There has been no attempt to obtain multi-spectral data beyond natural-color images using this camera. The combination of a 800 mm

lens and a digital camera has provided the highest spatial resolution of surface features (at ~ 8 m/pixel). Many hundreds of photographs have been obtained from the ISS; for example, the first three resident Space Station crews obtained nearly 13,500 pictures of the Earth. All of the Space Shuttle and ISS crew photographs are archived at the Johnson Space Flight Center, where users can access the images via a clickable map interface (<http://eol.jsc.nasa.gov/sseop/clickmap/>).

Surprisingly, fewer photographic and radar data exist for the Aleutian and Alaskan volcanoes than for Kamchatka. An explanation for why there is less coverage for the Aleutians (Figure 10.4), either hand-held photography from the Shuttle or from the ISS, is more problematic. Local meteorology undoubtedly plays a role in that many of the Space Shuttle photographs show greater cloud cover here than over Kamchatka. Visual targets along the Kamchatka Peninsula, particularly



Figure 10.3. Astronaut Donald Pettit on ISS Crew 6 waits for another target of opportunity to use the Kodak electronic camera and its giant 800 mm lens. Most of the photographs used in this chapter were taken using this camera system. This is image ISS006E13988.

Kliuchevskoi and Bezymianny, serve to attract the astronauts' attention and, hence, result in more photographs being taken. Further, in recent years the activity at Kamchatka and Kurile volcanoes has often been more frequent and spectacular than eruptions in the Aleutian Islands. Figure 10.5 is an example of a small eruption from Mt. Cleveland that attracted the attention of astronaut Jeffery Williams on the ISS. It is a relatively small strombolian eruption that occurred during good weather. Astronaut Jeffery Williams called the Alaska Volcano Observatory (AVO) from the ISS to report the eruption, exemplifying how this platform could be used to help monitor the Earth's surface and provide alerts of eruptions or other hazardous events. The Cleveland eruption had just occurred and had not yet been detected by AVO. In contrast, Figure 10.6 shows the 2009 eruption of Sarychev Peak, with a much larger ash plume, pyroclastic flows,

and it even appears to have affected the local weather.

With the exception of Shuttle Radar Topography Mission (SRTM) coverage, no high-resolution orbital radar data have been collected over the Aleutian or Alaskan volcanoes. In part this is due to the alignment of the targets on the ground, where turning the radar on and off for the few seconds when one of the Aleutian Islands was visible (the Space Shuttle had a speed of ~ 7 km/s over the Earth's surface) would not produce good-quality data; the small area of land would not allow for good calibration of the image.

One of the advantages for manned observations of the KKA lies in the fact that the orbit of the ISS only reaches poleward to $\sim 57^\circ$, so that at the latitude of Bezymianny volcano the ISS's orbits are aligned almost west–east (this was also the case with the Space Shuttle). This alignment means that during certain parts of a mission the same part of the Earth's surface can be viewed on several succes-



Figure 10.4. Space Shuttle photograph STS047-77-34 of Unimak Island and vicinity, Alaska including six volcanoes: Westdahl, Fisher, Shishaldin ($54^\circ 45'N$, $163^\circ 58'W$), Isanotski, Round Top, and Frosty. Heavy cloud cover, such as the banks of clouds coming in from the left of the image, is one of the primary limitations on photographic coverage of the Kuriles, Kamchatka, the Aleutians, and Alaska. The image was taken from the payload bay windows of the Space Shuttle on September 14, 1992 from an altitude of 317 km with a 100 mm lens. The tail of the Shuttle is at lower right. Unimak Island is approximately 100 km long.



Figure 10.5. Mt. Cleveland, Chuginadak Island, Aleutian Islands, Alaska erupting on May 23, 2006 at 22:57 GMT taken by astronaut Jeffery N. Williams of ISS Expedition 13. The image was taken from an altitude of 184 nautical miles with the E4 camera on board. The island is less than 10 km across.



Figure 10.6. The ash plume and pyroclastic flows from the June 12, 2009 eruption of Sarychev Peak in the Kurile Islands, Russia. This volcano was unmonitored at the time. Images like these provide insight into eruption mechanisms as well as the structure and composition of plumes. The image was taken from 182 nautical miles altitude with the N2 camera on the ISS.

sive orbits. Space Shuttle crews were also better able to respond to unexpected events like the October 1994 eruption of Kliuchevskoi Volcano, and were able to provide unique images of the plume from a variety of viewing geometries. In Section 10.6 we describe our observations of this eruption while in orbit on Space Shuttle flight STS-68. While there were some experiments that involved exact repeat

orbits (such as the second SIR-C/X-SAR mission in October 1994) most Space Shuttle flights utilized a drifting orbit, wherein the trace of the spacecraft's orbit over the Earth's surface does not repeat itself and different parts of the surface are observed on every orbit.

Finally, there is the issue of orbit altitude for photography. Not all Space Shuttle missions flew at

the same altitude (SIR-C/X-SAR was very low at ~ 205 km, while repair missions to the Hubble Space Telescope were as high as ~ 350 km), so that even the same camera systems provided different fields of view on different flights. This meant that with the same camera and lens combinations the spatial resolution of the photographs would vary. Typically, a focal length of 55 mm with a Hasselblad camera gives a ground resolution of ~ 50 m from an altitude of ~ 250 km.

10.3 TYPES OF OBSERVATIONS FROM THE SHUTTLE AND ISS

Several strong motivations exist for photography from the ISS (as was the case for the Space Shuttle). First, the ability to observe volcanoes in very remote locations enables their level of activity to be assessed far more frequently than on the ground. Low-level venting, such as that shown in Figure 10.7 for Mt. Cleveland, may be the only indication that a volcano is awakening. Even recently active volcanism can be detected from space. Warm lava flows, such as those produced by the 1997 eruption of Okmok Volcano, can be identified during winter months because of the absence of snow cover on

certain flanks for the volcano (Figure 10.8). Thermal activity within Akutan can also be detected (Figure 10.9). Observations of volcanoes that show no activity has taken place recently, such as Alaid Volcano (Kurile Islands; Figure 10.10), are also valuable when so few observations are made on the ground or provide valuable baseline observations.

Basic mapping is also possible from orbital images, particularly scenes obtained from the ISS using the 800 mm lens on the digital camera. For instance, a particularly fine set of images was collected in June 2002 of the central Kurile Islands (Figure 10.11). Geologists visit these islands only very rarely, and logistics are difficult on the ground, so that the ISS images can serve as surrogates for high-quality air photography (Figure 10.12). The ability of the astronauts and cosmonauts to obtain oblique views of volcanic centers in remote areas also aids analysis of the structural setting of these volcanoes (Figures 10.13–10.15).

Of course, the greatest contribution that ISS crews can make to volcanology lies in their observations of large, ongoing eruptions. This was also true of the Space Shuttle. The 1994 eruption of Kliuchevskoi Volcano met this criterion exactly. The crew of STS-68 had a bird's eye view of the



Figure 10.7. A faint gas plume is seen coming from 1,730 m high Mt. Cleveland (right center) on Chuginadak Island ($52^{\circ}49'N$, $169^{\circ}57'W$), Aleutian Islands, Alaska. Herbert Volcano is at left and Carlisle Volcano is at top. This is image number ISS001-E-5958 taken with a 400 mm lens and a Kodak DCS460 electronic camera on January 1, 2001 from an altitude of 367 km. After this photograph was taken, Cleveland experienced several explosive eruptions in February and March 2001. Chuginadak Island is less than 10 km across.

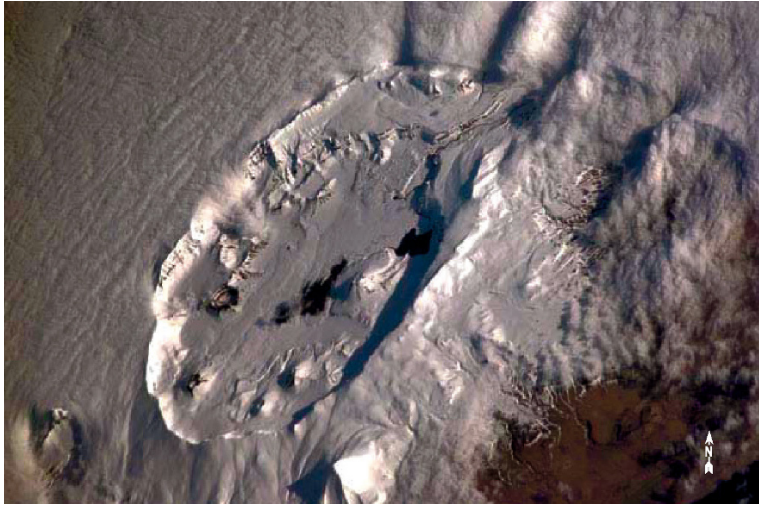


Figure 10.8. The outline of the 1997 lava flow on the floor of Okmok Caldera ($53^{\circ}24'N$, $168^{\circ}10'W$), Umnak Island, Aleutian Islands, Alaska can be identified here because of the absence of snow cover over the flow. The lava flow is estimated from the ground to be more than 20 m thick at the margins and 50 m maximum. This is image number ISS002-E-6065 taken with an 800 mm lens and a Kodak DCS460 electronic camera on May 18, 2001 from an altitude of 370 km. The caldera is approximately 10 km wide.



Figure 10.9. Akutan Volcano ($54^{\circ}08'N$, $165^{\circ}58'W$), Aleutian Islands, Alaska last erupted in May 1992 when localized steam and ash emissions took place. Lava extrusions within the summit caldera took place in 1929 and 1947. The circular summit caldera is ~ 2 km across and 60 to 365 m deep and there is an intra-caldera cinder cone. No evidence of current thermal anomalies can be detected in this photo. This is image number ISS005-E-18450 taken with an 800 mm lens on a Kodak DCS760C digital camera on October 24, 2002 from an altitude of 380 km.



Figure 10.10. Alaid Volcano ($50^{\circ}52'N$, $155^{\circ}34'E$), Kurile Islands, Russia. This is image number ISS005-E-19202 taken on October 30, 2002 from an altitude of 378 km with an 800 mm lens and a Kodak DCS760 electronic camera. The uniform snow cover around the peak indicates that no thermal anomaly is present and that there have not been any recent ash eruptions. The island is less than 17 km wide.



Figure 10.11. At an equivalent resolution of ~ 8 m/pixel, the best photographs from the ISS can serve as base images for mapping volcanoes such as Prevo Peak Volcano on Simushir Island, Kurile Islands, Russia ($47^{\circ}01'N$, $152^{\circ}07'E$). Prevo Peak is a stratovolcano with a summit crater 450×600 m that erupted in 1765 and 1825. See also Figure 10.24, which combines this image with digital topographic data collected by the SRTM instrument. The image was taken on June 30, 2002 from an altitude of 389 km with an 800 mm lens and a Kodak DCS760C electronic camera.

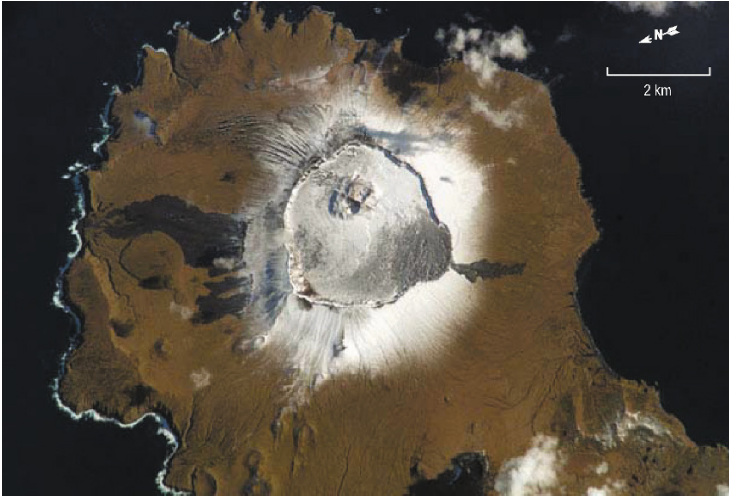


Figure 10.12. Yunaska Volcano, Aleutian Islands, Alaska ($52^{\circ}38'N$, $170^{\circ}37'W$) last erupted in 1937. Cinder cones and fissure-fed lava flows are visible on the western (left) end of the complex. The younger, 550 m high eastern complex consists of a shield volcano capped by two nested calderas that contain cinder cones and a lava field. Vents can also be seen on the upper flanks of the caldera. This is image number ISS005-E-18362 taken on October 23, 2002 from an altitude of 380 km with an 800mm lens and a Kodak DCS760C electronic camera.



Figure 10.13. Oblique view looking north across Bezymianny ($55^{\circ}58'N$, $160^{\circ}36'E$), Kliuchevskoi ($56^{\circ}06'N$, $160^{\circ}39'E$), and in the distance Shiveluch ($56^{\circ}38'N$, $161^{\circ}19'E$) Volcanoes, Kamchatka Peninsula, Russia. This is image number ISS001-E-6505, taken with an 800 mm lens on a Kodak DCS460 electronic still camera sometime in March 2001.



Figure 10.14. The two major volcanoes shown here are Kronotsky ($54^{\circ}45'N$, $160^{\circ}30'E$), the stratovolcano casting the shadow, and Kransheninnikov ($54^{\circ}35'N$, $160^{\circ}16'E$), a 9×10 km diameter caldera. Inside the caldera are younger and smaller volcanic calderas. The volcanoes are located on the Kamchatka Peninsula, Russia. The image was taken on May 8, 2002 from the ISS on orbit number 3792. This is image number ISS004-E-13788 taken with a 200 mm lens and a Kodak DCS760C electronic camera.

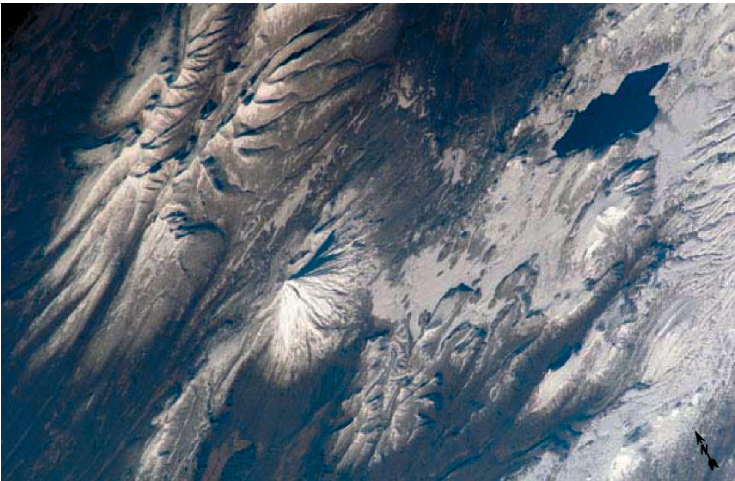


Figure 10.15. High oblique view of Opala Volcano, Kamchatka Peninsula, Russia (the prominent cone near the center of the image) at $52^{\circ}33'N$, $157^{\circ}20'E$. Opala has had several small historic eruptions and a large crater-forming eruption $\sim 1,500$ years ago. This is image number ISS005-E-19212 taken on October 30, 2002 from an altitude of 378 km with an 800 mm lens and a Kodak DCS760C electronic camera.



Figure 10.16. View of the early phase of the 1994 Kliuchevskoi eruption, Kamchatka Peninsula, Russia. Note the difference in plume structure between the near-vent turbulent plume and the downwind drifting plume. This is image number STS68-150-45 taken at 23:24:41 GMT on September 30, 1994 with a 250 mm lens on a Hasselblad camera during orbit number 9.

large eruption plume on several different orbits (Figure 10.16). In the following section we describe the excitement and scientific value of these observations.

10.4 SHUTTLE CREW OBSERVATIONS OF THE 1994 KLIUCHEVSKOI ERUPTION

The fortunate coincidence of an Earth observation Shuttle flight and the start of a major eruption of Kliuchevskoi Volcano just a few hours into the mission provided a unique opportunity to observe the evolution of an eruption. One of the authors (T.J.) was on board the Shuttle *Endeavour* during this mission (and the other SIR-C/X-SAR flight; STS-59 in April 1994), and the recollections of the crew as well as his notes recorded during the

flight makes fascinating reading. In this section, we therefore describe the eruption using these notes:

“Mission Elapsed Time, 0 days, 12 hours, 23 minutes, 20 seconds (0/12:23:20): The Shuttle Radar Laboratory (SRL) is all working perfectly—the big highlight of the observation so far is Kliuchevskoi erupting on the Kamchatka peninsula—it’s just like looking at the biggest volcano eruption you can imagine on the ground, and being able to view it from several different angles as we flew right over it on this last pass!”

These words from the on-orbit diary capture some of the crew’s excitement at witnessing the 1994 eruption of Kliuchevskoi Volcano in Kamchatka, Russia. The volcano had roared into life on the very day that the STS-68 mission started: September 30, 1994. The STS-68 crew benefited from sheer good luck, since the original launch date of August 18, 1994 had been scrubbed by a last second turbo-pump problem with an engine. On the first full day of operating the SRL, the Space Shuttle was heading toward Kamchatka on its 10th orbit when the crew spied a dark smudge of smoke on the horizon. At first they thought it might be a large thunderstorm, with its anvil streaming out far to the east. The clear air ruled out a storm system and, as the crew recognized the local geography, they were struck with a sudden realization: this was Kliuchevskoi Volcano and it was in full eruption.

The Kliuchevskoi volcanic complex is midway down the east coast of the Kamchatka Peninsula. During the first SRL mission in April 1994, the STS-59 crew had looked down over Kliuchevskoi, the tallest volcano in Asia at 4,850 m and saw that minor eruptive activity had dusted some ash on the summit of the volcano and the adjacent peak of Kamen Volcano. But on most of the passes, this volcano had looked quiet and pristine under its blanket of snow. In October, the mountain had changed dramatically.

Naturally, the crew had every camera on board pointed down at the eruption, and 45 images were collected of the plume on five different orbits. The crew was first struck by the scale of the eruption plume (Figure 10.17). From the summit, the plume rose ~15–20 km into the atmosphere. The ash plume appeared to rise straight up from the mountain, hit the stratosphere, and then sweep off with the jet stream to the east over the Pacific. The plume



Figure 10.17. Image number STS68-214-43 taken at 00:56:04 GMT on October 1, 1994 with a 250 mm lens on a Hasselblad camera. Compare with Figure 10.18b, which was taken 20 seconds earlier but ~140 km farther from the volcano. Image taken during orbit number 10.

clearly had two prominent layers, with lighter colored steam and dust rising highest, while a darker plume peeled off at medium altitude and streamed much farther off to the east. Perhaps the lighter plume was the most recent and more energetic of the pair.

As the Space Shuttle flew directly over the volcano, the crew had a dramatic down-the-throat view of this most active phase of the eruption (Figure 10.18). The volcano was generating a spectacular plume, and the summit of Kamen Volcano was shrouded in a dirty steam plume. A little farther to the south, adjacent Bezymianny Volcano (2,882 m) streamed a white steam plume, but no ash. Ash fall from the lower portions of the Kliuchevskoi plume coated the downwind slopes of all three mountains.

With a 250 mm telephoto lens attached to their Hasselblad camera (rolls 150 and 214), the crew discerned smaller scale activity on Kliuchevskoi's northern slopes, in the shadow of the main plume. They reported that smaller bursts of dirty steam and ash boiled from what appeared to be ash or pyroclastic flows down the northern flank. From their 204 km vantage point, the crew could see no motion in the plume, but the tight coils of the ash clouds rising into plume suggested a very vigorous eruption, both from the flanks and the summit. The video footage of the eruption received wide airplay on evening newscasts that first day.

For the first week of their mission, before the northernmost reach of the orbit (57° latitude) pre-

cessed too far westward, the STS-68 crew flew over or near Kamchatka on three successive orbits daily. These daily passes involving radar and photographic imaging occurred during local morning, with strong shadows outlining the peaks and plume.

On their 25th orbit, on October 1, 1994, the astronauts had another dramatic pass over Kliuchevskoi. The crew's onboard log records this observation:

“We observed two plumes from summit of Kliuchevskoi, one white, one smoky gray, and an ash plume from summit of Bezymianny, too. All plumes streamed together at summit height, and created an ash pall (mostly dirty smoke) downstream. Wind from west.”

By Flight Day 3, activity had subsided considerably. On the 42nd orbit:

“Kamchatka volcanoes show lots of ash on summit of Kliuchevskoi, but none on Tolbachik. No steam or plume present.”

Cloudy weather moved in soon after, but the Space Radar Lab (SRL) continued observing the waning eruption. By October 4 clear weather had returned; the astronauts observed no summit plume, but continued flows down the northern flanks generated dark ash plumes that cloaked the mountain in chocolate brown. Low-altitude winds carried the ash to the east to the nearby Pacific.

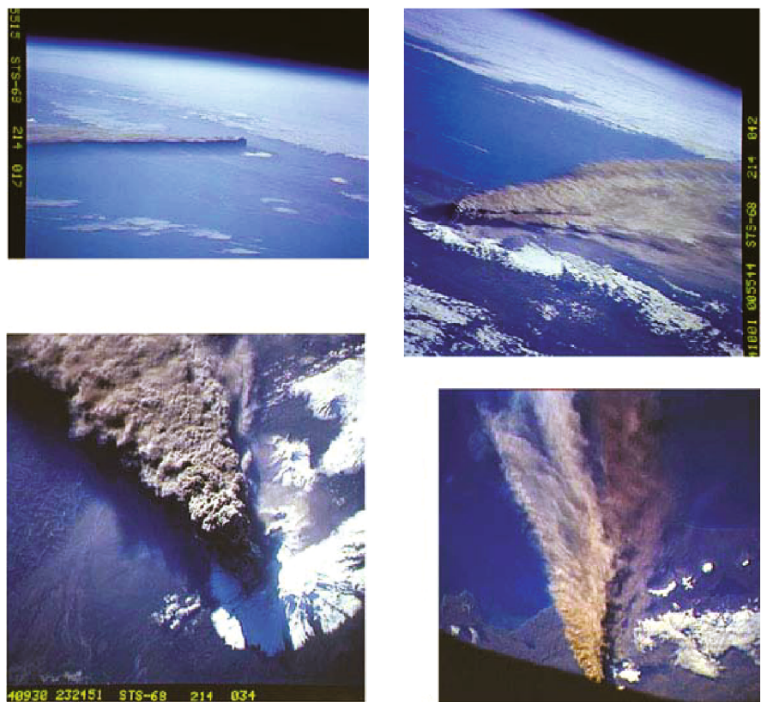


Figure 10.18. Four views of the ash plume from Kliuchevskoi Volcano: (a) image number STS68-214-17 taken at 21:55:15 GMT on September 30, 1994 with a 250 mm lens on a Hasselblad camera during orbit number 8; (b) the split level of the plume is clearly visible in this image (STS68-214-42) taken at 00:55:44 GMT on October 1, 1994 with a 250 mm lens on a Hasselblad camera during orbit number 10; (c) image number STS68-214-34 taken at 23:24:51 GMT on September 30, 1994 with a 250 mm lens on a Hasselblad camera during orbit number 9; (d) early in the eruption, the downwind segment of the plume clearly split into two different levels according to image number STS68-153-10 taken at 21:53:07 GMT on September 30, 1994 with a 250 mm lens on a Linhof camera during orbit number 8.

Kliuchevskoi’s southern peak was lightly dusted with ash, but no activity was visible.

By October 6, the orbit’s precession had the Space Shuttle arriving over Kamchatka too early in the morning for good photography, but the crew made this observation nonetheless:

“Kliuchevskoi looked like it had a steam plume rising through clouds that were close to the volcanic peaks.”

A fresh storm then moved in and blanketed the complex with fresh snow. Fortunately, SRL’s radars continued to track activity through the clouds. On October 9 the crew photographed the mountain again and could see almost no evidence of the spectacular eruption of a week earlier. Plainly visible were gray ash flows on the northwest and

northern flanks, still hot enough to melt the fresh snow. If anything, Kliuchevskoi looked more peaceful than it had in April on STS-59.

STS-68’s photographs, coupled with visual observations and the extensive radar imaging of the eruption, furnished the best available documentary record of Kliuchevskoi’s biggest outburst since the 1940s. Astronaut photography enabled volcanologists to correlate radar observations of hot ash and mudflows with Kliuchevskoi’s changing eruptive activity.

The success in capturing this eruption was aided by good luck and the particular mission profile. The altitude of ~210 km was a little over half that of the ISS or other Shuttle missions, and the high orbital inclination of 57°, coupled with Kliuchevskoi’s latitude of 56°, gave the Space Shuttle several passes over the volcano each day. Good

fortune played a large role: Kamchatka in October has about 12 hours of daylight, and the Space Shuttle *Endeavour* was laden with cameras and flown in a payload bay (and windows) down attitude for our SRL mission. While other spectacular volcanic episodes have been photographed from space (Rabaul and Etna, for example), the STS-68 experience with Kliuchevskoi is the best documented example of an eruption using visual observations from space.

10.5 SHUTTLE RADAR OBSERVATIONS OF THE KKA

In addition to facilitating optical photography, the Space Shuttle took four different radar systems into space over the time period 1981 to 2000. The first Space Imaging Radar (SIR-A) flew in November 1981 on STS-2, the second mission. Because this mission was a test flight for the Space Shuttle, it flew at an inclination of 28° , so that no coverage of targets poleward of 28° was obtained. The second radar, SIR-B, was flown on flight 41-G in October 1984. This mission had a 57° inclination orbit and so had the potential to image the southern parts of the KKA Arc. However, because this area was not one of the priorities of the mission's Science Team, no SIR-B data were collected over the KKA Arc.

The first radar images of the KKA from the Space Shuttle were obtained by SIR-C/X-SAR (Figure 10.19), on missions STS-59 (April 1994)

and STS-68 (October, 1994). Mouginis-Mark (1995) reviewed the volcano targets that were imaged during the two SIR-C/X-SAR missions in 1994. This radar system was unique among orbital radars at the time. Not only were radar data collected at three different wavelengths (X-, C- and L-band, or 3.0, 5.6, and 24.0 cm wavelength), but also multi-polarization data were collected (Stofan *et al.*, 1995). To facilitate the collection of research data, the mission featured a Science Team that had been working for several years prior to the first mission to identify priority targets. The Space Shuttle did not stay in orbit for a sufficient time for all of the Earth's surface to be accessible to the radar, nor was it possible to operate the radar in a continuous mode due to power and data storage constraints. Despite the fact that there were no targets in Kamchatka that were identified as a science target, by good fortune the orbit selected for the mission meant that the radar system was ready for the check-out phase of the mission as the Space Shuttle flew past Kamchatka. Thus, one of the first radar scenes collected by both the U.S. SIR-C radar and the German/Italian X-SAR radar was of Karymsky Volcano on orbit 10.

The radar check-out for STS-68 coincided with the first crew observations of the initial phase of the Kliuchevskoi eruption at 20:22:13 GMT on September 30, 1994, so that a rationale for additional acquisitions over Kamchatka developed during the flight. Furthermore, the orbit used for the mission was designed for several of the interferometry

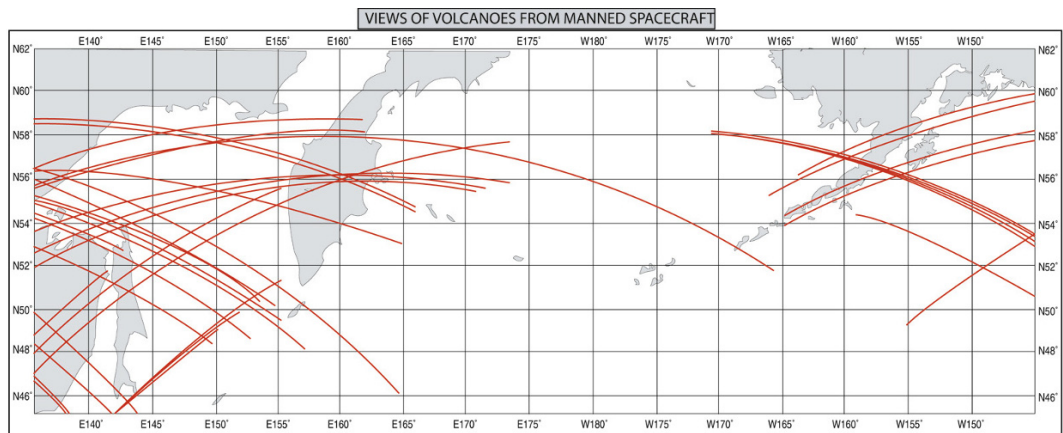


Figure 10.19. Plot of the ground tracks of STS-68, showing the data acquisitions of the SIR-C/X-SAR radar. There are fewer acquisitions over the Aleutians (compared with central Kamchatka) to collect data such as those shown in Figure 10.20.

experiments (over Hawaii, Galapagos, and the Philippines), and this orbit meant that there was repeat coverage of the same volcanoes in Kamchatka on several occasions. Swift and efficient planning of the radar by Tom Farr and Jeff Plaut of the Science Operations Team from the Jet Propulsion Laboratory meant that SIR-C data were obtained over Kliuchevskoi in a manner that allowed several interferometric scenes to be obtained.

While interferometric L-band data were collected over Kliuchevskoi on orbits 121, 137, 153, and 169 (October 7–10, 1994), little surface change was detected. Other day-to-day comparisons of SIR-C data over Kilauea Volcano, Hawaii, have shown the movement of active lava flows (Zebker *et al.*, 1996). No such surface changes were detected for Kliuchevskoi, although Harold Garbeil (1996, pers. commun.) was able to detect some changes in the lahar deposits on the eastern flank of the volcano.

However, one of the disappointments of the

STS-68 mission was the inability of the SIR-C/X-SAR radar to image the Kliuchevskoi plume. At the time of the mission, there had been no orbital radar data collected over an active eruption plume, so that there was great interest at the time to see how the radar systems would image the plume. It was expected that penetration of a plume would be achieved, with the least penetration associated with the X-band radar and greatest penetration with the L-band coverage from SIR-C. Doppler measurements of the vigorously rising plume might also have been accomplished. Unfortunately, because the most vigorous phase of the eruption took place very early in the mission, the SIR-C radar had not become operational on the orbits that would have produced the best views of the plume (orbit 7). While X-SAR was collecting data on this orbit, the narrow swath width and an inability to steer the radar to the required viewing geometry meant that no radar data were obtained on September 30. By the time that SIR-C/X-SAR were routinely collecting data, the next pass over Kliuchevskoi was on

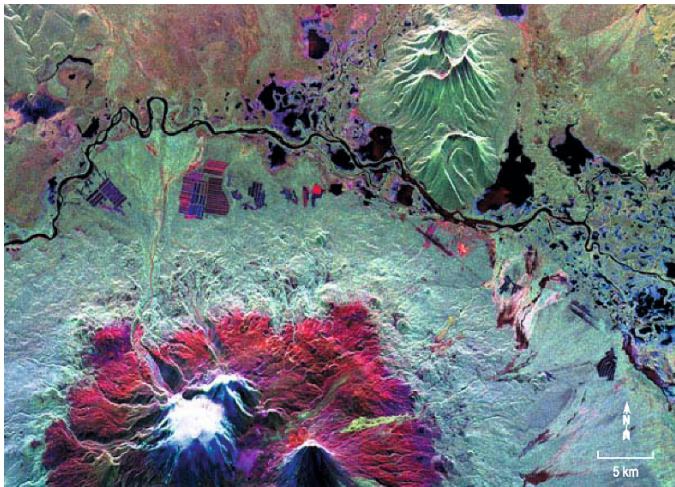


Figure 10.20. The radar image was acquired by SIR-C/X-SAR aboard the Space Shuttle *Endeavour* on its 25th orbit on October 1, 1994 of the north flank of Kliuchevskoi Volcano and the town of Klyuchi, Kamchatka Peninsula, Russia. The image shows an area $\sim 30 \times 60$ km that is centered at $56^{\circ}18'N$ and $160^{\circ}78'E$. This image was obtained in Mode 11 (Mouginis-Mark, 1995), which meant that C- and L-band signals were transmitted horizontally, but received in both like- and cross-polarizations channels. The colors in this image were obtained using the following radar channels: red represents the L-band (horizontally transmitted and received); green represents the L-band (horizontally transmitted and vertically received); blue represents the C-band (horizontally transmitted and vertically received). The Kamchatka River runs from left to right across the image. An older, dormant volcanic region appears in green on the north side of the river. New lava flows are visible on the flanks of Kliuchevskoi, appearing yellow/green in the image, superimposed on the red surfaces in the lower center. Melting snow triggered mudflows on the north flank of the volcano, which may threaten agricultural zones and other settlements in the valley to the north. Image prepared by the Jet Propulsion Laboratory.

orbit 25 (Figure 10.20) at 23:07:02 GMT and the most vigorous phase of the eruption had ended so that the plume was no longer highly active. For each of the passes of Kliuchevskoi, different combinations of wavelengths and polarizations were used, so that the area of coverage was not always the same. Figure 10.21 shows the field of view that was obtained with a more limited number of received channels, which gave a wider swath width.

The archive of all of the SIR-C radar data can be found at:

<http://edcsns17.cr.usgs.gov/sir-c/survey.html>

The second set of radar data that were collected for the KKA were obtained by the Shuttle Radar Topography Mission (SRTM) in February 2000, which provided a unique opportunity to collect digital elevation data for much of the Earth's surface (Farr and Kobrick, 2000; Rabus *et al.*, 2003). Flying at an inclination of 57° to the equator, the SRTM radar was able to look northward at the top of its orbit so that areas as far north as 60° were imaged. Working under the principle called "single-pass radar interferometry", the SRTM mission collected digital elevation data for the entire globe equatorward of 60° . One of the earliest products from the SRTM mission was a topographic map of the Kamchatka Peninsula (Figure 10.22).

SRTM data are particularly valuable for scene visualization as well as quantitative measures of volcano elevation, flank slope, and volume. Figure 10.23 displays a shaded relief version of Kunashir Island, in the southern Kuriles, which has been generated from 90 m SRTM elevation data. Such images are particularly helpful for the identification of structural trends, such as the graben that lies to the NW of Tyatya Volcano. SRTM data can also be combined with photographic data, such as the high-resolution ISS images shown in Figure 10.24. Such combination images allow for higher spatial resolution than the SRTM data provide, thereby allowing details of the morphology of the volcano (e.g., slump features, drainage channels, and collapse craters) to be more easily recognized.

The SRTM data that have been released to the science community have a spatial resolution of 90 m/pixel (30 m/pixel for the Aleutians) and a vertical accuracy of ~ 15 m (Farr and Kobrick, 2000; Rabus *et al.*, 2003). The seamless "finished" SRTM data archive can be found at:

<http://edc.usgs.gov/products/elevation/srtmbil.html>



Figure 10.21. Example of a single acquisition from the SIR-C radar in October 1994 of the north central Kamchatka Peninsula, Russia. This is data take 104-30 obtained at an incidence angle of 25.16° , mode 8, with two channels transmitted and received. Compare the swath width with that shown in Figure 10.20, which had more channels but a narrower swath width. The radar is looking from the right side of the image. Kliuchevskoi, Bezymianny, and Tolbachik Volcanoes are in the central part of this scene. The width of the swath is approximately 90 km.

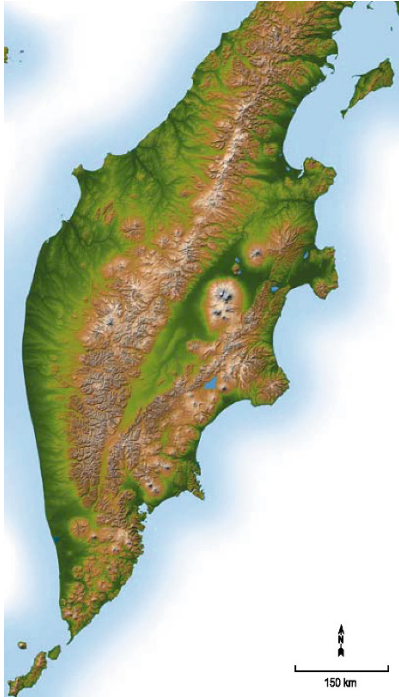


Figure 10.22. Two visualization methods using digital elevation data from the SRTM were combined to produce this image: shading and color-coding of topographic height of the Kamchatka Peninsula, Russia. The shade image was derived by computing topographic slopes in the north–south direction, so northern slopes appear bright and southern slopes appear dark. Color-coding is directly related to topographic height, with green at the lower elevations, rising through yellow and brown to white at the highest elevations. Image processed by the Jet Propulsion Laboratory.

10.6 SUMMARY

The views provided from the Space Shuttle and the ISS offer a unique perspective of volcanoes in the Kuriles, Kamchatka, the Aleutians, and Alaska that cannot be obtained from any unmanned spacecraft. The ability to select the optimum viewing geometry for photographs, from nadir to highly oblique, is particularly important. The opportunity to collect images at different times of day due to the non-Sun-synchronous orbits of the ISS also facilitate better recognition of geomorphic features due to longer shadows (once again, this was also true of the Space Shuttle). Some of the most useful observations that are routinely made by astronauts and

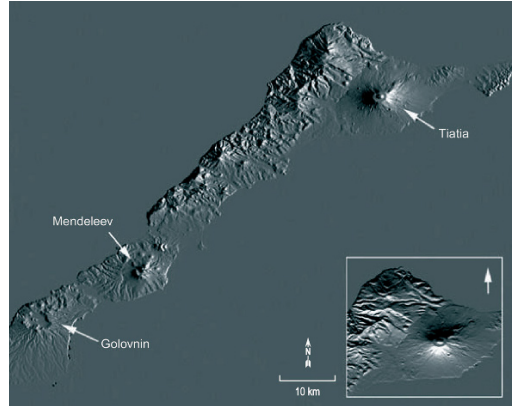


Figure 10.23. Shaded relief version of Kunashir Island, in the southern Kurile Islands, Russia just north-east of Hokkaido, Japan. Several volcanoes with different degradation states can be identified in this image: Golovnin ($43^{\circ}54'N$, $145^{\circ}30'E$) most recently erupted in 1848; Mendeleev ($44^{\circ}0'N$, $145^{\circ}42'E$) had a phreatic eruption in 1880; and Tyatya ($44^{\circ}21'N$, $146^{\circ}18'E$) had five eruptions between 1812 and 1973. Note the graben structure to the NW of the volcano. The inset shows a different lighting direction for Tyatya to demonstrate the utility of SRTM data for such structural studies of these remote islands.

cosmonauts include verification of low-level activity at remote volcanoes, and the acquisition of mapping quality images for areas that are rarely visited due to difficult field logistics. Rare opportunities to view major eruptions from above, such as the 1994 Klyuchevskoi eruption, can yield unique information on the structure and dispersal pattern of eruption plumes.

The Space Shuttle radar systems SIR-C/X-SAR and SRTM also provided unique information that could not be obtained from free-flying radars such as ERS, Radarsat, or Envisat. The power available on the Shuttle meant that multiple wavelength/multiple polarization data could be collected at one time. In the case of the SRTM, flying two radar antennas (one within the payload bay, the other on a 61 m long boom attached to the Shuttle) produced a topographic map of much of the Earth's surface in less than 2 weeks. These SRTM topographic data provide the best baseline information for geomorphic analysis of volcanoes in the KKA, where regional comparisons can be conducted of volcano geomorphology due to relative differences in the ages or rates of erosion (Wright *et al.*, 2006).

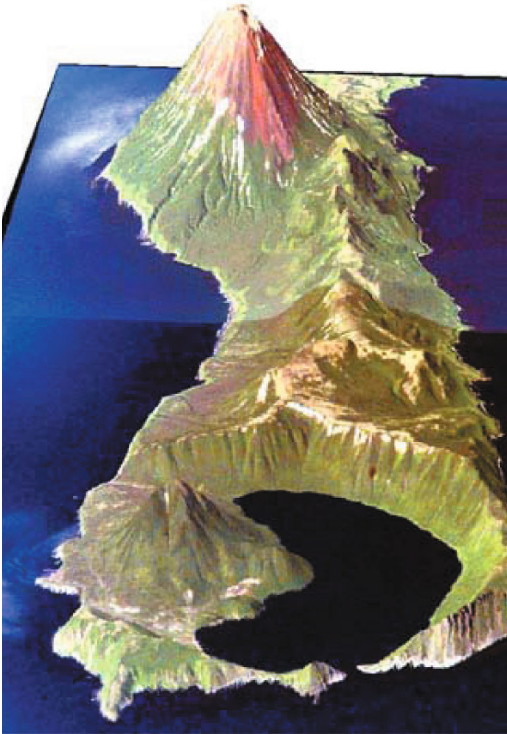


Figure 10.24. Oblique view of Urataman Volcano ($47^{\circ}06'N$, $152^{\circ}12'E$) and Prevo Peak on Simushir Island, Kurile Islands, Russia ($47^{\circ}01'N$, $152^{\circ}07'E$), looking towards the southwest. This image was generated by combining two ISS color images (frames ISS005-E-6513 and ISS-E-5614) with SRTM 90 m digital topographic data. Compare this image with the nadir view of this area shown in Figure 10.11. Vertical exaggeration is $\sim 2.4\times$.

10.7 ACKNOWLEDGMENTS

All Space Shuttle and ISS images courtesy of the Earth Sciences and Image Analysis Department, NASA Johnson Space Center.

10.8 REFERENCES

- De Silva, S.L.; Francis, P.W. (1990). Potentially active volcanoes of Peru: Observations using Landsat Thematic Mapper and Space Shuttle imagery, *Bull. Volcanol.*, **52**, 286–301.
- Evans, C.A.; Lulla, K.P.; Dessinov, L.V.; Glazovskiy, N.F.; Kasimov, N.S.; Knizhnikov, Yu.F. (2000). Shuttle–Mir Earth science investigations: Studying dynamic Earth environments from the Mir Space Station, in K.P. Lulla and L.V. Dessinov (Eds.), *Dynamic Earth Environments: Remote Sensing Observations from Shuttle–Mir Missions*, John Wiley & Sons, New York, pp. 1–14.
- Farr, T.G.; Kobrick, M. (2000). Shuttle Radar Topography Mission produces a wealth of data, *EOS, Transactions American Geophysical Union*, **81**, 583–585.
- Lowman, P. (1973). Geologic uses of Earth-orbital photography, in R.K. Holz (Ed.), *Surveillant Sciences: Remote Sensing of the Environment*, Houghton Mifflin, Boston, MA, 390 pp.
- Mouginis-Mark, P.J. (1995). Preliminary observations of volcanoes with the SIR-C radar, *IEEE Trans. Geosci. Rem. Sens.*, **33**, 934–941.
- Rabus, B.; Eineder, M.; Roth, A.; Bamler, R. (2003). The Shuttle Radar Topography Mission A new class of digital elevation models acquired by spaceborne radar, *Photogramm. Rem. Sensing*, **57**, 241–262.
- Rose, W.I.; Delene, D.J.; Schneider, D.J.; Bluth, G.J.S.; Krueger, A.J.; Sprod, I.; McKee, C.; Davies, H.L.; Ernst, G.G.J. (1995). Ice in the 1994 Rabaul eruption cloud: Implications for volcano hazard and atmospheric effects, *Nature*, **373**, 477–479.
- Stofan, E.R.; Evans, D.L.; Schmillius, C.; Holt, B.; Plau, J.J.; van Zyl, J.; Wall, S.D.; Way, J. (1995). Overview of results of spaceborne imaging Radar-C, X-band Synthetic Aperture Radar (SIR-C/X-SAR), *IEEE Trans. Geosci. Rem. Sens.*, **33**, 817–828.
- Wood, C.A.; Kienle, J. (1990). *Volcanoes of North America*, Cambridge University Press, Cambridge, U.K., 354 pp.
- Wright, R.; Garbeil, H.; Baloga, S.M.; Mouginis-Mark, P.J. (2006). An assessment of Shuttle Radar Topography Mission digital elevation data for studies of volcano morphology, *Rem. Sens. Environ.*, **105**, 41–53.
- Yoder, J.A.; Ackleson, S.G.; Barber, R.T.; Flament, P.; Balch, W.M. (2002). A line in the sea, *Nature*, **371**, 689–692.
- Zebker, H.A.; Rosen, P.; Hensley, S.; Mouginis-Mark, P.J. (1996). Analysis of active lava flows on Kilauea volcano, Hawaii, using SIR-C radar correlation measurements, *Geology*, **24**, 495–498.

The effects of volcanic eruptions observed in satellite images: Examples from outside the North Pacific region

Robert Wright, Andrew J.L. Harris, Ronnie Torres, Luke P. Flynn

11.1 CHAPTER SYNOPSIS

The effect of a volcanic eruption by liberating magma, gases, and energy is to modify the Earth's surface and its atmosphere. Quite how these changes are produced depends on the nature of the eruption; for example, whether it is explosive or effusive, the period of time over which the eruption occurs, the mass of material erupted, and the geographic area over which the erupted products are distributed. The eruption of lava flows, the emplacement of pyroclastic flows and lahars, and the deposition of volcanic ash all serve to change the landscape surrounding the volcano. The injection of ash and gas into the Earth's atmosphere not only alters its composition but, through this under certain conditions, has the ability to influence Earth's climate. These effects can be more than climatic or geomorphic. Indeed, the often close proximity between humans and erupting volcanoes means that these agents of change also constitute a hazard.

Many of the preceding chapters in this book have been concerned with describing how satellite data can be used to provide quantitative data regarding the nature of various eruptive products and processes. The purpose of this chapter is to illustrate how insights into the many effects of volcanic eruptions, at both the regional and global scales, can be gleaned from remotely sensed data sets. To this end, we begin by summarizing the ways in which volcanic eruptions can affect their surrounding environment and the attributes that make satellite remote sensing a suitable method for study-

ing these effects. Using a range of case studies for three contrasting volcanoes and eruption styles, we then illustrate how the regional and global effects of volcanic eruptions have been documented using satellite images.

11.2 INTRODUCTION: OBSERVING THE EFFECTS OF VOLCANIC ERUPTIONS USING SATELLITE IMAGES

The effect of a volcanic eruption, by transferring magma and gas from beneath the Earth's crust to a position above it, is to modify the Earth's surface and its atmosphere in a variety of ways and over a range of spatial and temporal scales. The exact nature of the effect of an eruption depends on the type of volcano, the chemistry of the magma erupted, the period of time over which the eruption occurs, and the geography of the area over which the erupted products are distributed. The eruption of lava flows, the emplacement of pyroclastic flows and lahars, and the deposition of volcanic ash can all serve to alter the geomorphological, hydrological, and ecological characteristics of the landscape surrounding the volcano, while the injection of ash and gas into Earth's atmosphere not only modifies its composition but can also, as a consequence, influence regional weather and global climate.

Significantly, the close proximity between humans and erupting volcanoes means that, in addition to simply impacting Earth's surface and atmosphere, the products of an eruption may also constitute a *hazard*. Blong (1984) identifies 13 volcanic hazards, defined as those products of an eruption that impact upon people, their possessions, their lifestyles, and their environments, a list which includes lava flows, ballistic projectiles, tephra fall, pyroclastic flows, debris avalanches, lahars, jökulhlaups, seismic activity, ground deformation, tsunami, atmospheric effects, acid rain, and acid gases. The effects of these hazards are many and varied and include the impact that eruptions have on humans both directly, as a result of physical and psychological trauma, and indirectly, through their impact on infrastructure, agriculture, commerce, and even tourism.

Some of the effects of volcanic eruptions, such as the destruction of houses by lava flows, can be detected and chronicled using satellite images; others, such as the psychological trauma inflicted on those evacuated from the houses, obviously cannot. This chapter is not intended to provide a detailed commentary of all the possible effects, physical and socio-economic, presented by volcanic hazards; for this we refer the reader to Blong (1984). Rather, the purpose of this chapter is to illustrate how insights into many of the products of volcanic eruptions, and some of their effects, can be gleaned from remotely sensed images.

The emplacement of lava flows, lahars, pyroclastic flows, and ash has a clear effect on the landscape surrounding a volcano: they re-surface it, often over short periods of time and sometimes over considerable areas. The effects of an explosive eruption are perhaps the most dramatic illustration of this. On May 18, 1980, Mt. St. Helens erupted approximately 0.2 km^3 of magma in 9 h, devastating $\sim 600 \text{ km}^2$ of the surrounding area (Christiansen and Peterson, 1981). Pyroclastic flows, ash fall, lahars, a directed blast and debris avalanche acted in concert to produce the changes depicted in Figure 11.1, which included the destruction of mature stands of coniferous forest and substantial changes to the local lacustrine and fluvial system. The eruption cost U.S.\$2.7 billion and the lives of 57 people (Fisher *et al.*, 1997). At Mt. St. Helens these changes occurred over a large area, with the majority (those associated with the initial directed blast), concentrated within several hours. At Soufrière Hills Volcano, Montserrat, many of the same volcanic processes have combined to significantly

alter the pre-eruption landscape, but this time over a relatively small geographic area and over a period of a decade (Figure 11.2). Although the eastern half of the island is obscured by clouds in the 1989 pre-eruption image the impact of pyroclastic flows, lahars, and ash fall on the southern half of the island is obvious.

However, the effects of an explosive eruption need not be as complex, and the processes that combined to produce the changes observed at Mt. St. Helens and Soufrière Hills Volcano can also act in relative isolation. The April 18, 1993 eruption of Lascar Volcano, Chile, resulted in the emplacement of pyroclastic flows that extended 7.5 km from the summit crater complex (Denniss *et al.*, 1996). The emplacement of these flows, which are clearly visible in Figure 11.3, was the major consequence of this eruption. Tephra fall is an obvious effect of explosive eruptions, although identification of the deposits in satellite images can prove difficult, unless the volumes involved are large or images are acquired quickly, as ash is quickly reworked by wind and rain. However, ash fall on snow and ice is particularly easy to identify. Mt. Belinda, only recently identified as an active volcano (Patrick *et al.*, 2005), lies in the South Sandwich Islands, an isolated archipelago in the South Atlantic Ocean (Figure 11.4). In this high spatial resolution ASTER image dark localized ash deposits, possibly produced during a recent strombolian explosion from the summit vent, can clearly be seen on the eastern side of the volcano's summit.

Volcanic sector collapses are relatively rare, and it would be misleading to say that their effects have been routinely observed during the era of satellite remote sensing, due to the limited opportunity for before-and-after image pairs. Satellite images did, however, play a key role in demonstrating that large sector collapses were more common than had at first been thought (Francis and Wells, 1988), and images such as the one depicted in Figure 11.5, which shows the landslide deposit produced by a collapse that occurred at Socompa Volcano in Chile (see Wadge *et al.*, 1995) make it easy to visualize just how potent a geomorphic agent such an event can be.

One of the most infamous volcanic disasters of recent years, the eruption of Nevado del Ruiz, Colombia in 1985, was caused by the rapid emplacement of lahars (volcanic mudflows) in response to the melting of the volcano's summit glacier during an eruption. More than 23,000 people, mainly in the village of Armero, were killed

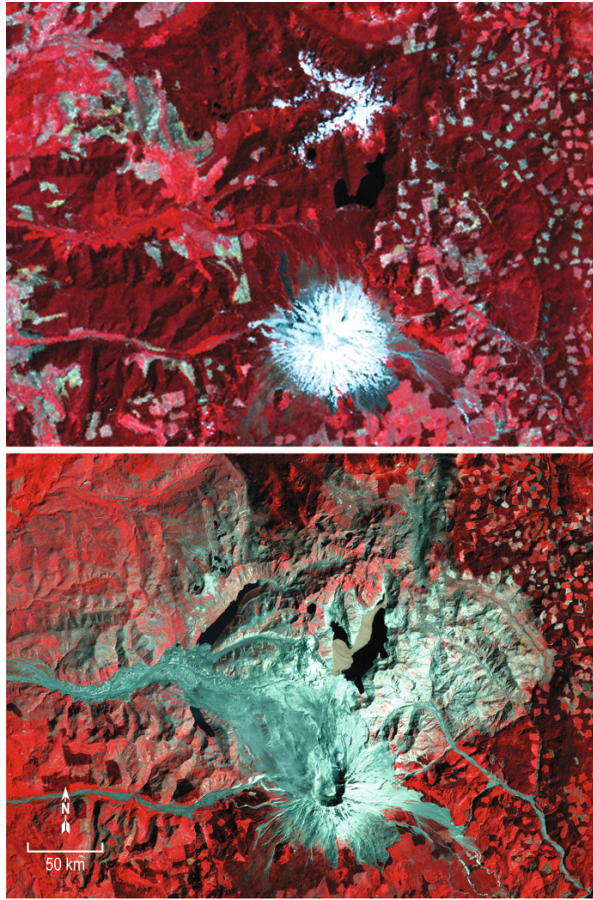


Figure 11.1. (Top) Landsat Multi-Spectral Scanner (MSS) standard false-color composite image of Mt. St. Helens, acquired on July 29, 1972. MSS bands 7 (0.8–1.1 μm), 5 (0.6–0.7 μm), and 4 (0.5–0.6 μm) are displayed in red, green, and blue, respectively. (Bottom) Landsat Thematic Mapper (TM) image of Mt. St. Helens, acquired on August 26, 1986. TM bands 4 (0.76–0.9 μm), 3 (0.63–0.69 μm), and 2 (0.52–0.60 μm) are displayed in red, green, and blue, respectively. MSS data have a nominal pixel size of $79 \times 79 \text{ m}$; TM pixels are 30 m on a side. In both images, healthy vegetation appears red, bare soil cyan, and ash gray. The pre-eruption Mt. St. Helens is snow-capped. The post-eruption image was acquired more than 6 years after the main May 18, 1980 eruption, but the effects of the eruption on the landscape are still obvious. Obvious changes have occurred with respect to the geomorphology of the volcano itself, the summit of which has been replaced with a 400 m diameter crater. Spirit Lake, the southern bank of which was directly impacted by the debris avalanche, can be seen immediately north of the volcano. Lahar deposits can be seen in many of the drainages radiating away from the volcano.

(Pierson *et al.*, 1990). Significantly, the impact of lahars is not necessarily constrained to the syn-eruptive period of a volcano's history. Casita Volcano, Nicaragua, last erupted 8,000 years ago (Scott *et al.*, 2001). However, anomalously heavy rainfall associated with the passage of Hurricane Mitch on October 30, 1998 resulted in both a sector collapse and the remobilization of unconsolidated volcanic

material on the volcano's flanks, producing lahars that killed more than 2,500 people (Figure 11.6; Kerle *et al.*, 2003).

Although perhaps less dramatic, the effusive eruption of basaltic lava also represents a formidable mechanism of Earth surface change and a hazard to human property and utilities, although rarely to human life. Whereas explosive eruptions often

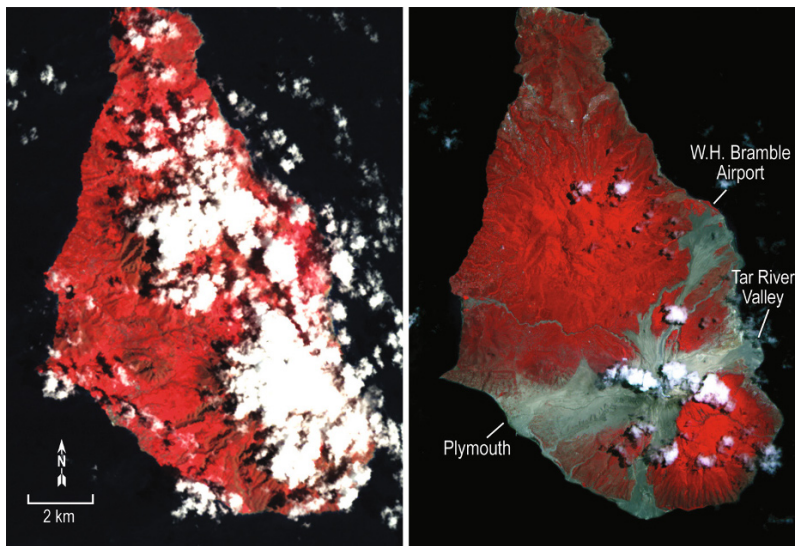


Figure 11.2. (Left) Landsat TM image of Montserrat, Lesser Antilles, acquired on October 9, 1989. TM bands 4, 3, 2 are shown in red, green, and blue. (Right) Terra ASTER (Advanced Spaceborne Thermal Emission and Reflection Radiometer) image of Montserrat acquired on September 4, 2002. ASTER bands 3 (0.76–0.86 μm), 2 (0.63–0.69 μm), and 1 (0.52–0.60 μm) are displayed in red, green, and blue, and the pixel size of this image is 15 m. The island is composed of four main volcanic massifs: Silver Hill, Centre Hills, Soufrière Hills, and South Soufrière Hills. Soufrière Hills Volcano began erupting on July 18, 1995, 350 years after the most recent previous activity. After an initial phase of phreatic activity the eruption entered its magmatic phase that comprised the emplacement of a series of andesitic lava domes. The capital city, Plymouth, first evacuated on August 22, 1995, was evacuated for the last time in April 1996 and has been all but destroyed by the combined effects of block-and-ash flows, pyroclastic surges, and lahars. The former runway at W. H. Bramble Airport is still visible, although the airport terminals were destroyed by block-and-ash flows on September 21, 1997. Pyroclastic flows, block-and-ash flows, and lahars impacted all major drainages in the southern half of the island. The new coastal fan of block-and-ash deposits produced during the eruption can be seen at the head of the Tar River Valley.

occur over relatively brief periods of time, perhaps hours or days, effusive eruptions can persist for months and even years. As this provides more opportunity for cloud-free image acquisitions, the effects of effusive eruptions are, arguably, easier to observe using satellites. Figure 11.7 shows a series of images of lava flows produced by two volcanoes with distinctly different eruptive styles. Pacaya Volcano in Guatemala has been continuously active since 1965, with explosive phases, characterized by strombolian and vulcanian activity, alternating with intermittent effusive eruptions (Bardintzeff and Deniel, 1992), which typically produce discrete channel-fed lava flows. Figure 11.8a shows a series of six images acquired by the Landsat Thematic Mapper and Enhanced Thematic Mapper+ sensors which depict several such flows. The ongoing eruption of Kīlauea volcano, Hawaii, began in 1983. Here, however, effusive activity is more persistent

and consists mainly of the gradual emplacement of pāhoehoe flow fields. Figure 11.7 shows a pair of images acquired by the Landsat Multispectral Scanner and the Landsat 7 Enhanced Thematic Mapper+ which show the impact of the steady emplacement of pāhoehoe lava flows on land on and adjacent to Kīlauea's Southeast Rift Zone.

The effects of an eruption on the landscape need not be so obvious. The last lava flow forming eruption at Masaya Volcano, Nicaragua, occurred in 1772 (Rymer *et al.*, 1998), while the last plinian eruption occurred approximately 6,500 years ago (Williams, 1983). The volcano remains, however, a prodigious emitter of sulfur dioxide gas, and at least five degassing “crises” have occurred since 1859 (Williams-Jones *et al.*, 2003). SO_2 can be detected and measured by satellite sensors such as MODIS and ASTER (see Prata *et al.*, this publication, Chapter 6). However, one of the *effects* of this

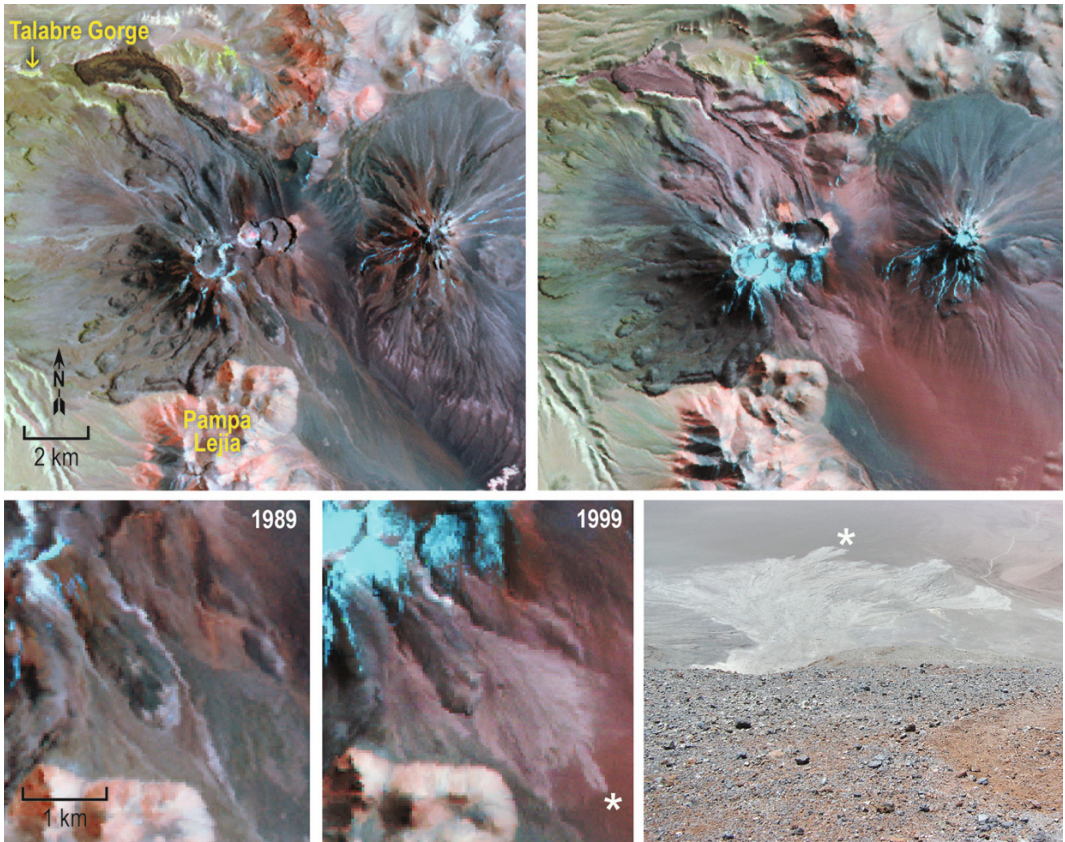


Figure 11.3. (Top left) Landsat TM image of Lascar Volcano, Chile, acquired on October 27, 1989. The summit of Lascar, which is at the center of the image, consists of a series of coalesced craters trending in a northeasterly direction; to the east is Volcán Aguas Calientes. (Top right) Landsat Enhanced Thematic Mapper Plus (ETM+) image of Lascar, acquired on May 16, 1999. In both cases, bands 7 (2.08–2.35 μm), 4 (0.76–0.90 μm), and 3 (0.63–0.69 μm) are displayed in red, green, and blue. Although this image was acquired 6 yr after the 1993 eruption, the low rate of weathering in this arid climate has left the pyroclastic flow deposit produced during the April 18, 1993 eruption extremely well preserved. In the 1999 image, the pyroclastic flows appear as pink pixels. Pyroclastic flows were emplaced adjacent to the Pampa Lejía to the southeast of the summit, and to the northwest, terminating in Talabre Gorge. (Bottom) Close-up showing the form of the pyroclastic deposit to the southeast. The photograph on the right was taken from the southeastern flank of the volcano in December 2004; the asterisk marks common points in the photo and the 1999 ETM+ image.

degassing can also be documented in satellite images. Prolonged exposure to acid gases in the plume is hazardous to human health, but has also served to degrade vegetation, including economically important coffee crops growing on the western flank of Masaya's summit caldera (Williams-Jones and Rymer, 2000; see Figure 11.8). The same effect has also been observed at Poás Volcano in Costa Rica.

The preceding examples have illustrated some

of the effects that volcanic eruptions can have on the Earth's surface. Volcanic eruptions also impact the Earth's atmosphere by loading it with variable quantities of ash and gas. Volcanic ash plumes produced during eruptions such as the June 15, 1991 eruption of Mt. Pinatubo, Philippines, have an obvious short-term impact: they block out the Sun. This causes a reduction in the amount of light reaching Earth's surface as well as a reduction in diurnal temperature variation, although in the case

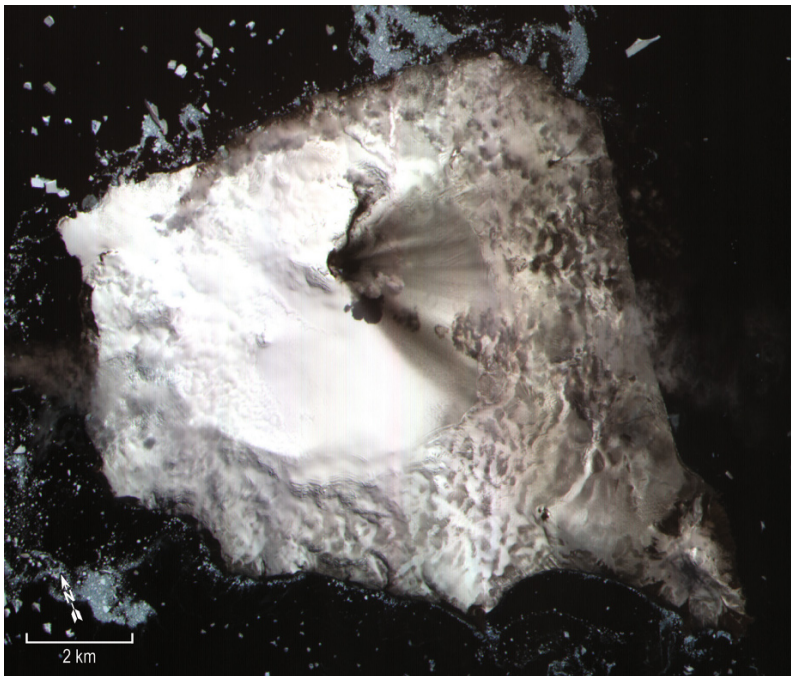


Figure 11.4. ASTER-simulated true-color image of Montagu, the largest island in the remote South Sandwich Island archipelago, acquired on December 7, 2003. Bands 3 (0.76–0.86 μm), 2 (0.63–0.69 μm), and 1 (0.52–0.60 μm) are displayed in red, green, and blue. The island comprises three volcanic cones: Mt. Belinda, the current center of activity located in the middle of the island; Mt. Oceanite at the extreme southeast tip of the landmass; and an unnamed cone about 2 km southeast of Belinda. The high latitude of Montagu Island (58.43°S) means that the island is \sim 90% covered by ice. As a result, contemporary volcanic eruption products are made conspicuous by the way they contrast starkly with the highly reflective snow and ice. Tephra-fall deposits are obvious as a contiguous group of gray pixels radiating away from Belinda’s summit and covering a 45° sector of the volcano’s eastern flank. The thin, sinuous group of black pixels extending to the north-northeast is a recently erupted lava flow. The dark, bulbous feature to the south of Belinda is the shadow of a diffuse plume, which can be seen moving to the east of the summit.

of Mt. St. Helens this effect persisted only for a couple of days until the ash cloud dispersed (Robock, 2000). Obviously, such an effect cannot be observed in satellite images. However, the cause, the ash plumes themselves, can, and Figure 11.9 shows a spectacular image acquired by NASA’s Aqua MODIS (Moderate Resolution Imaging Spectroradiometer) instrument of an eruption cloud produced during the September 25, 2002 eruption of Ruang Volcano, the southernmost volcano of the Sangihe Island Arc.

Sulfur dioxide affects human health, as well as soil and vegetation systems. If introduced into the atmosphere in sufficient quantities it can also have an effect on global climate via the generation of sulfuric acid (sulfate) aerosols (see Robock, 2000,

for a review). SO_2 oxidizes in the atmosphere, by reaction with H_2O and OH , to form sulfate aerosol clouds that cool the lower atmosphere by reducing the amount of sunlight that reaches the Earth’s surface. If confined to the troposphere the aerosols are removed through the combined effects of gravity and rain within a matter of hours to weeks, and the impact on climate is regional and limited to not much longer than the duration of the eruption. If, however, the eruption is energetic enough, these aerosols can be injected into the stratosphere, where they may reside for up to 3 years. Crucially, stratospheric winds allow these aerosols to be efficiently dispersed around the globe, and, as a result, such eruptions can affect Earth’s climate at the global scale. The Mt. St. Helens erup-

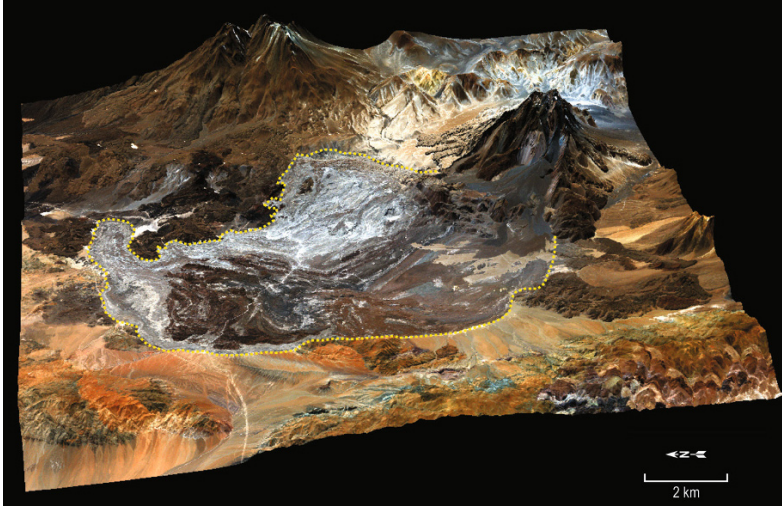


Figure 11.5. Landsat TM simulated true-color image (bands 3, 2, and 1 displayed in red, green, and blue, respectively) of Socompa Volcano, Chile. The multispectral satellite data have been draped over a 90 m resolution Shuttle Radar Topography Mission (SRTM; see Mougini-Mark and Jones, this publication, Chapter 10) digital elevation model (DEM), with a $\times 4$ vertical exaggeration. The northwestern flank of Socompa failed approximately 7,000 years ago, generating a debris avalanche that involved the movement of $\sim 50 \text{ km}^3$ of material (see Wadge *et al.*, 1995). The avalanche deposit itself, which extends 40 km from the volcano and covers an area of 490 km^2 , is delineated by the yellow dotted line. The amphitheater produced by the collapse is evident, although it has been partially filled by post-collapse volcanism. Low rates of weathering and the absence of significant vegetation cover make volcanic deposits in arid climates particularly well suited to remote-sensing analyses.

tion of May 1980 had a minimal impact on global climate because relatively little sulfur dioxide was injected into the stratosphere (Robock, 1981). However, recent eruptions at El Chichón, Mexico, in 1982 and Pinatubo, the Philippines, in 1991 perturbed the Earth's radiation budget enough to cause changes in global surface temperature of 0.1° and 0.2° (Robock and Mao, 1995). Figure 11.10 shows a Nimbus-7 TOMS image acquired on March 29, 1982 of the ash cloud produced by the eruption of El Chichón, which occurred one day earlier. The resulting aerosol cloud went on to circle the globe within 3 weeks.

The effects of volcanic eruptions are both varied and variable, acting as agents of change with respect to the Earth's surface and its atmosphere at a variety of spatial and temporal scales. Although not an exhaustive summary of all the possible effects and impacts that a volcanic eruption can have, we hope that the preceding discussion has succeeded in conveying that, despite their inherent variability, something that many of them have in common is their amenability to observation, measurement, and analysis by satellite remote-sensing

technologies. Assessing the impact of a volcanic eruption involves identifying the nature of the erupted products and resolving how their distribution and physical properties vary both spatially and temporally and, sometimes, determining how the Earth system responds when the eruption has finished. The value of Earth observation satellites as a tool for observing these effects can be summarized in terms of their ability to collect data synoptically, at regular and repetitive intervals, over extended periods of time, and in many different regions of the electromagnetic spectrum.

Many volcanoes are, geographically, very extensive and the products of their eruptions can be even more so. A technology that takes measurements over large areas quickly is clearly useful for mapping and otherwise observing many, if not all, of the volcanic processes described in the previous sections. Volcanic eruptions are also dynamic and, in order to evaluate them, their effects must be observed not only synoptically but also at regular intervals, and possibly over extended periods of time, a task for which satellite remote sensing is particularly adept. The scope of remote sensing as

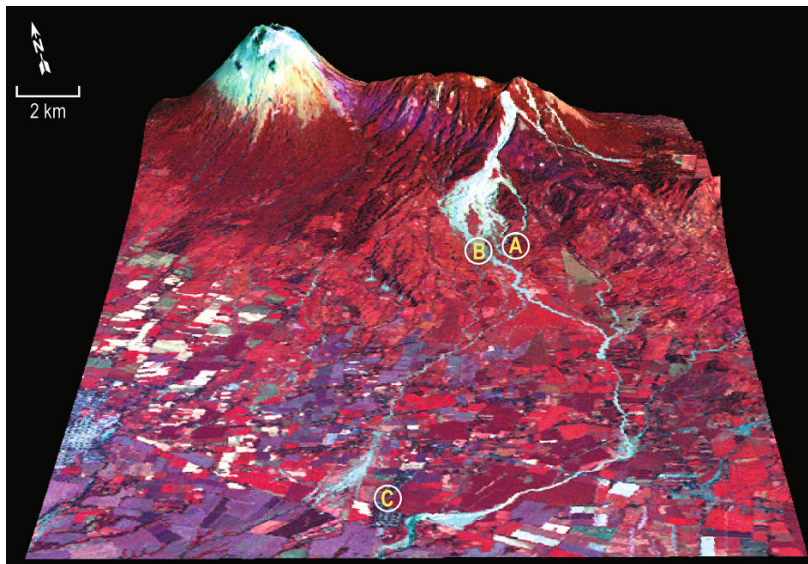


Figure 11.6. Landsat ETM+ false-color composite of Casita Volcano, Nicaragua, acquired on November 15, 1999. Bands 5 (1.55–1.75 μm), 3 (0.63–0.69 μm), and 1 (0.45–0.52 μm) are displayed in red, green, and blue, respectively. The multispectral satellite data have been draped over a 90 m SRTM-derived DEM ($\times 3$ vertical exaggeration). Casita is the dormant part of the San Cristóbal volcanic complex, the namesake of which is the peak to the west. On October 30, 1998, after receiving approximately 70 cm of rain in the previous 48 h, 1.6 million m^3 of hydrothermally altered and fractured rock detached from the volcano's southern flank. The rockslide fragmented close to the source, forming a debris avalanche, which eventually transformed into a lahar, apparent in this image as the bright cyan feature that extends from the summit of Casita. The mudflows destroyed the towns of Rolando Rodríguez and El Porvenir (the former positions of which are marked on the image as A and B, respectively) before bifurcating, extending across the Pan-American Highway, and finally coming to a halt on either side of Posoltega (C). Although this image was acquired just over one year after the event and substantial re-vegetation has occurred on the lahar deposit, the path and area covered during the mudflow is still apparent.

a means to study the effects of volcanic eruptions would be much diminished if data were only available in the visible part of the spectrum. However, remote determination of the sulfur dioxide content of volcanic plumes (see Watson and Prahash, this publication, Chapter 4), the mineralogy of lava domes (Ramsey *et al.*, this publication, Chapter 4), and the rate at which volcanic edifices deform (Lu *et al.*, this publication, Chapter 8), are made possible only by the acquisition of remotely sensed radiance data in different parts of the electromagnetic spectrum.

Establishing observational baselines against which the significance of contemporaneous volcanic unrest and eruptions can be judged is essential for understanding the long-term behavior of any volcanic system and the impact of this activity. This is as true for satellite image data as it is for more well-established technologies, such as seismic monitor-

ing. The benefits that arise from the regular, repetitive way in which remote-sensing data sets are collected, on time scales of days, to weeks, to months, are enhanced by the commitment of agencies such as the National Aeronautic and Space Administration (NASA), the National Oceanographic and Atmospheric Administration (NOAA), and the European Space Agency (ESA) to long-term data continuity. For example, the Advanced Very High Resolution Radiometer (AVHRR) has been carried on 10 different platforms since 1979, and constitutes a 25 yr archive of potentially useful volcanological data (e.g., Harris *et al.*, 1997a). Examination of AVHRR data for Mt. Etna (Italy) spanning the period 1980–1999 allowed the extraction of effusion rates from a total of 204 cloud-free images covering 11 different eruptions (see table 3 of Harris *et al.*, 2000). The Total Ozone Mapping Spectrometer (TOMS; Carn *et al.*,

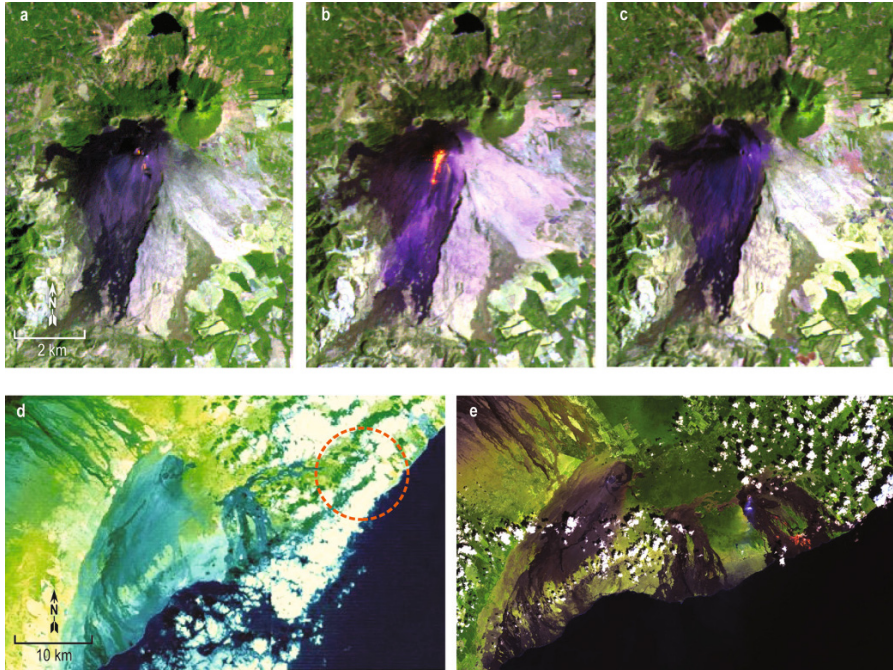


Figure 11.7. (Top) Landsat TM false-color composite images of Pacaya Volcano, Guatemala, acquired on January 19, 1990 (a), February 12, 1993 (b), and February 21, 1996 (c). (Bottom) Landsat TM false-color composite images of Kilauea Volcano, Hawaii which were acquired on January 19, 1990 (a), February 12, 1993 (b), and February 21, 1996 (c). Bands 7 (2.08–2.35 μm), 5 (1.55–1.75 μm), and 3 (0.63–0.69 μm) are displayed in red, green, and blue, respectively. When using this band combination, active lava, by virtue of its high temperature, appears red or yellow as a result of elevated levels of spectral radiance in the shortwave infrared. Pacaya is a composite volcano located about 45 km south of Guatemala City. After a period of repose that lasted almost 100 years, Pacaya erupted in March 1961, emplacing $1.5 \times 10^6 \text{ m}^3$ of basaltic lava onto the southern flank of the volcano (Eggers, 1983). Since this time, activity has been characterized by extended periods of relative quiet involving the presence (a) or absence (c) of strombolian eruptions within the summit crater, punctuated by sporadic and voluminous outpourings of lava onto the southern and western flanks of the volcano (b). The style of lava flow forming eruption at Pacaya contrasts sharply with that of Kilauea Volcano, Hawaii. The Pu'u 'Ō'ō-Kūpaianaha eruption began on January 3, 1983. Although the eruption has encompassed $\sim 500\text{ m}$ high lava fountains and the development of quasi-permanent lava ponds, the dominant characteristic has undoubtedly been the near-continuous low effusion rate emplacement of pahoehoe lava (see Heliker and Mattox, 2003 for an overview). Figure 11.8d shows a Landsat MSS (Multi-Spectral Scanner) image of Kilauea's Southeast Rift Zone acquired in 1973. Figure 11.8d shows the same area, this time imaged by Landsat ETM+ in 2000. Lava flows emplaced prior to 1973 are visible in both images. However, the flow field produced by the Pu'u 'Ō'ō-Kūpaianaha eruption is only visible in the 2000 image, marked by the dashed circle.

2003), which allows loading of the atmosphere with sulfur dioxide during major explosive eruptions to be determined, has been carried on board four different platforms since 1978 and, between 1978 and 2001, observed 102 eruptions at 61 different volcanoes (see tables 2–7 in Carn *et al.*, 2003). Extended data sets provided by these, and other, orbital sensors, constitute a powerful means for resolving the long-term effects of volcanic eruptions.

This section has provided an overview of some of the effects that volcanic eruptions can have and why satellite remote sensing can provide a useful means to document them. In the next section we recount more detailed case studies of how remote sensing has been used to observe the effects and hazards of several eruptions of contrasting styles, at varying scales, and at several volcanoes around the world.

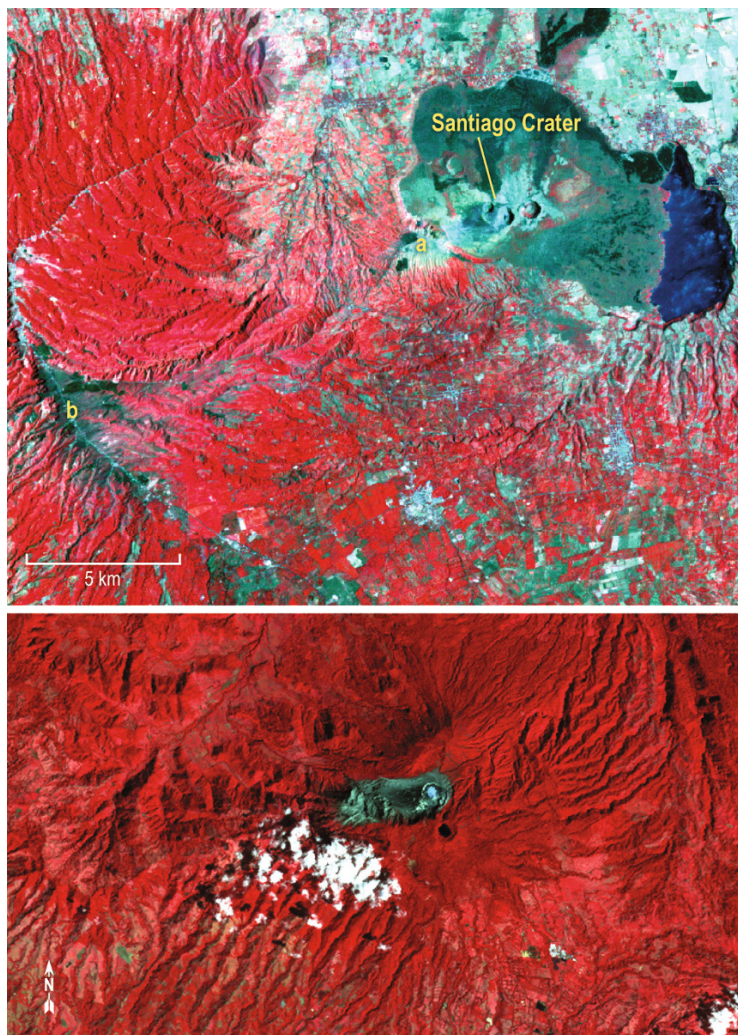


Figure 11.8. (Top) Landsat ETM+ false-color composite image of Masaya Volcano, Nicaragua, acquired on March 25, 2001. (Bottom) Landsat TM false-color composite image of Poás Volcano, Costa Rica, acquired on February 6, 1986. In both cases bands 4, 3, and 2 are displayed in red, green, and blue. Masaya is a large basaltic shield volcano characterized by persistent degassing. The current source of this gas is Santiago Crater, one of several nested craters contained within Masaya Caldera. Degassing at Masaya is apparently cyclic, the most recent episode having begun in the early 1990s. During this time total gas flux has been estimated to vary between 550 and 1,800 t per day (Williams-Jones *et al.*, 2003). The dominant easterly trade winds disperse the gas mainly over the western flank of the volcano, and the deposition of acid species from the plume stresses and ultimately kills vegetation in this region. The effect of this degassing is easily identified in this ETM+ image which has been processed to depict healthy vegetation in red. Two gray-green groups of pixels downwind of the crater, one on the edge of Masaya Caldera (a) and another on the edge of the older Las Sierras Caldera (b) correspond to areas that have been denuded of vegetation. Poás Volcano is a basaltic/andesitic stratovolcano that has been persistently active throughout historic times, hosting an acidic crater lake and a vigorously active shallow hydrothermal system (Rymer *et al.*, 2000). The volcano is a source of persistent gas emission into the atmosphere. The area impacted by these emissions, and the acid rain associated with them, is elliptical, with a major axis that trends approximately west-southwest (a function of the prevailing wind direction), and once more is easy to identify in this TM image. The active crater lake is visible at the eastern edge of this “de-vegetated” ellipse.

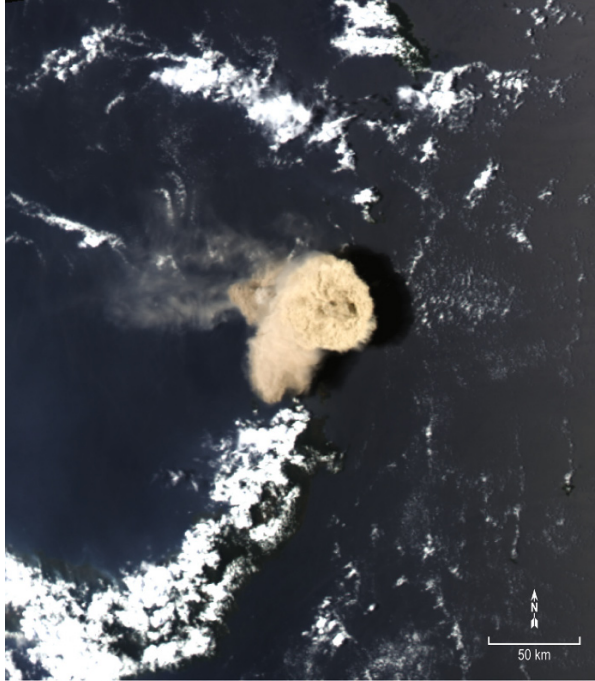


Figure 11.9. MODIS image of an eruption at Ruang Volcano, acquired at 12:50 (local time) on September 25, 2002. Bands 1 (0.62–0.67 μm), 4 (0.545–0.565 μm), and 3 (0.459–0.479 μm) are displayed in red, green, and blue, respectively, with a pixel size of 500 m. The eruption began about one hour before this image was acquired, and produced ash plumes that rose to approximately 20 km above sea level. By the time of image acquisition the diameter of the plume had exceeded 50 km. The shadow cast by the eruption plume can be seen to the east. A cloud-covered Sulawesi Island can be seen to the south.

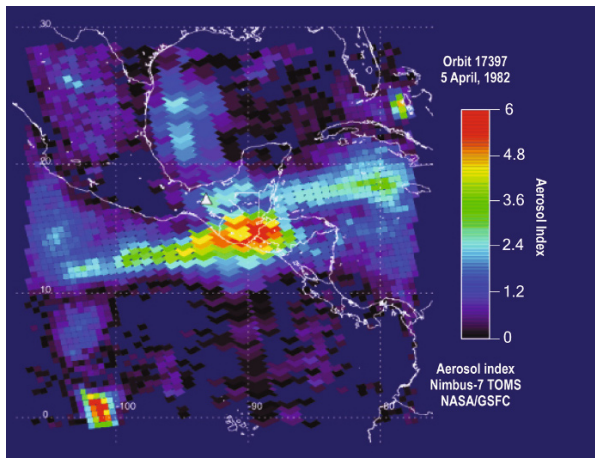


Figure 11.10. NIMBUS-7 TOMS image of the ash produced by the 1982 eruption of El Chichón, Mexico. The first historical eruptions of El Chichón began on March 28, 1982, culminating in the April 4 eruption, one of the largest of the 20th century. The TOMS Aerosol Index is positive for aerosols that absorb ultraviolet light, such as volcanic ash. This image shows the atmospheric loading of ash on April 5, 1982. The white triangle marks the location of the volcano (image processed by and courtesy of the TOMS Volcanic Emissions Group, JCET/UMBC).

11.3 MT. PINATUBO, PHILIPPINES, 1991

11.3.1 The effects on and response of a landscape to a large ignimbrite-forming eruption

The June 15, 1991 eruption of Mt. Pinatubo, which was the second largest of the 20th century, erupted between 8.4 and 10.4 km³ of magma (bulk volume; 3.7–5.3 km³ dense rock equivalent, DRE) in 9 h, devastating an area of more than 400 km² and covering most of South East Asia with ash (Wolfe and Hoblitt, 1996). Although eruptive activity began on June 12, most of the effects of the eruption were associated with the climactic stage, which included the emplacement of a thick non-welded pumice-rich ignimbrite, widespread pumiceous air fall deposits, lahars, and the formation of a 2.5 km diameter caldera.

Figure 11.11 shows a pair of SPOT (Satellite pour l'Observation de la Terre) images of Mt. Pinatubo and the surrounding region, spanning the period before and after the June 15, 1991 eruption. These false-color composite images have been produced so that vegetation appears red and unvegetated surfaces, such as pyroclastic deposits, exposed soil, alluvium, and bare rock, appear cyan. A bulk volume of 8.4 to 10.4 km³ of material was erupted during the climactic stage of the June 15, 1991 eruption (Wolfe and Hoblitt, 1996). Pyroclastic flows, which accounted for 5 to 6 km³ of this, filled valleys and mantled interfluvies creating an ignimbrite deposit up to 200 m thick in places (Scott *et al.*, 1996). The majority of the ignimbrite was emplaced to the west of the volcano's summit, with two thirds of its volume being distributed amongst three drainage basins: the Marella, the Balin-Baquero, and the Bucao (Bailey *et al.*, 2001). Pyroclastic flows extended up to 16 km from the vent and directly impacted an area of ~400 km² (Scott *et al.*, 1996). Pumiceous tephra fall accounted for the remaining 3.4 to 4.4 km³ of the erupted volume and was evenly distributed across all sectors of the volcano (Major *et al.*, 1996; Wolfe and Hoblitt, 1996). The maximum thickness of this deposit, measured 10.5 km from the vent, was 33 cm and an area of 2,000 km² was covered to a thickness of at least 10 cm (Paladio-Melosantos *et al.*, 1996). The total area affected by tephra fall was about 4 × 10⁶ km², although most fell into the South China Sea (Paladio-Melosantos *et al.*, 1996). The SPOT image shown in Figure 11.11 clearly reveals the distribution of these primary eruption products. Rain asso-

ciated with the passage of Tropical Storm Yunya quickly began to remobilize the 5.5 to 6.5 km³ of unconsolidated deposits on the volcano's flanks, triggering lahars along all major drainages around the volcano (Major *et al.*, 1996).

Although the climactic eruption itself only lasted for 9 h, its effects persisted for several years, many of which can be observed in the time series of SPOT images presented in Figures 11.12–11.14 which spans a 10 yr period before, during, and after the eruption. A significant change occurred at the volcano's summit, which was removed and replaced by a 2.5 km diameter caldera. The intra-caldera ignimbrite deposited during the climactic stage of the eruption was subsequently reamed out by phreatic explosions, and reworked by epiclastic processes and landslides. By September 1991 a crater lake fed by groundwater and rainwater had become established in the caldera (Campita *et al.*, 1996).

Post-eruption volcanism began with a series of phreatomagmatic explosions and the extrusion of a dacitic lava dome in the summit caldera lake between July and October 1992 (Daag and van Westen, 1996). After extruding a volume of 4 × 10⁶ m³ of magma, the eruptive activity stopped. By December 11, 1994 (Figure 11.12) the lake had expanded in area to cover most of the caldera floor, the peaks of the aforementioned lava dome complex manifest only as small islands on the lake surface. By February 12, 1996 (Figure 11.12) the crater lake had totally submerged the dome structure and expanded to approach low points in the caldera rim, notches formed by the truncation of the Maraunot and O'Donnell river valleys during formation of the caldera. The SPOT image acquired on December 5, 1998 shows continued areal expansion of the lake that by 2001 had grown to the extent that there was a serious risk that it would overtop the Maraunot notch, an event that would have triggered lahars on the northwestern flank of the volcano. In response to this hazard, a controlled breaching of the lake was conducted at the Maraunot notch in September of that year, causing the lake water to drain safely, rather than catastrophically, into the new Maraunot–Bucao river system.

The pyroclastic flows produced during the climactic stage of the eruption filled river valleys and mantled ridges producing a flat, featureless landscape, dramatically altering the watershed hydrology of the area. The easily eroded ignimbrite represented something of a blank canvas and a new drainage network quickly became established. Fig-

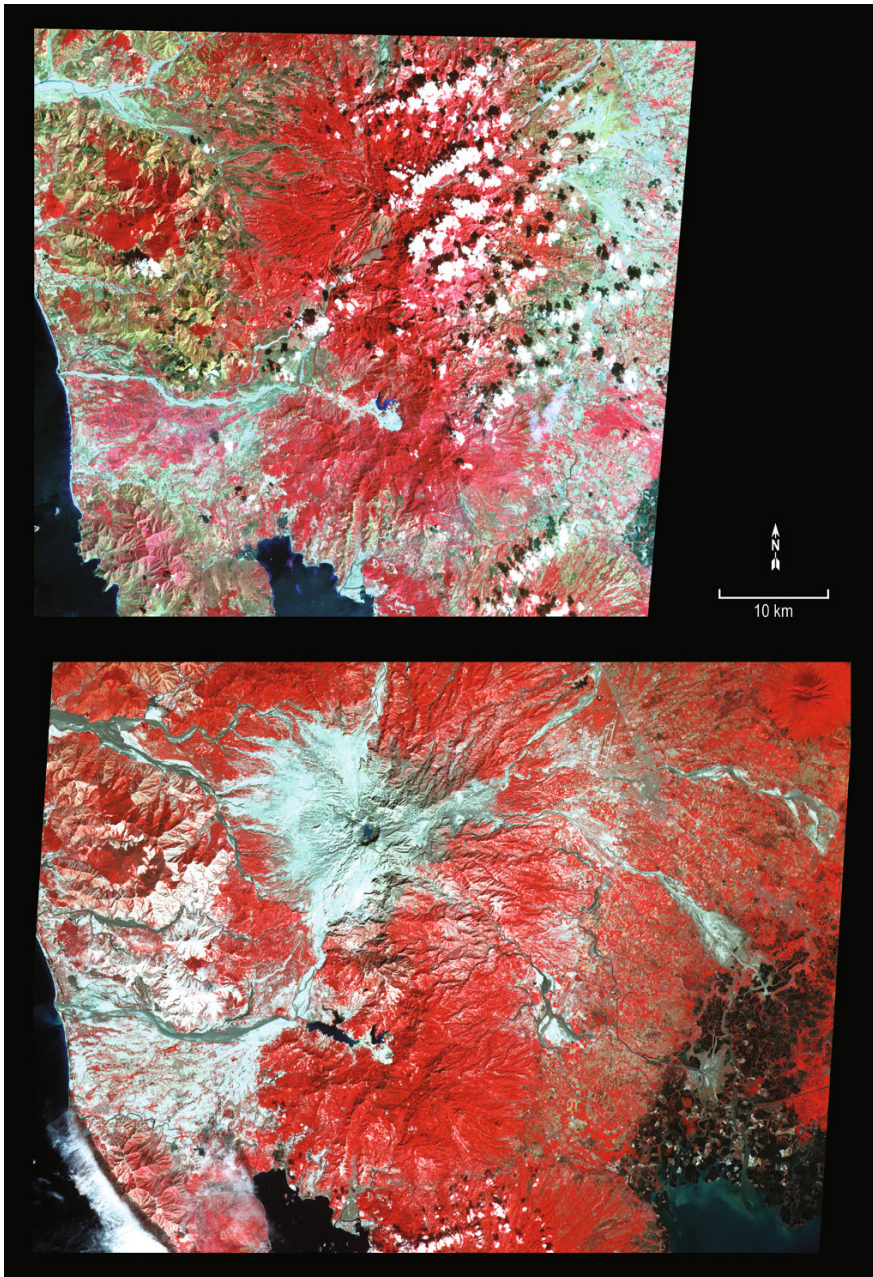


Figure 11.11. SPOT XS (multispectral mode) images of Mt. Pinatubo, Philippines. The image at the top was acquired on April 4, 1988; the image below, on December 18, 1991, six months after the June 15, 1991 eruption. The pixel size is 20 m in both cases, and bands 3 (0.79–0.89 μm), 2 (0.61–0.68 μm), and 1 (0.50–0.59 μm) are displayed in red, green, and blue, respectively. The 1991 image shows the situation at the end of the 1991 monsoon season, the rainfall associated with which did much to rework the original tephra deposits. The 1991 image, acquired at the end of the monsoon season, also shows how the eruption deposits were redistributed by lahar activity. Lahars impacted all major drainages of the volcano.

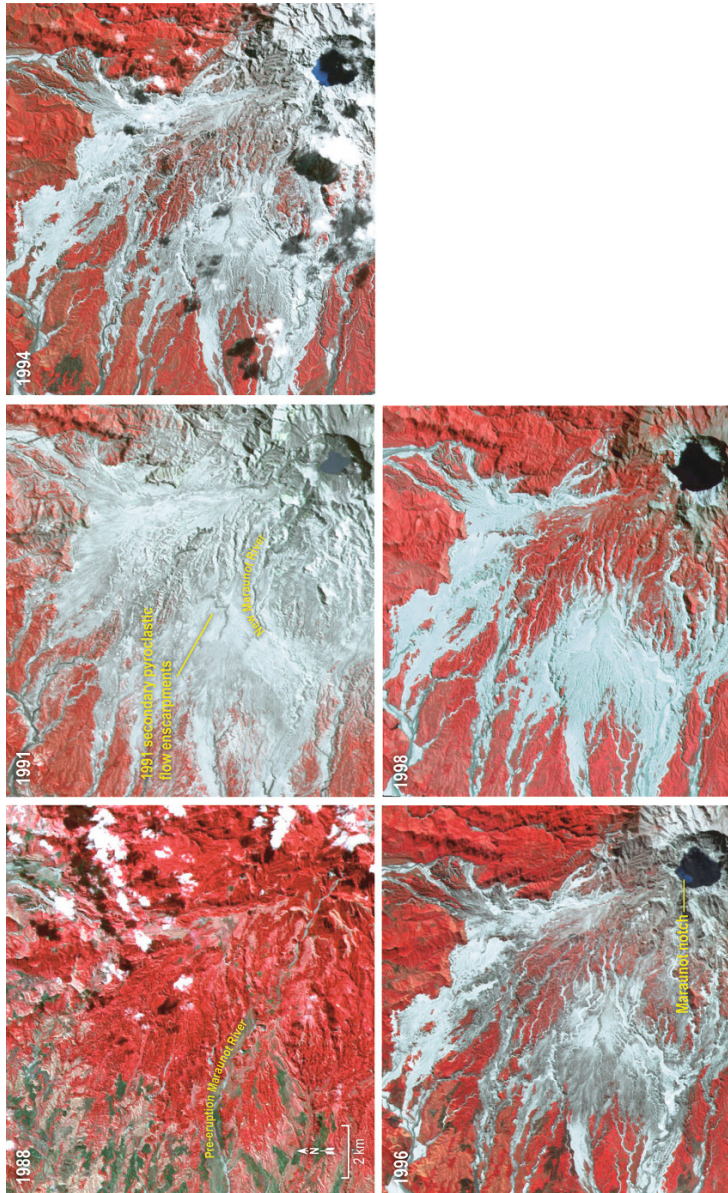


Figure 11.12. (Left to right, top to bottom) SPOT XS images acquired on April 4, 1988; December 18, 1991; December 11, 1994; February 12, 1996; and December 5, 1998 of the northwestern sector of Pinatubo Volcano, showing some of the most dramatic landscape changes to result from the eruption. The caldera formed during the climactic phase is visible in the southeast corner of the post-eruption images. By the time the December 18, 1991 image was acquired the intra-crater lake was well established although, as the following images show, the area it covered increased gradually during this time period. The resurgent dome that formed in the southern part of the caldera is barely visible in the December 1994 image and has been totally submerged by the time the February 1996 image was acquired. The Marauot River was destroyed during the eruption, a new Marauot River becoming established along a new course via erosion of the pristine ignimbrite fan.

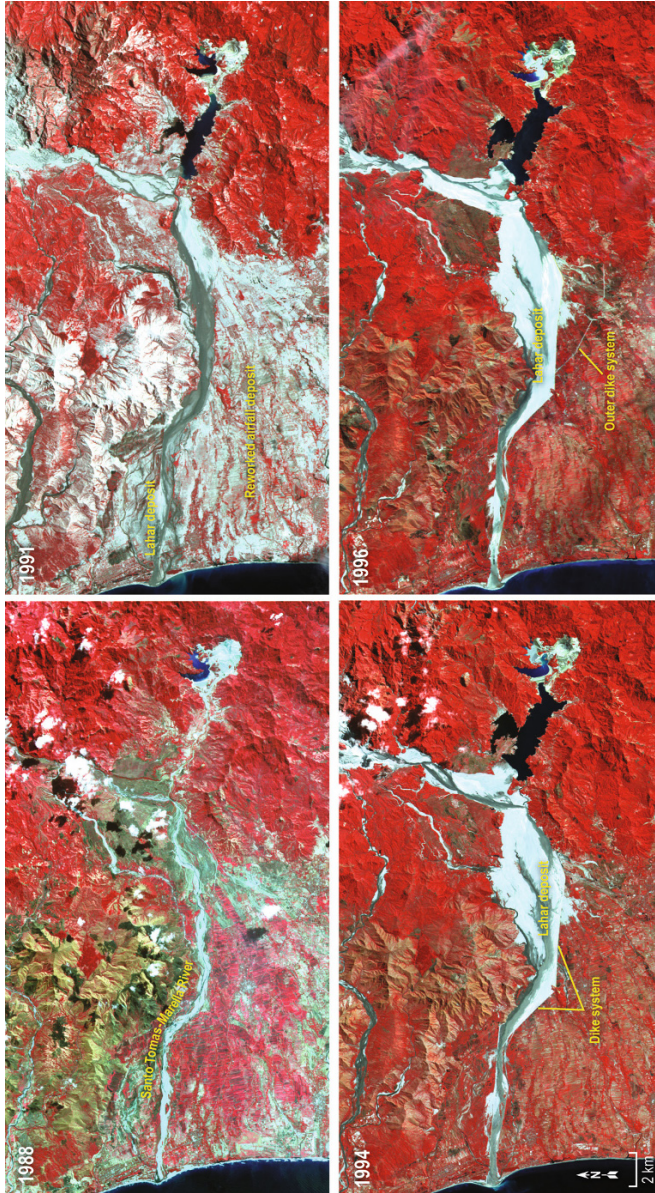


Figure 11.13. The development and containment of lahars on Pinatubo's western flank. Dikes were constructed after the eruption to reduce the area inundated by lahars. In 1993 a dike along the southern bank of the Santo Tomás River was built to protect the towns of Castillejos, San Marcelino, and San Narciso. Unfortunately, the dike did not work as planned and was overtopped by lahars in late 1993. After the failure of several dikes during the 1993 rainy season, stronger outer dikes were constructed in many cases. Although the intensity and frequency of lahars has and will continue to diminish as the volume of unconsolidated source material on the volcano's flanks is exhausted, the threat from lahars must still be taken seriously.

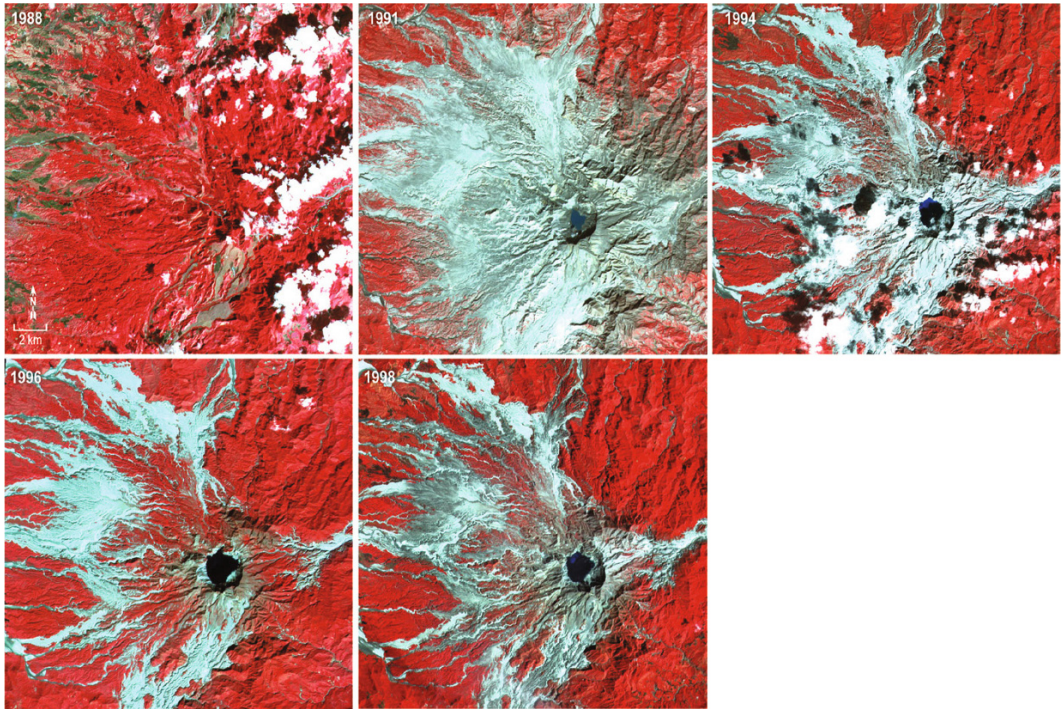


Figure 11.14. Sequence of SPOT images showing the denudation of vegetation caused by the June 1991 eruption and the spatial patterns of subsequent vegetation recolonization. The contrast between vegetated areas and those surfaces bereft of substantive vegetation cover is high in these images as a result of the very high near-infrared reflectance of vegetation.

ure 11.12 shows how the stream network within the Maraunot and Bucao ignimbrite fans developed in the 7 years following the eruption. Tropical Storm Yunya triggered the early development of channels and rills in the ignimbrite surface. An embryonic drainage pattern, identified in the field by linear associations of phreatic explosion pits and rootless fumaroles that formed where surface flow became concentrated in the still hot ignimbrite, was established as early as July 5, 1991. These streams were later entrenched and enlarged by typhoon-induced and rain-induced overland flow. With few exceptions, the post-eruption river valleys followed the pre-eruption drainage system configuration, although small-scale deviations from the pre-eruption channels did occur as new streams meandered into older terrains. Headward erosion and gullying during torrential rains transformed the 1991 pyroclastic fans into a heavily dissected ignimbrite terrain within 7 yr. This erosion has occurred much more rapidly, with 60% of the deposit remobilized in the first 6 years (Daag and van Westen,

1996), than has been observed at comparable ignimbrites, such as that formed during the 1912 Katmai eruption.

The thickness of the primary ignimbrite allowed it to maintain a hot, dry core enabling this region to act as a source of large dry-state remobilization (or deposit-derived) secondary pyroclastic flows that were emplaced after the eruption itself (Torres *et al.*, 1996, 2004). Several of the escarpments formed during the initiation of these secondary pyroclastic flows are visible in Figure 11.12. Cumulatively, these post-eruption deposit-derived flows have delivered large amounts of material into the valleys, allowing for significant bulking of subsequent lahars. Some secondary pyroclastic flows temporarily blocked tributary channels, creating localized ponding of water.

As much of the eruptive product has been confined to land-locked basins, the erosion of the ignimbrite has been balanced by aggradation of downstream regions by lahars. Rains associated with Yunya triggered lahars during the June 15,

1991 eruption itself. However, the effect of lahars on the landscape has persisted well beyond the syn-eruptive period, with lahars triggered by monsoon rains, volcanic thunderstorms (i.e., convective rain formed over localized heat sources in the ignimbrite), and breakouts from debris-dammed lakes that formed during the eruption (Pierson *et al.*, 1996) continuing to pose a serious hazard to the local population. Lahar deposits averaging 2 m in thickness and extending up to 52 km from the vent (Major *et al.*, 1996) were emplaced, mainly on alluvial fans to the east of the summit (Pierson *et al.*, 1996). Figure 11.11 shows the distribution of most of the lahar deposits at the end of the 1991 monsoon season. In response to the threat posed by lahars to downstream population centers, a series of giant concrete dikes totaling 85 km in length were built to channel them away from populated areas, at a cost of U.S.\$154 million (Mercado *et al.*, 1996). The images displayed in Figure 11.13 show the effects that these diversionary structures have had on lahar inundation patterns. Areas to benefit from these diversionary measures, such as the Pasig-Potrero River, have seen the impact of lahars much reduced, to the point where land has been able to be reclaimed for cultivation and construction. Areas not afforded such protection continue to be impacted by post-eruption lahars.

The 1991 Pinatubo eruption deposits also created a new lake west of the volcano. Figure 11.13 shows the geography of the Mapanuepe, Marella, and Santo Tomás Rivers prior to the 1991 eruption. Lahars produced during and after the June 15, 1991 eruption flowed down the Marella Valley and, aided by a bedrock constriction at the confluence of the Mapanuepe and Marella, blocked outflow from the Mapanuepe, promoting the formation of the new Mapanuepe Lake (Umbal and Rodolfo, 1996). At its largest the lake covered an area of 6.7 km² and contained approximately 75×10^6 m³ of water, although these dimensions fluctuated, particularly during the monsoon season. When lahar activity in the Marella waned, sediment supply to the constriction would decrease, allowing the lake to intermittently overtop the dam; when lahar activity in the Marella increased, the breaches were plugged and the lake level was allowed to recover. The formation of this new lake impacted the surrounding population in two ways. First, formation of the lake itself flooded the towns of Aglao, Buhawen, and Pili forcing the evacuation of 500 people (Umbal and Rodolfo, 1996). Second, lake breakout lahars constitute a continuing threat to communities

downstream on the Santo Tomás Plain, although artificial channels have been cut to stabilize the level of water in the lake.

The June 15, 1991 eruption had an enormous impact on regional vegetation. Areas impacted by pyroclastic flows were stripped of vegetation cover, while proximal slopes facing the vent were also deeply eroded. Figure 11.14 clearly shows that the re-colonization by vegetation progressed at different rates in different areas. The eastern sector of the volcano, mainly impacted by air fall deposits that were readily reworked and removed by wind and rain to expose the pre-eruption soil, was quickest to re-vegetate, recovering almost to pre-eruption levels in just 7 yr. The western sector bore the brunt of the effects of pyroclastic flows, and here vegetation re-growth has occurred more slowly and at a more variable rate. Proximal regions close to the summit that were denuded of soil entirely have failed to re-vegetate. Similarly, some distal regions of the ignimbrite show no more vegetation cover in the 1998 image than they do in the 1991 image. This is partly due to the continued inundation by lahars, but also because these areas correspond to the thickest ignimbrite deposits, remnant heat within which has retarded vegetation re-growth. However, vegetation in the medial regions of the western sector, upland areas, and interfluves, where the pyroclastic deposits were thinnest, began to re-establish itself prior to 1994 becoming almost fully re-established by the time the 1998 SPOT image was acquired.

11.4 MT. ETNA, ITALY, 1991–1993

11.4.1 Satellite observations of the emplacement and diversion of a large basaltic lava flow

The 1991–1993 eruption of Mt. Etna began with the opening of a discontinuous fracture system at the base of the summit's southeast crater in the early morning of December 14, 1991. These fractures extended in a south to southeasterly direction, intersecting the western wall of the Valle del Bove, a huge sector collapse feature on the volcano's eastern flank, later that day. Lava began to flow from the lower reaches of this fissure and within 6 h had extended 1.5 km from the main vent. Over the course of the next 473 days 235×10^6 m³ of lava were emplaced, forming a flow field 8.5 km long (Calvari *et al.*, 1994). The eruption, which ended

on March 30, 1993, remains, at least volumetrically, the largest to have occurred at Etna since the famous 1669 eruption that devastated Catania (see Corsaro *et al.*, 1996).

We have included this eruption in our list of case studies for two main reasons: one volcanological, the other anthropogenic. Empirical flow length–effusion rate relationships derived for Etnean flows predicted a final flow length of 5.5 km for the 1991–1993 lava (Calvari and Pinkerton, 1998). In fact, the lava extended 3 km farther and came within 700 m of the town of Zafferana (Figure 11.15e). It is recognized that lava tubes provide thermally efficient pathways for transmitting lava over long distances even at low effusion rates. This is because the roofs of tubes insulate the lava flowing beneath, retarding cooling and crystallization, and allowing the lava to advance farther before it stagnates than would be possible if the lava were flowing in an open channel (Keszthelyi and Self, 1998). The role played by lava tubes in the development of 'a'a lava flow fields at Etna has only recently been recognized (Calvari and Pinkerton, 1998), and the development of the tube system responsible for much of the expansion of the 1991–1993 lava can be observed in the series of Landsat TM images shown in Figure 11.15 (Wright *et al.*, 2000). The eruption is also of particular interest because it provides an excellent example of how humans have modified the impacts of an effusive volcanic eruption. Based upon advice from volcanologists that the eruption would have a long duration, Italian authorities approved construction of a containment barrier to safeguard the town of Zafferana, which numerical models predicted to be in the possible path of the lava (Barberi *et al.*, 1993). The flow was later diverted when engineers blasted a hole in the side of the tube close to the vent. The effect of this action in moving the location of flow activity from the vicinity of Zafferana to a new, safer, location was initially tracked and mapped using AVHRR time series (Harris *et al.*, 1997b). The sequence of satellite images we present illustrates the impact that this barrier had on the advance of the flows, as well as the effects of subsequent efforts to influence the course of the eruption.

A TM image acquired on December 9, 1991 shows the Valle del Bove 5 days before the eruption began (Figure 11.15a). Several historic flows, notably the 1978 and 1989 lavas, are apparent on the valley floor as dark, sinuous features. The information provided by the remainder of this suite of

satellite images provides useful insights into the development of the 'a'a lava flow field, the complex system of tubes that were responsible for much of its growth, and both the successful and unsuccessful diversion attempts. In these images, TM bands 7, 5, and 4 are displayed in red, green, and blue, respectively. Yellow pixels denote lava surfaces that were radiating substantial amounts of shortwave infrared energy at both 2.08 μm (band 7) and 1.65 μm (band 5), either because the surface crust was young and therefore hot, or the crust was extensively fractured, thus exposing hotter lava from the flow interior. Red pixels denote surfaces with a high enough effective surface temperature (i.e., the area-weighted temperature of the lava's crust and cracks) to emit significant energy at 2.08 μm , but which at the moment of image acquisition were too cool to radiate at the shorter wavelengths corresponding to TM band 5. Flow surfaces too cool to radiate energy at either of these wavelengths appear black in these false-color composites due to the low reflectivity of basalt at these wavelengths.

During the first phase of the eruption, which began on December 15, 1991 and ended on January 2, 1992 (Calvari *et al.*, 1994), the flow field was composed predominantly of 'a'a flow units, supplied by two main open channels that emanated from the main fissure (Figure 11.15b). Two contiguous groups of yellow pixels, consistent with the presence of open channel flows, or flows with heavily disrupted surface crusts, occupy the steep slopes at the headwall of the Valle del Bove (30°), and the Salto della Giumenta (25°). Between them, on the relatively flat slopes (<10°) of the Piano del Trifoglio, is a sinuous feature composed mainly of red pixels. By February 3, 1992 (Figure 11.15c), whereas no eastward expansion of the flow field had occurred, it had widened significantly in the Valle del Bove via merging and superposition of flows. However, the most obvious change to have occurred is the disappearance of highly radiant surfaces in the medial flow section. By February 3, 1992 elevated SWIR radiance (and therefore lava with an effective surface temperature in excess of 120°C) was restricted to the proximal and distal flow regions. This change is consistent with the complex system of tubes that had formed on the floor of the Valle del Bove by the time this image was acquired, a tube system that had begun to form within 2 weeks of the beginning of the eruption (Calvari and Pinkerton, 1998). At this time, lava issuing from the primary vent was being diverted below ground into the tube system, and transmitted

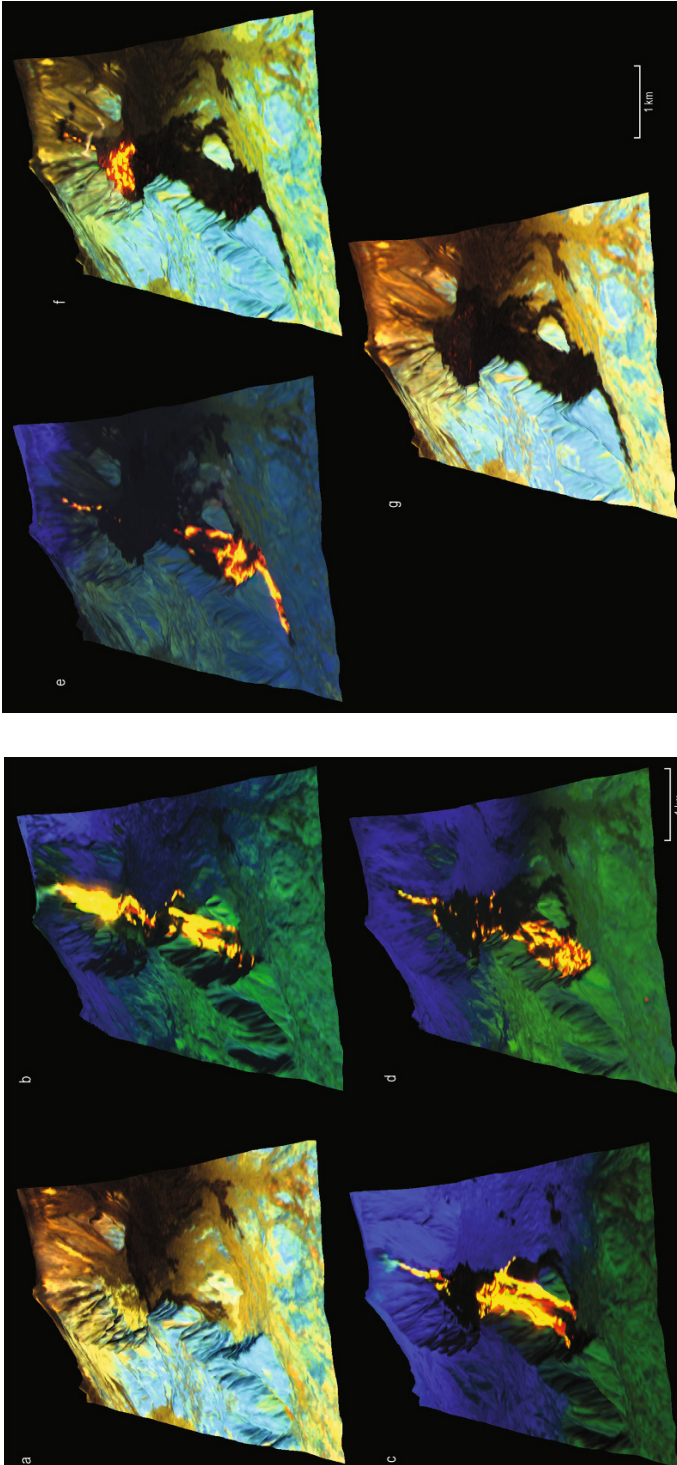


Figure 11.15. Time series of Landsat TM images showing the development of the 1991–1993 Mt. Etna lava flow. Bands 7, 5, and 4 are displayed in red, green, and blue, respectively. The multispectral satellite data have been draped over a DEM to aid interpretation of the relationships between flow surface radiance (and hence temperature and structure) and underlying slope. Vertical exaggeration is $\times 3$. Color changes in areas adjacent to the flow field are due to seasonal variations in snow cover and the effect this has on overall band-to-band image contrast. Although the eruption lasted 473 days, only five cloud-free TM images were acquired, highlighting the problems that can be encountered when trying to construct detailed time series of volcanic eruptions using high spatial, but low temporal resolution satellite images. Fortunately, the five images that were acquired each coincide with a significant phase of the eruption's development.

along its length before re-emerging at ephemeral vents several hundred meters above Salto della Giumenta. From here, lava flowed at the surface via three open channels into Val Calanna.

By March 22, 1992 (Figure 11.15d) the tube system had expanded eastward, with the previously mentioned ephemeral vents occupying a position directly on the edge of Val Calanna. The position of the tube is well identified by TM as a series of discrete clusters of yellow pixels, corresponding to elevated SWIR radiance from skylights and tumuli. Beyond this point active surface flows are confined by the topography of Val Calanna, with little lengthening of the flow field having occurred. In response to the perceived threat of lava inundation to the town of Zafferana, construction of an earthen containment barrier had begun on January 2, 1992. The barrier, 234 m long and 21 m high, was constructed at the exit of the Val Calanna (Portella Calanna). Flows reached the barrier on March 14, 1992 and proceeded to fill the valley. By March 28, 6 days after the image shown in Figure 11.15d was acquired, lava had accumulated to within 7 m of the top of the earthen dam. Accumulation of lava in the Val Calanna continued until April 10, 1992 when the barrier was overtopped and lava flows began advancing towards the town (Barberi *et al.*, 1993).

Figure 11.15e shows the flow field as it appeared on May 9, 1992, with active lava extending from the site of the containment barrier towards the town. Importantly, the TM images also reveal that the situation in the Valle del Bove had changed little since early February, with lava from the main vent continuing to be fed to the active flow fronts by the well-established tube system. After the failure of the containment barrier (and several smaller barriers constructed between April 10 to 14) to halt the flows' advance, the attention of the Italian Civil Defense authorities turned instead to interrupting the lava supply pathway. If the lava could be prevented from entering the tube system near the source, the flow fronts threatening Zafferana would be starved of fresh supply, causing them to stagnate. Several attempts were made to block the tube system in the upper region of the Valle del Bove, by dropping concrete blocks into skylights and using controlled explosions to block the tubes with lava fragments. However, on May 27, 1992, after four unsuccessful attempts, a new approach was adopted. Rather than simply trying to block the lava tubes, explosions were used to divert lava from the main feeder channel into an artificial channel

that had been excavated adjacent to it. Blocks of lava and artificial obstacles were then dumped into the natural channel in an attempt to seal it. As a result of this final successful intervention, approximately two thirds of the lava were diverted into the artificial channel (Barberi *et al.*, 1993), lava that would otherwise have been transmitted along the tube to the flow fronts approaching the town. Further infilling of the natural channel on May 29 succeeded in diverting the remainder. The ephemeral vents in Val Calanna continued to vent lava for eight more days as lava within the tube system drained (Calvari and Pinkerton, 1998). However, starved of fresh supply, the flows that had threatened Zafferana came to a halt.

The effects of the successful diversion are recorded in a TM image acquired on August 13, 1992 (Figure 11.15f), with active flows confined to the upper reaches of the Valle del Bove. By forcing the lava from the main fissure to flow at the surface, rather than below ground, the diversion attempts caused the flow front to revert to the position it had occupied 5 months earlier (Barberi *et al.*, 1993). However, a substantial drop in the lava effusion rate in early June 1992 meant that these new flows remained confined to the Valle del Bove, where a new flow field and tube system developed (Calvari and Pinkerton, 1998). The last active lava flows were observed and the eruption ended on March 30, 1993. Figure 11.15g shows the Valle del Bove as it appeared on June 29, 1993, almost 3 months later.

11.5 SANTIAGUITO, GUATEMALA, 1902–2000

11.5.1 Satellite observations of drainage basin impacts and hazards of prolonged effusive silicic eruption

In 1902, a plinian eruption on the south flank of Santa María Volcano in Guatemala spewed out around 8.5 km^3 of ash, which covered more than $1.2 \times 10^6 \text{ km}^2$ to a thickness of up to 2 m (Williams and Self, 1983). Lahar activity followed, as the unconsolidated ash was washed into the surrounding rivers, causing a dramatic increase in sediment supply so that riverbeds downstream of Santa María rose by 10 to 15 m (Kuenzi *et al.*, 1979). By 1922 the sediment supply had waned.

In 1922, after 20 years of quiescence, a phase of continuous dome extrusion began within the 1902 eruption crater of Santa María (Rose, 1987). Between 1922 and 2000, continuous lava extrusion

at a time-averaged rate of $\sim 0.44 \text{ m}^3 \text{ s}^{-1}$ formed a $\sim 1.1 \text{ km}^3$ dome complex (Harris *et al.*, 2003). Although the four main units comprising this complex are named El Caliente, Monje, Mitad, and Brujo, the complex itself has been named Santiaguito. While continuous, the rate of extrusion has alternated between 3 to 5 yr periods of above-average extrusion rates, separated by 9 to 12 yr below-average periods (Rose, 1987; Harris *et al.*, 2003).

The continuous extrusion at Santiaguito has provided a persistent, if variable, sediment supply to the fluvial system. Here, mobilization of loose volcanic material on and around the dome during the wet season triggers lahars and riverbed aggradation each rainy season. As a result, river channels become clogged with volcanic material, causing riverbeds to aggrade, the damming of tributaries, and the diversion of river channels. Lahar activity and aggradation thus impacts a fluvial system extending 60 km from Santa María and Santiaguito to the Pacific coast of Guatemala (Figure 11.16). This is a heavily populated and farmed zone such that the activity has widespread impacts on communities across this zone.

One of the best ways to track such a persistent yet widespread phenomena is to use the repeat, synoptic coverage afforded by satellite data. Here, 30 m spatial resolution multispectral data of the Landsat Thematic Mapper (TM) and Enhanced Thematic Mapper Plus (ETM+) provides data capable of creating regular maps of impacted zones. Thus, in Harris *et al.* (2006) a time series of 21 TM and ETM+ images were used to document and examine lahar inundation and aggradation in Santiaguito's drainage system between 1987 and 2000. Indeed, the impact of lahar inundation, by replacing zones of healthy vegetation with barren volcanic material, is easy to detect in such satellite images due to the extreme spectral contrast, especially in the visible and near-infrared, between these two distinct surface types.

At the dome, the TM image clearly shows the horseshoe-shaped scar open to the southwest which represents the 1902 crater on the flank of the otherwise symmetrical cone of Santa María (Figure 11.17). Around Santa María, the lush vegetation of this tropical country is apparent from the rich blue colors that, in this false-color rendition, represent healthy vegetation. However, the barren surfaces represented by the Santiaguito dome complex are apparent as a light-brown mass within and over-spilling the 1902 crater. During each rainy season,

where the monsoon in Guatemala usually begins during May and lasts until October, loose material is washed from this mass into the river valleys that have their source on the flanks of Santiaguito. Subsequent downstream deposition of rain-mobilized volcanic material causes river channel aggradation such that ravines that were once tens of meters deep are now filled. Ravine-filling, in turn, promotes stream diversion, capture, and channel abandonment. The emplacement of volcanic material along these river valleys is apparent from the broad zones of dark-brown, unvegetated, volcanic material that mark the courses of these rivers.

We can use these images to map and track the annual impact of lahar activity, where Harris *et al.* (2005) used a simple approach based on the Normalized Difference Vegetation Index to locate vegetation-free pixels. These maps clearly reveal changes in the location and area of lahar activity. Figure 11.18, for example, shows a 3 yr long time series revealing change in the inundated area across the medial section of the drainage basin. We first notice a general decline in the inundated area during these three years; clearly vegetation regrowth is outpacing lahar inundation. However, at the extreme west of the map is the Río Ixpatz. During this period, inundation along the course of this river appears to die out completely. This reflects the success of human intervention, where the construction of dikes to prevent lahars from entering this river was responsible for the recovery of vegetation along this stretch.

At the coast, the effects of the persistent, post-1922 lahar inundation are apparent, as in the medial and proximal sections of the drainage system, from swaths of sediment that cut through the vegetation every year (Figure 11.19). However, across this distal drainage section the effects of the 1902 eruption are also still plainly apparent. The huge quantity of material washed through the system emplaced a triangular wedge of sediment at the coast with its apex pointing upstream. This wedge is still apparent from lineaments caused by slight variations in the vegetation but which delineate this feature (Figure 11.19). The constructional effect of this new wedge of sediment caused tributaries, especially those entering the Río Samala from the east, to become dammed. This created a series of lakes aligned along the eastern edge of the wedge. Sediment washed to the coast caused the shoreline to prograde building a new arcuate delta, still readily apparent on the Landsat imagery.

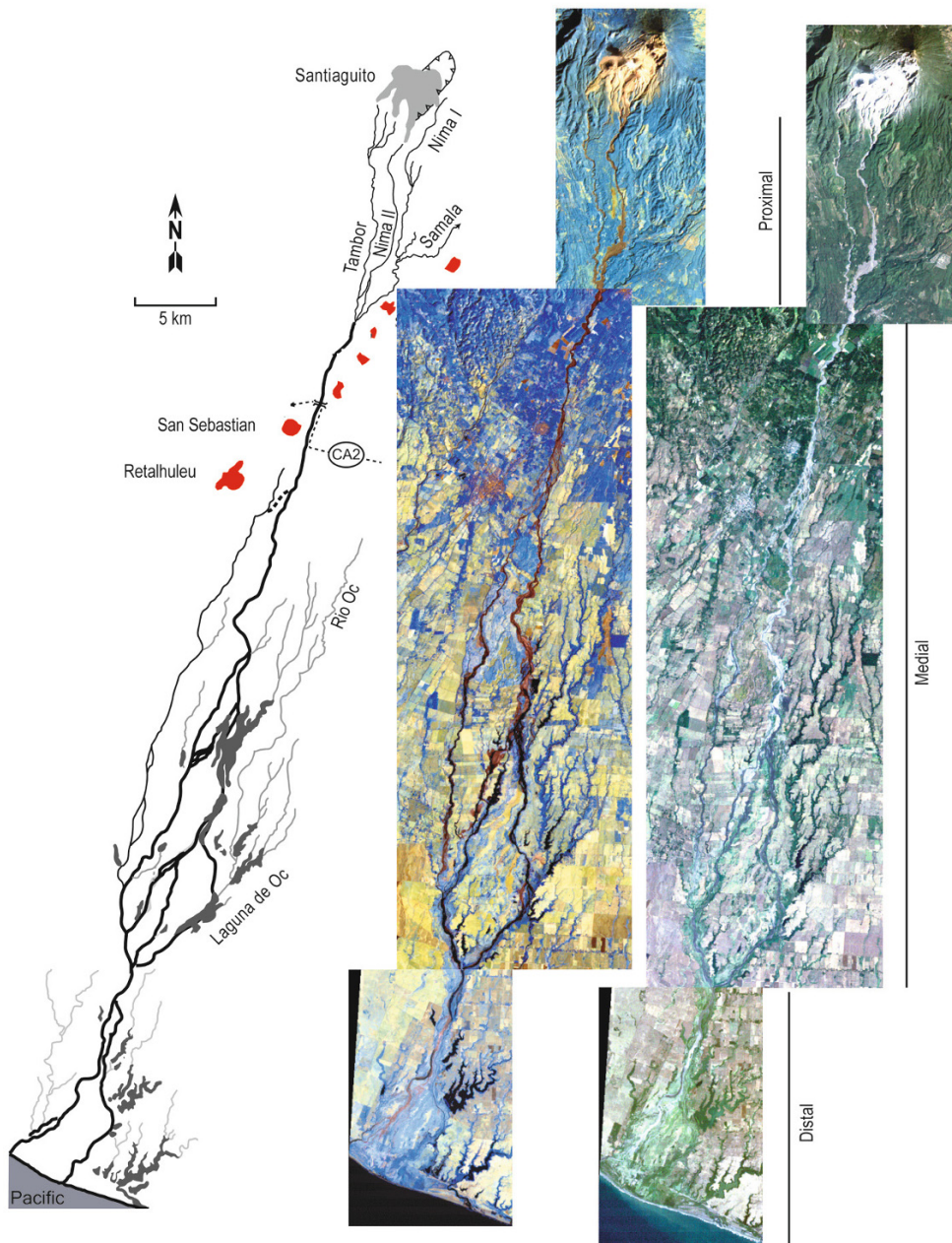


Figure 11.16. Landsat TM false-color and simulated true-color composites of Santa María Volcano and the surrounding area. Bands 7, 5, 4 and 3, 2, 1 are displayed in red, green, and blue, respectively. A map is provided to aid interpretation of the complex distribution of rivers and tributaries in the area between Santa María and Guatemala’s Pacific coastline. Persistent extrusion of dacitic lava from the Santiaguito dome complex has occurred since 1922, producing a series of west–east trending domes and associated block lava flows. Collapse of these lava features produces an ample supply of unconsolidated material, which is mobilized during the wet season each year and transported downslope. The accumulation of this material has resulted in aggradation of rivers and streams, eventually forcing a change in their direction. This has resulted in widespread loss of cultivable land.

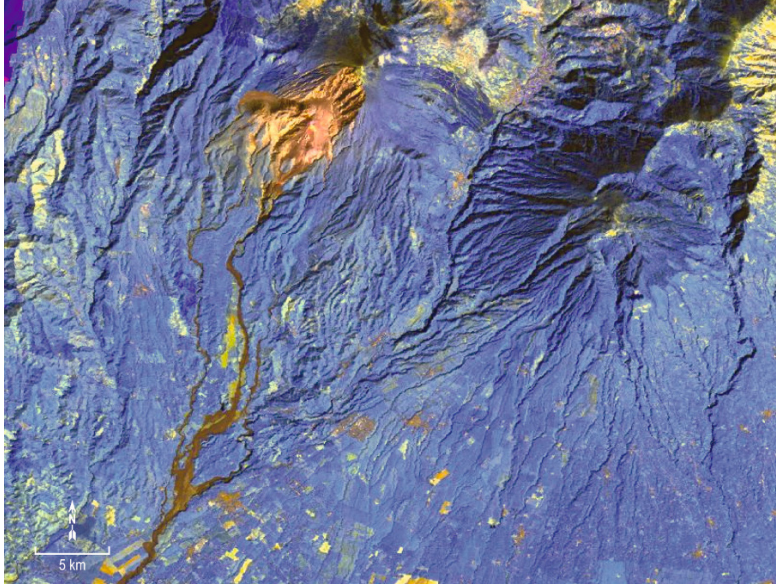


Figure 11.17. Landsat TM false-color composite of Santa María Volcano and the surrounding area. Bands 7, 5, and 4 are displayed in red, green, and blue, respectively. Pale-blue pixels contain vegetation; Santa María is apparent as a group of brown pixels in the upper middle portion of the image. The horseshoe-shaped feature is the scar left by the 1902 eruption. About 2 km south of this lie a series of domes erupted in the crater left by the 1902 eruption, collectively referred to as Santiaguito, of which El Caliente is the most recent and currently active.

The ETM+ image of 2000 revealed that 23 km², or 3%, of the 825 km² drainage basin downstream of Santiaguito was covered by barren volcanoclastic material. The year-on-year estimated TM-derived extrusion rate (Harris *et al.*, 2003) and aggradation area show that both the extrusion rate and aggradation area are variable and related (Harris *et al.*, 2005). Here, in years of increased extrusion (E_r) at the dome complex and/or increased rainfall ($Rain$), the area of inundation across the proximal zone (A_{prox}) increases following the empirical relationship:

$$A_{prox} = 3.92 + 0.5E_r + 0.39 \ln(Rain).$$

Given that the rivers are bordered by significant agricultural and man-made structures, this continues to inflict significant damage on the local population, where Kimberly (1995) estimates U.S.\$2 million to U.S.\$14 million of damage is caused by lahar-related activity every year. The direct impact on human populations is even more apparent when we consider the case of El Palmar, a village located on the banks of the Río Nimá I and about 8 km south of Santiaguito. Aggradation caused river diversion at this location such that

lahars and stream courses have become diverted through the village center, resulting in the village being now effectively abandoned. Most buildings are now either destroyed and/or partially buried. A new 20 m wide, 23–27 m deep ravine also formed through the center of village, adding to the damage.

11.6 MT. PINATUBO, PHILIPPINES, 1991

11.6.1 Satellite observations of the atmospheric effects of a VEI-6 eruption

The ability of volcanic eruptions to influence weather and climate has been recognized for at least 2,000 years, and has been the subject of serious scientific investigation for almost a century (e.g., Humphreys, 1913; Mitchell, 1961; Lamb, 1970). Volcanic eruptions cause a range of chemically and physically active particles and gases to be injected into the atmosphere (we refer the reader to Robock, 2000 for a detailed discussion of their

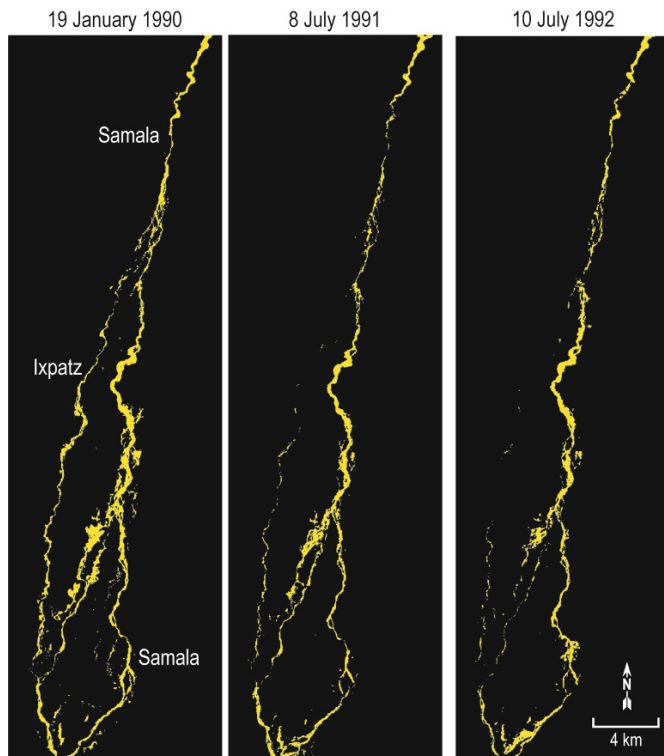


Figure 11.18. Normalized Difference Vegetation Index (NDVI) images showing temporal variations in river aggradation downslope from Santa María Volcano. Due to the marked contrast in near-infrared reflectance of dacite and healthy vegetation, the NDVI is an excellent way of mapping the changing patterns of river aggradation and lahar inundation that have resulted from the ongoing eruption of Santiaguito. The NDVI is much higher for vegetated surfaces than it is for lahar deposits. In these images, surfaces with high NDVI values have been masked. Yellow pixels correspond to low-NDVI, unvegetated riverbeds.

effects) In short, if these gases and aerosols are confined to the troposphere their effects on the atmosphere are short-lived and localized, as they are efficiently removed from the atmosphere (within a matter of weeks) by the combined effects of gravity and rain. However, if the gas and ash is injected into the drier and more stable stratosphere, the residence times of these volcanogenic gases increases and the effects of an eruption on Earth's atmosphere can be long-lived and truly global in scale. Sulfur gases, most notably sulfur dioxide, convert into sulfuric acid via reaction with hydroxyl, which condenses to an aerosol within about a month (Schoeberl *et al.*, 1993). If injected into the stratosphere, these aerosols remain in Earth's atmosphere for an extended period of time, typically with a decreasing abundance for up to 3 years. The individual sulfate aerosol particles are about the same

size as the wavelength of visible light, and act as very efficient scatterers. Enhanced backscattering of incoming solar radiation causes a reduction in the amount of energy that reaches Earth's surface, which cools as a result. The 1815 eruption of Tambora, Indonesia is thought to have caused Northern Hemisphere temperatures to decrease by 1 to 1.5° in the following summer (see Crowley and Kim, 1999 and Self *et al.*, 2004 for details). Although the stratospheric aerosol blanket causes a net cooling of the troposphere and surface, it simultaneously absorbs infrared energy emitted by Earth's surface and troposphere, causing the temperature of the stratosphere itself to increase, which produces the paradoxical phenomenon of Northern Hemisphere winter warming that has been observed to follow large explosive eruptions. This stratospheric warming is partially, but not wholly, offset by the volca-

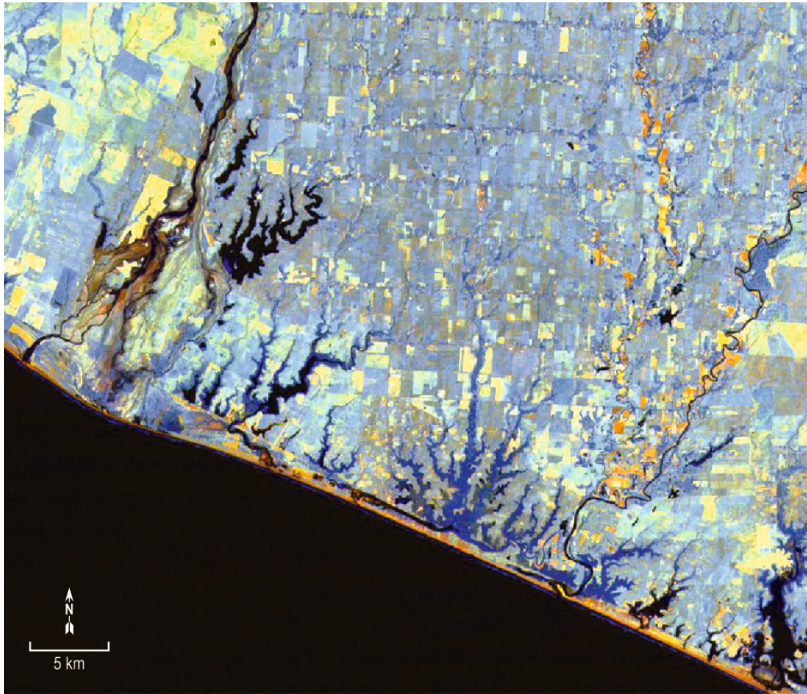


Figure 11.19. Landsat TM false-color composite of the Pacific coast of Guatemala, showing the distribution of lahars and lahar-dammed lakes that have been produced by the ongoing activity at Santiaguito. Bands 7, 5, and 4 are displayed in red, green, and blue, respectively.

nically enhanced destruction of stratospheric ozone. The injection of sulfate aerosols into the stratosphere vastly increases the number of surfaces on which reactions that de-nitrify the stratosphere can occur, promoting the survival of anthropogenic ozone-destroying chlorine.

The climatic “effectiveness” of an eruption depends on four main factors: the sulfur content of the magma; the explosivity of the eruption; the latitude of the volcano (stratospheric aerosol clouds from high-latitude eruptions tend to remain in the hemisphere of origin, while those from tropical eruptions can spread between hemispheres); and the height of the tropopause above it (which influences the likelihood that the aerosols will enter the stratosphere). In a previous section we demonstrated how satellite images could be used to document some of the effects of the 1991 eruption of Mt. Pinatubo on the landscape. Here, we show how satellite images can also be used to chronicle the impact that the eruption had on Earth’s atmosphere.

The main eruption of June 15, 1991 produced a

mushroom-shaped cloud that extended more than 1,000 km from the vent in less than 11 hours (Holasek *et al.*, 1996). Figure 11.20 shows a sequence of visible wavelength images acquired by the Japanese Geostationary Meteorological Satellite (GMS-4) which document the expansion of the main eruption cloud during the first 3 hours after the onset of the climactic phase. This cloud attained a height of at least 35–40 km above sea level, more than sufficient to penetrate the tropopause, which was about 17 km above the volcano. This, combined with the relatively high bulk sulfur content of the magma body, resulted in a large amount of SO_2 being injected into the stratosphere during the paroxysmal eruption (Robock, 2002; Guo *et al.*, 2004). Eruption columns with sufficient energy to pierce the tropopause were produced on at least 14 occasions between June 12 and 16, 1991 (table 1 in Self *et al.*, 1996).

The SO_2 cloud produced during the June 15 eruption circled the globe within 22 days (Bluth *et al.*, 1992). Figure 11.21 shows images acquired by the Nimbus-7 Total Ozone Mapping Spectrometer

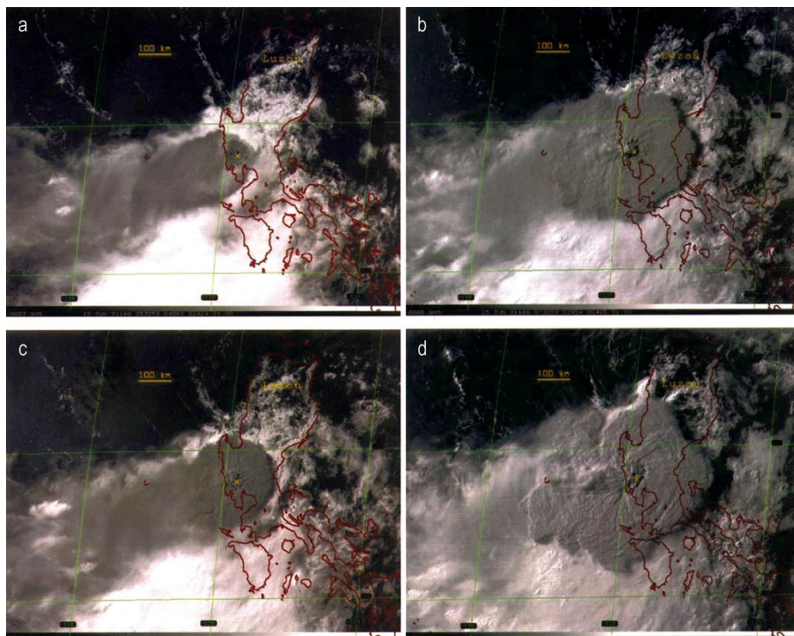


Figure 11.20. GMS-4 visible wavelength ($0.50\text{--}0.75\mu\text{m}$) images of the Pinatubo eruption cloud acquired at 13:41 (a), 14:41 (b), 15:41 (c), and 16:41 (d) on June 15, 1991 (all times local). The first image coincides almost exactly with the onset of the climactic phase of the eruption (images from Holasek *et al.*, 1996).

(TOMS) instrument which depict the changing size and location of this cloud for an 11-day period spanning the paroxysmal eruption. As the name suggests, TOMS was designed to produce high-resolution global maps of atmospheric ozone, by making measurements of backscattered UV light in the ultraviolet part of the spectrum, a wavelength region in which ozone absorbs energy. However, SO_2 molecules also absorb energy at these wavelengths, allowing TOMS to be used for mapping the distribution and abundance of volcanic gas clouds (e.g., Krueger, 1983; Carn *et al.*, 2003). Within 9 days of the main eruptive event, the SO_2 cloud had extended meridionally as far as central Africa, some 10,000 km from the vent. In the sequence of images (Figure 11.21), the raw TOMS data have been processed to depict the concentration of SO_2 present in the atmospheric column in milli-atmospheres per centimeter. This unit represents the amount of gas affecting the reflection of ultraviolet energy from Earth's surface to the satellite in terms of a one-dimensional gas layer at standard temperature and pressure which, by integrating over the area of the cloud to obtain a volume, can be converted to a mass. In this way,

TOMS data have been used to estimate that the main eruption produced approximately 20 Mt of SO_2 (1 Mt is equal to 10^9 kg; see Bluth *et al.*, 1992 and Guo *et al.*, 2004).

Once in the stratosphere, conversion of this SO_2 into sulfate aerosol began, increasing the optical thickness of Earth's atmosphere. Measurements of optical depth made by the Stratospheric Aerosol and Gas Experiment II instrument (SAGE II), flown onboard NASA's Earth Radiation Budget satellite, are shown in Figure 11.22 for the period before and after the eruption. In these images, a transition from green to yellow to red indicates increasing optical depth and aerosol abundance. Figure 11.22a shows the optical depth of Earth's atmosphere prior to the eruption. The eruption caused a 2-order-of-magnitude increase in optical depth at tropical latitudes (Figure 11.22b) with aerosols apparent at a maximum altitude of 29 km (McCormick and Veiga, 1992). Although initially confined to latitudes between 20°S and 30°N , the aerosol blanket soon began to spread and by the end of September 1991 had almost covered the entire globe (Figure 11.22c). Figure 11.22d shows how the aerosol cloud appeared in January

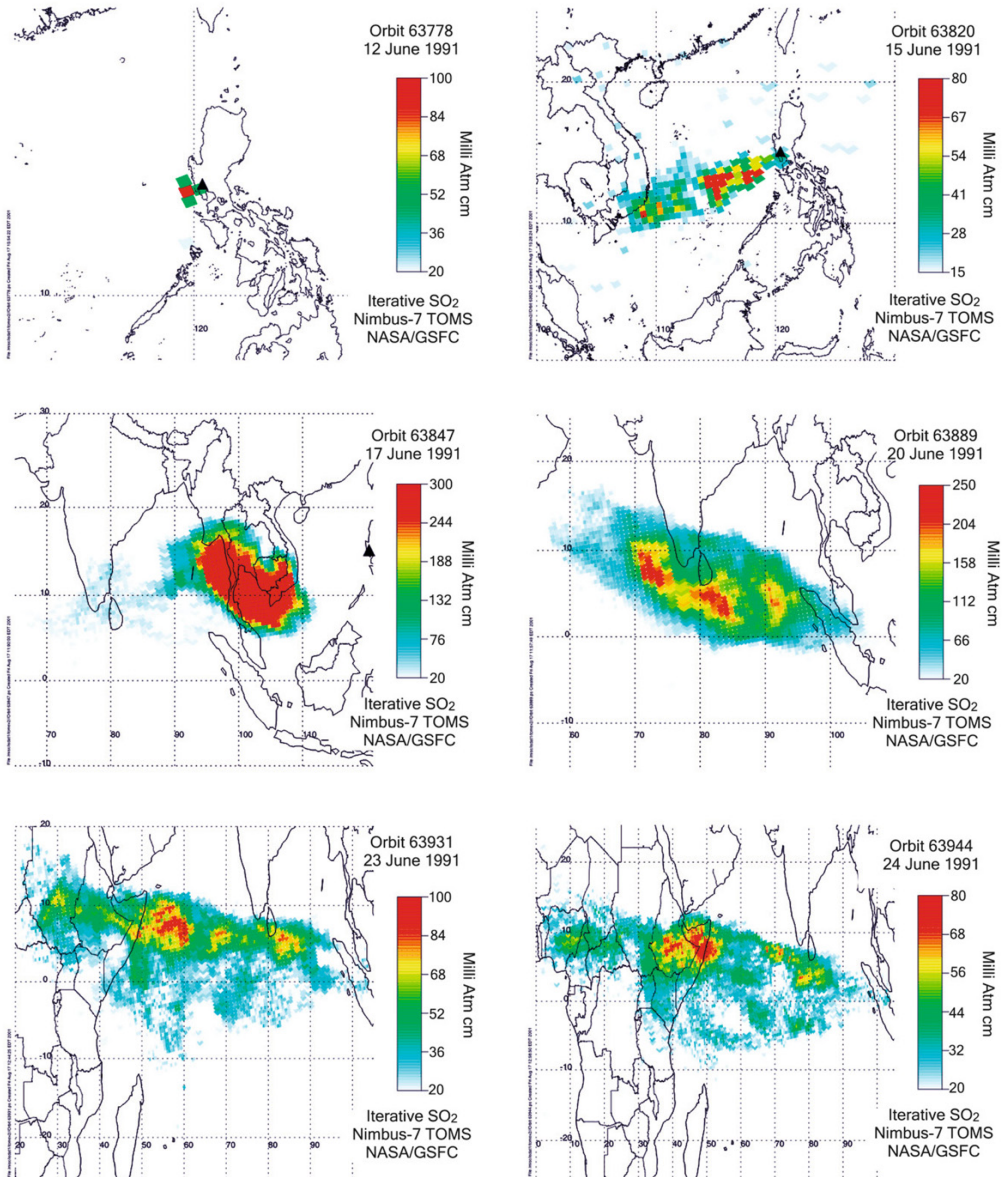


Figure 11.21. NIMBUS-7 TOMS images of the SO₂ produced by the June 15, 1991 eruption of Pinatubo, Philippines. TOMS allows the SO₂ abundance in the atmosphere to be determined by making measurements of scattered radiance in the ultraviolet region of the electromagnetic spectrum, a region where the SO₂ molecule absorbs strongly. The black triangle marks the location of the volcano (images processed by and courtesy of the TOMS Volcanic Emissions Group, JCET/UMBC).

1994, some 30 months later. Although optical thickness had by this time decreased by about an order of magnitude relative to the high values observed immediately following the eruption, it is still 10 times greater than the pre-eruption “background” levels

depicted in Figure 11.22a. By relating the extinction values measured by SAGE II to the assumed properties of the aerosol, McCormick and Veiga (1992) estimate that between 20 and 30 Mt of sulfate aerosol was produced by the eruption.

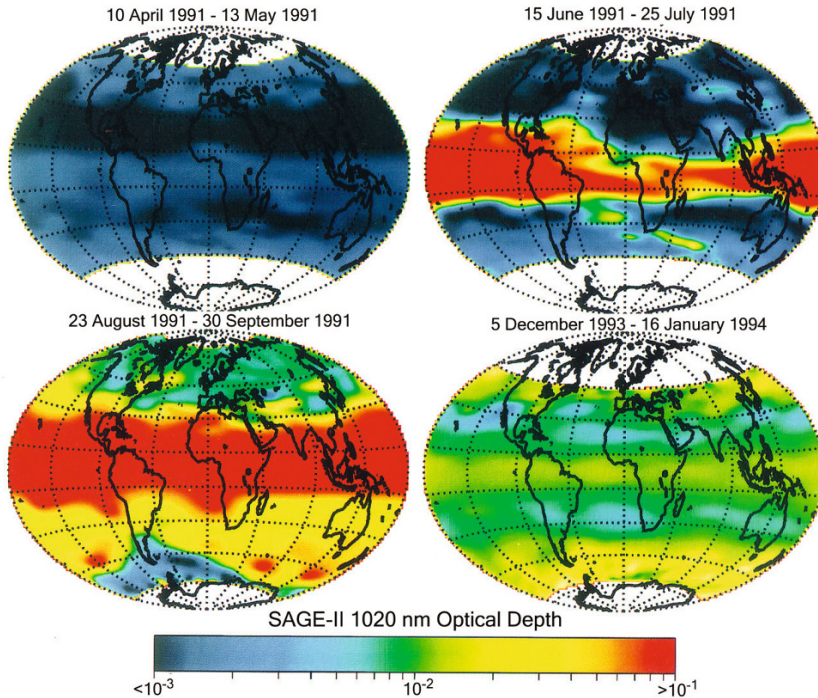


Figure 11.22. SAGE-II optical depth measurements made for a period spanning the June 1991 eruption of Pinatubo (images from Self *et al.*, 1996).

11.7 CONCLUSIONS

Satellite images can provide unique perspectives on the effects of volcanic eruptions. This stems largely as a result of the ability of Earth observation satellites to acquire multispectral images that cover large geographic areas, at regular and repeated intervals, for any active volcanic region on Earth. In this chapter we have demonstrated how images from a wide range of operational satellite sensors can be used to catalogue the effects of a wide range of eruption products and styles on Earth's surface and atmosphere.

Volcanoes lend themselves to satellite monitoring, as we know where most of the active and potentially active volcanoes on Earth are. Unfortunately, the eruptions of most volcanoes are localized in time and space, and the periods of inactivity between eruptions are often far longer than the duration of the eruptions themselves (Wadge, 2003). As such, acquiring satellite image data sets to observe the effects of eruptions may be considered a question of "when" rather than "where". For low spatial resolution sensors such as MODIS

and AVHRR, this is irrelevant; these sensors acquire data for all regions of the globe all of the time. Indeed, routine, near-real time thermal monitoring of all Earth's volcanoes has been achieved using low spatial resolution satellite data (Wright *et al.*, 2002, 2004; Wright and Flynn, 2004), as has the automated detection and mapping of ash clouds and volcanic SO_2 (see Carn *et al.*, 2003 for details).

Unfortunately, routine acquisition of the kind of high spatial resolution images that have been the main focus of this chapter poses a different set of problems. Scheduling conflicts, mission priorities, and low duty cycles means most of Earth's $\sim 1,500$ potentially active volcanoes are imaged only sporadically at high spatial resolutions and, as a result, detailed images of the effects of such eruptions may not be acquired. Fortunately, these problems are being addressed. Under several guises, efforts are currently being made to increase the efficiency with which high spatial resolution imaging resources are deployed during volcanic eruptions, by automatically re-tasking them to acquire images whenever a volcano exhibits a change in "behavior". Two programs, the Auton-

omous Sciencecraft Experiment (ASE) and the Volcano Sensor Web (VSW) experiment are currently being tested (Davies *et al.*, 2006a,b). The VSW experiment relies upon changes in the level of activity at a volcano, which may be the onset of a new eruption or an escalation in the intensity of existing activity, being detected either by ground-based instruments (e.g., tiltmeters) or near-real time satellite thermal-monitoring systems (e.g., the Hawaii Institute of Geophysics and Planetology's "MODVOLC" system; Wright *et al.*, 2004). Detection events are then used to trigger the acquisition of a high spatial, high spectral resolution image by the Earth Observing-1 Hyperion sensor (Pearlman *et al.*, 2003), at the next available opportunity. The ASE runs a series of classification algorithms onboard the EO-1 platform itself to detect thermal emission from erupting volcanoes; if the thermal signature of an erupting volcano is detected, Hyperion is re-tasked to acquire an image. In this case, the re-tasking is done entirely on board. These and similar efforts will ensure that, in the future, detailed high spatial resolution data sets from a variety of different sensors will be available with which to help analyze and catalogue the effects of volcanic eruptions.

11.8 ACKNOWLEDGMENTS

Support for R.W., A.J.L.H., and L.P.F. was provided by NASA grant NNG04G064G. We would like to thank the University of Maryland Global Land Cover Facility (<http://glcf.umiacs.umd.edu/index.shtml>) for providing an excellent online resource, from which we obtained several of the images used in this chapter. Dave Pieri provided the Landsat TM time series of the 1991–1993 Etna eruption. Many of the other TM and ETM+ images were purchased using funding provided by Landsat Science Team Grant NAG 5-3451. ASTER images are courtesy of NASA/GSFC/MITI/ERSDAC/JAROS. We thank Steve Self for his generous review.

11.9 REFERENCES

- Bailey, J.E.; Self, S.; Mougini-Mark, P.J. (2001). Has dynamic equilibrium been re-established for the fluvial landscape on the 1991 Mt. Pinatubo ignimbrite sheet? *EOS, Transactions American Geophysical Union*, **82**(47), F16–F17.
- Barberi, F.; Carapezza, M.L.; Valenza, M.; Villari, L. (1993). The control of lava flow during the 1991–1992 eruption of Mt. Etna, *J. Volcanol. Geothermal Res.*, **56**, 1–34.
- Bardintzeff, J.-M.; Deniel, C. (1992). Magmatic evolution of Pacaya and Cerro Chiquito volcanological complex, Guatemala, *Bull. Volcanol.*, **54**, 267–283.
- Blong, R.J. (1984). *Volcanic Hazards: A Sourcebook on the Effects of Eruptions*, Academic Press, London, 424 pp.
- Bluth, G.J.S.; Doiron, S.D.; Schnetzler, C.C.; Krueger, A.J.; Walter, L.S. (1992). Global tracking of the SO₂ clouds from the June, 1991 Mount Pinatubo eruptions, *Geophys. Res. Lett.*, **19**, 151–154.
- Calvari, S.; Pinkerton, H. (1998). Formation of lava tubes and extensive flow field during the 1991–1993 eruption of Mount Etna, *J. Geophys. Res.*, **103**, 27291–27301.
- Calvari, S.; Coltelli, M.; Pompilio, M.; Scribano, V. (1994). The 1991–1993 Etna eruption: Chronology and lava flow-field evolution, *Acta Vulcanologica*, **4**, 1–14.
- Campita, N.R.; Daag, A.S.; Newhall, C.G.; Rowe, G.L.; Solidum, R.U. (1996). Evolution of a small caldera lake at Mount Pinatubo, in C.G. Newhall and R.S. Punongbayan (Eds.), *Fire and Mud: Eruptions and Lahars of Mount Pinatubo, Philippines*, University of Washington Press, Seattle, pp. 435–442.
- Carn, S.A.; Krueger, A.J.; Bluth, G.J.S.; Schaefer, S.J.; Krotkov, N.A.; Watson, I.M.; Data, S. (2003). Volcanic eruption detection by the Total Ozone Mapping Spectrometer (TOMS) instruments: A 22-year record of sulphur dioxide and ash emissions, in C. Oppenheimer, D.M. Pyle, and J. Barclay (Eds.), *Volcanic Degassing*, Special Publication 213, Geological Society of London pp. 177–202.
- Chien, S.; Davies, A.; Tran, D.; Chichy, B.; Rabideau, G.; Castaño, R.; Sherwood, R.; Jones, J.; Grosvenor, S.; Mandl, D. *et al.* (2004). Using automated planning for sensorweb response.
- Christiansen, R.L.; Peterson, D.W. (1981). Chronology of the 1980 eruptive activity, *The 1980 Eruptions of Mount St. Helens, Washington*, USGS Professional Paper 1250, U.S. Geological Survey, Reston, VA, pp. 17–30.
- Corsaro, R.A.; Cristofolini, R.; Patane, L. (1996). The 1669 eruption at Mount Etna: Chronology, petrology and geochemistry, with inferences on the magma sources and ascent mechanisms, *Bull. Volcanol.*, **58**, 348–358.
- Crowley, T.J.; Kim, K.-Y. (1999). Modelling the temperature response to forced climate change over the last six centuries, *Geophys. Res. Lett.*, **26**, 1901–1904.
- Daag, A.S.; van Westen, C.J. (1996). Cartographic modelling of erosion in pyroclastic flow deposits of Mount Pinatubo, Philippines, *ITC J.*, **2**, 110–124.

- Davies, A.; Chien, S.; Baker, V.; Doggett, T.; Dohm, J.; Greeley, R.; Ip, F.; Castaño, R.; Cichy, B.; Rabideau, G. *et al.* (2006a). Monitoring active volcanism with the Autonomous Sciencecraft Experiment on EO 1, *Remote Sensing of Environment*, **101**, 427–446.
- Davies, A.G.; Chien, S.; Wright, R.; Miklius, A.; Kyle, P.R.; Welsh, M.; Johnson, J.B.; Tran, D.; Schaffer, S.R.; Sherwood, R. (2006b). Sensor web enables rapid-response to volcanic activity, *EOS, Trans. Am. Geophys. Union*, **87**(1), 5.
- Denniss, A.M.; Harris, A.J.L.; Carlton, R.W.; Francis, P.W.; Rothery, D.A. (1996). The 1993 Lascar pyroclastic flow imaged by JERS-1, *Int. J. Remote Sensing*, **17**, 1975–1980.
- Eggers, A.A. (1983). Temporal gravity and elevation changes at Pacaya volcano, Guatemala, *J. Volcanol. Geothermal Res.*, **19**, 223–237.
- Fisher, R.V.; Heiken, G.; Hulen, J.B. (1997). *Volcanoes: Crucibles of Change*, Princeton University Press, Princeton, NJ, 317 pp.
- Forsyth, P.Y. (1988). In the wake of Etna, 44 B.C., *Classical Antiquity*, **7**, 49–57.
- Francis, P.W.; Wells, G.L. (1988). Landsat thematic mapper observations of debris avalanche deposits in the Central Andes, *Bull. Volcanol.*, **50**, 258–278.
- Guo, S.; Bluth, G.S.; Rose, W.I.; Watson, I.M.; Prata, A.J. (2004). Re-evaluation of SO₂ release of the 15 June 1991 Pinatubo eruption using ultraviolet and infrared satellite sensors, *Geochem. Geophys. Geosyst.*, **5**, doi: 10.1029/2003GC000654.
- Harris, A.J.L.; Butterworth, A.L.; Carlton, R.W.; Downey, I.; Miller, P.; Navarro, P.; Rothery, D.A. (1997a). Low cost volcano surveillance from space: Case studies from Etna, Krafla, Cerro Negro, Fogo, Lascar and Erebus, *Bull. Volcanol.*, **59**, 49–64.
- Harris, A.J.L.; Blake, S.; Rothery, D.A.; Stevens, N.F. (1997b). A chronology of the 1991 to 1993 Etna eruption using AVHRR data: Implications for real time thermal volcano monitoring, *J. Geophys. Res.*, **102**, 7985–8003.
- Harris, A.J.L.; Murray, J.B.; Aries, S.E.; Davies, M.A.; Flynn, L.P.; Wooster, M.J.; Wright, R.; Rothery, D.A. (2000). Effusion rate trends at Etna and Krafla and their implications for eruptive mechanisms, *J. Volcanol. Geothermal Res.*, **102**, 237–269.
- Harris, A.J.L.; Flynn, L.P.; Rose, W.I. (2003). Temporal trends in lava dome extrusion at Santiaguito 1922–2000, *Bull. Volcanol.*, **65**, 77–89.
- Harris, A.J.L.; Vallance, J.W.; Kimberly, P.; Rose, W.I.; Matías, O.; Flynn, L.P.; Garbeil, H. (2004). Downstream aggradation owing to lava dome extrusion and rainfall runoff at Volcán Santiaguito, Guatemala, *Volcanic Hazards in Central America*, GSA Special Paper, Geological Society of America, Boulder, CO.
- Harris, A.J.L.; Vallance, J.W.; Kimberly, P.; Rose, W.I.; Matías, O.; Bunzendahl, E.; Flynn, L.P.; Garbeil, H. (2006). Downstream aggradation owing to lava dome extrusion and rainfall runoff at Volcán Santiaguito, Guatemala, in W.I. Rose (Ed.), *Volcanic Hazards in Central America* (GSA Special Paper 412), Geological Society of America, Boulder, CO, pp. 85–104.
- Heliker, C.; Mattox, T.N. (2003). The first two decades of the Pu'u Ō'ō-Kūpaianaha eruption: Chronology and selected bibliography, in C. Heliker, D.A. Swanson, and T.J. Takahashi (Eds.), *The Pu'u Ō'ō-Kūpaianaha Eruption of Kīlauea Volcano, Hawai'i: The First 20 Years*, USGS Professional Paper 1676, U.S. Geological Survey, Reston, VA, pp. 1–28.
- Holasek, R.; Self, S.; Woods, A.W. (1996). Satellite observations and interpretation of the 1991 Mount Pinatubo eruption plumes, *J. Geophys. Res.*, **101**, 27635–27655.
- Humphreys, W.J. (1913). Volcanic dust and other factors in the production of climatic changes, and their possible relation to ice gases, *J. Franklin Institute*, August, 131–172.
- Kerle, N.; van Wyk de Vries, B.; Oppenheimer, C. (2003). New insight into the factors leading to the 1998 flank collapse and lahar disaster at Casita volcano, Nicaragua, *Bull. Volcanol.*, **65**, 331–345.
- Keszthelyi, L.; Self, S. (1998). Some physical requirements for the emplacement of long basaltic lava flows, *J. Geophys. Res.*, **103**, 27447–27464.
- Kimberly, P. (1995). Changing volcanoclastic sedimentary patterns at Santa Maria volcano, Guatemala, detected with sequential Thematic Mapper data, 1987–95, Unpublished M.S. thesis, Michigan Technological University, 59 pp.
- Krueger, A.J. (1983). Sighting of El Chichón sulfur dioxide clouds with the Nimbus 7 Total Ozone Mapping Spectrometer, *Science*, **220**, 1377–1379.
- Kuenzi, W.D.; Horst, O.H.; McGehee, R.V. (1979). Effect of volcanic activity on fluvial-deltaic sedimentation in a modern arc-trench gap, southwestern Guatemala, *Geol. Society Amer. Bull.*, **90**, 827–838.
- Lamb, H.H. (1970). Volcanic dust in the atmosphere, with a chronology and assessment of its meteorological significance, *Philosophical Trans. Royal Society London A*, **266**, 425–533.
- Major, J.J.; Janda, R.J.; Daag, A.S. (1996). Watershed disturbance and lahars on the east side of Mount Pinatubo during the mid-June 1991 eruptions, in C.G. Newhall and R.S. Punungbayan (Eds.), *Fire and Mud: Eruptions and Lahars of Mount Pinatubo, Philippines*, University of Washington Press, Seattle, WA, pp. 895–919.
- McCormick, M.P.; Veiga, R.E. (1992). SAGE II measurements of early Pinatubo aerosols, *Geophys. Res. Lett.*, **19**, 155–158.

- Mercado, R.A.; Lacsamana, J.B.T.; Pineda, G.L. (1996). Socioeconomic impacts of the Mount Pinatubo Eruption, in C.G. Newhall and R.S. Punungbayan (Eds.), *Fire and Mud: Eruptions and Lahars of Mount Pinatubo, Philippines*, University of Washington Press, Seattle, WA, pp. 1063–1070.
- Mitchell, J.M. (1961). Recent secular changes of the global temperature, *Annals of the New York Academy of Sciences*, **95**, 235–250.
- Paladio-Melosantos, L.O.; Solidum, R.U.; Scott, W.E.; Quiambao, R.B.; Umbal, J.V.; Rodolfo, K.S.; Tubianosa, B.S.; Delos Reyes, P.J.; Alonso, R.A.; Ruelo, H.B. (1996). Tephra falls of the 1991 eruptions of Mount Pinatubo, in C.G. Newhall and R.S. Punungbayan (Eds.), *Fire and Mud: Eruptions and Lahars of Mount Pinatubo, Philippines*, University of Washington Press, Seattle, WA, pp. 513–536.
- Patrick, M.R.; Smellie, J.L.; Harris, A.J.L.; Wright, R.; Dean, K.; Izbekov, P.; Garbeil, H.; Pilger, E. (2005). First recorded eruption at Mount Belinda Volcano, (Montagu Island), South Sandwich Islands, *Bull. Volcanol.*, in press.
- Pearlman, J.; Barry, P.; Segal, C.; Shepanski, J.; Beiso, D.; Carman, S. (2003). Hyperion, a space-based imaging spectrometer, *IEEE Trans. Geosci. Remote Sensing*, **41**, 1160–1173.
- Pierson, T.C.; Janda, R.J.; Thouret, J.-C.; Borrero, C.A. (1990). Perturbation and melting of snow and ice by the 13 November 1985 eruption of Nevado del Ruiz, Colombia, and consequent mobilization, flow and deposition of lahars, *J. Volcanol. Geothermal Res.*, **41**, 17–66.
- Pierson, T.C.; Daag, A.S.; Delos Reyes, P.J.; Regalado, M.T.M.; Solidum, R.U.; Tubianosa, B.S. (1996). Flow and deposition of posteruption hot lahars on the east side of Mount Pinatubo, July–October 1991, in C.G. Newhall and R.S. Punungbayan (Eds.), *Fire and Mud: Eruptions and Lahars of Mount Pinatubo, Philippines*, University of Washington Press, Seattle, WA, pp. 921–950.
- Punongbayan, R.S.; Newhall, C.G.; Hoblitt, R.P. (1996). Photographic record of rapid geomorphic change at Mount Pinatubo, 1991–94, in C.G. Newhall and R.S. Punongbayan (Eds.), *Fire and Mud: Eruptions and Lahars of Mount Pinatubo, Philippines*, University of Washington Press, Seattle, pp. 21–66.
- Robock, A. (1981). The Mount St. Helens volcanic eruption of 18 May 1980: Minimal climatic effect, *Science*, **212**, 1383–1384.
- Robock, A. (2000). Volcanic eruptions and climate, *Reviews of Geophysics*, **38**, 191–219.
- Robock, A. (2002). The climatic aftermath, *Science*, **295**(5558), 1242–1244.
- Robock, A.; Mao, J. (1995). Winter warming from large volcanic eruptions, *Geophys. Res. Lett.*, **19**, 2405–2408.
- Rose, W.I. (1987). *Volcanic Activity at Santiaguito Volcano, 1976–1984*, GSA Special Paper 212, Geological Society of America, Boulder, CO, pp. 17–27.
- Rymer, H.; van Wyk de Vries, B.; Stix, J.; Williams-Jones, G. (1998). Pit crater structure and processes governing persistent activity at Masaya volcano, Nicaragua, *Bull. Volcanol.*, **59**, 345–355.
- Rymer, H.; Cassidy, J.; Locke, C.A.; Barboza, M.V.; Barquero, J.; Brenes, J.; Van der Laat, R. (2000). Geophysical studies of the recent 15-year eruptive cycle at Poás Volcano, Costa Rica, *J. Volcanol. Geothermal Res.*, **97**, 425–442.
- Schoeberl, M.R.; Bhartia, P.K.; Hilsenrath, E.; Torres, O. (1993). Tropical ozone loss following the eruption of Mt. Pinatubo, *Geophys. Res. Lett.*, **20**, 29–32.
- Scott, K.M.; Macias, J.L.; Naranjo, J.A.; Rodriguez, S.; McGeehin, J.P. (2001). *Catastrophic Debris Flows Transformed from Landslides in Volcanic Terrains: Mobility, Hazard Assessment, and Mitigation Strategies* (USGS Professional Paper 1630), U.S. Geological Survey, Reston, VA
- Scott, W.E.; Hoblitt, R.P.; Torres, R.C.; Self, S.; Mylene, Ma.; Martinez, L.; Nillos Jr., T. (1996). Pyroclastic flows of the June 15, 1991 climactic eruption of Mount Pinatubo, in C.G. Newhall and R.S. Punungbayan (Eds.), *Fire and Mud: Eruptions and Lahars of Mount Pinatubo, Philippines*, University of Washington Press, Seattle, WA, pp. 545–570.
- Self, S.; Zhao, J.; Holasek, R.E.; Torres, R.C.; King, A.J. (1996). The atmospheric impact of the 1991 Mount Pinatubo eruption, in C.G. Newhall and R.S. Punungbayan (Eds.), *Fire and Mud: Eruptions and Lahars of Mount Pinatubo, Philippines*, University of Washington Press, Seattle, WA, pp. 1089–1115.
- Self, S.; Gertisser, R.; Thordarson, T.; Rampino, M.R.; Wolff, J.A. (2004). Magma volume, volatile emissions, and stratospheric aerosols from the 1815 eruption of Tambora, *Geophys. Res. Lett.*, **31**, L20608, doi: 10.1029/2004GL020925.
- Stothers, R.B. (1984). The great Tambora eruption of 1815 and its aftermath, *Science*, **224**, 1191–1198.
- Torres, R.C.; Self, S.; Martinez, M.L. (1996). Secondary pyroclastic flows from the June 15, 1991, ignimbrite of Mount Pinatubo, in C.G. Newhall and R.S. Punongbayan (Eds.), *Fire and Mud: Eruptions and Lahars of Mount Pinatubo, Philippines*, University of Washington Press, Seattle, pp. 665–678.
- Torres, R.C.; Mougini-Mark, P.J.; Self, S.; Garbeil, H.; Kallianpur, K.; Quiambao, R. (2004). Monitoring the evolution of the Pasig–Potrero alluvial fan, Pinatubo volcano, using a decade of remote sensing data, *J. Volcanol. Geothermal Res.*, **138**, 371–392.
- Umbal, J.V.; Rodolfo, K.S. (1996). The 1991 lahars of southwestern Mount Pinatubo and evolution of the lahar-dammed Mapanuepe Lake, in C.G. Newhall and R.S. Punungbayan (Eds.), *Fire and Mud: Eruptions and Lahars of Mount Pinatubo, Philippines*,

- University of Washington Press, Seattle, WA, pp. 951–970
- Wadge, G. (2003). A strategy for the observation of volcanism on Earth from space, *Philosophical Trans. Royal Society London A*, **361**, 145–156.
- Wadge, G.; Francis, P.W.; Ramirez, C.F. (1995). The Socompa collapse and avalanche event, *J. Volcanol. Geothermal Res.*, **66**, 309–336.
- Wen, S.; Rose, W.I. (1994). Retrieval of the size and total masses of particles in volcanic clouds using AVHRR bands 4 and 5, *J. Geophys. Res.*, **99**, 5421–5431.
- Williams, S.N. (1983). Plinian air-fall deposits of basaltic composition, *Geology*, **11**, 211–214.
- Williams, S.N.; Self, S. (1983). The October 1902 Plinian eruption of Santa Maria Volcano, Guatemala, *J. Volcanol. Geothermal Res.*, **16**, 33–56.
- Williams-Jones, G.; Rymer, H. (2000). The hazards of volcanic gases, in H. Sigurdsson, B. Houghton, S.R. McNutt, H. Rymer, and J. Stix (Eds.), *Encyclopedia of Volcanoes*, Academic Press, San Diego, pp. 97–1004.
- Williams-Jones, G.; Rymer, H.; Rothery, D.A. (2003). Gravity changes and passive SO₂ degassing at the Masaya caldera complex, Nicaragua, *J. Volcanol. Geothermal Res.*, **123**, 137–160.
- Wolfe, E.W.; Hoblitt, R.P. (1996). Overview of the eruptions, in C.G. Newhall and R.S. Punungbayan (Eds.), *Fire and Mud: Eruptions and Lahars of Mount Pinatubo, Philippines*, University of Washington Press, Seattle, WA, pp. 3–20.
- Wright, R.; Flynn, L.P. (2004). Space-based estimate of the volcanic heat flux into the atmosphere during 2001 and 2002, *Geology*, **32**, 189–192.
- Wright, R.; Rothery, D.A.; Blake, S.; Pieri, D.C. (2000). Visualising active volcanism with high spatial resolution satellite data: The 1991–1993 eruption of Mount Etna, *Bull. Volcanol.*, **62**, 256–265.
- Wright, R.; Flynn, L.P.; Garbeil, H.; Harris, A.J.L.; Pilger, E. (2002). Automated volcanic eruption detection using MODIS, *Remote Sensing of Environment*, **82**, 135–155.
- Wright, R.; Flynn, L.P.; Garbeil, H.; Harris, A.J.L.; Pilger, E. (2004). MODVOLC: Near-real-time thermal monitoring of global volcanism, *J. Volcanol. Geothermal Res.*, **135**, 29–49.

- Alaska Volcano Observatory (AVO) 96
- absolute zero 27
- absorption 31, 35–37, 104, 107, 126, 130, 138, 150–151, 153, 156–157, 162, 164, 169, 171, 174, 177, 282, 284
- absorption coefficient 28–29, 40
- absorption efficiency 131
- absorption length 29
- acid gases 327
- acid rain 332
- active volcanoes 2, 4, 13
- Adak Volcano 7
- Adams Volcano 8
- Advanced Baseline Imager (ABI) 145, 171, 297
- Advanced Spaceborne Thermal Emission and Reflection (ASTER) 45, 57, 80, 164, 326
- Advanced Very High Resolution Radiometer (AVHRR) 45, 80, 263, 330
- advection 189–192, 197, 200, 287
- aerial photographs 81
- aerial photography 83
- aerosols 20, 121, 130, 145, 147–148, 150–151, 171, 177, 188, 289, 328, 329, 333, 348–349
- aerosol cloud 348
- aerosol optical depth 29
- aggradation 345
- aggregate 193–194
- aggregation 106, 190, 193–194, 202
- aggregation parameter 194
- Aglao Town 339
- Agung Volcano 148
- air traffic 3, 16, 19, 109–110, 197, 215, 228, 248, 261, 294
- air traffic routes 16, 18
- air transport 1
- air transportation 1
- airborne ash 13, 18–20, 22
- airborne ash probability distribution (AAPD) 226
- airborne volcanic ash 18
- aircraft 262, 283, 287, 289, 291
- aircraft encounter 149
- aircraft exposure 21
- aircraft operations 131
- airport closures 16–17, 19
- AIRSAR 92
- Akademia Nauk Caldera 51
- Akutan Volcano 7, 8, 227, 244–245, 251–252, 254, 270, 309–310
- Akutan Island 253
- Akutan Village 252
- Alaid Volcano 3, 4, 14–15, 197, 309, 311
- Alaska 1–3, 5–6, 13, 16–17, 19, 197–198, 200, 214, 245, 262–263, 267–268, 282, 284, 290, 307, 310, 312, 320
- Alaska Peninsula 2, 5–6, 19
- Alaska Trench 2
- Alaska Volcano Observatory (AVO) 1, 80, 261, 307
- albedo 125, 130, 133, 269, 279–280
- Aleutian Islands 1–2, 5, 7, 16, 17, 20, 80, 197, 307–308, 310, 312
- Aleutian Trench 2
- Aleutian Volcanic Arc 19
- Aleutians 27, 261, 303–304, 307, 320
- Along Track Scanning Radiometer (ATSR) 61
- Ambrym Volcano 123, 124
- amplitude 29
- Amukta Volcano 7
- Anatahan Volcano 158, 165
- Anchorage 6, 16, 18–19, 114, 214, 262–263, 289–290
- Anchorage International Airport 263
- Anchorage VAAC 292
- Anchorage, Alaska Airport 3
- Angstrom coefficient 155
- Aniakchak Volcano 6, 88–89
- Arctic Ocean 2
- Argentina 9
- Armero 324
- Asama 174
- aseismically 19
- ash 197
- ash and sulfur in cabin 17
- ash clouds 15, 18–20, 21, 102, 103, 109, 123–124, 133–134, 150, 167, 187, 188, 190–191, 195, 202, 204, 209–213, 215, 217, 219, 220, 223, 225, 261, 271, 274, 283, 290–291, 294, 297, 315, 350
- ash cloud dispersion 220

- ash column 134, 140, 194, 196
 ash concentrations 188, 194, 203, 204, 208–211, 215, 217, 220, 288
 ash deposition 288
 ash deposits 262, 271, 275
 ash detection 123, 134, 136–137, 140, 209
 ash dispersion modeling 16
 ash distribution 225, 227
 ash encounter 209, 213, 217–218, 287
 ash fall 16–17, 19, 203, 229, 287, 315, 324
 ash flows 16, 316
 ash hazard 18, 137, 294
 ash particles 263
 ash plumes 131, 136, 248, 307, 314, 315, 333
 ash retrieval 120, 136
 ash tracking 230
 ash volume 287
 ASTER 91–95, 102
 ASTER, ETM+ 79
 at-satellite radiance 29, 44
 Atka Island 136
 Atka Volcano 7
 atmosphere 41, 109–110, 146, 157, 168, 187, 281, 323, 328, 346, 350
 atmosphere corrections 176
 atmosphere temperature profile 115, 285
 atmospheric aerosol 44
 atmospheric column 127, 217
 atmospheric conditions 21
 atmospheric correction 42–43
 Atmospheric Infrared Sounder (AIRS) 45
 atmospheric models 113
 atmospheric moisture 111
 atmospheric pressure 109
 atmospheric profile 114, 286
 atmospheric radiation 124
 atmospheric temperature profile 284
 Atmospheric transmission 29
 atmospheric transmissivity 61
 atmospheric windows 42, 153, 174
 ATSR 120
 attenuation 35–36
 Augustine Volcano 6–7, 14–17, 65, 83–84, 109–110, 112, 114, 118–121, 135, 164, 166, 168, 198, 203–204, 219–224, 270, 281, 285
 automated alarms 281
 automated detection 70, 350
 Avachinsky Volcano 5, 14–16, 197
 avalanches 16
 AVHRR 10–11, 18
 aviation 149, 180, 197, 199, 209, 223, 295
 aviation color code 293–294
 aviation hazards 145, 173
 AVO 1, 3, 6, 11, 16, 19, 21, 81
 back trajectory 196–197
 backscatter 94–95, 237–238, 243
 backscatter remote-sensing 81
 Baker Volcano 8, 16
 baseline 239, 243
 Becharof Lake 241, 254, 256
 Beer–Bouguer–Lambert Law 36
 Belinda 328
 Bezymianny Volcano 3–5, 13–15, 64–65, 70, 85, 87, 89–90, 92, 197, 227, 270, 277, 279, 281, 307, 312, 315, 319
 bidirectional reflection function (BRDF) 37
 bifurcated plume 288
 bifurcating cloud 198
 bistatic scattering coefficient 28
 Black Peak Caldera 88
 Black Peak Volcano 6, 89, 95
 blackbody 31, 36, 40, 44, 126, 153, 174
 blackbody radiance 28
 block-and-ash flows 65, 326
 Bogoslof Volcano 7–8, 14–15
 Boltzmann constant 28, 31, 56
 boundary conditions 196
 brightness temperatures (BTs) 130, 138, 139, 162, 164, 277, 280
 brightness temperature difference 107, 127, 163, 169, 210
 brightness temperature differences (BTDs) 16, 106
 brittle–ductile transition 250
 Brujo Volcano 343
 Brunt–Väisälä frequency 102
 BTD *see* brightness temperature differences
 Bucao Volcano 338
 Buenos Aires VAAC 292
 Buhawen Town 339
 buoyancy 107–108, 111, 113
 C band 31
 calderas 3, 4, 6–7, 9
 calibration baseline 20
 CALIPSO 131
 Canada 2, 19, 214, 262
 Canadian Emergency Response Model (CanERM) 199, 204, 209–211, 215, 217, 220–221, 223, 288, 298
 carbon dioxide 101
 Carlisle Volcano 7
 Cascade Range 2, 8, 16, 20, 270
 Cascade Volcanoes 1
 Cascades 270
 see also Cascade Range
 Cascades Volcano Observatory (CVO) 1, 8, 16, 21
 Casita Volcano 325, 330
 Castillejos Town 337
 Catania Volcano 340
 Central Africa 27
 Central America 2
 Centre Hills 326
 Cerro Galán 9
 Cerro Galán Caldera, Argentina 9
 Cerro Negro 229
 Chaitén Volcano 139–140
 chemical variations 20
 Chikurachki Volcano 3, 4, 14–15, 275
 Chile 327, 329
 Chirinkotan Volcano 4
 Chuginadak Island 7, 213, 308–309
 cinder cones 3, 6–7, 9, 85, 312
 Cleveland Volcano 7–8, 14–17, 21, 116, 134–135, 161, 167–171, 203–204, 213–214, 216–219, 223, 281–282, 284–286, 288–289, 294–296, 307–309
 climate 146–148, 150, 153, 180, 323, 328, 345
 climate change 151
 climatic 347
 cloud heights 120, 283, 287–288, 290
 CO₂ 21
 coherence 247, 256
 Cold Bay 6, 214
 Colo Volcano 11
 color composite 12
 column height 101
 commercial remote sensing 79
 complex volcanoes 9
 concentration 28
 condensation 107
 conduction 59
 convection 59
 convective column 113
 convective heat transfer coefficient 61
 Cook Inlet 6, 16, 83

- Copper River Basin 85
 Correlation Spectrometer (COSPEC) 153, 173, 178
 Cosiguina Volcano 148
 COSPEC *see* Correlation Spectrometer
 Costa Rica 327, 332
 crater 8
 Crater Lake Volcano 8
 crater lakes 3, 8
 cumulonimbus 135
 CVO *see* Cascades Volcano Observatory
- damaged aircraft 17
 dark-pixel correction 43
 Darwin VAAC 292
 data fusion 92, 94, 96
 debris avalanches 83, 324, 329–330
 debris flows 13, 62, 66, 261, 271, 277
 decorrelation 243
 Defense Meteorological Satellite Program (DMSP) 73
 Defense Support Program (DSP) 73
 deflation 13, 20, 249
 deflation rate 250
 deformation 20, 239, 242, 250
 deformation field 251
 deformation patterns 257
 degassing 265
 Denali Volcano 198
 deposition 200
 dielectric constant 89
 differential Global Positioning System (dGPS) 93
 differential radar interferometry 13
 diffraction approximation 34
 diffraction limit 34
 diffusion 189–193, 200, 287–288
 diffusion coefficients 192, 200, 202
 diffusion rate 202, 288
 digital camera 306
 digital elevation models (DEM) 11, 21, 89, 90, 202, 238, 288, 291
 digital number 52
 dike 252
 dike intrusion 252
 dilution 192
 directed blast 16, 324
 dislocation sources 242, 244, 251
 dispersion 111, 178, 190–192, 197, 200–201, 213, 217–218, 220, 229, 288
 dispersion coefficient 199
 dispersion modeling 16, 22
 dispersion models 21, 115, 117, 120, 283, 285, 288–289, 291, 298
 displacement field 246
 domes 6, 8, 12–13
 dormant volcanoes 19
 downward flux density 29
 downwelling 156
 drag coefficient 193
 Drift River 67
 Drift River valley 66
 dual-band method 10, 58
 Dutch Harbor 7, 18, 214
 dynamic overshoot 113
- earthquakes 2
 earthquake displacements 235
 Eastern Africa 27
 eastern Aleutian Islands 19
 Ebeko Volcano 3, 4
 effusion rates 11, 291
 effusive processes 20
 effusive rates 20, 266
 Ekarma Volcano 4
 El Caliente Volcano 343, 345
 El Chichón Volcano 11, 13, 129–130, 148, 172, 329, 333
 El Palmar Town 345
 El Porvenir Town 330
 El Reventador Volcano 197
 electromagnetic (EM) radiation 27, 83
 electromagnetic energy 30
 electromagnetic spectrum 30, 81, 153, 264
 electromagnetic waves 30
 electrostatic attraction 193
 ellipsoid source 242
 EM *see* electromagnetic radiation
 EM radiation *see* electromagnetic radiation
 emission 35–36, 39, 124, 163
 emission monitoring 178
 emission rates 145–146, 148, 150, 157, 160, 174, 178, 180, 201
 emissivity 28, 43, 171
 emittance 281
 energy 28–30
 engine failure 18
 Enhanced Thematic Mapper 326
 Enhanced Thematic Mapper Plus (ETM+) 57, 80, 87, 343
 ensemble 230
 ensemble approach 201
 entrainment 135
 environmental factor 21
 Erebus Volcano 147
 Erebus in Antarctica 11
 ERS *see* European Remote-sensing Satellite
 Erta Ale Volcano, Ethiopia 11, 12, 64
 eruption clouds 16, 79, 101, 138, 284
 eruption column 107, 109, 135, 188, 190, 194, 198, 209, 281, 287, 347
 eruption detection 21
 eruption detection algorithms 266
 eruption forecasting 254
 eruption plumes 21, 190, 314
 eruption precursor 70
 eruption rate 101
 eruption response time 264
 eruptions 15, 18
 Etna Volcano 13, 120, 139, 146, 176, 235, 317, 340–341
 eulerian 190, 199
 Europe 8, 16–17
 European Remote-sensing Satellite (ERS)-2 80, 94
 evacuated aircraft 17
 exitance angle 28
 explosive eruptions 7, 16, 20
 explosive processes 20
 extinction 35
 extinction coefficient 29, 44, 133
 extinction cross-section 28, 38
 extinction efficiency 38, 130
 extinction efficiency factor 28
 extrusion rates 343, 345
- Fairbanks 214, 262, 267–268, 289
 fallout 106, 193, 229
 false color composites 9
 Fernandina Volcano 10
 Fick's law 192
 finite aperture 34
 Fisher Volcano 307
 fissure eruption 248
 fissures 3
 flight cancellations 17
 floods 16
 flow terminus (ft) 86
 fluid dynamics 102, 193
 forecasting 18, 187
 forecasts 188, 189, 196, 200, 204, 214, 229, 288, 295
 fossil fuels 146
 Fourier transform infrared 173
 Fourpeaked Volcano 51
 fragmentation 101
 frequency 28–30, 36
 Frosty Volcano 307

- fumaroles 12, 69, 70, 81, 146
 Fuss Peak Volcano 4
- Galapagos Islands 10
 Galunggung Volcano 18, 102
 gamma ray 31
 Gareloi Volcano 7, 14–15, 197
 Garibaldi Lake Volcano 8
 Garibaldi Volcano 8
 gas cloud 21
 gas concentration 153
 gas diffusivity 192
 gas emissions 145, 172, 332
 gas flux 332
 gas plume 174
 gas retrieval 174
 gas thrust 107
 Gaussian function 200
 Geostationary Operational
 Environmental Satellite
 (GOES) 11, 33, 45, 59, 80,
 145, 263
 geostationary or geosynchronous
 (GEO) 33
 geostationary orbit 33
 geothermal lakes 62, 69
 Glacier Peak Volcano 8
 glaciers 6
 global 17
 global climate 145
 global effects 323
 Global Ozone Monitoring
 Experiment (GOME) 45, 157
 global positioning systems
 (GPS) 19, 257
 GOES *see* Geostationary
 Operational Environmental
 Satellites
 Golovnin Volcano 320
 Gorely Volcano 5, 161
 gravity waves 283
 graybody 163
 Great Lakes 16
 greenhouse effect 147
 Greenland 16, 19
 Grimsvotn Volcano 160
 ground deformation 244
 ground truthing 43
 Guatemala Volcano 331, 342, 344
 Guatemala City 331
 Gulf of Alaska 2, 197
- Hawaii 2, 65, 331
 hazard 334, 339
 hazard assessments 16, 21, 202,
 254, 293
 hazard awareness 229
- hazard evaluation 283
 hazard forecasts 290
 hazard mitigation 21, 112, 197,
 212, 254, 257, 281, 283, 287
 hazard response 20, 112
 hazards 291, 323–325
 height distribution 198
 Hekla Volcano 119, 148, 171–172
 Herbert Volcano 7
 high spatial resolution 79–82, 85–
 86
 high temporal resolution 80
 Hokkaido, Japan 275
 Homer Volcano 6, 214, 219
 Hood Volcano 8, 16
 hot spots 79
 Hot Springs Valley 252
 Hybrid Single-Particle Lagrangian
 Integrated Trajectories
 (HYSPLIT) 199, 201–202,
 204, 207, 209–211, 215–216,
 217, 220–223, 288, 298
 hydrothermal 83
 hydrothermal system 148
 HYSPLIT *see* Hybrid Single-
 Particle Lagrangian Integrated
 Trajectories
- Iceland 10
 ignimbrite 334, 336, 338–339
 IKONOS 79, 81–82, 91
 incandescence 10
 incidence angle 28, 240
 incident flux density 28
 incoming intensity 28
 index of refraction 243
 Indonesia 346
 inflation 13, 20
 inflation rate 246, 250, 254
 infrared (IR) 30–31, 50
 InSAR *see* interferometric SAR
 instantaneous field of view
 (IFOV) 34
 integrated pixel temperature
 value 277
 interferograms 237–243, 245, 246,
 247–248, 249–251, 253, 256
 interferometric coherence 238, 243,
 249, 251, 255, 257
 interferometric radar 80
 interferometric synthetic aperture
 radar (InSAR) 19, 90, 91, 235,
 236
 interferometry 235, 317
 International Civil Aviation
 Organization 200
- International Space Station (ISS)
 21, 303, 306, 320
 inverse Planck function 56
 Inverse problems 32
 irradiance 156
 Isanotski Volcano 307
 Islands of Four Mountains
 Volcano 7, 213
 ISS *see* International Space Station
 Italy 2
- Japan 297
 Japanese Geostationary
 Meteorological Satellite
 (GMS-4) 347
 JCET/UMBC 333
 JERS 92
 jökulhlaups 324
 JPL 96
- K band 31
 K-theory 200
 Kagamil Volcano 7
 Kamchatka 1, 16–17, 20, 197, 265,
 267, 303–304, 307, 317, 320
 Kamchatka Peninsula 1–3, 5, 13,
 16, 80, 89, 119, 261, 275, 306,
 312–314, 318–320
 Kamchatka River 318
 Kamchatka Volcanic Eruption
 Response Team (KVERT) 1,
 16, 21, 212, 273
 Kamchatka–Aleutian Tectonic
 (KAT) connection 2, 3, 5
 Kamchatski Trench 2
 Kamen Volcano 89, 314–315
 Kanaga Volcano 7, 8, 14–15
 Karthala Volcano 123, 124, 128–
 129
 Karymsky Volcano 5, 14–15, 68–
 69, 161, 165, 227, 270, 279,
 281, 317
 Karymsky Lake 5
 Kasatochi Island 7
 Kasatochi Volcano 7, 8, 14–17, 19,
 109–110, 134–137
 Katmai Lake 69
 Katmai Volcano 6, 13, 108–110,
 338
 Kharimkotan Volcano 3
 Kilauea Volcano 10, 65, 70, 102,
 250, 318, 326, 331
 kinematic viscosity 193
 King Salmon Volcano 6, 214
 Kirchhoff's Law 36
 Kiska Volcano 7, 270
 Kizimen Volcano 14, 65–66

- Kliuchevskoi Volcano 3–4, 5, 14–15, 17, 51, 60, 90, 105, 115–116, 148, 172, 203–204, 209, 211–212, 225, 227, 276, 278, 281, 303, 307–309, 312, 314–315, 317–320
- Klyuchevskoi *see* Kliuchevskoi 210
- Klyuchi Town 5, 7, 318
- Kodiak Volcano 6, 18, 214
- Kolokol Gp. Volcano 4
- Komandorsky Islands 226
- Korovin Volcano 7, 8, 14–15, 270
- Koryaksky Volcano 5, 16
- Krafla Volcano 250
- Krakatau Volcano 148, 150
- Kransheninnikov Volcano 313
- Kronotsky Volcano 313
- Ksudach Volcano 5
- Kunashir Island 319–320
- Kupaianaha Volcano 65
- Kurile Islands 1–4, 16, 17, 20, 27, 80, 119, 261, 265, 303, 304, 307, 308–309, 311, 319, 320–321
- Kurile–Kamchatski Trench 2
- Kuriles *see* Kurile Islands
- KVERT *see* Kamchatka Volcanic Eruption Response Team
- L band 31
- laboratory spectroscopy 86
- lagrangian 190–192, 199, 202
- Laguna de Oc Volcano 344
- lahar warms 67
- lahars 13, 62, 66, 323–324, 325, 326, 330, 334, 335, 337–339, 342, 343, 345, 347
- Lake Nyos 147
- lakes 6
- Laki Volcano 148
- Lambertian 125, 156
- Lambertian scattering 37
- laminar 193
- Landsat 4, 6, 10, 45, 52, 83, 87, 92–94, 326
- Landsat Multispectral Scanner (MSS) 9–10, 326
- Landsat Thematic Mapper (TM) 9–10, 12, 325, 343
- lapilli 118
- Las Sierras Caldera 332
- Lascar Volcano 10–12, 64, 65, 70, 324, 327
- laser 27
- lava 10
- lava channel 10
- lava discharge rate 72
- lava domes 62–66, 70, 72, 83, 86, 88, 261, 326, 334
- lava flows 3, 6, 7, 10, 12, 13, 20, 27, 61–63, 72, 89, 244, 248, 251, 261, 277, 291, 309, 310, 312, 323–324, 326, 328, 331, 339, 340–342, 344
- lava fountaining 248, 278
- lava lakes 12, 64–65, 72, 146, 279
- Lava Point 252
- lava tubes 340, 342
- longer wavelength infrared 11
- look angle 239
- low Earth orbit 33
- low-temperature volcanism 85
- LOWTRAN 44
- maars 6, 9
- magma 21
- magma accumulation 254
- magma chambers 244
- magma flux 246–247
- magma intrusion 254, 257
- magma storage 21
- magma withdrawal 250
- magmatic intrusion 254
- Makushin Volcano 7, 270
- Maly Semiachik Volcano 5
- Manam Volcano 172, 198
- Mapanuepe Lake 339
- Mapanuepe River 339
- Maraunot Volcano 338
- Marella River 339
- Marella Valley 339
- Masaya Volcano 326, 332
- mass eruption rate 106
- mass loading 106, 129–131, 194
- Mauna Loa Volcano 10, 250
- Mauna Ulu Volcano 65
- Max Planck 31
- Maxwell's equation 27
- mean optical depth 106
- melt inclusions 21
- Mendelev Volcano 320
- mesopause 41, 108–110
- mesosphere 41, 107, 109, 150
- meteorological hazards 20
- Mexico 329, 333
- microwave 31, 172
- Microwave Limb Sounder (MLS) 45, 171
- mid and thermal infrared (MIR and TIR) 58
- mid-infrared (MIR) 20, 31
- Mie scattering 38, 107, 128
- Mie theory 128
- mini-DOAS 178
- MISR 120
- Mitad Volcano 343
- mitigation 21
- Miyakejima Volcano 158
- Moderate Resolution Imaging Spectroradiometer (MODIS) 45, 57, 80, 102, 263, 328
- Moderate Resolution Infrared Sounder 167
- MODIS *see* Moderate Resolution Imaging Spectroradiometer
- MODIS/ASTER airborne simulator (MASTER) 81
- MODTRAN 44
- MODVOLC 70
- Mogi models 254
- Mogi source 242, 244, 248, 251
- monitoring 177
- monitoring volcanic gases 153
- Monje Volcano 343
- Montagu Volcano 328
- Montreal VAAC 292
- Montserrat Volcano 326
- Mosses Lake 19
- MSG 73
- MSS *see* Multispectral Scanner
- Mt. Augustine 11, 12, 16, 79
- Mt. Belinda 64, 324
- Mt. Cleveland 16, 80–81
- Mt. Erebus 12, 64
- Mt. Etna 102, 339
- Mt. McKinley 198
- Mt. Pinatubo 327, 334–335
- Mt. Rainier 8, 16
- Mt. Redoubt 16
- Mt. Spurr 16, 81–82, 89, 106
- Mt. St. Helens 8, 11, 13–17, 51, 81, 108–110, 119, 129–130, 194, 272, 324–325, 328
- MTSAT 59, 73
- mudflows 16, 219, 318, 324, 330
- Multi-Functional Transport Satellite 263
- Multispectral Infrared and Visible Imaging Spectrometer 164
- Multispectral Scanner (MSS) 9, 331
- Mutnovsky Volcano 161
- NASA 4–5, 7–8
- National Environmental Satellite Data and Information Services (NESDIS) 264
- National Polar Orbiting Environmental Satellite System

- (NPOESS) Preparatory Project (NPP) 296
- National Science Foundation (NSF) 96
- near-infrared (NIR) 31, 83
- near-real time monitoring 20
- Nevado del Ruiz Volcano 324
- NEXRAD 118, 122
- Nicaragua 330, 332
- Nikolski Volcano 7, 213–214, 289
- Nimá I River 344–345
- Nimá II River 344
- Nimbus 11
- Nimbus High Resolution Infrared Radiometer (HRIR) 52
- Nimbus I 10
- Nimbus II data 10
- NOAA 10
- NOAA SMS-1 10
- noise-equivalent temperature difference 162
- non-specular radiance 29
- non-Sun-synchronous orbit 21
- NOPAC 13
- Normalized Difference Vegetation Index (NDVI) 343, 346
- North America 8–9, 17, 19–20
- North American Plate 3
- North Pacific 1–3, 6, 9, 13–21, 297
- Northern Hemisphere 16
- northwestern U.S.A. 1, 16
- NOTAM (Notice To Airmen) 294
- Novarupta Volcano 6, 148
- nucleation 135
- numerical weather prediction 195, 200
- Nyamuragira Volcano 147
- Nyiragongo Volcano 157
- O₃ 21
- Oc River 344
- Okmok Volcano 7, 8, 14–17, 19, 51, 63, 81, 91–92, 109–110, 244–248, 270, 279–281, 309–310
- OMI *see* Ozone Monitoring Instrument
- Opala Volcano 313
- opaque clouds 285
- Open Bight 252
- optical depth 106, 125, 131–132, 163, 177
- optical thickness 348–349
- Oregon 1
- Ostry Tolbachik Volcano 89
- Otvazhny Volcano Crater 275
- outgoing intensity 28
- oxidation 85
- ozone 150, 154, 156, 347–348
- Ozone Monitoring Instrument (OMI) 45, 145, 160, 263
- P band 31
- Pacaya Volcano 326, 331
- Pacific Northwest 19
- Pacific Ocean 2, 136, 197, 214
- Pampa Lejía Volcano 327
- Papua New Guinea 197–198, 200
- particle aggregation 189
- particle concentration 281
- particle radius 132
- particle size 140, 282, 288
- particle size distribution 129, 133, 281
- Pasig-Potrero River 339
- passive degassing 160, 165
- Pavlof Volcano 6, 14–15, 197, 227, 270, 276, 279, 281
- penny crack source 242
- permeability 28–29
- permittivity 27–28
- Petropavlovsk-Kamchatsky 16, 18, 268, 272
- Petropavlovsk 5, 209, 213, 262, 267
- Peulik Volcano 237, 241–242, 244–245, 254–256
- phase difference 238
- phase function 130
- phase unwrapping 241
- phase value 237–241
- Philippines 327, 329, 349
- photographs 303, 305–306, 309, 311, 320
- photography 309, 316
- phreatomagmatic 334
- Piano del Trifoglio Volcano 340
- Pili Town 339
- pilot reports (PIREPs) 120, 209, 213, 287, 294
- Pinatubo Volcano 108, 110, 120, 146–148, 162, 172, 187, 329, 336–337, 339, 345, 347–350
- pixel-integrated temperature 57
- Planck curve 58
- Planck function 124, 162, 168
- Planck's constant 28, 30, 56
- planetary boundary layer (PBL) 117
- plinian 1, 62
- Plosky Tolbachik Volcano 89–90
- plume heights 110, 119–120, 200, 202
- plume shape 194, 202, 204
- plume structure 314
- Plymouth 326
- Poás Volcano 327, 332
- Popocatepetl Volcano 146, 149
- Port Graham 219
- Port Moller 6
- Portella Calanna 342
- Portland Volcano 8, 16, 262
- Posoltega Town 330
- precursor 279
- precursor activity 150
- Prevo Peak 311
- probability distribution 225–228, 291
- propagation 30
- Puff dispersion model 16, 20, 115, 116, 202, 204, 208–211, 215, 217, 220, 223–224, 226–228, 283, 285–286, 288, 298
- pumice 83–84
- Pu'u 'O'o-Kupaianaha 331
- pyroclastic deposits 80, 89
- pyroclastic flows (PF) 62, 65, 79, 83–85, 87, 219, 251, 261, 277, 307, 323–324, 326–327, 334, 338–339
- QuickBird 81, 91
- Rabaul Volcano 197, 200, 303, 317
- radar 11, 27, 112, 117, 119, 316–317, 320
- radar interferometry 11, 254, 319
- radars 303
- Radarsat 90, 92
- radiance 52
- radiance due to aerosol 29
- radiant temperature 279
- radiant thermal sources 10
- radiation 59, 124
- radiative transfer 125, 162, 164, 166, 170, 176
- radiative transfer equation 39–40
- radiative transfer models 44, 127, 130
- radiosondes 112, 191, 195–196, 220
- radiowave 31
- Raikoke Volcano 148
- Rainier Volcano 8
- RAT (Robust AVHRR Technique) 70
- rawinsonde 191, 196
- Rayleigh radiance 29
- Rayleigh scattering 44, 122, 151, 177
- Rayleigh scattering formula 38
- real-time monitoring 22
- Redoubt Volcano 6–7, 11, 14–17,

- 19, 66–67, 102–103, 109–110, 114–115, 117, 119–121, 131, 197, 201, 226, 228, 263–264, 281
- reduced displacement 287
- reflectance 125
- reflectance spectra 84–85
- reflection 35–36, 150, 156, 348
- reflectivity 28, 36, 160
- refraction 35
- refractive indices 28, 37, 132, 133
- rerouted 17
- resurgent dome 9
- resuspension 193, 202
- Retalhuleu Volcano 344
- reverse absorption 107, 137–138
- Reynolds number 193, 202
- Richardson number 200
- Río Ixpatz 343
- Río Samala 343
- rockslides 16
- Rolando Rodríguez Town 330
- Round Top Volcano 307
- Ruang Volcano 124, 136, 138, 328, 333
- Russia 2, 197, 214, 262, 267, 308, 311–314, 318–321
- S band 31
- Sakhalin Volcanic Eruption
Response Team (SVERT) 1, 16, 21
- Sakurajima Volcano 174
- Salto della Giumenta 340, 342
- Samala River 344
- San Cristóbal Volcano 330
- San Francisco 16
- San Marcelino Town 337
- San Narciso Town 337
- San Sebastián Volcano 344
- Sanaka Volcano 4
- Sangihe Island Arc 328
- Santa María Volcano 148, 342–346
- Santiago Crater 332
- Santiaguito Volcano 63–64, 342–347
- Santo Tomás Plain 339
- Santo Tomás River 337, 339
- Sarychev Peak 3, 14, 17, 307–308
- satellite monitoring 262, 350
- Satellite pour l'Observation de la Terre (SPOT) 91, 334
- Scanning Imaging Absorption Spectrometer for Atmospheric Chartography (SCIAMACHY) 45, 158
- scattering 35–37, 104, 107, 125, 130–131, 154, 156–157, 243
- scattering coefficient 29, 40
- scattering efficiency 130
- SCIAMACHY *see* Scanning Imaging Absorption Spectrometer for Atmospheric Chartography
- scoria cones (sc) 85, 86
- Seattle 8, 262
- sedimentation 107, 189–191, 197
- Seguam Volcano 7
- seismic data 19
- seismic monitoring 20
- settling 193
- Severgin Volcano 274
- SEVIRI *see* Spinning Enhanced Visible and Infrared Imager
- Sheveluch Volcano 227, 270
- shield volcanoes 3, 6, 9
- Shishaldin Volcano 6–7, 14–15, 51, 93, 111, 227, 244–245, 256–257, 270, 279, 281, 307
- Shiveluch Volcano 3–5, 14–15, 17, 64, 70, 111, 148, 280, 312
- short-wavelength infrared 10–11
- shortwave infrared 12, 31
- shortwave infrared (SWIR) 80, 83
- Shuttle radar instrument 21
- Shuttle Radar Topography Mission (SRTM) 80, 91–94, 235, 303, 307, 319, 329
- Sierra Negra Volcano 10
- significant meteorological information release (SIGMETs) 17, 189, 223, 294, 295
- Silver Hill 326
- Simushir Island 4, 311
- Sinarka Volcano 274
- single scattering albedo 29
- single scattering approximation (SSA) 44
- Skylab 9–10
- SMS-1 10
- SO 147
- SO₂ 21, 101, 123, 136–137, 140, 145–146, 148, 150–151, 153–158, 160, 162, 164, 166, 169–171, 173–175, 177–179, 281, 284, 291, 297, 326, 328, 347–350
- SO₂ absorption 166
- SO₂ cloud 102
- SO₂ plume 178
- Socoma Volcano 324, 329
- solar angle 287
- solar heating 279
- solar radiation 31, 154
- soma volcanoes 3
- Soufrière Hills Volcano 149, 160, 172, 324, 326
- source term 198
- South America 197
- South Sandwich Islands 324, 328
- South Sister Volcano 51
- South Soufrière Hills Volcano 326
- Space Imaging Radar (SIR) 317
- Space Radar Lab (SRL) 315
- Space Shuttle 21, 303–306, 308, 316–317, 320
- spatial decorrelation 243
- spatial resolution 33–34, 154, 263–266, 288, 291, 298, 350
- spectral resolution 33–34, 86, 151, 264–266
- spectral signals 21
- specular radiance 29
- Spinning Enhanced Visible and Infrared Imager (SEVIRI) 45, 59
- Spirit Lake 325
- split-window 43, 107, 205, 210–211, 213–214, 217, 220, 265, 274, 276, 277, 283–285, 289, 297–298
- split-window ash detection 204
- Spokane Volcano 16, 19
- SPOT *see* Satellite pour l'Observation de la Terre
- Spurr Volcano 6–7, 14–15, 17, 19, 103, 108, 111–113, 166–167, 200, 203–205, 207–209, 225, 285–286, 290
- SRTM *see* Shuttle Radar Topography Mission
- station mask 268
- Stefan–Boltzmann constant 28, 61
- Stefan–Boltzmann equation 32
- stereoscopic imaging 120
- Stokes' law 193
- stratocones 3, 6
- stratopause 41, 108–109
- stratosphere 41, 107–110, 145–146, 150, 157, 166–167, 171–172, 283, 314, 328–329, 346, 348
- stratospheric ozone 31
- stratovolcanoes 3, 9, 311
- Stromboli Volcano 62, 68, 176
- Strombolian 62, 67–68, 229, 324, 326, 331
- Strombolian activity 68, 72
- submarine volcanoes 3
- subsidence 253

- Sulawesi Island 333
 sulfur 4, 16, 21
 sulfur dioxide 11, 13
 sulfur dioxide clouds 16
 Sun-synchronous 33
 supervised classification 95
 surface deflation 246
 surface deformation 19, 235, 240, 244, 248, 254
 surface deposits 22
 surface emissivity 125
 surface tension 194
 Surtsey 10
 SVERT *see* Sakhalin Volcanic Eruption Response Team
 Synthetic Aperture Radar (SAR) 80, 89, 235
 synthetic interferogram 238
- Tacoma Volcano 8
 Talabre Gorge 327
 Tambor River 344
 Tambora Volcano 148, 150, 346
 Tana Volcano 7
 Tar River Valley 326
 Television and Infrared Operational Satellite (TIROS) 50
 temperature 169
 temperature profiles 112
 temperature reversal 108
 temporal decorrelation 243
 temporal frequency 79
 temporal resolution 33–34, 154, 263, 265–266, 298
 tephra 107, 209, 251, 324, 328, 334
 terminator effect 33
 Texas 16
 textural variations 20
 Thematic Mapper (TM) 11, 52, 85, 326
 thermal anomalies 12, 20, 49, 72, 85, 219, 261, 263–267, 271–273, 275, 277, 279, 291, 298
 thermal conductivity 61
 thermal decorrelation 243
 thermal flux 20, 262, 264–266, 291
 thermal gradient 108
 thermal infrared (TIR) 20, 31, 80
 thermal radiation 27
 thermosphere 107, 109
 TIROS Operational Vertical Sounder (TOVS) 45, 166
 TIROS VHRR 10
 TM *see* Thematic Mapper
 Toba Volcano 150
 Tobachik Volcano 4
- Tokyo 262–263
 Tokyo VAAC 292
 Tolbachik Volcano 3, 5, 13–15, 51, 85–86, 89–91, 319
 TOMS 13, 156
 TOMS *see* Total Ozone Mapping Spectrometer
 TOPSAR 91–92
 Total Ozone Mapping Spectrometer (TOMS) 11, 45, 145, 263, 330
 trajectory models 180
 translucent clouds 285
 transmission 35, 306
 transmittance 162
 tropopause 41, 108–110, 112, 119–120, 150, 283, 347
 troposphere 41, 107, 109–110, 147, 150–151, 157, 166–167, 169, 171, 243, 283, 328, 346
 tropospheric water vapor 13
 turbulence 117
 turbulent 193
 two-component mixture model 57
 two-component model 58
 Tyatya 275, 319, 320
- U.S.A. 13, 16
 Ugashik 254, 256
 Ukinrek Maars Volcano 6, 14–15, 254, 256
 Uliaga Volcano 7
 ultraviolet (UV) 20, 21, 31, 80, 145, 154, 172, 333, 348
 ultraviolet spectroscopy 11
 umbrella cloud 111, 114
 Umnak Island 213
 Unimak Island 307
 United States 7, 19, 297
 University of Alaska Fairbanks (UAF) 96
 University of Alaska Fairbanks, Geophysical Institute 1
 Unmak Island 136
 Unzen Volcano 64
 upward flux density 29
 upwelling 156
 upwelling (forward) radiance 29
 upwelling radiation 124
 Urataman Volcano 321
 USGS 96
 Ushkovsky Volcano 89–90
- vacuum 28
 Val Calanna 342
 Valdez Volcano 214
 Valle del Bove 339–340, 342
- Valley of Ten Thousand Smokes 6
 Vancouver Volcano 8, 16, 262
 VAST 70
 vegetation detection 83
 VEI 3, 5–6, 8
 Veniaminof Volcano 6, 14–15, 88–89
 Very High Resolution Radiometer (VHRR) 10, 52
 Villarrica Volcano 178–179
 visible 31
 visible to near-infrared (VNIR) 81, 83
 VNIR *see* visible to near-infrared
 Volcán Aguas Calientes 327
 volcanic activity 3, 16, 21, 27
 volcanic advisory 189
 volcanic ash 1, 17, 21, 101, 103, 105, 107, 123, 127, 133, 137, 149, 151, 171, 188, 191, 195, 197–199, 201, 215, 225, 229, 262, 283, 294–295, 323, 327
 Volcanic Ash Advisories (VAAs) 189, 294, 295
 Volcanic Ash Advisory Centers (VAACs) 133, 187, 200, 230, 283, 292
 volcanic ash clouds 18
 Volcanic Ash Collaboration Tool (VACT) 295
 volcanic ash dispersion and tracking models 287
 volcanic ash eruption clouds 138
 volcanic ash hazard mitigation 193
 volcanic ash hazards 150
 volcanic ash transport and dispersion 187
 volcanic cloud height 285
 volcanic clouds 2, 19–22, 101, 105–106, 107, 114, 120, 121, 127, 130, 132, 140, 171, 173, 188, 200, 218, 261–267, 271, 274, 275, 281–283, 285, 287, 288, 289, 291–292, 298
 volcanic deformation 235, 242, 245, 256–257
 volcanic degassing 69
 volcanic emissions 45, 101
 Volcanic Explosivity Indices (VEI) 3, 209, 248, 287
 volcanic forcing 151
 volcanic gases 20, 62, 145–151, 153, 155, 172–174, 177, 178, 180, 348
 volcanic gas detection 11
 volcanic hazards 21, 146, 149, 187, 324

- volcanic plumes 80, 102, 130–131, 164, 282, 330
- volcanic processes 27, 45
- volcanic surfaces 20
- volcanic unrest 146, 173
- volcano deformation 19, 244
- volcano monitoring 1, 80, 187, 257, 264–268, 271, 272, 277, 287–288, 293, 296–298
- volcanogenic CO₂ 146
- volume mixing ratio 172
- Vsevidof Volcano 270
- vulcanian 1, 62, 67, 326
- Vulcano 69

- Washington 1
- Washington VAAC 292
- water vapor correction 127

- wave number 56
- wave propagation 27
- wavelength 28–30
- weather forecasting 21
- weathering 85
- Wellington VAAC 292
- Westdahl Volcano 6–7, 14–15, 79, 81, 89, 93–95, 244–245, 248–250, 307
- White Island 147
- Wien's constant 28
- Wien's displacement law 31, 58, 281
- wind field model 188
- wind field patterns 16
- wind fields 196, 201–203, 212, 286–288, 290–291, 298
- Wrangell 270

- X band 31
- X-ray 31

- Yakima Volcano 16, 19
- Yellowstone 69, 146
- Yunaska Volcano 90, 312
- Yuzhno-Sakhalinsk Volcano 268, 274

- Zafferana Town 340, 342
- Zasaritzki Volcano 4
- Zavaritzki Volcano 4
- zenith angle 29, 125, 276, 281
- Zhupanovsky Volcano 14